Proceedings of the 39th International Conference of the Polymer Processing Society (PPS-39)

Cartagena de Indias, Colombia

19-23 May, 2024

Editors:

Jairo Ernesto Perilla
Cesar Sierra
Felipe Salcedo
Jorge Alberto Medina

Polymer Processing Society

Content

PREFACE

Proceedings of the 39th International Conference of the Polymer Processing Society (PPS-39)

December 2024

View Online

Export Citation

Preface: Proceedings of the 39th International Conference of the Polymer Processing Society (PPS-39)

We are honored to present the Proceedings of the 39th International Conference of the Polymer Processing Society, which took place on May 19-23, 2024, at the Hilton Hotel, Cartagena de Indias, Colombia.

The PPS 39 international conference was organized by Universidad de los Andes and ICIPC, leading Colombian institutions in polymer science and technology, and was attended by nearly 435 participants from 41 countries. The program progressed to eight plenary lectures, four industrial keynotes lectures, seven distinguished keynotes lectures, forty-nine keynotes, two hundred and two oral presentations, and sixty-six poster presentations. Besides traditional symposia about polymer processing, the PPS-39 program included four special symposia on Biopolymers, Biocomposites and Bioprocessings; Circular Economy of Polymers; Degradation; Biodegradation and Composting and Polymers in the Sustainable Development Goals of the United Nations, for a total number of 20 symposia. For the first time, the conference included a Machine Learning in Polymer Processing General Symposium.

We thank all the authors for their contributions and the reviewers for their relevant comments and corrections.

The success of this event would not have been possible without the invaluable participation of the organizing committee, the symposium organizers, and the chairs of the different sessions. The contributions by sponsors and trade exhibitors helped ensure an enjoyable and distinguished event.

DOI: https://doi.org/10.51573/Andes.PPS39.PF.0

Summary of This Volume

The 39th International Conference of the Polymer Processing Society (PPS-39) was hosted by Universidad de los Andes and ICIPC and attended by nearly 435 participants from 41 countries. Besides traditional symposia about polymer processing, the PPS-39 program included four special symposia on Biopolymers, Biocomposites, and Bioprocessings; Circular Economy of Polymers; Degradation; and Biodegradation and Composting, and Polymers in the United Nations Sustainable Development Goals, for a total of 20 symposia. These proceedings contain papers from prominent professors, scientists, students, and engineers active in the field of polymer processing.

These proceedings will be of interest to Researchers from academia and industry, students, and postdoctoral fellows.

Additional Information About This Volume

Pages: 460

Language: English

Publisher: Ediciones Uniandes

Editors of the PPS-39 Proceedings:

Jairo Ernesto Perilla, Chemical Engineering Department of Universidad Nacional de Colombia

Cesar Sierra, Chemical Department of Universidad Nacional de Colombia

Felipe Salcedo, Chemical and Food Engineering Department of Universidad de los Andes

Jorge Alberto Medina, Mechanical Engineering of Universidad de los Andes

ISBN: 978-958-798-779-9

GENERAL SYMPOSIA | EXTRUSION

Analysis of Spiral Mandrel Dies with Novel Channel Geometries to Draw Conclusions on the Purging Time of the Melt Using CFD

Felix Vorjohann and Reinhard Schiffers

DOI: https://doi.org/10.51573/Andes.PPS39.GS.EX.1

December 2024

Analysis of Spiral Mandrel Dies with Novel Channel Geometries to Draw Conclusions on the Purging Time of the Melt Using CFD

Felix Vorjohann and Reinhard Schiffers[1]

Abstract: Spiral mandrel dies are deeply integrated into the extrusion process and are the predominant die type for manufacturing products with a ring-shaped cross-section, e.g. blown film. The geometry of the axial spiral mandrel die is characterized by a spiral mandrel with one or more feed holes that merge into the spiral channels. The spiral channels themselves are embedded in the mandrel and have a characteristic u-shape in cross-section, which is dictated by the milling head used during manufacturing. In the past, numerous geometric parameters of the conventional axial spiral mandrel distributor have been examined in the course of optimizations, but the general design is still largely based on the concept of the 1960s. Therefore, this paper presents four concepts for new channel geometries that deviate from the conventional spiral channel cross-sectional shape. All variants were analyzed using a CFD-based algorithm for the automated geometry optimization by varying the general parameters describing the spiral channel. Other defining parameters were kept constant. The results provide insights into the influence of geometry parameters for spiral mandrel dies on purging time.

Keywords: Extrusion, Die Design, Spiral Mandrel Die, Novel Channel Geometries, Purging, CFD, Simulation, Optimization, Parameter Study, Plastics Processing, Plastics Machinery

1 The authors Felix Vorjohann (felix.vorjohann@uni-due.de) and Reinhard Schiffers (reinhard.schiffers@uni-due.de) are affiliated with the Institute of Product Engineering (IPE), Engineering Design and Plastics Machinery at the University of Duisburg-Essen in Germany.

DOI: https://doi.org/10.51573/Andes.PPS39.GS.EX.1

Introduction

In the extrusion process, purging of the extrusion die is often carried out on-line during operation, as this practice is faster than a die change. However, this can lead to long purging times if the extrusion tool has not been specifically optimized in terms of its purgeability. Long purging times are associated with lost production and wasted material and not only affect productivity, but also increase production costs and impact the environment. Optimizing the purgeability of extrusion dies such as the spiral mandrel die is therefore of significant importance to minimize these negative effects and increase the efficiency and sustainability of production.

Approach

The intention of this paper is to investigate novel channel geometries for axial spiral mandrel dies. The overall research objective is to optimize the purgeability of the spiral mandrel distributor, which is why purgeability is used as a quality criterion to evaluate the results for the different geometry variants. The integration of this quality criterion will be discussed later in this paper.

The following investigation is based on the fully parameterized CAD models of the tool variants considered. From these, a total number of 3886 unique design points (DP) with novel channel geometries are generated, which are then transferred individually to the ANSYS Workbench programs to perform the CFD simulations in ANSYS Fluent. The results of the simulations are processed and saved in the form of quality criteria. This process of the described parameter study is illustrated in Figure 1.

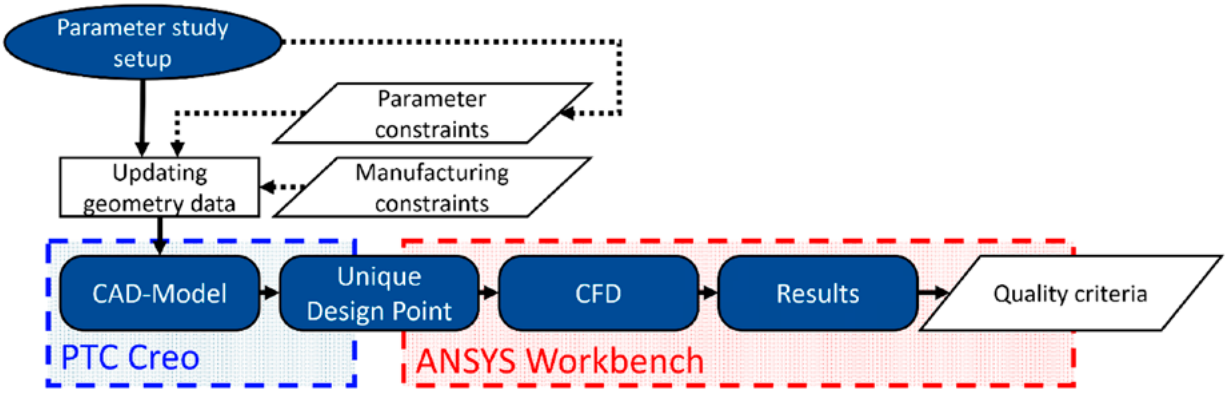

Figure 1. Algorithm for the conducted parameter study.

DOI: https://doi.org/10.51573/Andes.PPS39.GS.EX.1

Analyzed Geometries

This paper examines four variants of an axial spiral mandrel die. The CAD model of the conventional axial spiral mandrel distributor was created in PTC Creo and is the subject of work by te Heesen et al. [1,2]. The variants investigated in this paper differ from the conventional design in the cross-sectional shape of the spiral mandrel channel. Four CAD models were used, each representing one of the cross-sectional shapes. Within these models, the parameters describing the basic geometry as well as those defining the channel geometry can be freely changed. Only the fluid volume was modeled, as this forms the flow domain for the subsequent CFD simulation. Since the spiral mandrel manifold has a periodicity, only a 90° segment was modeled for the considered die with four feed holes to reduce the simulation time. The investigated channel geometries and the describing geometry parameters are shown in Figure 2.

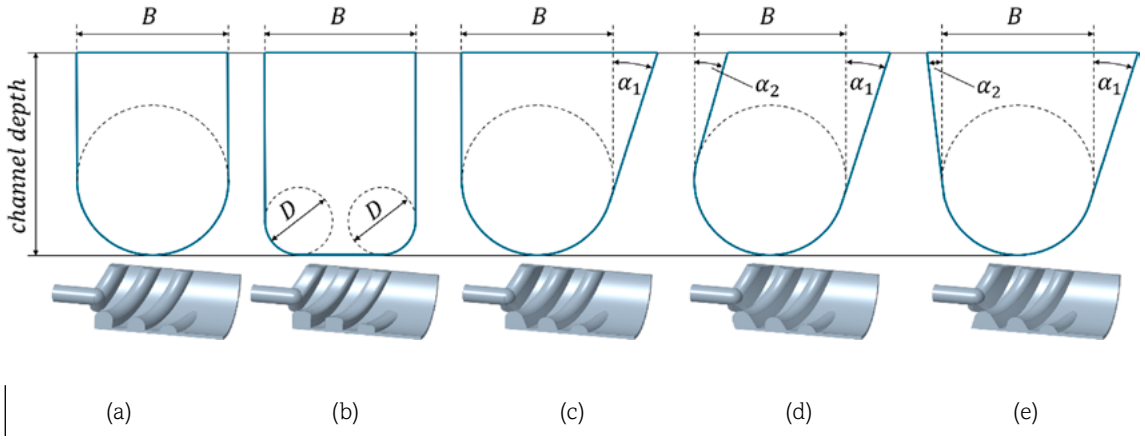

Figure 2. Cross-sectional shapes within the spiral channel: (a) conventional crest-shape, (b) double-circle crest, (c) one-sided flank angle, (d) two-sided flank angle "Parallelogram", (e) two-sided flank angle "Pyramid".

The naming of the different variants also refers to these cross-sectional shapes, which differ from the conventional crest shape shown as variant (a) in Figure 1. The relevant geometry parameters for the geometry variants (a) to (e) are listed in Table 1. A distinction is made between the parameters that were varied during the investigation to generate different DP and those that were kept constant to ensure comparability of the results. In addition, the minimum and maximum values, as well as the step sizes with which the respective parameters were varied.

DOI: https://doi.org/10.51573/Andes.PPS39.GS.EX.1

Table 1. Excerpt of the parameters used in the study to describe the channel geometry.

Parameter	Type	min	max	Step size
D [mm]	Variable	4	16	2
α_1 [°]	Variable	5	40	5
α_2 [°]	Variable	5	40	5
B [mm]	Fixed	18	18	-
$channel\ depth_n$ [mm]; n = [0 ..1]	Function	See Figure 3		
$gap\ width_n$ [mm]; n = [0 ..1]	Function			

The channel depth and the gap width change depending on the spiral height and are described by a continuous function for each DP. The index n describes the normalized spiral height. n assumes values between 0 and 1. These values act as supporting points and are used to describe the spiral channel depth and the gap width at the different heights. Different values for channel depth and gap width can be assumed at each supporting point. The considered value range is highlighted in Figure 3.

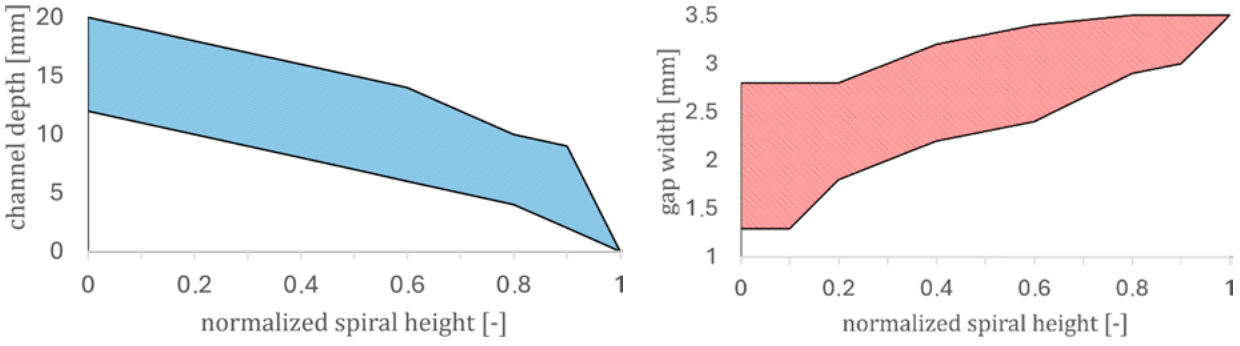

Figure 3. Channel depth (a) and gap width (b) as a function of the normalized spiral height.

Other characteristic parameters for the spiral mandrel die, like the total die height, feed length, spiral height, outer diameter, and wrap angle, as well as the number of channels and the gap width at the outlet were kept constant.

For a general description of the axial spiral mandrel die and the parameters describing the geometry, refer to the works of te Heesen et al. [1,2] and Michaeli et al. [3].

DOI: https://doi.org/10.51573/Andes.PPS39.GS.EX.1

Simulation Set-up and Boundaries

The CFD simulations were performed in a steady state for a total mass flow of 40 kg/h. The material parameters for the low-density polyethylene used (Lupolen 2420D – LyondellBasell Industries) were imported into the solver via a user-defined function and included data on density, heat capacity, thermal conductivity and viscosity, using a cross-WLF model. Figure 4 shows the applied boundary conditions for the reference geometry.

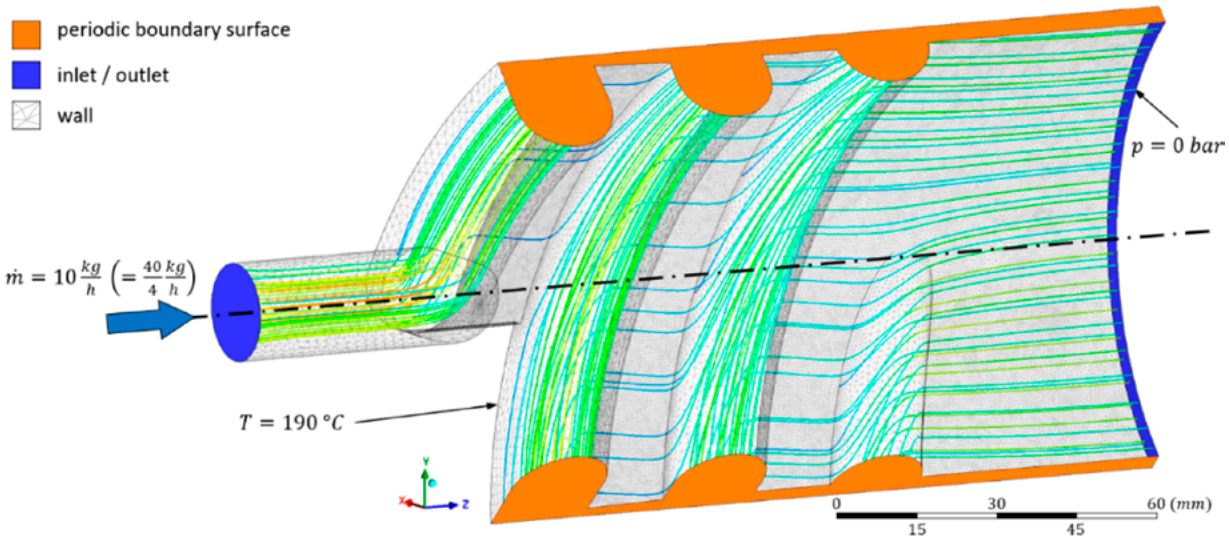

Figure 4. Boundary conditions for the spiral mandrel die.

Quality Criteria Used for the Evaluation

As the focus of the study is on purgeability, the fluid change effectiveness (FCE) is used as an evaluation criterion to identify and quantify stagnation zones. The FCE ε is based on the work of Kummerow et al. [4] and describes the ratio of the mean absolute residence time τ to the local melt age θ for each cell in the flow domain. Therefore, the FCE describes how often a local volume is purged in the time it takes for a plug flow to flow through the entire volume:

$$\varepsilon = \frac{\tau}{\theta} = \frac{\overline{\theta}_{outlet}}{\theta} \qquad 1)$$

The combined volume of all cells with a purgeability below a threshold value ε is referred to as V_ε and is normalized by the total volume of the fluid domain V_{total}. The resulting value Q_ε can then be used as a quality criterion for different values of ε:

DOI: https://doi.org/10.51573/Andes.PPS39.GS.EX.1

$$Q_\varepsilon = \frac{V_\varepsilon}{V_{total}} \quad 2)$$

For example, $Q_{\varepsilon = 0.2}$ describes the percentage of fluid volume that is replaced less than 0.2 times by a plug flow. In other words, this percentage of the fluid volume cannot be replaced with five plug flows, passing through the die. The aim is therefore to minimize the value of Q_ε. In this work, 16 quality criteria were calculated for each DP to describe the purgeability in the range between $Q_{\varepsilon = 0.025}$ and $Q_{\varepsilon = 0.4}$.

Results of the Simulations

The linear correlation coefficient is used to evaluate the results of the geometry variants and in particular the relationship between purgeability and the geometry parameters. This is calculated between all geometry parameters and the 16 quality criteria of Q_ε. For each geometry parameter, the correlation is then summarized to an averaged correlation coefficient $\bar{r}$. These aggregated correlation coefficients are listed in Table 2.

Table 2. Linear correlation coefficients for parameters describing the channel geometry.

Parameter \ Variant	(b)	(c)	(d)	(e)
D [mm]	-0.64			
α_1 [°]		-0.36	-0.21	+0.11
α_2 [°]			-0.14	+0.46
channel depth$_n$ [mm]; n = [0 .. 0.3]	+0.14	+0.33	+0.40	+0.34
gap width$_n$ [mm]; n = [0 .. 0.3]	+0.16	+0.20	+0.24	+0.15

To evaluate the results, variants (b) and (e) are discussed first. For (b), the negative correlation between the rounding diameter D and Q_ε shows that an increase in D results in improved purgeability. It should be noted that for large values of D, the geometry of the double-circle crest approaches that of a conventional crest shape. In terms of purgeability, the double-circle variant offers no advantages over the conventional cross-section (a) and can be discarded for further optimization.

The same applies to the geometry of (e): here, the back flank angle α_2 proves to be the most disadvantageous parameter for purgeability; the best results are achieved with the smallest flank angles. The preferred geometry variant of (e) is therefore variant (c), which effectively has a back flank angle α_2 of 0°.

DOI: https://doi.org/10.51573/Andes.PPS39.GS.EX.1

As for variant (c), a negative mean linear correlation coefficient exists between the values of Q_ε and the flank angle α_1 ($\bar{r} = -0.36$). Thus, higher values of α_1 can lead to better purgeability. However, the flank angle α_1 cannot be increased indefinitely to improve purgeability. Hence, a non-zero optimum exists, which is dependent on the other geometry-determining parameters. Accordingly, variant (c) is suitable for further consideration in future investigations.

Finally, geometry variant (d) will be evaluated here. Negative correlations with purgeability were found for both α_1 ($\bar{r} = -0.21$) and α_2 ($\bar{r} = -0.14$). However, these are significantly lower than the influence of the initial gap width and the initial spiral depth. Increasing both the outlet-side flank angle and the inlet-side flank angle can contribute to improved purgeability. Further research is also advisable here.

For future research, variant (c) can be investigated as a subset of variant (d) by extending the value range by the value $\alpha_2 = 0°$. The recommendations from the exclusion of variants (b), (e), and (c) for future investigations in favor of variants (a) and (d) are shown in Figure 5.

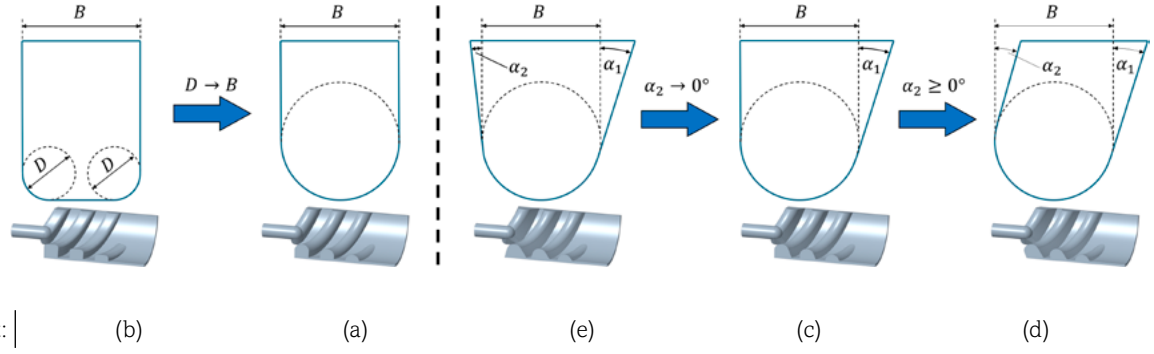

Figure 5. Recommended exclusion of variants (b), (e), and (c) in favor of variants (a) and (d).

Conclusion and Outlook

Based on the results presented, this paper shows that the channel shape in the spiral channel has a fundamental influence on purgeability and should be considered in the context of detailed die optimizations. It has already been shown that a reasonable design decision to improve purgeability is the integration of flank angles. Spiral channels that are inclined in the direction of the die outlet have proven to be advantageous.

The geometry variant (b) of the double-circle crest could not lead to any improvement in purgeability and can be excluded for future optimizations. The variant (d) of the two-sided flank angle "Parallelogram" offers the greatest potential for optimizing the spiral channel. In future studies, detailed investigations of the interactions between the angles of the outlet-side and inlet-side flanks must

DOI: https://doi.org/10.51573/Andes.PPS39.GS.EX.1

be carried out, and the optimum must be determined as a function of the gap width and channel depth profile, as well as the other geometry parameters. The interaction of purgeability with other quality parameters for the spiral mandrel die, such as pressure loss and mass flow homogeneity of the melt at the outlet, should also be investigated. Finally, the results of the simulations must be subjected to experimental validation.

Acknowledgments

We like to thank the German Research Foundation (Deutsche Forschungsgemeinschaft, DFG) for funding this research project titled "Novel Channel Geometries for Spiral Mandrel Dies," Project-No.: SCHI 1475/10-1, as well as our industrial partner ETA Kunststofftechnologie GmbH for the valuable input and the good cooperation.

References

1. O. te Heesen, "Ganzheitlicher Ansatz zur Dimensionierung und Optimierung von Extrusionswerkzeugen am Beispiel von Wendelverteilern". *Dissertation*, Universität Duisburg-Essen, Duisburg, 2015.
2. O. te Heesen, J. Wortberg, M. Humpa, P. Hungenberg, P. Köhler, "Automatic Optimization of Spiral Mandrel Dies by a Coupled Approach Using the Methods of Flow Analysis Networks and Three Dimensional CFD-Simulations", *Proceedings of Polymer Processing Society 31st (PPS-31)*, Jeju Island, Korea, 07.06-11.06.2015.
3. W. Michaeli and C. Hopmann, "Extrusion Dies for Plastics and Rubber", 4th ed. Munich, Cincinnati: Hanser Publishers, 2016.
4. J. Kummerow and J. Wortberg, "Local mean age of melt: New approaches for die optimization", *Proceedings of PPS-34: the 34th International Conference of the Polymer Processing Society (PPS-34)*, Taipei, Taiwan, 2019.

GENERAL SYMPOSIA | EXTRUSION

Evaluation of Temperature Impact During Extrusion on the Mixing Levels of PS/PA6 by Optical Monitoring

Felipe O. C. Bernardo, Sebastião V. Canevarolo and José A. C. G. Covas

DOI: https://doi.org/10.51573/Andes.PPS39.GS.EX.2

December 2024

Evaluation of Temperature Impact During Extrusion on the Mixing Levels of PS/PA6 by Optical Monitoring

Felipe O. C. Bernardo, Sebastião V. Canevarolo and José A. C. G. Covas[1]

Abstract: This work uses on-line monitoring of turbidity to ascertain the temperature impact on the mixing performance of kneading blocks with different geometries. For this purpose, one of the barrel segments of the extruder was modified to incorporate four sampling devices and a slit die containing optical windows. The experiments consisted in reaching steady extrusion and then adding a small amount of tracer. Upon opening each sampling device, material was laterally detoured from the local screw channel and its turbidity were measured by the optical detector. Residence time distribution (RTD) curves were obtained at various axial positions along three different kneading blocks and under different temperatures. It is hypothesized that K, a parameter related to the area under each RTD curve, is a good indicator of dispersive mixing, whereas variance can be used to assess distributive mixing. The experimental data confirmed that these mixing indices are sensitive to changes in processing conditions and that they translate the expected behavior of each kneading block geometry.

Keywords: Mixing, Optical Properties, Temperature, Twin-Screw Extrusion, RTD Curves

1 Felipe O. C. Bernardo (felipeocb@hotmail.com) is affiliated with the Graduate Program in Materials Science and Engineering at the Federal University of São Carlos in Brazil. Sebastião V. Canevarolo (caneva@ufscar.br) is affiliated with the Federal University of São Carlos in Brazil, and José A. C. G. Covas (jcovas@dep.uminho.pt) is affiliated with the University of Minho in Portugal.

DOI: https://doi.org/10.51573/Andes.PPS39.GS.EX.2

Introduction

Mixing with co-rotating twin-screw extruders (TSE) has been the focus of numerous modeling and experimental studies, which usually aim to characterize either the distributive or the dispersive aspects of the process. In the case of distributive mixing, Fard et al. [1] proposed a mapping method based on the tracking of particles in the velocity fields, while Wang et al. [2] calculated the evolution of the Renyi relative entropies of the minor component along the extruder. However, most studies predicted and/or measured the residence time distribution (RTD) [3-6]. The width of the RTD curves is generally considered a measure of distributive mixing, which can be interpreted as the variance factor (Equation 1), but other parameters of the curves (e.g., minimum and mean residence times) can be used to gain an understanding of the effect of screw geometry and operating conditions on the machine's response. Another parameter, the total area under a RTD curve (A), is a direct and quantitative measure of tracer content and can be calculated accordingly Equation 2.

$$\sigma^2 = \int_0^\infty (t - t_n)^2 E(t) dt = \sum_0^\infty (t - t_n)^2 E(t) \Delta t \quad 1)$$

$$A = \int_0^\infty c dt = \sum_{t_i}^{t_f} c_i * \Delta t = \sum_{t_i}^{t_f} V_{Ni} * (t_i - t_{i-1}) \quad 2)$$

In these equations, $E(t)$ is the residence distribution function, t_i and t_n are the minimum and mean residence time, Δt is the time interval determined by the on-line data collection frequency, usually at 5 Hz or 0.2 s and, c is the tracer/pulse concentration at time t, which is taken here as V_N, the normalized transmitted light intensity response. To better analyze the experimental curves obtained from the measurements, they were fitted by theoretical pulse curves accordingly Equation 3 [7],

$$I = I_0 + K \left[1 - e^{-\left(\frac{t-t_i}{R_1}\right)}\right]^p . e^{-\left(\frac{t-t_i}{R_2}\right)} \quad 3)$$

where I_0 is the initial intensity or base line value (here set to zero), K is an area constant, t_i is the minimum residence time, R_1 and R_2 are the rise and fall time rates, respectively, and p is a power exponent. R_1 relates to the first part of the RTD curve, before the maximum, hence representing its rise time rate. The higher the R_1, the lower this rate. R_2 is associated with the region of the RTD curve beyond the maximum, thus quantifying its fall time rate. Again, the greater its value, the lower the rate of the RTD curve returning to its base line. The p parameter shifts the peak of the RTD curve down and forward, thus spreading the curve and reducing its area. This means a reduction in the number of particles and an increase in the axial spreading of the dispersed phase. Changes

DOI: https://doi.org/10.51573/Andes.PPS39.GS.EX.2

in p are much more perceptive than changes in R_2. R_1 is even less sensitive, as it is obtained from fitting a short portion of curve. K is a constant related to the area under the curve and is very sensitive both to changes in intensity of the RTD and to changes in R_1, R_2, and p, i.e., with changes in the number and dispersion of particles.

Here, we propose using the parameter K as an indicator of dispersive mixing performance, whereas the variance is used to assess distributive mixing. Both were chosen because they are related to the number and shape of dispersed particles and they are simple and easy to quantify, especially when compared to other more widespread mixing indicators.

Materials and Methods

Materials

A commercial grade of polystyrene, Styrolution 124 N/L with MFR of 12 cm^3/10 min (5.0 kg, 200°C) and density of 1.04 g/cm^3 was extruded as matrix. A polyamide 6, Domamid® 6NC01 with MFR of 165 cm^3/10 min (5.0 kg, 275°C) and density of 1.00 g/cm^3 was used as tracer/pulse.

Experimental Set-up

The experiments were carried out on a Collin ZK 25P co-rotating modular twin-screw extruder with L/D = 48. Figure 1(a) shows the modified barrel segment (1) containing two axial sets of on-off valves (2a and 2b). Each assembly consists of 4 openings that allow material to flow out of the extruder. A multislit die (3) containing 4 slits (L/D = 13, 14, 15, and 16) was fixed to the upper assembly (2a). Figure 1(b) shows the optical detection system used to quantify any changes in the intensity of light transmitted through the polymeric flow. The latter contains an aligned pair of light emitters (6a) and light receiver (6b), which are held in position by a C-shaped support (4).

DOI: https://doi.org/10.51573/Andes.PPS39.GS.EX.2

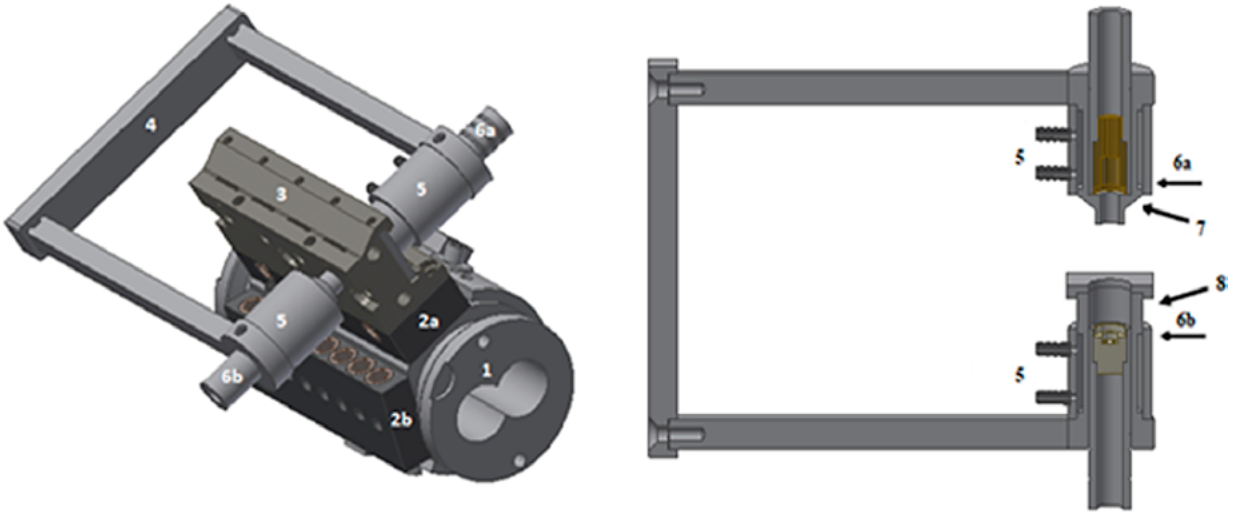

a) b)

Figure 1. (a) Experimental set-up: modified barrel segment (1) with two axial rows of sampling devices (2a, 2b); multi-slit die (3); sliding optical detector with a C-shaped support (4); water-cooling system (5); light source (6a) and receptor (6b) for optical measurements and (b) Optical detector system: LED (6a) with a polarizer (7) and two LDRs (6b) with a polarizing filter (8).

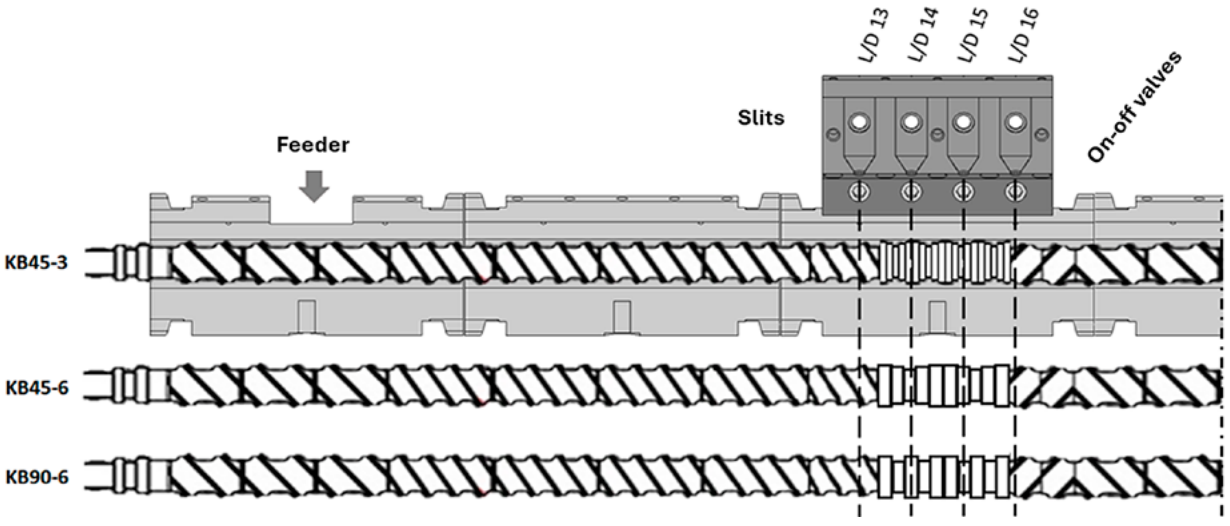

Figure 2. Screw profiles containing a 60 mm long mixing zone with different geometries: KB45-3–four kneading blocks with positive 45° stagger, each containing five 3 mm thick disks; KB45-6–two kneading blocks with 45° positive stagger, each containing five 6 mm thick disks; KB90-6–two kneading blocks with neutral 90° stagger, each containing five 6 mm thick disks.

DOI: https://doi.org/10.51573/Andes.PPS39.GS.EX.2

Three screw profiles were used and are presented in Figure 2.

To keep the experimental effort within reasonable limits, all the experiments were performed with a feed rate of 2 ± 0.1 kg/h and a uniform screw rotation speed of 100 rpm, while temperature was varied between 220°C, 230°C, and 240°C. For each processing run, upon reaching steady state extrusion of PS, a pulse of PA6 is added (0.105 g, corresponding to a concentration lower than 0.1% w/w relative to the matrix), the valve of a specific sampling device is opened, and the optical detector starts synchronously recording the transmitted light intensity as turbidity. The presence of the dispersed phase in the flow through the slit-die produces light scattering and retardation, which are recorded in real-time. Data comes out as a typical residence time distribution (RTD) curve. This procedure was repeated for the three remaining sampling positions and then the entire experiment was replicated for a different temperature and for the various screw profiles.

Results and Discussion

Turbidity Evaluation

Figure 3 below shows the normalized turbidity curves obtained with the addition of pulses under the measurement conditions for each L/D and for each of the 3 screw profiles. At L/D = 13, the local flow rate for screws KB45-3 and KB45-6 is either low or nil; for this reason, measurements on this position were not performed in this work.

Analyzing the data present in Figure 3, a different behavior is evident for each assembled thread profile. For the first profile of KB45-3, there is a greater discrepancy in the values found for the temperature 220°C, while for the other two thread profiles we have a few differences in values regardless of the temperature applied. Another evident point is the higher turbidity values found for the outlet valve of L/D = 14, something already expected as turbidity is expected to decrease downstream.

Mixing Evaluation

Once the obtained normalized turbidity values were analyzed, pulse function (Equation 3) was applied and the variance and area under the curve values were removed from each curve obtained. Thus, the mixing factors were quantified.

The data presented in Figure 4 confirms better mixing performance in elements with an angle between their kneading discs of 90°. Although the differences are low from one profile to another, they are present and easily identified graphically. For the analysis conditions with 45° elements varying the thickness of the discs, few differences were observed, therefore showing that the angulation of the elements stands out over their thickness.

DOI: https://doi.org/10.51573/Andes.PPS39.GS.EX.2

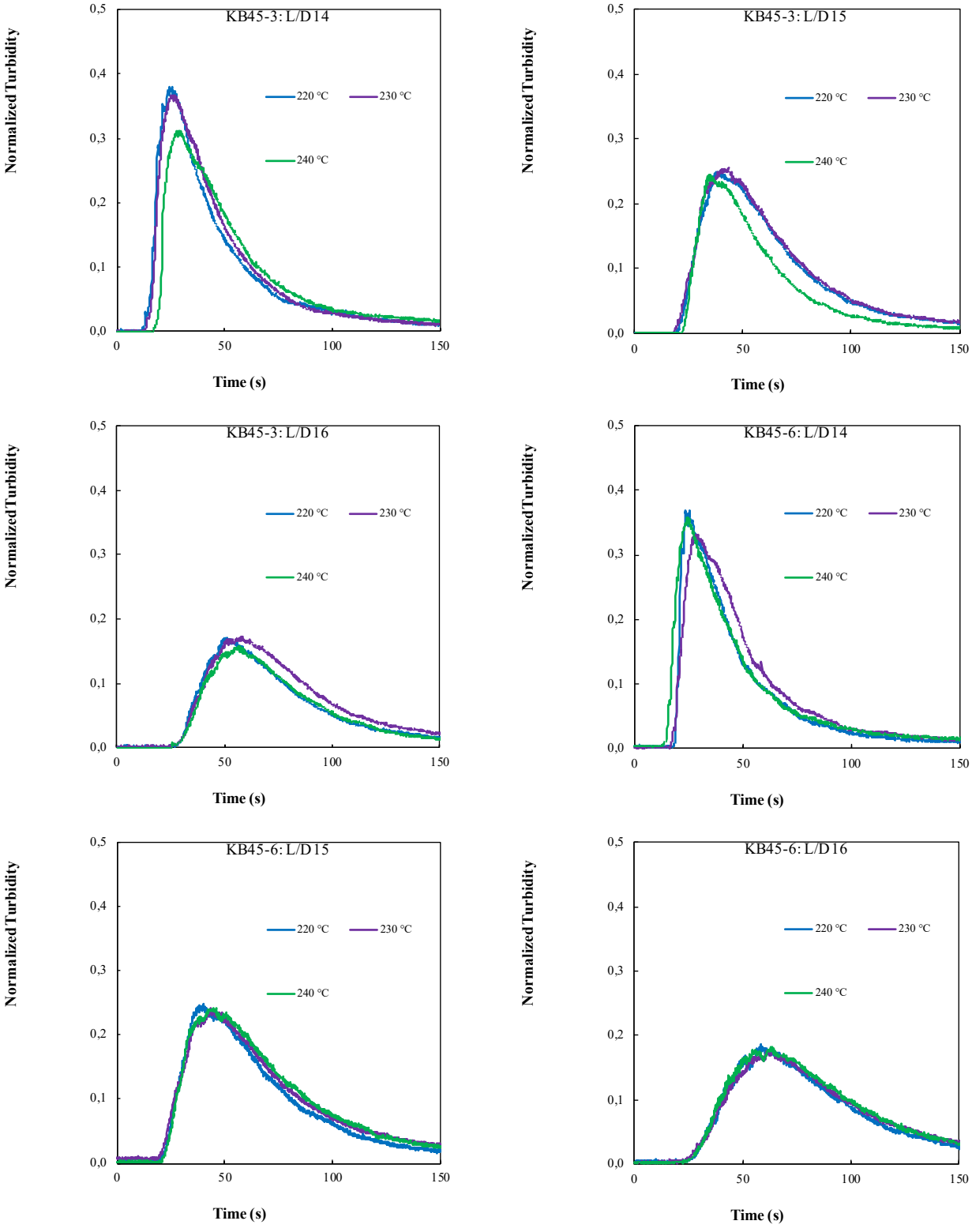

DOI: https://doi.org/10.51573/Andes.PPS39.GS.EX.2

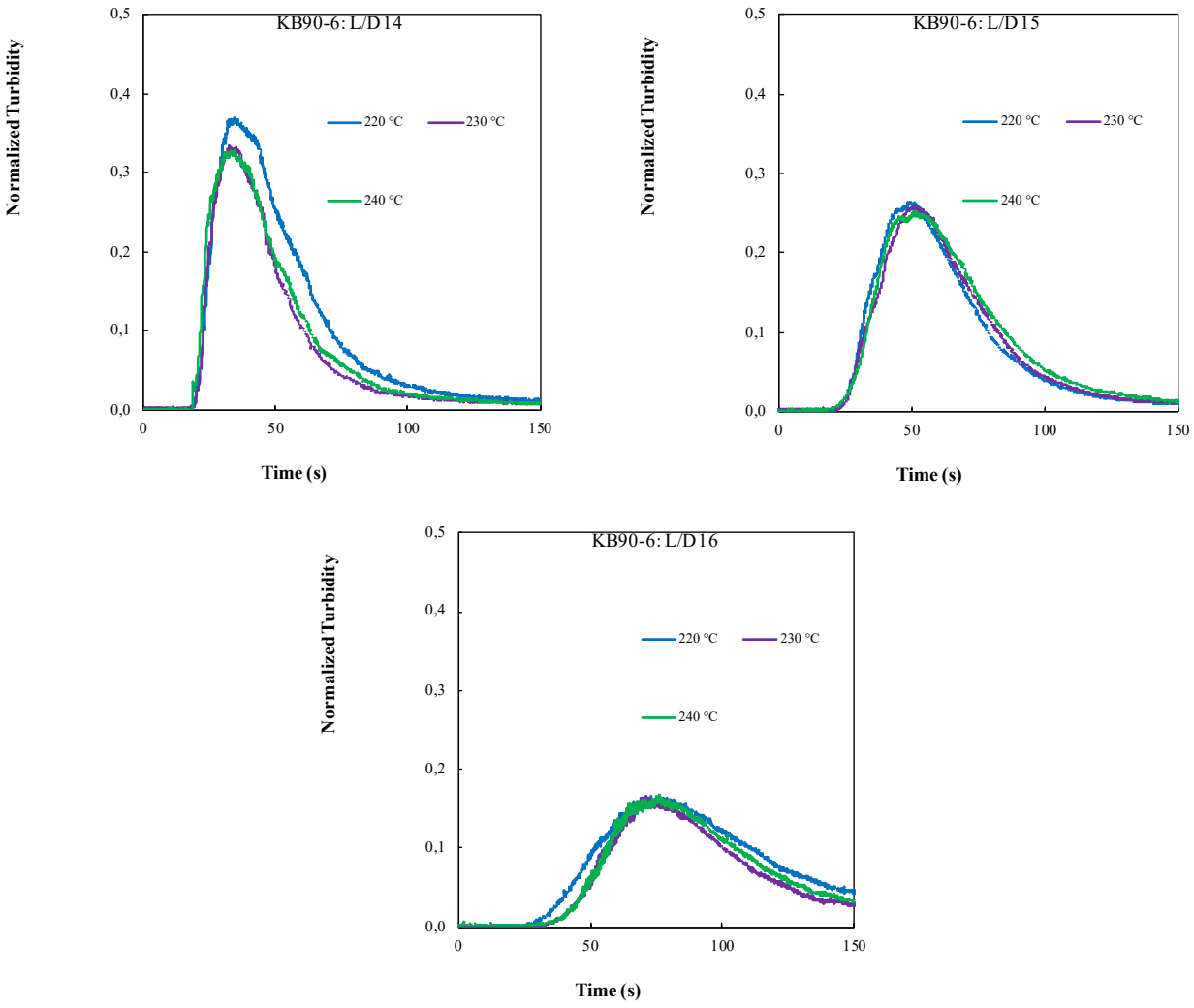

Figure 3. Normalized turbidity as function of time (s) for each screw profile: KB45-3, KB45-6, and KB90-6 for each measurement temperature. Screw rotation speed at 100 rpm for all measures.

DOI: https://doi.org/10.51573/Andes.PPS39.GS.EX.2

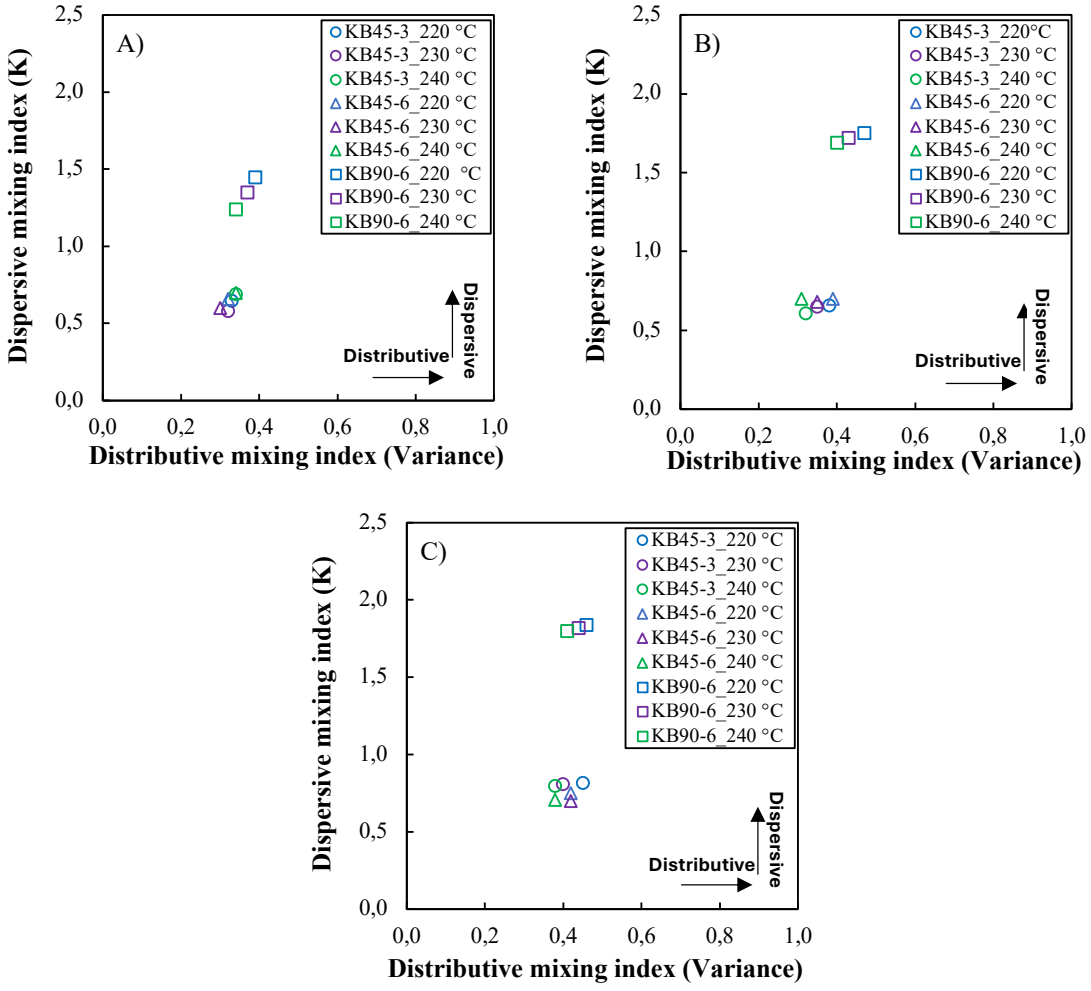

Figure 4. Mapping the mixing performance: Dispersive mixing index (K) versus Distributive mixing index (Variance) for different kneading blocks (KB45-3, KB45-6, and KB90-6) and temperatures 220°C, 230°C, and 240°C at ports: A) L/D = 14, B) L/D = 15, and C) L/D = 16.

Conclusion

In this study, a real-time optical detection system was employed to monitor the melt mixing behavior of a diluted polymer blend along a kneading section of a co-rotating twin screw extruder. The system utilizes light scattering and retardation caused by dispersed phase particles, providing information on particle number. By introducing the second phase component as a pulse at the extruder entrance and tracking its exit at various axial positions along the mixing zone, residence time distribution (RTD) curves were generated. The parameter K (a constant in the pulse curve, corresponding to the area under an RTD curve) and the variance of the RTD curves were utilized as dispersive and distributive mixing indicators, respectively. Analysis of K and the variance of

DOI: https://doi.org/10.51573/Andes.PPS39.GS.EX.2

the RTD curves revealed that higher dispersive mixing occurred in zones comprising disks staggered at 90°, which are associated with longer residence times compared to zones with smaller angles (45°). Thus, the experimental set-up and methodology employed in this work offer a way to rapidly evaluate the mixing performance of screw zones. This capability is valuable for optimizing screw configuration, establishing processing parameters, or designing new screw elements for twin-screw extruders.

Acknowledgments

The authors acknowledge the Coordenação de Aperfeiçoamento de Pessoal de Nível Superior -Brasil (CAPES) for funding this work as well as the Programa de Pós-Graduação em Ciência e Engenharia de Materiais (PPG-CEM) of Federal University of São Carlos and the Institute for Polymers and Composites (IPC) of the University of Minho for providing access to the laboratorial facilities.

References

1. Sarhangi Fard, A., Hulsen, M.A., Meijer, H.E.H., Famili, N.M.H. and Anderson, P.D., "Tools to simulate distributive mixing in twin-screw extruders", *Macromolecules*, vol. 21, pp. 217–240, 2012.
2. Wang, W., Manas-Zloczower, I. and Kaufman, M., "Entropic characterization of distributive mixing in polymer processing equipment", *AIChE Journal*, vol. 49, pp. 1637–1644, 2003.
3. Puaux, J.P., Bozga, G., and Ainser, A., "Residence time distribution in a corotating twin-screw extruder", *Chemical Engineering and Science*, vol. 55, pp. 1641–1651, 2000.
4. Lawal, A. and Kalyon, D.M., "Mechanisms of mixing in single and co-rotating twin screw extruders", *Polymer Engineering and Science*, vol. 35, pp. 1325–1338, 1995.
5. Wesholowski, J., Berghaus, A. and Thommes, M., "Investigations concerning the residence time distribution of twin-screw-extrusion processes as indicator for inherent mixing", *Pharmaceutics*, vol. 10, p. 207, 2018.
6. Kim, N., Kim, H. and Lee, J., "Numerical analysis of internal flow and mixing performance in polymer extruder II: Twin screw element" *Korea-Australia Rheology Journal*, vol. 18, pp. 153–160, 2006.
7. Canevarolo, S.V., Mélo, T.J.A. Covas, J.A. and Carneiro, O.S., "Direct method for deconvoluting two residence time distribution curves" in International Polymer Processing, vol. 16, 2001, pp. 334–340.

GENERAL SYMPOSIA | FUNCTIONAL ADDITIVES AND REACTIVE PROCESSING

Thin Films from Modified Poly(Glycolic Acid) with Excellent Water Vapor Barrier

Marieke Hilhorst, Sara Caliari, Wouter Post, Lambertus J. Kuijpers and Fresia Alvarado Chacon

DOI: https://doi.org/10.51573/Andes.PPS39.GS.FARP.1

December 2024

Thin Films from Modified Poly(Glycolic Acid) with Excellent Water Vapor Barrier

Marieke Hilhorst, Sara Caliari, Wouter Post, Lambertus J. Kuijpers and Fresia Alvarado Chacon[1]

Abstract: Commercial biodegradable polymers that combine high oxygen and water vapor barrier properties are scarce. In the packaging industry multilayer materials are usually used to achieve the barrier requirements, however they are usually not recyclable and will not biodegrade when discarded. The outstanding barrier properties of poly(glycolic acid) (PGA) make it an excellent candidate for a biodegradable oxygen and water vapor barrier packaging material. At the same time, its processability into films using standard converting equipment is a major challenge. Low melt strength, high processing temperatures, and fast crystallization at the die limit its use in conventional packaging applications. Chain extenders are typically used to improve the melt strength of polymers and thereby the overall processability, however they may affect the intrinsic barrier properties of the material. This work studied the reactivity of PGA with different chain extenders. It found that by using less than 2% reactive chain extenders the processability of PGA could be highly improved while keeping the intrinsic barrier properties of the material. After compounding PGA with the chain extenders Joncryl and carbodiimide, stable flat sheet extrusion of the material was possible resulting in sheets thinner than 10 µm. The multidirectional stretchability of the melt was improved, showing an increase in the melt strength of the polymer. Barrier properties were measured, and it was found that the water vapor transmission rate (WVTR) is not affected by the addition of the chain extender. This improvement in the processability of PGA offers a promising solution for biodegradable high-barrier packaging materials.

Keywords: Poly(glycolic acid) (PGA), Barrier properties, Chain Extenders, Thin Films

1 The authors Marieke Hilhorst (marieke.hilhorst@wur.nl), Sara Caliari, Wouter Post, Lambertus J. Kuijpers, Fresia Alvarado Chacon (fresia.alvaradochacon@wur.nl) are affiliated with the Wageningen Food and Biobased Research in The Netherlands.

DOI: https://doi.org/10.51573/Andes.PPS39.GS.FARP.1

Introduction

Poly(glycolic acid) (PGA) is a remarkably interesting polyester for film and coating applications due to its excellent barrier properties and its fast biodegradability in natural environments [1,2]. In recent years more cost-effective production technologies were installed at an industrial level which resulted in a reduction in market price. PGA is now an interesting material for cost-competitive markets such as packaging. As a result, multiple PGA producers have appeared in the commodity market [3,4]. In addition, innovative technologies have been developed to derive PGA from biomass, which aids the decoupling of plastic products and packaging from fossil resources [5].

However, PGA's processability in conventional thermoplastic equipment is a challenge. PGA has a high melting point; therefore, it needs to be processed at temperatures above 200°C [6]. It also has high crystallinity [7] and poor melt strength [8]. These properties limit the production of films and sheets from this material with conventional processing equipment.

Copolymerization of glycolic acid, for example with lactic acid, offers the possibility to reduce processing temperatures. It also influences the crystallinity of the polymer which, in turn, improves processability. However, when changing the molecular structure, the gas and water vapor barrier properties (highly dependent on the crystallinity) will be reduced. Even though barrier properties reported for these copolymers can be comparable to other bench market polymers, they are outperformed by the PGA homopolymer [7].

Mixing polyesters with other polymers is a conventional approach that is used to improve processability and/or mechanical properties. However, there are practical and theoretical risks in this approach. One potential issue is the possible de-mixing of the blend due to non-compatibility of the polymers. Another challenge, specific to PGA, is that few other biodegradable polymers can be processed at its high processing temperature. The alternative of blending PGA with non-biodegradable polymers will completely negate the unique selling point of the material. The final and most critical issue is the potential negative effect of blending on the excellent intrinsic barrier properties of the PGA. Until now, studies on PGA enhancement have focused on improving mechanical properties without looking into the effect on the barrier properties [9-11].

Chain extenders are known to improve polyesters' processability. A chain extender will connect the different polymer chains by reacting with the end-groups. In the case of PGA, it is expected that there are hydroxyl and/or carboxyl end-groups available for reacting. Literature show that isocyanate-based chain extenders in amounts up to 3 wt.% are more efficient than methacrylate-based ones due to differences in reactivity, resulting in improved thermal stability [8]. Furthermore, chain extenders have been proven to reduce hydrolytic degradation, resulting in improved material and product lifetime [12]. To obtain more insights on the effect of chain extenders on both processability and functionality, this study investigates five different chain extenders for PGA. Results on processability into thin sheets and barrier properties of the resulting products are reported.

DOI: https://doi.org/10.51573/Andes.PPS39.GS.FARP.1

Materials and Methods

This research is conducted in two phases: phase 1 in 2021 with virgin PGA (V-PGA) with MFI of 18 g/10 min, and phase 2 in 2023 with the same batch PGA aged over time (A-PGA) with MFI of 66 g/10 min. In the meantime, PGA is stored in a vacuum sealed bag at 4°C. PGA Vytal J116 with batch code 20210515-G-0304 supplied by PJChem is used in both phases. Carbonyl bis caprolactam (CBC) supplied by DSM, Pyromellitic dianhydride (PMDA) supplied by Sigma Aldrich, Joncryl ADR-4400 and Joncryl ADR-4468 supplied by BASF, and Carbodiimide Nexoll CDI/W supplied by Euro-Chemicals are used as chain extenders. Zinc stearate supplied by Sigma Aldrich is used as catalyst. V-PGA, A-PGA and their compounds are dried at 120°C in a Gerco dry-air desiccant dryer. All additives are dried at 40°C in a vacuum oven for at least 4 hours prior to any type of processing.

A Haake Rheomix Polylab kneader is used to screen the reactivity with different agents. The kneader is set to 225°C. The PGA is kneaded for 5 to 7 minutes (ensuring all material is melted), then the additives are added and the mixture is kneaded for a total of 30 minutes. The following amounts are added to V-PGA for the reactivity study: 0.5 wt.% CBC, 0.5 wt.% PMDA, 0.2, 0.5 wt.% Joncryl ADR-4400, 0.2, 0.5, and 1wt.% Joncryl ADR-4468.

The compounding is performed on a twin screw Berstorff ZE 25*40D extruder at a throughput of 5k g/h, 300 rpm screw speed with the following temperature profile: 20/80/160/180/190/190/200/205/205/205/215°C. V-PGA extruded only once without additives (VE-PGA) is also analyzed. The following compounds are made V-PGA with 0.2 wt.% and 0.5 wt.% Joncryl ADR-4468 (V-0.2J and V-0.5J respectively), both with and without zinc stearate (V-0.2JZ, V-0.5JZ). A-PGA is compounded with 0.5 wt.% Joncryl ADR-4468 (A-0.5J) and 1.5 wt.% carbodiimide (A-1.5C). Melt flow index (MFI) of the pure and produced compounds is measured according to ISO-1133 with Zwick MFLOW MFI. All samples are measured using a standard weight of 2.16 kg and a temperature of 230°C.

Sample sheets are produced on a Dr. Collin tech line A20T single screw extruder equipped with a 150 mm wide adjustable slit die. The line extruder is run at 80 rpm with a temperature profile per zone of 210/233/240°C and die temperature per section of 225/229/230°C.

Water vapor transmission rate (WVTR) is measured according to ASTM method E96-16 following the desiccant method: silicate gel inside the cup, store cup with sample in room with higher relative humidity. Samples are kept under controlled conditions (climate chamber) and weighed with analytical balance (3-digit number). Weight gain or weight loss are plotted against time. Linear regression analysis allows the results to be expressed in g (water)/m² (foil) day or corrected to 100 µm foil thickness. WVTR is applied at the temperature and specific relative humidity gradient shown in the data.

DOI: https://doi.org/10.51573/Andes.PPS39.GS.FARP.1

Oxygen transmission rate (OTR) is measured according to ASTM D3985-17 for dry condition and ASTM F1927-14 at a specific relative humidity using an Ametek Mocon machine. Automatic controlled relative humidity testing range is between 0 and 90% ± 3%. Standard film test area (50cm²) and film thickness: up to 3 mm. Result are expressed in mlO2/m². day.bar and corrected to 100µm thickness.

Results and Discussion

Reactivity of Poly(glycolic acid)

Kneading experiments are performed to verify the reactivity of the selected additives with PGA at the chosen temperature. Amounts chosen are based on known amounts typically used for PET, because of the similar polymer end-groups and the high processing temperature. For the V-PGA evaluated without additives, it was observed that at 225°C, 5 minutes are needed for complete melting of the polymer and homogeneous viscosity distribution. This value is set as the minimum processing time to study the reactivity with the different additives.

Chain extenders used are known to react either with the carboxyl or with the hydroxy groups available in the PGA. The functional epoxide groups of Joncryl react with the carboxyl groups of PGA polymers. In the case of carbodiimide, the carboxyl group will directly form an amide bond with the primary or secondary amine. CBC and PMDA connect to the hydroxyl groups, CBC as a monofunctional chain extender and PMDA as a multifunctional.

From the executed tests, it can be derived that additives reacting with carboxyl end-groups are the most efficient when adding them in the same amount (1%). Figure 1 shows the torque measured at the kneader for two trials with 1 wt.% PMDA and 1 wt.% Joncryl ADR-4468. When adding 1 wt.% Joncryl ADR-4468, a huge increase in torque at around 10 minutes (7 times higher than the molten PGA) is observed. In contrast, for PMDA a decreasing line is observed; this shows that by adding 1 wt.% PMDA at this temperature, no reaction takes place. After 30 minutes of kneading, the torque with Joncryl is twice as high as the initial molten PGA, despite the expected thermal degradation (torque decline with time). It was suspected that 1 wt.% of this type of Joncryl might be too high to process the compound into sheets via sheet extrusion due to abundant crosslinking. Therefore, lower amounts are used for further experiments. Enough reactivity is seen when adding 0.2 and 0.5 wt.%, but significantly lower torques are observed. The reactivity is lower because less amounts of molecules with reactive groups are available.

DOI: https://doi.org/10.51573/Andes.PPS39.GS.FARP.1

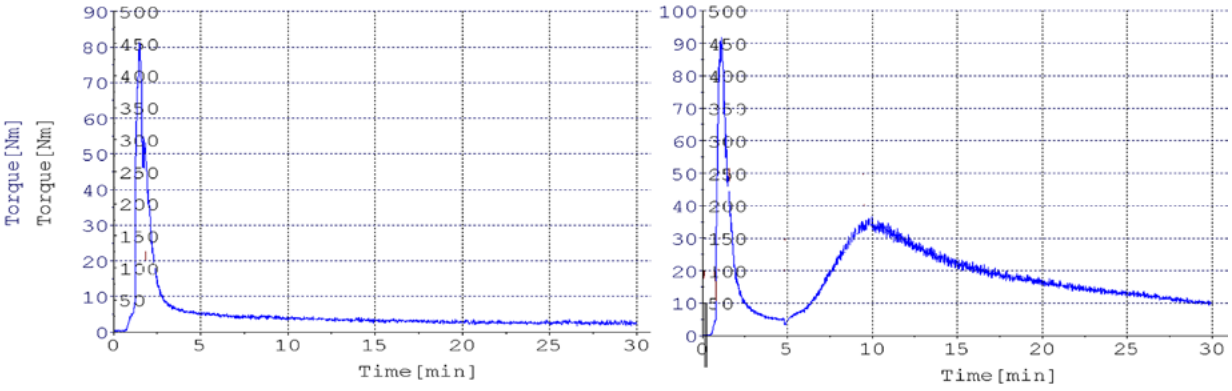

Figure 1. Torque (Nm) vs time (min) as measured by the kneader. Left: PGA with 1 wt.% PMDA and no reaction, right: PGA when 1wt.% Joncryl ADR-4468 is added.

Amounts of 0.2 wt.% and 0.5 wt.% of Joncryl ADR-4400 did not show any reactivity with the PGA. Joncryl ADR-4400 has only 5 functional epoxide groups, while Joncryl ADR-4468 has 9 epoxide groups available for reacting. Apparently, these amounts of Joncryl ADR-4400 are not enough.

When adding 0.5wt.% CBC or PMDA, no increase in torque was observed. This shows that no reaction took place at the temperature and amounts used. It could be either that not enough hydroxyl groups are available or that the required reaction temperatures are higher than the used temperature. PMDA and CBC are typically used in the chain extending of PA6 and PET, usually processed at higher temperatures, above 230°C [6]. These tests were performed at a maximum temperature of 225°C to avoid extensive thermal degradation of PGA, while reducing the viscosity enough to allow mixing.

For polylactic acid, it is well known that zinc stearate can be used as a catalyst in combination with Joncryl to accelerate its reaction time. Trials were done to confirm if the use of this catalyst will also work with PGA. When adding 0.5 wt.% Joncryl ADR-4468, the measured reaction times with PGA were as long as 7 minutes. By adding 150 ppm zinc stearate, the reaction times could be decreased from 7 to approximately 3 minutes. Torque graphs are shown in Figure 2, where reaction times are indicated between the orange lines.

DOI: https://doi.org/10.51573/Andes.PPS39.GS.FARP.1

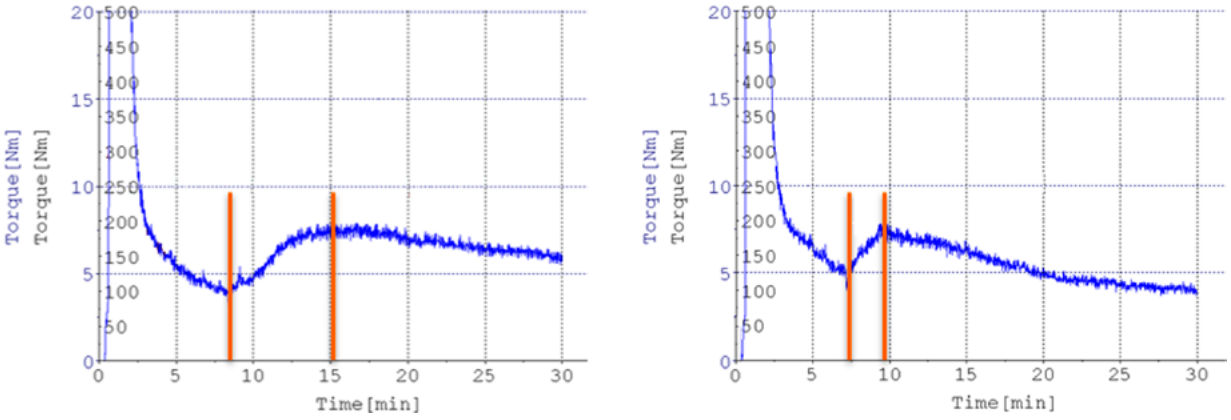

Figure 2. Kneader raw data showing the torque vs. time (blue curves) with the reaction time (between orange lines). Left: PGA with 0.5 wt.% Joncryl ADR-4468, right: PGA with 0.5 wt.% Joncryl ADR-4468 and 150 ppm zinc stearate.

Melt Flow Properties

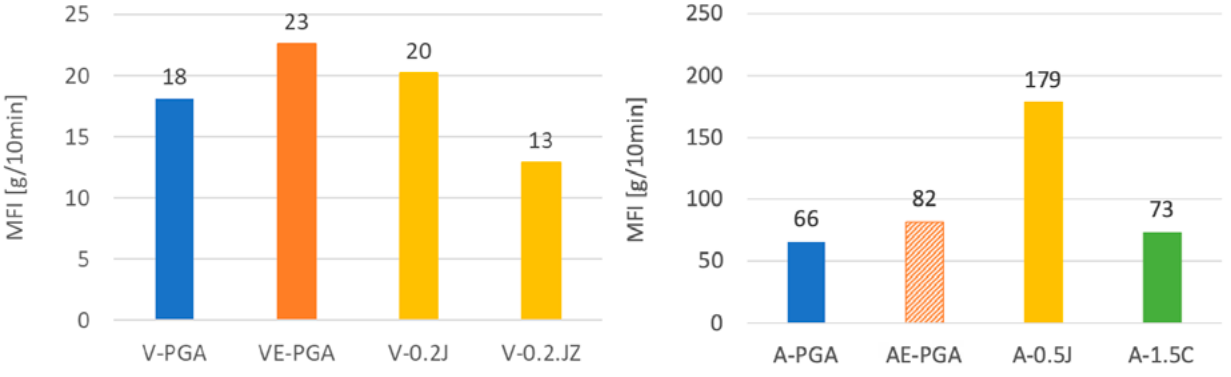

Figure 3. Melt flow index–MFI (230°C 2.16 kg) of the different pure and modified PGA materials. Top: Results for virgin PGA (phase 1). Down: Results for aged PGA (phase 2). The pattern filled bulk corresponds to a predicted value since no data is available.

Figure 3 shows the MFI results of a selection of manufactured PGA samples. The results of the virgin PGA trial (phase 1) show that the compounding step has a significant effect on the polymer viscosity. MFI increases by more than 20% which can be attributed to thermal degradation. The decrease in MFI of this PGA after extrusion with the addition of Joncryl shows the effect of the chain extender on the viscosities, probably due to crosslinking. In phase 2 of this study, PGA has aged over time as the MFI more than tripled. This indicates a drastic decrease in molecular weight over time. This is probably due to the rapid hydrolysis of PGA despite storing it at low temperatures and in sealed bags.

DOI: https://doi.org/10.51573/Andes.PPS39.GS.FARP.1

The addition of 0.5 wt.% Joncryl ADR-4468 to the aged PGA does not counteract the ongoing thermal degradation, it even seems to increase it. However, the addition of 1.5 wt.% carbodiimide (not used in phase 1) has a significant effect, counteracting the ongoing thermal degradation.

PGA Flat Sheet Processing

The PGA grades and modified PGA compounds were processed via flat sheet extrusion where the maximal sheet-width of 15 cm is achievable. The thickness, highest achievable width and width variation of the produced sheets can be found in Table 1. Some example sheets are also shown in Figure 4. The processing of the virgin PGA leads to very narrow sheets that do not reach 5 cm at a thickness lower than 20 µm. The intrinsic low melt strength of the PGA results in a large variation in thickness and width. At similar or lower thickness than the virgin PGA, the Joncryl modified sheets showed to be much more stable with less necking, resulting in wider sheets with small variation. These are the thinnest sheets that have been produced up to now with modified PGA.

Unfortunately, this effect was not observed for thicker sheets made with the aged PGA (A-0.5J). This could be explained by the reaction speed of Joncryl, which could be too slow when competing with the extremely fast thermal degradation at the extruder for these aged materials with expected low molecular weights.

Sheets using combinations of Joncryl and zinc stearate could not be analyzed further. Though zinc stearate helped increase the reaction speed of Joncryl ADR-4468, as seen in Figure 2, the flat extrusion process is very unstable for thin sheets, so unstable that it was not possible to collect samples for further analysis. Also, specks were seen in the sheets, probably due to alter crystallization mechanisms during re-processing.

Due to the low viscosity of the aged PGA, it was necessary to drastically increase the thickness of the sheets to values around 100 µm, this is why A-0.5J and A-1.5C are thicker as well. Again, a large variation in the width of the sheets for the pure PGA can be observed and surprisingly also for the Joncryl modified sheets. However, when modifying the aged PGA with carbodiimide, the sheet extrusion process stabilizes and sheets at full width with small width variations are obtained. The MFI of the modified aged PGA grade showed to be slightly higher than the aged PGA. Most probably, the viscosity is at the level of the predicted value of the extruded aged PGA or even lower. Figure 4 shows an example of three typical sheets with lengths of around 20 cm and a maximum width of 12 cm, only obtained for the sample A-1.5C.

DOI: https://doi.org/10.51573/Andes.PPS39.GS.FARP.1

Figure 4. Left A-PGA, middle A-0.5J, right A-1.5C.

Table 1. Dimensions of flat sheets produced.

Material	Thickness (μm)	Highest achievable width (cm)	Width variation (cm)
V-PGA	10 to 20	<5	~ 2.5
V-0.2J	6	11	< 0.5
A-PGA	80	9.5-13	~ 4
A-0.5J	100	8-11	~ 4
A-1.5C	70	12	< 0.5

Barrier Properties of PGA Sheets

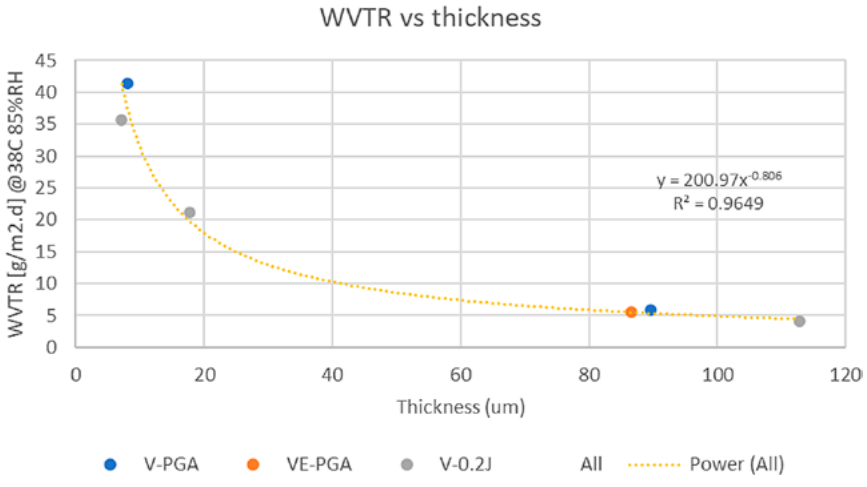

Figure 5. Water vapor barrier properties dependence on the thickness of the film.

DOI: https://doi.org/10.51573/Andes.PPS39.GS.FARP.1

Barrier properties are largely dependent on the thickness of a product; therefore, water vapor and oxygen transmission rates are usually corrected for thickness. However, this relationship is not linear and especially for polyesters, depending on the crystallinity of the material [13]. When looking into flat sheets, crystallinity and therefore barrier properties will also be affected by processing conditions such as temperature and stretching at the die. Linear regression models have been built, for example, for PE to allow the prediction of the minimum required thickness for achieving the peak performance of the material [14]. Figure 5 shows the dependence of uncorrected water vapor transmission rates on film thickness. Even with the limited amount of data input caused by the inability to process all formulations, this model can help predict the layer thickness needed to achieve the desired WVTR. It is interesting to notice that not only the pure PGA is fitted in the model but also the Joncryl modified PGA. Transmission rates corrected for thickness are shown in Table 2.

When correcting the values for thickness, water vapor transmission rates measured at two different conditions are at the same level of around 3 g/m².day for pure and modified PGA (see Table 2). These values are independent of the starting material (virgin or aged) and of the chain extender used. Oxygen transmission rates are only evaluated for virgin PGA, pure and modified. Due to the low OTR, measuring times are lengthy. Results show that the addition of chain extender does not negatively affect the barrier properties. The modification of PGA with the reported chain extenders preserves the excellent barrier properties of PGA. From this, it can be derived that the original crystalline structure of the PGA polymer remains intact. More research into the crystalline and molecular structure of the PGA is recommended to confirm this hypothesis.

Table 2. Top: water vapor transmission rate (WVTR) and bottom: oxygen transmission rate (OTR) at the given conditions corrected for 100µm thickness.

Material	Sheet thickness (µm)	WVTR (23°C, 85% RH) [g/m².day]	WVTR (23°C, 90% RH) [g/m².day]
V-PGA	10-20	3.4 ± 0.5	
V-0.2J	6	2.5 ± 0.8	
A-PGA	80		2.9 ± 0.6
A-0.5J	100		3.0 ± 0.2
A-1.5C	70		2.5 ± 0.1
Material	**Sheet thickness (µm)**	**OTR (25°C, 0% RH, 100% O_2) [mlO_2/m².day.bar]**	**OTR (25°C, 90% RH, 100% O_2) [mlO_2/m².day.bar]**
V-PGA	10-20	0.3 ± 0.1	0.2 ± 0.1
V-0.2J	6	0.3 ± 0.1	0.5 ± 0.2

DOI: https://doi.org/10.51573/Andes.PPS39.GS.FARP.1

Conclusions

The use of Joncryl ADR-4468 and carbodiimide chain extenders to modify PGA has a positive effect on processing properties. Full width sheets could be obtained, achieving for the first-time flat sheets with thickness below 10 µm when using 0.2 wt.% Joncryl as an additive. The water vapor and oxygen barrier properties of the modified PGA are preserved when using Joncryl and carbodiimide as chain extenders, even when the virgin material has aged for two years. CBC and PMDA do not show sufficient reactivity at the concentrations and conditions used in this study. Chain extenders that react with PGA seem to counteract the effect of thermal degradation at the extruder during processing; more research on the exact mechanism is needed. A simple model to predict the WVTR values of flat sheets made of pure and modified PGA is proposed. With this model the thickness of the PGA-layer needed to achieve certain WVTR can be estimated. This study shows how the processing of PGA can be enhanced, which is one of the biggest hurdles to using PGA as functional material in biodegradable barrier packaging products.

Acknowledgments

The authors acknowledge the government and the industrial partners for funding the project LWV19220 Paper-based food packaging. This project was a public-private partnership funded by the Top Sector Agri-Food and with the commitment of Unilever Innovation Centre Wageningen B.V., Koninklijke Douwe Egberts B.V., and Vaassen Flexible Packaging B.V. part of Clondalking Group. Also, the "KB 34 Circular and climate neutral society" program under grant number KB-34-010-001.

References

1. P. K. Samantaray et al., "Poly (glycolic acid) (PGA): a versatile building block expanding high performance and sustainable bioplastic applications," *Green Chemistry,* vol. 22, no. 13, pp. 4055-4081, 2020, https://doi.org/10.1039/d0gc01394c
2. F. Wu, M. Misra, and A. K. Mohanty, "Challenges and new opportunities on barrier performance of biodegradable polymers for sustainable packaging," *Progress in Polymer Science,* vol. 117, 2021, https://doi.org/10.1016/j.progpolymsci.2021.101395
3. K. Yamane, H. Sato, Y. Ichikawa, K. Sunagawa, and Y. Shigaki, "Development of an industrial production technology for high-molecular-weight polyglycolic acid," *Polymer Journal,* vol. 46, no. 11, pp. 769-775, 2014, https://doi.org/10.1038/pj.2014.69
4. K. J. Jem and B. Tan, "The development and challenges of poly (lactic acid) and poly (glycolic acid)," *Advanced Industrial and Engineering Polymer Research,* vol. 3, no. 2, pp. 60-70, 2020, https://doi.org/10.1016/j.aiepr.2020.01.002

5. T. M. Gadda, M. M. Pirttimaa, O. Koivistoinen, P. Richard, M. Penttila, and A. Harlin, (2014, January) The industrial potential of bio-based glycolic acid and polyglycolic acid. *Appita* [Innovation]. 1.

6. H. de Beukelaer, M. Hilhorst, Y. Workala, E. Maaskant, and W. Post, "Overview of the mechanical, thermal and barrier properties of biobased and/or biodegradable thermoplastic materials," *Polymer Testing,* vol. 116, 2022, https://doi.org/10.1016/j.polymertesting.2022.107803

7. M. A. Murcia Valderrama, R. J. van Putten, and G. M. Gruter, "PLGA Barrier Materials from CO2. The influence of Lactide Co-monomer on Glycolic Acid Polyesters," *ACS Applied Polymer Materials Journal,* vol. 2, no. 7, pp. 2706-2718, Jul 10, 2020, https://doi.org/10.1021/acsapm.0c00315

8. L. Chen, X. Sun, Y. Ren, R. Wang, W. Liang, and X. Duan, "Influence of chain extenders on the melt strength and thermal stability of polyglycolic acid," *Journal of Applied Polymer Science,* vol. 138, no. 23, 2021, https://doi.org/10.1002/app.50551

9. R. Wang, X. Sun, L. Chen, and W. Liang, "Morphological and mechanical properties of biodegradable poly (glycolic acid)/poly (butylene adipate-co-terephthalate) blends with in-situ compatibilization," *RSC Advances,* vol. 11, no. 3, pp. 1241-1249, Jan 4, 2021, https://doi.org/10.1039/d0ra08813g

10. K. Wang, J. Shen, Z. Ma, Y. Zhang, N. Xu, and S. Pang, "Preparation and Properties of Poly(ethylene glycol-co-cyclohexane-1,4-dimethanol terephthalate)/Polyglycolic Acid (PETG/PGA) Blends," *Polymers (Basel),* vol. 13, no. 3, Jan 31 2021, https://doi.org/10.3390/polym13030452

11. L.-F. Chang, Y.-G. Zhou, Y. Ning, and J. Zou, "Toughening Effect of Physically Blended Polyethylene Oxide on Polyglycolic Acid," *Journal of Polymers and the Environment,* vol. 28, no. 8, pp. 2125-2136, 2020, https://doi.org/10.1007/s10924-020-01752-5

12. X. Sun, L. Chen, R. Wang, M. Jiang, M. Sun, and W. Liang, "Control of hydrolytic degradation of polyglycolic acid using chain extender and anti-hydrolysis agent," *Journal of Applied Polymer Science,* vol. 139, no. 25, 2022, https://doi.org/10.1002/app.52398

13. S. Marano, E. Laudadio, C. Minnelli, and P. Stipa, "Tailoring the Barrier Properties of PLA: A State-of-the-Art Review for Food Packaging Applications," *Polymers (Basel),* vol. 14, no. 8, Apr 18, 2022, https://doi.org/10.3390/polym14081626

14. K. Lahtinen and J. Kuusipalo, "Prediction of WVTR with General Regression Models," presented at the 11th Tappi European PLACE Conference, 2007.

DOI: https://doi.org/10.51573/Andes.PPS39.GS.FARP.1

GENERAL SYMPOSIA | INJECTION MOLDING

Design of an Injection Mold with Local Placement of Heating Coatings for Warpage Compensation

Christian Hopmann, Christoph Zimmermann, Daniel C. Fritsche, Kirsten Bobzin, Hendrik Heinemann, Marvin Erck and Nicole Lohrey

DOI: https://doi.org/10.51573/Andes.PPS39.GS.IM.1

December 2024

Design of an Injection Mold with Local Placement of Heating Coatings for Warpage Compensation

Christian Hopmann, Christoph Zimmermann, Daniel C. Fritsche, Kirsten Bobzin, Hendrik Heinemann, Marvin Erck and Nicole Lohrey[1]

Abstract: The influence of the thermal injection mold design crucially affects the geometric precision of injection molded parts. However, the adjustability of the heat flux distribution established with the conventionally used cooling channels is limited and cannot cover the variable cooling demand. The proposed approach of using heating coatings on the cavity surface to manipulate the part's cooling rate shows that it may be advantageous, due to the close and localized application to the part. A simulative optimization routine determines the necessary position and surface power of the heating coating. The objective of this methodology is to homogenize the surface temperature, inner cooling rate, and freeze time inside the part. This work applies the simulative design method for the optimized placement and heating power on a mold for a three-dimensional part. As the temperature field of the heating coating depends on the contacting, the electro-thermal simulation is analyzed and confirmed as sufficient to establish the optimal heat flux distribution. A process simulation study shows the dimension with the most critical warpage is decreased by 90%.

Keywords: Heating Coating, Injection Molding, Local Heating, Process Simulation, Thermal Mold Design, Warpage

1 The authors, including Daniel C. Fritsche (daniel.fritsche@ikv.rwth-aachen.de), are affiliated to the Lehrstuhl für Kunststoffverarbeitung of the RWTH Aachen University in Germany and the Institut für Oberflächentechnik of the same university.

DOI: https://doi.org/10.51573/Andes.PPS39.GS.IM.1

Introduction

Thermal mold design is a crucial step in creating an injection mold. Its primary objective is to rapidly cool down the molded part, ensuring an efficient manufacturing process. It must simultaneously allow for mold filling under moderate process conditions while preventing premature solidification of the melt. Balancing these conflicting goals, the cooling conditions also impact the optical and geometric properties of the part. Variations in part wall thickness and localized mass accumulation lead to significant differences in temperature, cooling rate, and solidification time. These state variables influence the material's specific volume during cooling. Non-uniform 3D-specific volume states or shrinkage during cooling induce local stress within the part, resulting in warping upon demolding due to unconstrained geometric shrinkage. Properly adjusting the heat balance of the mold through temperature homogenization, cooling rate, and freezing time distribution within the molded part helps reduce discrepancies in locally specific volumes [1].

Conventionally, the part is cooled down by heat transfer into a fluid like water or oil running through cooling channels inside the mold, close to the cavity. Various research is conducted to create methods and design rules on how to design the cooling channel layout for injection molds [2]. The approaches to inverse thermal mold design have the advantage that no initial tempering channel layout is necessary and that the user cannot influence the result by his choice of starting conditions [3,4]. The term "inverse" is derived from the objective: At the end of the cooling phase, a thermally homogeneous molded part is to be produced. The central tool is an objective function, which evaluates the thermal state of the molded part [7,8]. Based on this target definition, the heat balance of the injection mold is iteratively adjusted until an optimality condition is reached. The automized thermal design and cooling channel derivation have shown that the boundary conditions for cooling channels limit the level of detail with which the optimal heat balance can be set. Consequently, the necessary heat flux cannot be supplied locally. One example is the minimum diameter of the cooling channel or minimum distance between the cavity and the cooling channel [5,6].

In order to establish a well-defined heat flux profile, extremely high temperature gradients are necessary. A prior simulation study demonstrated the advantages of applying localized heat input to the edges of an injection-molded part to mitigate warpage [7]. The practical implementation and extent of localized heat input is promising. A newly developed heating coating consisting of two electrically isolating ceramic layers around a electrically contacted ceramic layer was applied on the cavity wall of a plate geometry and practically tested [8-10]. The electric flow creates a heat source according to the joule heating. The coating's low mass ensures a high heating and cooling rate of the wall temperature. An adjustable influence on the part warpage is also validated and, therefore, the use of this technology for higher geometric precision is suggested [8]. The heating power distribution, which is derived by the temperature field on the surface, is homogeneous but depends on the contacting positions of the coating. The position determines the resistance for the electric current between the different contacts and, consequently, the electric current density distribution and direction within the coating.

DOI: https://doi.org/10.51573/Andes.PPS39.GS.IM.1

An adaptation of the inverse thermal mold design shows the applicability of this methodology for heating coatings on the cavity wall [11]. Heat sources on the cavity wall make it possible to significantly reduce the result of the optimization's objective function. For example, more homogeneous surface temperatures on the part and cooling rates inside the part are achieved. To experimentally validate the effect of the heating coating, a three-dimensional part and the optimal heating coating layout is calculated. A test was performed to determine if a thermo-electrical simulation calculating the joule heating and the resulting heat flow can be used to set up different contacting positions of the coating and whether it predicts the resulting heating power distribution. Finally, a commercial process simulation is conducted to compare the warpage of the part with and without a heating coating to ensure the positive effect before the manufacturing of the mold.

Electric Simulation and Calibration of the Heat Transfer Coefficient

The influence of the electrical contacting and position indicates that it needs to be considered to actually create the optimal heating power distribution. Therefore, an electro-thermal simulation of the experiments in [8] is modelled with Comsol Multiphysics 6.1, Comsol AB, Stockholm, Sweden, and compared to define the unknown boundary conditions with a reverse engineering approach. As the temperature dependent electrical resistance of the coating is known through the measured current and voltage, the remaining parameter is the heat transfer coefficient between the coating and substrate.

The experimental setup is a mold insert with a heating coating which is cooled by the mold's cooling channel [8]. The mold insert is a flat surface usually used for injection molding of plates. Figure 1 shows the temperature distribution of the numerical model and the experimental setup measured with a thermography camera. The temperature level is considered approximately equal and the electric contacts are recognized by the temperature hot spots. However, the simulation shows that the hottest area is between the two contacts at the bottom instead of the two contacts in the middle. Since the contacts are in a parallel connection and are the same distance apart, no path with a lower electrical resistance is expected. However, a reduced heat flow at the bottom or increased heat flow at the top in x-direction would lead to a temperature gradient in x-direction. Thus, the coating's electrical resistance is lower in the hotter area. Further adaptations of the heat flow were tested by increasing the natural convection at the bottom and decreasing the heat transfer coefficient between the top of the insert with the coating and the mold base. Currently no significant improvement of the correspondence of the temperature field's quantitative conformity is achieved.

DOI: https://doi.org/10.51573/Andes.PPS39.GS.IM.1

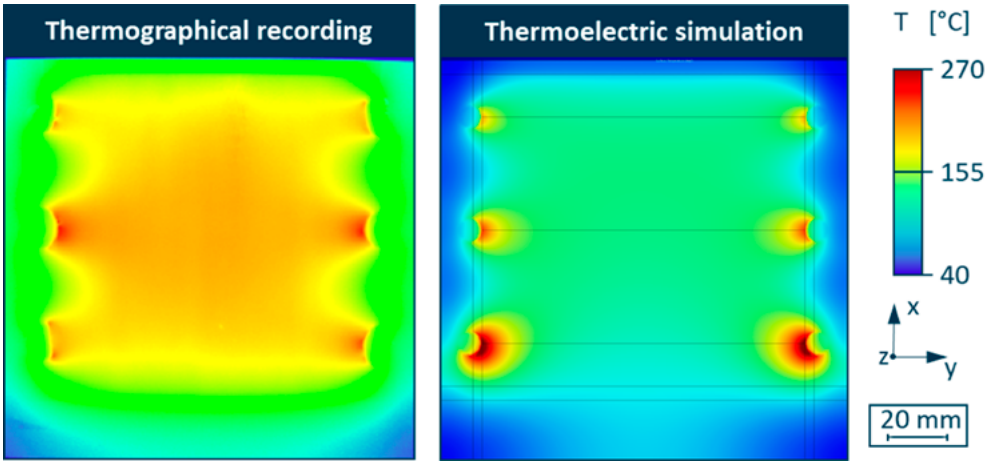

Figure 1. Comparison of the temperature distribution between thermography and simulation.

Optimization of the Heating Coating Position and Power

The design and optimization routine developed in previous works is applied on a three dimensional geometry [11]. The chosen geometry is a simplification of a stacking box (Figure 2). The simplifications are necessary to ensure the access of the thermal spray gun to the whole mold surfaces during the coating process. Additionally, the decreased structural stiffness increases the risk of warpage and therefore poses a more critical case to validate the warpage compensation due to local heating coatings. Figure 2 shows the cooling channel layout designed by professional mold manufacturers. It serves as an industrial example to demonstrate whether additional and more localized control of the cooling of the part brings advantages for the existing conventional mold cooling. The inlet is realized by a cold runner and located in the back of the bottom of the box.

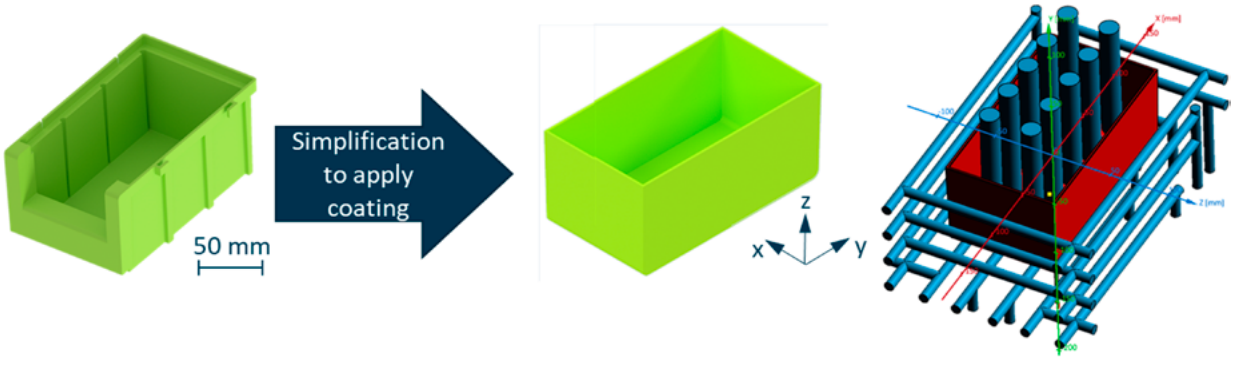

Figure 2. Part geometry and cooling channels for the validation case.

DOI: https://doi.org/10.51573/Andes.PPS39.GS.IM.1

The material of the mold and part as well as the process parameters are chosen for the design routine to calculate the initial conditions of the part after injection (Table 1). The simulation software, Sigmasoft, Sigma Engineering GmbH, Aachen, Germany, is used to determine and export the temperature and pressure distribution of the mold and melt.

Table 1. Material and process parameter for calculating the initial conditions for the subsequent thermal optimization. An unreinforced polybutylene terephthalate (PBT) is used for the mold design.

Parameter	Value/Name	Unit
Melt material	PBT–Pocan B1305, Envalior GmbH, Düsseldorf, Germany	-
Mold steel	1.2311 / 40CrMnMo7	-
Melt temperature	255	[°C]
Mold temperature	80	[°C]
Injection rate	100	[cm^3/s]
Ejection temperature	98	[°C]
Cooling time	15	[s]

The optimization routine is conducted with the Comsol Multiphysics software. Firstly, the heating power on the cavity surface as the design variable is optimized with a gradient based optimization algorithm. The algorithm minimizes the objective function [11,12] and thus homogenizes the temperature on each part's surface and the cooling rate as well as the freeze time inside the part. The first optimization results in an optimal heating power distribution. Secondly, a non-gradient based optimization algorithm assigns the heating power distribution to either the discrete heating zone or no heating. The optimal result is a heating zone of 6,000 W/m^2 assigned to each position with a value above 3,500 W/m^2 from the first optimization step.

The simulation without a heating coating shows a wide temperature distribution on the surface, with the lowest temperature on the edges and corners and the maximum temperature in the edges inside the box (Figure 3). The area with higher temperatures originates due to the proximity of the inlet and the four surfaces in this area that transport energy to the cooling channel in the middle, whereas the cooling channels withdraw energy from one side of one wall. This area can also not be optimized by applying heating coating, which is why the maximum value in all optimized layouts is similar (Figure 3).

The potential of the heating coating is visible in the area, which is colder than 98°C in simulation result without heating. The optimal heating distribution homogenizes this area to a high degree, (Figure 3). The minimum temperature is a lot closer to the average temperature and half of the temperature values lie within a range of 2.5 K. This is smaller than the range of 6.0 K without heating. The minimum values from the discrete solutions are in-between the optimal distribution and the one without heating, and the temperature distribution is also narrower. Half the values lie within

DOI: https://doi.org/10.51573/Andes.PPS39.GS.IM.1

a range of 3.4 K. This shows that the discrete optimization focuses on a narrow distribution rather than increasing minimum temperature significantly to achieve the best compromise in terms of the objective function.

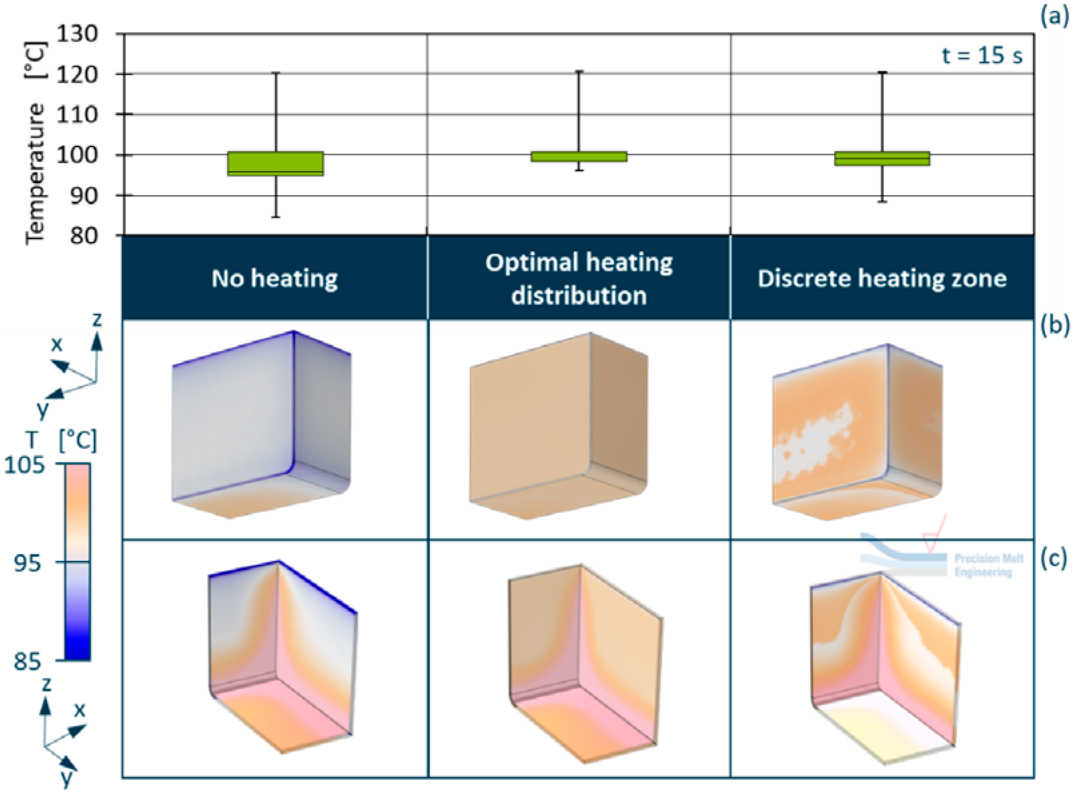

Figure 3. Box plot showing the temperature distribution on the part's surface without a heating coating, with the optimal heating coating distribution and one discrete heating coating zone (a). False color plots displaying the temperature distribution on a quarter model with a view of the outside (b) and inside (c) of the box.

Simulative Validation of the Heating Coating's Warpage Compensation

The process is simulated with and without the developed heating coating, according to the predefined parameters in Moldex3D 2023, CoreTech System Co., Ltd, Taiyuan St. Zhubei City, Taiwan (Table 1). The first comparison in terms of temperature distribution shows a more similar temperature level on the inside and outside of the box with heating coatings (Figure 4). However, the temperature influence of the heating coatings is seen on the outer walls in terms of hot spots. The temperature distribution is less homogenic compared to the simulation in Comsol. This is explained by the differing heat transfer coefficient implemented in all process simulation software.

DOI: https://doi.org/10.51573/Andes.PPS39.GS.IM.1

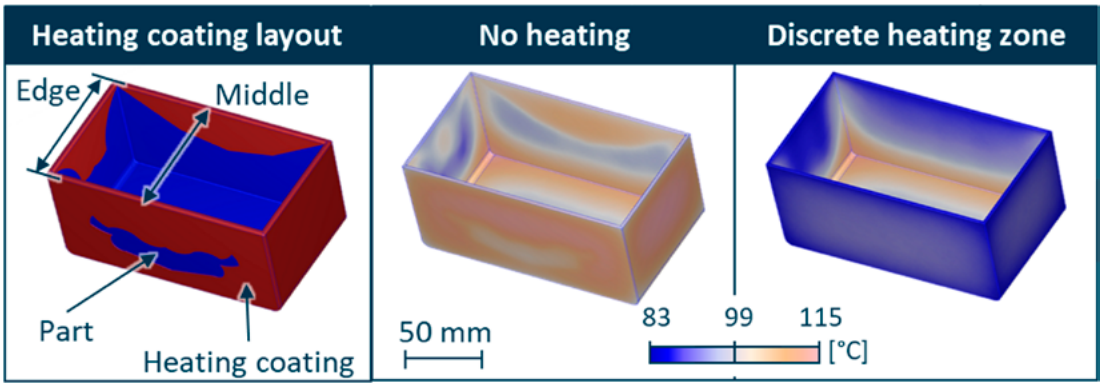

Figure 4. Temperature distribution on the part's surface displayed regarding the Moldex3D model.

An indicator for the geometric precision the typical warpage for box-shaped geometries is the wall collapse. The difference between the width of the part in the middle and the edge is supposed to be the same (Figure 4). Table 2 shows that the wall collapse is 90% lower with -0.15 mm compared to the 1.46 mm without heating coatings.

Table 2. Distances of the part in the middle and edge of the long wall after 15 s cooling.

Measurement	Edge [mm]	Middle [mm]	Wall collapse [mm]
Nominal	94.6	94.6	0
No heating	93.03	91.57	1.46
Discrete heating zone	92.71	92.86	-0.15

Conclusion

The methodology presented in previous works is applied on a three-dimensional part. A discrete heating power is derived and created as a geometry to create a heating layout. The thermo-electrical simulation was established for this heating coating technology and can be used in the future for developing the electrical contacting. The ideal heating power distribution ignoring the influence of the contacting in an injection molding simulation already shows that the warpage is reduced. However, the different heat transfer coefficient model used in the design software and the validation software led to different boundary conditions. A more comparable set of boundary conditions for the different simulations will be used in the future, by defining a constant heat transfer coefficient.

All in all, the result is a significant layout that will be manufactured in the future and iterate design changes of the heating coatings position and size should be reduced.

DOI: https://doi.org/10.51573/Andes.PPS39.GS.IM.1

Acknowledgments

The presented investigations were carried out at RWTH Aachen University within the framework of the Collaborative Research Centre SFB1120-236616214 "Bauteilpräzision durch Beherrschung von Schmelze und Erstarrung in Produktionsprozessen" and funded by the Deutsche Forschungsgemeinschaft e.V. (DFG, German Research Foundation). The sponsorship and support are gratefully acknowledged.

Research Data

This work's research data can be accessed here: http://hdl.handle.net/21.11102/ce52d6c9-906e-49ea-a5eb-a600675fd4f1

References

1. R. Spina, M. Spekowius, K. Küsters, and C. Hopmann, "Thermal Simulation of Polymer Crystallization during Post-Filling," *KEM*, pp. 1699–1706, 2013, https://doi.org/10.4028/www.scientific.net/KEM.554-557.1699
2. S. Feng, A. M. Kamat, and Y. Pei, "Design and fabrication of conformal cooling channels in molds: Review and progress updates," vol. 171, 2021.
3. P. Nikoleizig, "Inverse thermische Spritzgießwerkzeugauslegung auf Basis des lokalen Kühlbedarfs," Dissertation, RWTH Aachen, 2018.
4. A. Agazzi, V. Sobotka, R. Le Goff, D. Garcia, and Y. Jarny, "A Methodology for the Design of Effective Cooling System in Injection Moulding," *International Journal of Material Forming*, vol. 3, S1, pp. 13–16, 2010, https://doi.org/10.1007/s12289-010-0695-2
5. G. R. Berger, D. Zorn, W. Friesenbichler, F. Bevc, and C. J. Bodor, "Efficient cooling of hot spots in injection molding. A biomimetic cooling channel versus a heat-conductive mold material and a heat conductive plastics," *Polymer Engineering and Science*, vol. 59, s2, E180-E188, 2019, https://doi.org/10.1002/pen.25024
6. S. Mayer, Optimised mould temperature control procedure using DMLS, 2009. [Online]. Available: https://www.3dimpuls.com/sites/default/files/download/eos_optimizedmouldtemperaturecontrolprocedureusing_dmls.pdf
7. C. Hopmann et al., Eds. Identification and compensation of part warpage in injection molding using on-cavity thermally sprayed heating coatings, 2023.
8. D. C. Fritsche et al., Eds. Einsatz und Einflussnahme von thermisch gespritzten Heizschichten im variothermen Spritzgießprozess, 2021.

9. K. Bobzin, W. Wietheger, M. A. Knoch, and A. Schacht, "Heating behaviour of plasma sprayed TiOx/Cr2O3 coatings for injection moulding," *Surface and Coatings Technology*, vol. 399, 2020, https://doi.org/10.1016/j.surfcoat.2020.126199

10. K. Bobzin et al., Eds. Thermisch gespritzte Heizschichtsysteme für den Einsatz im Spritzgießen. Düsseldorf, 2020.

11. C. Hopmann et al., "Methodology of a thermal injection mold design with locally applied heating coatings on the cavity wall," *Materialwissenschaft Werkst*, vol. 55, no. 4, pp. 518–532, 2024, https://doi.org/10.1002/mawe.202300156

12. T. Hohlweck, D. Fritsche, and C. Hopmann, "Validation of an extended objective function for the thermal optimisation of injection moulds," *International Journal of Heat and Mass Transfer*, vol. 198, p. 123365, 2022, https://doi.org/10.1016/j.ijheatmasstransfer.2022.123365

DOI: https://doi.org/10.51573/Andes.PPS39.GS.IM.1

GENERAL SYMPOSIA | INJECTION MOLDING

Impact of Glass Fiber Content and Packing Pressure on Weld Line Integrity in Injection Molded Short Glass Fibre Reinforced Polyamide

Majid Mokarizadehhaghighishirazi, Bart Buffel, Stepan V. Lomov and Frederik Desplentere

DOI: https://doi.org/10.51573/Andes.PPS39.GS.IM.2

December 2024

Impact of Glass Fiber Content and Packing Pressure on Weld Line Integrity in Injection Molded Short Glass Fibre Reinforced Polyamide

Majid Mokarizadehhaghighishirazi, Bart Buffel, Stepan V. Lomov and Frederik Desplentere[1]

Abstract: Managing the challenge of weld lines of short-fiber reinforced polymers (SFRPs) in injection molding is crucial for enhancing the mechanical performance of these composites. This study evaluates the impact of various glass fiber contents (0 to 50 wt%) within a polyamide 6 (PA6) matrix on the tensile and flexural properties at weld lines, comparing each sample to its counterpart without a weld line. Our findings indicate that weld lines have minimal impact on the mechanical properties of composites with low fiber content (10 wt%). However, at higher fiber contents, the strength, modulus, and strain at fracture are significantly reduced due to unfavorable fiber orientations at the weld lines. Increasing the packing pressure during injection molding can partially recover these properties by promoting favorable fiber orientation at the weld line. This signifies the importance of carefully controlling processing parameters to optimize the mechanical performance of SFRPs at weld lines.

Keywords: Injection Molding, Short-Fiber Reinforced Polymers, Weld Lines, Fiber Orientation

1 The authors Majid Mokarizadehhaghighishirazi (majid.shirazi@kuleuven.be), Bart Buffel (bart.buffel@kuleuven.be), Stepan V. Lomov (stepan.lomov@kuleuven.be) and, Frederik Desplentere (frederik.desplentere@kuleuven.be) are affiliated with the Department of Materials Engineering at KU Leuven University in Belgium.

DOI: https://doi.org/10.51573/Andes.PPS39.GS.IM.2

Introduction

Injection molding is a widely used process for producing thermoplastic polymers and composites. A significant challenge in this process is the formation of weld lines, which occur when multiple flow fronts merge within the mold cavity. These weld lines can significantly deteriorate the mechanical properties of the finished product, particularly in short-fiber reinforced polymers (SFRPs). Stagnating weld lines, formed by the direct collision of flow fronts, are especially problematic as they restrict polymer flow and result in poor interface bonding [1].

In unfilled polymers, the mechanical properties at weld lines are degraded due to insufficient molecular diffusion and the presence of voids and V-notches, which create localized stress points. The reduction of mechanical performance is more severe in SFRPs featuring stagnating weld lines, where unfavorable fiber orientation at the weld line can lead to a reduction in mechanical properties of up to 50% . Near the weld line, fibers are oriented perpendicular to the flow direction as a result of elongational flow, whereas fibers near the mold walls outside the weld region align parallel to the flow direction due to the high shear stress. The perpendicular fiber alignment at the weld line disrupts the load transfer efficiency and creates weak points in the composite, thereby significantly diminishing its mechanical properties [2].

Extensive research has been conducted on how injection molding parameters affect weld line strength. For non-reinforced polymers, increasing the melt and mold temperatures generally improves weld line strength by promoting better polymer chain interdiffusion [3]. However, the effect of packing pressure remains debated. For reinforced polymers, fiber orientation at the weld line is a critical factor, and the literature presents conflicting views on how processing parameters influence this orientation [4].

Our previous study investigated the effects of weld lines on the mechanical properties of unfilled and glass fiber-reinforced PA6 [4]. We found that weld lines minimally impacted the mechanical properties of unfilled PA6 due to the matrix's high healing capability, as confirmed by DSC and oscillatory shear measurements. In contrast, glass fiber-reinforced PA6 composite showed significant reductions in mechanical performance at the weld lines due to unfavorable fiber orientation, with fractures primarily occurring at the weld line. We identified a bell-shaped fracture surface structure linked to the 'underflow' phenomenon caused by flow imbalances during injection molding, which affects fiber orientation. Processing parameters such as melt and mold temperatures had negligible effects on weld line strength, while increased packing pressures improved mechanical properties by intensifying the underflow and promoting more favorable fiber orientation at the weld line.

Building on our previous research, which focused solely on pure PA6 and its composite reinforced with 50 weight percent (wt%) glass fiber, the current study aims to investigate the impact of varying fiber content on the mechanical behavior of composites featuring stagnating weld lines. Specifically, we examined composites incorporating 0, 10, 20, 30, 40, and 50 wt% glass fibers within a PA6 matrix. This investigation seeks to clarify how different fiber contents affect the tensile and

DOI: https://doi.org/10.51573/Andes.PPS39.GS.IM.2

flexural properties of the composites. We have extended our analysis by incorporating both tensile and flexural tests, thereby providing a more comprehensive evaluation of the mechanical behavior of these materials.

Materials and Methods

Materials

For this study, a PA6 matrix equivalent to the one used in DOMAMID 6LVG50H2BK was used to compound various composites with different glass fiber content. This particular PA6 matrix is not commercially available and was thus supplied directly by Domo Chemicals. Composites containing 0, 10, 20, 30, 40, and 50 weight percent (wt%) of glass fibers were compounded using the supplied PA6 matrix. Advantex® chopped glass fibers, measuring 4 mm in length and 10 μm in diameter, were used in the compounding process. Tensile bars with and without weld lines were molded from each composite pellet. Prior to injection molding, both the PA6 matrix and glass fibers were dried for a minimum of 4 hours at 80°C.

Sample Preparation

To investigate the impact of fiber content on weld line strength, composites were produced using a two-step manufacturing process. Initially, chopped glass fibers were blended into virgin PA6 through compounding with a Leistritz ZSE18MAXX corotating twin-screw laboratory extruder. This process produced composites containing varying glass fiber content from 0 to 50 wt%. Following this, dog-bone-shaped tensile samples were produced via injection molding using an Arburg 320S machine. The mold cavity, designed with a cold sprue and runners, adheres to the ISO 527 standard and can produce two samples simultaneously. Dual gates positioned at opposite ends of each sample facilitate the formation of weld lines at the midpoint of each tensile bar. Filling the cavity from one side with the opposite gates closed results in samples without weld lines. The details and dimensional specifications of the mold cavity are shown in Figure 1. The packing pressure was systematically varied across three levels (40, 60, and 80% of the maximum injection pressure) to examine its effect on weld line strength.

DOI: https://doi.org/10.51573/Andes.PPS39.GS.IM.2

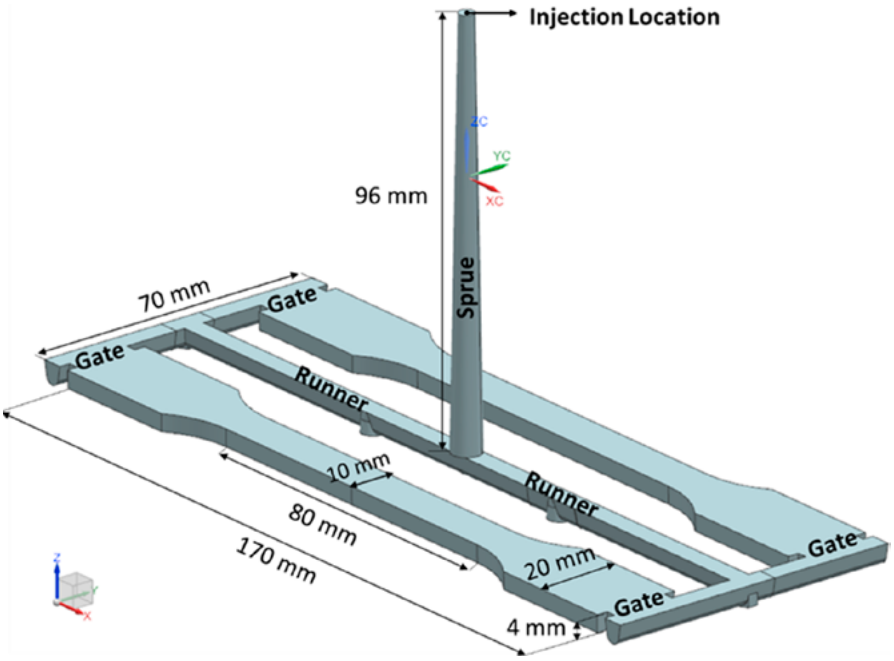

Figure 1. Details of the mold cavity used for producing dog-bone-shaped samples.

Tensile and Flexural Testing

Tensile tests were conducted on specimens with varying fiber content processed at different levels of packing pressure to measure tensile properties of samples, both with and without weld lines. Using an Instron 3367 two-column tensile bench equipped with a 30 kN load cell, and an extensometer for precise strain measurements, samples were tested at a crosshead speed of 1 mm/min following the ISO 527 standard. Mechanical properties such as maximum tensile stress, strain at fracture, and tensile modulus were recorded. Each category was tested with three specimens and the average results were reported. For flexural testing, three-point bending tests were performed according to the ISO 178 standard using an Instron 3345 single-column tensile bench with a 1 kN load cell. Samples were tested at a crosshead speed of 2 mm/min, and properties such as maximum flexural stress, strain at fracture, and flexural modulus were evaluated. To prevent moisture absorption, the injection molded samples were sealed immediately after injection molding.

DOI: https://doi.org/10.51573/Andes.PPS39.GS.IM.2

Results and Discussions

In this section, we analyze the mechanical properties of PA6 composites reinforced with varying percentages of glass fibers to investigate the impact of weld lines and injection molding processing parameters on their tensile and flexural performance. Our previous research demonstrated that while melt and mold temperatures have minimal influence on weld line strength, packing pressure does play a critical role. By examining various fiber contents and adjusting packing pressures to 40%, 60%, and 80% of the maximum injection pressure during the molding process, we aim to clarify the complex interactions among mechanical properties at the weld lines, fiber content, and packing pressure.

Tensile and Flexural Strength

The effect of fiber content and packing pressure on the tensile and flexural strength of composites with stagnating weld lines is shown in Figure 2. Initial observations show minimal impact of weld lines on the tensile and flexural strength of pure PA6 and PA6 composite reinforced with 10 wt% glass fiber. This can be attributed to the lower fiber content, which does not significantly disturb the polymer matrix healing at the weld lines. As the glass fiber content increases to 20 wt% and beyond, a noticeable reduction in both tensile and flexural strength in samples with weld lines is evident, compared to their counterparts without weld lines. This reduction is more pronounced with increasing fiber content. Increased packing pressures show a mitigating effect on this strength reduction. For composites with 20 wt% or higher glass fiber content, higher packing pressures help improve the tensile and flexural strength, thereby partially restoring the mechanical properties. This suggests that the application of higher packing pressures facilitates better distribution and orientation of fibers at the weld lines, as shown in our previous study [4], contributing to a more effective fiber role in carrying tensile and flexural stresses.

It is also observed that flexural strength generally surpasses tensile strength across all composites. This phenomenon can be explained by the nature of the loading conditions during the tests. Flexural tests involve both tension and compression within the material, allowing the composites to better distribute and withstand stresses. In contrast, during tensile tests, the composite is subjected to a unidirectional force, which can lead to earlier failure due to the lack of fiber reinforcement, as many fibers are aligned perpendicular to the force direction at the weld line.

DOI: https://doi.org/10.51573/Andes.PPS39.GS.IM.2

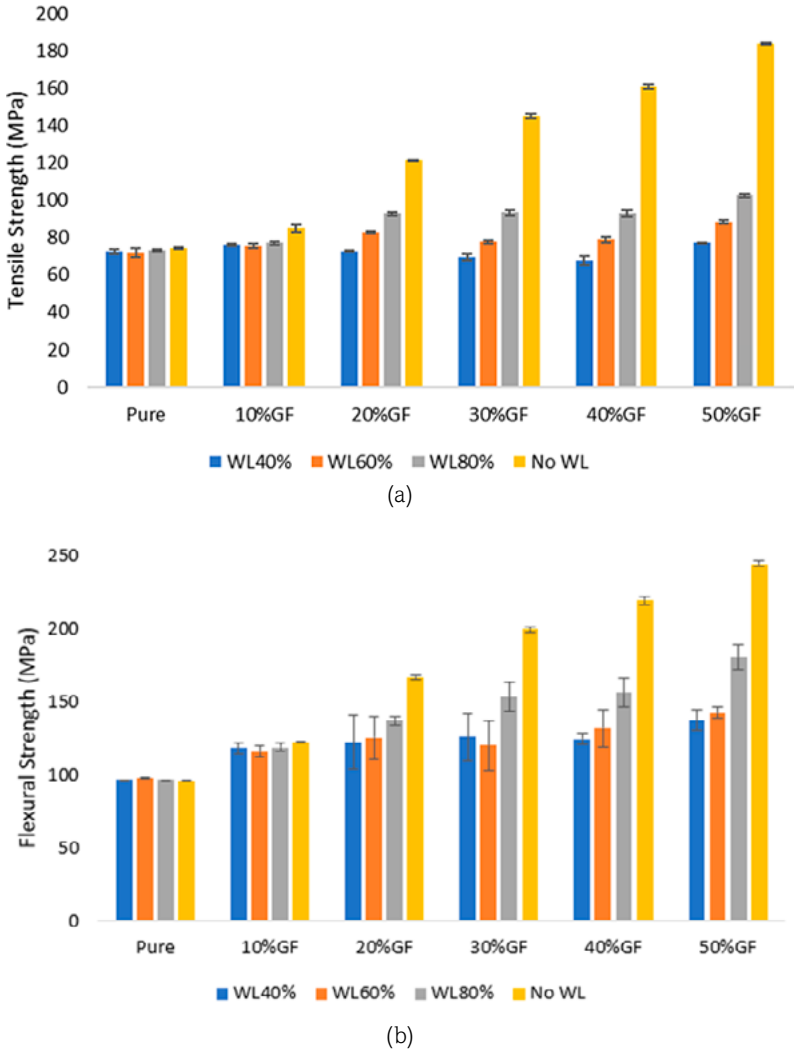

Figure 2. The effects of fiber content and packing pressure on the strength of composites with and without weld lines in (a) tension and (b) bending modes.

Tensile and Flexural Modulus

Similar trends in the influence of fiber content and packing pressure on the tensile and flexural modulus of composites with stagnating weld lines are observed, mirroring those seen in tensile and flexural strength. The presence of weld lines in pure and 10 wt% glass fiber composites shows minimal impact on their modulus, suggesting that the material's stiffness is predominantly governed by

DOI: https://doi.org/10.51573/Andes.PPS39.GS.IM.2

the polymer matrix in these lower fiber content composites. However, as the fiber content increases to 20 wt% and above, a significant reduction in both tensile and flexural modulus is observed at the weld lines. This reduction is primarily due to unfavorable fiber orientation at the weld line and the resulting inefficiency in load transfer capabilities within the composite.

The recovery of modulus with increased packing pressure further supports the concept that the fiber orientation at the weld lines is improved by increasing the packing pressure. The lack of a deflectometer during bending tests prevents a direct comparison between tensile and flexural modulus, highlighting a potential area for methodological improvement in future studies.

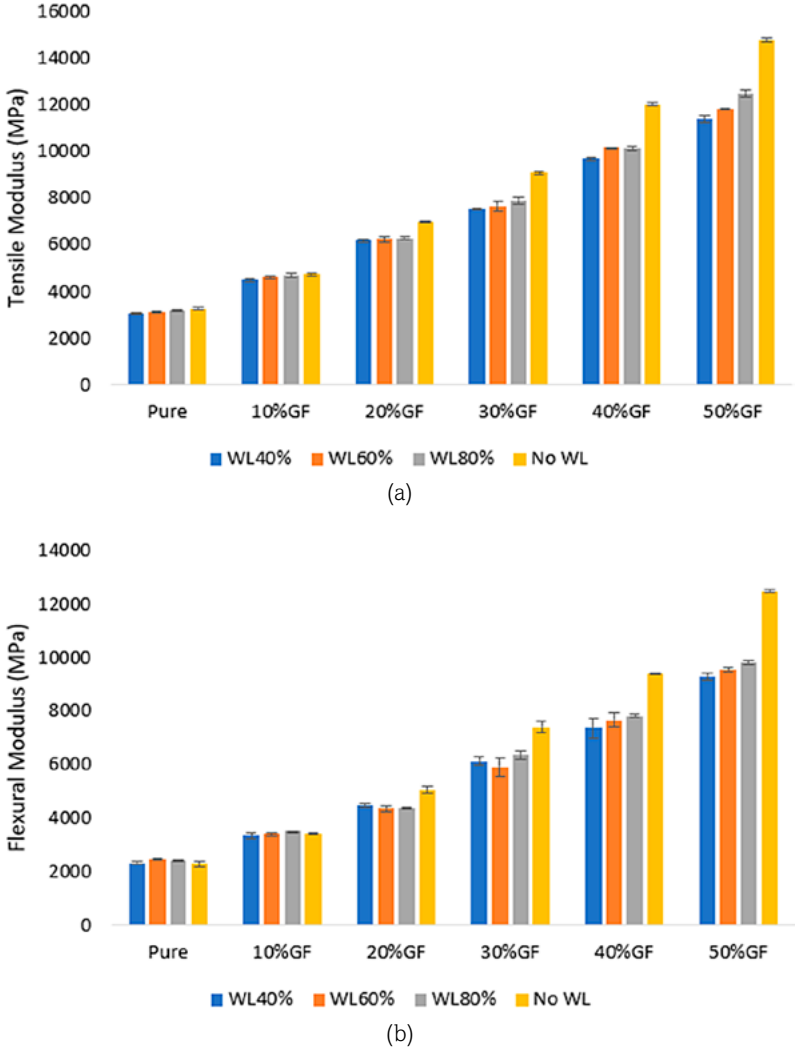

Figure 3. The effects of fiber content and packing pressure on the modulus of composites with and without weld lines in (a) tension and (b) bending modes.

DOI: https://doi.org/10.51573/Andes.PPS39.GS.IM.2

Strain at Fracture

The strain at fracture in tension and bending modes provides further insights into the ductility of the composites (Figure 4). Pure PA6 samples exhibit relatively high strains (>10%) in tensile tests. This property is maintained in bending tests, where no fractures were observed, suggesting an inherent ductility in the material, which is not affected by the presence of weld lines. However, in composites with 10 wt% or more glass fibers, significant reductions in tensile fracture strains are evident at weld lines. The reductions in flexural fracture strains are less pronounced than in tensile tests. This could be due to the triaxial stress state in bending, which may allow the material to sustain higher deformations before fracture, compared to the uniaxial tension where stress concentration at weld lines leads to earlier failure.

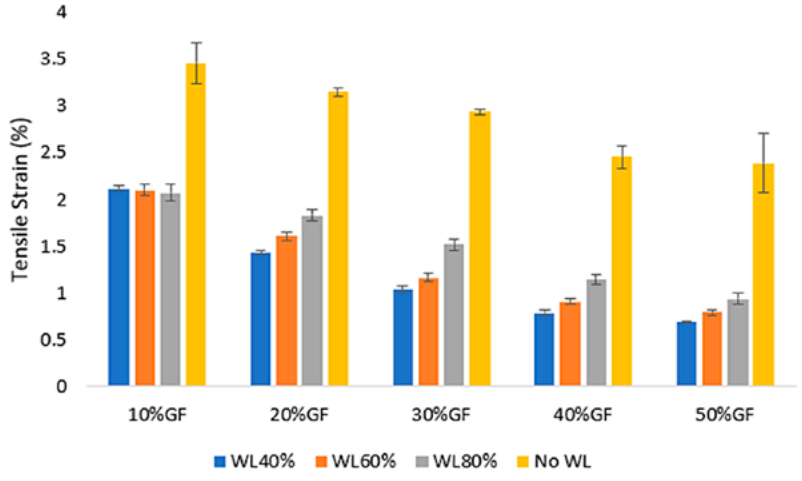

(a)

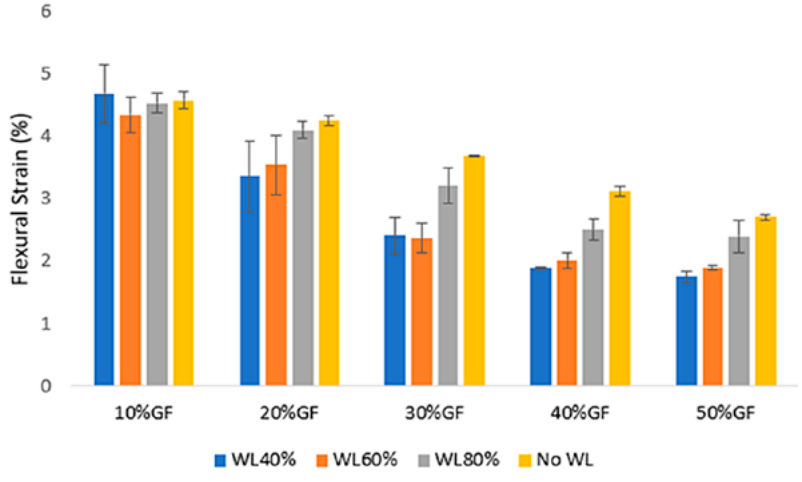

(b)

Figure 4. The effects of fiber content and packing pressure on the strain at fracture for composites with and without weld lines in (a) tension and (b) bending modes.

DOI: https://doi.org/10.51573/Andes.PPS39.GS.IM.2

Conclusion

This study highlights the significant impact of weld lines on the mechanical properties of PA6 composites with varying glass fiber contents. While pure PA6 and low fiber content composites (10 wt%) are minimally affected by weld lines, composites with ≥20 wt% glass fiber exhibit substantial reductions in tensile and flexural strength, modulus and fracture strain due to weld lines. However, increased packing pressure can partially mitigate these reductions by promoting a more favorable fiber orientation at the weld line. These findings underscore the importance of optimizing processing parameters to enhance the mechanical performance of fiber-reinforced composites in the presence of weld lines.

Acknowledgments

The work leading to this paper has been funded by the ICON project "ProPeL", which fits in the MacroModelMat (M3) research program, coordinated by Siemens (Siemens Digital Industries Software, Belgium), and funded by SIM (Strategic Initiative Materials in Flanders) and VLAIO (Flemish government agency Flanders Innovation & Entrepreneurship). The authors would like to thank Domo Chemicals for providing the material.

References

1. J. Onken and C. Hopmann, "Prediction of weld line strength in injection-moulded parts made of unreinforced amorphous thermoplastics", 2016.
2. M. B. Baradi, C. Cruz, T. Riedel, and G. Régnier, "Frontal weld lines in injection-molded short fiber-reinforced PBT: Extensive microstructure characterization for mechanical performance evaluation," *Polymer Composites*, vol. 40, no. 12, pp. 4547–4558, Dec. 2019, https://doi.org/10.1002/pc.25310
3. R. Seldén, "Effect of processing on weld line strength in five thermoplastics," *Polymer Engineering and Science*, vol. 37, no. 1, pp. 205–218, 1997, https://doi.org/10.1002/pen.11663
4. M. Mokarizadehhaghighishirazi, B. Buffel, S. V. Lomov, and F. Desplentere, "Investigation of microstructural and mechanical properties of weld lines in injection-molded short glass fiber-reinforced polyamide 6," *Polymer Composites*, 2024, https://doi.org/10.1002/pc.28384

GENERAL SYMPOSIA | INJECTION MOLDING

Investigations on Injection Mold Inserts with Reduced Thermal Masses using Additive Manufacturing

Milan Fitzlaff, Gibran Khoury, Moritz Käß, Martin Werz, Bernd Gundelsweiler and Stefan Weihe

DOI: https://doi.org/10.51573/Andes.PPS39.GS.IM.3

December 2024

Investigations on Injection Mold Inserts with Reduced Thermal Masses using Additive Manufacturing

Milan Fitzlaff, Gibran Khoury, Moritz Käß, Martin Werz, Bernd Gundelsweiler and Stefan Weihe[1]

Abstract: This work examined previously developed injection mold inserts with reduced thermal mass, with regard to lightweight construction approaches. These were optimised for oil-variothermal temperature control using simulative support. Additive manufacturing (AM), with its high degree of freedom in design, enables the implementation of individual, conformal cooling channels and can additionally support the efficiency of the variothermal process. The thermal mass of the injection mold is often a limiting factor in terms of process efficiency, which is also addressed in the analysis and optimisation considering the possibilities of additive manufacturing. A comparison of lightweight inserts with comparable variants made of solid material revealed a significant difference, with consideration of several tempering cycles. The validation of selected inserts confirmed the simulation. These investigations show that AM combined with lightweight construction approaches can support an additional increase in efficiency as well as a reduction in cycle times for the fluid-variothermal process control.

Keywords: Variotherm, Additive Manufactured Inserts, Injection Molding, Thermal Simulation

1 The authors Milan Fitzlaff (milan.fitzlaff@ikff.uni-stuttgart.de), Gibran Khoury and Bernd Gundelsweiler are affiliated with the Institute of Precision Engineering (IKFF) at the University of Stuttgart in Germany. Moritz Käß, Martin Werz and Stefan Weihe are affiliated with the Materials Testing Institute (MPA) at the University of Stuttgart in Germany.

DOI: https://doi.org/10.51573/Andes.PPS39.GS.IM.3

Introduction

Injection molding (IM) enables the economical mass-scale production of complex plastic components [1]. Variothermal temperature control is often required for parts with complex geometry or optical requirements. In this process, the mold is heated to a defined, required temperature prior to filling and cooled down afterwards for demolding [2]. In most cases, this is associated with an increase in cycle time. Faster and more efficient heating processes have therefore been the subject of several studies and can be achieved by various methods [3-6]. The least complex variant to implement regarding the mold design, and thus the dominating technology [6], is heating with fluids such as oil or water, since the same temperature control channels can be used for heating and cooling. A disadvantage is that the heat is generated outside the mold, which limits the dynamics of the process [7].

Due to the high degree of design freedom in the production of any component, additive manufacturing (AM) allows a decoupling of the design of cooling channels from the constraints of conventional manufacturing methods [8]. This enables a reduction of the thermal mass of the mold and is increasingly used for isothermal processes.

Fundamentals

Heat transfer must be differentiated into three mechanisms, all of which occur in IM: conduction, convection (also: convective heat transfer), and radiation [9]. The resulting heat flows based on these mechanisms, regarding the injection mold as a system boundary, is shown in Figure 1 [10].

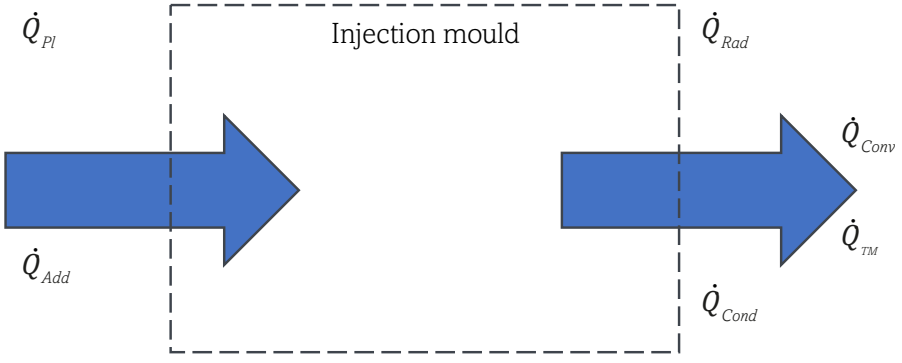

Figure 1. Heat flows at an injection mold (schematic).

The resulting total heat flow balance is given by equation 1 [11]:

DOI: https://doi.org/10.51573/Andes.PPS39.GS.IM.3

$$\dot{Q}_{Pl} - (\dot{Q}_{Cond} + \dot{Q}_{Conv} + \dot{Q}_{Rad}) + \dot{Q}_{Add} - \dot{Q}_{TM} = 0 \quad 1)$$

$\dot{Q}_{Pl}$ describes the heat flow coming into the system by the plastic melt. $\dot{Q}_{Cond}$, $\dot{Q}_{Conv}$ and $\dot{Q}_{Rad}$ are the heat losses due to conduction, convection, and radiation. $\dot{Q}_{Add}$ considers additional heat flows (e.g. using hot runner systems) and $\dot{Q}_{TM}$ gives the heat flow leaving the system with the cooling medium. The calculation of the heat flows is given in [9]. Another important factor is the thermal mass of a mold [7]. The heat Q supplied to or dissipated from a body with a mass m and a specific isobaric heat capacity c_p for a change in temperature ΔT is calculated using equation 2 [9]:

$$Q = c_p \cdot m \cdot \Delta T \quad 2)$$

Assuming Q and c_p are given and constant, the relationship given in equation 3 applies:

$$\frac{1}{m} \sim \Delta T \quad 3)$$

Accordingly, the smaller the mass of a body, the greater the change in temperature. This can also be achieved by thermally decoupling individual mold sections by means of insulating layers [7].

Scope of This Work

In this research, an oil-variothermal temperature control is optimized using AM. By combining the state-of-the-art and new developments, investigations are carried out for additive manufactured mold inserts. The aim of this work is to show suitable measures to make this process more efficient. As shown schematically in Figure 2, this on-going research project is divided into different phases. The overall development of the mold has already been subject in Fitzlaff et al. [12]. This research focuses on the third row of the process: thermal simulation and validation.

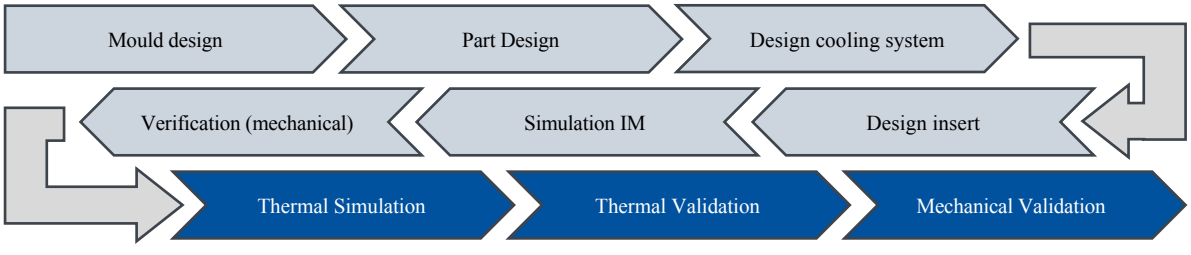

Figure 2. Schematic of the development process.

DOI: https://doi.org/10.51573/Andes.PPS39.GS.IM.3

Preparations and Implementation

Thermal Simulation

The inserts shown in Figure 3 are considered for thermal simulation. Insert V_{01} (a) consists of a component additive manufactured from stainless steel AISI 316L with conformal cooling channels to produce a cup-shaped part. This insert is back-casted with ultra-high performance concrete (UHPC) (in blueish grey). Due to its lower specific heat capacity and density [13], UHPC provides a lower thermal mass compared to the 316L. Furthermore, its lower thermal conductivity provides an additional insulation to the master mold. The V_{02} (b) insert made entirely of 316L bulk material serves as a reference in the simulation. In Fitzlaff et al. [12] a complex arcade like cooling system (ACS) with only 2 mm distance to the cavity surface has been developed. The V_{Gen} variant (c) uses the ACS in addition to an external lightweight structure for the production of a tensile test bar. Two additional reference inserts were modelled for this purpose. $V_{Gen,ref}$ (d) also uses the ACS, but does not have an external lightweight structure. $V_{Gen,ref-cc}$ (e) has an external lightweight structure and uses a conformal cooling system.

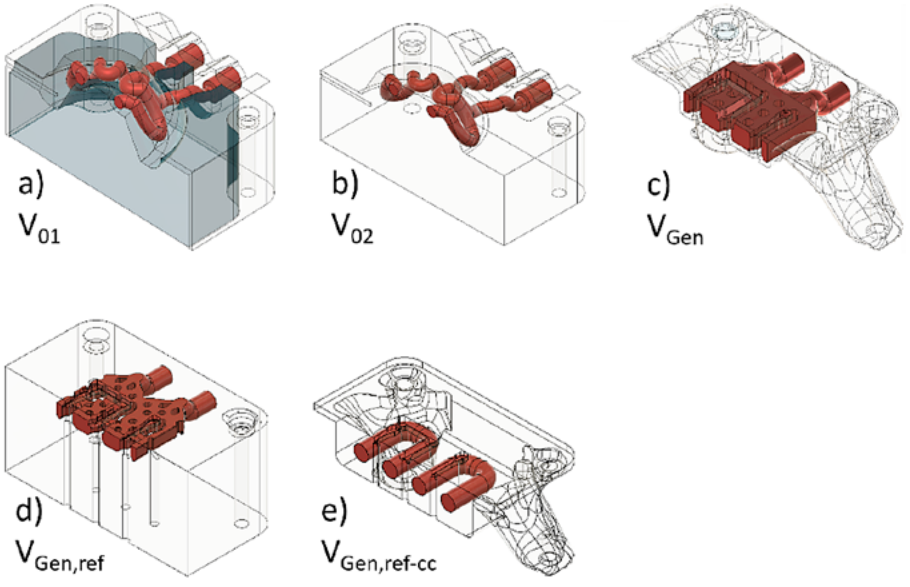

Figure 3. Designed inserts for the simulation (half section, cooling channel in red).

For the thermal simulation, a transient thermal simulation (ATTS) in "Ansys Workbench" (Ansys, Inc., Canonsburg, U.S.) in view of the similarity theory of heat transfer [9,14] is considered. The equations to determine the heat transfer coefficient α are given in [9]. Radiation was considered with an emission coefficient $\varepsilon = 0.36\ldots0.9$, [15]. Natural convection is included using the heat transfer coefficient $\alpha_n = 10\ \frac{W}{m^2 \cdot K}$ [14]. For the simulation, a mold target temperature $\vartheta_t = 125°C$ is

DOI: https://doi.org/10.51573/Andes.PPS39.GS.IM.3

defined for the process for V_{01} and V_{02}, using a fluid temperature ϑ_F = 145°C, limited in these investigations considering the properties of the UHPC used. For the inserts V_{Gen}, $V_{Gen,ref}$ and $V_{Gen,ref\ cc}$ a fluid temperature ϑ_F = 195°C is taken into account, for a mold target temperature of ϑ_t = 170°C. The target temperature already corresponds for V_{01} and V_{02} to the melt temperature of a polyethylene (PE)–Eraclene MS 80 U (Versalis S.p.A., Italy) [16], which was also used in the subsequent IM trials. The parameters of the simulation are summarized in Table 1.

Table 1. Parameters of the thermal simulation.

Variation	Fluid flow $\dot{V}\left[\frac{l}{min}\right]$	Fluid temp. $\vartheta_F[°C]$	Heat coefficient $\alpha\left[\frac{W}{m^2 \cdot K}\right]$
V_{01} and V_{02}	2x4.5	145–60	2359–860
V_{Gen} and $V_{Gen,ref}$	9	195–60	614 – 543
$V_{Gen,ref-cc}$	9	195–60	4318–1061

Thermal Validation

Thermal validation is carried out by taking thermographic images using a FLIR A655sc (Teledyne FLIR, Täby, Sweden) while the mold is open. The temperature is evaluated at ten points across the cavity, see Figure 4. The validation is performed on V_{01} and V_{Gen} with five repetitions each.

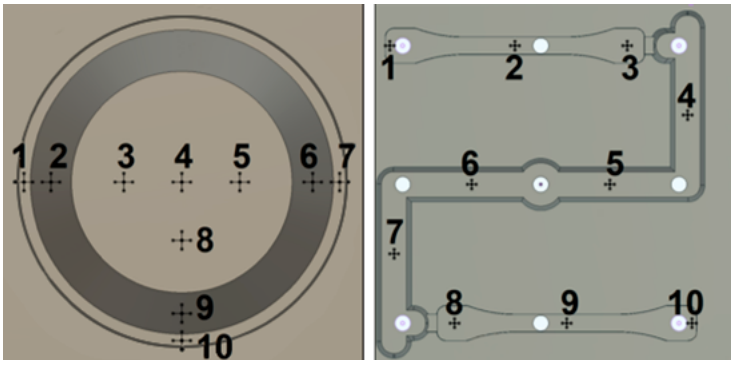

Figure 4. Measuring points for inserts V_{01} (left) and V_{Gen} (right).

Mechanical Validation

The investigations for mechanical validation are performed using the selected inserts on an injection molding machine, Arburg Allrounder 170S, (Arburg GmbH, Loßburg, Germany). The machine parameters are given in Table 2. Prior to the molding, as well as after 10 and 100 cycles, inserts V_{Gen} and V_{01} are inspected for visible damage by means of an optical inspection by the naked eye.

DOI: https://doi.org/10.51573/Andes.PPS39.GS.IM.3

In the same intervals, the inserts are inspected for deformations using a coordinate measuring machine “Prismo 7” (Zeiss GmbH, Oberkochen, Germany). Additional non-destructive examinations using a computer tomography (CT) “Phoenix V|tome|x M”, (Waygate Technologies, Huerth, Germany) enable an evaluation of the material condition inside the inserts and, thus, the detection of material failure.

Table 2. Parameters of the mechanical validation for selected inserts.

	V_{01}	V_{Gen}
clamping force [*kN*]	35	25
injection pressure [*MPa*]	20	16,5

Results and Discussion

Thermal Simulation and Validation

Figure 5(a) gives a comparison of the simulations and measurements for the inserts V_{01} and V_{02} for ϑ_F = 145°C and Figure 5 (b) for the inserts V_{Gen}, $V_{Gen,ref}$ and $V_{Gen,ref-cc}$ with ϑ_F = 195°C, showing the mean value of all points. The minimum and maximum temperatures are represented by error bars.

The measurements show a high consistency of the experiment with the simulation for cooling channels with a regular cross-section (V_{01}) for the considered inserts. The mold target temperature for V_{01} is reached at every point after only 22.2 s, which is consistent with the simulation (25.6 s). According to the simulation, a heating time of 90 s is to be expected for the insert V_{02}.

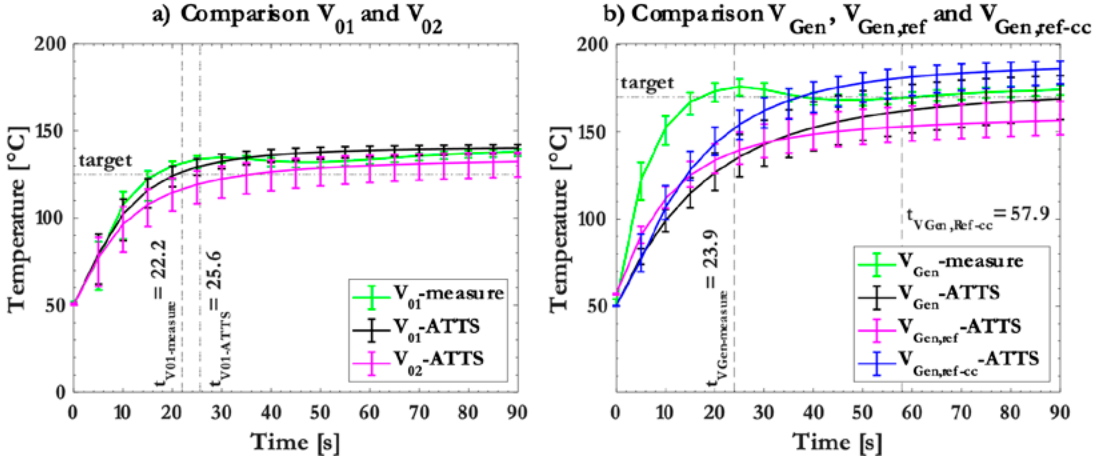

Figure 5. Comparison of V_{01} and V_{02} (a) and V_{Gen}, $V_{Gen,ref}$ and $V_{Gen,ref-cc}$ (b).

DOI: https://doi.org/10.51573/Andes.PPS39.GS.IM.3

For the insert with ACS (V_{Gen}), there is initially a higher deviation from the simulation and the mold target temperature is reached for the first time at every point after only 23.9 s. However, the temperature drops afterwards because remaining cold oil from the backflow of the mold is mixed with the oil from the hot circuit. As a result, the experiment and simulation are again consistent. This drop in temperature has been addressed in Regloplas AG [17] and can be counteracted with a suitable system. According to the simulation, the target mold temperature for the insert $V_{Gen,ref\text{-}cc}$ is reached after 57.9 s. Hence, with optimised peripheral equipment the ACS can outperform a conformal cooling system. Furthermore, the use of an ACS results in a more homogeneous surface temperature. It is also shown that the ATTS approach in the known method is only partially suitable for highly irregular cooling systems, such as the ACS.

These investigations suggest that a reduction of the thermal mass can reduce the required time to reach a target temperature in an oil-variothermal process by up to 50% to 66%.

Mechanical Validation

The measurements on the inserts on the coordinate measuring machine show no noticeable mechanical defects in the area around the cavity, even after 100 cycles. The CT results show no damage to the cooling systems. However, the visual inspection of insert V_{01} revealed the presence of microcracks and hairline fractures in the UHPC after ten cycles. The crack propagation progresses slightly after 100 cycles. Due to the high intensity of the x-ray beam, the CT is limited to further characterize the extent of these cracks. The hairline fractures in the concrete do not result in immediate failure of the mechanical stability of the insert. Endurance tests with periodic monitoring can provide a more precise prediction of the long-term stability of such an insert. Further methods for a reliable non-destructive testing must be evaluated.

Conclusion

The approaches used in this work show the possibility of reducing the cycle time for an oil-variothermal IM process and thus an improvement in efficiency. In simulation studies, the reduction of the thermal mass, the selection of materials with low thermal conductivity, and the reduction of contact surfaces between the insert and the master mold show a reduction in heat losses.

The simulative approach using the similarity theory of heat transfer is only of limited significance for complex cooling systems and therefore is initially less consistent. This discrepancy is compensated over time by a temperature drop in the system due to the cold oil in the return flow.

It has also been shown that the distance from the cooling system to the cavity can be reduced by using a complex, large-area cooling system, while still enabling a homogeneous temperature. This also has a positive effect on shortening the temperature control time. The use of thermally optimized

DOI: https://doi.org/10.51573/Andes.PPS39.GS.IM.3

inserts such as those developed in this research can therefore further increase the efficiency of a fluid-variothermal process and thus contribute to saving energy and cycle time.

References

1. C. Hopmann et al., *Spritzgießwerkzeuge: Auslegung, Bau, Anwendung,* 7th ed. München: Hanser; Ciando, 2018.
2. C. Bonten, *Kunststofftechnik: Einführung und Grundlagen,* 3rd ed. München: Hanser, 2020.
3. M. Deckert, "Beitrag zur Entwicklung eines hochdynamischen variothermen Temperiersystems für Spritzgießwerkzeuge," Dissertation, Technische Hochschule Chemnitz, Chemnitz, 2012.
4. S. Jacob, "Thermo-KonSens: Sachbericht (Schlussbericht) zum Verwendungsnachweis zu FuE Vorhaben," Leipzig, 2018.
5. M. Zülch, *Temperierung von Spritzgusswerkzeugen durch vollständig integrierte induktive Beheizung.* Dissertation. Stuttgart: IKFF, 2011.
6. W. Berlin et al., "Variothermie im Wandel der Zeit," *Kunststoffe*, vol. 109, no. 08, pp. 20-23, 2019.
7. C. Bleesen, "Variotherme Spritzgießtechnologie zur Beeinflussung tribologischer Eigenschaften thermoplastischer Formteile," Dissertation, TU Chemnitz, Chemnitz, 2016.
8. A. Kirchheim, "Additive Fertigung generiert Mehrwert," *Maschinenbau*, vol. 46, no. 8, pp. 32–33, 2018.
9. P. Stephan, S. Kabelac, M. Kind, D. Mewes, K. Schaber, and T. Wetzel, Eds., *VDI Wärmeatlas,* 12th ed. Berlin: Springer Vieweg, 2021.
10. G. Menges, G. Wübken, and B. Horn, "Einfluß der Verarbeitungsbedingungen auf die Kristallinität und Gefügestruktur teilkristalliner Spritzgußteile," *Colloid and Polymer Science*, vol. 254, no. 3, pp. 267–278, 1976.
11. M. Berghoff, "Perspektiven bei der Temperierung von Problemzonen im Werkzeug," Iserlohn, n. d.
12. M. Fitzlaff, G. Jäkle, and B. Gundelsweiler, "Additiv gefertigte Werkzeugeinsätze für den variothermen Spritzgießprozess," *Schriftenreihe / Institut für Kunststofftechnik, 28. Stuttgarter Kunststoffkolloquium: 28. Februar–2. März 2023*, C. Bonten and M. Kreutzbruck, Eds., Stuttgart: IKT Universität Stuttgart, 2023, pp. 259–266.
13. T. Litwin and B. Gundelsweiler, "Induktives Heißpressen von elektrisch leitfähigen Compound Werkstoffen," in *27. Stuttgarter Kunststoffkolloquium*, C. Bonten and Kreutzbruck Marc, Eds., 1st ed., Stuttgart, 2021, pp. 163–168.
14. H. Gröber and S. Erk, *Die Grundgesetze der Wärmeübertragung,* 3rd ed. Berlin: Springer, 1988.
15. KLEIBER Infrared GmbH, *Emissionsgradtabelle* Accessed: Nov. 6 2023. [Online]. Available: https://www.kleiberinfrared.com/index.php/de/amanwendungen/emissionsgrade.html
16. Versalis S.p.A, "Eraclene MS 80 U BCA: Technical Data Sheet," Milano, 2021.
17. Regloplas AG, *Einsparpotenzial bei der dynamischen Temperierung* Accessed: May 28 2024. [Online]. Available: https://www.regloplas.com/de/technologien/temperier-technologie/einsparpotenzial-bei-der-dynamischen-temperierung

DOI: https://doi.org/10.51573/Andes.PPS39.GS.IM.3

GENERAL SYMPOSIA | INJECTION MOLDING

Material Selection for Injection Molding Hollow Microneedles

Tim Evens, Pol Vanwersch, Sylvie Castagne and Albert Van Bael

DOI: https://doi.org/10.51573/Andes.PPS39.GS.IM.4

December 2024

Material Selection for Injection Molding Hollow Microneedles

Tim Evens, Pol Vanwersch, Sylvie Castagne and Albert Van Bael[1]

Abstract: Hollow microneedles are designed to perform intradermal medical substance delivery or fluid extraction, with polymers standing out as cost-effective materials for mass production via injection molding. However, existing research lacks a comparative analysis of different polymers in terms of processability and performance in skin penetration tests. This study addresses this gap by evaluating hollow microneedles fabricated from five biocompatible thermoplastic materials: polycarbonate (PC), polybutylene terephthalate (PBT), polylactic acid (PLA), polyamide 12 (PA12), and glass-fiber reinforced polyarylamide (PARA). Significant differences in replication fidelity were found among the thermoplastics, with a higher calculated solidification time resulting in better replication fidelity due to extended deformability during the packing phase. PBT microneedles deformed during demolding and were excluded from penetration tests. Penetration tests on piglet ears showed no penetration for PA12 and PLA microneedles due to deformation of the needles. PARA demonstrated consistent penetration results, while PC exhibited an inconsistent penetration behavior, with some needles successfully penetrating while others deformed. High mechanical properties were found to be critical for achieving consistent and successful penetration.

Keywords: Hollow Microneedles, Injection Molding, Material Selectionv

1 The authors Tim Evens (tim.evens@kuleuven.be), Pol Vanwersch (pol.vanwersch@kuleuven.be), and Albert Van Bael (albert.vanbael@kuleuven.be) are affiliated with the Department of Materials Engineering at the KU Leuven University in Belgium. Sylvie Castagne (sylvie.castange@kuleuven.be) and Pol Vanwersch are also affiliated with the Department of Mechanical Engineering and Flanders Make@KU Leuven at the same university.

DOI: https://doi.org/10.51573/Andes.PPS39.GS.IM.4

Introduction

Hollow microneedles are miniature needle-like structures designed to perform intradermal medical substance delivery or fluid extraction [1]. Over the years, various types of materials, including silicon, metals, ceramics, and polymers have been reported in literature for manufacturing microneedles [2]. Polymers particularly stand out as an excellent material for microneedles, as they can be cost-effective for mass production through injection molding [3]. While several polymers have been proposed in literature for microneedle fabrication, there is a notable absence of studies comparing their processability and performance during skin penetration tests. Existing research tends to highlight individual polymers, emphasizing their advantages without providing a systematic exploration of differences among various candidates.

This study addresses this gap by conducting a comprehensive analysis of hollow microneedles fabricated from five biocompatible thermoplastic materials: polycarbonate, polybutylene terephthalate, polylactic acid, polyamide 12, and glass-fiber reinforced polyarylamide. First, each material is assessed for its injection molding characteristics and replication fidelity. Secondly, the penetration behavior, an essential aspect of microneedle functionality, is tested through penetration tests on piglet ears.

Materials and Methods

Materials

The selected mold material is a low corrosion tool steel AISI 420, which is a common mold material within polymer injection molding. Five biocompatible thermoplastic materials were selected for this study: polyamide 12 (PA12, Vestamid Care ML67, Evonik), polycarbonate (PC, Lexan HPX8R, SABIC), polybutylene terephthalate (PBT, Valox HC325HP, SABIC), polylactic acid (PLA, MedEco ICB, BioVox), and 50% glass-fiber reinforced polyacrylamide (PARA, Ixef HC1022, Syensqo). Table 1 presents material properties of the thermoplastics, sourced from the suppliers and the material databases of Autodesk Moldflow 2023 and Moldex3D 2023.

Table 1. Material properties of the thermoplastics, sourced from the material suppliers and the material databases of Autodesk Moldflow 2023 and Moldex3D 2023.

	PA12	PC	PBT	PLA	PARA
Density (kg/m³)	1033	1100	1316	1240	1622
Young's Modulus (MPa)	1080	2400	2550	3450	19500
Tensile strength (MPa)	41	59	60	65	280
Thermal conductivity (W/m °C)	0.235	0.185	0.146	0.225	0.300
Specific heat (J/g °C)	2098	1128	1259	1167	1766
No-flow temperature (°C)	150	167	200	92	190

DOI: https://doi.org/10.51573/Andes.PPS39.GS.IM.4

Representation of the Process Chain

The process chain for manufacturing and testing hollow polymer microneedles developed by Evens et al. is illustrated in Figure 1 [4]. First, a micromachining system with a laser source ablates hollow microneedle cavities into a mold insert. The insert is then positioned within the mold housing. During the injection molding process, the polymer melt is forced into the laser-ablated cavities, forming the microneedles. Finally, the functionality of the microneedles is evaluated through skin penetration experiments.

Injection Molding

The injection molded part selected for this study is a 60×55×1.5 mm flat plate, featuring 6 different microneedles arranged in a 2×2 array. By design, these microneedles vary in shape and dimensions, with lengths ranging from 1000 µm to 1700 µm. They are centrally positioned on the plate, located 3 mm from the edge opposite to the gate. The polymer is injected through a hot runner positioned 17 mm from the edge of the plate. The mold insert corresponding to this product was designed and manufactured in a previous study [5]. Injection molding is done on an Engel ES 200/35 HL injection molding machine. The injection molding parameters for each thermoplastic are given in Table 2 and are defined to achieve a high replication fidelity. The geometry of the replicated thermoplastic microneedles is assessed using a Keyence VH-S30 digital microscope.

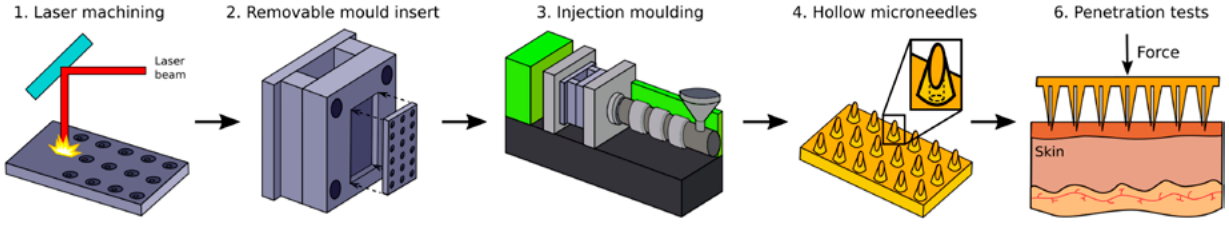

Figure 1. Illustration of the process chain to produce and test hollow polymer microneedles.

Table 2. Process parameters for injection molding.

	PA12	PC	PBT	PLA	PARA
Barrel temperature (°C)	195	310	270	210	290
Volumetric injection rate (cm^3/s)	150	150	150	150	150
Holding pressure (MPa)	95	71	95	71	95
Mold temperature (°C)	145	110	165	60	170

DOI: https://doi.org/10.51573/Andes.PPS39.GS.IM.4

The geometry of the replicated thermoplastic microneedles is assessed using a Keyence VH-S30 digital microscope. Six injection molded samples are collected and six microneedles are measured on each sample. The average of these measurements along with the standard deviation is reported in the results.

Penetration Tests

The penetration tests are designed to gain insights into the mechanisms of skin piercing and to compare the microneedles to each other in different thermoplastics. A piglet ear is used as a skin model due to its similitude to human skin [6]. For the penetration tests, a motorized tension and compression tester (BZ2.5/TS1S, Zwick) equipped with a 500-N load cell is used. For each thermoplastic, the skin penetration tests were conducted using needle type 5, the sharpest needle, (as shown in Figure 2). Each test was repeated three times using a new, unused needle. The penetration testing procedure involves placing a piglet ear beneath a downward-facing microneedle. The needle is slowly lowered towards the skin at 1 mm per minute until contact, identified by a 0.01 N threshold force. Upon contact, the needle is descended into the skin at 2 mm per minute while recording force and displacement at a rate of 1 MHz. A penetration event is defined by a sudden decrease in force, as described in [5].

Results and Discussion

Microneedle Replication Through Injection Molding

Figure 2 shows microscopic images of the six different microneedles replicated in five different thermoplastics. A clear difference in geometry can be observed among the various types of microneedles. Additionally, there is a noticeable variation in replication fidelity between the different thermoplastics, which will be further discussed in the following section. During the injection molding experiments, deformation of PBT microneedles could be observed during demolding. An example of this is Needle 2 in Figure 2. This deformation is not due to insufficient solidification, as increasing the cooling time significantly did not resolve the issue. Therefore, PBT has been excluded from the penetration experiments. Furthermore, since the PARA compound is glass-fiber reinforced grade, fibers can be seen protruding from the needles. As these fibers might cause complications if they break off in the skin during penetration, they should therefore be the subject of further analysis.

DOI: https://doi.org/10.51573/Andes.PPS39.GS.IM.4

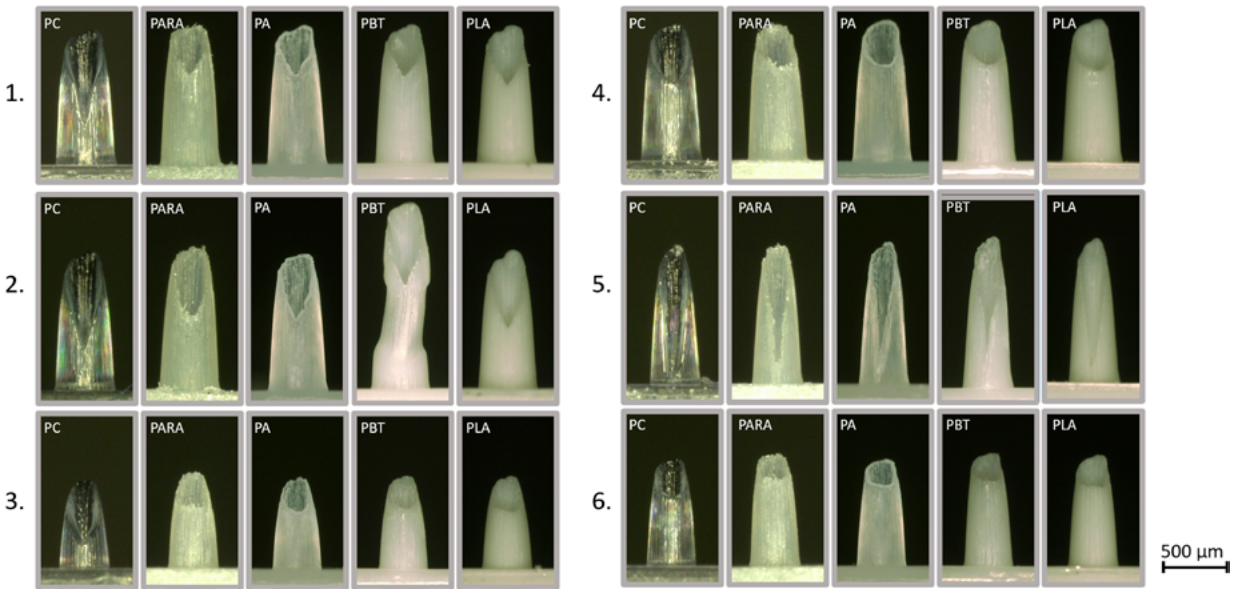

Figure 2. Microscopic images of the six different microneedles replicated in the different thermoplastics.

Figure 3 shows the average replication fidelity of the needle length and ridge height (the vertical dimension of the surrounding ridge structure) for each of the thermoplastics, alongside a micro computed tomography slice of a hollow microneedle cavity. Difference in replication fidelity between the needle length and ridge height are evident across all thermoplastics. This difference in replication fidelity is caused by the fact that the aspect ratio of the ridge-forming trench (forming the ridge height) is higher than that of the main needle cavity. This increased surface/volume ratio leads to faster freezing of the polymer and thus a lower replication fidelity. A similar relationship between aspect ratio and replication fidelity was noted by Evens et al. [7].

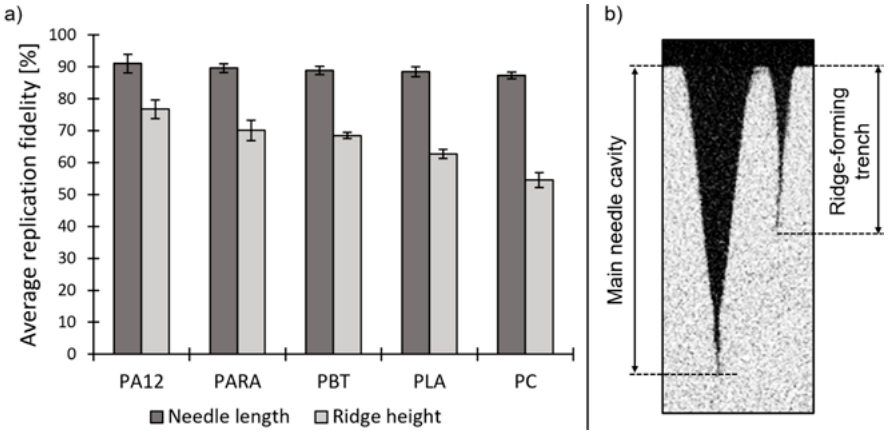

Figure 3. (a) Average replication fidelity of the needle length and ridge height for each of the thermoplastics. (b) Illustration of a micro computed tomography slice of a hollow microneedle cavity.

DOI: https://doi.org/10.51573/Andes.PPS39.GS.IM.4

Difference in Microneedle Replication Fidelity Between the Thermoplastics

Each of the thermoplastics has different material properties, which affects the replication fidelity during injection molding. Using Equation 1, we can estimate the time (t) required for the average temperature of the polymer to reach the no-flow temperature ($T_{no\text{-}flow}$), as shown in [8],

$$t = \frac{a^2}{\pi^2 \cdot \alpha} \cdot ln\left[\frac{8}{\pi^2} \cdot \left(\frac{T_{injection} - T_{mould}}{T_{no-flow} - T_{mould}}\right)\right] \quad 1)$$

with a the thickness of the polymer part, α the thermal diffusivity (calculated using the thermal conductivity, specific heat, and density), $T_{injection}$ the injection temperature, and T_{mould} the mold temperature. Using this equation and the data from Table 1 and Table 2, the time required for PA12, PARA, PBT, PLA, and PC to reach the no-flow temperature are 6.9 s, 5.4 s, 3.6 s, 3.1s, and 1.8 s, respectively. Figure 4 now shows the average replication fidelity of (a) the needle length and (b) the ridge height, along with the time to reach the no-flow temperature for each of the thermoplastics. A clear trend can be observed between the solidification time and the replication fidelity, where a longer solidification time leads to a higher replication fidelity. With a longer solidification time, the polymer melt remains at a higher temperature during the packing phase, ensuring the polymer remains deformable and can continue to fill the microneedle cavity. Conversely, when the solidification time is short, the skin layer of polymer solidifies quickly, preventing further filling of the microneedle cavity.

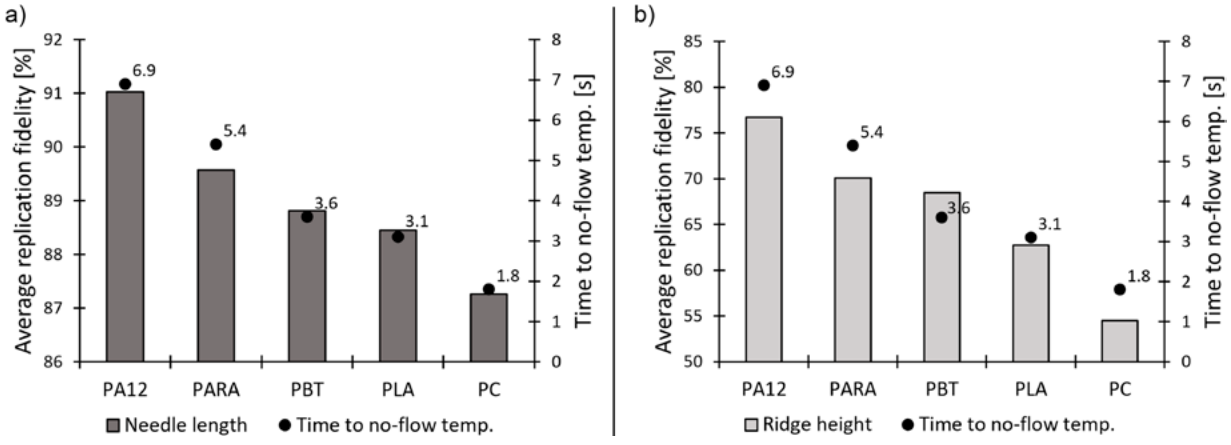

Figure 4. Average replication fidelity of (a) the needle length and (b) the ridge height, together with the time to reach the no-flow temperature for each of the thermoplastics.

DOI: https://doi.org/10.51573/Andes.PPS39.GS.IM.4

Penetration Performance of the Microneedles

Figure 5 shows the force-displacement graphs for penetration tests performed on single microneedles in (a) PA12, (b) PARA, (c) PLA, and (d) PC. In the cases of PA12 (Figure 5[a]) and PLA (Figure 5[c]), no drop in force is observed in the graphs, indicating that there is no penetration event. Microscopic inspection of the microneedles after the penetration tests clearly revealed deformation of the needles, indicating that the needles do not maintain their structural integrity during the penetration test. For PARA (Figure 5[b]), a clear drop in force is consistently observed between 3 to 4 N in every graph. Microscopic inspection of a needle before and after the penetration tests shows no visible deformation. However, it is not possible to determine whether the fibers protruding from the surface were broken or left in the skin after the penetration tests. This issue necessitates further investigation to confirm the integrity and safety of PARA microneedles. For PC (Figure 5[d]), two of the three force-displacement curves show a clear drop in force, occurring between 3.5 to 2.2 N, suggesting that penetration occurs inconsistently. The needle that did not show a drop in force was found to be deformed after the penetration test, indicating an inconsistent performance of PC microneedles.

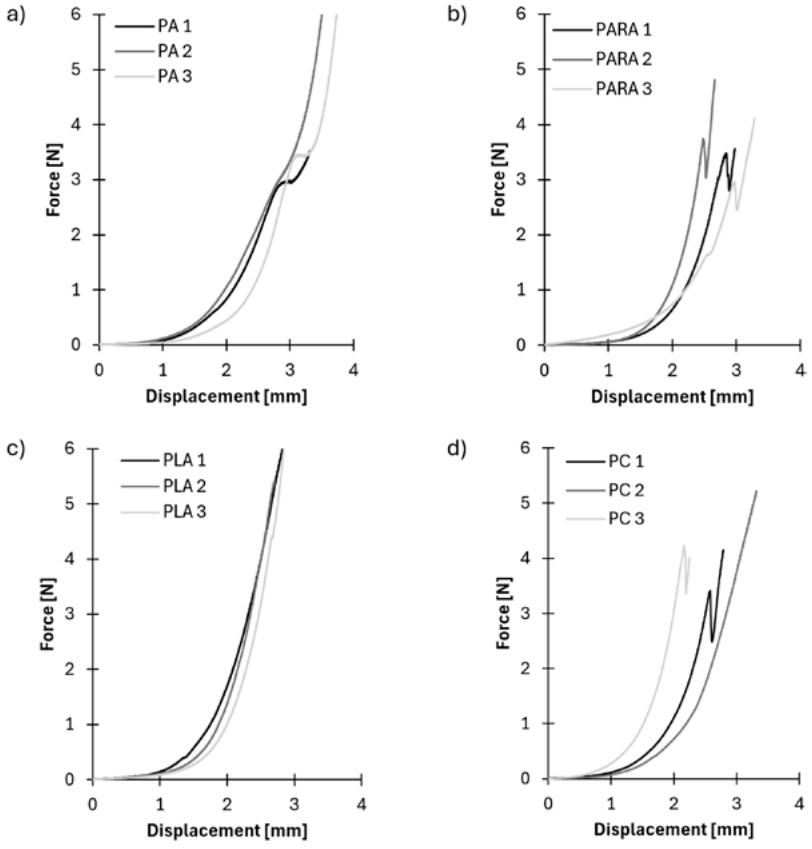

Figure 5. Force-displacement graphs for penetration tests performed on single microneedles in (a) PA12, (b) PARA, (c) PLA, and (d) PC.

DOI: https://doi.org/10.51573/Andes.PPS39.GS.IM.4

A notable trend is observed between the mechanical properties of the thermoplastics, as shown in Table 1, and the penetration success rate. This correlation suggests that achieving consistent and successful penetration requires thermoplastics with higher mechanical properties, particularly the Young's modulus and tensile strength, as seen with PARA.

Conclusion

In this study, we compared five different thermoplastics – PA12, PC, PBT, PLA, and PARA – based on their injection molding characteristics and skin penetration behavior. Significant differences in replication fidelity were observed, influenced by the solidification time of the polymers. Higher solidification times led to better replication fidelity due to extended deformability during the packing phase. Penetration tests revealed that high mechanical properties are essential for successful penetration. PARA exhibited consistent penetration but requires further investigation on the safety of protruding glass fibers. PA12 and PLA microneedles did not penetrate due to the microneedles deforming during the penetration, and PC showed inconsistent performance.

Acknowledgments

This work was funded by the KU Leuven Interdisciplinary Network project IDN/20/011 MIRACLE, as well as the Fonds Wetenschappelijk Onderzoek (FWO)–Vlaanderen SBO S003923N project and SB fellowship 1S31022N. The authors would like to thank Olivier Malek from the company Sirris for laser ablating the microneedle cavities in the mold inserts, and the companies SABIC, Evonik, BioVox, and Syensqo for providing the thermoplastic injection molding materials.

References

1. E. Larrañeta, et al., "Microneedle arrays as transdermal and intradermal drug delivery systems", *Materials Science and Engineering R Reports*, vol. 104, pp. 1–32, 2016.
2. A. Tucak, et al., "Microneedles: Characteristics, materials, production methods and commercial development", *Micromachines*, vol. 11, 2020.
3. T. Evens, et al., "Comparing the Replication Fidelity of Solid Microneedles Using Injection Compression Moulding and Conventional Injection Moulding", *Micromachines*, vol. 13, 2022.
4. T. Evens, et al., "Producing Hollow Polymer Microneedles Using Laser Ablated Molds in an Injection Molding Process", *Journal of Micro and Nano Manufacturing*, vol. 9, pp. 1–9, 2021.
5. P. Vanwersch, et al., "Design, fabrication, and penetration assessment of polymeric hollow microneedles with different geometries", *The International Journal of Advanced Manufacturing Technology*, vol. 132, pp. 533–551, 2024.

6. J.C. Wei, et al., "In vivo, in situ and ex vivo comparison of porcine skin for microprojection array penetration depth, delivery efficiency and elastic modulus assessment", *Journal of the Mechanical Behavior Biomedical Materials*, vol. 130, 2022.

7. T. Evens, et al., "Predicting the replication fidelity of injection molded solid polymer microneedles", *Journal of the Mechanical Behavior of Biomedical Materials*, vol. 37, pp. 237–254, 2022.

8. K.A. Stelson, "Calculating cooling times for polymer injection moulding", *Proceedings of the Institution of Mechanical Engineers, Part B: Journal of Engineering Manufacture*, vol. 217, pp. 709–713, 2003.

DOI: https://doi.org/10.51573/Andes.PPS39.GS.IM.4

GENERAL SYMPOSIA | INJECTION MOLDING

Modeling of Polymer Processing of Thermoplastic Polymers: Application to the Injection Molding Process

Vito Speranza, Sara Liparoti, Giuseppe Titomanlio and Roberto Pantani

DOI: https://doi.org/10.51573/Andes.PPS39.GS.IM.5

December 2024

Modeling of Polymer Processing of Thermoplastic Polymers: Application to the Injection Molding Process

Vito Speranza, Sara Liparoti, Giuseppe Titomanlio and Roberto Pantani[1]

Abstract: In the transformation operations of polymeric materials, there is a complex interplay between transport phenomena and crystallization. In particular, the polymer in the molten state is a viscoelastic fluid with rheological parameters depending on temperature, pressure, crystallinity, and molecular stretch. The molecular stretch is a tensor variable with values determined by the history of the flow, temperature, and pressure fields. During polymer processing operations, several phenomena proceed simultaneously by interacting with each other. The combination and interplay of the models that describe each of the phenomena mentioned above provides the evolution of all the relevant quantities and, therefore, also the overall model that describes the evolution of the solidification that generally proceeds starting from the walls (where the temperature is lower and furthermore the shear is higher). This work presents an overall model of the behavior of an isotactic polypropylene during the injection molding process. The model includes the kinetics of spherulitic and fibrillar crystallization and their dependence on the level of molecular stretch; the modeling is carried out up to the prediction of molecular stretch and morphology distributions along the molded part thickness. The model predictions satisfactorily describe the evolution of temperature and pressure during the process and the fundamental aspects of the morphology distribution inside the part.

Keywords: Rapid Heat Cycle Molding (RHCM), Crystallization Kinetics Model, Flow Induced Crystallization, Spherulites' Evolutions, Fibers' Evolutions

1 Vito Speranza (corresponding author)(vsperanza@unisa.it), Sara Liparoti (sliparoti@unisa.it), Giuseppe Titomanlio (gtitomanlio@unisa.it) and Roberto Pantani (rpantani@unisa.it) are affiliated with the Department of Industrial Engineering at the University of Salerno in Italy.

DOI: https://doi.org/10.51573/Andes.PPS39.GS.IM.5

Introduction

Injection molding is a largely adopted transformation process to quickly produce parts with high dimensional accuracy that can be used for a wide range of applications (i.e. automotive, biomedical etc.). Polypropylene (iPP) is one of the most widespread semi-crystalline polymers adopted for such a process. During injection molding, the polymer is melted and is then forced into a (generally) cold cavity in which it solidifies and crystallizes. Finally, it completes its cooling allowing for the part ejection. Performances of the parts can be tailored by properly changing the process conditions. In particular, upon increasing the mold temperature a fast filling of the cavity and a reduction of the molecular stretch can be achieved. However, an increase of the cooling time (and thus of the production time) can occur. To prevent this drawback, the cavity surface temperature can be rapidly heated and cooled during the process. Rapid heat cycle molding (RHCM) processes are designed by adopting several heat sources such as cartridge heaters, steam, or induction coil [1-4]. The part surface defects reduce in the presence of the RHCM and the reproduction accuracy improves with a negligible increase in the cycle time. In semi-crystalline molded parts, the final properties, such as mechanical properties and volumetric shrinkage, are determined by the operating parameters that in turn influence the morphology and crystallinity developed during the process. Several approaches [6,7] were adopted to predict the final properties of the parts by including the crystallization kinetics in the models adopted for injection molding. In particular, a multiscale approach was adopted by Kim and Jeong [7] to predict the spherulite formation. Temperature and flow field were simulated at the macroscale and spherulite growth at the mesoscale. However, these models neglect the material properties evolution induced by the process and the interplay between the material properties.

This work proposes a model for the formation of different morphologies (spherulites and fibers) in an iPP. The model considers the effect of injection molding variables (temperature and pressure) and is coupled with a macromolecular evolution model to consider the effect of flow on crystallinity evolutions through the molecular stretch. The model for the crystallization kinetics has been implemented in the model for the description of the injection molding process previously developed at the University of Salerno (namely UNISA code) [7]. The UNISA code accounts for the interplay between the crystallinity and material properties (i.e. density, viscosity, and relaxation time). The robustness of the model has been proven through comparison with the experimental results in terms of morphology developed along the sample thickness.

Materials and Methods

Injection molding tests were carried out with a commercial grade iPP supplied by Basell, Ferrara, Italy. An extensive characterization campaign was conducted on the iPP. A 1.5 mm thick rectangular cavity was adopted for the tests. To analyze the effect of the cavity surface temperature on the morphology distribution in the part, the conventional injection molding process was coupled

DOI: https://doi.org/10.51573/Andes.PPS39.GS.IM.5

with a rapid heating device. Only a first part of the cavity was covered by the heaters. The RHCM process was implemented by locating thin heaters (240 μm) on both cavity surfaces. A 100 μm steel layer was adopted in order to protect the heaters from the melt contact. A single cavity surface temperature (i.e. 150°C) and two different activation times for the heaters (i.e., 1.3 s and 12 s) were adopted for the injection molding tests.

The numerical simulation of the performed injection molding tests was conducted with the UNISA code, a software developed at the University of Salerno. Such a code considers the filling, packing, and cooling stages. It describes the RHCM process by simultaneously solving the energy balance in both the polymer and the heater. The UNISA code adopts a complete characterization of the iPP. Two competing crystallization kinetics are considered: one for the meso phase and another for the alpha spherulitic phase. The effect of flow on the alpha phase is accounted for. The effect of crystallinity on polymer density, viscosity, and relaxation time is also considered. To predict the different morphologies (fibers and spherulites) of the iPP alpha phase, a recent purpose-built kinetics model [8] was implemented in the UNISA code. The kinetics model describes the competing evolution of fibers and spherulites, for the alpha phase. The effect of flow on nucleation and growth processes of both morphologies is accounted for.

Results

Before checking if simulations correctly describe the final morphology distribution in the part, we will analyze the process evolutions during the process. Figure 1 shows predicted evolutions of process variables for the condition with 150°C cavity surface temperature and 1.3 s heating activation time. It considers the evolutions in a position covered by the heating system, at 15 mm downstream from the cavity entrance.

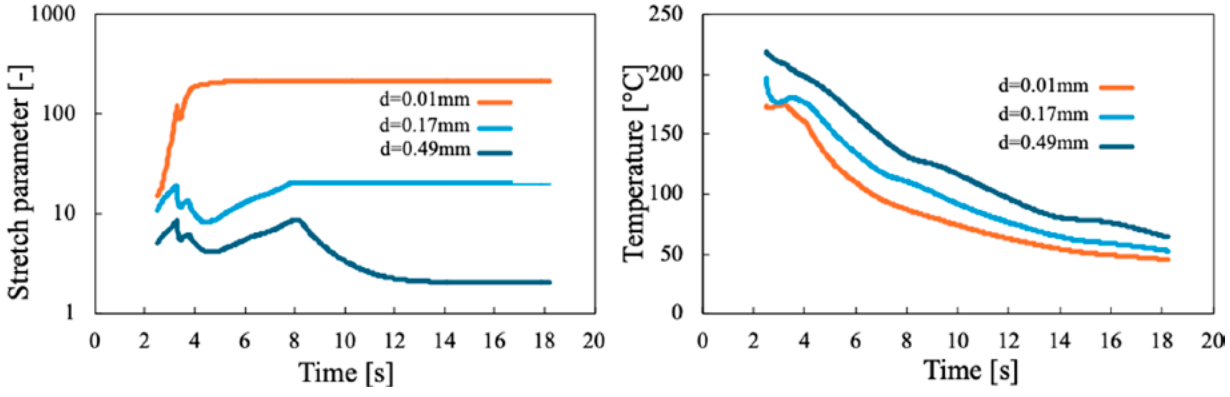

(a) (b)

DOI: https://doi.org/10.51573/Andes.PPS39.GS.IM.5

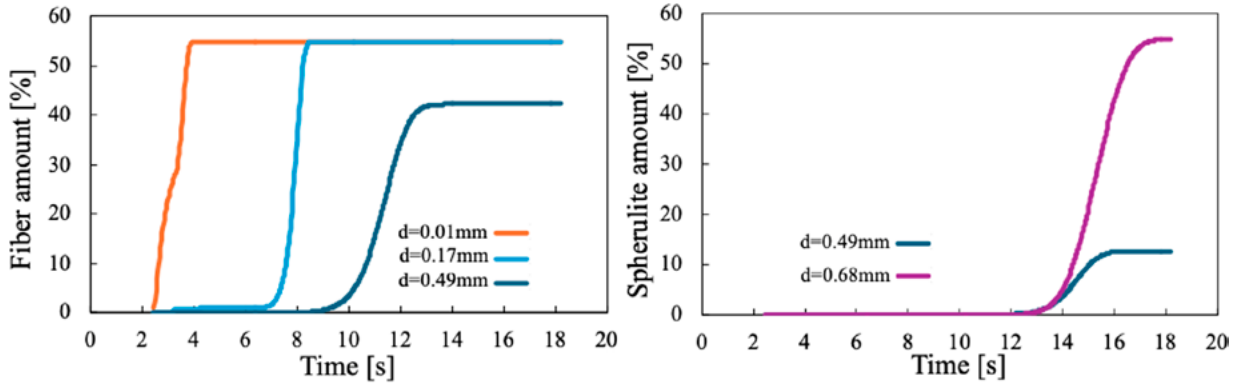

(c) (d)

Figure 1. Predictions at 15 mm downstream from the cavity entrance under the heater system, for the condition with 150°C cavity surface temperature and 1.3 s activation time: (a) stretch parameter, (b) temperature, (c) fiber amount, and (d) spherulite amount.

Figures 1(a-d) report the evolutions of the calculated molecular stretch parameter, temperature, fiber formation, and spherulite formation, respectively, at different distances, d, from the sample surface (0 mm and 0.75 mm identify the sample surface and the sample mid-plane, respectively). The evolutions start from about 2 s, i.e., the time required to the flow front to reach the position. The activation of the heater for the first 1.3 s, after the melt touches the position, limits the cooling to about 150°C for the outer layers of the sample. In Figure 1(a), during the filling, namely up to about 4 s, the stretch increases close to the sample surface (i.e., d=0.01 mm). The fiber formation (see Figure 1[c]) immediately starts and during the filling reaches the maximum allowable degree of crystallinity, namely 55%. The molecular stretch exhibits a plateau when the fibers completely fill the space. Even if the temperature is high, due to the low packing flow and the long relaxation times, induced by the high level of crystallinity, the molecular stretch is essentially constant. In the internal layers (i.e., 0.17 mm and 0.49 mm), the stretch increase during the filling is followed by a stretch decrease during the early stage of packing: the relaxation phenomena, due to the high temperature and the crystallinity absence, efficiently counteracts the effect of flow. During the later stage of packing, although the temperature continues to cool down (see Figure 1[b]), the effect of the packing flow overcomes the relaxation phenomena, determining an increase of the molecular stretch. At d=0.17 mm the fiber formation starts later, at around 6 s, and completes at the end of the packing phase, namely at 8 s. Due to the highest level of crystallinity and the absence of flow, which is characteristic of the cooling phase, the stretch remains constant. Closer to the sample mid-plane, due to the reduced flow and thus low level of stretch, the fiber formation starts during the cooling phase. The simultaneous formation of spherulites (see Figure 1[d]), however, competes with the formation of fibers and both fibers and spherulites fill the available amorphous space. Only spherulites form for distances higher than 0.5 mm.

DOI: https://doi.org/10.51573/Andes.PPS39.GS.IM.5

Figures 2(a-d) show, for the same molding condition, predicted evolutions of variables in the cavity at 100 mm downstream from the cavity entrance, i.e., well outside of the heating system.

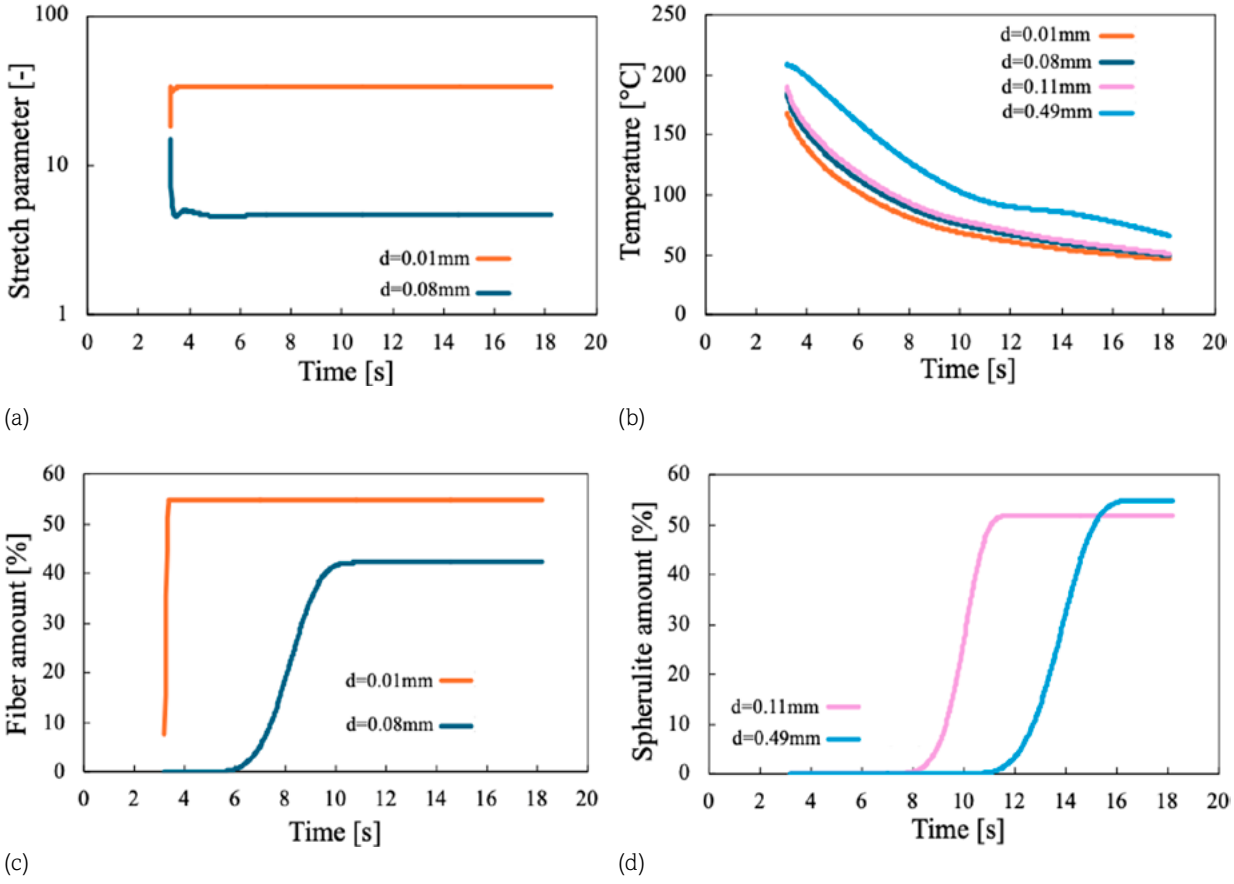

Figure 2. Predictions at 100 mm downstream from the cavity entrance outside of the heating system, for the condition with 150°C cavity surface temperature and 1.3 s activation time: (a) stretch parameter, (b) temperature, (c) fiber amount, and (d) spherulite amount.

The direct contact of the polymer with the unheated mold surface causes a continuous rapid cooling of the material even during the first second of the process (see Figure 2[b]). Due to proximity to the cavity tip, the flow fields are much less intense and the molecular stretch remains remarkably lower (see Figure 2[a]) with respect to the previous position depicted in Figure 1(a). However, very close to the sample surface, a sharp but small increase of the stretch can be observed as soon as the polymer reaches the position; a subsequent stretch plateau corresponding to the fiber evolutions can also be observed. At d=0.08 mm, the level of stretch permits the fiber formation only after 6 s, with a final crystallinity level below 55% (see Figure 2[c]). At inner layers, as the distance from the sample surface increases, only the formation of spherulites occurs with an increasing crystallization time (see Figure 2[d]). Interestingly, the temperature evolution shows an inflection

DOI: https://doi.org/10.51573/Andes.PPS39.GS.IM.5

(see Figure 2[c]), especially at d=0.49 mm, when the material locally crystallizes due to the latent heat generation term accounted for in the energy balance.

Figures 3(a-d) show, at the same position along the flow path considered in Figure 1, i.e., 15 mm downstream from the cavity entrance, the evolutions calculated for the condition with 150°C cavity surface temperature and 12 s heating time.

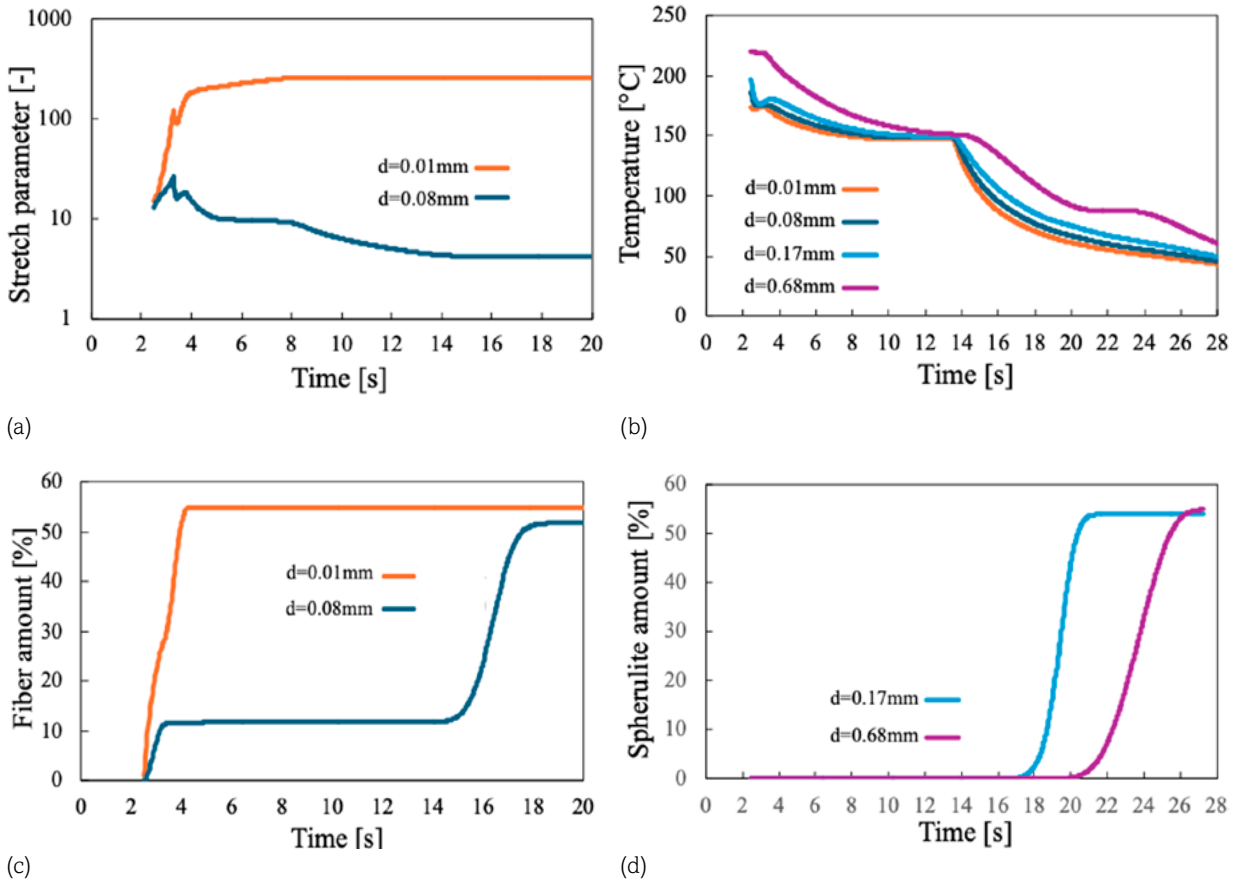

Figure 3. Predictions at 15 mm downstream from the cavity entrance under the heater system, for the condition with 150°C cavity surface temperature and 12 s activation time: (a) stretch parameter, (b) temperature, (c) fiber amount, and (d) spherulite amount.

Close to the sample surface at d=0.01 mm, the stretch evolution (see Figure 3[a]) and fiber formation (see Figure 3[c]) correspond to the ones showed in Figure 1(a) and Figure 1(c), namely calculated for the condition with 1.3 s heating time. The long heating time induces a plateau at about 150°C in the temperature evolutions (see Figure 1[b]). Therefore, after the early stage of packing, at a distance of 0.08 mm from the sample surface, the stretch remains essentially constant (the low packing flow is actively counteracted by the relaxation). The fiber formation starts during filling (see Figure 3[c]),

DOI: https://doi.org/10.51573/Andes.PPS39.GS.IM.5

when the stretch increases, and presents a plateau due to the nearly constant temperature and low stretch; it completes during the second cooling that occurs at the heater deactivation, namely at about 14 s. At d=0.17 mm, spherulite formation occurs during the second cooling (see Figure 3[d]) and all the available space is occupied by spherulitic structures. In the internal layers close to the sample mid-plane, spherulitic crystallization occurs later. An inflection in the temperature evolution is observed when the material locally crystallizes (see Figure 3[b]).

Finally, comparisons between polarized optical micrographs (POM) captured at 15 mm downstream from the cavity entrance and predicted distributions of spherulites and fibers along the sample half thickness are shown in Figure 4.

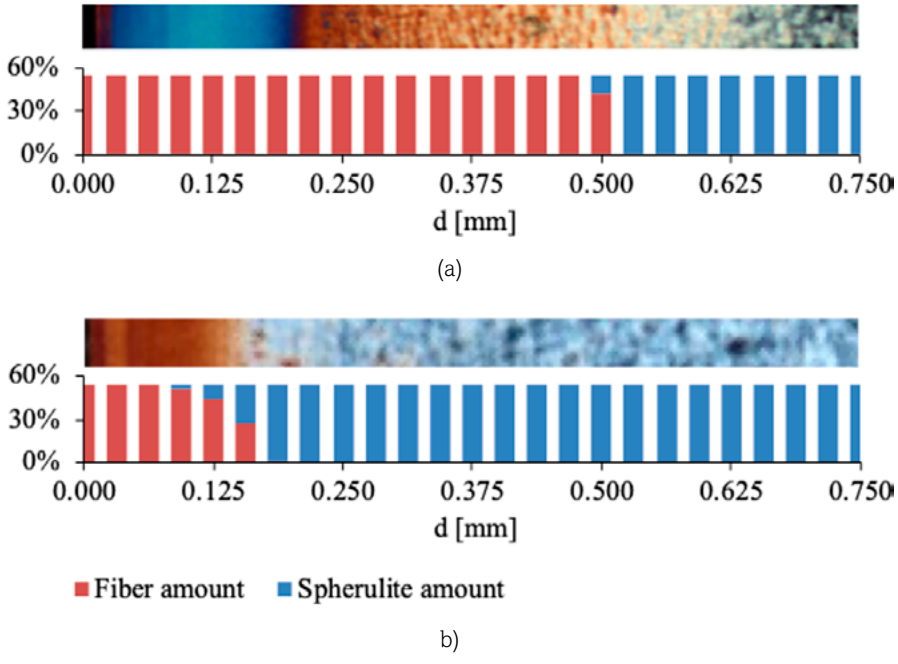

Figure 4. Comparisons between optical micrographs and predicted final morphology distribution along the sample thickness at 15 mm downstream from the cavity entrance, for condition 150°C and 1.3 s (a) for condition 150°C and 12 s (b).

The colored bands in micrographs close to the sample surface are characteristic of the fibrillar layers while the grained area detectable towards the midplane identifies the spherulitic layer. The thickness of such a spherulitic grained area increases as the heating time increases. Coherent with the experimental observations, in the predictions only fibers form close to the sample wall, filling all the local available space; instead, at the sample mid-plane, only spherulites form. The thickness of the fiber and spherulite layers depends on the molding conditions adopted, consistent with experimental observations. In particular, the thickness of the fibrillar layer decreases as the heating time increases. Predicted final morphology distribution correctly describes the experimental

DOI: https://doi.org/10.51573/Andes.PPS39.GS.IM.5

finding in the condition with 12 s heating time while an overestimation of the fibrillar layer thickness is found in the condition with 1.3 s heating time.

Conclusions

An injection molding machine coupled with a rapid heating system was adopted to carry out iPP molding tests under different conditions. The heating system made it possible to control cavity surface temperature and heating system activation time. In particular, two different conditions were considered both with 150°C cavity surface temperature and two heating times: 1.3 s and 12 s. The morphology distributions in the parts were simulated by adopting the UNISA code. The results reasonably predicted the process variable evolutions. The experimental final distribution of morphology, composed by fibers and spherulites, was coherently described by the simulations, especially for long heating activation times. The dependence on molding conditions was also correctly predicted. A slight overestimation of the fibrillar layer thickness was observed for short heating activation times.

References

1. Nian, S.-C., Wu, C.-Y., Huang, M.-S, "Warpage Control of Thin-Walled Injection Molding Using Local Mold Temperatures", *International Communications in Heat and Mass Transfer*, vol. 61, pp. 102–110, 2015, https://doi.org/10.1016/j.icheatmasstransfer.2014.12.008
2. Liparoti, S., Sofia, D., Pantani, R., "Rapid Heating of Mold: Effect of Uneven Filling Temperature on Part Morphology and Molecular Orientation", *Processes*, vol. 11, p. 273, 2023, https://doi.org/10.3390/pr11010273
3. Minh, P.S.; Uyen, T.M.T., Do, T.T., Nguyen, V.-T., Nguyen, V.T.T., "Enhancing the Fatigue Strength of the Weld Line in Advanced Polymer Injection Molding: Gas-Assisted Mold Temperature Control for Thermoplastic Polyurethane (TPU) Composites", *Polymers (Basel)*, vol. 15, p. 2440, 2023, https://doi.org/10.3390/polym15112440
4. Dong, G., Zhao, G., Zhang, L., Hou, J., Li, B., Wang, G., "Morphology Evolution and Elimination Mechanism of Bubble Marks on Surface of Microcellular Injection-Molded Parts with Dynamic Mold Temperature Control", *Industrial & Engineering Chemistry Research*, vol. 57, pp. 1089–1101, 2018, https://doi.org/10.1021/acs.iecr.7b04199
5. Hong, J., Kim, S.K., Cho, Y.-H., "Flow and Solidification of Semi-Crystalline Polymer during Micro-Injection Molding", *International Journal of Heat and Mass Transfer*, vol. 153, pp. 119–576, 2020, https://doi.org/10.1016/j.ijheatmasstransfer.2020.119576
6. Kim, S.K., Jeong, A., "Numerical Simulation of Crystal Growth in Injection Molded Thermoplastics Based on Monte Carlo Method with Shear Rate Tracking". *International Journal of Precision Engineering and Manufacturing*, vol. 20, pp. 641–650, 2019, https://doi.org/10.1007/s12541-019-00089-x

7. Pantani, R., Speranza, V., Titomanlio, G., "Thirty Years of Modeling of Injection Molding. A Brief Review of the Contribution of UNISA Code to the Field", *International Polymer Processing*, vol. 31, pp. 655–663, 2016.

8. Speranza, V., Liparoti, S., Volpe, V., Titomanlio, G., Pantani, R., "Modelling of Morphology Development towards Spherulites and Shish–Kebabs: Application to Isothermal Flow-Induced Crystallization Experiments on Isotactic Polypropylene", *Polymer (Guildf)*, vol. 196, pp. 122–459, 2020, https://doi.org/10.1016/j.polymer.2020.122459

GENERAL SYMPOSIA | POLYMERIZATION AND SYNTHESIS

Incorporation of Aminoalcohols to Tune the Properties of Polyurethane Systems

Alexandre Adam, Saadane Rezaiguia, Romain Severac and Michel Bouquey

DOI: https://doi.org/10.51573/Andes.PPS39.GS.PS.1

December 2024

Incorporation of Aminoalcohols to Tune the Properties of Polyurethane Systems

Alexandre Adam, Saadane Rezaiguia, Romain Severac and Michel Bouquey[1]

Abstract: It is common practice to incorporate low molecular weight molecules, known as chain extenders, to enhance the performance of polyurethane (PU) material. They usually increase the phase separation between the soft and hard domains, which has a significant impact on the density of hydrogen bonds. Aminoalcohols, molecules with both hydroxyl and amine functional groups, are important building blocks in the synthesis of pharmaceuticals but are also widely used in cosmetics or paints and coatings. Easily derived from abundant natural sources, such as amino acids, aminoalcohols align with the need for renewable and sustainable sources. Despite their importance, the specific reactivity of aminoalcohols towards isocyanates and their contribution to PU-based formulations remain underexplored. They can act as chain extenders as well as crosslinkers and catalysts. This study addressed this knowledge gap by assessing the feasibility of adding various aminoalcohols to create hybrid poly(urethane-urea) formulations. By measuring the exothermicity of the polymerization and gel times, we calculated that all tested aminoalcohols have a catalytic activity on the formation of the polymer network. We also identified DMAMP as a promising reactive catalyst whose integration into the network is of primary interest to formulate products that do not emit volatile organic compounds. Moreover, increasing the amount of aminoalcohols stiffened the foams while maintaining the density constant. X-ray tomography completed the characterizations of the foams. Taken together, these results open possibilities for using aminoalcohols to enhance and tune material performances while contributing to more environmentally friendly PU formulations.

Keywords: Aminoalcohols, Polyurethanes

1 The authors Alexandre Adam (aadam@inano.au.dk), Saadane Rezaiguia (srezaiguia@advancionsciences.com), Romain Severac (rseverac@advancionsciences.com) and Michel Bouquey (michel.bouquey@unistra.fr) are affiliated with the Institut Charles Sadron UPR22 at the Université de Strasbourg in France.

DOI: https://doi.org/10.51573/Andes.PPS39.GS.PS.1

Introduction

PU foams represent more than half of total PU consumption worldwide and can be divided into two main groups: rigid and flexible foams [1]. Rigid foams are used mainly for insulation purposes in the building industry, refrigeration, and transportation industry. On the other hand, flexible foams are recognized for their excellent reversible deformation and are widely used in the transportation industry, with cars, aircraft, seats, and for applications like pillows, mattresses etc. [2,3].

The production of PU foams with controlled and tailored properties involves the use of many additives, such as a UV stabilizer, flame retardants, silicones, catalysts, and chain extenders. Many studies highlighted the importance of these additives on the final properties of the PU materials [4-6]. PU are segmented polymers that comprise hard and soft segments and the use of chain extenders deeply modifies the organization of both domains [7]. However, very few molecules have been investigated as chain extenders, primarily glycols such as diethylene glycol, butanediol or small diamines such as putrescine, ethylene diamine [8,9]. Aminoalcohols (AA) are a class of molecules containing both hydroxyl and amino (primary, secondary, tertiary) groups around an alkane backbone. They are widely used in many industries and find applications in chemical manufacturing, paints, coatings, and personal care. Their diverse structures as well as physical and chemical properties may provide new features to PU materials. The primary amines of AA are more reactive with isocyanates than alcohol groups and lead to the formation of urea bonds. Urea bonds are tougher and less flexible than urethane bonds because of the higher density of the hydrogen bonds that can be built. Hence, a new material can be obtained based on a mixed poly(urethane-urea) network with a controlled density of urea bonds. Polyurea are materials with interesting properties but are generally more expensive to produce than PU. Adding urea bonds in PU through the chain extenders is thus very promising. In this paper, several AA were studied, and their reactivity with isocyanates, their behavior as potential catalysts in standard PU mixtures, and the consequences of their addition in a standard flexible PU foam formulation were specifically researched.

Materials and Methods

All AA were obtained from Advancion Sciences company. They are defined by their molecular weight (MW) and their number of functional groups (f) (the sum of alcohol and primary amine groups). Those molecules are: 2-amino-2-methyl-1-propanol (AMP, MW=89.1 g/mol, f=2), 2-amino-2-ethyl-1,3-propanediol (AEPD, MW= 119.2 g/mol, f=3), Tris(hydroxymethyl)-aminomethane (Tris, MW=121.1 g/mol, f=4), 2-dimethylamino-2-methylpropanol (DMAMP, MW=117.2 g/mol, f=1), *N,N*-dimethyl-3-methoxypropylamine (DMMOPA, MW= 117.2 g/mol, f=0). Their structure is detailed in Table S1. Polyols Alcupol F-2832, C-5571, X-7510, R-3810 were obtained from Repsol. Silicone and catalyst agents Tegostab® B8724 LF2, B8737 LF2, DABCO 33LV and DABCO BL11 were acquired from Evonik. 1,2-diamino-2-methylpropane (DMP), 1,3-propanediol (1,3-PD) and 1,3-butanediol were purchased from Sigma-Aldrich.

DOI: https://doi.org/10.51573/Andes.PPS39.GS.PS.1

AMP was distilled under low pressure to remove excessive water content. The water content of all aminoalcohols was measured by the Karl-Fisher method before any use.

FTIR spectroscopy:

The IR data were acquired using the transmission method. Demountable Omni-cell Specac liquid cell with NaCl windows were used. Infrared spectra were collected at 4 cm^{-1} resolution with a Brucker Vertex 70 apparatus equipped with a DTGS detector, a KBr beam splitter and a blackbody source.

Exothermicity measurements:

Temperature probes (thermocouples) connected to a cDAQ-T1101 Bundle from National Instruments and linked to the computer were used to monitor the temperature changes inside the reactive mixture. SignalExpress software was used to acquire the signals from the thermocouples with a time interval of 200 ms. The reaction tube was covered with a block of PE foam to increase the insulation of the system and be as close as possible to an adiabatic system.

Gel times:

Alcupol X-7510, a triol, was added to a 10 mL polypropylene tube followed by the addition of a defined amount of AA. The amount of AA (called %mol cat) corresponds to a molar fraction of the total OH functions coming from the triol. The correct concentration of AA is obtained by diluting a concentrated mixture of 8 %mol cat. Typically, 8 %mol cat. mixture is prepared as follows: Alcupol X-7510 is added to a tube (5 g, 7.46 mmol, 100 eq) as well as the studied catalyst (0.60 mmol, 8 eq). The mixture is mixed well by strong manual shaking. The mixtures are then heated to 60°C. TDI (118 eq) is quickly added, and the tube is shaken for 10 s. The timer is started and the tube is kept at 60°C. The time necessary until no more flowing of the system is observed is noted as the gel time.

Stress-strain measurements:

Compression tests were performed on a INSTRON ElectroPuls E300 testing machine. A 100N load cell has been used and measurements were performed at room temperature and ambient humidity. The curves were acquired on cubic samples (3 cm x 3 cm x 3 cm) of the synthesized PU foams, cut with a hot wire. The strain rate was 0.04 s-1 and the maximum strain (end of loading) was set at 80%.

X-Ray tomography:

PU foams were imaged with a micro-CT scan (RXSolutions EasyTom 150-160). A microfocus X-Ray source (Hamamatsu L12161-07) was used and acquisitions were carried out at 70 kV tube

DOI: https://doi.org/10.51573/Andes.PPS39.GS.PS.1

voltage and 142 µA tube current for voxel dimensions of 0.010x0.010x0.010 mm^3 (distance source-detector 398.9 mm and source-sample 31.4 mm). The detector was a VARIANT PaxScan 2520DX (1920x1536 pixels on 127 µm pixel pitch, 16-bit). Each saved projection is an average of 20 frames captured at 5 frames per second.

Results and Discussion

Reactivity of AA with Isocyanates

To produce homogeneous PU foams, the kinetic parameters of the reaction are crucial. Because the isocyanate (NCO) functional group strongly absorbs infrared light (around 2700 cm^{-1}), FTIR spectroscopy is the technique of choice to monitor the reactivity of isocyanate functions with different AA molecules. By following the change of transmittance of each sample, we can establish the main reactivity trends. The change of intensity directly indicates the conversion of the isocyanate functions:

$$p(t) = 1 - \frac{A_t - A_\infty}{A_0 - A_\infty}$$

where p(t) is the isocyanate conversion and A_0, A_t and A_∞ are the initial absorbance, the absorbance at a reaction time t, and the absorbance at equilibrium after an infinite reaction time, respectively.

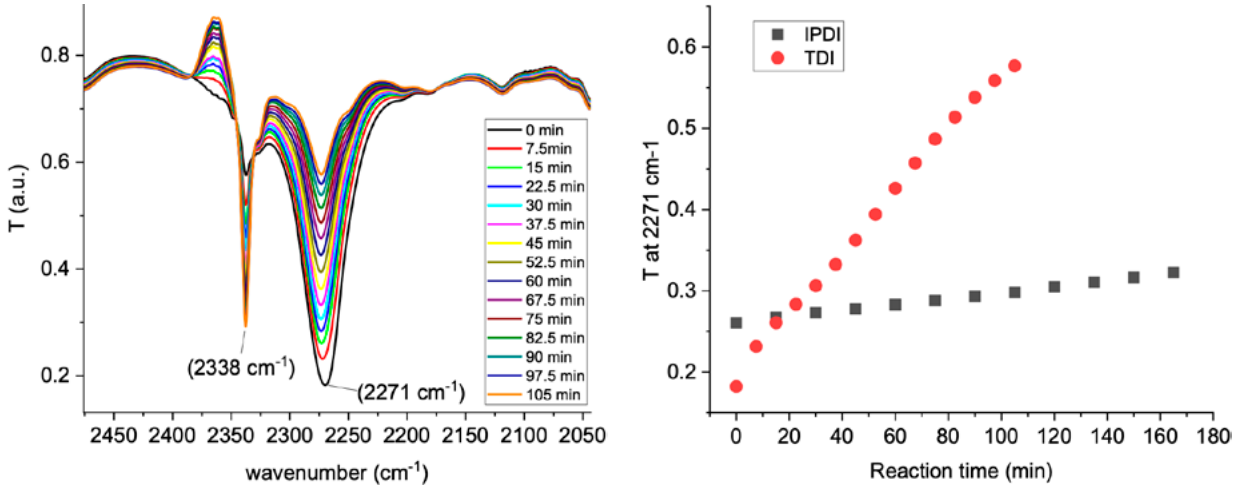

a) b)

DOI: https://doi.org/10.51573/Andes.PPS39.GS.PS.1

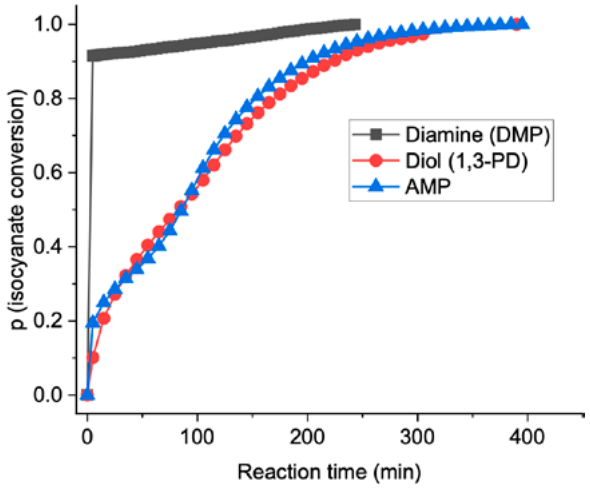

c)

Figure 1. (a) Evolution of the transmittance as a function of reaction time for a system containing AMP and TDI, (b) comparison of the reaction kinetics of TDI and IPDI with AMP, (c) isocyanate conversion as a function of reaction time for DMP, 1,3-PD and AMP.

Figure 1(a) illustrates the decrease of the intensity of the NCO band as a function of time and the conversion of isocyanate. To decide between which isocyanate was the best suited for evaluating the reaction kinetics of AA, AMP was first allowed to react with IPDI and TDI, two different diisocyanates. As expected, TDI reacts much faster than IPDI due to the aromaticity of TDI that activates the isocyanates groups by mesomeric effect (Figure 1[b]). TDI was thus used for the following experiments because a high reactivity is needed to build PU foams. Then, several reactants were tested to evaluate and compare the reactivity towards TDI of one AMP and model molecules, a diol 1,3-PD and a diamine DMP, chosen for their structure close to the AMP (Figure 1[c]). The diamine reacts much faster with NCO than AMP and the diol 1,3-PD. Indeed, most of the NCO groups were already consumed by the beginning of the measurement. The fast reaction takes place in the very first moment after mixing the chemicals. It was possible to confirm that aminoalcohols molecules bearing amine and alcohol groups have an intermediate reactivity between the corresponding diamine (DMP) and diol (1,3-PD).

Another way to evaluate the relative reactivity between different samples consisted in measuring the exothermicity of the reaction, i.e. the temperature elevation to determine the heat released. The method has been previously theorized and explained. For example, Li et al. employed this method to evaluate the isocyanate conversion as a function of reaction time [6]. Different AA were tested: DMP, 1,3-PD, AMP, AEPD, DMAMP, and DMMOPA. The concentration of active chemical functions ($OH+NH_2$) was kept constant between the different samples (Figure 2).

DOI: https://doi.org/10.51573/Andes.PPS39.GS.PS.1

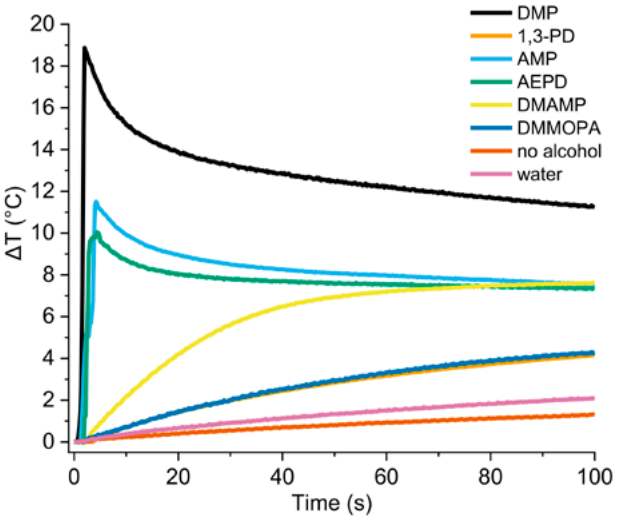

Figure 2. Temperature profile of dilute systems when different AA are used; the amount of reactive chemical functions from AA is kept constant.

It can be observed that for every product containing a primary amine function, i.e. DMP, AMP, and AEPD, there is a temperature peak at the first moment of the reaction, immediately after the addition of TDI (less than 2 s after addition), most certainly due to the rapid formation of urea bonds. On the other hand, for AA bearing only OH groups and/or a tertiary amine (DMAMP, 1,3-PD), the temperature increase is exponential and reaches a plateau after few minutes. It can be noted that the temperature elevation is more significant in the solution containing DMAMP than 1,3-PD, which tends to confirm the catalytic activity of the tertiary amine on the formation of the urethane bond of this molecule.

When introducing DMMOPA without other reactive molecules, the temperature elevation profile is equivalent to the one obtained for 1,3-PD, even if there are no OH or NH_2 functions. The temperature increase was also recorded when adding TDI in a solution containing nothing more than solvent and catalyst (no alcohol) and in a solution that also contains water, always with the same total number of functions. The temperature rises only very slightly, less than 2°C, which is far less than what is obtained when DMMOPA is added in the solution, confirming the catalytic properties of this molecule that has no alcohol nor primary amine.

Influence of AA on PU Polymerization – Catalytic Potential of AA

The chemical structure of some AA is very close to the structure of the amine-catalysts used in the PU industry. Thus, the catalytic properties of AA were investigated to reveal any potential interesting properties by measuring the gel time of a mixture of TDI and a triol, Alcupol X-7510, in the presence of either AA, diol, diamine or DABCO BL11 and DABCO 33 LV, which are catalysts widely used to produce PU foams (Figure 3[a] and 3[b]).

DOI: https://doi.org/10.51573/Andes.PPS39.GS.PS.1

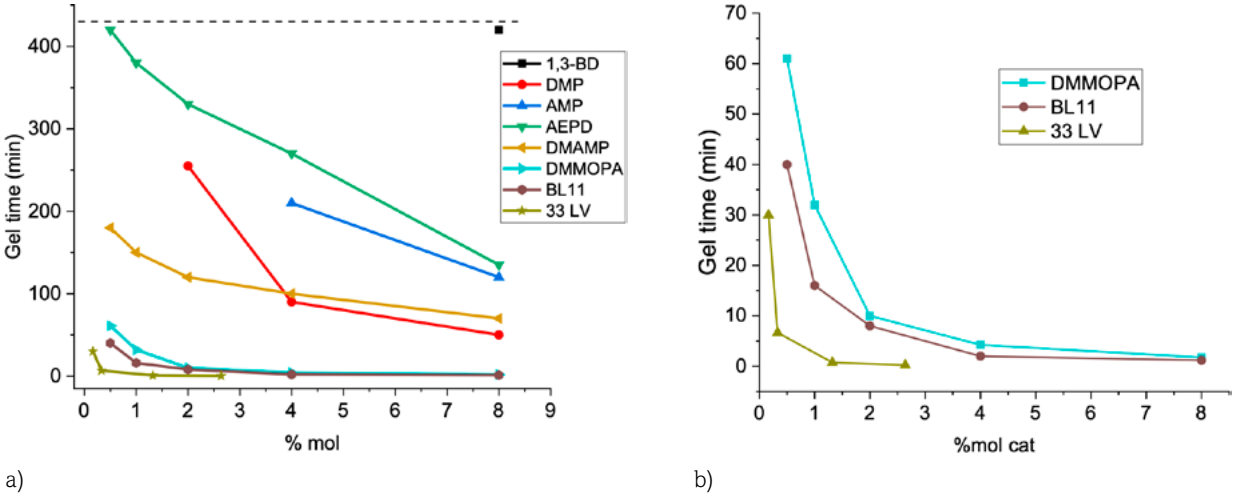

a) b)

Figure 3. (a) Gel times of TDI and Alcupol X-7510 in the presence of increasing amounts of different potential catalysts, (b) zoom on the results obtained after the addition of DMMOPA, BL11 and 33LV.

For mixtures without any catalyst (i.e. without AA, diol, diamine), the gel time is over 400 min. Approximately the same gel time is obtained with an addition of 1,3-BD, which confirms that it has no catalytic activity towards the formation of the PU network. However, the gel times are systematically shorter for any other added molecules, confirming the catalytic activity of all AA. The more AA or standard catalysts are added, the lower the gel times, which means that the polymerization is speeded up. AMP have the smallest effect of all the AA. This can be explained by the fact that the reactive primary amines groups will quickly react and immobilize these molecules in the PU/PUrea network, preventing them from later helping the bond formation. DMP, the diamine, has a similar behavior. DMAMP is more interesting from a catalytic point of view. The gel times are clearly reduced compared to the reference system. The DMAMP structure possesses one tertiary amine and one alcohol group. The presence of this tertiary amine certainly explains this behavior, efficiently catalyzing the formation of the polyurethane/polyurea network. During polymerization, the presence of the alcohol group also contributes to the integration of DMAMP into the polymer network. It can thus be classified as a reactive catalyst.

Non-reactive catalysts are obviously more efficient due to their mobility in the reactive mixture. Common commercial amine catalysts, DABCO BL11 and 33LV, are also very efficient for catalyzing the formation of urethane/urea bonds. 33LV, which is specially designed and recommended for this application, is the most efficient. But DMMOPA, which has a chemical structure very close to BL11, also shows a very good catalytic activity, confirming that the structure directly impacts the catalytic behavior.

DOI: https://doi.org/10.51573/Andes.PPS39.GS.PS.1

Influence of AA in PU Foams

PU foams represent a very large part of the total PU market. Here we have already shown that AA react with isocyanates and can also act as polymerization catalysts. So, after confirming the possibility of including AA in PU systems, the influence of AA on PU foam production was studied. By comparing the mechanical properties of foams built with and without AA, it is possible to determine the main trends of the influence of AA. This consisted in measuring the impact of increasing amounts of AMP, AEPD, and Tris on the stiffness and pore morphology.

A standard formulation of TDI-based flexible foams was chosen as a reference for comparison. Then the amounts of polyol and all the additives (Tegostab 8727, 8737, Dabco, and water) were kept constant in the whole study. TDI was adjusted accordingly to compensate the excess of alcohol and primary amine functions coming from the addition of AA. Typical foam formulations used for this study are reported in Table 1 and pictures are shown in Figure 4(a). The amount of functional groups (OH+NH2) coming from a specific added AA is expressed as a ratio of the number of functions from the AA ($n_{OH,AA}$) to the number of functions from the polyol ($n_{OH,polyol}$). X is defined as:

$$X = \frac{n_{OH,AA}}{n_{OH,polyol}} \quad (1)$$

Table 1. Details of the PU Foam Formulations.

Component	Reference	AMP X=1	AMP X=4	AEPD X=1
Alcupol F2832	15 g	15 g	15 g	15 g
Tegostab 8724	112.5 µL	112.5 µL	112.5 µL	112.5 µL
Tegostab 8737	37.5 µL	37.5 µL	37.5 µL	37.5 µL
Dabco 33LV	44.1 µL	44.1 µL	44.1 µL	44.1 µL
Dabco BL11	13.5 µL	13.5 µL	13.5 µL	13.5 µL
Water	525 µL	525 µL	525 µL	525 µL
AA		0.33 g	2.67 g	0.29 g
TDI	4.96 mL	5.52 mL	9.48 mL	5.52 mL

The structural analysis was done using X-ray tomography and the mechanical properties were evaluated by density and compression tests. Compression testing is the most classic way of evaluating the flexibility and recovery of a foam. Different information can be obtained from these curves, in particular the slope of the linear elastic region which corresponds to the apparent modulus E of the material (Figure 4[b]).

DOI: https://doi.org/10.51573/Andes.PPS39.GS.PS.1

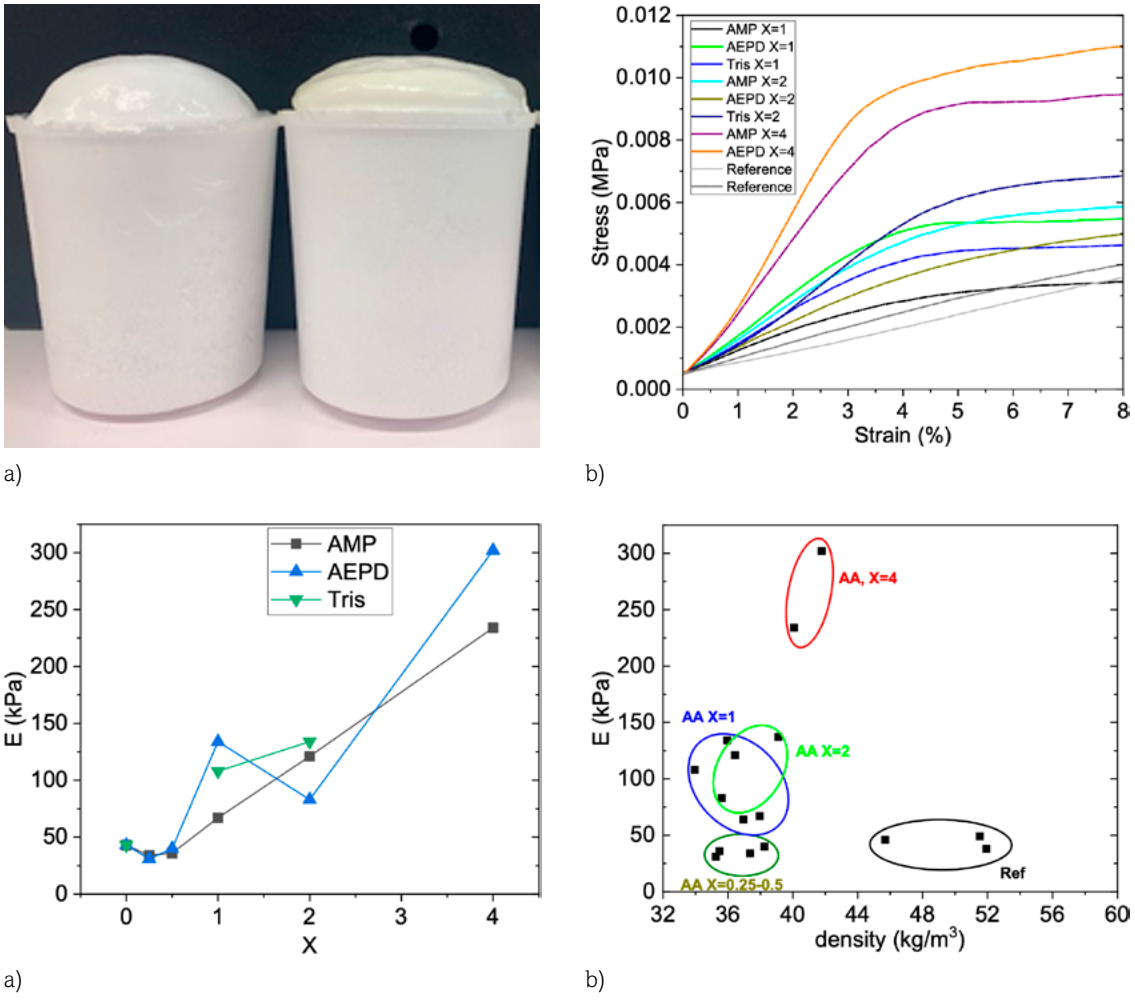

Figure 4. (a) Photograph of two foams obtained with the reference formulation (left) and with AMP X=1 (right), (b) Compression curves between 0 and 8 % strain, (c) Young's moduli vs density plot, and (d) Young's moduli as a function of the amount of AA added.

The reference samples have an average modulus of E = 43.5 ± 8 kPa for an average density of d = 51.7 ± 0.3 kg/m^3. From Figure 4(b) and 4(c), a clear tendency of the modulus E to increase when adding an increasing amount of AA can be observed. This means that AA introduce rigidity in the material. This is typically what is expected with the addition of small molecules, with a functionality above 2, that can act as crosslinking points. Small diols and diamines are also typically used in the PU synthesis to act as chain extenders to promote phase segregation between the apolar and soft domains of the polyol and the polar and rigid domains rich in urea and urethane bonds.

To sort the data obtained and distinguish the main effect of adding AA, the results were sorted according to a modulus-density plot (Figure 4[d]). This plot reveals the main trends of the influence of AA in a PU formulation. Compared to the reference samples (black circle), it is clear that the addition of AA increases the apparent elastic moduli of the obtained foams. The more AA is added,

DOI: https://doi.org/10.51573/Andes.PPS39.GS.PS.1

the tougher the foams are. At the same time, we can also notice a decrease in density even when very low amounts of AA were added (small X values). These observations suggest that the addition of AA results in a lower degree of cell opening. The closer the cells are, the tougher the foams are and the more CO_2 gas is trapped within the foam cells. This would explain the two observed phenomena: decrease in density and increase of Young's moduli. Structural analyses were then performed by X-ray tomography to visualize the cells in the foam.

X-ray tomography is a powerful technique that allows scanning of the internal structure of a variety of samples. It can reconstruct the porous structure of foam material, making it possible to identify the size and distribution of the porosities.

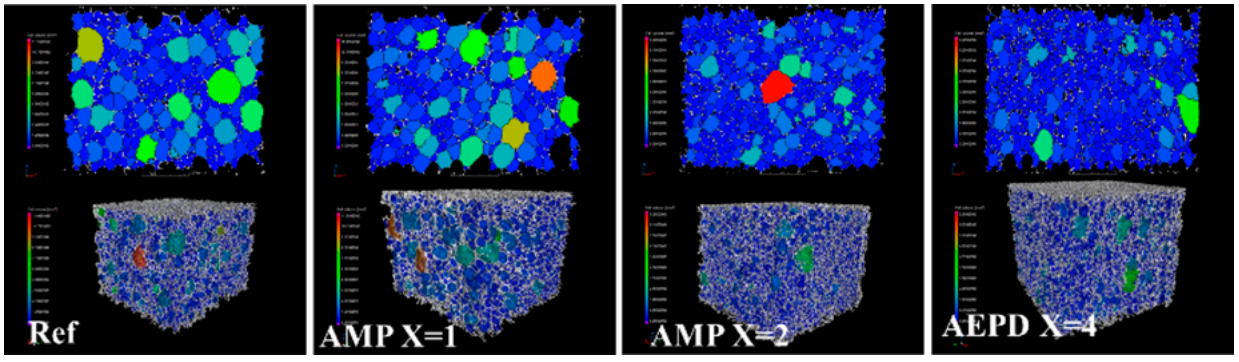

Figure 5. Pictures obtained from X-ray tomography of 4 foam cubes: a reference sample (Ref), a foam with addition of AMP (X=1 and X=2) and AEPD (X=4).

Figure 5 shows an example of the detailed structure that can be obtained using this technique. The figures obtained for all the samples are presented in Figure S4. First, it appears that the structure of all the foams produced with comparable amounts of AA is very close. There is no significant divergence in the pore size, wall thickness, and pore morphology. For all samples, the pores are of various sizes, between 1 and 0.1 mm. The pores are slightly anisotropic, oval-shaped, due to the compression exerted by the sides of the beaker during the blowing of the material. Foams produced with the reference formulation exhibit the same morphology as the foams produced by adding AA.

However, the addition of increasing amounts of AA resulted in the formation of smaller pores, which greatly contribute to stiffening of the material. PU are segmented polymers with hard and soft domains. Hard segments form hydrogen bonds and crystallize to create hard domains. The hard domains, linked by strong hydrogen bonds, are dispersed within the soft domain matrix. The dispersion and morphology of these hard domains determine the final properties of PUs. In the PU foam formation, AA act as chain extenders and build urea and urethane groups by reacting with isocyanates. Thus, AA integrate the hard segments and alter the organization of the hydrogen bonding. The microphase separation between hard and soft domains is thus less pronounced. By increasing the compatibility of the hard and soft domains, the microphase separation, which

DOI: https://doi.org/10.51573/Andes.PPS39.GS.PS.1

leads to cell rupture, is delayed and thus more closed cells are produced [6,10] and tougher material is obtained.

Conclusion and Perspectives

The aim of this study was to investigate: (i) the reactivity of AA in PU formulations and (ii) the effect of these molecules on flexible cold-cure PU foams. For this purpose, different AA with different structures, molecular weights, and functionality numbers were tested. Among the reactive molecules tested, AMP, AEPD, and Tris are di-, tri-, and quadrifunctional, respectively, while DMAMP contains one tertiary amine and one hydroxyl group. DMMOPA with no alcohol and a tertiary amine was considered as non-reactive. Results showed that the reactivity of AA with isocyanates is adapted to play the role of chain extenders, and that AA are catalyzing the formation of the PU network. Thus, they could partially replace classic tertiary amine-based catalysts in industrial PU foams. Finally, AA were added to PU foams and the structure and mechanical properties were examined. By increasing the apparent Young's modulus, AA stiffen the PU foams while increasing the number of closed cells. Consequently, AA could be used to finely tune the properties of PU foams. Detailed structural analyses of the produced PU materials will be done to understand the influence of AA on the ordering of the hard versus soft domains that leads to the observed mechanical properties.

Acknowledgements

This work was supported by the Institut Charles Sadron (ICS) and the Institut Carnot MICA, with financial support from Advancion company under contract CNRS 257110. All authors acknowledge the CarMac (Anaïs De Maria and Mélanie Legros) for the IR measurements, the MiNaMec plateform and Antoine Egele for X-ray tomography and data interpretation. Authors especially acknowledge Damien Favier for the compression measurements.

References

1. N. V. Gama, A. Ferreira, and A. Barros-Timmons, "Polyurethane Foams: Past, Present, and Future," *Materials*, vol. 11, no. 10, Art. no. 10, Oct. 2018, https://doi.org/10.3390/ma11101841
2. M. Ates, S. Karadag, A. A. Eker, and B. Eker, "Polyurethane foam materials and their industrial applications," *Polymer International*, vol. 71, no. 10, pp. 1157-1163, 2022, https://doi.org/10.1002/pi.6441
3. J. Bicerano et al., "Flexible Polyurethane Foams," in *Polymeric Foams: Mechanisms and Materials*, 2004, https://doi.org/10.1201/9780203506141.ch6

4. H. Singh and A. K. Jain, "Ignition, combustion, toxicity, and fire retardancy of polyurethane foams: A comprehensive review," *Journal of Applied Polymer Science*, vol. 111, no. 2, pp. 1115-1143, 2009, doi:10.1002/app.29131

5. G. S. Dhaliwal, S. Anandan, M. Bose, K. Chandrashekhara, and P. Nam, "Effects of surfactants on mechanical and thermal properties of soy-based polyurethane foams," *Journal of Cellular Plastics*, vol. 56, no. 6, pp. 611-629, Nov. 2020, https://doi.org/10.1177/0021955X20912200

6. W. Li, A. J. Ryan, and I. K. Meier, "Effect of Chain Extenders on the Morphology Development in Flexible Polyurethane Foam," *Macromolecules*, vol. 35, no. 16, pp. 6306-6312, Jul. 2002, doi:10.1021/ma020231l

7. I. Yilgör, E. Yilgör, and G. L. Wilkes, "Critical parameters in designing segmented polyurethanes and their effect on morphology and properties: A comprehensive review," *Polymer*, vol. 58, pp. A1–A36, Feb. 2015, https://doi.org/10.1016/j.polymer.2014.12.014

8. T. J. Touchet and E. M. Cosgriff-Hernandez, "1–Hierarchal structure–property relationships of segmented polyurethanes," in *Advances in Polyurethane Biomaterials*, S. L. Cooper and J. Guan, Eds., Woodhead Publishing, 2016, pp. 3-22. https://doi.org/10.1016/B978-0-08-100614-6.00001-9

9. K. C. Frisch, "Chemistry and technology of polyurethane adhesives1," in *Adhesion Science and Engineering*, D. A. Dillard, A. V. Pocius, and M. Chaudhury, Eds., Amsterdam: Elsevier Science B.V., 2002, pp. 759-812. https://doi.org/10.1016/B978-044451140-9/50016-0

10. A. Sohrabi, "Effects of di- and trifunctional chain extenders on the properties of flexible cold-cure polyurethane foams," *Journal of Cellular Plastics*, vol. 60, no. 1, pp. 41-57, Jan. 2024, https://doi.org/10.1177/0021955X231224776

GENERAL SYMPOSIA | POLYMER BLENDS AND ALLOYS

Study of HDPE/PET/E-GMA Blends: Toughening, Rigidity, and Thermal and Morphology Behavior

C. Feregrino, S. A. Ospina, L. Flórez, A. Henao and B. L. López

DOI: https://doi.org/10.51573/Andes.PPS39.GS.PBA.1

December 2024

Study of HDPE/PET/E-GMA Blends: Toughening, Rigidity, and Thermal and Morphology Behavior

C. Feregrino, S. A. Ospina, L. Flórez, A. Henao and B. L. López[1]

Abstract: The purpose of this study was to utilize E-GMA as a compatibilizer to enhance the mechanical properties of recycled blends of high-density polyethylene, polyethylene terephthalate, and ethylene-glycidyl methacrylate copolymer (HDPE/PET/E-GMA), with the aim of manufacturing plastic soda crates. The results showed that toughness increased without losing rigidity. Flexural strength improved by 11% and impact strength by 8% when the PET content was 20%, indicating that E-GMA acts as a compatibilizer. These results can be applied to improve the mechanical properties of recycled materials in an upcycling context.

Keywords: HDPE, PET, E-GMA, Blends, Recycled

1 C. Feregrino (ciro.feregrino.montes@gmail.com) is affiliated with Plásticos Técnicos Mexicanos S.A. de C.V. company. The authors S. A. Ospina (sospina@icipc.org), L. Flórez (lflorez@icipc.org) and A. Henao are affiliated with the Instituto de Capacitación e Investigación del Plástico y del Caucho (ICIPC). B.L. López (blopez@udea.edu.co) is affiliated with the Grupo de Investigación Ciencia de los Materiales Instituto de Química at the University of Antioquia.

DOI: https://doi.org/10.51573/Andes.PPS39.GS.PBA.1

Introduction

Current approaches to resource efficiency focus on recycling and a circular economy. Recycling is considered one of the best options in waste management to reduce the impacts of post-consumer plastic packaging waste. Recycling offers opportunities for using polymers in sustainable manufacturing. However, each time a product reaches the end of its life cycle, the recycling process results in a loss of molecular weight and degradation of mechanical properties, primarily due to exposure to environmental factors and high temperatures [1].

As a result, the use of recycled material is limited or restricted to lower performance products. This limitation is particularly significant given that plastics constitute an increasingly large proportion of municipal solid waste worldwide. The bulk of this plastic waste comprises polyolefin-based plastics, such as high-density polyethylene (HDPE), low-density polyethylene (LDPE), polypropylene (PP), and polyethylene terephthalate (PET) [2].

PE and PP alone account for 50% of the 150 million metric tons of thermoplastics demanded globally, with PE making up two-thirds of all polyolefins used. Polyethylene terephthalate (PET) is an important polymer among plastics globally, contributing approximately 8% by weight and 12% by volume of global solid waste due to its desirable properties, applications, and industrial advancements, leading to a rapid increase in its generation [3].

This context highlights the critical need for improved recycling processes and innovative solutions capable of maintaining or even enhancing the quality and performance of recycled plastics. A significant area of research is the development of PET/HDPE blends, primarily focused on improving compatibility due to the substantial differences in their solubility parameters, which naturally render them incompatible. Key issues for high-performance polymer blend production include dispersion and embedding of the dispersed phase, strong interfacial interaction, and morphology design. Factors determining phase morphology include material characteristics and processing parameters. Some authors have shown that ternary blends of HDPE, PET, and E-GMA enhance matrix impact strength, including Lei et al. [2,4-6].

Experimental Section

Materials and Blends

Commercial grade HDPE (PADMEX 65080, MFI=8.0 g/10 min @ 190°C 2.16 kg, Petróleos Mexicanos), PET, and E-GMA copolymer (Lotader AX8840, MFI=5.0 g/10 min @ 190°C 2.16 kg, SK Functional Polymer) were used in this work to analyze their individual properties, prepare binary blends (HDPE/PET 95%/5% w/w, HDPE/E-GMA 95%/5% w/w, PET/E-GMA 95%/5% w/w), and prepare ternary blends (HDPE/PET/E-GMA 85%/10%/5% w/w, HDPE/PET/E-GMA 75%/20%/5%

DOI: https://doi.org/10.51573/Andes.PPS39.GS.PBA.1

w/w, HDPE/PET/E-GMA 65%/30%/5% w/w). The decision to set the concentration of E-GMA at 5% w/w and use PET only up to 30% w/w was based on the previous work reported by [5], which showed that using more than 5% of E-GMA does not improve mechanical properties, and adding more than 30% of PET reduces the impact strength of the blend.

Blend Preparation

For the preparation of binary and ternary blends, the components were weighed at the designated mass ratio and blended in a Labtech Twin Screw extruder (LTE-2640, 26 mm diameter, L/D 40, OD/ID 1.3) at 280°C (flat profile) and 800 RPM. All the blends were produced at the same feed rate of 25 kg/h. The screw configuration was the same for all the blends and included distributive (30°, 60°) and dispersive (90°) mixing elements. A degassing vacuum zone at the end of the extruder was used to produce 30 cm Hg vac. In order to get rid of residual moisture, PET was dried prior to extrusion at 120°C for 4 hours in a Motan Bin S 15L dryer.

Test Specimen Preparation

All the test specimens for Izod impact strength and flexural tests were injection molded using a 35 A Boy Machine with an Axxicon AIM Quick Change mold and an ISO type B insert. All individual materials and blends were injected using the same parameters. The temperature profile was set to 250°C in the feeding zone and nozzle, and 280°C in the middle zone. Apart from adjusting the temperature due to the PET content, all injection molding parameters were defined according to the ISO 1872-2 standard. The mold temperature was 40°C. The theoretical flow front velocity was 100 mm/s in the cross-section of the test specimen. The specific hold pressure was set to 575 bar for 25 seconds and an additional 10 seconds for cooling. The tangential velocity during plastification was 0.2 m/s. The cycle time was approximately 40 seconds.

Impact Strength Test

The Izod impact tests were performed in a Tinius Olsen IT 504 pendulum according to ISO 180, with a type A notch. The capacity of the pendulum was 2.8 J.

Flexural Properties Test

The flexural properties were measured in a Shimadzu AGS-X 5 universal testing machine, according to ISO 178, at a test speed of 2 mm/min and a 64 mm span.

DOI: https://doi.org/10.51573/Andes.PPS39.GS.PBA.1

Scanning Electron Microscope Observation (SEM)

SEM Micrographs were obtained in a JEOL JXA8530F electron microscope. Fractured specimens from the test were polished. After this, the samples were gold coated in order to increase their electric conductivity for SEM observation. The operating voltage was 20 KV.

Differential Scanning Calorimetry Measurement (DSC)

DSC tests were conducted according to ASTM D3418-15 using a TA instrument DSC Q200. The samples were heated from 25°C to 280°C at a heating rate of 10°C/min, then cooled at the same rate to 40°C and reheated until reaching the melting temperature.

Dynamic Mechanical Analysis Measurement (DMA)

A TA Instrument DMA 850 was used in dual cantilever mode. The samples were heated to approximately 150°C at a heating rate of 5°C/min. The oscillatory frequency was 1 Hz, and the amplitude was 35 μm.

Results and Discussion

Mechanical properties. Table 1 shows the results of the mechanical properties.

Table 1. Mechanical properties of binary and ternary blends.

	Impact Strength (KJ/m²)			Flexural Strength (MPa)			Flexural Modulus (MPa)		
	Value	σ	%Vs HDPE	Value	σ	%Vs HDPE	Value	σ	%Vs HDPE
HDPE	4.44 C	0.15		25.18	0.22		1136	36	
PET	2.62 C	0.05		79.93	0.26		2318	64	
HDPE/PET (95/5)	3.47 C	0.14	-21.85	26.22	0.36	4.13	1177	68	3.61
HDPE/E-GMA (95/5)	4.19 H	0.12	-5.63	23.6	0.3	-6.27	1094	76	-3.70
PET/E-GMA (95/5)	9.93 C	0.62		74.23	0.59		2282	62	
HDPE/PET/E-GMA (85/10/5)	4.72 H	0.28	6.31	26.28	0.59	4.37	1119	43	-1.50
HDPE/PET/E-GMA (75/20/5)	4.78 H	0.10	7.66	28.02	0.53	11.28	1214	39	6.87
HDPE/PET/E-GMA (65/30/5)	5.51 H	0.15	24.10	29.46	0.43	17.00	1231	38	8.36

DOI: https://doi.org/10.51573/Andes.PPS39.GS.PBA.1

PET/HDPE blends are inherently incompatible due to the significant difference in their solubility parameters [2]. This incompatibility is evident in the impact strength of the binary HDPE/PET blend, which decreased by 21.85% compared to unmodified HDPE. On the other hand, ternary HDPE/PET/E-GMA blends exhibited higher impact strength than pristine HDPE, with a trend of improving in this property as PET concentration increased. Traditionally, adding elastomeric (rubbery) polymers to polyolefins could soften and toughen them, enhancing impact strength but at the cost of reduced rigidity, as expressed by the flexural modulus [7]. In our study, the ternary HDPE/PET/E-GMA blends demonstrated enhanced impact strength and flexural properties compared to pristine HDPE. A similar behavior has been reported by Chen et al. [8] for PP/EPR/HDPE blends, attributed to the reduction of the interparticle distance between the EPR domain, explained by the formation of a core-shell morphology where the PP content is located inside the EPR domain.

Scanning Electron Microscope Observation (SEM)

Figures 1a, 1b, and 1c show the morphology of HDPE/PET (95/5) binary blend, HDPE/PET/E-GMA (85/10/5), and ternary HDPE/PET/E-GMA (65/30/5) blend, respectively.

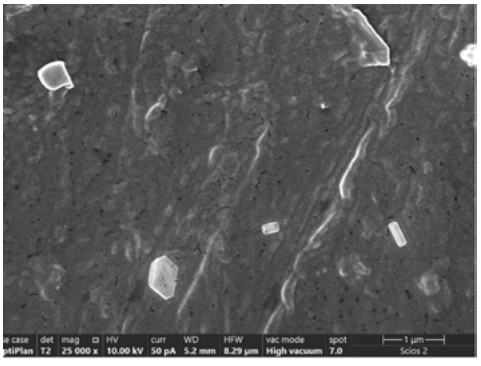

(a)

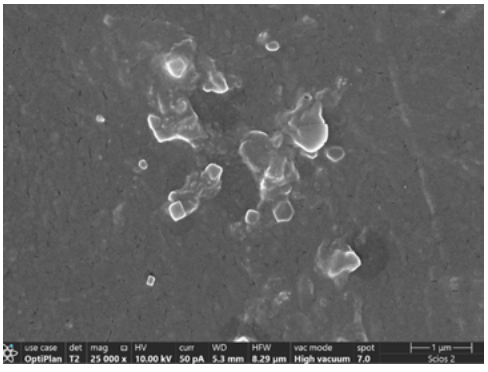

(b)

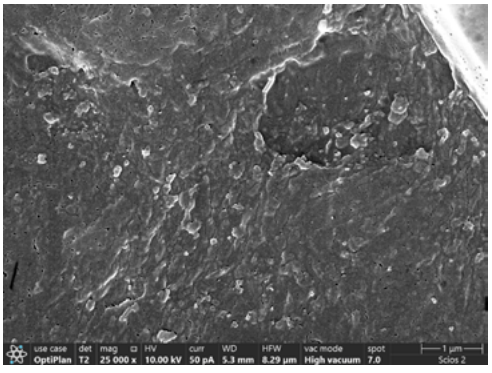

(c)

Figure 1. (a) HDPE/PET (95/5) binary blend, (b) HDPE/PET/E-GMA (85/10/5) ternary blend, (c) HDPE/PET/E-GMA (65/30/5) ternary blend.

DOI: https://doi.org/10.51573/Andes.PPS39.GS.PBA.1

PET dispersed phase within an HDPE matrix can be observed in Figure 1(a). The addition of E-GMA in the HDPE/PET blends improves the dispersion of the PET dispersed phase within the HDPE matrix, as evidenced by a smaller particle size (Figure 1[b], Figure 1[c]).

Analyzing the mechanical properties alongside the SEM images it is possible to correlate the improved impact strength of HDPE/PET/E-GMA (65/30/5) compared to HDPE/PET/E-GMA (85/10/5), which can be attributed to the interparticle distance of the dispersed phase observed (Figure 1[b], Figure 1[c]). While pure PET exhibits low impact strength and poor miscibility in HDPE, PET itself has a toughening effect for HDPE, as can be deduced for the impact strength value of the HDPE/PET binary blend.

The addition of PET to the HDPE/E-GMA blend in the ternary blend demonstrates an excellent toughness, although E-GMA alone does not improve HDPE properties. This suggests a synergistic effect between PET and E-GMA in toughening HDPE. These results indicate that the increased toughness of the ternary HDPE/PET/E-GMA blends is due to E-GMA acting as a compatibilizer, improving the interfacial adhesion between HDPE and PET.

Differential Scanning Calorimetry Measurement (DSC)

The results of the DSC test are shown in Figure 2. As can be seen, the main melting transitions of PET and HDPE remain virtually unchanged compared with HDPE/PET/E-GMA (65/30/5). According to ASTM D3418-15, this minimal displacement in the transition temperature can be attributed to the method´s repeatability. The compatibilizer does not affect the melting temperature and crystallinity of PET and HDPE, which is advantageous because their mechanical properties are not affected.

The melting temperature of E-GMA was detected at 106.02°C, but it was not observed in the ternary blend. This is because the GMA part (8%) reacts with PET to form ester groups [6] Figure 3.

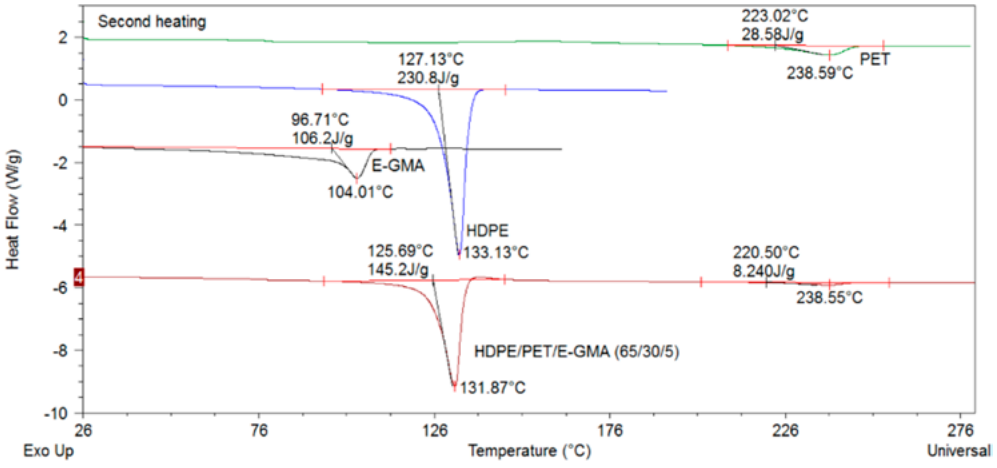

Figure 2. DSC thermogram of PET, HDPE, E-GMA, and HDPE/PET/E-GMA (65/30/5) samples.

DOI: https://doi.org/10.51573/Andes.PPS39.GS.PBA.1

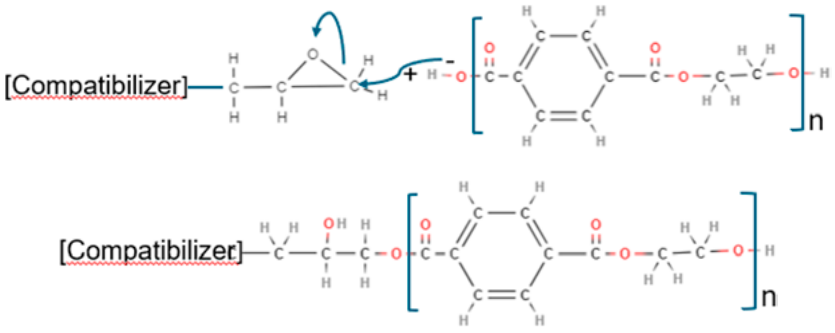

Figure 3. Reaction proposed by Kalfoglou et al. [6].

Dynamic Mechanical Analysis Measurement (DMA)

Figure 4 shows the DMA results for the pristine polymers and the ternary blend. The main α transition of PET is located at 83.2°C, HDPE has its broad α relaxation centered around 51.3°C, and E-GMA presents its main transition at -13.6°C. On the other hand, the ternary blend HDPE/PET/E-GMA (65/30/5) presents two transitions: one at 56.8°C, associated with the HDPE content, and another at 82.5°C, related to PET. Under these test conditions, in the HDPE/PET/E-GMA (65/30/5) ternary blend it is not possible to observe the transition associated with E-GMA. This fact, and the shift in the HDPE and PET transition temperatures towards each other, suggests that E-GMA functions solely as a compatibilizer, assisting in the dispersion of PET in the HDPE matrix.

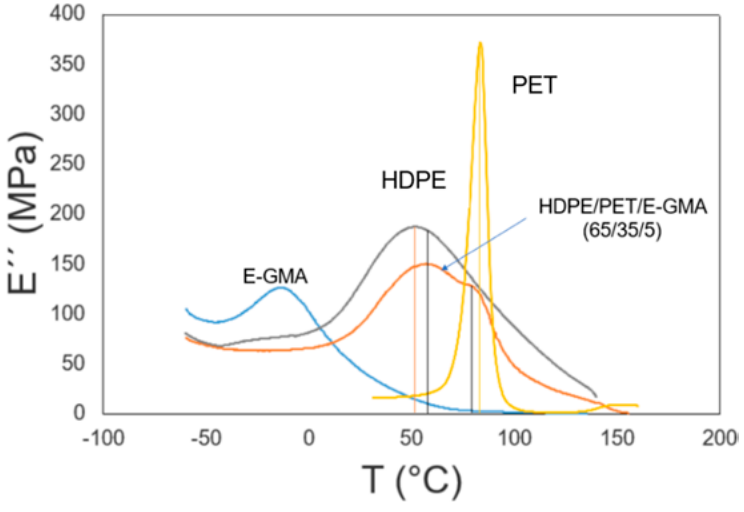

Figure 4. DMA test results showing loss modulus Vs temperature for HDPE, PET, E-GMA and HDPE/PET/E-GMA (65/30/5) (heating rate 5°C/min and oscillatory frequency 1 Hz).

DOI: https://doi.org/10.51573/Andes.PPS39.GS.PBA.1

Conclusion

To improve the mechanical properties of recycled materials, the morphology of HDPE/PET/E-GMA ternary blends demonstrates how the compatibilizer aids in the dispersion of PET in the HDPE matrix, improving the flexural modulus and impact strength of recycled materials in an upcycling context. E-GMA acts as a good compatibilizer.

The impact strength of the HDPE/PET/E-GMA ternary blends increases with higher PET content, which can be attributed to the decrease in the interparticle distance of the homogenous dispersed phase, as observed in SEM micrographs. Additionally, E-GMA helps reduce the size of the dispersed PET phase within the HDPE matrix, a fact also evident in the SEM micrographs. These results will be applied to recycled products, ultimately aiding in the design of materials from an upcycling perspective, which will enable the production of products with enhanced properties.

References

1. B. G. Mwanza and C. Mbohwa, "Drivers to Sustainable Plastic Solid Waste Recycling: A Review," *Procedia Manufacturing*, vol. 8, no. October 2016, pp. 649–656.
2. Y. Lei, Q. Wu, and Q. Zhang, "Morphology and properties of microfibrillar composites based on recycled poly (ethylene terephthalate) and high density polyethylene," *Composites Part A: Applied Science and Manufacturing*, vol. 40, no. 6–7, pp. 904–912, 2009.
3. A. B. Raheem, Z. Z. Noor, A. Hassan, M. K. Abd Hamid, S. A. Samsudin, and A. H. Sabeen, "Current developments in chemical recycling of post-consumer polyethylene terephthalate wastes for new materials production: A review," *Journal of Cleaner Production*, vol. 225, pp. 1052–1064, 2019.
4. Y. Wang, D. Mi, L. Delva, L. Cardon, J. Zhang, and K. Ragaert, "New approach to optimize mechanical properties of the immiscible polypropylene/poly (ethylene terephthalate) blend: Effect of shish-kebab and core-shell structure," *Polymers (Basel).*, vol. 10, no. 10, 2018.
5. M. N. Salleh, S. Ahmad, M. H. A. Ghani, and R. S. Chen, "Effect of compatibilizer on impact and morphological analysis of recycled HDPE/PET blends," *AIP Conference Proceedings*, vol. 1571, no. 2013, pp. 70–74, 2013.
6. N. K. Kalfoglou, D. S. Skafidas, J. K. Kallitsis, J.-C. Lambert, and L. Van der Stappen, "Comparison of compatibilizer effectiveness for PET/HDPE blends," *Polymer (Guildf).*, vol. 36, no. 23, p. 4453, 1995.
7. M. Tolinski, "Introduction," *Additives for Polyolefins*, pp. 3–7, 2015.
8. F. Chen, Y. Shangguan, Y. Jiang, B. Qiu, G. Luo, and Q. Zheng, "Toughening with little rigidity loss and mechanism for modified polypropylene by polymer particles with core-shell structure," *Polymer (Guildf)*, vol. 65, pp. 81–92, 2015.

DOI: https://doi.org/10.51573/Andes.PPS39.GS.PBA.1

GENERAL SYMPOSIA | POLYMER COMPOSITES

Influence of the Processing Temperature in the Calendaring Process of Staple Fiber Yarns on the Degree of Consolidation and the Thermal Properties

Martin Detzel, Peter Mitschang and Ulf Breuer

DOI: https://doi.org/10.51573/Andes.PPS39.GS.PC.1

December 2024

Influence of the Processing Temperature in the Calendaring Process of Staple Fiber Yarns on the Degree of Consolidation and the Thermal Properties

Martin Detzel, Peter Mitschang and Ulf Breuer[1]

Abstract: In this study, carbon/polyamide 6 staple fiber yarns were heated above the melting temperature of the polymer in a modified impregnation and calendaring process using two hot air blowers, stretched to align the fibers in the yarns, and formed into tapes. Tapes were produced at different process temperatures and the influences on the degree of consolidation and the thermal properties of the tapes were characterized. While improved impregnation quality can be achieved at higher temperatures, a decrease in the crystallization peak temperature of the impregnated tape was observed, indicating thermal degradation.

Keywords: Recycled Carbon Fiber, Thermal Properties, Staple Fiber Yarn, Tape Manufacturing

1 The authors Martin Detzel (martin.detzel@leibniz-ivw.de), Peter Mitschang and Ulf Breuer are affiliated with the Leibniz-Institut fuer Verbundwerkstoffe GmbH in Germany.

DOI: https://doi.org/10.51573/Andes.PPS39.GS.PC.1

Introduction

Depending on the manufacturing process, during the production of carbon fiber reinforced polymers approximately 40% of carbon fibers become waste, even though they are high-quality production offcuts [1]. Due to their high manufacturing costs and energy requirements, it is worthwhile to use these fibers in components with the highest possible fiber orientation. One way of using recycled carbon fibers (rCF) in an automated and conventional composite processing method is through the production of rCF tapes. For short rCF in the range of 1-12 mm, it is possible to produce rCF tapes using a wet-laid process [2,3], while textile processes can be used for fibers longer than 25 mm [4-6]. In textile processes, either slivers [7] or yarns [4,8] are produced, to which thermoplastic fibers are added as a manufacturing aid and for subsequent fiber impregnation. Depending on the weight amount of thermoplastic fibers in the textile intermediate, thermally stabilized or fully consolidated tapes can be produced by melting the polymer. During the tape production process, the polymer must be in a fully molten state until consolidation but should not be heated above the degradation onset temperature of the polymer. The aim of this study was to determine the material temperature during processing in the tape production line as a function of the fixed hot air blower temperature and to investigate the resulting degree of consolidation and the thermal properties of the produced tape.

Experimentation

Material

Staple fiber yarns with a content of 60 wt.-% CF staple fibers and 40 wt.-% PA6 staple fibers were produced with a titer of 500 tex by Wagenfelder Spinnerei GmbH, using the wrap spinning process. To ensure the stability of the yarn, a PA6 wrapping filament was used, a different PA6 type than the PA6 staple fibers due to its processability. Winding the staple fiber yarns with the wrapping filament leads to the undulation of the yarn and thus to misalignment of the fibers. The utilized rCF fibers are of the Panex® type 35 from the manufacturer Zoltek (St. Louis, MO, USA), which are spool remnants cut to a length of 80 mm for the spinning process. An image of an rCF staple fiber yarn spool and a microscopic image showing the components are presented in Figure 1.

DOI: https://doi.org/10.51573/Andes.PPS39.GS.PC.1

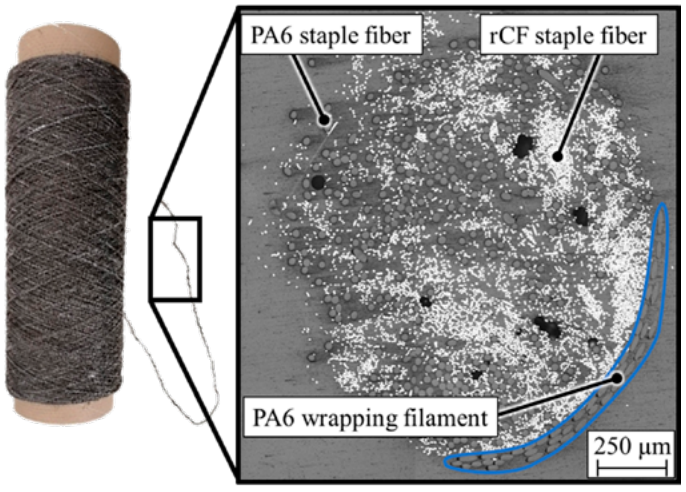

Figure 1. Spool with staple fiber yarn and microscopy image of the staple fiber yarn (PA6 wrapping filament highlighted in blue).

Determination of the Process Window and the Thermal Properties of the Produced Tapes

To determine the process window, both differential scanning calorimetry (DSC) to measure the melting point in the first heating cycle and thermogravimetric analysis (TGA) to detect the degradation onset temperature for the two PA6 types were conducted. The thermal properties (peak melting and recrystallization peak temperatures) of the produced tapes were determined using DSC in the second heating cycle and the cooling cycle. In both DSC heating cycles, the samples were heated from 20°C to 280°C under a nitrogen flow of 30.0 mL/min at a heating rate of 10 K/min. The cooling cycle from 280°C to 20°C, was carried out under a nitrogen flow of 30.0 mL/min at a cooling rate of -10 K/min. The TGA was conducted under an airflow of 30.0 mL/min in the temperature range of 30-520°C at a heating rate of 10 K/min.

Tape Production

Tape production can be described as a modified calendaring and impregnation process and was carried out on the tape production line shown in Figure 2.

DOI: https://doi.org/10.51573/Andes.PPS39.GS.PC.1

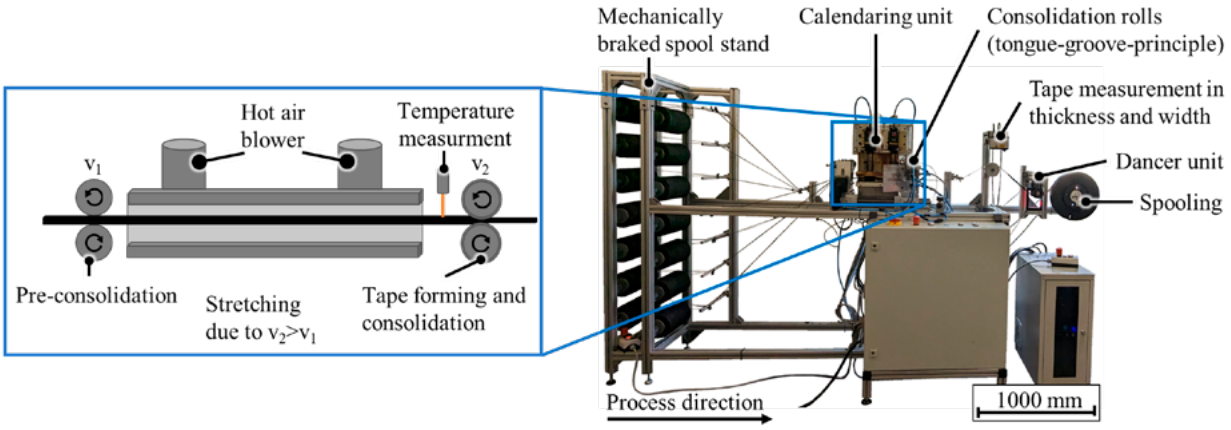

Figure 2. Tape production line with a schematic illustration of the calendaring process.

14 spools of yarn are used to produce a 12.7 mm wide tape. These are stored in a mechanically braked spool stand and pulled into the calendaring unit by the pre consolidation rollers. In the 250 mm long heating zone of the calendaring unit, the yarns are heated above the melting temperature of the polymer by two adjustable hot air blowers. The yarns are stretched by the speed difference (stretching factor) between the consolidation rollers and the pre-consolidation rollers, which leads to an alignment of the rCF in the process direction.

Table 1. Temperature, speed and stretching factor used in tape production.

Parameter set	Temperature in °C (Hot air blower) Pass 1 / Pass 2	Speed v_1 in m/min Pass 1 / Pass 2	Stretching factor $v_2>v_1$ Pass 1 / Pass 2
450°C (Pass 1) / (Pass 2)	450 / 450	1.4 / 1.1	1.1 / 1.09
475°C (Pass 1) / (Pass 2)	475 / 475	1.4 / 1.1	1.1 / 1.09
500°C (Pass 1) / (Pass 2)	500 / 500	1.4 / 1.1	1.1 / 1.09
525°C (Pass 1) / (Pass 2)	525 / 525	1.4 / 1.1	1.1 / 1.09
550°C (Pass 1) / (Pass 2)	550 / 550	1.4 / 1.1	1.1 / 1.09

The actively cooled consolidation rollers work on the tongue-and-groove principle and form a 12.7 mm wide tape from the yarns. The consolidation force was applied by a pneumatic cylinder and set to 120 N. Following consolidation, the produced tape was geometrically measured using a laser profile sensor and then wound onto Häfner spools. Further information on the production process can be found in [8], which describes that a second pass through the tape production line had a positive effect on fiber orientation and mechanical properties compared to tapes produced with the identical stretching factor in a single pass. Therefore, in this parameter study, all tapes were produced with a second pass at the same speeds and stretching factor. Only the hot air blower

DOI: https://doi.org/10.51573/Andes.PPS39.GS.PC.1

temperature was varied in increments of 25 K within the range of 450-550°C. The parameter sets are listed in Table 1 and abbreviated in the subsequent figures according to the hot air blower temperature used.

Determination of the Material Temperature During Processing

The temperature in the middle of the material during production was determined by in-situ temperature measurements. For this purpose, a type K thermocouple was inserted into a yarn, fixed and processed with the parameters listed in Table 1 for the first pass through the tape production line. To determine the temperature during the second pass, tapes were previously produced with the parameters for the first pass, then a type K thermocouple was inserted, fixed, and processed with the second pass parameters. To ensure statistical reliability, ten repetitions were carried out.

Determination of the Degree of Consolidation

The degree of consolidation was assessed by determining the void volume content using microscopic images. Five tapes per parameter level were tested for both the first and second pass through the tape production line. The void volume content was determined at three positions of the tapes: left, middle, and right. It was automatically evaluated using the gray value analysis.

Results

Determination of the Process Window

Figure 3(a) shows the DSC results of the first heating cycle for the two PA6 types. There is no significant difference between the two PA6 types. The peak melting temperature for the PA6 staple fiber is 219.7°C, while for the PA6 wrapping filament it is 219.9°C. Both melting temperatures are within the expected range for PA6. Figure 3(b) shows the results of the TGA, which reveal a clear difference in the degradation behavior of the two PA6 types. The first degradation onset temperature of the PA6 staple fiber is 320°C, while for the PA6 wrapping filament it is 380°C. The lower degradation onset temperature of the PA6 staple fibers may be attributed to additives present in the polymer. A process window of 220°C to 320°C was derived from this peak melting temperature and the onset of degradation temperature.

DOI: https://doi.org/10.51573/Andes.PPS39.GS.PC.1

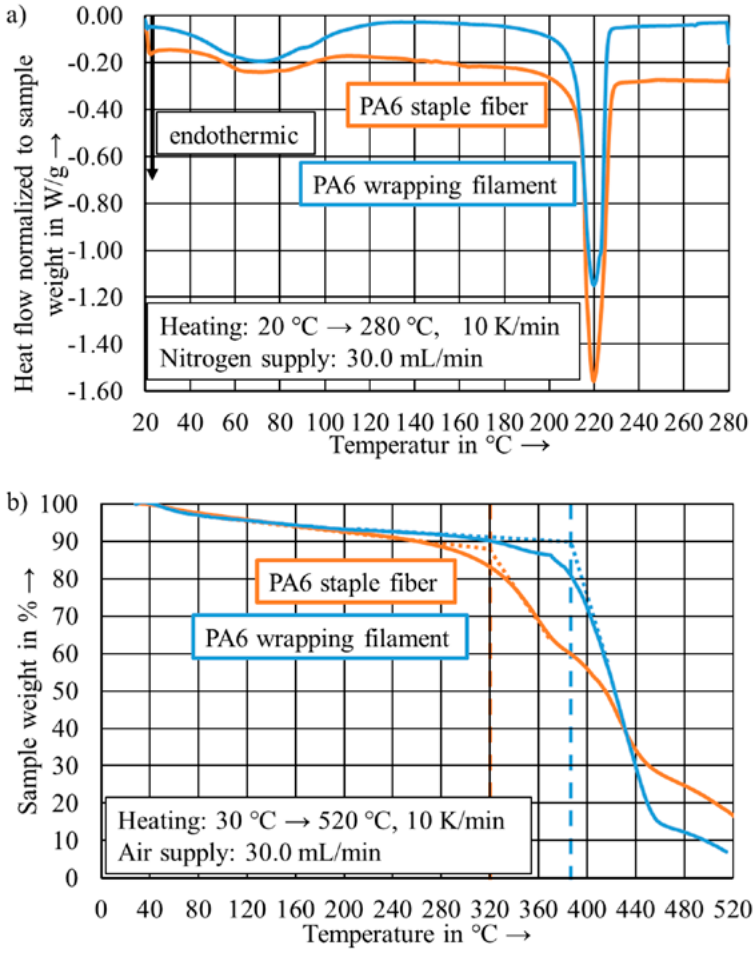

Figure 3. (a) DSC-thermogram of the PA6 staple fiber and the PA6 wrapping filament and (b) TGA-thermogram of the PA6 staple fiber and the PA6 wrapping filament.

Determination of the Material Temperature During Processing

Figure 4(a) shows the temperatures in the center of the yarn for the hot air blower temperatures ranging from 450 to 550°C for the first pass through the tape production line. The increase in yarn temperature immediately after leaving the pre-consolidation rollers is due to the hot air exiting the heating zone. Upon entering the heating zone, the yarns quickly heat up above the melting temperature of the PA6. The passage of the first hot air blower is clearly indicated by a change in the temperature gradient. The maximum temperature in the material is reached at the second hot air blower. The material temperature decreases slightly until it reaches the consolidation rollers. During the consolidation process, the material temperature is rapidly lowered to about 100°C by the actively cooled consolidation rollers. The subsequent slow cooling occurs passively through ambient temperature. For the set hot air blower temperatures of 525°C and 550°C, the degradation onset temperature of the PA6 staple fiber in the center of the yarn is exceeded. Taking into account

DOI: https://doi.org/10.51573/Andes.PPS39.GS.PC.1

the standard deviation of the experiments, the degradation onset temperature is also reached in some experiments with a hot air blower temperature of 500°C. Figure 4(b) shows the temperatures for the second pass through the tape production line for previously produced tapes. A comparable heating behavior to that of the yarns (Figure 5[a]) is observed. Due to the lower processing speed, the dwell time of the tapes in the heating zone is longer; but the degradation onset temperature in the center of the tape is not reached for any of the set hot air blower temperatures. The more open structure of the yarns allows faster heating of the sample's center. A statement about the temperature at the sample surface cannot be provided at this time but should be measured in future studies.

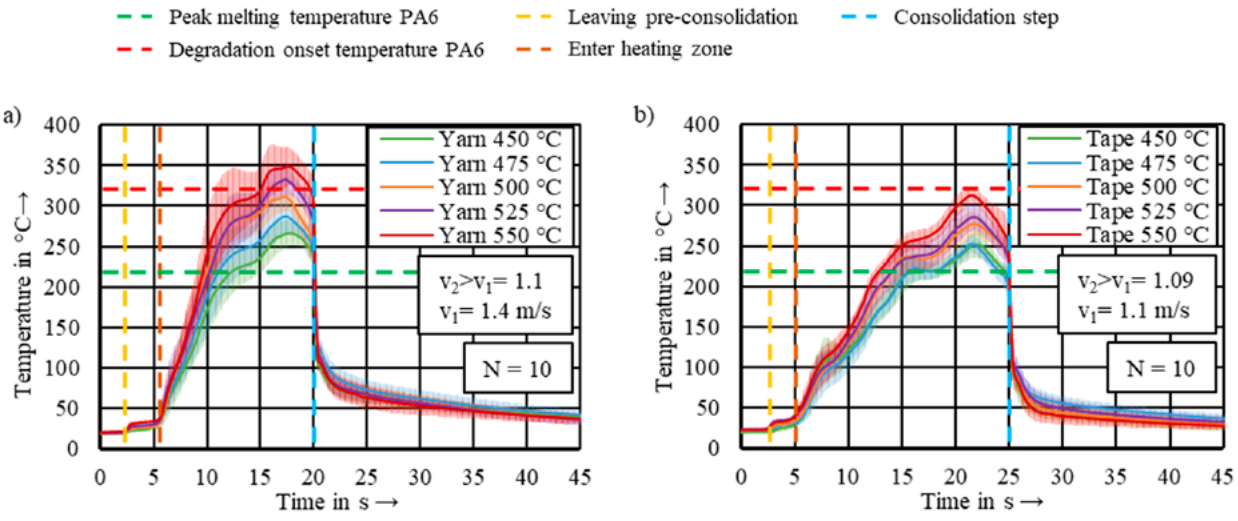

Figure 4. (a) Temperature in the center of the staple fiber yarn during the first and (b) temperature in the center of previously produced tape during the second pass through the tape production line.

Determination of the Degree of Consolidation

Figure 5 shows the results of the void volume analysis to evaluate the degree of consolidation. The results are divided into the first and second system runs. In some microscopy images for temperatures 450°C and 475°C, unmelted PA6 fibers can be observed at the edges of the tape after the first pass through the tape production line, see Figure 5(b). Except for the temperature of 450°C, higher temperatures during the first pass result in lower void volume content. At 475°C, the void volume content is 7.3%; increasing the temperature to 550°C reduces the void volume content to 2.6%. The low void volume content at 450°C (2.2%) is due to a poorly consolidated tape surface, which led to post-impregnation with embedding material, see Figure 5(c).

DOI: https://doi.org/10.51573/Andes.PPS39.GS.PC.1

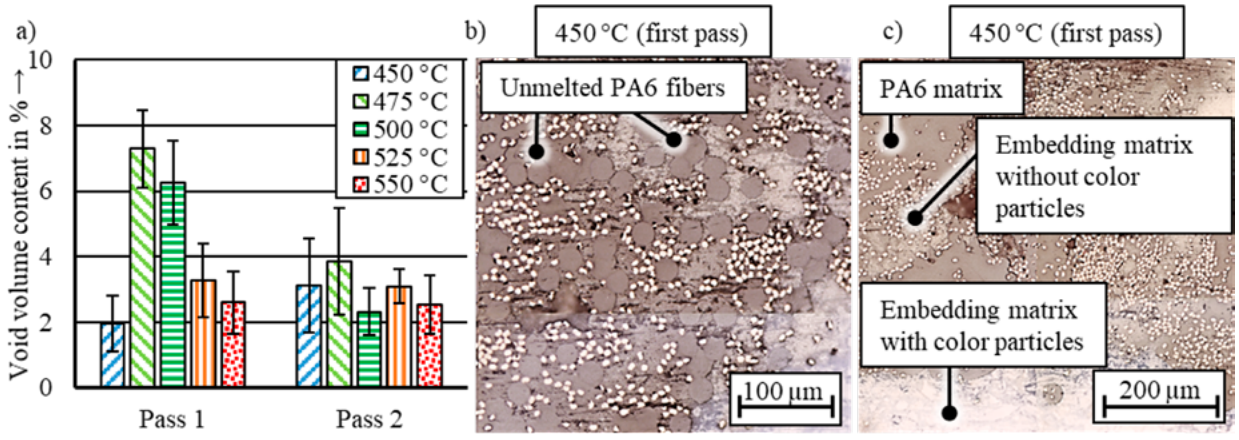

Figure 5. (a) Void volume content after the first and second pass for different hot air blower temperatures, (b) unmelted PA6 fibers at the edge of produced tapes at 450°C after the first pass and (c) tape produced at 450°C after the first pass with post-impregnation of embedding material.

These areas could not be detected as voids by the automatic evaluation. For future research, compression thermal analysis [9] should be used to measure the degree of consolidation, as this method can evaluate samples without a closed surface. The results of the tapes after the second pass through the tape production line show no clear influence of the hot air blower temperature. The void volume content decreases after the second pass through the equipment and ranges from 2.3% to 3.8%.

Determination of the Thermal Properties of the Produced Tapes

The results of the DSC measurements are shown in Figure 6 for the hot air blower temperature used during tape production. Compared to the PA6 wrapping filament and the PA6 staple fiber, the peak melting temperature of the tapes decreases regardless of the selected hot air blower temperature. The peak melting temperature of the produced tapes ranges from 214.2°C to 216.8°C, while the PA6 wrapping filament is at 219.9°C and the PA6 staple fiber at 221.5°C. At temperatures of 450°C and 475°C, the crystallization peak temperature of 188.5°C and 188.6°C is in the range between PA6 staple fiber 186.1°C and PA6 wrapping filament 193.5°C. A decrease in the crystallization peak temperature is observed, starting from a hot air blower temperature of 500°C. For 500°C and 525°C, the crystallization peak temperature is 184.4°C. Increasing the temperature to 550°C leads to a drop in the crystallization peak temperature (182.6°C). A change in the crystallization peak temperature can be attributed to a change in molecular weight due to thermal degradation [10].

DOI: https://doi.org/10.51573/Andes.PPS39.GS.PC.1

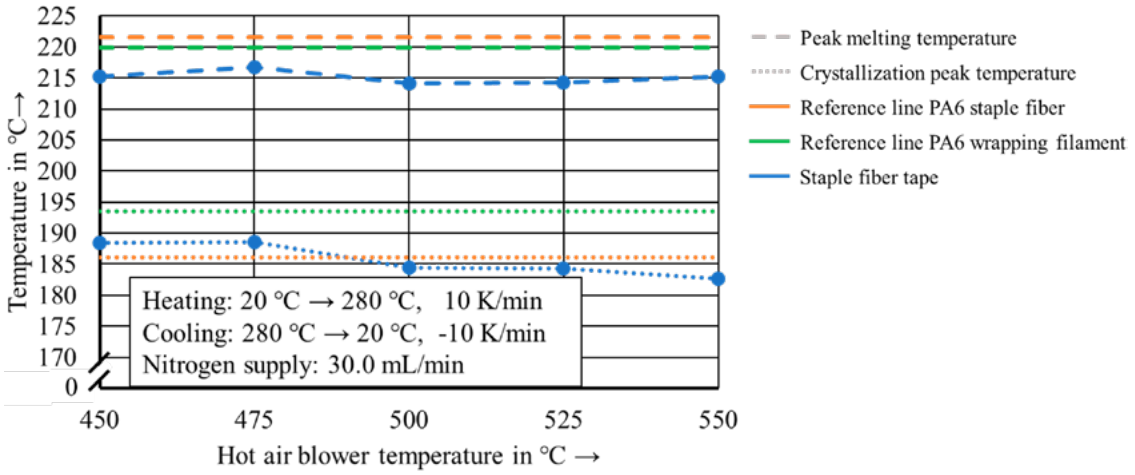

Figure 6. Influence of hot air blower temperature on peak melting and crystallization peak temperature.

Conclusion

By combining the results of the DSC and TGA tests, the processing window for the staple fiber yarns was determined. The subsequent in-situ temperature measurements showed that hot air blower temperatures above 500°C led to material temperatures exceeding the degradation onset temperature of the PA6 staple fibers. Exceeding the degradation onset temperature in these experiments may have contributed to the observed decrease in the crystallization peak temperature. However, these higher temperatures resulted in the lowest void volume contents after the first pass. Improved consolidation was achieved without noticeable influence from the hot air blower temperature after the second pass. For the future production of SF tapes, a processing temperature of 450°C or 475°C should be selected at the utilized processing speed to prevent thermal damage while ensuring good material consolidation.

Acknowledgments

This study has been conducted within the framework of the research project 'Process analysis of pseudo-plastic behavior of unidirectional reinforced staple fiber organic sheets' funded by the German Research Foundation (DFG)—funding reference 471480678.

References

1. M. F. Khurshid, M. Hengstermann, M. M. B. Hasan, A. Abdkader, and C. Cherif, "Recent developments in the processing of waste carbon fibre for thermoplastic composites – A review," *Journal of Composite Materials,* vol. 54, no. 14, pp. 1925–1944, Jan. 2020, https://doi.org/10.1177/0021998319886043

2. S. Yarlagadda, J. Deitzel, D. Heider, J. Tierney, and J. W. Gillespie Jr., "Tailorable Universal Feedstock for Forming (TUFF): Overview and Performance," no. SAMPE Conference Proceedings, Jan. 2019, [Online]. Available: https://doi.org/10.33599/nasampe/s.19.1605

3. H. Yu, K. D. Potter, and M. R. Wisnom, "A novel manufacturing method for aligned discontinuous fibre composites (High Performance-Discontinuous Fibre method)," *Composites Part A: Applied Science and Manufacturing,* vol. 65, pp. 175–185, Oct. 2014, https://doi.org/10.1016/j.compositesa.2014.06.005

4. M. Hengstermann, M. M. B. Hasan, A. Abdkader, and C. Cherif, "Development of a new hybrid yarn construction from recycled carbon fibers (rCF) for high-performance composites. Part-II: Influence of yarn parameters on tensile properties of composites," *Textile Research Journal*, vol. 87, no. 13, pp. 1655–1664, Jan. 2017, https://doi.org/10.1177/0040517516658511

5. M. Hengstermann, N. Raithel, A. Abdkader, M. M. B. Hasan, and C. Cherif, "Development of new hybrid yarn construction from recycled carbon fibers for high performance composites. Part-I: basic processing of hybrid carbon fiber/polyamide 6 yarn spinning from virgin carbon fiber staple fibers," *Textile Research Journal*, vol. 86, no. 12, pp. 1307–1317, Jan. 2016, https://doi.org/10.1177/0040517515612363

6. C. Goergen, D. Schommer, M. Duhovic, and P. Mitschang, "Deep drawing of organic sheets made of hybrid recycled carbon and thermoplastic polyamide 6 staple fiber yarns," *Journal of Thermoplastic Composite Materials*, vol. 33, no. 6, pp. 754–778, Jan. 2020, https://doi.org/10.1177/0892705718811407

7. M. H. Akonda, M. Stefanova, P. Potluri, and Du Shah, "Mechanical properties of recycled carbon fibre/polyester thermoplastic tape composites," *Journal of Composite Materials*, vol. 51, no. 18, pp. 2655–2663, Jan. 2017, https://doi.org/10.1177/0021998316672091

8. M. Detzel, P. Mitschang, and U. Breuer, "New Approach for Processing Recycled Carbon Staple Fiber Yarns into Unidirectionally Reinforced Recycled Carbon Staple Fiber Tape," *Polymers*, vol. 15, no. 23, p. 4575, Nov. 2023, https://doi.org/10.3390/polym15234575

9. K. M. Nelson, J.-A. E. Manson, and J. C. Seferis, "Compression Thermal Analysis of the Consolidation Process for Thermoplastic Matrix Composites," *Journal of Thermoplastic Composite Materials*, vol. 3, no. 3, pp. 216–232, Jul. 1990, https://doi.org/10.1177/089270579000300304

10. G. W. Ehrenstein, G. Riedel, and P. Trawiel, *Praxis der Thermischen Analyse von Kunststoffen*, 2nd ed. München: Hanser Fachbuchverlag, 2003.

GENERAL SYMPOSIA | POLYMER COMPOSITES

Formulation of Highly Electro-Conductive Thermoplastic Composites using PEDOT-based Fillers with Controlled Shape Factor

Adèle Karst, Michel Bouquey, Jérémie Soulestin, Cédric Samuel and Thibault Parpaite

DOI: https://doi.org/10.51573/Andes.PPS39.GS.PC.2

December 2024

Formulation of Highly Electro-Conductive Thermoplastic Composites using PEDOT-based Fillers with Controlled Shape Factor

Adèle Karst, Michel Bouquey, Jérémie Soulestin, Cédric Samuel and Thibault Parpaite[1]

Abstract: The objective of this study is to develop a new conductive thermoplastic material with superior electrical properties. Currently, conductive polymers are typically filled with carbon or metallic particles [1]. However, these filled thermoplastics exhibit drawbacks such as high rigidity, toxicity, and high viscosity [2]. An alternative approach investigated in this work is to substitute these fillers with intrinsically conductive polymers like Poly(3,4-ethylenedioxythiophene) (PEDOT). PEDOT can achieve exceptional electrical conductivities (over 1000 $S.cm^{-1}$) when combined with polymeric dopants like poly(styrene sulfonate) (PSS) and is frequently used in thin films or gels in medical and energy applications [3]. However, incorporating PEDOT into the conventional hot melt processes of the plastic industry remains challenging [1].

Keywords: Conductive Polymers, PEDOT, Oxidative Polymerization, Conductive Composites, Extrusion, Electrical Conductivity, Shape Factor

1 The authors Adèle Karst, Michel Bouquey and Thibault Parpaite (thibault.parpaite@ics-cnrs.unistra.fr) are affiliated with the Institut Charles Sadron in France. Jérémie Soulestin and Cédric Samuel are affiliated with the IMT Nord Europe which in turn is affiliated to the Institut Mines-Télécom and partnered with the University of Lille in France. Thibault Parpaite is also affiliated with INSA Strasbourg.

DOI: https://doi.org/10.51573/Andes.PPS39.GS.PC.2

Introduction

In a previous study, we synthesized electro-conductive PEDOT particles for incorporation into a polyethylene oxide (PEO) matrix via an extrusion process [4]. Composites with notable conductivities of up to 12 $S{\cdot}cm^{-1}$ were achieved, but a high amount of PEDOT fillers was required to reach the electrical percolation threshold. To reduce this percolation threshold, this work investigates a new approach based on a supported polymerization process. The goal is to control the shape factor of the synthesized conductive PEDOT particles by using different fillers, such as silica, graphene, or clays, for EDOT polymerization. The objective is to coat these fillers with a conductive PEDOT shell and then study the impact of various shape factors on the electrical percolation threshold of the resulting composites. Relationships between the process, morphology, and properties were analyzed using SEM, X-ray tomography, and four-probe resistivity measurements. Percolation curves for different shape factors were also obtained and compared to the initial curve obtained with micrometric PEDOT particles.

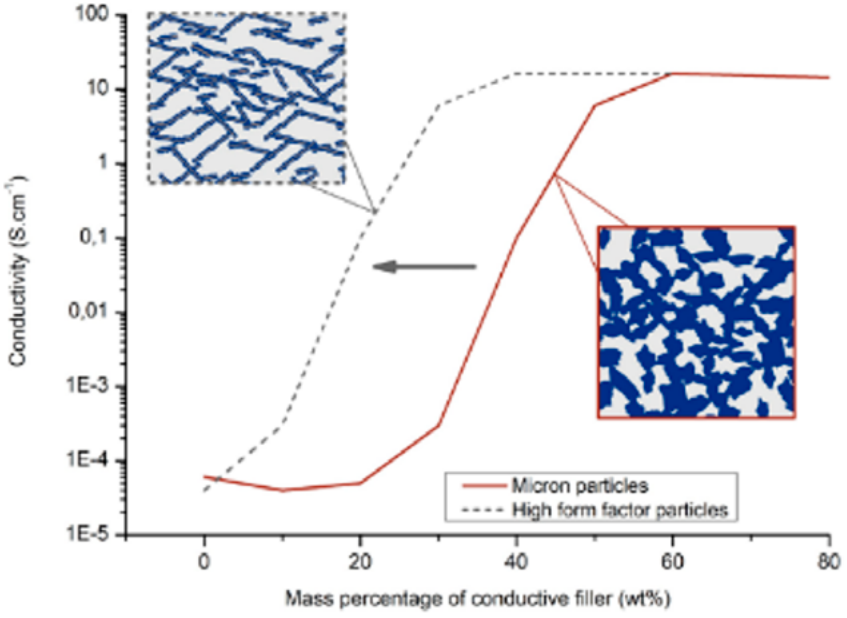

Figure 1. Illustration of the objective of reducing the percolation threshold by optimizing the form factor of the fillers.

DOI: https://doi.org/10.51573/Andes.PPS39.GS.PC.2

Experimental Section

Materials

3,4-Ethylenedioxythiophene (EDOT, 99%, Acros Organics), iron (III) chloride ($FeCl_3$; 97%, Sigma-Aldrich), sodium dodecyl sulfate (SDS, 98.5%, Sigma-Aldrich), natural clays with interesting shape factor (L/D ratio > 50) were used as received for the synthesis of PEDOT-Clay particles. Poly(ethylene oxide) (PEO, 100.000 g/mol, Sigma-Aldrich) was used as received for the extrusion of PEO / PEDOT-Clay composites.

Synthesis of PEDOT-Clay Particles Using Oxidative Polymerization Process

The synthesis of PEDOT-Clay was performed by chemical oxidative polymerization of EDOT in the presence of clay particles, as presented in a previous work [4]. The clays were dispersed in 100 mL of demineralized water, and Sodium Dodecyl Sulfate (SDS, 0.00056 mmol) was dissolved in the solution. EDOT (0.007 mol) was added dropwise, and the solution was stirred for 2 hours. The oxidant (FeCl3, 0.0023 mol) was then added to the solution. The solution was placed under magnetic stirring for 48 hours to allow polymerization at room temperature.

The polymerized solution was filtered using a Büchner funnel and filter paper. During suction, the PEDOT-Clay particles were retained by the filter paper and the oxidizing solution was collected in the vacuum flask. The polymerized particles were washed twice on the filter paper during suction, first with acetone:methanol (3:10) and then with ethanol:water (1:1). The PEDOT-Clay particles were dried at 60°C for 48 hours.

Incorporation of Synthesized PEDOT-Clay Particles into the PEO Matrix by Twin Screw Extrusion

The result of the polymerization step, which is a dry dark blue powder, is directly used as a filler for the twin screw extrusion process. Agglomerates of synthesized PEDOT-Clay particles were separated using a mortar and then blended with PEO powder. The proportions of PEDOT-Clay in PEO were varied from 10 wt.% to 40 wt.%. The blended dry powders were then introduced into a twin screw extruder at a temperature of 100°C and a screw rotation speed of 30 rpm. The microcompounder (Haake Minilab 2, Thermo Fisher Scientific) was used in direct extrusion mode. Under these conditions, the residence time of the material inside the microcompounder is approximately 1 minute.

DOI: https://doi.org/10.51573/Andes.PPS39.GS.PC.2

Characterizations

Conductivity Measurements on PEDOT-Clay Particles and Extruded PEO/PEDOT-Clay Composites

To perform electrical conductivity measurements, the PEDOT-Clay powder was compressed into pellets. Infrared equipment normally used for making KBr pellets was employed for this purpose. The pellets were compressed at 45 bars for 30 seconds. With this method, all the samples are 13 mm in diameter, but with varying thicknesses. The thickness of each pellet was measured with a slide caliper.

The composite strip could be used immediately after the extrusion step. The width and thickness of the strip were also measured with a slide caliper. Both the PEDOT-Clay pellets and the extruded strips were then placed in a homemade four-probe system, developed specifically for this study and equipped with a Keithley 2611B multimeter, with constant pressure applied for resistance measurements.

Morphological Analyses by SEM and X-Ray Tomography

The morphology of PEDOT-Clay powders and extruded PEO/PEDOT-Clay ribbons was analyzed primarily by scanning electron microscopy (SEM, Hitachi SU 8010). The extruded ribbons were also subjected to X-ray tomography using an EasyTom 150/160 apparatus (RX Solution, voltage 100 kV, spatial resolution 5 µm) for better visualization of the aggregation state of PEDOT-Clay particles within the PEO.

Results & Discussions

Processing of PEO/PEDOT Composites

Previous work by our team demonstrated the synthesis of conductive PEDOT particles and their incorporation into a thermoplastic matrix [5]. Electrically conductive PEDOT particles were obtained through chemical oxidative polymerization. Using these particles as fillers, electrically conductive thermoplastic composites were manufactured by twin screw extrusion to determine the electrical percolation threshold and the maximum conductivity of the composite. PEDOT particles were blended with PEO having a molecular weight of 100,000 $g.mol^{-1}$ at a processing temperature of 100°C, which is compatible with the maximum processing temperature of PEDOT, close to 170-180°C [5]. At approximately 30 wt.% PEDOT, the electrical conductivity begins to increase, reaching a maximum conductivity of around 12 $S.cm^{-1}$ with 60 wt.% of conductive particles.

DOI: https://doi.org/10.51573/Andes.PPS39.GS.PC.2

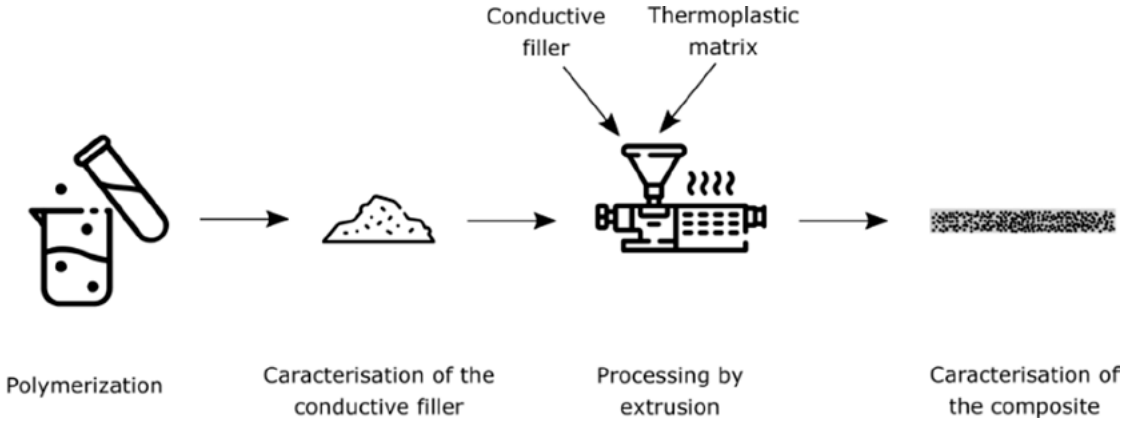

Figure 2. Schematic representation of the electrically conductive thermoplastic composite processing.

Influence of the Form Factor on the Percolation Threshold

Interesting properties were obtained in the previous study, but a high percolation threshold was observed, which can lead to certain issues. In fact, aside from cost concerns, a high percolation threshold results in high viscosities and a reduction in the mechanical properties of the composite [6]. Therefore, reducing the percolation threshold is necessary while maintaining the electrical properties of the composite materials. To this end, some studies have demonstrated the influence of the form factor and aspect ratio on the percolation threshold. Audoit and Matthews, for example, showed that the higher the form factor of the filler, the lower the percolation threshold [7,8].

Supported Polymerization of PEDOT in Literature

To modify the form factor of PEDOT, using a polymerization support to obtain a core-shell structure with controlled morphology is a promising strategy. To achieve a very high form factor, Chen et al. and Zhang et al. demonstrated the possibility of polymerizing EDOT onto polypropylene fibers or glass fibers [9,10]. Supported oxidative polymerization on graphene particles has also been presented in literature, as shown by the work of Xu et al. [11], leading to the formation of 2D particles. This method can also be used to synthesize coated nanoparticles, such as silica@PEDOT nanoparticles [12] or carbon black@PEDOT [13].

Supported Polymerization of PEDOT on High Form Factor Clays

To reduce the percolation threshold of our PEO/PEDOT thermoplastic composites and lower the material cost, a supported polymerization of PEDOT on clay particles with a very high aspect ratio (L/D > 50) was performed. Figure 3 shows the morphology of PEDOT/clay particles obtained by

DOI: https://doi.org/10.51573/Andes.PPS39.GS.PC.2

chemical oxidative polymerization of EDOT in water at 20°C. SEM and cryo-TEM images illustrate the clay particles before polymerization ([a] and [c]) and covered by a PEDOT shell ([b] and [d]).

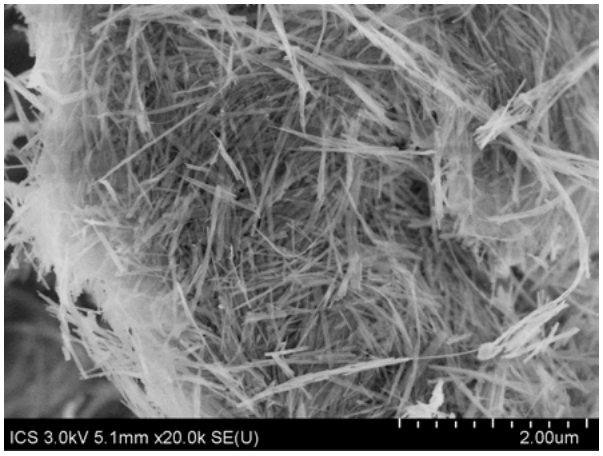

(a) Pure Clay – Before polymerization

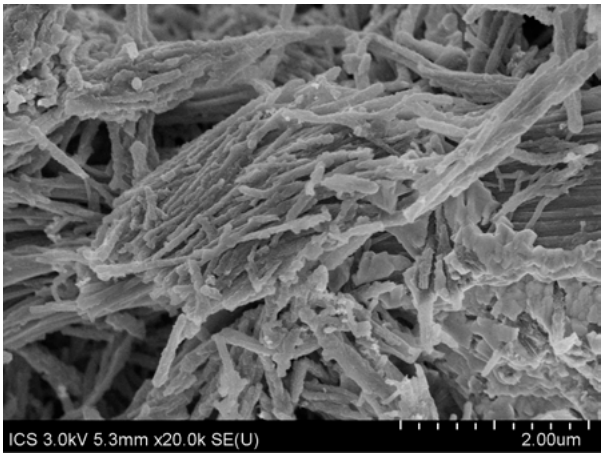

(b) Clay-PEDOT – After polymerization

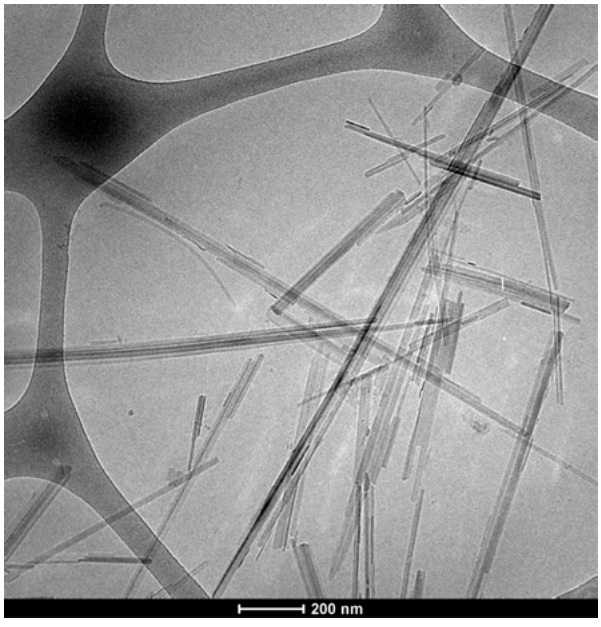

(c) Pure Clay – Before polymerization

(d) Clay-PEDOT – After polymerization

Figure 3. SEM images of clay particles before polymerization (a) and after supporting EDOT (b); cryo-TEM images of clay particles before polymerization (c) and after supporting EDOT (d).

Figure 3(b) shows a complete coverage of the clay particles by PEDOT, while Figure 3(d) indicates that all PEDOT chains surround the clay particles, with no PEDOT chains appearing to be independent of the clay particles. Moreover, conductivity characterizations were also performed on compressed powders, with conductivities reaching up to 47 $S.cm^{-1}$.

DOI: https://doi.org/10.51573/Andes.PPS39.GS.PC.2

Effect of Form Factor on the Percolation Threshold of PEO Composites

Electrically conductive thermoplastic composites PEO/PEDOT-Clay were manufactured by twin screw extrusion using the same process described in paragraph 1. To determine the electrical percolation threshold, extrusion experiments were conducted with varying amounts of PEDOT-Clay particles, ranging from 10 wt% to 40 wt%. Figure 4 shows that the electrical conductivity of PEO/PEDOT-Clay composites begins to increase from 20 wt% of fillers. A shift of approximately 10 wt% in the percolation threshold is observed between the percolation curves of composites loaded with high aspect ratio versus low aspect ratio particles, which is consistent with literature.

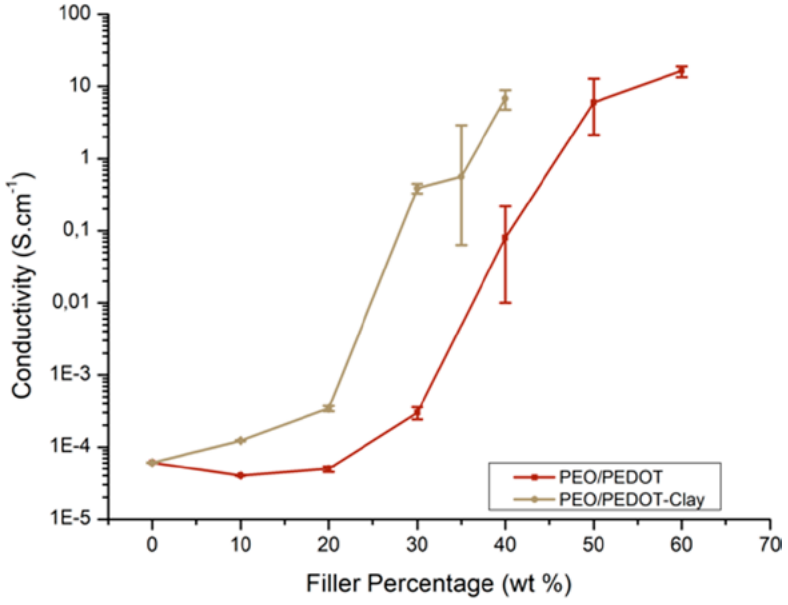

Figure 4. Evolution of the electrical conductivity of PEO/PEDOT and PEO/PEDOT-clay thermoplastic composites as a function of the PEDOT weight content (red) or PEDOT-Clay weight content (dash line).

Moreover, a drastic improvement in filler dispersion is evident from the X-ray tomography images presented in Figure 5.

DOI: https://doi.org/10.51573/Andes.PPS39.GS.PC.2

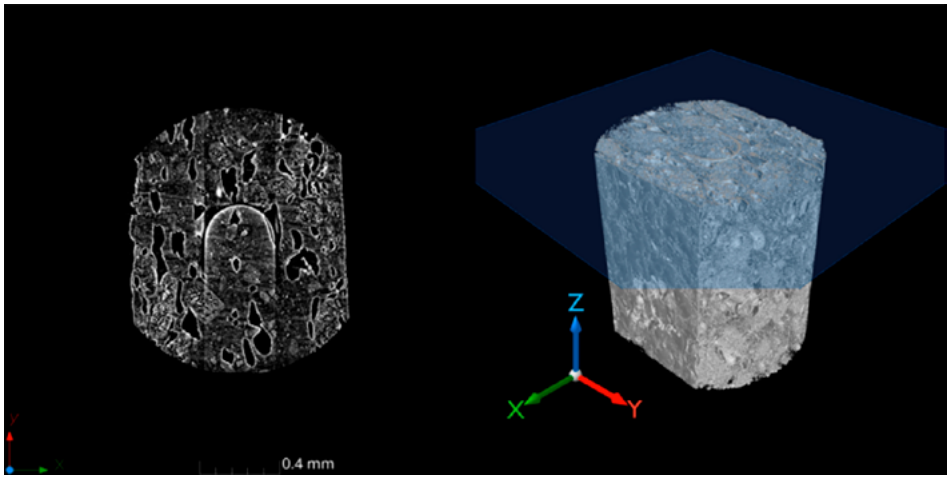

PEO/μPEDOT 60/40 wt%

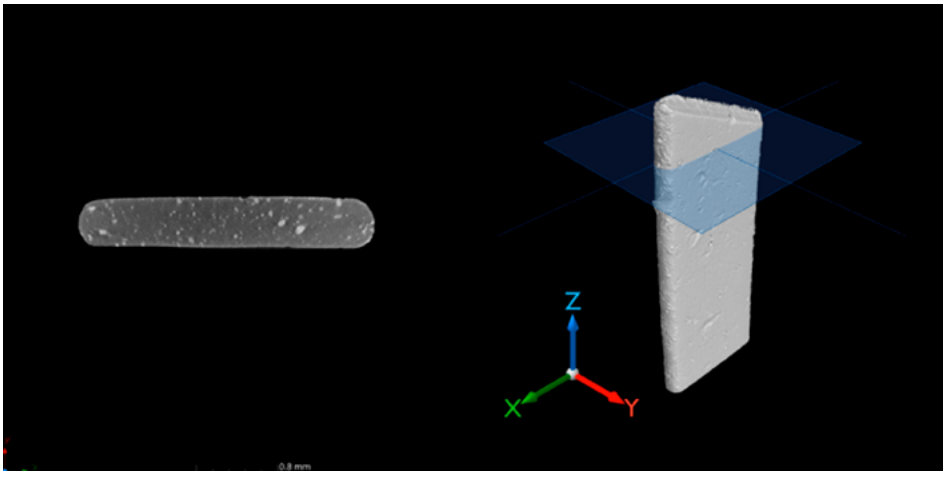

PEO/CLAY-PEDOT 60/40 wt%

Figure 5. X-Ray tomography of PEO/PEDOT and PEO/PEDOT-clays thermoplastic composites filled with 40 wt% of filler.

Conclusion

Electrically conductive PEDOT-Clay particles were successfully produced, with conductivities reaching up to 47 $S \cdot cm^{-1}$. These micron-sized fillers were then incorporated into a thermoplastic matrix. PEO/PEDOT-Clay thermoplastic composites were obtained through an extrusion process, and a significant reduction in the percolation threshold was observed due to form factor optimization. Additionally, improved filler dispersion within the matrix was noted, leading to better homogeneity and enhanced mechanical resistance of the material.

DOI: https://doi.org/10.51573/Andes.PPS39.GS.PC.2

Acknowledgments

All authors acknowledge the MINAMEC platform (Antoine Egele) for conductivity measurements, X-ray tomography, and data interpretation. The authors especially acknowledge Damien Favier for the realization of the four probes conductivity measurement device. The authors acknowledge the PLAMICS microscopy facility of ICS. CS and JS particularly acknowledge the Wallonia Region/ Service Public de Wallonie (Belgium), West Vlaanderen Region (Belgium), Agentschap Innoveren Ondernemen (Belgium), and European Commission (FEDER) for the financial support regarding important chemicals in the framework of the INTERREG France-Wallonie-Vlaanderen program (BIOHARV project, GoToS3 portofolio).

References

1. C. Duc, G. Stoclet, J. Soulestin, and C. Samuel, "Poly(ethylene oxide)/Poly(3,4-ethylenedioxythiophene):Poly(styrene sulfonate) (PEDOT:PSS) Blends: An Efficient Route to Highly Conductive Thermoplastic Materials for Melt-State Extrusion Processing ?," ACS Appl Polym Mater, vol. 2, no. 6, pp. 2366–2379, Jun. 2020, https://doi.org/10.1021/acsapm.0c00303
2. K. Gnanasekaran et al., "3D printing of CNT- and graphene-based conductive polymer nanocomposites by fused deposition modeling," Appl Mater Today, vol. 9, pp. 21–28, 2017, https://doi.org/10.1016/j.apmt.2017.04.003
3. C. Jiang, G. Chen, and X. Wang, "High-conversion synthesis of poly(3,4-ethylenedioxythiophene) by chemical oxidative polymerization," Synth Met, vol. 162, no. 21–22, pp. 1968–1971, 2012, https://doi.org/10.1016/j.synthmet.2012.09.008
4. A. Karst et al., "Synthesis and characterization of PEDOT, an intrinsically conductive polymer," 2023, p. 150001. https://doi.org/10.1063/5.0135837
5. A. Karst, T. Parpaite, M. Bouquey, H. Pelletier, J. Soulestin, and C. Samuel, "Synthesis of PEDOT particles and manufacturing of electrically-conductive PEO / PEDOT thermoplastic composites by twin-screw extrusion," *Polymer (Guildf)*, vol. 290, Jan. 2024, https://doi.org/10.1016/j.polymer.2023.126577
6. F. Godard, M. Vincent, J.-F. Agassant, and B. Vergnes, "Étude Du Comportement Rhéologique Et Des Propriétés Mécaniques De Composites Sciures De Bois-Polyéthylène Haute Densité," *Rhéologie*, vol. 136, pp. 9–21, 2008.
7. Jérémie AUDOIT, "Optimisation de la conductivité électrique transverse de composites structuraux PAEK–fils submicroniques d'argent / fibres de carbone continues avec ensimage conducteur," p. 147, 2017, [Online]. Available: http://thesesups.ups-tlse.fr/3432/1/2017TOU30001.pdf
8. M. Mathew, T. Schilling, and M. Oettel, "Connectivity percolation in suspensions of hard platelets," *Physical Review E: Statistical, Nonlinear and Soft Matter Physics*, vol. 85, no. 6, pp. 1–7, 2012, https://doi.org/10.1103/PhysRevE.85.061407

9. X. Zhang et al., "Worm-Like PEDOT:Tos coated polypropylene fabrics via low-temperature interfacial polymerization for high-efficiency thermoelectric textile," *Progress in Organic Coatings*, vol. 149, no. August, p. 105919, 2020, https://doi.org/10.1016/j.porgcoat.2020.105919

10. X. Chen, G. Tang, J. Pan, and H. Wang, "Synthesis and Thermoelectric Property of 1D Flexible PEDOT: p-TSA/Glass Fiber," *Journal of Minerals and Materials Characterization and Engineering*, vol. 06, no. 03, pp. 448–463, 2018, https://doi.org/10.4236/jmmce.2018.63032

11. K. Xu, G. Chen, and D. Qiu, "Convenient construction of poly(3,4-ethylenedioxythiophene)-graphene pie-like structure with enhanced thermoelectric performance," *Journal of Materials Chemistry A*, vol. 1, no. 40, pp. 12395–12399, 2013, https://doi.org/10.1039/c3ta12691a

12. D. Eun Park, Y. Zhen Dong, and H. Jin Choi, "Fabrication and electric stimuli-response of semiconducting poly(3,4-ethylenedioxythiophene)/silica nanocomposite particles," *European Polymer Journal*, vol. 101, pp. 255–261, Apr. 2018, https://doi.org/10.1016/j.eurpolymj.2018.02.033

13. Y. Xie et al., "Properties of carbon black-PEDOT composite prepared via in-situ chemical oxidative polymerization," *e-Polymers*, vol. 19, no. 1, pp. 61–69, May 2019, https://doi.org/10.1515/epoly-2019-0008

GENERAL SYMPOSIA | POLYMER COMPOSITES

Braided Composite System with Haptic Feedback for Teleoperation

Nathalia Diaz Armas, Shilpa Thakur, Jinde Zhang, Geet Bhandari, Sevil Turkoglu, Drupad Kadiyala Bhavani, Pratap M. Rao, Cagdas D. Onal and Joey Mead

DOI: https://doi.org/10.51573/Andes.PPS39.GS.PC.3

December 2024

View Online

Export Citation

Braided Composite System with Haptic Feedback for Teleoperation

Nathalia Diaz Armas, Shilpa Thakur, Jinde Zhang, Geet Bhandari, Sevil Turkoglu, Drupad Kadiyala Bhavani, Pratap M. Rao, Cagdas D. Onal and Joey Mead[1]

Abstract: A pneumatic-driven soft robotic actuator made from braided nylon coated with silicone elastomer was created using a new fabrication process, with the aim of providing haptic feedback to the fingers in teleoperation applications. The resulting haptic actuator was designed to be flexible, lightweight, and wearable, offering a comfortable user experience. Through the manipulation of the braiding angle, multiple devices were fabricated, focusing on their effectiveness in transmitting haptic sensations to the user's finger.

Keywords: Braided Composites, Haptic Glove, Silicone Matrix, Pneumatic Subsystem

Introduction

Wearable haptic interfaces have been explored for various applications, including teleoperation, virtual reality, healthcare, human-computer interaction, and more [1,2]. When remotely performing teleoperation tasks under unpredictable or non-repetitive conditions, relying solely on visual feedback is not sufficient. Therefore, the presence of haptic feedback becomes crucial, allowing humans to effectively control a robot from a distance and also ensuring operator safety [3].

1 The authors Nathalia Diaz Armas (nathalia_diazarmas@student.uml.edu), Jinde Zhang (jinde_zhang@uml.edu), Geet Bhandari (geet_bhandari@student.uml.edu), Sevil Turkoglu (sevil_kaynar@student.uml.edu), Drupad Kadiyala Bhavani (drupad_kadiyalabhavani@student.uml.edu) and Joey Mead (joey_mead@uml.edu) are affiliated with the University of Massachusetts Lowell in the United States. The authors Shilpa Thakur (sthakur@wpi.edu), Pratap M. Rao (pmrao@wpi.edu) and Cagdas D. Onal (cdonal@wpi.edu) are affiliated with the Worcester Polytechnic Institute in the United States.

DOI: https://doi.org/10.51573/Andes.PPS39.GS.PC.3

Significant efforts have been dedicated to advancing pneumatic-operated systems for haptic feedback, which provides important advantages such as high power-to-weight ratio and increased safety [4,5]. S. Li et al. [3] introduced a haptic glove composed of pneumatic actuators fabricated from heat-sealable plastic. These actuators were rolled into a toroid shape, enabling them to encircle the user's fingers. When inflated, these actuators effectively conveyed the sensation of grasp force. However, the sealed plastic system exhibited wrinkling, suggesting potential for refinement through the adoption of alternative materials. After this work, Rameshwar et al. [6] developed a device constructed from a fabric-silicone composite configured in a toroidal shape. The fabric-silicone composite showed a 35% reduction in applied force during teleoperation compared to the plastic-sealed device, facilitating the manipulation of delicate objects with increased finesse. In addition, the use of a fabric-silicone composite addressed the plastic-like tactile sensation experienced by users with the sealable plastic device. However, the fabric-silicone device developed by Rameshwar et al. showed considerable thickness, had a visible stitch line, and the manufacturing process lacked scalability. The fabric-silicone composite was a promising option for finger-based devices, offering the potential to enhance haptic feedback sensitivity, but further research on alternative fabric types and designs, as well as alternative manufacturing techniques that are less reliant on manual labor, is an exciting opportunity.

Braided composites in the form of elastomer-coated fibers are of particular interest, as they allow for the customization of mechanical properties, as well as flexibility in design [7]. Elastomer braided composites offer impermeability to air and superior foldability, making them remarkably suitable for use in a pneumatic finger-based devices [8].

In this work, an industrially relevant process is presented for the manufacturing of a pneumatic-driven soft robotic actuator from braided nylon coated with a silicone elastomer. The nylon structure was manufactured using a braiding machine that wove the yarns in a circular pattern at different angles and subsequently impregnated them with a silicone elastomer matrix. The resulting pneumatic finger-based haptic device was specifically designed to encase the knuckles of a hand and facilitate the transfer of forces perceived in a robotic hand to the user's own fingers, with the aim of achieving a more sensitive, highly immersive, and realistic teleoperation experience. By investigating a range of braiding angles, this work explored how the braiding structure influences the effectiveness of haptic sensation transmission to the user's finger.

Material, Design, and Fabrication

This study used bonded nylon thread #69 (SGT.KNOTS) for the fiber material. The elastomeric matrix material consisted of a silicone elastomer (DOW DOWSIL 92-009 Dispersion Coating Clear, manufactured by Dow Inc.). According to the supplier specifications, the silicone was diluted with thinner (Varnish Maker and Painter's Naphtha, manufactured by Klean-Strip) in a ratio of 4 parts thinner to 3 parts silicone (v/v). To determine the diameter of the braided tubular structures, rigid

DOI: https://doi.org/10.51573/Andes.PPS39.GS.PC.3

Teflon rods with diameters of 25.4 mm and 22.2 mm were used. The nylon-silicone pneumatic actuator consisted of two composite tubes of different diameters stacked together and sealed at the ends, forming an inner bladder between them. This bladder was pressurized via a small 3 mm polyurethane tube, which was connected to one end of the actuator to deliver air, as shown in Figure 1.

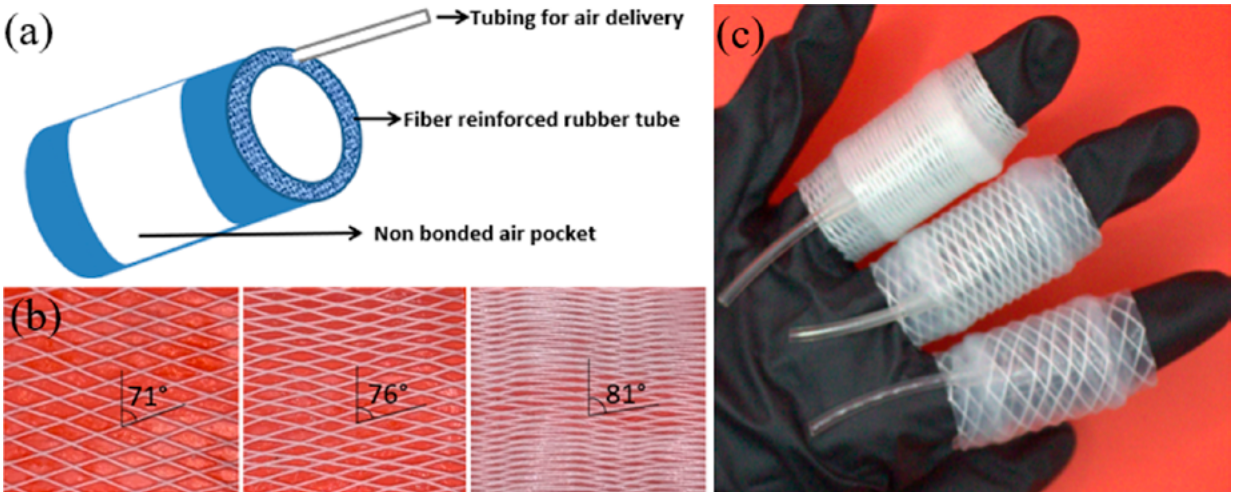

Figure 1. Nylon-silicone pneumatic actuators, (a) conceptual design with an inner pneumatic subsystem, (b) nylon structure coated with silicone elastomer with variations in braiding angles, (c) actuators with different braiding angles.

Fabrication Method

The manufacturing process of the nylon-silicone pneumatic actuator involved four stages, as described below.

Braiding

Nylon tubular structures of two different diameters were braided using a HERZOG braiding machine (model LZ 1/17-80 FZR) equipped with 16 rotating Nylon yarns. The dimensions of each tubular structure were determined using Teflon rods of two different diameters for braiding: 22.2 mm for the inner tubular structure and 25.4 mm for the outer tubular structure. Three braiding angles were systematically evaluated: 71°, 76°, and 81°. The rotational speed of the braider carrier was kept constant at 50 rpm, while the lay length was adjusted to 30 mm, 20 mm, and 10 mm. The resulting braid angles for each condition were measured using the image processing software, ImageJ.

DOI: https://doi.org/10.51573/Andes.PPS39.GS.PC.3

Coating

The tubular structures mounted on the Teflon rods were impregnated with silicone elastomer solution, while rotating in a custom-built automatic spinner at 30 rpm, forming the elastomeric matrix composite (Figure 1[b]). The coating process was repeated four times. The first three coatings were cured for 30 minutes at room temperature before applying the subsequent coating. The fourth coating was cured for 72 hours at room temperature.

Stacking

The composite with a 25.4 mm diameter was removed from the Teflon tube and trimmed to a length of 3 mm. Similarly, the composite extracted from the Teflon tube with a 22.2 mm diameter was trimmed to a length of 5 mm. Subsequently, the 25.4 mm diameter composite was assembled by sliding it over the 22.2 mm diameter composite. Once precise alignment and stacking of the two tubes were ensured, a polyurethane rubber tube with an internal diameter of 1.8 mm and an outer diameter of 3 mm was inserted between them.

Sealing

The edges of the 3 mm length tubular structure were coated with undiluted silicone while the automatic spinner was in motion, closing the gap between both composites and ensuring the air tube connection. After curing, the assembled structure was extracted from the Teflon tube, resulting in the nylon-silicone pneumatic actuator.

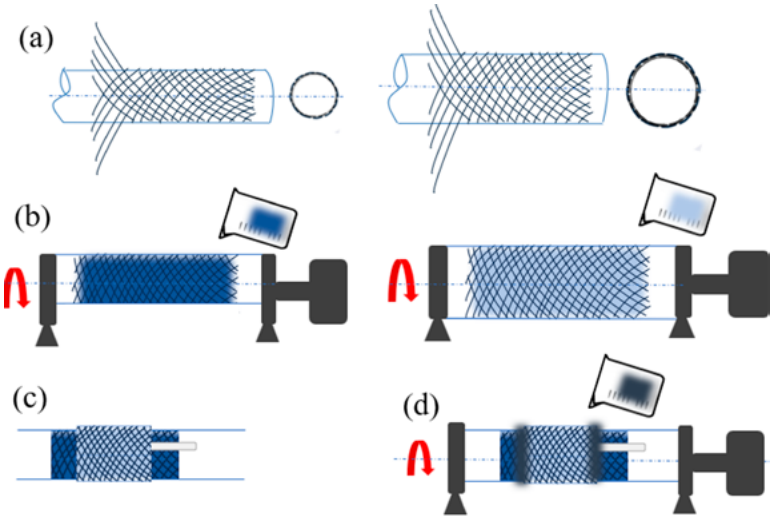

Figure 2. Schematic of the haptic device manufacturing process: (a) braided yarn around Teflon cores of two sizes, (b) braided yarns coated with silicone elastomer solution while placed on automatic spinner, (c) cut and stacked braided composite, and (d) edges coated with non-diluted silicone.

DOI: https://doi.org/10.51573/Andes.PPS39.GS.PC.3

Experimental

The haptic feedback capability of the nylon-silicone pneumatic actuator was characterized by studying its inflation behavior and force response. During testing, the pressurization of the haptic device was controlled through pneumatic solenoid valves (S070C-VAG-32 manufactured by SMC), actuated by a pulse-width modulation (PWM) signal, which is precisely what regulates the proportion of the source pressure directed through the valve into the haptic device and controls the degree of haptic feedback to the user's finger. Three versions of the nylon-silicone pneumatic actuator with different braiding angles (71°, 76°, and 81°) were tested, as well as one without fiber (only silicone). The experimental procedure was divided into 2 categories: inflation test and force test.

Inflation Test

The inflation test was performed to assess the response of each device to the pressure input and verify control over feedback. The nylon-silicone pneumatic actuators were connected to a pneumatic valve, while placing a digital I^2C interfaced MPRLS pressure sensor into the air pocket to measure the internal pressure. The internal pressure of the devices was monitored under two conditions: first, a stepwise rise in the PWM input and holding each pressure increment for one second and, separately, full inflation input to the pneumatic valve from 0% to 100%.

Force Test

The force response of the nylon-silicone pneumatic actuator was measured using a 3D-printed human-like finger, following a methodology similar to our previous work [6]. The custom-designed device consisted of a tendon-driven finger connected to a load cell and equipped with a flexible sensing resistor (FSR) on the finger. These configurations made it possible to measure the two forces that the user's finger would experience when using the nylon-silicone pneumatic device: compression force and restoration force. The compression force reflects the pressure exerted during contact, detected by the FSR. The restoration force, measured by the load cell, is the resistance keeping the fingers open, while transmitting the grasp of the robotic arm.

Results and Discussion

The nylon-silicone pneumatic actuator created using the braiding manufacturing process weighed less than 5 grams. The device was easy to wear and when pressurized the air pocket inflated to provide haptic feedback to the user's fingers. Direct control over the inflation of the nylon-silicone actuator was verified by observing the linear relationship between the air proportioned by the valve and the pressure registered inside the actuators when subjected to the stepwise rise in the

DOI: https://doi.org/10.51573/Andes.PPS39.GS.PC.3

PMW input, as depicted in Figure 3(a). These results show it is possible to provide specific haptic feedback to the user through controlled inflation. As shown in Figure 3(a), the actuators did not respond prior to 10% PMW input. After the initial 10%, all actuators showed a linear relationship up to 100% full inflation. The initial 10% is the threshold, where the pressure supplied is sufficient to provide the necessary force for valve opening and to initiate inflation. Within this framework, the nylon-silicone actuators should operate solely within the 10%-100% duty cycle range.

System delays in tactile output under 61 ms are negligible for human users [9]. During the inflation test from 0% to 100%, the nylon-silicone actuators achieved pressures exceeding 10 kPa in less than 61 ms (Figure 1[b]). The minimum detectable pressure, the smallest change a user could perceive with the inflated actuator, is reported to be below 2 kPa [6]. These results indicate that the actuators can provide feedback with virtually no delay.

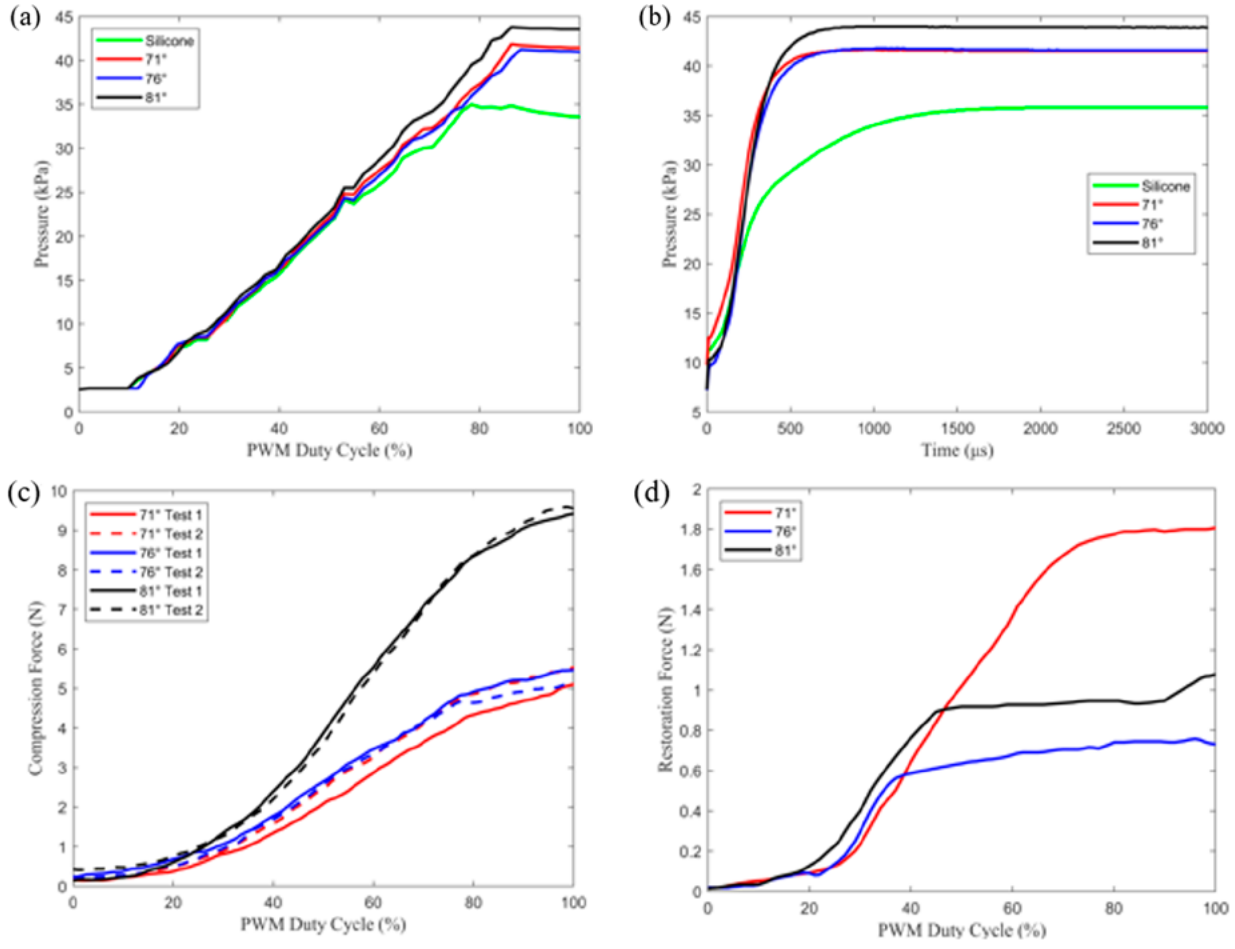

Figure 3. (a) Stepwise pressure rise, (b) Full inflation test results, (c) Compression test, and (d) Restoration test.

DOI: https://doi.org/10.51573/Andes.PPS39.GS.PC.3

The results for the compression force (Figure 3[c]), or squeezing around the finger, indicated that the maximum pressure registered did not exceed the minimum pressure pain threshold reported by Özcan et al. [10], which is approximately 20 N. The highest compression force, 9.6 ± 0.3 N, was observed with the 81° braiding, followed by the 76° braiding, and lastly the 71° braiding. The results demonstrated that larger braiding angles provided greater applied pressure. This behavior aligns with observations in literature for braided pneumatic systems such as McKibben muscles [11]. Angles closer to 90 degrees mean that the nylon fibers in the composite are more perpendicular to the actuator's length, enhancing force capability in the radial direction. Therefore, greater braiding angles can provide higher haptic feedback forces to the human hand with the designed actuator, allowing the actuators to be tailored for specific applications. It is important to note that the silicone actuators without braiding were not included in the force results, as they were unable to withstand the applied pressure during the tests. This underscores the essential role of fiber reinforcement in ensuring the effective functionality of the designed actuator.

The restoration force results, shown in Figure 3(d), exhibit a linear relationship with air input for the lower braiding angle (71°). However, this relationship was found to be uneven for the samples with higher braiding angles. Throughout this test, the 3D-printed hand undergoes initial flexion, and the inflation of the nylon-silicone actuator facilitates the opening of the hand. Reduced braiding angles, situated nearer to the longitudinal axis, facilitate a higher contraction ratio, empowering the actuator to shorten more noticeably. Moreover, reduced braiding angles and lower fiber density within the composite may promote improved airflow by reducing reinforcement. As a result, smaller braiding angles have demonstrated an increase in restoration force.

Conclusions

A new manufacturing technique has been created for fabricating fiber-reinforced silicone haptic muscles with an integrated pneumatic subsystem that is flexible, lightweight, and wearable. The pneumatic system demonstrates a near-linear correlation between air input and resulting pressure. Moreover, the system's delays in tactile output remain imperceptible to users, remaining below the threshold of human detection. Safety is assured with contact forces kept below 20 N. Evaluation of actuators with varying braiding angles reveals that higher angles yield increased haptic feedback forces, albeit with a less linear relationship to air input compared to lower angles. Thus, braiding angles can be changed to provide optimal performance.

Acknowledgments

This work received financial support from SEMI-FlexTech under Grant number FT19-21-215. The authors gratefully acknowledge this support.

References

1. M. Zhu, S. Biswas, S. I. Dinulescu, N. Kastor, E. W. Hawkes, and Y. Visell, "Soft, Wearable Robotics and Haptics: Technologies, Trends, and Emerging Applications," *Proc. IEEE*, vol. 110, no. 2, pp. 246–272, 2022, doi: 10.1109/JPROC.2021.3140049.
2. Y. Huang et al., "Recent advances in multi-mode haptic feedback technologies towards wearable interfaces," *Materials Today Physics*, vol. 22, 2022, doi: 10.1016/j.mtphys.2021.100602
3. S. Li, R. Rameshwar, A. M. Votta, and C. D. Onal, "Intuitive Control of a Robotic Arm and Hand System with Pneumatic Haptic Feedback," *IEEE Robotics and Automation Letters*, vol. 4, no. 4, pp. 4424–4430, 2019, doi: 10.1109/LRA.2019.2937483
4. M. W. Uddin, X. Zhang, and D. Wang, "A pneumatic-driven haptic glove with force and tactile feedback," *Proceedings of the 2016 International Conference on Virtual Reality and Visualization ICVRV*, pp. 304–311, 2017, doi: 10.1109/ICVRV.2016.57
5. B. Jumet et al., "A Textile-Based Approach to Wearable Haptic Devices," *2022 IEEE 5th International Conference on Soft Robotics (RoboSoft 2022)*, pp. 741–746, 2022, doi: 10.1109/RoboSoft54090.2022.9762149
6. R. Rameshwar, E. H. Skorina, and C. D. Onal, "Fabric-Silicone Composite Haptic Muscles for Sensitive Wearable Force Feedback," *ACM International Conference Proceeding Series*, pp. 33–41, 2023, doi: 10.1145/3594806.3594853
7. J. P. Carey, "Handbook of Advances in Braided Composite Materials: Theory, Production, Testing and Applications," *Woodhead Publishing Series in Composites Science and Engineering*, pp. 1–479, 2017, doi: 10.1016/C2014-0-03943-3
8. Z. Shang, J. Ma, Z. You, and S. Wang, "A foldable manipulator with tunable stiffness based on braided structure," *Journal of Biomedical Materials Research–Part B Applied Biomaterials*, vol. 108, no. 2, pp. 316–325, 2020, doi: 10.1002/jbm.b.34390
9. A. J. Doxon, D. E. Johnson, H. Z. Tan, and W. R. Provancher, "Human detection and discrimination of tactile repeatability, mechanical backlash, and temporal delay in a combined tactile-kinesthetic haptic display system," *IEEE Transactions on Haptics*, vol. 6, no. 4, pp. 453–463, 2013, doi: 10.1109/TOH.2013.50
10. A. Özcan, Z. Tulum, L. Pinar, and F. Başkurt, "Comparison of pressure pain threshold, grip strength, dexterity and touch pressure of dominant and non-dominant hands within and between right- and left-handed subjects," *Journal of Korean Medical Science*, vol. 19, no. 6, pp. 874–878, 2004, doi: 10.3346/jkms.2004.19.6.874
11. C. S. Kothera, M. Jangid, J. Sirohi, and N. M. Wereley, "Experimental characterization and static modeling of McKibben actuators," *Journal of Mechanical Design*, vol. 131, no. 9, pp. 0910101–09101010, 2009, doi: 10.1115/1.3158982

GENERAL SYMPOSIA | POLYMER COMPOSITES

Effect of Pigments on Laser Beam Transmission in Diode Laser Transmission Welding of Poly(propylene)

Foram Dave, Mahmood Ali, Mozaffar Mokhtari, Richard Sherlock, Alistair McIlhagger and David Tormey

DOI: https://doi.org/10.51573/Andes.PPS39.GS.PC.4

December 2024

Effect of Pigments on Laser Beam Transmission in Diode Laser Transmission Welding of Poly(propylene)

Foram Dave, Mahmood Ali, Mozaffar Mokhtari, Richard Sherlock, Alistair Mcllhagger and David Tormey[1]

Abstract: Welding technologies are state of the art for joining polymer composites, with one of the two joining parts considered laser transmissive (LT) and the other laser absorptive (LA). Pigments are often added to LT to enhance the crystallinity of the polymer matrix. However, pigments lead to internal scattering of the laser beam and the rate of transmission or the laser energy density decreases. Depending upon the type and amount of pigments added in the formulation of LT, the percentage of the laser beam transmitted, absorbed, or scattered differs. Laser welding performance depends on the laser energy available for welding after considering the losses. In the present study, optical transmission of injection molded isotactic polypropylene (iPP) samples were analyzed with a varying dosage of organic pigment (neat PP, 2%, 3%, 4%, 5%, 6%, 8%, and 10%) using a LPKF TMG 3 transmission tester. The device uses a wavelength of 980 nm and simulates the optical radiation conditions of diode laser transmission welding (LTW). The percentage transmission varied with the sample thickness and the composition percentage of pigment. The modified Bouguer-Lambert law described the transmission energy and apparent extinction coefficient. The model was validated with the experimental value of transmittances of the samples with varying sample thicknesses of iPP. There was a decrease in the percentage of laser transmission with an increase in the pigment content of the samples. It was found that the apparent extinction coefficient is a function of the pigment levels.

Keywords: Polymer Composites, Pigments, Optical Transmission, Polypropylene, Extinction Coefficient

1 The authors Foram Dave, Mahmood Ali and David Tormey (david.tormey@atu.ie) are affiliated with the Department of Mechanical and Manufacturing Engineering and the Centre for Precision Engineering, Materials and Manufacturing (PEM) Centre at the Atlantic Technological University Sligo in Ireland. Mozaffar Mokhtari is affiliated with the National Graphene Institute and Department of Materials of the School of Natural Sciences at the University of Manchester in the United Kingdom. Richard Sherlock is affiliated with the Department of Life Sciences of School of Science at the Atlantic Technological University Sligo in Ireland. Alistair Mcllhagger is affiliated with the Engineering Research Institute of the School of Engineering at the Ulster University in the United Kingdom.

DOI: https://doi.org/10.51573/Andes.PPS39.GS.PC.4

Introduction

Laser transmission welding (LTW) is a technique that is used to join two thermoplastic (TP) materials: laser-transmissive (LT) and laser-absorptive (LA). An incident beam of radiation containing nucleating agents (NA) or pigments passes through LT [1]. The amount of radiation transmitted depends on the size, type, dispersion, distribution, etc., of the pigments. After transmission, the radiation gets absorbed by LA depending on the laser-absorbing pigment (mostly carbon black: CB) in LA. As a result, thermal energy is transferred from LA to LT, leading to the inter-diffusion of the polymer and ultimately forming a weld joint upon cooling. The optical properties of LT and LA determine the amount of laser beam energy transmitted and distributed over the interface. Optical characteristics of polymers are related to the welding performance, considering polymer thickness, wavelength, and various additives for joining two surfaces. For a strong joint, sufficient thermal energy must be available at the weld interface to melt the polymer and at the same time not degrade the polymer due to excessive energy [2]. Various models were developed to understand the effect of some of the factors on the melting and re-solidification phenomenon [3].

Theory

Most of the polymeric materials are transparent to the near-infrared (NIR) laser beam (800~ 1064nm) [4]. Depending on the type and amount of pigments added in the formulation, the amount of laser beam transmitted, scattered or reflected differs. The rate of transmission for organic pigments is higher compared to inorganic pigments [5]. For semi-crystalline (SC) polymers, the phenomenon depends upon the spherulite structure size. Finer spherulites have higher transmittance than coarse spherulites [6]. Due to reflections and refractions, the light gets scattered randomly [7]. The actual optical path of the laser beam is prolonged in SC polymers as the rays get refracted and scattered on the crystalline superstructures. As a result, the absorption increases [8]. In LTW, preferential energy deposition occurs with subsequent TP material melting at the interfacial zone, as shown in Figure 1. The interaction between the laser radiation and TP depends on three crucial parameters: total transmittance (TT), total absorbance (AT), and total reflectance (RT). They are related, as shown in Eq. (1)

$$1 = T_T + A_T + R_T \quad 1)$$

Depending on the polymer morphology, sample thickness, and compounding ingredients, the percentage of T_T, A_T, and R_T differs.

DOI: https://doi.org/10.51573/Andes.PPS39.GS.PC.4

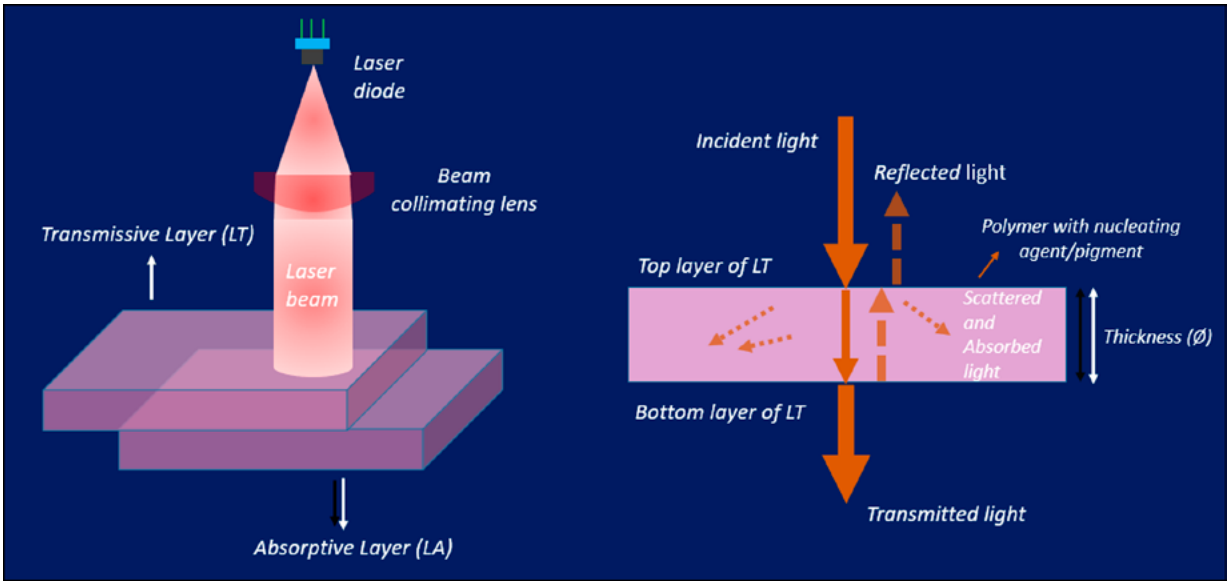

Figure 1. Schematic of transmission laser welding of lap geometry of materials (left) and light transmission through a transmissive layer with reflected, scattered, and absorbed light phenomena (right) [9]. Reproduced with permission from [9]. Copyright (2021)CC BY 4.0, Frontiers in Materials.

For LT, it is difficult to separate absorption and scattering [8,9]. Some studies measure the laser light scattering, such as x-y scanning pinhole [8], charged coupled device, small light sensor [10], etc. The presence of pigments increases the internal scattering of the laser beam, which increases the effective beam diameter. With an increase in the pigment level, the percentage of scattering may vary [11]. When laser radiation falls on the laser transmissive surface, the intensity of the radiation decreases as it propagates, which can be elaborated by integrating Eq. (2) over a definite path length F [12]:

$$\int_{I_\lambda=I_\lambda(0)}^{I_\lambda(F)} \frac{dI_\lambda}{I_\lambda} = -\int_{F^*=0}^{F} \beta_\lambda(F^*)dF^* \quad 2)$$

where $I\lambda(0)$ is the incident laser radiation from the laser head on a given volume at F = 0 (F is a dummy variable of integration), and $\beta\lambda$ is the extinction coefficient. The integration yields the radiation intensity at location F in the given direction ω:

$$I_\lambda(F) = I_\lambda(0)\, e^{\left[-\int_0^F \beta_\lambda(F^*)dF^*\right]} \quad 3)$$

Eq. 3 is known as the Beer's, Bouguer's or Lambert-Bourguer law, which shows that as the laser radiation passes through an absorbing-scattering medium, the intensity is attenuated exponentially. The local emission or scattering into the direction ω is not taken into consideration in this

DOI: https://doi.org/10.51573/Andes.PPS39.GS.PC.4

law. The extinction coefficient (βλ) is a summation of absorption coefficient (κλ) and scattering coefficient (ϕλ) [12].

$$\beta_\lambda = \kappa_\lambda + \varphi_\lambda \quad 4)$$

Considering that the scattering of the radiation in the laser transmissive part is negligible, Eq.(4) reduces to

$$\beta_\lambda = \kappa_\lambda \quad 5)$$

The interaction between the laser radiation and the crystalline structure of the polymer occurs if the size of the spherulites is in the range of the visible or near-infrared (NIR) light (400-1060 nm) which determines the amount of scattering. Pigment distribution, size, and nature of scattering centers influence the scattering behavior. Beam broadening occurs in polymers with higher crystallinity [13]. Many simulations have been carried out using the Bouguer-Lambert law [14,16]. However, an assumption is made that the laser radiation travels in a straight line through LT and LA, but there will be specular reflective losses (ηi) apart from the absorptive losses, which can be calculated by Eq. (7)

$$\eta_i = \left(\frac{n_1 - n_0}{n_1 + n_0}\right)^2 \quad 6)$$

Model Development

In the case of polymers that are non-scattering, single-scattering or multi-scattering, the total energy transmission can be described by the Bouguer-Lambert law [7]. M. Chen et al. [16] developed and modified a model for measuring the absorption coefficient for LA material filled with CB using the measured transmittances with varying thicknesses. The total laser radiation intensity (Iλ) after passing through the polymer of a given thickness can be given by [7]:

$$I_\lambda = T_T I_\lambda(0) = I_\lambda(0)(1 - R_T)(1 - \eta)e^{-\beta_\lambda t} \quad 7)$$

where,

RT: total reflectance of the polymer from the top incident surface as well as the polymer bulk
η: surface reflectance at the polymer bottom surface
t: total thickness of the laser transmissive part or laser absorptive part

DOI: https://doi.org/10.51573/Andes.PPS39.GS.PC.4

Eq. (7) will be referred to as the modified Bouguer-Lambert law derived from Beer-Lambert law. For simplification, it is assumed that the total reflectance (RT) contribution from the polymer bulk takes place in a local volume close to the top of the incident surface.

$$\ln T_T \approx \ln(1 - R_T - \eta) - \kappa_\lambda t \quad 8)$$

Eq. (8) will be used in the experimental analysis for validating the modified Bouguer-Lambert law. The samples of 2 mm thickness were stamped by cutting the polypropylene (PP) coupons (Figure 2) with varying pigment content with neat PP, 2%, 3%, 4%, 5%, 6%, 8%, and 10%. Thin cross-sections were also taken as 120 μm, 240 μm, and 360 μm using a microtome.

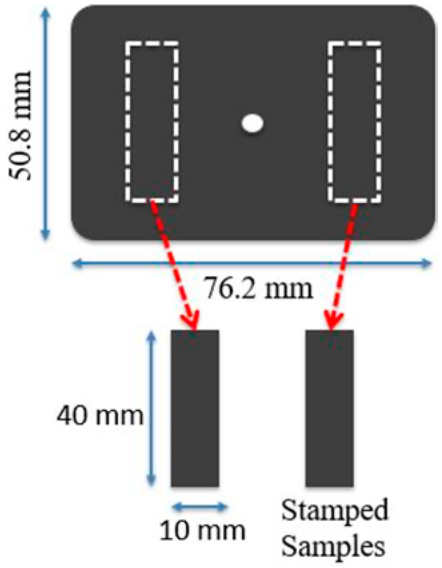

Figure 2. PP sample stamped for analysis.

The LPKF TMG 3 transmission tester (class 1 according to DIN EN 60825-1) was utilized to determine the optical transmission of thermoplastics. The maximum radiation intensity is on the aperture plate of the device. The specifications of the device are mentioned in Table 1. The device is designed to simulate the optical radiation conditions of laser transmission welding of thermoplastic as realistically as possible. The laser beam is emitted from a diode of the tester and penetrates the thermoplastic sample to be measured. The intensity of the radiation after the transmission is calculated based on the photoelectric effect, representing the value for the optical permeability of the thermoplastic at a wavelength of 980 nm. The scattered rays are blocked with an aperture of 3 mm, and the remaining photons are measured on the detector. The data obtained was utilized to validate the modified Bouguer-Lambert law.

DOI: https://doi.org/10.51573/Andes.PPS39.GS.PC.4

Table 1. Specification of LPKF TMG 3.

Data	Value	Unit
Laser class	1	
Wavelength	980	Nm
Max. power	<1	mW
Diameter of the measuring aperture	3	mm
Focus diameter on the measuring aperture	~1.5	mm

Three measurements on the samples were taken, and an average was considered. The data was utilized to validate the modified Bouguer-Lambert law. The measured transmission values vary according to the wall thickness and the visual properties of a thermoplastic component. The diameter of the measuring beam is approximately 1.5 mm.

Results and Discussion

The addition of NA/pigments changes the crystallinity of the semi-crystalline polymers (PP). Due to changes in the morphology and thickness of the samples, the amount of laser radiation (optical properties) passing through the laser transmissive sample differs. It can be observed in the graph, Figure 3, there is a decrease in the percentage of laser transmission with an increase in the pigment content. Figure 3(b) shows that the fraction of the laser beam energy transmitted depends on the thickness of the laser transmissive layer. It decreases with an increase in thickness [17].

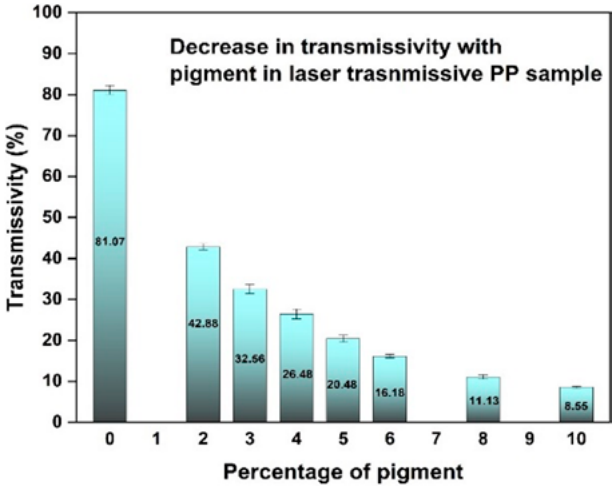

(a)

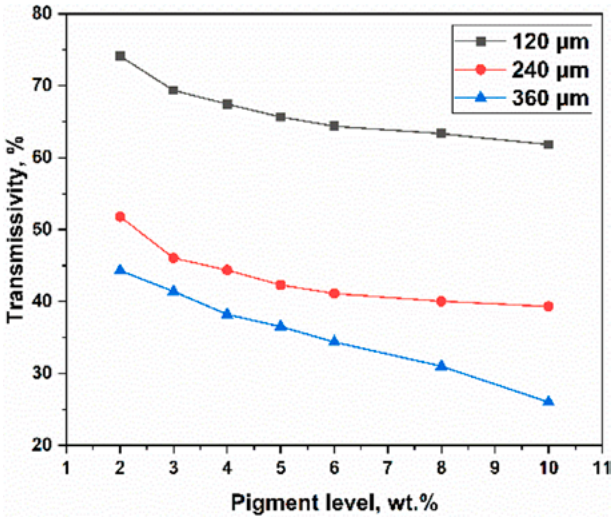

(b)

Figure 3. Decrease in transmissivity with (a) pigment content (b) thickness variation.

A linear relationship between lnTT and thickness t validates the modified Bouguer-Lambert law (Figure 4). The apparent **κλ** for every pigment content was determined as shown in Table 2 with the R-square value.

Table 2. Apparent κλ for samples with varying pigment content.

Sl. No.	Pigment level (wt.%)	Apparent κλ (1/mm)	$R_T + \eta = 2\eta$	R-Square
1	2	0.85	0.05	80.64
2	3	0.86	0.13	62.65
3	4	1.08	0.12	77.54
4	5	1.16	0.14	76.78
5	6	1.33	0.14	83.82
6	8	1.69	0.10	94.12
7	10	2.32	0.03	99.99

The values of the apparent **κλ** are plotted with the pigment level, as shown in Figure 4. A linear relationship between the apparent **κλ** and pigment level with R2: 95.51% was observed experimentally. Equation 9 obtained from the graph can be used to determine apparent **κλ** as a function of pigment for PP samples. Apparent **κλ** increased from 0.85 1/mm for 2 wt.% pigment to 2.32 1/mm for 10 wt.% pigment. Higher **κλ** at higher pigment content can affect the thermal profile, which may facilitate the welding process.

DOI: https://doi.org/10.51573/Andes.PPS39.GS.PC.4

$$y = 0.204x + 0.194 \quad (9)$$

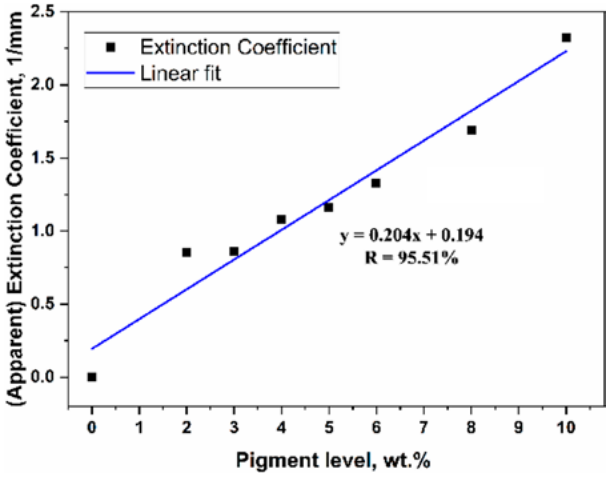

Figure 4. κλ Vs pigment level for PP.

Conclusion

The Bouguer–Lambert law was utilized to study the effect of pigment content and sample thickness on the laser beam transmission. A linear relationship between the apparent **κλ** and the pigment content was observed. At higher pigment content, the percentage of transmission decreases. Hence, there is less energy available for the laser absorptive layer to absorb the laser beam. The amount of melting may not be sufficient for the interdiffusion for welding. This could decrease the weld strength. However, higher **κλ** at higher pigment content can affect the thermal profile, which may help the welding process. Hence, an optimum pigment percentage needs to be quantified in future work. Also, the effect of pigment size and its distribution on **κλ** and polymer crystallinity will be carried out.

Acknowledgements

The North-West Centre for Advanced Manufacturing (NWCAM) project is supported by the European Union's INTERREG VA Programme, managed by the Special EU Programmes Body (SEUPB). The views and opinions in this document do not necessarily reflect those of the European Commission or the Special EU Programmes Body (SEUPB). If you would like further information about NWCAM, please contact the lead partner, Catalyst Inc, for details.

References

1. F. Dave, M. M. Ali, R. Sherlock, A. Kandasami, and D. Tormey, "Laser Transmission Welding of Semi-Crystalline Polymers and Their Composites: A Critical Review," *Polymer 2021, vol. 13, Page 675*, vol. 13, no. 5, p. 675, Feb. 2021.
2. E. Ghorbel, G. Casalino, and S. Abed, "Laser diode transmission welding of polypropylene: Geometrical and microstructure characterisation of weld," *Materials & Design*, vol. 30, no. 7, pp. 2745–2751, 2009.
3. L. S. Mayboudi, A. M. Birk, G. Zak, and P. J. Bates, "Laser transmission welding of a lap-joint: Thermal imaging observations and three-dimensional finite element modeling," *Journal of Heat and Mass Transfer*, vol. 129, no. 9, pp. 1177–1186, 2007.
4. M. Chen, G. Zak, and P. J. Bates, "Absorption coefficient measurement in laser transmission welding of thermoplastics," *International Polymer Procesing.*, vol. 30, no. 1, pp. 38–43, 2015.
5. V. A. Kagan and G. P. Pinho, "Laser Transmission Welding of Semicrystalline Thermoplastics–Part II: Analysis of Mechanical Performance of Welded Nylon," *Journal of Reinforced Plastics and Composites*, vol. 23, no. 1, pp. 95–107, Jan. 2004.
6. L. S. Mayboudi, *Heat transfer modelling and thermal imaging experiments in laser transmission welding of thermoplastics*. 2008.
7. M. Chen, G. Zak, and P. J. Bates, "Effect of carbon black on light transmission in laser welding of thermoplastics," *Journal of Materials Processing Technology*, vol. 211, no. 1, pp. 43–47, 2011.
8. M. G. Æ. T. F. Æ. M. Schmidt, "Optical properties of plastics and their role for the modelling of the laser transmission welding process," pp. 49–55, 2009.
9. M. M. Ali, F. Dave, R. Sherlock, A. Mcilhagger, and D. Tormey, "Simulated Effect of Carbon Black on High Speed Laser Transmission Welding of Polypropylene With Low Line Energy," *Frontiers in Materials*, vol. 0, p. 407, Sep. 2021.
10. M. Ilie, J. C. Kneip, S. Mattei, and A. Nichici, "Effects of laser beam scattering on through-transmission welding of polymers," *24th International Congress on Applications of Lasers and Electro-Optics, ICALEO 2005–Congress Proceedings*, vol. 802, pp. 388–393, 2005.
11. V. A. Kagan, R. G. Bray, and W. P. Kuhn, "Laser transmission welding of semi-crystalline thermoplastics-Part I: Optical characterisation of nylon based plastics," *Journal of Reinforced Plastics and Composites*, vol. 21, no. 12, pp. 1101–1122, 2002.
12. R. Siegel and J. R. Howell, *Thermal Radiation Heat Transfer*, 4th ed. New York, NY, USA: Taylor & Francis, 2002. Available: https://books.google.ie/books?hl=en&lr=&id=FBjSBQAAQBAJ [Accesed: Aug 27, 2020].
13. U. A. Russek, "Laser beam welding of polymers with high power diode lasers joining innovation for micro and macro technologies," *20th Icaleo 2001, Vols 92 93, Congress Proceedings*, vol. 483, pp. 483–491, 2001.
14. H. Potente, G. Fiegler, H. Haferkamp, M. Fargas, A. von Busse, and J. Bunte, "An approach to model the melt displacement and temperature profiles during the laser through-transmission welding of thermoplastics," *Polymer Engineering & Science*, vol. 46, no. 11, pp. 1565–1575, Nov. 2006.

DOI: https://doi.org/10.51573/Andes.PPS39.GS.PC.4

15. L. S. Mayboudi, A. M. Birk, G. Zak, and P. J. Bates, "A 2-D thermal model for laser transmission welding of thermoplastics," *24th Icaleo 2005–Congress Proceedings*, vol. 2005, no. 1, pp. 402–409.

16. C. Lu, Y. J. Juang, L. J. Lee, D. Grewell, and A. Benatar, "Numerical simulation of laser/IR assisted micro-embossing," *Annual Technical Conference–ANTEC, Conference Proceedings*, 2004, vol. 1, no. 1, pp. 1200–1204.

17. D. Grewell, P. Rooney, and V. A. Kagan, "Relationship between Optical Properties and Optimised Processing Parameters for through-Transmission Laser Welding of Thermoplastics," *Journal of Reinforced Plastics and Composites*, vol. 23, no. 3, pp. 239–247, Feb. 2004.

DOI: https://doi.org/10.51573/Andes.PPS39.GS.PC.4

GENERAL SYMPOSIA | POLYMER FOAMS AND MEMBRANES

From Vibrating Molecules to a Running Shoe: Connecting Dielectric Properties with Process Feedback in Radio-Frequency welding of TPU Bead Foams

Marcel Dippold, Makrina A. Chairopoulou, Maximilian Drexler, Michael Scheiber and Holger Ruckdäschel

DOI: https://doi.org/10.51573/Andes.PPS39.GS.PFM.1

December 2024

From Vibrating Molecules to a Running Shoe: Connecting Dielectric Properties with Process Feedback in Radio-Frequency welding of TPU Bead Foams

Marcel Dippold, Makrina A. Chairopoulou, Maximilian Drexler, Michael Scheiber and Holger Ruckdäschel[1]

Abstract: Besides new material solutions, innovative processing technologies are key for working towards a more sustainable future for bead foam products. Compared to standard steam chest molding, innovative radio frequency (RF) welding shows great potential based on its direct energy input, which results in reduced energy consumption. Thus, the present study provides fundamental insights into the correlation of dielectric properties of expanded thermoplastic polyurethane (ETPU) bead foams with the processing behavior. Impedance spectroscopy is used to analyze the complex relative permittivity ε_r^* of both polymer and respective beads. The dielectric properties of polymers are dictated by their molecular structure and hence resulting dipoles. Thus, significant dependency on temperature and frequency is observed due to changes in chain flexibility and therefore alignment with the oscillating electromagnetic field. As cellular structures, the introduction of a second air phase leads to generally attenuated values at equal trends. Within the RF process, changes, predominantly in the imaginary part of ε_r^* from initial starting temperatures up to welding, are directly reflected in the power curve as process feedback. Furthermore, temperature evolution and derived heating rate within the bead foams demonstrate excellent conformity with previous results with minor deviations due to the thermal inertia of the fiber optic temperature sensor.

Keywords: Radio Frequency, Bead Foams, Dielectric Properties, ETPU, Welding

1 Marcel Dippold, Michael Scheiber and Holger Ruckdäschel (holger.ruckdaeschel@uni-bayreuth.de) are affiliated with the University of Bayreuth in Germany. Makrina A. Chairopoulou and Maximilian Drexler are affiliated with Adidas AG in Germany.

DOI: https://doi.org/10.51573/Andes.PPS39.GS.PFM.1

Introduction

From packaging to sports equipment, bead foam products are integral to our daily lives. In recent decades, the market and research landscapes have seen the emergence of numerous new materials based on bio-based or recycled polymers [1]. Additionally, there has been a significant focus on developing technical and high-performance materials to expand their application range to higher operating temperatures. Alongside advancements in materials, new processing technologies have been introduced. These include the welding together of individual beads to create three-dimensional, durable parts in a more energy and resource efficient manner [2]. Among these innovations, the most notable is the direct dielectric heating of beads using an external electromagnetic field in the radio-frequency range [3]. This method generates heat through intermolecular friction within the polymer volume itself as dipoles within the affected volume interact with the oscillating field and undergo constant realignment [4-6]. A thorough investigation of these physical phenomena is essential to optimize the process for maximum energy efficiency and part quality. As shown in previous studies, the dielectric properties of these materials are key in order to understand and predict their interaction within the electromagnetic field and consequently their heating behavior [7]. In terms of values, the complex relative permittivity ε_r^* is a material property, influenced both by temperature and frequency [8]. Due to this superposition, changes over the length of the welding cycle starting with beads at room temperature up to the welding temperature are essential for fundamental process knowledge [7, 9, 10]. The direct link between permittivity and heating behavior is established by the volumetric power input P_v in Equation (1). [5,11].

$$P_V = 2 \times \pi \times f \times \varepsilon_0 \times \varepsilon_r'' \times E_{RMS}^2 \quad 1)$$

ε_0 represents the permittivity of vacuum and f the frequency of the oscillating electromagnetic field with E_{RMS} as the root mean square (RMS) value of the peak field strength. The imaginary part ε_r'' of the complex-valued relative permittivity ε_r^* is therefore in linear dependency to the intrinsic heating power of any material within an oscillating electromagnetic field. Despite no visible correlation to the real part of the relative permittivity ε_r' within the shown Equation (1), an indirect impact is known via the electromagnetic field strength E_{RMS}. This interaction is based on the influence of this material property on the capacity within a serial stack as well as the field displacement between phases with different permittivity [12]. For the intricate multi-phase system of RF bead foam welding, both phenomena may occur. However, their magnitude is difficult to estimate without complex simulative approaches. Thus, the present study first analyzes the permittivity of both bulk polymer and bead foams in order to subsequently link these material properties with the direct process feedback during the RF welding.

DOI: https://doi.org/10.51573/Andes.PPS39.GS.PFM.1

Materials and Methods

Materials

Within this study, the commercially available ETPU grade Infinergy® 32-100 U10 from BASF SE (Ludwigshafen, Germany) was used with an average bead density of 183 kg/m³. For the analysis of the bulk polymer properties, hot pressing was utilized to compact the beads and produce solid platelets with a diameter of 25 mm and a height of 1 mm.

Impedance Spectroscopy

The permittivity of the material was measured with RF I-V method by the E4991A RF impedance analyzer from Keysight Technologies, Inc. (Santa Rose, USA) and an UF55plus universal oven by Memmert GmbH + Co. KG (Schwabach, Germany). The bulk material and bead foams at defined densities were analyzed within two specially designed measurement cells. A detailed explanation of the setup can be found in a previous study [7].

Radio Frequency Welding

The radio frequency welding trials were conducted on a Wave Foamer C from Kurtz GmbH & Co. KG (Kreuzwertheim, Germany). A schematic representation of the setup with active and ground electrodes, PTFE mold, and filled beads is illustrated in Figure 1(a).

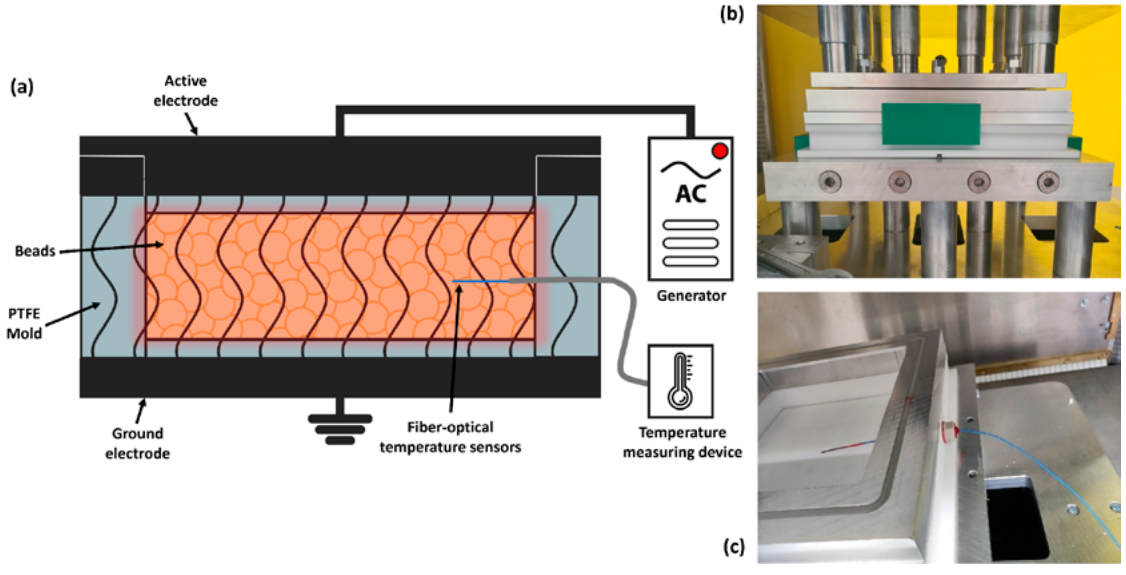

Figure 1. Schematic cross-section of the mold with beads and temperature sensor (a), real PTFE mold with upper and lower electrode installed in the RF machine (b), and detailed view of the temperature sensor entering the empty mold (c).

DOI: https://doi.org/10.51573/Andes.PPS39.GS.PFM.1

The alternating current generator is connected to the upper active electrode, setting the potential difference to the lower ground electrode, thus resulting in an oscillating electromagnetic field with a fixed frequency of 27.12 MHz. The maximum voltage for all trials was set to 9 kV with a short ramp-up time of around 4 s. Durations at this maximum voltage varied between 12.5 and 25 s. The density of the plates was controlled by weight and set to a fixed 25 vol.-% of polymer with respect to the mold volume. This results in a part density of 276 kg/m³. Before demolding, a stabilization time of 200 s was set in order to ensure sufficient cooling. A PTFE frame with an internal rectangular geometry of 200 x 200 mm² was used as a mold (Figure 1[b]). PTFE isolation plates below and above the foam beads set the height of the final foam sample to 10 mm. Since conductive materials would strongly interact with the electromagnetic field, a special fiber optic temperature sensor was placed within the bead foam to measure its temperature increase. As shown in Figure 1(c), the cable is fed through a sealed entry port on the right side of the frame. To ensure representative results, a central positioning of the sensor within the plate was analyzed after each trial throughout the cross-section.

Results and Discussion

Dielectric Properties of ETPU

The permittivity of polymers and their dependency on temperature and frequency is based on their chemical structure and resulting molecular interactions across individual chains. As shown in literature, ε_r' exhibits a step down behavior over frequency [7]. Due to internal relaxation processes, this phenomena is also visible for the investigated TPU in Figure 2.

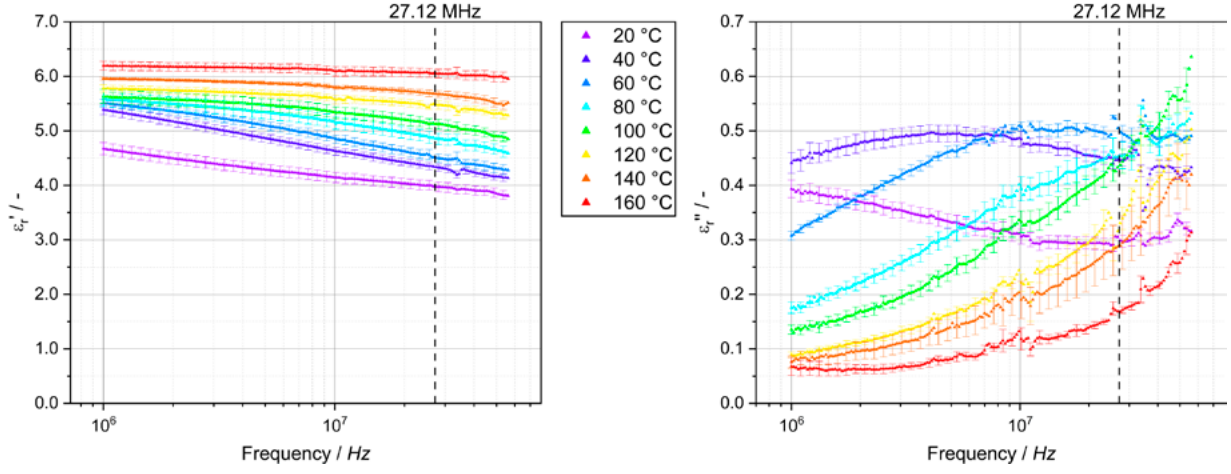

Figure 2. Real and imaginary parts of the complex relative permittivity ε_r^* of TPU as a function of frequency from 20 to 160°C.

DOI: https://doi.org/10.51573/Andes.PPS39.GS.PFM.1

Enhanced flexibility of the polymer chains at elevated temperatures resulting in a shift of that step to higher frequencies resulted in increased permittivity values at a constant frequency. Since the analysis frequency range is limited by the setup from 1 to 50 MHz, the step down is only partially visible at each temperature. A similar behavior is observed for ε_r''. Here, a peak is formed over frequency, which constantly shifts upwards if the temperature is increased. The peak of ε_r'' corresponds to the inverse relaxation time of the orientational polarization phenomena within the chain's dipoles. Elevated flexibility allows the dipoles to align up to faster alternating fields and therefore lower their specific relaxation time. At temperatures above 60°C, the tip of the peak is out of the observable frequency range and only the left shoulder of the peak is visible.

Since the frequency of the electromagnetic field within the RF process is fixed at 27.12 MHz for regulatory reasons, the real and imaginary part over the temperature at individual frequencies are shown in Figure 3.

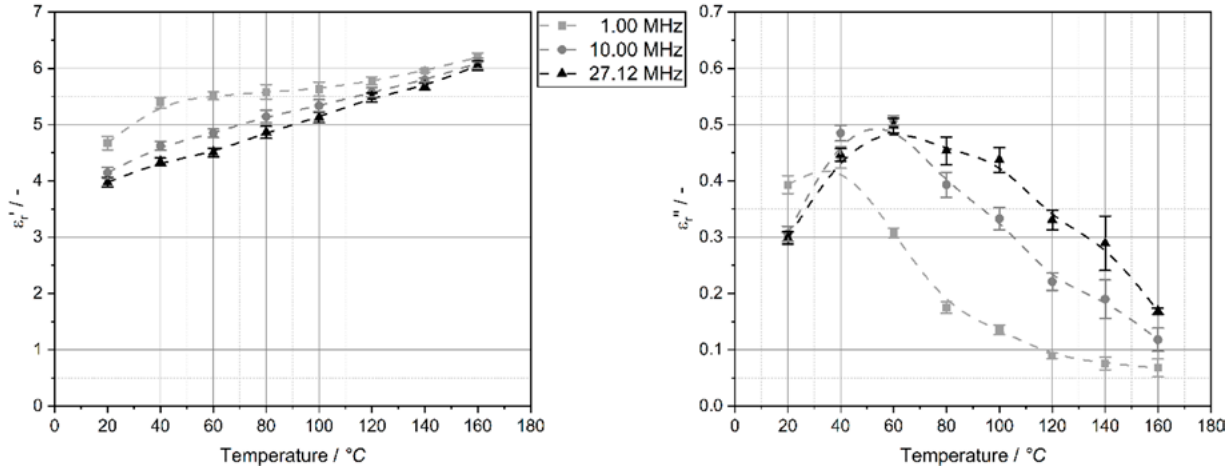

Figure 3. Real and imaginary part of the complex relative permittivity ε_r^* of TPU as a function of temperature at frequencies of 1, 10, and 27.12 MHz.

The previously mentioned superposition of temperature and frequency is clearly observable in ε_r'. Over the temperature, this behavior results in a step up towards higher temperatures, visible for 1 MHz. At higher frequencies of 10 and 27.12 MHz, this feature is less distinctive, and a more gradual incline can be observed. This material response is based on a combination of relaxation phenomena and an overall increased chain flexibility with increasing temperature, thus leading to reduced intermolecular interactions [13, 14]. Similar to ε_r', the ε_r'' peak exhibits a shift to elevated temperatures with an increase in analysis frequency. At the fixed frequency of 27.12 MHz, changes in the real but primarily imaginary part of the complex relative permittivity over the welding period must be considered. These changes will directly impact the heating of the material based on the volumetric power input from Equation (1).

DOI: https://doi.org/10.51573/Andes.PPS39.GS.PFM.1

In addition to the bulk TPU material, a second bigger measurement cell allows for direct analysis of the complex relative permittivity of the beads at defined densities and temperatures [7]. Dielectric properties of multi-phase systems are subject to complex interactions within and between the individual materials. This causes them to deviate from a simple linear mixing rule [15-17]. Figure 4 shows a similar behavior in ε_r' and ε_r'' of the beads at a density of 15 vol.-% of the polymer at all temperatures compared to the prior bulk TPU.

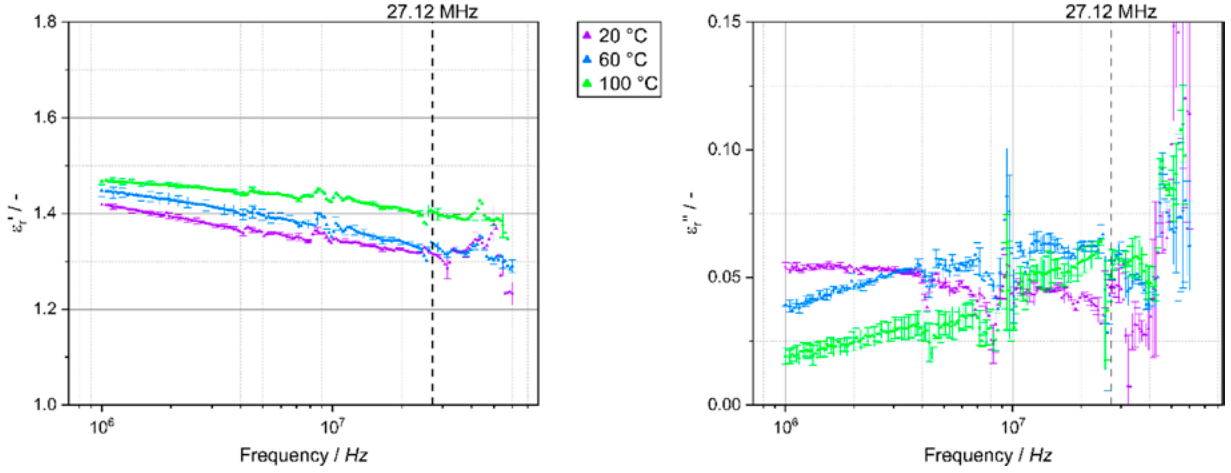

Figure 4. Real and imaginary part of the complex relative permittivity ε_r^* of ETPU as a function of frequency at a defined density of 15 vol.-% at 20, 60 and 100°C.

Despite showing a similar overall trend over the frequency, the quantity of both parts of the complex relative permittivity is attenuated since the second phase air has generally lower values ($\varepsilon_r^* = 1 - 0i$). Thus, the average response of the material within the measurement cell is reduced. This results in increased deviations, which is especially visible in ε_r'' at higher frequencies limited by internal resonances.

At a fixed temperature, the ratio of polymer within the analyzed volume of beads is the determining parameter, as shown in Figure 5. As expected, the values for ε_r' and ε_r'' are in between the two polymer and air phases, depending on the volumetric ratio with again similar trends to the bulk TPU. During the production of parts with increased density, this will automatically lead to elevated power input. However, a higher amount of polymer will also increase the volumetric heat capacity of the system linearly with density. This leads to theoretically similar heating rates independent of the density for a fixed material. Nevertheless, this only represents a highly simplified assumption. Elements like local displacement of the electromagnetic field within the cellular structure and to the mold is excluded as well as thermal conductivity within the bead foam and towards the PTFE frame and isolation plates.

DOI: https://doi.org/10.51573/Andes.PPS39.GS.PFM.1

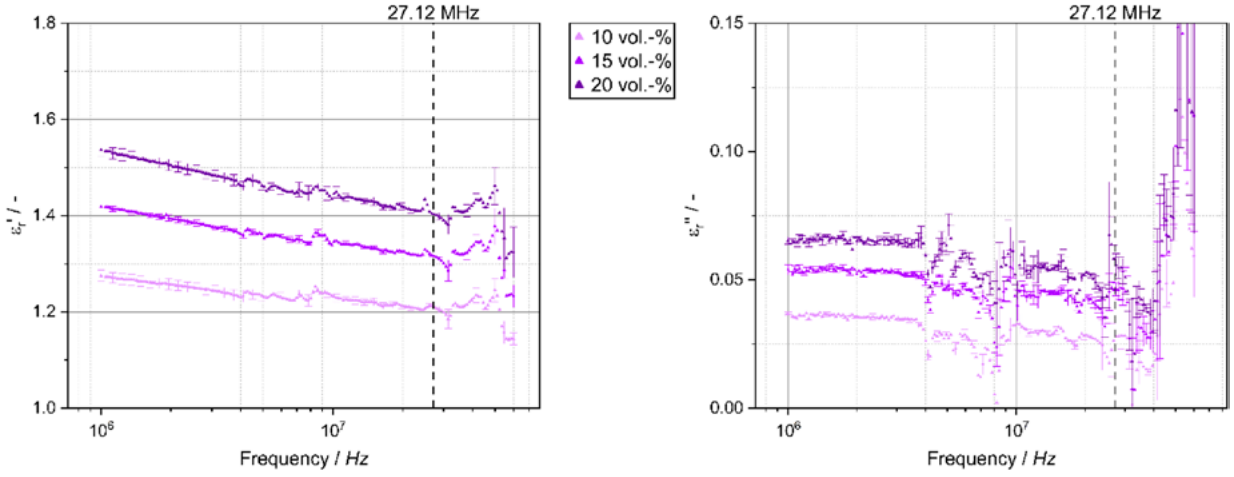

Figure 5. Real and imaginary part of the complex relative permittivity ε_r^* of ETPU as a function of frequency at 20°C and defined densities of 10, 15 and 20 vol.-%.

Influence of Dielectric Properties on Radio Frequency Welding

In order to verify the connection between material properties and the RF process, multiple welding trials were conducted. The real voltage present at the active electrode is shown in Figure 6.

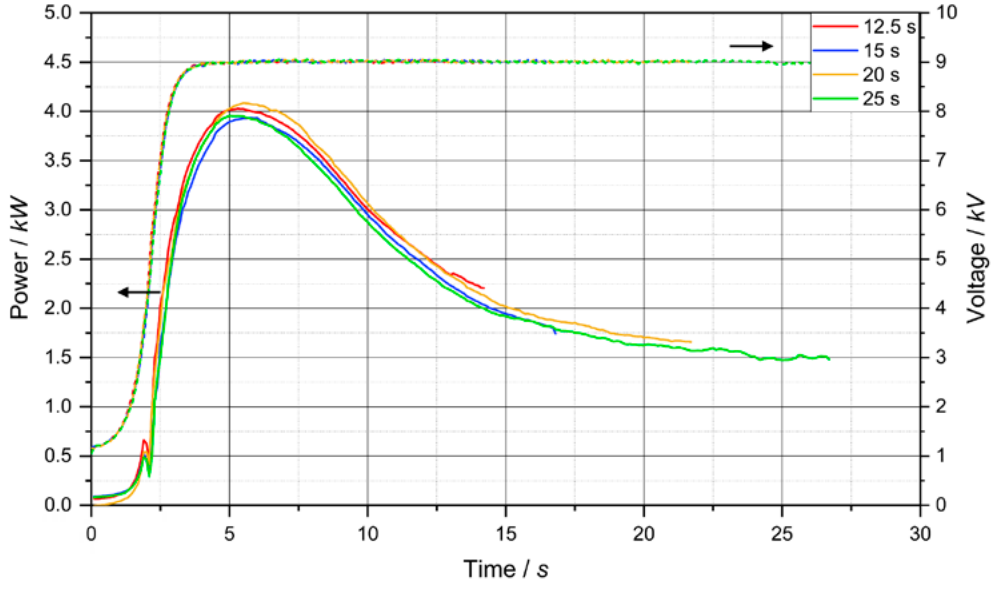

Figure 6. Power and voltage as a function of time for the welding trials at 9 kV with 25 vol.-% of beads for times at maximum voltage at 12.5, 15, 20, and 25 s.

DOI: https://doi.org/10.51573/Andes.PPS39.GS.PFM.1

The voltage curve over time is predetermined by the operator with a linear ramp-up at the beginning of 2 s until the maximum voltage of 9 kV is reached. Due to machine-related inertia within the voltage regulation, the initial phase deviates from that specification. This results in a slight delay in the ramp-up. A constant voltage is reached after approximately 4 s. Neglecting the only slight changes in ε_r', a fixed voltage results in a constant electromagnetic field strength. Based on the plate geometry it can be assumed to be homogeneous with only minor edge effects. Thus, the observable changes in power over the welding time may be attributed to evolving ε_r'' with increased temperature. As expected, all curves with changing time at maximum voltage from 12.5 to 25 s are overlapping. This indicates a high reproducibility of the process and feedback data. Within the range of constant voltage, an initial slight increase in power up to a maximum is followed by an elongated decline. By comparing the results of ε_r'' (Figure 3) with this behavior, the linear dependency between this material property and the process feedback is clearly visible. With the peak power at around 5 to 6 s a temperature of around 60°C can be reversely attributed.

This indirect temperature observation can be compared to the data of the fiber optic temperature sensor placed inside the beads during the welding process (Figure 7).

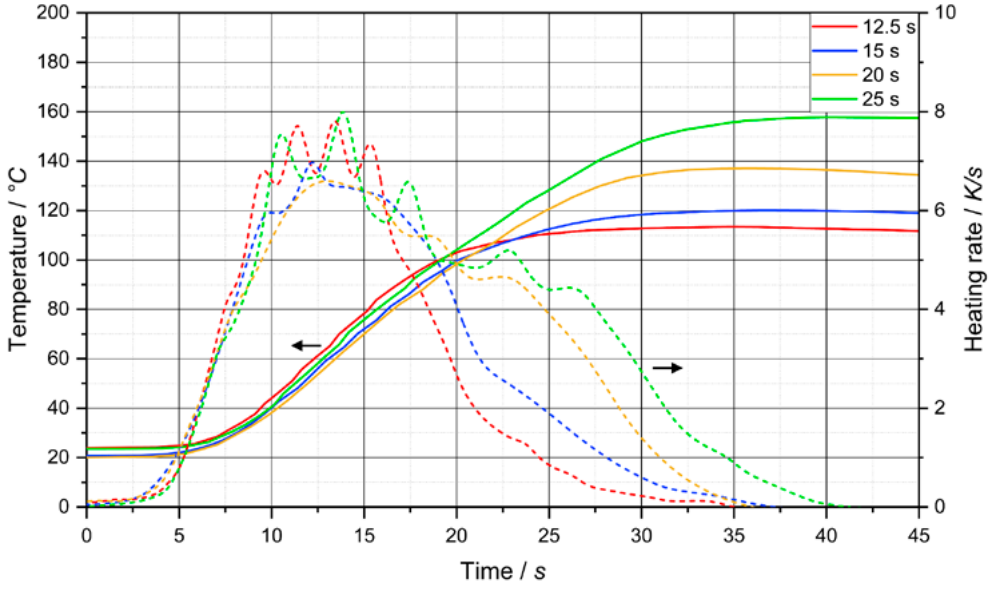

Figure 7. Temperature and calculated heating rate as a function of time for the welding trials at 9 kV with 25 vol.-% of beads for times at maximum voltage at 12.5, 15, 20, and 25 s.

A significant delay is clearly visible in the expected temperature to the measured one. Despite the small diameter of the 1 mm sensor tip, the apparent thermal inertia must be considered when interpreting the data. Furthermore, this phenomenon is reflected in the initial delay of around 5 s until the temperature starts to rise. Additionally, a continuous temperature increase is observed exceeding the time frame of applied voltage by up to 15 s. This also suggests that the maximum

DOI: https://doi.org/10.51573/Andes.PPS39.GS.PFM.1

temperatures measured during the process underestimate the actual ones with a high probability. Temperature is by far the most important parameter for the welding of the individual beads to a final part. This deviation must therefore be considered in understanding and optimizing the process in combination with the respective material. Additionally, the heating rate can be calculated from the temperature curve over time. At a constant heat capacity, the heating rate is directly proportional to the volumetric power input by the dielectric heating of the polymer. After an initial peak in heating rate a slight drop is observable for all welding times. Once the voltage is switched off, the thermal inertia still leads to positive heating rates, but with decreasing strength until cooling occurs. Thus, by comparing all individual results, a direct correlation between the temperature-dependent dielectric properties of the polymer and both feedback curves power and heating rate at the RF process is visible.

Conclusion

This study provides a clear correlation between the material properties and process feedback during the novel RF welding process. The permittivity of the TPU as bulk material shows significant changes throughout the analyzed frequency and temperature range. For ε_r', a step down is visible towards higher frequency with an overall increase for elevated temperature. Within the imaginary part ε_r'', however, a peak is formed that similarly shifts towards higher frequency at increased temperature. Focusing on fixed frequencies, as in the case of the RF process at 27.12 MHz, this leads to an initial rise in ε_r'' followed by a slow decline towards temperatures close to melting of the polymer. Switching to bead foams, the inclusion of a second air phase with constant properties when heated results in overall similar curves in permittivity, but with attenuated values in between the two individual materials. The power consumption within the RF process is directly correlated to material and process parameters. This behavior is clearly visible at a constant voltage after the initial ramp-up time. Here the temperature-induced changes in power over the welding time can be attributed to an evolving imaginary part of the relative permittivity ε_r''. Observations gained by the fiber optic temperature sensor are again mainly consistent with these theoretical correlations. Only a significant delay due to thermal inertia of the sensor was monitored. This indicates that an indirect analysis of the temperature via power appears to provide feedback without time delay. Thus, the insights gained within this study into the novel RF process for ETPU bead foams expand to new possibilities for a more sustainable future for lightweight products.

Acknowledgments

The authors would like to acknowledge Marc Norridge and Korbinian Berner for supporting the trials at the RF welding machine. Additionally, the Bavarian Polymer Institute (BPI) must be acknowledged for providing access to different analytical methods.

This research was funded by the "Bavarian Ministry of Economic Affairs, Regional Development and Energy" within the funding program "Verbundforschungsprogramm Förderlinie Materialien und Werkstoffe" (grant number MW-2104-0005).

References

1. D. Raps, N. Hossieny, C. B. Park, and V. Altstädt, "Past and present developments in polymer bead foams and bead foaming technology," *Polymer (Guildf).*, vol. 56, pp. 5–19, 2015, https://doi.org/10.1016/j.polymer.2014.10.078
2. J. Kuhnigk, T. Standau, D. Dörr, C. Brütting, V. Altstädt, and H. Ruckdäschel, "Progress in the development of bead foams – A review," *Journal of Cellular Plastics*, vol. 58, no. 4, pp. 707–735, 2022, https://doi.org/10.1177/0021955X221087603
3. V. Romanov, "Device and method for producing a particle foam part," WO 2017/125412 A1, 2017.
4. N. Hossieny, M. Nofar, V. Shaayegan, and C. B. Park, "Effects of glycerol monosterate on TPUs crystallization and its foaming behavior," *AIP Conference Proceedings*, vol. 1593, pp. 374–377, 2014, https://doi.org/10.1063/1.4873803
5. M. Mehdizadeh, *Microwave/RF Applicators and Probes for Material Heating, Sensing, and Plasma Generation: Second Edition*. 2015.
6. Zhou Y.; Breyen M, *Joining and assembly of medical materials and devices*. Woodhead Publishing Limited, 2013.
7. M. Dippold, C. Töpfer, and H. Ruckdäschel, "Influence of dielectric properties of polybutylene terephthalate and respective foam beads on process behavior in radio-frequency welding," *Journal of Applied Polymer Science*, vol. 141, no. 8, pp. 1–12, Feb. 2024, https://doi.org/10.1002/app.54988
8. A. K. Jonscher, "A new model of dielectric loss in polymers," *Colloid and Polymer Science*, vol. 253, no. 3, pp. 231–250, 1975, https://doi.org/10.1007/BF01470233
9. D. C. Campos, "Dielectric properties of polyols, at frequency range 0.2–3 GHz and temperature range 293–473 K: an analysis in the frequency and temperature domain," *Journal of Microwave Power and Electromagnetic Energy*, vol. 54, no. 2, pp. 125–160, 2020, https://doi.org/10.1080/08327823.2020.1755482
10. T. Sabu, T. Raju, K. Z. Ajesh, and K. M. Raghvendra, *Spectroscopy methods for nanomaterials characterization*, vol. 2. Amsterdam: Elsevier Inc., 2017.
11. H. Sussner, D. E. Horne, and D. Y. Yoon, "A new method for determining the pyroelectric coefficient of thin polymer films using dielectric heating," *Applied Physics Letters*, vol. 32, no. 3, pp. 137–139, 1978, https://doi.org/10.1063/1.89974
12. K. Schneider, C. Ott, and D. Drummer, "Simulative study of polymeric core–shell foam particles for the enlargement of the material portfolio in 3-D high-frequency welding ," *Polymer Engineering & Science*, November, pp. 1–11, 2021, https://doi.org/10.1002/pen.25861

13. C. B. Roth and J. R. Dutcher, "Glass transition and chain mobility in thin polymer films," *Journal of Electroanalytical Chemistry*, vol. 584, no. 1, pp. 13–22, 2005, https://doi.org/10.1016/j.jelechem.2004.03.003

14. V. A. Bershtein, M. Z. Petkevich, L. G. Razgulyayeva, and V. A. Stepanov, "The temperature dependence of intermolecular interaction in polymers in the glassy state," *Polymer Science U.S.S.R.*, vol. 20, no. 12, pp. 3005–3013, 1978, https://doi.org/10.1016/0032-3950(78)90514-2

15. A. H. Sihvola, "How strict are theoretical bounds for dielectric properties of mixtures?," *IEEE Transactions on Geoscience and Remote Sensing*, vol. 40, no. 4, pp. 880–886, 2002, https://doi.org/10.1109/TGRS.2002.1006369

16. H. Looyenga, "Dielectric constants of heterogeneous mixtures," *Physica*, vol. 31, no. 3, pp. 401–406, 1965, https://doi.org/10.1016/0031-8914(65)90045-5

17. A. H. Sihvola and J. A. Kong, "Effective permittivity of dielectric mixtures," *IEEE Transactions on Geoscience and Remote Sensing*, vol. 26.4, pp. 420–429, 1988.

DOI: https://doi.org/10.51573/Andes.PPS39.GS.PFM.1

GENERAL SYMPOSIA | FIBERS AND FILMS

Polyketone-Polypropylene Core-Shell Fibers for Concrete Reinforcement

Jonas Herz, Sophia Hefenbrock, Katharina Lorenz, Dirk Muscat and Nicole Strübbe

DOI: https://doi.org/10.51573/Andes.PPS39.GS.FF.1

December 2024

Polyketone-Polypropylene Core-Shell Fibers for Concrete Reinforcement

Jonas Herz, Sophia Hefenbrock, Katharina Lorenz, Dirk Muscat and Nicole Strübbe[1]

Abstract: Corrosion of commonly used steel reinforcements weakens the structural strength of concrete. To address this issue, research was conducted on concrete reinforcements in the form of polymer fibers. These polymer fibers need concrete bonding ability and good mechanical properties. This study investigates core-shell fibers produced from polyketone and polypropylene mixed with a compatibilizer. The core-shell fibers were produced by coextrusion and drawing. The fibers were analyzed by tensile tests, a single fiber pull-out test, contact angle measurements, scanning electron microscopy, and thermogravimetric analysis.

Keywords: Concrete Reinforcement, Core-Shell Fiber, Polyketone, Polypropylene

1 The authors Jonas Herz (jonas.herz@th-rosenheim.de), Sophia Hefenbrock, Katharina Lorenz, Dirk Muscat and Nicole Strübbe are affiliated with the Faculty of Engineering at the Rosenheim Technical University of Applied Sciences in Germany.

DOI: https://doi.org/10.51573/Andes.PPS39.GS.FF.1

Introduction

Concrete is currently the principal material used in the building industry [1]. However, because of the corrosion of steel reinforcements, the concrete industry is searching for alternative reinforcement possibilities. Different solutions, like stainless steel [2] as well as carbon fiber reinforcements [3] and polymer fibers [4], have been investigated. To be considered an alternative reinforcement, a polymer fiber needs to simultaneously provide high mechanical properties and good bonding ability to the concrete matrix [5]. However, other fiber properties should also be considered. In case of fire, decomposition of polymer fibers creates a porous system. This porous system allows vapor to clear out of the concrete with decreased spalling [6]. Accordingly, tests concerning the thermal stability are also performed. Previous research indicated good bonding abilities through the addition of calcium carbonate and wood particles in the shell of polypropylene (PP) core-shell fibers [7]. Further, polyketone (PK) showed high mechanical properties [8]. Nevertheless, the processing temperature of PK is too high for the addition of wood particles. As a first step in this direction, this research investigates core-shell fibers that combining PK in the core and PP in the shell, in relation to their mechanical properties, concrete bonding ability, and thermal stability. A subsequent addition of filler particles to the shell material could be considered for future research.

Experiments

Materials

A combination of three materials was used in this research. An aliphatic polyketone with a density of 1.19 g/cm³ and a melt volume rate of 21 g/10 min at 240°C and 5 kg [9] was used as core material. In the shell, polypropylene with a density of 0.905 g/cm³ and a melt flow rate (MFR) of 1 g/10 min at 230°C and 2.16 kg [10] was used as base material. A maleic anhydride grafted polypropylene (MAH) with a density of 0.91 g/cm³ and a melt flow rate of 9.1 g/10 min at 230°C and 2.16 kg [11] worked as a compatibilizer to the PP in the shell.

Processing

Compounding

Three different shell-material combinations were compounded using a Coperion ZSK 26 MC^{18} twin screw extruder with a screw diameter of 26 mm and a l/d-ratio of 48. The MAH was added to the PP by 25, 50, and 75 wt.-%. The compounding parameters are shown in Table 1.

DOI: https://doi.org/10.51573/Andes.PPS39.GS.FF.1

Table 1. Compounding parameters for shell-material production.

Shell Material	Screw Speed	Mass Temperature	Pressure	Throughput
	[rpm]	[°C]	[bar]	[kg/h]
PP75-MAH25	250	227	21	12
PP50-MAH50	250	227	25	12
PP25-MAH75	250	225	18	12

Fiber Production

The core-shell fibers were processed by a two-step process. First, a strand was produced using coextrusion. The same Coperion ZSK 26 MC[18] twin screw extruder used for compounding the shell materials was connected to a HAAKE polydrive single screw extruder with a screw diameter of 19 mm and a l/d-ratio of 25 via a coextrusion die. The core material (C) was processed by the twin screw extruder (Extruder 1) and the shell material (S) by the single screw extruder (Extruder 2). After extrusion, the strand was cooled in a water bath and taken-up by a godet. The coextrusion parameters are shown in Table 2. Second, the strand was drawn to a fiber using a Collin Teach Line MDO stretching unit. The strand was placed in front of the stretching unit. The speed of the first godet before the furnace was set at 1 m/min. Fiber drawing was induced by temperature and tension applied by a higher speed of the second godet after the furnace. The roll-temperature of both godets was set at 80°C and the furnace was heated up to 188°C. All fibers were drawn until fiber failure occurred. A draw ratio (DR) was calculated by the ratio between the speeds of the two godets.

Table 2. Coextrusion parameters for strand production.

Fiber	Extruder 1				Extruder 2			Strand Handling	
	Screw Speed	Mass Temperature	Pressure	Throughput	Screw Speed	Mass Temperature	Pressure	Water-bath Temperature	Take-up Speed
	[rpm]	[°C]	[bar]	[kg/h]	[rpm]	[°C]	[bar]	[°C]	[m/min]
C-PK-S-PP100	120	237	98	1.5	17	210	125	20	12
C-PK-S-PP75-MAH25	120	237	112	1.5	17	209	72	14	12
C-PK-S-PP50-MAH50	120	237	112	1.5	17	209	59	14	12
C-PK-S-PP25-MAH75	120	237	110	1.5	14	208	45	14	12

DOI: https://doi.org/10.51573/Andes.PPS39.GS.FF.1

Fiber Analysis

The mechanical properties of the fibers were examined by tensile tests using a Zwick universal testing machine (Z100) equipped with a 10 kN load cell and 90° deflection grips. The sample length was 250 mm. The test speed was set at 1 mm/min during determination of Young's modulus and increased to 10 mm/min until fiber break. Five samples were tested per fiber material.

Single fiber pull-out tests (SFPT) were used to investigate the bonding between fiber and concrete. For specimen preparation, single fibers were fixed with 15 mm embedment length in molds with a size of 60 x 60 x 30 mm³. The molds were filled with the concrete mixture presented in Table 3. The concrete mixture was manufactured using a Kitchen Aid ProLine Series 6 equipped with a flat beater. First, the concrete was cured for 24vh in a climate-regulated chamber at a humidity of 67% and a temperature of 20°C. Then, the specimens were demolded and stored for another 13 days in the same environment as the first curing step. Finally, six specimens per fiber material were tested at a specimen curing time of 14 days using a Zwick universal testing machine (Zwick 1474) equipped with a 500 N load cell. The pull-out speed was 2 mm/min. The test ended after complete fiber pull-out. As the fiber was clamped directly on top of the specimen surface, the free fiber length can be ignored.

Table 3. Concrete mixture.

Material		Sand	Portland Cement (CEM I)	Limestone	Water	Superplasticizer 1	Superplasticizer 2
Amount	[g]	1350	450	75	220	6.2	3.0

For every fiber, the interfacial shear strength (IFSS) τ_{IFSS} was calculated from the pull-out curves by:

$$\tau_{IFSS} = \frac{F_{max}}{\pi\, d_f l_e} \quad (1)$$

where F_{max} represents the maximum extraction force, d_f the equivalent fiber diameter, and l_e the embedment length.

Surface energies and polarities of the core-shell fibers were examined at their maximum DR using contact angle measurements by a KRÜSS EasyDrop FM40. The test liquids used were water and diiodomethane. The fiber surfaces were cleaned, and eight small droplets of each liquid were set on the surface to measure the contact angle. The calculation of the surface energy was done using the Krüss ADVANCE software accordingly to the method of Owen, Wendt, Rabel, and Kaelble. This method allows splitting of the surface energy into a dispersive and a polar part [12].

DOI: https://doi.org/10.51573/Andes.PPS39.GS.FF.1

Optical analysis of the different fiber surfaces prior and after SEPT was performed on the scanning electron microscope MIRA3 from Tescan using the secondary electron detector. The samples were gold sputtered and inspected at different magnifications using an accelerating voltage of 10kV.

The fiber decomposition was tested via thermogravimetric analysis (TGA) using a TA Instruments TGA 5500. The different fibers were analyzed under nitrogen atmosphere at temperatures between ≈30°C and 650°C at a heat rate of 20 K/min. The mass loss was recorded as a function of temperature.

Results and Discussion

Fiber Production

The furnace temperature for all fibers was above the melting temperature of PP to draw the PK core. Similarly to the argument in previous research, this could be caused by a high melt stiffness of the PP [8]. The maximum DR and the equivalent fiber diameters are shown in Table 4.

Table 4. Attained draw ratios and fiber diameters.

Shell Material		C-PK-S-PP100	C-PK-S-PP75-MAH25	C-PK-S-PP50-MAH50	C-PK-S-PP25-MAH75
Maximum Draw Ratio	[1]	10	9	8	9
Equivalent Fiber Diameter	[mm]	0.54 ± 0.2	0.57 ± 0.1	0.62 ± 0.1	0.58 ± 0.1

Tensile Tests

The results from tensile tests are presented in Figure 1. The highest Young's modulus is reached by C-PK-S-PP100, and C-PK-SPP50-MAH50 shows the lowest value. In case of the materials containing MAH, the Young's modulus seems to follow the DR. C-PK-SPP75-MAH25 shows the highest tensile strength, while higher amounts of MAH decrease the tensile strength. This could be a result of the shorter polymer chains of the MAH, which are indicated by the higher MFR compared to the PP.

DOI: https://doi.org/10.51573/Andes.PPS39.GS.FF.1

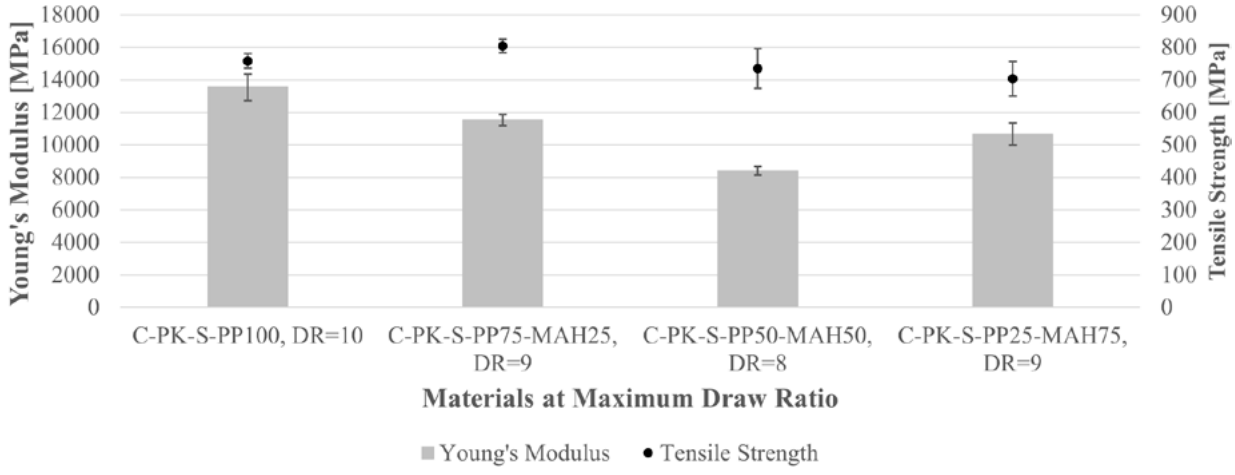

Figure 1. Results from tensile tests.

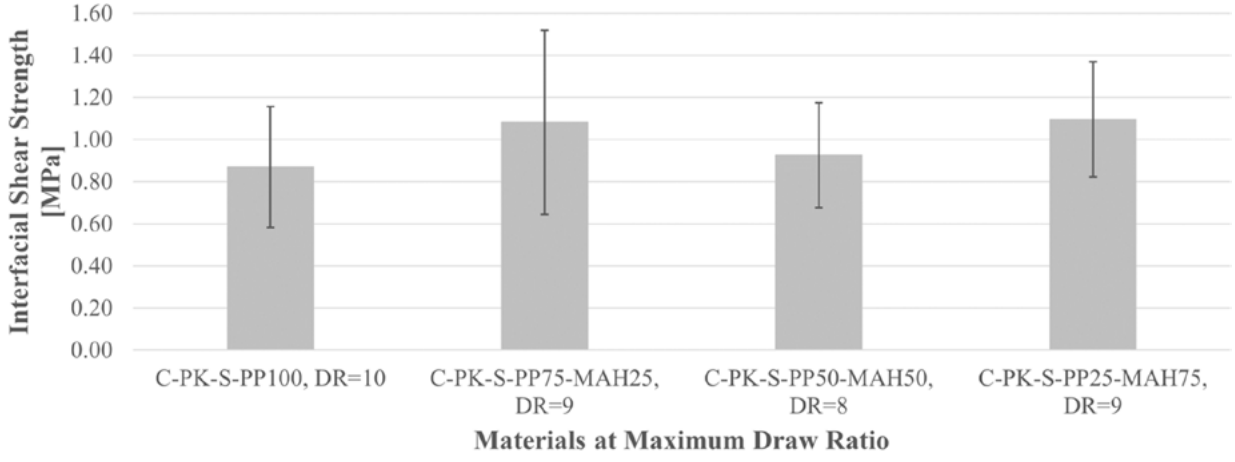

Figure 2. Results from single fiber pull-out tests.

Single Fiber Pull-out Tests

The results from SFPT in Figure 2 demonstrate an increased IFSS for the materials containing MAH. Further, a comparison with Figure 1 indicates a correlation of IFSS and Young's modulus for the MAH containing fibers. As the Young's modulus is influenced by the DR, the DR could also be considered an influencing factor on the IFSS. Nevertheless, the influence of MAH and the Young's modulus respectively DR on the IFSS seems to be rather small.

DOI: https://doi.org/10.51573/Andes.PPS39.GS.FF.1

Contact Angle Measurements

An increase in surface energy for the fibers containing MAH is clearly visible in Figure 3. A slightly increased polarity is also shown. Furthermore, surface energy correlates with the IFSS presented in Figure 2, which allows the assumption that the higher surface energy causes a better wetting of the fiber surface by the concrete.

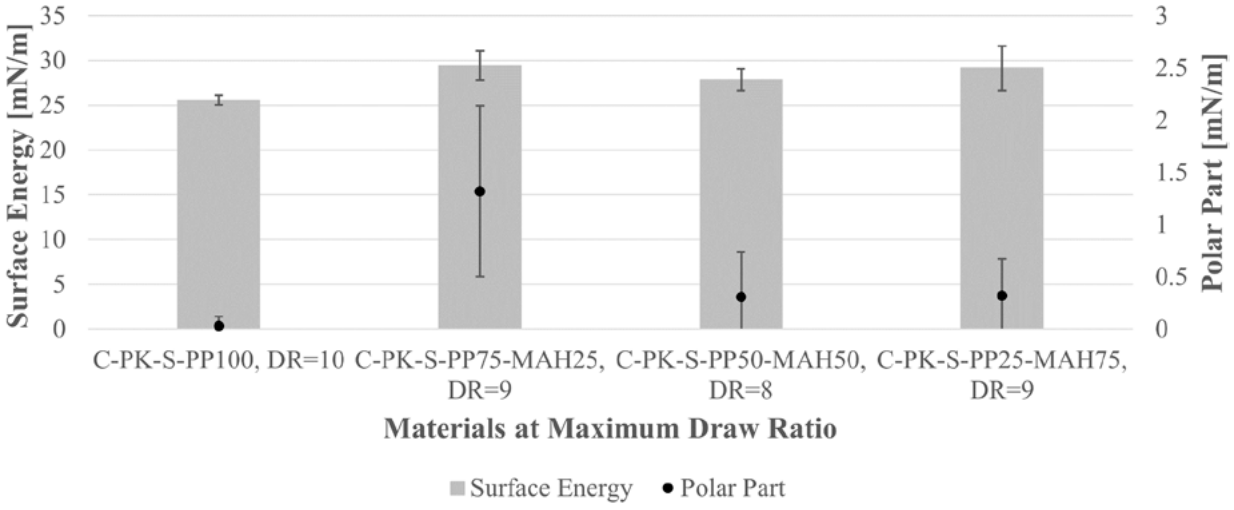

Figure 3. Results from contact angle measurements.

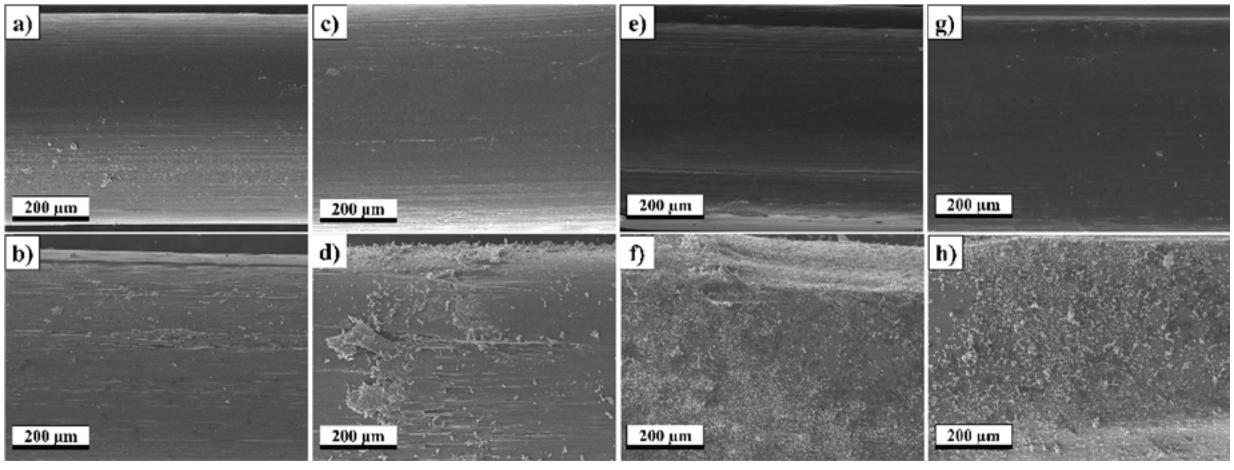

Figure 4. Scanning electron microscopy pictures, C-PK-S-PP100, DR=10 before a) and after b) pull-out, C-PK-S-PP75-MAH25, DR=9 before c) and after d) pull-out, C-PK-S-PP50-MAH50, DR=8 before e) and after f) pull-out, C-PK-S-PP25-MAH75, DR=9 before g) and after h) pull-out.

DOI: https://doi.org/10.51573/Andes.PPS39.GS.FF.1

Scanning Electron Microscopy

Figure 4 shows SEM pictures of the fiber surfaces prior and after pull-out test. It can be clearly seen that adding MAH into the shell of the fibers leads to higher adhesion to the concrete. There is no significant difference in adhesion depending on the MAH-content observable.

Thermogravimetric Analysis

Figure 5 shows the results from TGA and Table 5 shows the temperature at a weight loss of 5%, 10%, 30%, and 70% mass loss. It is visible that the decomposition takes place primarily between 375°C and 525°C. Two decomposition steps are visible, which are shifted slightly by the addition of MAH. The first step is shifted to higher temperatures while the second step happens at lower temperatures.

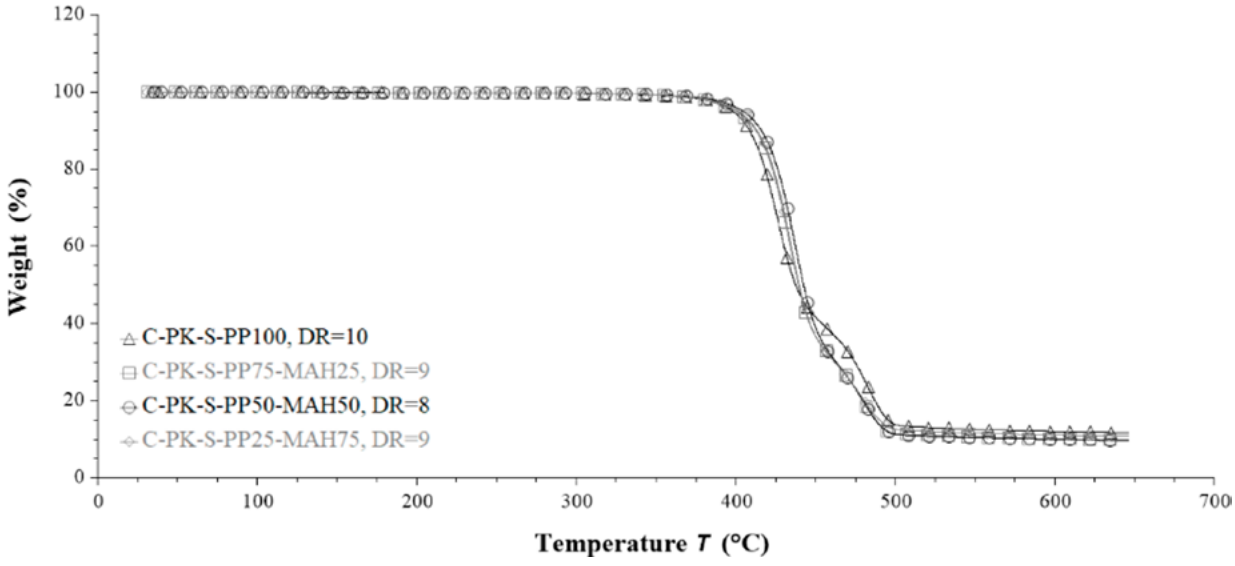

Figure 5. Results from thermogravimetric analysis.

Table 5. Temperature at certain mass loss.

Shell Material	Draw Ratio	Temperature of 5% Mass Loss	Temperature of 10% Mass Loss	Temperature of 30% Mass Loss	Temperature of 70% Mass Loss
	[1]	[°C]	[°C]	[°C]	[°C]
C-PK-S-PP100	10	398.19	408.60	424.53	474.60
C-PK-S-PP75-MAH25	9	400.29	412.61	429.06	462.77
C-PK-S-PP50-MAH50	8	404.37	415.96	432.36	462.85
C-PK-S-PP25-MAH75	9	401.53	413.28	429.75	461.81

DOI: https://doi.org/10.51573/Andes.PPS39.GS.FF.1

Conclusion

This study shows that MAH in the fiber shell has a high potential for core-shell fibers made from PK and PP. The MAH shows a positive influence on the bonding between core-shell fibers and concrete. Furthermore, MAH increases the surface energy of the fibers and concrete adheres to the fibers surface as shown by the SEM pictures. For 25 wt.-% of MAH, an increased tensile strength was observed compared to the fiber without MAH. The thermal stability is just slightly influenced by the added MAH.

The tensile strength of all fibers presented in this study surpass that of common steel rebars. The tensile strength of common steel rebars reaches values above 600 MPa. Specialized types can also reach a tensile strength of 800 MPa [13]. Accordingly, the core-shell fibers presented herein show a high potential for applications in building industries. But further research, as for instance 3-point bending tests, need to be carried out before a final conclusion can be drawn.

Acknowledgments

The authors wish to acknowledge the support of Aline Huber and Wolf Schmederer for the support of this study.

References

1. J. Hegger, M. Curbach, A. Stark, S. Wilhelm, and K. Farwig, "Innovative design concepts: Application of textile reinforced concrete to shell structures," *Structural Concrete*, vol. 19, no. 3, pp. 637–646, 2018, https://doi.org/10.1002/suco.201700157
2. U. Nürnberger and Y. Wu, "Stainless steel in concrete structures and in the fastening technique," *Materials and Corrosion*, vol. 59, no. 2, pp. 144–158, 2008, https://doi.org/10.1002/maco.200804150
3. B. Beckmann et al., "Collaborative research on carbon reinforced concrete structures in the CRC / TRR 280 project," *Civil Engineering Design*, vol. 3, no. 3, pp. 99–109, 2021, https://doi.org/10.1002/cend.202100017
4. R. Rostami, M. Zarrebini, S. B. Abdellahi, D. Mostofinejad, and S. M. Abtahi, "Investigation of flexural performance of concrete reinforced with indented and fibrillated macro polypropylene fibers based on numerical and experimental comparison," *Structural Concrete*, vol. 22, no. 1, pp. 250–263, 2021, https://doi.org/10.1002/suco.201900374
5. M. Sigrüner, D. Muscat, and N. Strübbe, "Investigation on pull-out behavior and interface critical parameters of polymer fibers embedded in concrete and their correlation with particular fiber properties," *Journal of Applied Polymer Science*, vol. 138, no. 28, p. 50745, 2021, https://doi.org/10.1002/app.50745

6. B. Wietek, *Fiber Concrete: In Construction*, 1st ed. Wiesbaden: Springer Fachmedien Wiesbaden; Imprint: Springer, 2021.

7. J. Herz, M. Sigrüner, D. Muscat, and N. Strübbe, "Co-extruded polymer fibers for concrete reinforcement," in *Proceedings of the 37th International Conference of the Polymer Processing Society (PPS-37)*, Fukuoka City, Japan, 2023, p. 80002, https://doi.org/10.1063/5.0168511

8. J. Herz, K. Lorenz, D. Muscat, and N. Strübbe, "Polymeric core-shell and mono-material fibers for concrete reinforcement," in *Proceedings of the 38th International Conference of the Polymer Processing Society (PPS-38)*, St. Gallen, Switzerland, 2024, p. 40004, https://doi.org/10.1063/5.0204946

9. RIA-Polymers GmbH, RIAMAXX HR 00 EX natur.

10. M-Base Engineering+Software GmbH, ISPLEN PP020G3E.

11. Mitsui Chemicals Europe GmbH, ADMER™ QE800E.

12. D. K. Owens and R. C. Wendt, "Estimation of the surface free energy of polymers," *Journal of Applied Polymer Science*, vol. 13, no. 8, pp. 1741–1747, 1969, https://doi.org/10.1002/app.1969.070130815

13. H. Kämpfe, Bewehrungstechnik: Grundlagen, Praxis, Beispiele, Wirtschaftlichkeit, 2nd ed. Wiesbaden, Germany: Springer Vieweg, 2020.

Influence of Coating Structure of an SiOx Barrier Coating on a PET Substrate on Water Vapor Permeation Activation Energy

J. Franke, M.O. Liedke, P. Dahmen, M. Butterling,
A. G. Attallah, A. Wagner, P. Alizadeh and R. Dahlmann

DOI: https://doi.org/10.51573/Andes.PPS39.GS.NN.1

December 2024

Influence of Coating Structure of an SiOx Barrier Coating on a PET Substrate on Water Vapor Permeation Activation Energy

J. Franke, M.O. Liedke, P. Dahmen, M. Butterling, A. G. Attallah, A. Wagner, P. Alizadeh and R. Dahlmann[1]

Abstract: The application of plasma polymerized silicon-based coatings on plastic substrates is an effective way to adjust the permeability of the substrate. However, the permeation mechanisms are yet not fully understood. Here, the activation energy of permeation can offer valuable insights. In order to understand how the activation energy of permeation depends on the coating structure, five silicon-based coatings with varying oxygen content were analyzed, which led to property modifications ranging from silicon-oxidic to silicon-organic. Positron annihilation spectroscopy was employed to characterize the free volume and quartz crystal microbalance measurements were used to determine the density of the coating. These results were compared to water vapor permeation measurements with a temperature variation in the range of 15°C to 50°C. As expected, the silicon-organic coatings do not significantly impact the permeation rates, while the silicon-oxidic coatings do exhibit a barrier effect. The density of the coatings increases for the more silicon-oxidic coatings. A coating with an unusually high oxygen to precursor ratio forms the exception in both permeation and density. The free volume appears to increase for the more silicon-organic coatings. The pore wall chemistry is also affected, hinting at a structural transition from silicon-organic to silicon-oxidic. With this approach, we aim for an in-depth understanding of the chemical structure of silicon-based thin film coatings and its influence on gas permeation through those coatings.

Keywords: PECVD, SiO_x, Coating Structure, Structural Transition, Positron Annihilation Spectroscopy

1 The authors J. Franke (jonas.franke@ikv.rwth-aachen.de), P. Dahmen, P. Alizadeh and R. Dahlmann are affiliated with the Institute for Plastics Processing (IKV) at the RWTH Aachen University in Germany. The authors M.O. Liedke, M. Butterling, A. G. Attallah and A. Wagner are affiliated with the Institute of Radiation Physics, Helmholtz-Zentrum Dresden-Rossendorf in Germany.

DOI: https://doi.org/10.51573/Andes.PPS39.GS.NN.1

Introduction

For applications such as food packaging or membranes, the gas permeability of plastics must be adjusted. This can be achieved via Plasma Enhanced Chemical Vapor Deposition (PECVD) with the use of Hexamethyldisiloxane (HMDSO) as a precursor. Depending on the process parameters, the degree of fragmentation of HMDSO can be tuned to adjust the organic content of the resulting coating. Lowering the organic content leads to silicon-oxidic coatings, referred to primarily as SiO_x, which have excellent gas barrier properties. In contrast, coatings with higher organic content do not have a significant gas barrier but show good gas separation properties for membrane applications [1]. This paper examines the structural transition from silicon-organic membrane coatings to silicon-oxidic gas barrier coatings.

Methods

PECVD Coating of PET Film and Si-Wafer Substrates

PECVD Coatings were applied with a variation of O_2 and HMDSO flow in the *Large Area Microwave Plasma System* (LAMPS) reactor, which is described elsewhere [2]. The parameter variation is shown in Table 1; the name of the coatings refers to their HMDSO:O_2 ratio. Increasing the O_2 flow in the process leads to a higher oxygen content in the resulting coating and changes its structure from silicon-organic to silicon-oxidic [3]. All coatings were carried out with a microwave peak power of 16 kW, pressure of 5 Pa, pulsation of 5/45 ms and a purging time of 20 s. Different substrates were used, each of which are each described in the following sections.

Table 1. PECVD Parameter Variation.

Coating	O_2 Flow [sccm]	HMDSO Flow [sccm]
1:0	0	20
1:1	20	20
1:5	100	20
1:10	200	20
1:100	1000	10

DOI: https://doi.org/10.51573/Andes.PPS39.GS.NN.1

Measurement of Water Vapor Transmission Rate (WVTR) and Calculation of Permeation Activation Energy

For the WVTR measurement, biaxially orientated polyethylene terephthalate (PET) film with a thickness of 12 µm by Flex Films Inc. was coated with a thickness of approximately 30 nm. Each coating was measured with a Permatran-W 700 (Ametek, Inc.) on five samples. Temperature has been varied between 15°C and 50°C in increments of 5°C. The temperature dependence of the water vapor permeability can be expressed as equation 1.

$$P(T) = P_0 * e^{-\frac{E_A}{RT}} \quad 1)$$

P_0 is the pre-exponential Arrhenius factor, E_A is the apparent activation energy of permeation, R is the ideal gas constant, and T is the absolute temperature. On an Arrhenius plot, the slope of a linear fit between the data points yields the value for E_A. This has been conducted for each sample, to subsequently determine mean and standard deviation of E_A for each coating. A change in E_A is a sign for a change in permeation mechanism and as such can yield valuable insights [4].

Determination of Coating Density

The coating mass was measured using the Quartz Crystal Microbalance (QCM) openQCM Q-1 by Novaetech Srl and corresponding 10 MHz Quartz Sensors. In a first step, each sensor's resonance frequency of the fundamental mode f_0 was determined. After coating the sensors with a thickness of approximately 100 nm, the resonance frequency was measured again, and the mass Δm_c of the coating could be determined from the frequency shift Δf using the Sauerbrey Equation (equation 2).

$$\Delta m_c = -\Delta f \frac{A\sqrt{\rho_q \mu_q}}{2f_0^2} \quad 2)$$

Here, A is the area of the coated electrode, and ρ_q and μ_q are the quartz's density and shear modulus, respectively. In a second step, measurements of the coating thickness d_c were conducted by stylus profilometry using Alpha-Step® D-600 Stylus Profiler by KLA-Tencor. The coating density ρ_c could be calculated with equation 3.

$$\rho_c = \frac{\Delta m_c}{A \cdot d_c} \quad 3)$$

DOI: https://doi.org/10.51573/Andes.PPS39.GS.NN.1

Characterization of Free Volumes via Positron Annihilation Spectroscopy

The porosity of the coating was characterized via Doppler broadening variable energy positron annihilation spectroscopy (DB-VEPAS). For this, the coatings were applied on gold-coated silicon wafers with a thickness of approx. 100 nm. DB-VEPAS measurements have been conducted at the apparatus for in-situ defect analysis (AIDA) [5]. Positrons have been accelerated and monoenergetically implanted into samples in the range $0.05\ keV \leq E_p \leq 35$, which allowed for depth profiling. After a short diffusion, they annihilate in delocalized lattice sites or localize in vacancy-like defects usually emitting two anti-collinear 511 keV gamma photons once they meet electrons. Since at the annihilation site thermalized positrons have negligible momentum compared to the electrons, a broadening of the 511 keV line is observed mostly due to momentum of the electrons. This broadening is characterized by two distinct parameters, S and W, defined as a fraction of the annihilation line in the middle (511 keV ± 0.70 keV) and outer regions (508.56 keV ± 0.30 keV and 513.44 keV ± 0.30 keV), respectively. The S-parameter is a fraction of positrons annihilating with low momentum valence electrons and scales with concentration and size of vacancy type defects.

The W-parameter approximates overlap of positron wave function with high momentum core electrons and is a fingerprint of local chemistry of the annihilation spot. Plotting S over W is helpful to examine atomic surrounding of the defect site and its size (type) [6]. A fraction of positrons, which approaches a pore, have a chance to bound to electrons from the pore wall and create each a bound positron-electron particle, the so-called Positronium (Ps). Then, the fraction of Ps, having spins of positron and electron parallel to each other, the so-called ortho-Ps (o-Ps), can residue in a pore or pore network for a defined time before the inevitable annihilation with another pore wall electron of the opposite spin, the so-called “pick-off” process. The pick-off process leads to emission of two gamma photons in contrast to o-Ps self-annihilation where 3 photons are emitted. How long o-Ps exists inside of free volumes (pores) scales with the pore size [7]. Since o-Ps annihilates with 2 photons, it will contribute to the S-parameter and can be detected using the DB-VEPAS method.

Results

Water Vapor Permeability

The temperature dependent WVTR profiles of all coatings are shown in Figure 1. The curves of the uncoated PET and the higher HMDSO:O_2 ratios down to 1:5 can barely be distinguished. Only the lowest ratios, 1:10 and 1:100, show a significant difference and as such exhibit barrier properties. While this is in accordance with experience, the 1:100 coating was anticipated to have superior barrier properties due to a higher degree of crosslinking and as a result, more glass-like barrier properties. It must be considered that this ratio is unusually low for the setup used and may

DOI: https://doi.org/10.51573/Andes.PPS39.GS.NN.1

lead to increased internal stress cracking or detachment of the coating. Also, the high uncertainty for both barrier coatings hinders interpretation of the data. On the right side of Figure 1, the corresponding Arrhenius plots are shown for all samples, which is used to determine the activation energy using equation 1.

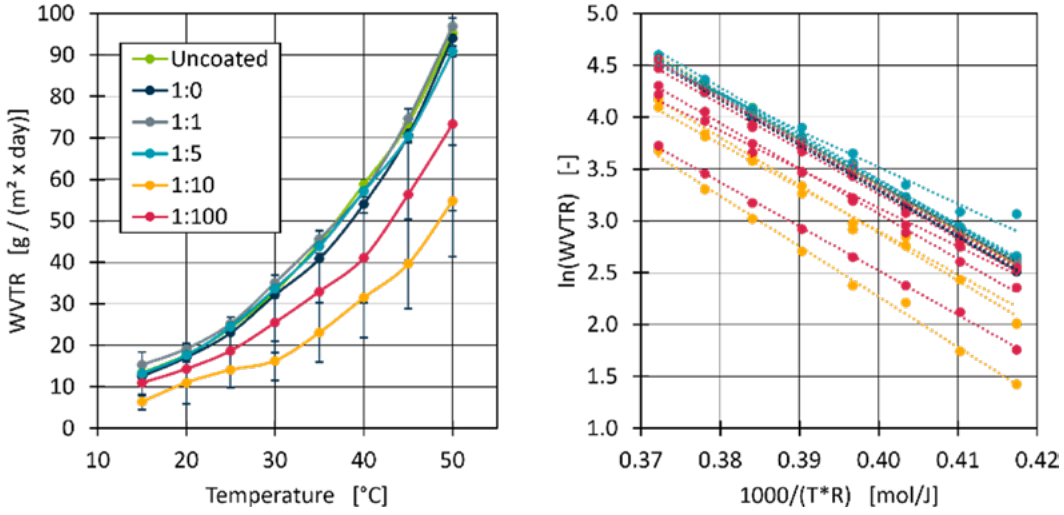

Figure 1. Measured water vapor permeation for all coatings (mean & standard deviation) over temperature (left) and corresponding Arrhenius plot where each sample is shown individually (right).

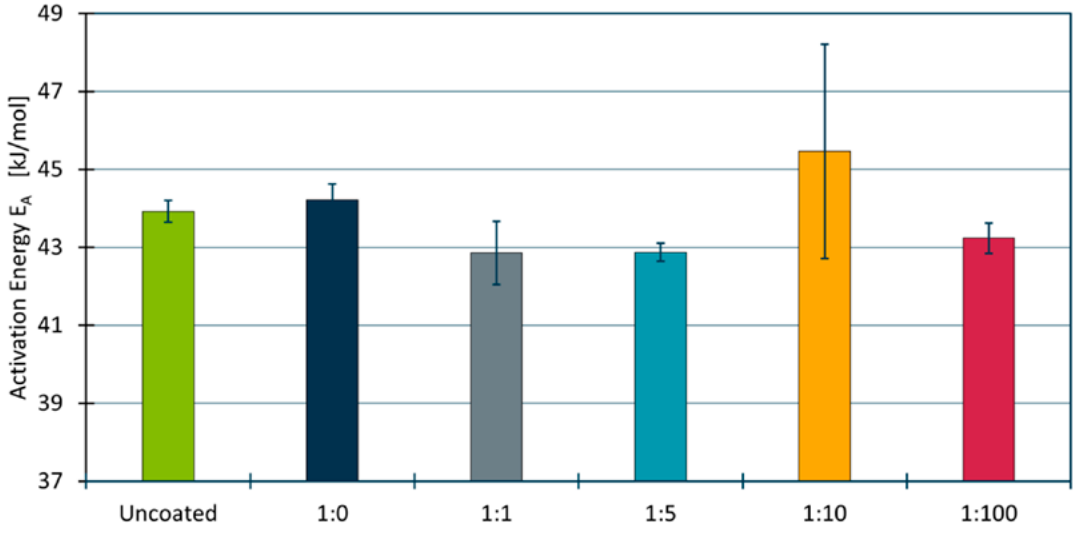

Figure 2. Calculated water vapor permeation activation energies.

As can be observed, the linear fit matches well, meaning that the samples exhibit Arrhenius behavior, and the activation energy can be calculated. The results, shown in Figure 2, suggest that the

DOI: https://doi.org/10.51573/Andes.PPS39.GS.NN.1

activation energy remains mostly the same for all coatings and the uncoated substrate, apart from the 1:10 ratio, where both mean and standard deviation are increased.

The rise in activation energy suggests that the permeation mechanism is altered for the 1:10 coating, where the permeating molecules must overcome an effective barrier coating [4]. It is remarkable that this does not occur for the 1:100 coating, which results either from internal stress cracking (see above) or an unchanged permeation mechanism.

Morphological and Chemical Structure of the Coatings

The density of the coatings determined via QCM are shown in Figure 3. A rise in density occurs with HMDSO:O_2 ratios < 1. Our hypothesis is that an increase in oxygen tends to lead to a higher degree of cross-linking in the coating, which will be examined in future studies. Once again, the 1:100 coating is noteworthy, as its density is still increased compared to higher ratios, but shows a decline compared to the ratios 1:5 and 1:10. The determination of the coating density is performed under the assumption of a homogenous coating with a constant thickness. This means that cracks in the coating that generate void volume will reduce the measured value, while the actual density is higher.

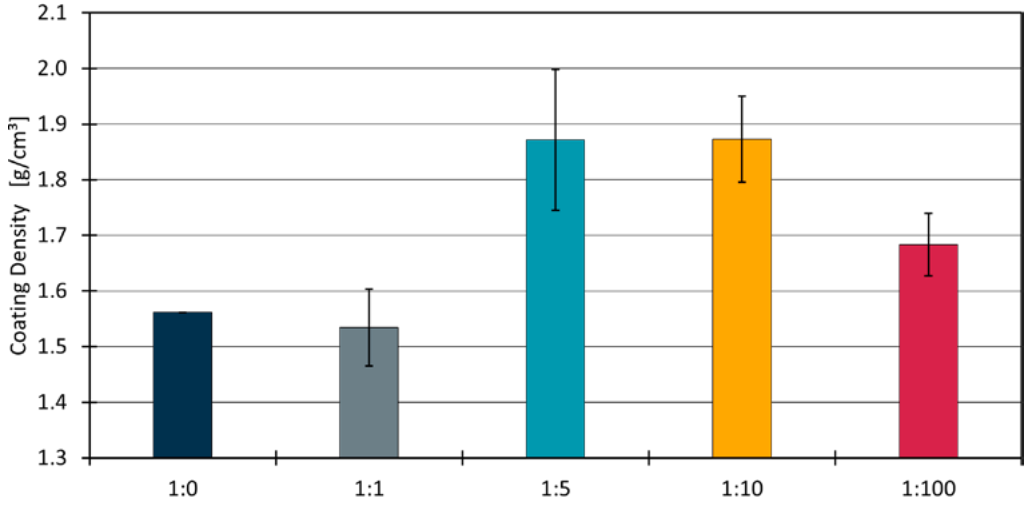

Figure 3. Calculated water vapor permeation activation energies.

Figure 4 shows the evaluated parameters S and W for vitreous carbon (C) and silica (SiO_2) as a reference, and for all coatings for implantation energies of 1.05 keV to 2.05 keV, which corresponds to implantation depths in the center of the coatings, where surface and interface effects are attenuated. The S parameter can be used as a qualitative measure for porosity, where an increase can be caused by either increased pore size or concentration. It includes, however, the other contributions

DOI: https://doi.org/10.51573/Andes.PPS39.GS.NN.1

that originate from point defects and their agglomerations. Consideration of the W parameter can yield information on the pore wall chemistry. With decreasing ratio, the coatings show a decrease in S (hence porosity) and an increase in W (corresponding to a chemical shift at the annihilation site from C to SiO_2). This suggests that the coatings are changing both in porosity and pore wall chemistry. Between ratios of 1:5 and 1:10, a structural transition seems to occur, where the porosity remains similar, while a change in pore wall chemistry is observed. This structural transition can be used to separate silicon-organic and silicon-oxidic coating structures. The silicon-organic coatings (ratios 1:0 to 1:5) exhibit a linear correlation in S-W, which is similar but less pronounced for the silicon-oxidic coatings. To illustrate this, two dashed lines are added to Figure 4 as a visual guide.

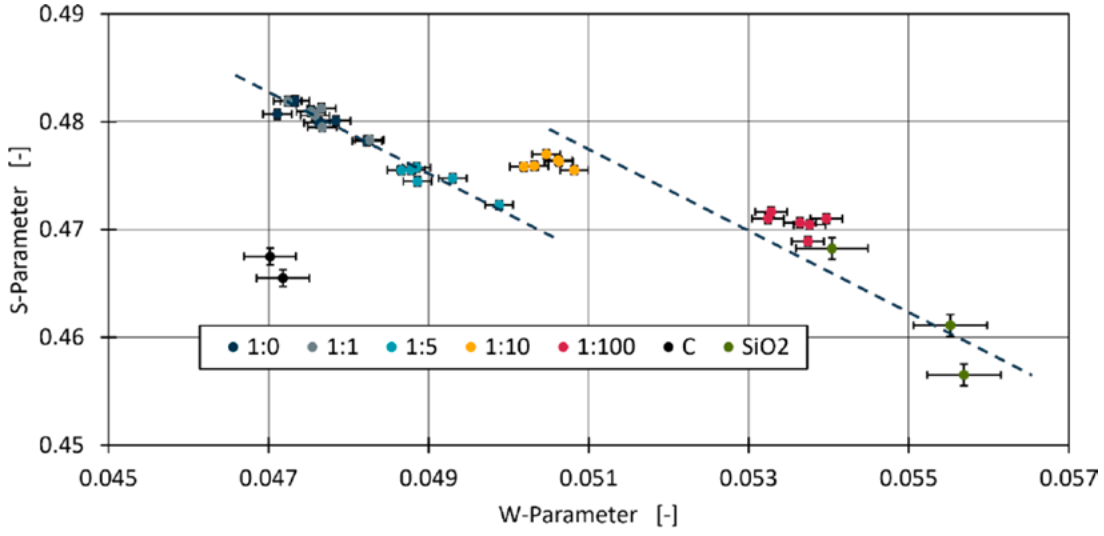

Figure 4. S-W Plot of PAS data, supplemented by reference data on vitreous carbon (C) and silica (SiO_2).

Discussion

The characterization methods in this study show different aspects of an apparent structural transition for silicon-based PECVD coatings. The highest HMDSO:O_2 ratios (1:0 and 1:1) show similar properties for WVTR (i.e., no barrier effect), E_A, density, porosity, and pore wall chemistry. It is reasonable to assume that the slight increase in oxygen flow does not significantly alter the coating structure. The 1:5 coating has the same permeation properties, but its density is increased, while porosity decreased and the pore wall chemistry is slightly shifted. This is a sign that the increase in oxygen flow starts to impact the coating structure, although no barrier effect is created. The most interesting change concerns the 1:10 coating, which constitutes the best barrier of all coatings, including an increased E_A that suggests a different permeation mechanism. While it resembles the 1:5 coating in density and porosity, the shift in pore wall chemistry seems to be the decisive factor to create an efficient gas barrier. Finally, the 1:100 coating exhibits odd behavior in almost

DOI: https://doi.org/10.51573/Andes.PPS39.GS.NN.1

all properties, which most likely results from a high degree of crosslinking that leads to high inner tensions and thus stress cracking. This affects the macroscopic WVTR and QCM measurements, whereas PAS explores the coating on a nanoscale, which is not influenced by cracks. This formation of cracks will be the subject of future studies.

Conclusion

Comprehensive research of the coating structure of silicon-based PECVD coatings with a variation of HMDSO:O_2 ratio during the process has been conducted. The coatings cover a spectrum from silicon-organic to silicon-oxidic structures, which includes a structural transition where a gas barrier effect emerges between 1:5 and 1:10. This structural transition is observed both in permeability and apparent permeation activation energy, as well as pore wall chemistry. It is not observable in density and porosity, which suggests that these properties are less important for a barrier effect, at least in this range. Further research should be conducted to confirm and better understand this structural transition.

Acknowledgments

We thank the Deutsche Forschungsgemeinschaft (DFG, German Research Foundation) for the funding of project 470287198. Parts of this research were carried out at ELBE at the Helmholtz-Zentrum Dresden-Rossendorf e.V., a member of the Helmholtz Association. We would like to thank the facility staff (Eric Hirschmann) for their assistance. This work was partially supported by the Impulse-und Net-working fund of the Helmholtz Association (FKZ VH-VI-442 Memriox), and the Helmholtz Energy Materials Characterization Platform (03ET7015).

References

1. J. Rubner et al., “On the Mixed Gas Behavior of Organosilica Membranes Fabricated by Plasma-Enhanced Chemical Vapor Deposition (PECVD),” *Membranes*, vol. 12, no. 10, 2022, https://doi.org/10.3390/membranes12100994
2. H. Behm, “Investigation of plasma processes and their influence on the composite properties of polypropylene coated by means of plasma polymerization,” RWTH Aachen, 2016.
3. P. Alizadeh et al., “Stretch-tolerant PECVD gas barrier coatings for sustainable flexible packaging,” *Plasma Processes and Polymers*, 2024, https://doi.org/10.1002/ppap.202400018
4. A.P. Roberts et al., “Gas permeation in silicon-oxide/polymer (SiOx/PET) barrier films: role of the oxide lattice, nano-defects and macro-defects,” *Journal of Membrane Science*, vol. 208, 1-2, pp. 75–88, 2002, https://doi.org/10.1016/S0376-7388(02)00178-3

5. M.O. Liedke et al., "Open volume defects and magnetic phase transition in Fe60Al40 transition metal aluminide," *Journal of Applied Physics*, vol. 117, no. 16, 2015, https://doi.org/10.1063/1.4919014

6. M. Clement et al., "Analysis of positron beam data by the combined use of the shape- and wing-parameters," *Journal of Applied Physics*, vol. 79, no. 12, pp. 9029–9036, 1996, https://doi.org/10.1063/1.362635

7. S.J. Tao, "Positronium Annihilation in Molecular Substances," *The Journal of Chemical Physics*, vol. 56, no. 11, pp. 5499–5510, 1972, https://doi.org/10.1063/1.1677067

Process Transfer of PECVD Gas Barrier Coatings Between PE-HD and PP Hollow Bodies

Philipp Alizadeh, Kevin Oberle and Rainer Dahlmann

DOI: https://doi.org/10.51573/Andes.PPS39.GS.NN.2

December 2024

Process Transfer of PECVD Gas Barrier Coatings Between PE-HD and PP Hollow Bodies

Philipp Alizadeh, Kevin Oberle and Rainer Dahlmann[1]

Abstract: This study investigates the plasma enhanced chemical vapor deposition (PECVD) coating process transfer between PE and PP substrates. An inverse relationship is observed between the barrier improvement factor (BIF) and applied energy density (E), with PE showing a stronger response. The same process gas ratio optimizes both materials, suggesting geometry influences the barrier effect more than material. However, the barrier on PP is limited, indicating poorer compatibility to functionalization. The development of the intermediate layer did not improve the barrier performance. FESEM analyses and scratch tests suggest material damage during coating application. Further research is needed to optimize the coating process.

Keywords: PECVD, Barrier Coating, Substrate Influence, FESEM, OTR, Energy Density

1 The authors Philipp Alizadeh (philipp.alizadeh@ikv.rwth-aachen.de) and Rainer Dahlmann are affiliated with the Institute for Plastics Processing (IKV) in Industry and Craft at the RWTH Aachen University in Germany. Kevin Oberle is affiliated with the global manufacturer DWK Life Sciences GmbH.

DOI: https://doi.org/10.51573/Andes.PPS39.GS.NN.2

Introduction

In the realm of surface technology, Plasma Enhanced Chemical Vapor Deposition (PECVD) coatings have emerged as a promising solution for creating completely recyclable and highly functional barrier packaging [1,2]. The flexibility of the PECVD process with regard to the coating chemistry is one of its most significant advantages. However, to harness this potential, it is imperative to understand the coating-substrate interface, especially when different substrate materials are involved. This understanding is crucial as it directly influences the coatability of the substrate material.

In light of this, coating systems are often designed with at least two layers: a functional barrier layer and an interface layer. The interface layer serves as a bridge between the functional coating and the substrate, with its chemistry tuned to form covalent bonds with both the substrate and the barrier. This paper presents a study that investigates the influence of both layers on the coatability of two polyolefinic materials, namely polypropylene (PP) and polyethylene (PE). The substrates were bottles with a volume of 125 ml. Geometry was identical for both materials. A definitive screening design (DSD) was implemented for both layers, incorporating six parameters: power, pulse on time, pulse off time, precursor and oxygen gas flow, and process pressure.

The findings from this study provide valuable insights into the PECVD process and its application in the development of recyclable and functional barrier packaging. They also contribute to a broader understanding of the interaction between coating systems and substrate materials, paving the way for further advancements in this field.

Methods and Materials

Reactor for the Inner Coating of Hollow Bodies

The concept of internal coating of hollow bodies by means of microwave ignited PECVD was first presented by IKV [3]. In the case of this study, four magnetrons (Muegge GmbH, Reichelsheim) generate microwaves with a peak power of 1000 W, each of which is fed into the reactor via concentrically arranged and slotted waveguides. Process gases are fed into the hollow body through a gas lance made of polytetrafluoroethylene (PTFE) and also dosed by means of a mass flow controller (MKS Instruments Deutschland GmbH, Munich).

Energy Density Parameter

Different descriptions have been proposed [4,5] to assess the energy introduced into the coating process. An equation (equation 1) that specifically describes pulsed microwave processes has been formulated by Hegemann [6].

DOI: https://doi.org/10.51573/Andes.PPS39.GS.NN.2

$$\varepsilon = \frac{P \cdot \frac{t_{on}}{t_{on} + t_{off}}}{F_P + r_{gas} F_A}$$

Power (P) is multiplied by the duty cycle, which describes the ratio of the pulse on time (t_{on}) to a whole pulse duration ($t_{on} + t_{off}$). The averaged power is divided by the corrected gas flow, which consists of the precursor flow (F_P) and the auxiliary gas flow (F_A) multiplied by the gas correction factor (r_{gas}). The gas correction factor has been empirically derived by Hegemann and accounts for the partial fragmentation and integration of the auxiliary gas (here oxygen) into the coating [7].

Oxygen Transmission Rate (OTR)

An O_2-permeability tester (M8700, Systech Instruments Ltd., Thame, UK) was used to measure the OTR. All measurements were carried out at a constant temperature and relative humidity (23.0 ± 0.1°C), in accordance with DIN 53380-3 and ASTM D3985. At least two samples were tested for each test point.

FESEM

A Sigma HD VP type Field Emission Scanning Electron Microscope (FESEM) from Carl Zeiss Microscopy GmbH, Jena, Germany, was used to observe the surface topography. The electron beam was generated by a Schottky field emission cathode and has a diameter of a few nanometers, thus achieving high focusing.

Coating Development and Process Parameters

Two separate coating developments were conducted iteratively for the development of the dual layer (barrier/intermediate layer) coating. First, the barrier layer was subjected to parameter variation while the intermediate layer was held constant. The statistical analysis of the parameter-barrier relationship was assessed and parameters for improved barrier performance derived. Next, the barrier layer was held constant while the intermediate layer was developed in order to achieve improved barrier-substrate bonding. The coating developments were conducted using a definitive screening design (DSD). Process parameters are varied on three levels, which are given in Tables 1 and 2. Further information about the utilization of DSD for the development of PECVD coatings can be obtained elsewhere [8].

The hypothesis for the role of the intermediate layer in enhancing the coating-barrier interface is twofold. Firstly, the chemical bond of the highly polar SiO_x-coating to unpolar plastic substrates is bridged by a silicon organic SiOCH-coating that has organic and inorganic functional groups. Secondly, oxygen ion bombardment during application of the SiO_x layer can cause degradation of the

DOI: https://doi.org/10.51573/Andes.PPS39.GS.NN.2

substrate due to the surplus energy from the process. A thin SiOCH layer can be utilised to absorb the surplus energy by the oxidization process during oxygen ion bombardment [9].

Table 1. Process parameter space for the barrier layer development.

Level	Power [W]	Pulse on time [ms]	Pulse off time [ms]	Oxygen flow [sccm]	HMDSO flow [sccm]	Pressure [Pa]
1	800	6	80	100	3	10
2	900	8	100	200	4	15
3	1000	10	120	300	5	20
Optimized	800	10	80	237	3.5	10

Table 2. Process parameter space for the intermediate layer development.

Level	Power [W]	Pulse on time [ms]	Pulse off time [ms]	Oxygen flow [sccm]	HMDSO flow [sccm]	Pressure [Pa]
1	750	2	80	-	5	30
2	850	3	100	-	10	33
3	950	4	120	-	15	36

Results and Discussion

The results of the coating development are assessed by analyzing the barrier performance and evaluated by FESEM analysis in the following section.

Influence of the Energy Density on Barrier Performance

The first iteration of the coating development focuses on the barrier layer. The barrier improvement factor (BIF, $OTR_{uncoated}/OTR_{coated}$) is plotted over the applied energy density (E) in J/cm³ in Figure 1. Uncoated OTR values are 0.2036 $\frac{cm^3\ (std)}{bottle\ \times\ day}$ for PE and 0.1172 $\frac{cm^3\ (std)}{bottle\ \times\ day}$ for PP. During development of the barrier layer the intermediate layer has been constantly kept at parameters displayed for level 2 in Table 2. It is striking that an inverse relationship can be observed between the two variables, indicating that BIF decreases as energy density increases. Regarding the influence of the substrate material, a more pronounced response by PE is observed compared to PP. The higher structural integrity under thermal load or ion bombardment of PE can be posited as a hypothesis for this behavior. A similar increase of the BIF for PP at lower energy densities is conceivable. It should be mentioned, however, that energy density levels cannot be decreased indefinitely in order to sustain high cross linking levels for the SiO_x coating.

DOI: https://doi.org/10.51573/Andes.PPS39.GS.NN.2

It should be emphasized that the statistical analysis of the test plans for both materials shows that the parameters HMDSO and oxygen flow are significant. In addition, the same process gas ratio (3.5 sccm HMDSO and 237 sccm oxygen) is identified as the local optimum for both materials. This is an interesting observation, as the barrier effect seems to be determined more by the geometry than by the material. The BIF values are of course significantly higher for PE due to the higher OTR values in the uncoated state. The trend in connection with energy densities is less pronounced for PP. In conclusion, the barrier layer appears to reach an optimum under the same conditions, but the absolute functionality of PP is clearly limited in direct comparison. Consequently, the PP shows poorer coatability under the same process conditions. The intermediate layer was therefore subsequently subjected to a development.

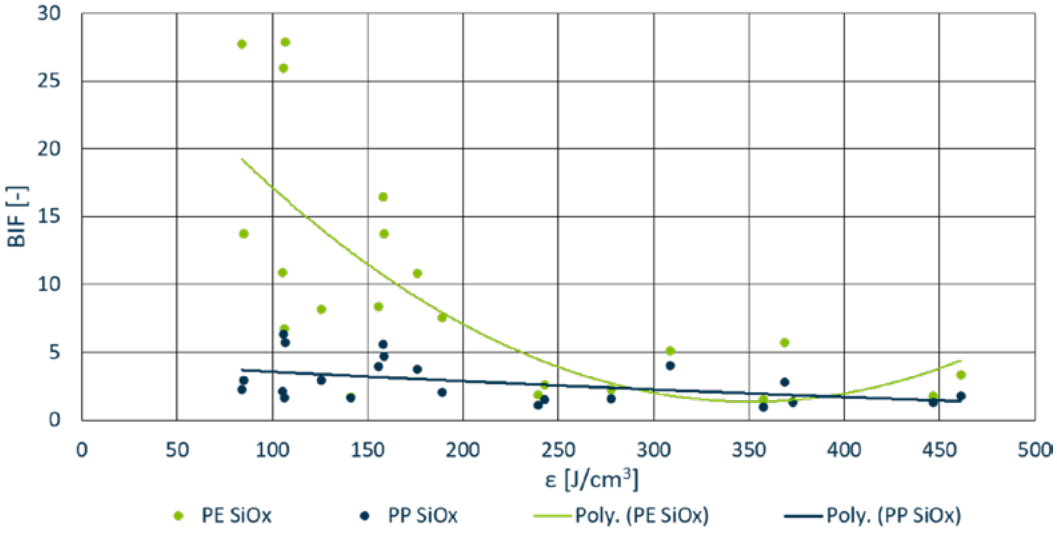

Figure 1. Barrier improvement factor over energy density (Barrier layer).

For the development of the intermediate layer the barrier layer has been kept constantly kept at the derived parameters from the first iteration displayed in the last line of Table 1. In direct comparison to the development of the barrier layer, the development of the intermediate layer shows no further improvement to the previously best barrier performance (Figure 2).

Therefore, the initial hypothesis of the protective function of the intermediate layer during the application of the barrier layer could not be confirmed. The discussed process window might not have been sufficient, since a protective layer should be applied that combines a thin and homogeneous cover of the whole sample surface. Further research should be conducted to clarify the cause for this observation.

DOI: https://doi.org/10.51573/Andes.PPS39.GS.NN.2

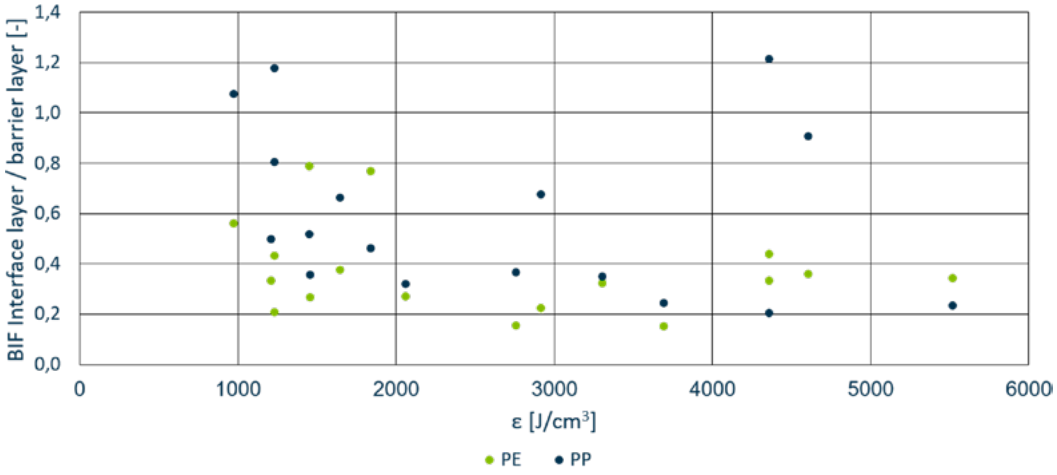

Figure 2. Barrier improvement factor over energy density (Intermediate layer).

Field Emission Scanning Electron Microscopy

FESEM analyses have been carried out to understand how the significantly lower barrier function of coated PP in comparison to PE came about. Representative images are presented in Figure 3. Before coating, both surfaces appeared very smooth. PE had some deformations that indicate cold deformations during production. The surface structure of coated PE appears very smooth while a noticeable deformation of the surface structure is observed for PP. This deformation appears to be a combination of wrinkles in the plastic and a droplet-like pattern. The droplets could be a sign of local delamination. A similar error pattern can be observed in etching experiments [10]. Delamination can be a sign for degradation of the substrate material. The direct comparison illustrates a strong indication of material damage as the cause of the inhibited coatability of PP.

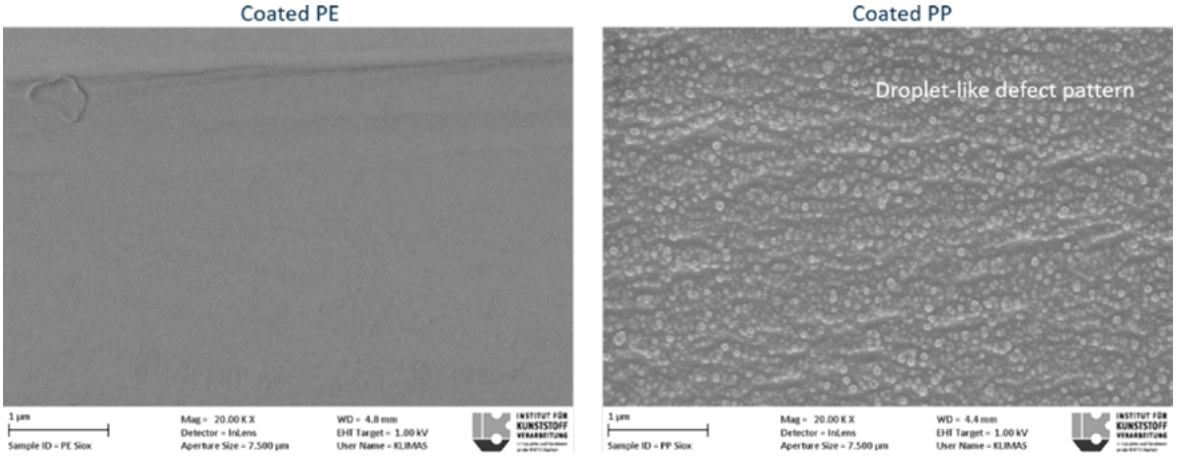

Figure 3. Comparison of coated PE and PP (SiOCH/SiOx).

DOI: https://doi.org/10.51573/Andes.PPS39.GS.NN.2

In order to further clarify the cause for the damage pattern, scratch tests have been conducted. The images can be observed in Figure 4. Coated samples have been scratched with a scalpel in order to visualise a mechanical damaging of the coatings on both materials. For PE, a very sharp edge can be observed that represents the scalpel incision very well. The surrounding coating surface is interspersed with fine, close-meshed cracks, which indicate a high degree of brittleness and strong adhesive bonding to the substrate. For PP, the coating seems much more loosely bonded to the substrate and delamination occurs far beyond the edge of the incision. The chemical bond seems to be inhibited by the degraded material. In conclusion, the inhibited coatability of PP seems to be closely linked to the damage of the substrate surface as a result of temperature load and ion bombardment.

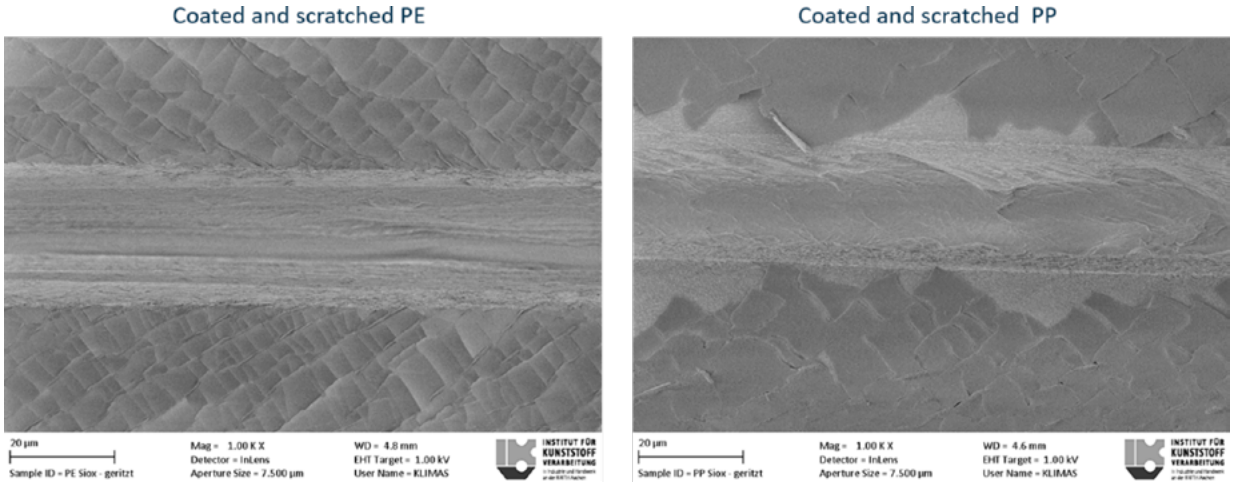

Figure 4. Investigation of scratched coatings on PE and PP.

Conclusion

The process transfer of PECVD coatings between different substrate materials, specifically PE and PP, reveals significant differences in their response to the coating process. The BIF shows an inverse relationship with the applied energy density, with PE demonstrating a more pronounced response compared to PP. This could be attributed to PE's higher structural integrity under thermal load or ion bombardment. Interestingly, the same process gas ratio is identified as the local optimum for both materials, suggesting that the barrier effect is influenced more by the geometry than by the material itself. However, the absolute functionality of PP is limited in comparison to PE, indicating poorer coatability under the same process conditions.

The development of the intermediate layer did not result in further improvement to the barrier performance, contradicting the initial hypothesis of its protective function during the application

DOI: https://doi.org/10.51573/Andes.PPS39.GS.NN.2

of the barrier layer. This calls for further research of the hypothesis. FESEM analyses and scratch tests provide strong indications of material damage during coating application as a cause for the inhibited coatability of PP. The surface structure of coated PP shows noticeable deformation, which could be a sign of substrate material degradation.

In conclusion, the inhibited coatability of PP seems to be tightly linked to the damage of the substrate surface as a result of temperature load and ion bombardment. Further research is needed to fully understand these observations and to optimize the coating process for different substrate materials.

References

1. H. Yasuda and Y. Matsuzawa, "Economical Advantages of Low-Pressure Plasma Polymerization Coating," *Plasma Processes and Polymers*, vol. 2, no. 6, pp. 507–512, 2005.
2. L. Kleines, T. Blasius, and R. Dahlmann, "PECVD barrier coating systems on post-consumer recyclates for food contact applications," *Surface Engineering*, vol. 38, 10-12, pp. 968–976, 2022, https://doi.org/10.1080/02670844.2023.2181258
3. P. Plein, "Method of coating hollow bodies" DE 3632748 C2.
4. R. Hippler, Ed. *Low temperature plasma physics: Fundamental aspects and applications,* 1st ed. Berlin, Weinheim: Wiley-VCH, 2001.
5. H. Yasuda, "Plasma polymerization for protective coatings and composite membranes," *Journal of Membrane Science*, vol. 18, pp. 273–284, 1984, https://doi.org/10.1016/S0376-7388(00)85039-5
6. D. Hegemann, "Plasma Polymer Deposition and Coatings on Polymers," in *Comprehensive Materials Processing*: Elsevier, 2014, pp. 201–228.
7. D. Hegemann and M.-M. Hossain, "Influence of Non-Polymerizable Gases Added During Plasma Polymerization," *Plasma Processes and Polymers*, vol. 2, no. 7, pp. 554–562, 2005, https://doi.org/10.1002/ppap.200500041
8. P. Alizadeh, S. Wilski, and R. Dahlmann, "Definitive screening design for the development of alkali resistant PECVD coatings for returnable PET bottles," *Progress in Organic Coatings*, vol. 172, p. 107064, 2022, https://doi.org/10.1016/j.porgcoat.2022.107064
9. T. d. l. Arcos et al., "PECVD and PEALD on polymer substrates (Part II): Understanding and tuning of barrier and membrane properties of thin films," 2023.
10. S. Wilski et al., "Mechanisms of oxygen permeation through plastic films and barrier coatings," *Journal of Physics D: Applied Physics*, vol. 50, no. 42, p. 425301, 2017, https://doi.org/10.1088/1361-6463/aa8525

GENERAL SYMPOSIA | MECHANICAL PROPERTIES AND FRACTURE

Electrolyte Resistance of Amine Based Epoxy's used for Lithium-Ion Battery Cell Housings

Niclas Emrich Moritz Rayer and Reinhard Schiffers

DOI: https://doi.org/10.51573/Andes.PPS39.GS.MPF.1

December 2024

Electrolyte Resistance of Amine Based Epoxy's used for Lithium-Ion Battery Cell Housings

Niclas Emrich Moritz Rayer and Reinhard Schiffers[1]

Abstract: Filled epoxy potting materials are seen as promising polymer for applications in future automotive battery systems. Hence the electrolyte resistance is of crucial importance. This work examines the electrolyte resistance of potential material candidates for such applications. The material is stored hermetically in electrolyte for several weeks at an elevated temperature of 45°C. Swelling values are determined, and the mechanical behavior of the specimens is analyzed. Additionally, the electrolyte contamination is measured using head space injected gas chromatography and mass spectroscopy. Based on procedure of exclusion, the impact of filler- and matrix-system upon the swelling behavior is derived. The aim of this work is to identify possible amine-based epoxy materials, that are suitable for polymer metal joint applications, while being in contact with battery electrolytes.

Keywords: Epoxy, Electrolyte Resistance, Battery Storage Systems, Automotive Industry

1 The authors Niclas Emrich (niclas.emrich@bmw.de), Moritz Rayer (moritz.rayer@uni-due.de) and Reinhard Schiffers (reinhard.schiffers@uni-due.de) are affiliated with the Institute of Product Engineering at the University of Duisburg-Essen in Germany.

DOI: https://doi.org/10.51573/Andes.PPS39.GS.MPF.1

Introduction

Applications for automotive battery systems require hybrid joints of copper and polymer with high demands towards helium seal tightness and long-term durability. Such hybrid joints are seen as a promising prospect to reduce costs in future battery systems. This work examines epoxy systems that can be used for vacuum potting to achieve such hybrid bonds. Epoxy systems are chosen due to a low processing viscosity, so that fine, nanoscopic metal oxide surface structures of the metal joining partner can be infiltrated. Thus, epoxy systems are also well established for electronic encapsulation, which can be seen as a comparable field of application. An iterative approach is chosen to develop and qualify an epoxy system that meets the requirements in battery packs. Derived from automotive battery pack requirements the following hurdles are defined to qualify a particular material as electrolyte resistant:

- Material swelling post exposure to battery electrolyte.
- Tensile Strength post exposure to battery electrolyte.
- Contamination of battery electrolyte.

In each iteration step, properties (such as filler content, filler type or glass transition temperature) of the epoxy system are modified to improve the results on achieving these hurdles. As a result of this work an amine-based epoxy system is qualified to meet these criteria. Additionally, several conclusions are found on how to impact the electrolyte resistance of epoxy systems.

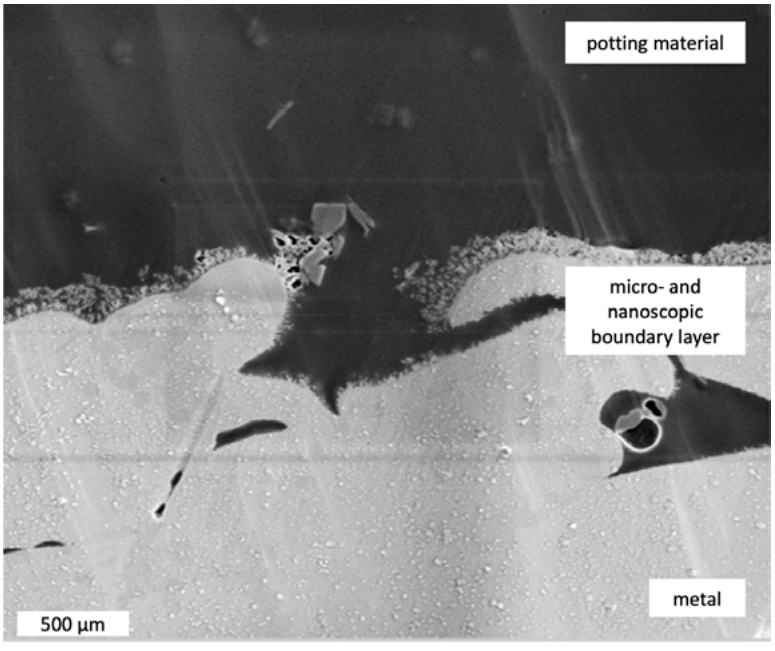

Figure 1. Exemplary copper to polymer metal hybrid.

DOI: https://doi.org/10.51573/Andes.PPS39.GS.MPF.1

Fundamentals and State of the Art

Polymers used as functional components in battery packs can be exposed to liquid battery electrolytes to a certain extent. The electrolytes in lithium-ion battery cells consist of conducting salts, organic aprotic solvents and additives [3]. In the case of non-crosslinked polymers, organic solvents can cause strong swelling or even dissolution. For crosslinked polymers, a less strong swelling can be expected, depending on the macromolecular structure of the material. Swelling processes are strongly dependent on external factors, such as contact duration, ambient temperature and applied mechanical stresses. In many cases, swelling processes are reversible, but the superposition of material swelling and embrittlement or stress cracking can lead to degradation of the desired material properties. This is because the solvent can dissolve ingredients and additives out of the polymer. [2,4] Immersion tests can be used to determine the behavior of polymers exposed to liquid chemicals. For this purpose, DIN EN ISO 175 specifies appropriate test methods and conditions. The standard allows an isolated analysis of the influence of chemicals without the impact of external factors. [1] In addition to the swelling and dissolution behavior of the polymers studied, the influence of the dissociated conducting salts is unknown. When combining lithium-hexafluorophosphat and water, hydrofluoric acid (HF) is formed (Equation 1) [4]. This may be the case, when water intrudes into a battery system. As production facilities for battery systems are not perfectly isolated from humidity in the ambient atmosphere, there is also a very low residual degree of water contained in battery systems.

$$LiPF6 + H2O \rightarrow LiF + 2HF + POF3 \quad 1)$$

State of the art research on the resistance of polymers to battery electrolytes shows that there are few published study results. Existing resistance tables in the literature do not list results for lithium hexafluorophosphate-containing electrolytes. Furthermore, for filled thermoset potting compounds, the resistance of the matrix as well as the resistance of the fillers is crucial. [5] examined the electrolyte resistance of epoxy resin-based adhesives used on sandwich structures for battery cell applications by performing swelling tests as well as tensile tests and tensile shear tests on specimens after immersion in liquid electrolyte. The study examines the solvents of the electrolyte as well as the solvents containing the dissociated lithium-hexafluorophosphate. It is demonstrated that the contact of the polymer with the solution of conducting salt and solvents causes a strong swelling as well as a decrease in the strength of the adhesive. [5] The mechanical properties of polymers in technical applications are in many cases optimized via fillers and reinforcing materials. Glass fibers are proposed as a promising solution in many applications. However, glass, quartz and silicate ceramics are considered unresistant to hydrofluoric acid [6]. Therefore, it may be assumed that the glass fibers are chemically attacked and partly dissolve. Therefore, in this case metal oxide fillers are used. This work can be seen as a first step, to show a generally feasibility study for epoxy potting systems in applications with direct contact to electrolytes for battery lithium-hexafluorophosphate.

DOI: https://doi.org/10.51573/Andes.PPS39.GS.MPF.1

Materials and Experimental Setup

Electrolyte, Storage Conditions and Handling

The electrolyte used for in this work is a standard reference electrolyte used for automotive battery systems. It is based on four organic solvents (Dimetyl Carbonate–DMC, Ethylene Carbonate–EC, Ethyl Methyl Carbonate–EMC, Vinylene Carbonate–VC), the conductive salt lithium-hexafluorophosphate and further additives. To segregate the observations from the impact caused by hydrofluoric acid, the specimens are handled in a protected argon environment, containing less than 1 ppm water. For the swelling examination 5 specimens are stored in one container, filled with a volume of 30 ml of electrolyte. Each container is pre-dried under vacuum conditions for a duration of 12h at 60°C. The storage of the sealed containers is done at an elevated temperature of 45°C and under dry atmosphere, containing approximately 100 ppm residual humidity. This minimizes the gradient of humidity from the container inside to the outside, thus mitigating humidity intrusion due to imperfections in the sealing of the container. When extracting the polymer specimen, the sample is dried for 15 min and is then weighted.

Epoxy Potting Material Specimen

The epoxy material is fabricated in laboratory conditions and modified in specific properties for the purpose of this work. Generally, the following schematic is used for the composition of the material:

- All amine-based variants contain a similar resin matrix.
- When modifying the matrix, changes affect by additives and not the monomer molecules (e. g. to enhance processability).

The variants resulting from this can be classified as shown in Table 1. By procedure of exclusion, inference can be made on the impact of resin matrix / fillers towards the analyzed properties.

Table 1. Overview and composition of the investigated epoxy resin systems.

Iteration	Resin	Hardener	Matrix classification	Filler Approach
IT 1	R1	H1	anhydride based	no fillers
	R2	H2	amine based	no fillers
	R3	H2	amine based	metal oxide (~60 wt-%)
	R4	H2	amine based	metal oxide + mineral filler (~60 wt-%)
IT 2	R5	H3	amine based, high T_G	metal oxide + mineral filler (~60 wt-%)
	R5	H2	amine based, low T_G	

DOI: https://doi.org/10.51573/Andes.PPS39.GS.MPF.1

Iteration	Resin	Hardener	Matrix classification	Filler Approach
IT 3	R6	H3	amine based, optimization	metal oxide + mineral filler (~60 wt-%)
	R6	H2	amine based, optimization	

The material modification is carried out in three iteration steps. First, the influence of fillers is investigated. Then the formulation of the hardener is adjusted to vary the glass transition temperature (T_G). In a subsequent optimization, the chemical formulation of the matrix is investigated for the two-component composition of the material. Figure 2 shows two different types of specimens: a tensile test specimen and a swelling test specimen. The tensile test specimen is fabricated from resin sheet material according to DIN EN ISO 527 Typ 1BA using waterjet cutting. The swelling test specimens are mechanically fabricated from sheet materials with a thickness of 4 mm. Each specimen has a quadratic shape with a dimension of 10 mm x 10 mm.

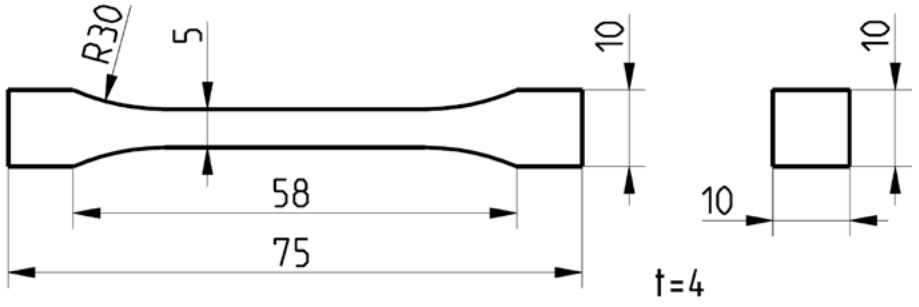

Figure 2. Tensile test specimen (left) and swelling test specimen (right).

Analyzing Swelling, Mechanical Performance and Electrolyte Contamination

The swelling behavior is evaluated by comparing the pre-storage-mass (m_1) with the post-storge-mass (m_2). The swelling percentage is calculated by the ratio of the gained mass and the pre-storage mass. The outer appearance is documented visually. Each swelling value is the average of five specimen. To observe the changes in the structural properties of the material, the tensile strength and elasticity are considered. Analogue to the swelling, the mechanical performance is evaluated before and after being exposed to the storage procedure. The mass change is recorded after 7 as well as after 21 days and the results are then compared. The tensile tests are based on DIN EN ISO 527 and are performed on a ZwickRoell ProLine universal testing machine under laboratory atmosphere using a pulling velocity of 1 mm/min. Additionally, the contamination of electrolyte is tested by using gas chromatography method. The key data of the testing system and the methodology is summarized in Table 2. The electrolyte contamination is determined by comparing the constituents of the electrolyte from the swelling test to an uncontaminated electrolyte sample. By

DOI: https://doi.org/10.51573/Andes.PPS39.GS.MPF.1

using head space injection gas chromatography, the qualitative composition of the injected liquid sample is analyzed. The retentions duration within the separation column segregates the volatile constituent, that are injected. Each constituent is detected at a characteristic point of time and its intensity is measured by a subsequent mass spectroscopy. The result is typical GC-MS peak diagram.

Table 2. Parameters of gas chromatography to analyze the composition of the battery electrolyte.

Head Space Injection GC-FID (Clarus 680)	
Thermostatic control	10 min @ 120°C
Needle Temperature	130°C
Transver-Line Temperature	150°C
Injection Time	0,04 min
Separating column	Restek Rtx-200MS–30m, 0,25mm, 0,5µm
Electrolyte amount	100 µl

Results and Discussion

Swelling

Figure 3 shows the increase in mass of all compounds after 7 and after 21 days of electrolyte contact in percentage. The R1-H1 batch is an anhydride-based system that shows a particularly strong swelling behavior with a mass increase of about 14% after 21 days. The unfilled material amine-based system (R2-H2) also shows strong swelling with a mass increase of about 12% after 21 days, but generally lower than the anhydride-based approach. Consequently, the amine-based approach is pursued for further investigation. Adding metal oxide filler (R3-H2) reduces the material swelling significantly down to 7% and a combination of metal oxide and mineral fillers (R4-H2) decreases the swelling behavior even further.

In iteration step 2, the combination of metal oxide and mineral filler is continued (resin R5). By varying the hardener, the glass transition temperature T_G is adjusted. The T_G for the material R5-H3 is only slightly above the storage temperature. This results in increased swelling, particularly for a longer storage over 21 days. When using the hardener H2 with the modified resin R5, a swelling of less than 4% can be achieved instead. Also, the difference between 7 and 21 days storage is marginal, which indicates that the electrolyte absorption is terminated. The T_G of this material setup is even higher than the best approach from Iteration 1 (R4-H2). The swelling value of less than 4% can be seen as a plausible value for the targeted field of application.

Iteration step 3 focuses on the chemical improvement of the resin system. The target is to further decrease the swelling behavior. While one approach fails (R6-H3 show much higher swelling

DOI: https://doi.org/10.51573/Andes.PPS39.GS.MPF.1

than previous), the other approach shows that swelling can be reduced even further. However, the tendency of swelling increase between 7 and 21 days, is higher than previous. Further long-term investigations need to be carried out to observe if this tendency is decreasing over time.

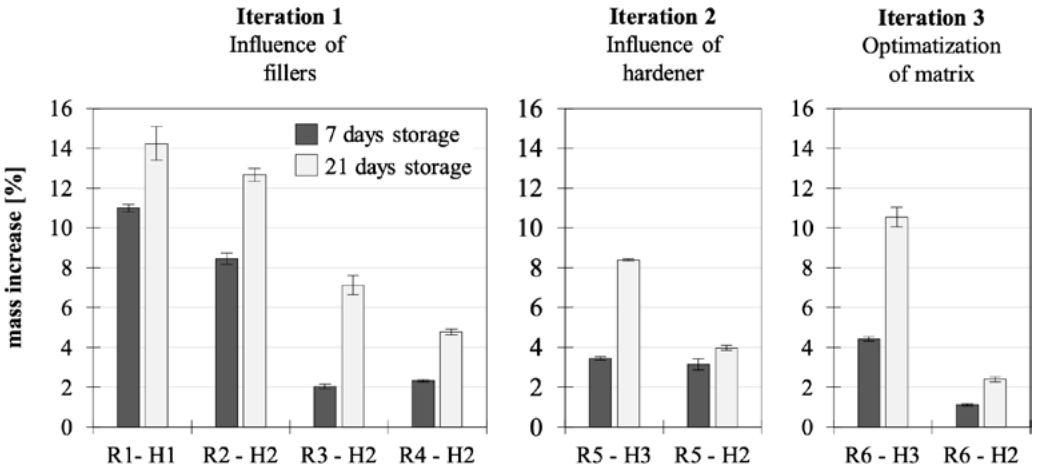

Figure 3. Results of the swelling tests for all 3 iteration steps (5 samples per measurement).

Mechanical Performance

The swelling behavior does not allow a direct prediction of the mechanical behavior of the materials when being exposed to battery electrolyte. Figure 4 shows a representative selection of the tested materials. Therefore, the anhydride-based (R1-H1) system was compared to three filled amine-based material systems. The results show the tensile strength as well as the corresponding elongation at break.

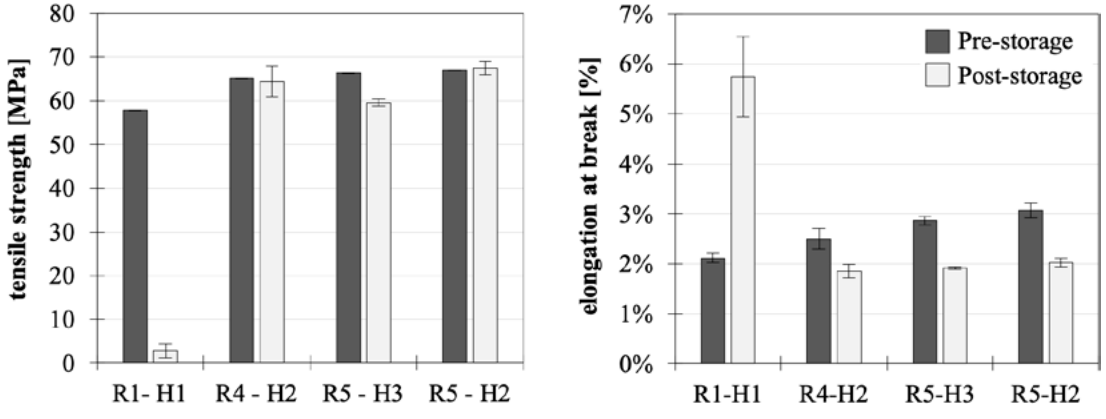

Figure 4. Mechanical properties of tensile strength specimen before and after 21 days (5 specimens per measurement).

DOI: https://doi.org/10.51573/Andes.PPS39.GS.MPF.1

The R1-H1 system, which shows very high swelling values, loses over 90% strength and the elongation at break increases significantly. This is most probably related to the anhydride hardener formulation. The other three materials show only a slight decrease from the initial strength, which is in the range of around 65 MPa. The R5-H3-system (relatively low T_G) shows the biggest difference in tensile strength after a 21 day exposure to battery electrolyte. Overall, the amine-based epoxy resin systems show some embrittlement due to contact with electrolyte. The most promising approach from the 2nd iteration of the swelling test (R4-H2) also proves to be technically suitable according to the mechanical properties.

Electrolyte Contamination

Figure 5 shows a peak diagram as a result of using the HS-GC-MS analysis for a sample of reference electrolyte that is extracted from the capsulation vessel post storage. The intensity of detected constituents is plotted against time. From a material database, deflections can be compared with the typical deflections of materials listed in the database. The reference sample is a sample of uncontaminated electrolyte. Figure 5 (R5-H2) shows the typical deflections of the solvents EMC, DMC, VC and EC, but no unexpected components.

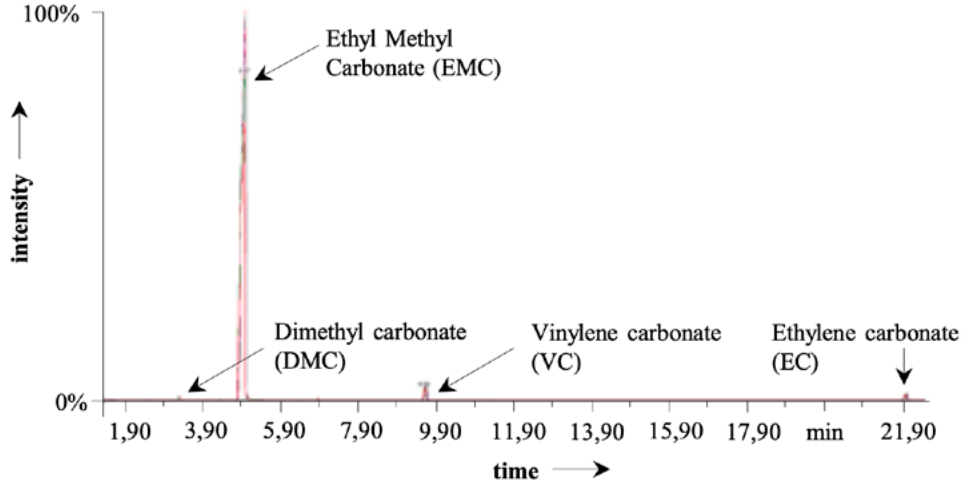

Figure 5. Retention time for GC-MS analysis of battery electrolyte.

The promising material approach R5-H2 as well as the unsuitable and strongly swelling approach R1-H1 were stored for 21 days. To be able to classify the results, a typical thermoplastic material for this application field (Polyamide 12), was also stored and measured. In the Polyamide 12 sample, Xylene and Dioxane were detected in addition to the known substances from the reference measurement. Xylene was also detected in both epoxy resin systems, while dioxane was detected only in the R1-H1 system. The peak of Dioxane and of the known Dimethyl Carbonate was significantly higher in this sample and is thus interpreted as a fraction that results from electrolyte decay

DOI: https://doi.org/10.51573/Andes.PPS39.GS.MPF.1

unrelated to the polymer contact. Overall, the result for R5-H2 shows significantly less contamination than the PA 12 that is commonly used for the application.

Conclusions

To summon up: the anhydrite system is not suitable for application in lithium-ion battery storage systems, but a basic feasibility is demonstrated for the amine-based epoxy systems. For the latter it is found that: Electrolyte resistance can be increased using specific fillers. Best a combination of metal-oxide and mineral fillers. The glass transition temperature should be significantly higher than the expected operating temperature. The mechanical properties of amine-based epoxy resin systems with high filler contents are not or only slightly affected by contact with battery electrolyte.

The iterative approach indicates further optimization potential. The consequent next step building on this work would target the resistance of the entire polymer-metal hybrid structure.

References

1. DIN–German Institute for Standardization, *DIN EN ISO 175: Plastics – Methods of test for the determination of the effects of immersion in liquid chemicals*, 2011.
2. H. Frick and C. Stern, *Einführung in die Kunststoffprüfung. Prüfmethoden und Anwendungen*, Munich, Germany: Carl Hanser, 2017.
3. C. Hartnig and M. Schmidt, "Electrolytes and conducting salts," in *Lithium-Ion Batteries: Basics and Applications*, R. Korthauer, Ed. Berlin, Germany: Springer-Verlag, 2013.
4. S. F. Lux, I. T. Lucas, E. Pollak, S. Passerini, M. Winter, and R. Kostecki, "The mechanism of HF formation in LiPF6 based organic carbonate electrolytes," *Electrochemistry Communications*, vol. 14, no. 1, 2012, https://doi.org/10.1016/j.elecom.2011.11.009
5. G. Menges, E. Haberstroh, W. Michaeli, and E. Schmachtenberg, *Menges Werkstoffkunde Kunststoffe*, Munich, Germany: Carl Hanser, 2011.
6. J. Seo, S. K. Singh, Y. Zhang, J. Ma, C. E. Bakis, C. D. Rahn, and M. A. Hickner, "Electrolyte-resistant epoxy for bonding batteries based on sandwich structures," *Journal of Applied Polymer Science*, vol. 135, no. 15, p. 46059, 2018, https://doi.org/10.1002/app.46059
7. S. Verhaverbeke, I. Teerlinck, C. Vinckier, G. Stevens, R. Cartuyvels, and M. M. Heyns, "The etching mechanisms of SiO2 in hydrofluoric acid," *Journal of The Electrochemical Society*, vol. 141, no. 10, pp. 2852–2859, 1994, https://doi.org/10.1149/1.2059267

DOI: https://doi.org/10.51573/Andes.PPS39.GS.MPF.1

GENERAL SYMPOSIA | MODELING AND SIMULATION

Fatigue Lifetime Analysis of POM Gears for Generalized Tooth Root Shapes

Robert Eberlein and Sven Düzel

DOI: https://doi.org/10.51573/Andes.PPS39.GS.MS.1

December 2024

Fatigue Lifetime Analysis of POM Gears for Generalized Tooth Root Shapes

Robert Eberlein and Sven Düzel[1]

Abstract: The current calculation methods for determining the tooth root load capacity of polymer gears (e.g., VDI 2736) are based on the same assumptions as those for steel gears. However, due to the non-linear material behavior, temperature, and rate dependency of polymers, these predictions are often inaccurate. A previous study employed rate-dependent nonlinear viscoplastic finite element (FE) modelling of polyoxymethylene (POM) to quantify material influences not considered in standard metal gear assumptions. A lifetime model was developed and validated to predict tooth root fracture based on rotational speed for a constant tooth root geometry. In this study, the existing damage model is adapted and validated to include the dependency on notch (tooth root) geometry. The extension of the model to two damage parameters allows for a geometry-independent representation of the nonlinear speed dependency of tooth root breakage. This correlative modelling approach incorporates two independent damage mechanisms inside the material which lead to tooth root breakage failure of the gear. To map these mechanisms, local material states at the crack initiation point are used as damage parameters. Calibration of the bi-parametric damage model with experimental data shows that model predictions fall within the experimental scatter. Further research is ongoing to extend the damage model regarding generalized torque loading conditions.

Keywords: Lifetime Modelling, Polymer Gears, Tooth Root Fracture, Viscoplastic Material Modelling, Finite Element Analysis, Local Damage Criterion

1 The authors Robert Eberlein (robert.eberlein@zhaw.ch) and Sven Düzel (sven.duezel@zhaw.ch) are affiliated with the Institute of Mechanical Systems (IMES) at the Zurich University of Applied Sciences (ZHAW) in Switzerland.

DOI: https://doi.org/10.51573/Andes.PPS39.GS.MS.1

Introduction

Polymer gears are increasingly popular in various industries due to their low weight, corrosion resistance, quieter operation, lack of lubrication requirements, and cost-effectiveness compared to steel gears. However, current standard calculation methods like VDI 2736, which are based on assumptions for steel gears, are inadequate for polymer gears and lead to inaccurately predicted polymer gear lifetimes [1]. These methods assume rigid body behavior, linear elastic material properties, and rotational speed independent lifetimes, which do not align with the nonlinear, rate-dependent properties of polymers [1-3]. This paper investigates tooth root breakage, a common failure mode in both dry and lubricated applications, occurring when tensile load at the tooth root exceeds the material's fatigue limit [3,4].

Researchers have tried to predict this failure analytically by adjusting current standards [2] or through lifetime modelling consisting of a numerical finite element (FE) simulation combined with fatigue models [5-8]. Common simulation methods use quasi-static FE modeling and assume linear elastic behavior, but these are insufficient for polymers due to their nonlinear and transient material properties and the dynamic nature of gear meshing [9-11]. Previous studies often used steel fatigue models, focusing on strain-based criteria, but these are unsuitable for polymers because of significant differences in material characteristics [12]. In [13], a lifetime modelling approach consisting of a damage model based on an FE model, including a physical material modelling approach utilizing the Three-Network-Viscoplastic (TNV) model [14,15] that is based on the original work by [18,19], showed the ability to predict the lifetime dependency on rotational speed for a constant load torque level and root geometry. The damage model extrapolates the increase of the maximal principal strain at the crack initiation point in the tooth root, based on the values of five simulated loading cycles (revolutions), to the experimental determined lifetime for defining a strain criterion at which the gear fails. The critical strain in the tooth root is increasing continuously as it can be shown for the uniaxial case [16]. This damage modeling approach is based on the physical material behavior and has the capacity to incorporate dynamic effects. However, damage modeling based on extrapolation has the disadvantage that it requires the simulation of 5 consecutive cycles and that the extrapolation is sensitive to these 5 simulated support points when extrapolating to cycle numbers over 10^5. Thus, new approaches considering the unique properties of polymers are necessary for accurate prediction of tooth root breakage and fatigue life in polymer gears.

DOI: https://doi.org/10.51573/Andes.PPS39.GS.MS.1

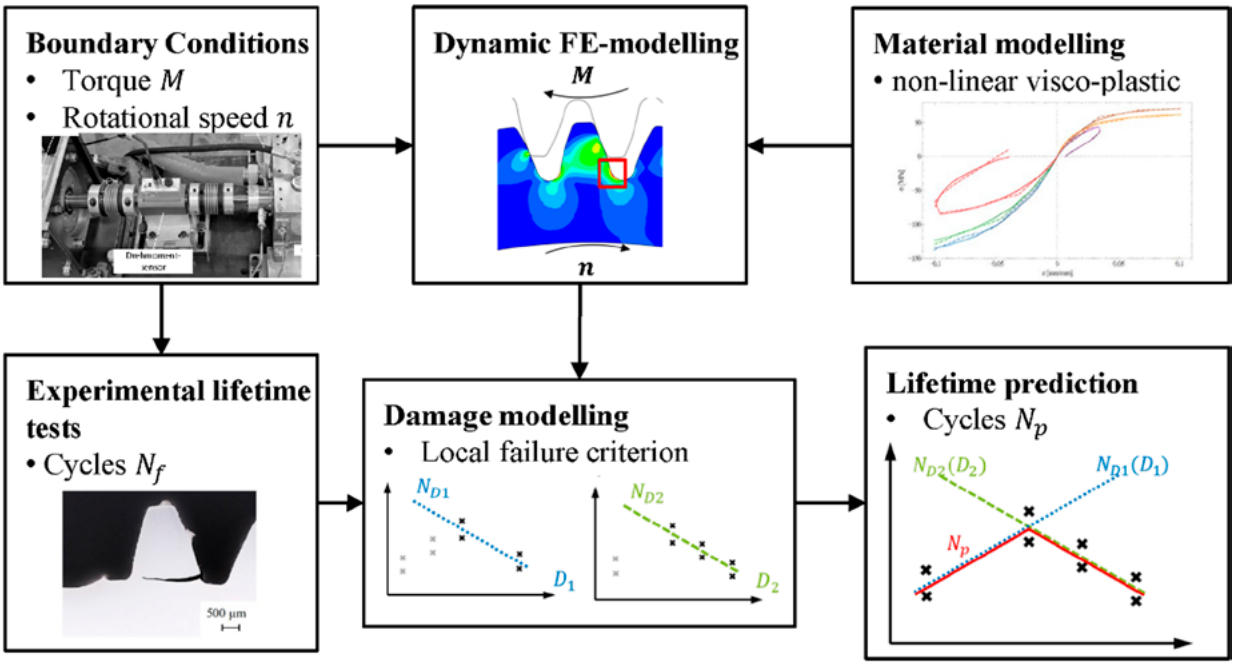

Figure 1. Structure of the lifetime model.

The objective of this study is to generalize the lifetime model from the previous study [13] with the ability to work independently from rotational speed and root geometry at a constant torque level. With regard to the structure of the lifetime model in Figure 1, this implies an adaptation of the damage model, which combines the results from experimental lifetime tests and FE-simulations. Consequently, the experimental lifetime tests conducted in the previous study with the reference tooth root geometry are supplemented with tests of an optimized geometry at the same conditions on the test rig. The tests are conducted under constant loading torque at different rotational speeds with a tempered oil lubrication at 50°C. The dynamic FE-modeling scheme remains unchanged and is still based on physical material modeling with the TNV model. Another objective is to alter the methodology employed in damage modeling from an extrapolative to a correlative approach, as is the case with classical fatigue models [12,17]. This addresses the inherent limitations of the extrapolating approach, whereby minor alterations to the simulated support points result in significant changes in the calculated damage values for high numbers of cycles. Consequently, this approach is highly susceptible to the damage values derived from the initial five revolutions. A correlative approach circumvents this issue and is computationally less costly. This holds, because the damage parameters and the material behavior are assumed to be unchanged in each revolution, thus only one cycle must be simulated.

DOI: https://doi.org/10.51573/Andes.PPS39.GS.MS.1

Experimental Results

Figure 2 shows the results of the experimental lifetime tests for both tooth root geometries, shown at the right side of the figure. The results of the reference geometry are taken from [13]. The optimized geometry is an adaptation of the reference root shape, which reduces the stress concentrations from the notch effect and thus increases lifetime. Figure 2 illustrates that the increase in lifetime is dependent on rotational speed. This can be attributed to time-dependent local material states at different rotational speeds. Compared to the reference geometry, the optimized geometry can be tested up to 3000 min^{-1} without causing a change in the failure mode of the gear (tooth root fracture to temperature induced failure). The lifetime of both geometries is characterized by speed dependency, which results in a local lifetime maximum. As the speed increases, the trend reverses from this maximum, with a subsequent decrease in lifetime. This suggests that there are two opposing effects, i.e. mechanical or thermal destruction of molecular bonds. In other words, two damage mechanisms that are contrary dependent on the dynamics of the load, with one or the other dominating at different speeds. This hypothesis requires the introduction of a second damage parameter.

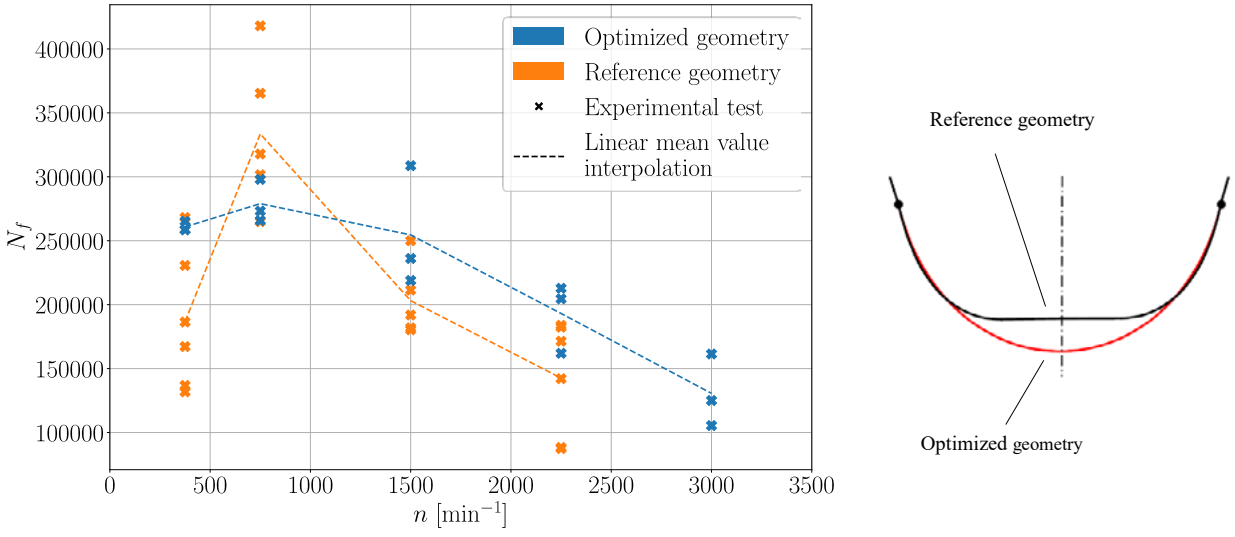

Figure 2. Experimental lifetime tests at constant torque level for two root geometries.

Bi-Parametric Damage Model

The bi-parametric damage model introduced here is based on two independent damage mechanisms that lead to the same failure mechanism (tooth root breakage) of the gear with the corresponding lifetimes N_{D1} and N_{D2}. As they are independent of each other, the first one reached (lower

DOI: https://doi.org/10.51573/Andes.PPS39.GS.MS.1

one in value) is decisive for the failure and the resulting predicted lifetime N_p of the model. Hence, no cumulative interactions of the damage mechanisms are assumed, see equation 1.

$$N_p = \min(N_{D1}, N_{D2}) \tag{1}$$

Regarding the experimental results, it can be concluded that with increasing rotational speed, the first damage mechanism becomes dominant for lifetime limitation. Once a critical speed n_{crit} is reached, the dominant damage mechanism is altered as illustrated in Figure 3(b). Therefore, for loading conditions at low rotational speed, one mechanism is limiting lifetime, whereas at high rotational speed, the other mechanism is restricting lifetime. Each damage mechanism depends on a damage parameter D_n, which correlates with the corresponding mechanism lifetime N_{D1} and N_{D2}, see Figure 3(a). This dependency is for both mechanisms characterized by the damage function *f*. In general, the type of this function must be monotonically decreasing with increasing damage parameter. In equation 2, the damage function is presented. It is assumed to be linear.

$$N_{Dn} = f(D_n) = a_n \cdot D_n + b_n \tag{2}$$

In order to achieve a contrary speed dependency of the lifetimes N_{D1} and N_{D2} in Figure 3(b), the respective damage parameters D_1 and D_2 must have a contrary dependency on rotational speed. This means that with increasing speed, the damage parameter D_2 will increase and thus lead to a lower lifetime N_{D2}, while the other damage parameter D_1 will decrease and thus the lifetime N_{D1} will increase. This represents the condition for a suitable choice of damage parameters, which must be based on local material states at the crack initiation point in order to ensure a physically motivated correlation.

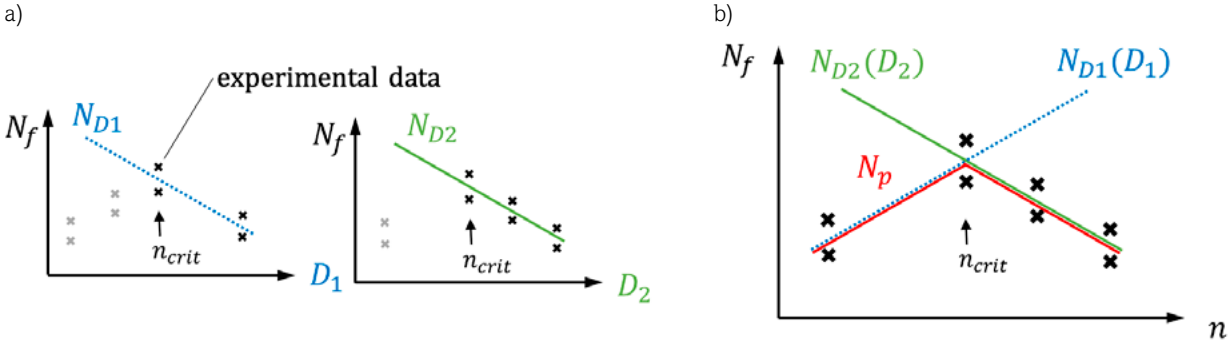

Figure 3. (a) Calibration of damage functions, (b) Evaluation of predicted lifetime N_p.

DOI: https://doi.org/10.51573/Andes.PPS39.GS.MS.1

Damage Parameters

The damage parameter D_1, defined in equation 3, consists of the amplitude of the maximal principal strain scaled with the loading period T to increase the dependency on rotational speed. The strain amplitude describes the difference between the minimal and maximal value of the maximal principal strain in the crack initiation point, which is an indicator of the tension load in the direction of the crack opening. The period T is proportional to time, in which the tooth is loaded. This represents an extension of the damage parameter used in the previous study [13], where the maximal principal strain was used exclusively. Physically, the damage mechanism of D_1 can be interpreted as a mechanical destruction of the polymer's molecular bonds. In contrast, the damage parameter D_2, defined in equation 4, equals the amplitude of the viscoplastic strain energy density rate at the point of crack initiation, indicating how fast energy is dissipated. This is a direct indicator of local heating, hence the mechanism of D_2 can be regarded as a measure for thermal destruction of molecular bonds. Figure 4 shows both damage parameters with their contrary dependency on rotational speed, as the influence of the geometries is a direct result of physical material modeling.

$$D_1 = T \cdot \Delta\varepsilon_1 \tag{3}$$

$$D_2 = \Delta\dot{U}_{vp} \tag{4}$$

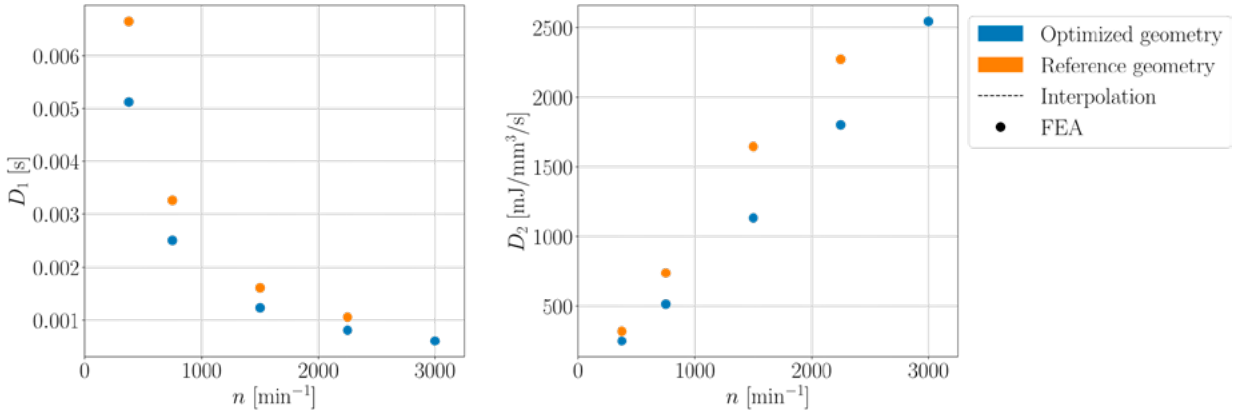

Figure 4. Damage parameters in dependence of rotational speed.

Application to Experimental Results

In order to apply the bi-parametric damage model with the specified damage parameters to the experimental results, the experimental data must first be associated with respect to the governing damage mechanism as shown in Figure 3(b). This step is necessary to calibrate the two damage functions and leads to the condition that both mechanisms are represented in the data by the chosen

DOI: https://doi.org/10.51573/Andes.PPS39.GS.MS.1

speed sampling. The transition of the mechanisms is defined by the splitting method, which may occur either on or between data points. Here the former one is assumed, hence a critical speed n_{crit} exists, where the damage of both mechanisms is minimized. Figure 5 shows the damage mechanisms lifetimes N_{D1} and N_{D2} predicted by the calibrated damage functions as well as the effective predicted lifetime N_p along the rotational speed. The damage functions of both mechanisms were fitted to the damage parameter data of both geometries, so the criterion is independent of the geometry. The figure shows that the variation of the tooth root geometry influences the mechanisms' lifetimes. This is a result of the change in the damage parameters due to the changed notch shape. Furthermore, two different speed dependencies are evident, N_{D1} multi-linear and N_{D2} linear, which can be attributed to the different speed dependencies of the damage parameters D_1 and D_2. The lifetime prediction N_p of the model reproduces the experimental data within its scatter as well as the local lifetime maxima.

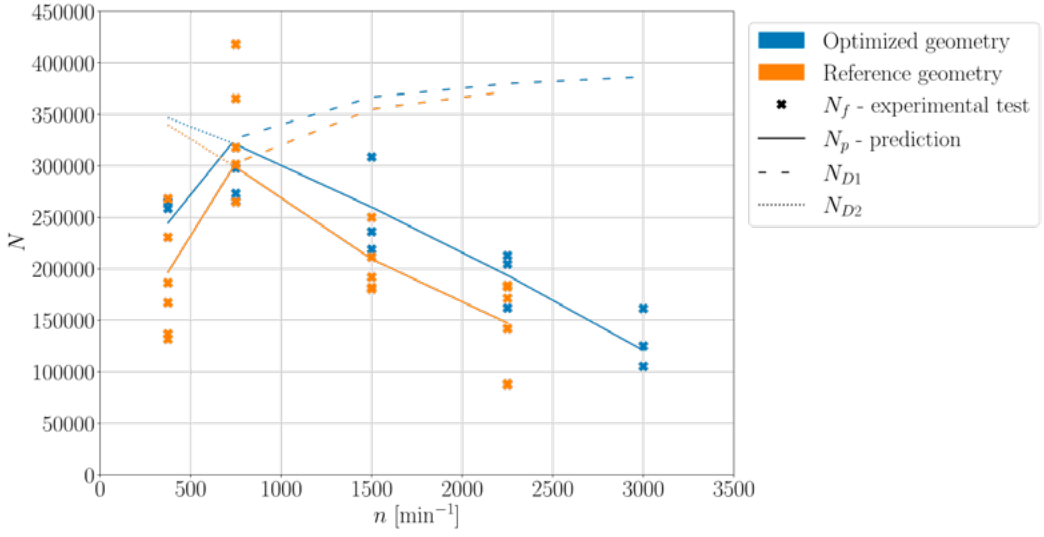

Figure 5. Evaluation of predicted lifetime N_p out of damage mechanisms lifetime.

Conclusion

The tooth root fracture failure mechanism exhibits a speed dependency with a trend reversal, which leads to a local lifetime maximum. The bi-parametric damage model postulates two independent damage mechanisms of the polymer, which can be attributed to this behavior and depend on local material states at the crack initiation point. The first damage parameter is based on the maximum principal strain, which is a direction-dependent variable. It can be interpreted as a mechanical destruction of the polymer's molecular bonds. The second damage parameter considers the thermal destruction of these bonds by considering the dissipation rate. This is a direction-independent variable and can be related to short-term local heating. Although the model does not include any

DOI: https://doi.org/10.51573/Andes.PPS39.GS.MS.1

interaction between the damage mechanisms, the predictions are within the experimental scatter and the local lifetime maximum can be modeled. Further research is required to investigate the interaction between damage mechanisms and changes in linear or even nonlinear damage functions in order to generalize the damage model for varying loading boundary conditions.

Acknowledgments

The financial support of FVA (Forschungs Vereinigung Antriebstechnik, Germany) is gratefully acknowledged for the 951 KuFuGeo project.

References

1. C. Hasl, C. Illenberger, P. Oster, T. Tobie, and K. Stahl, "Potential of oil-lubricated cylindrical plastic gears," *Journal of Advanced Mechanical Design, Systems, and Manufacturing*, vol. 12, p. JAMDSM0016, 2018, https://doi.org/10.1299/jamdsm.2018jamdsm0016
2. C. Hasl, H. Liu, P. Oster, T. Tobie, K. Stahl, and Forschungsstelle fuer Zahnraeder und Getriebebau (Gear Research Centre), "Method for calculating the tooth root stress of plastic spur gears meshing with steel gears under consideration of deflection-induced load sharing," *Mechanism and Machine Theory,* vol. 111, pp. 152–163, 2017.
3. S. Senthilvelan and R. Gnanamoorthy, "Effect of rotational speed on the performance of unreinforced and glass fiber reinforced nylon 6 spur gears," *Materials Design*, vol. 28, pp. 765–772, 2007, https://doi.org/10.1016/j.matdes.2005.12.002
4. M. Hribersek, M. Erjavec, G. Hlebanja, and S. Kulovec, "Durability testing and characterization of pom gears," *Engineering Failure Analysis*, vol. 124, p. 105377, 2021, https://doi.org/10.1016/j.engfailanal.2021.105377
5. Z. Lu, Z. Li, H. Liu, P. Wei, B. Xia, and M. Ye, "An accelerated fatigue test method of polymer gears based on thermostress conversion relation," *Engineering Fracture Mechanics*, vol. 266, p. 108388, 2022, https://doi.org/10.1016/j.engfracmech.2022.108388
6. A. Bravo, D. Koffi, L. Toubal, and F. Erchiqui, "Life and damage mode modeling applied to plastic gears," *Engineering Failure Analysis*, vol. 58, pp. 113–133, 2015, https://doi.org/10.1016/j.engfailanal.2015.08.040
7. Z. Lu, H. Liu, P. Wei, C. Zhu, D. Xin, and Y. Shen, "The effect of injection molding lunker defect on the durability performance of polymer gears," *International Journal of Mechanical Sciences*, vol. 180, p. 105665, 2020, https://doi.org/10.1016/j.ijmecsci.2020.105665
8. R. Wu, P. Wei, Z. Lu, H. Liu, D. Zorko, and H. Xie, "A comparative study of fatigue behavior between S-shaped and involute POM gears," *Journal of Computational Design and Engineering*, vol. 9, pp. 2483–2494, 2022, https://doi.org/10.1093/jcde/qwac121

9. Y.-j. Wu, J.-j. Wang, and Q.-k. Han, "Contact finite element method for dynamic meshing characteristics analysis of continuous engaged gear drives," *Journal of Mechanical Science and Technology* , vol. 26, pp. 1671–1685, 2012, https://doi.org/10.1007/s12206-012-0416-5

10. H. Jia, J. Zhang, and X. Xu, "Dynamic modeling and analysis of epoxy gear considering material viscoelasticity," *Machines*, vol. 11, 2023, https://doi.org/10.3390/machines11010076

11. H. Dresig and A. Fidlin, "Schwingungen mechanischer Antriebssysteme: Modellbildung, Berechnung, Analyse, Synthese," *Springer Verlag*, 2020.

12. A. Winkler and G. Kloosterman, "A critical review of fracture mechanics as a tool for multiaxial fatigue life prediction of plastics," *Frattura ed Integrita Strutturale*, vol. 9, pp. 262–288, 2015, https://doi.org/10.3221/IGF-ESIS.33.32

13. S. Düzel, R. Eberlein, H.-J. Dennig, "Fatigue life analysis of POM gears with transient material modeling," *AIP Conference Proceedings*, vol. 3158, p. 110015, 2024, https://doi.org/10.1063/5.0204543

14. PolymerFEM, PolyUMod Manual (Version 6.3.4).

15. J. Bergström, "Mechanics of Solid Polymers", William Andrew Publishing, 2015.

16. M. Shariati, H. Hatami, H. Yarahmadi, and H. R. Eipakchi, "An experimental study on the ratcheting and fatigue behavior of polyacetal under uniaxial cyclic loading," *Materials & Design*, vol. 34, pp. 302–312, 2012, https://doi.org/10.1016/j.matdes.2011.08.017

17. Fatemi and N. Shamsaei, "Multiaxial fatigue: An overview and some approximation models for life estimation," *International Journal of Fatigue*, vol. 33, no. 8, pp. 948–958, 2011, issn: 0142-1123, https://doi.org/10.1016/j.ijfatigue.2011.01.003

18. G.A. Holzapfel, T.C. Gasser, and R.W. Ogden, "A new constitutive framework for arterial wall mechanics and a comparative study of material models," *Journal of Elasticity*, 61:1-48, 2000.

19. T.C. Gasser, R.W. Ogden, and G.A. Holzapfel, "Hyperelastic modelling of arterial layers with distributed collagen fibre orientations," *Journal of the Royal Society Interface*, 3:15-35, 2006.

GENERAL SYMPOSIA | MODELING AND SIMULATION

Simulative Approach for Predicting the Heating Behavior of Elastomers in the Solid-State Microwave Heating Process

Jonas Petzke, Dennis Kleinschmidt and Florian Brüning

DOI: https://doi.org/10.51573/Andes.PPS39.GS.MS.2

December 2024

Simulative Approach for Predicting the Heating Behavior of Elastomers in the Solid-State Microwave Heating Process

Jonas Petzke, Dennis Kleinschmidt and Florian Brüning[1]

Abstract: The increasing demand for energy efficient vulcanization of rubber extrusions requires the optimization and further development of existing processes. Microwave vulcanization allows the energy required for this process to be coupled directly into the material via dielectric losses. Microwave heating requires the polarity of the rubber so that the electromagnetic wave can cause the polar components of the material to vibrate. These vibrations cause internal friction, resulting in an increase in the temperature of the rubber compound. In this research project, microwaves were used to heat a rubber strand placed in a specially prepared waveguide. This method offers advantages over conventional methods, such as hot air vulcanization. A key advantage is that the energy is coupled directly into the material, resulting in low losses. In contrast to hot air vulcanization, where the air must first be heated, the heating of the material also takes place within the product to be heated. This results in a significant increase in energy efficiency, reaching up to 90 %. In addition, internal heating provides a more homogeneous heat distribution in the rubber strand compared to external heating by hot air vulcanization. To predict the heating behavior of rubber in the microwave process, a simulative model is created in the multiphysics simulation environment CST Studio Suite®. The model describes the microwave heating behavior of rubbers based on the thermodynamic and electromagnetic material data of the rubber compound. This simulation is known as a bi-directional simulation, so that temperature-dependent variables such as dielectric loss and thermal conductivity can be considered. The model is used to analyze parameter variations of the electromagnetic wave frequency, waveguide geometry, and strand orientation in the waveguide. Finally, optimized settings for the real process are recommended.

Keywords: Microwave Heating, Solid-State, Rubber, Simulation, CST Studio Suite, Dielectric Loss, Efficiency, Optimization, Waveguide, Microwave, Heating, Vulcanization

1 The authors Jonas Petzke (jonas.petzke@ktp.uni-paderborne), Dennis Kleinschmidt and Florian Brüning are affiliated with the Paderborn University in Germany.

DOI: https://doi.org/10.51573/Andes.PPS39.GS.MS.2

Introduction

In rubber extrusion processes, it is important to achieve homogenous crosslinking throughout the material's cross-section to ensure consistent properties in the final product [1-3]. Achieving high energy efficiency is also crucial for the vulcanization process from an economic point of view, as it allows for high throughput in a short time while minimizing energy consumption [3-5]. In conventional vulcanization processes like hot-air vulcanization, heat is conducted from the outside to the inside of the material. Thus, the heat capacity, thermal conductivity, and heat transfer between the elastomer and the intermediate medium play significant roles in the vulcanization process. Elastomers generally have low thermal conductivity, which can result in thermal damage in the edges of thick-walled profiles while the core remains insufficiently heated and in a plastic state. With good insulation and a vulcanization energy requirement of 0.1 kWh/kg, the total system energy requirement is approximately 0.3 kWh/kg. This results in a relatively low efficiency of 33 % [6].

To ensure a higher efficiency of energy input, a uniform temperature distribution, and consistent vulcanization across the cross-section, dissipative heat input is necessary within the extrudate. Microwave irradiation provides an effective means of achieving this internal heat input. The heating process primarily occurs through the electrical component of the electromagnetic wave. As the wave penetrates the material, a phase shift occurs between the electric field and the polarization of the polar components within the material [7]. This reorientation of dipoles generates internal friction, which leads to a heating of the elastomer. This phenomenon is known as dielectric loss. To describe this process, the materials loss angle is required [8], equation 1.

$$tan\delta = \frac{\epsilon_r''}{\epsilon_r'} \tag{1}$$

In the given equation, the loss angle is denoted as δ, the imaginary part of the permittivity as ϵ_r'', and the real part as ϵ_r'. The loss angle represents a material-specific parameter that exhibits an increase with greater polarity. Furthermore, the value of the loss angle is contingent on both the material's temperature and the frequency of the electromagnetic field. By employing the loss angle, the energy P_V imparted into the material volume can be determined through the utilization of the field strength $\vec{E}$ and the fields frequency *f*. The energy P_V can be evaluated based on the field strength, as indicated by equation 2 [8].

$$P_V = 2 \cdot \pi \cdot f \cdot \epsilon_0 \int_V \epsilon_r' \cdot tan\,\delta \cdot \left|\vec{E}\right|^2 \cdot dV \tag{2}$$

Microwave rubber profile vulcanization emerged in the 1960s to enhance productivity and quality. Early microwave ovens employed either a waveguide or resonant design but faced issues with uniform heating. Due to an inadequate dielectric loss factor and narrow, intricate profiles, satisfactory

DOI: https://doi.org/10.51573/Andes.PPS39.GS.MS.2

results could not be obtained. Furthermore, certain products had metal cores that acted as antennas for the electromagnetic wave, making microwave heating difficult. Moreover, rapid heating of certain materials caused thermal degradation of the extrudate.

As in 1994 [9], Krieger investigated the microwave heating behavior of rubber extrudates, taking into account the temperature inhomogeneity at the extruder outlet. He found that the areas of the extrudate with higher temperatures are heated more intensively. Thus, temperature differences already present during the shaping of the extrudate are amplified during microwave treatment. In addition, he has already shown that polar rubbers such as acrylonitrile-butadiene rubber (NBR) or polychloroprene rubber (CR) can be heated significantly faster than non-polar rubbers such as natural rubber (NR) or polyisobutylene rubber (IIR). However, he did not describe this behavior in detail but carried out general studies of heating behavior.

In 2010, Makul et al. [10] further investigated the pre-curing behavior of NR using a rectangular waveguide under varying sulfur content. They found that treatment with a microwave frequency of 2.45 GHz in the pre-curing process led to crosslinking of NR already below the vulcanization temperature. It was also shown that the sulfur content had only a minor influence on the absorption behavior of the rubber, while an increase in the carbon black content led to a higher absorption of the microwave energy. Furthermore, an initial basis for a mathematical model of the microwave heating of NR in a stationary process could be generated.

In 2022, Okumura et al. [11] investigated the heating behavior of microwaves in the in-mold tire manufacturing process. They were also able to show that blended carbon black serves as a heat source for microwave vulcanization. As a result, rapid vulcanization was achieved by microwave irradiation compared to conventional processes. However, it should be noted that the heating has an exponential temperature curve over time, which leads to problems in process control. By using a variable frequency microwave between 5.85GHz – 6.65 GHz, this problem could be reduced in the stationary vulcanization process.

Materials

In order to generate a comparatively high absorption behavior of the electromagnetic waves, a material with a high dielectric loss is initially selected for the simulative approach explained in this paper. This material is Nitrile Butadiene Rubber (NBR). The temperature-dependent material parameters permittivity, loss angle, thermal conductivity, specific heat capacity and density have been determined from a real compound. The thermal conductivity was determined using a Laser Flash Analyzer (LFA 467 HyperFlash ©) from NETZSCH-Gerätebau GmbH. The heat capacity was determined by using dynamic differential calorimetry, employing a DSC 3+ apparatus from Mettler-Toledo. The material density was determined using the ME204T/00 analytical balance from Mettler-Toledo. The electrical material parameters, permittivity, and dielectric loss angle were

DOI: https://doi.org/10.51573/Andes.PPS39.GS.MS.2

measured externally at the Fraunhofer Institute for Chemical Technology (ICT) in the field of microwave and plasma technology. The material parameters thus determined are presented in Table 1.

Table 1. Material parameters for the simulation.

Material Parameter	Unit	Value
Permittivity	-	4.11
Loss angle (at 2.56 GHz)	-	0.04
Thermal conductivity	W/K · m	0.24
Specific heat capacity	J/K · kg	2000
Density	kg/m³	1166

In the simulation environment, a 30 mm x 30 mm x 4 mm cuboid was created based on the material data in Table 1. In addition, a more complex geometry was analyzed based on a sealing profile. The geometry of the sealing profile is shown in the Figure 1.

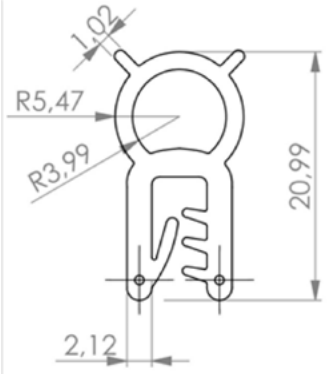

Figure 1. Geometry – Sealing profile (dimensions are given in mm).

Equipment

CST Studio Suite® software is used in this paper for microwave-based heating simulations. This comprehensive software simulates electromagnetic fields and, with additional solvers, can address thermal, mechanical, and other problems. Thermal calculations are facilitated by the CST MPhysics Studio® package, which includes an ACIS-based 3D modeling environment and automatic meshing. A key feature of CST MPhysics Studio® is complete parameterization, allowing easy adjustments of dimensions and automatic maintenance of aspect ratios. Multiphysics simulations in CST Studio Suite® link electromagnetic and thermal models, with options for unidirectional

DOI: https://doi.org/10.51573/Andes.PPS39.GS.MS.2

or bidirectional transfer of calculated values. If the models depend on each other, e.g., if the field-determining material parameters such as permittivity are temperature-dependent, a bi-directional coupling can be selected. Knowledge of the temperature dependence of the material parameters is critical. For this type of coupling, the number of iterations must be specified, which determines how often both models are to be calculated with the respective changed variables. CST Studio Suite® then proceeds as follows: First, the electromagnetic field is calculated in the model, then the thermal losses are calculated from the simulation results and passed to the thermal solver, which calculates the thermal fields based on the values. The results are used as modified parameters for the new calculation of the EM field. This is repeated for the selected number of iterations. Both solvers base their calculations on the same master model, and global parameters can be defined that are shared between the two subprojects. A schematic representation of the simulation process is shown in Figure 2 [12].

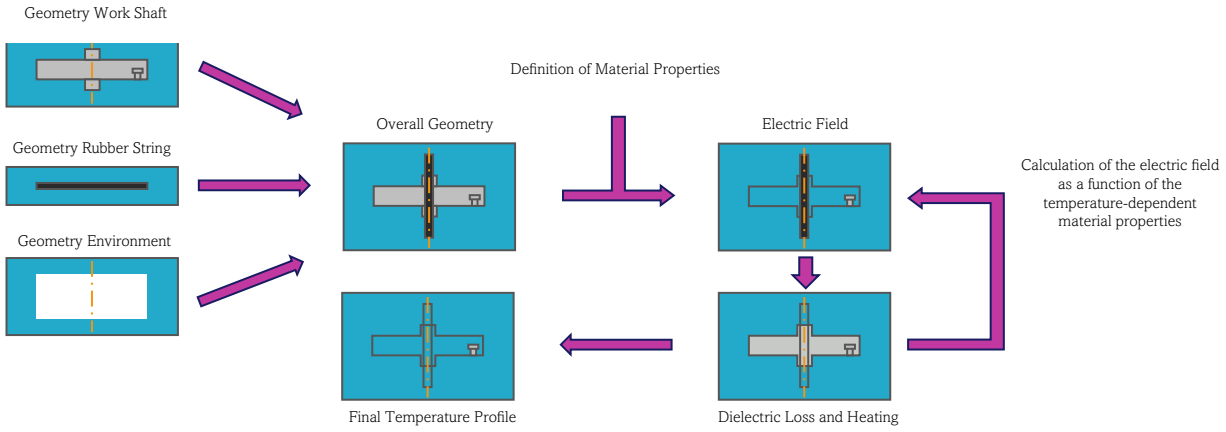

Figure 2. Schematic representation of the iterative heating simulation with consideration of the temperature-dependent material parameters.

Results

The temperature distribution across the cross section of the rubber specimen and the homogeneity of the temperature distribution were used to analyze the simulation results. As described in equation 3, the assessment of the temperature distribution is calculated by the difference between the maximum temperature T_{max} and the minimum temperature T_{min} in relation to the difference between the average temperature T_{mean} and the ambient temperature T_0. This results in an ideal homogeneity of the temperature distribution for a homogeneity index of zero.

DOI: https://doi.org/10.51573/Andes.PPS39.GS.MS.2

$$Homogeneity\ index = \frac{T_{max} - T_{min}}{T_{mean} - T_0} \quad 3)$$

A rectangular waveguide, a common tool in electrical engineering, was employed in the model to guide the electromagnetic wave. This metallic structure enables the almost loss-free transmission of microwaves while ensuring effective shielding from the surrounding environment. As shown in Figure 3, it was observed that an H_{10} standing wave forms in the rectangular waveguide. The index 10 indicates the number of half waves of the electric field components in the corresponding directions within the rectangular waveguide. Here, "1" means that there is a half-wave in the wider dimension of the rectangle and "0" means that there is no half-wave in the narrower dimension of the rectangle. It should be noted that the field distribution is uneven, particularly in the region near the waveguide opening where the rubber string passes through, compared to the rest of the structure. It was also observed from the electric field that the introduction of a dielectric, in this case rubber, leads to a reduction in the field strength. Both phenomena are shown in Figure 3.

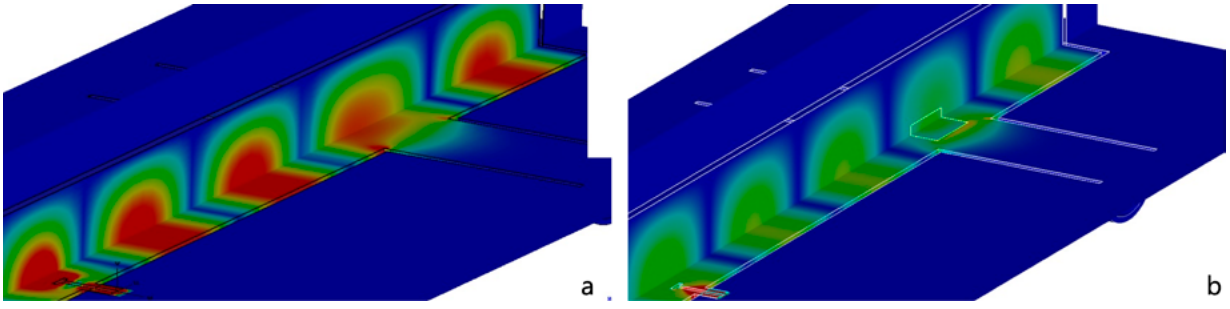

Figure 3. (a) Expansion of the E-field without test specimen (empty waveguide) f = 2450 MHz, (b) Expansion of the E-field with cuboid test specimen f = 2450 MHz.

The process parameters were also optimized. This was done by varying the length of the rectangular waveguide. The output length of the waveguide l_c was extended by an offset as shown in Figure 4. During the simulations, the power consumption was kept constant at 450 W.

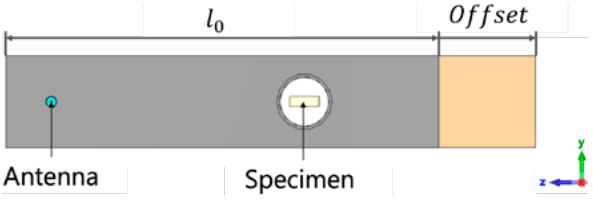

Figure 4. Parametrization of the waveguide length.

DOI: https://doi.org/10.51573/Andes.PPS39.GS.MS.2

The results of the waveguide length sweep for the cuboid after 80 s of heating at a frequency of 2450 MHz are shown in Figure 5(a). The offset length in mm is shown on the abscissa, the temperature in °C on the left ordinate, and the homogeneity index in dimensionless form on the right ordinate. The simulations show that the mean temperature (dark blue), the maximum temperature (red), and the minimum temperature (green) increase from an offset length of 36 mm to 68 mm. This suggests that the maximum of the e-field at 68 mm is almost entirely in the region of the rubber specimen. This means that maximum temperatures of almost 300°C are reached. The average temperature is about 225°C. As the offset length increases, the temperatures decrease and reach a local minimum at 116 mm. The maximum temperatures there are only about 50°C. The homogeneity index of the heating, shown in light blue, reaches a local maximum of about 1.6 at 44 mm. It decreases with increasing offset length, with the best homogeneity at 84 mm and a homogeneity index of about 0.4. With further increase of the offset length, the homogeneity index increases and reaches a maximum of 1.8 at 108 mm. Thus, for a microwave heating process of a cuboid, an optimized process can be achieved at an offset length of 84 mm. At this point, the highest homogeneity is achieved as well as comparatively high temperatures of about 140°C, on average.

An offset length sweep was also performed for the sealing profile (Figure 5[b]). The cross section of the profile is smaller than that of the cuboid. Since an 80 s heating duration led to significantly higher temperatures, the heating time was subsequently reduced to 28 s. The average, maximum and minimum temperatures also decrease up to an offset length of approximately 32 mm and then increase up to a length of 74 mm. This means that temperatures of about 125°C can be reached on average. The temperature of this profile also decreases as the offset length increases. As with the cuboid, the shift of the field maxima can be observed, with the field maximum in the 74 mm range being very centered in the specimen. The homogeneity is best in the region around 80 mm with a homogeneity index of about 0.3. Therefore, an optimum at 80 mm could also be determined.

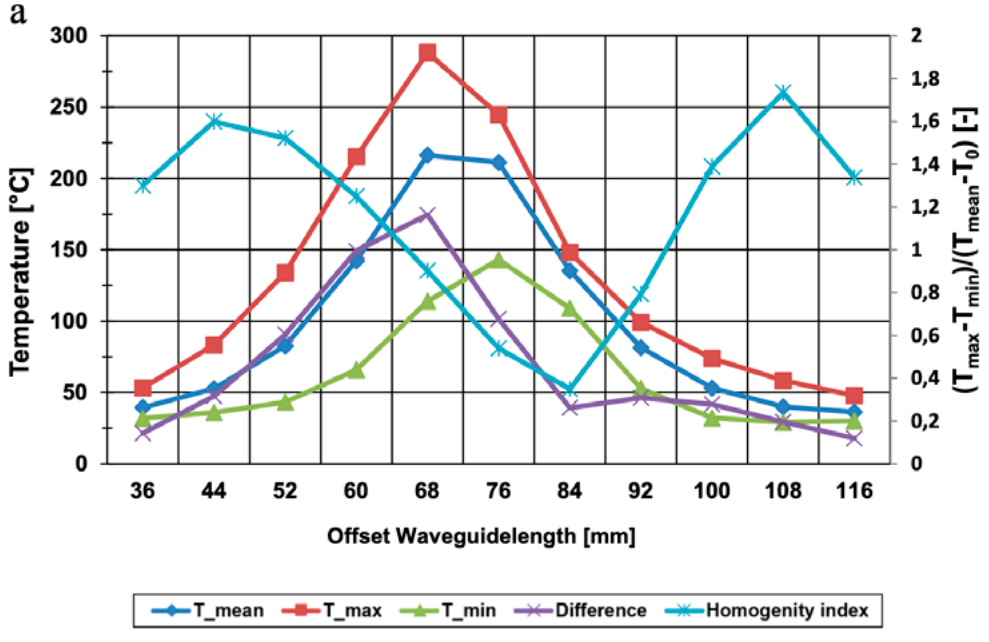

DOI: https://doi.org/10.51573/Andes.PPS39.GS.MS.2

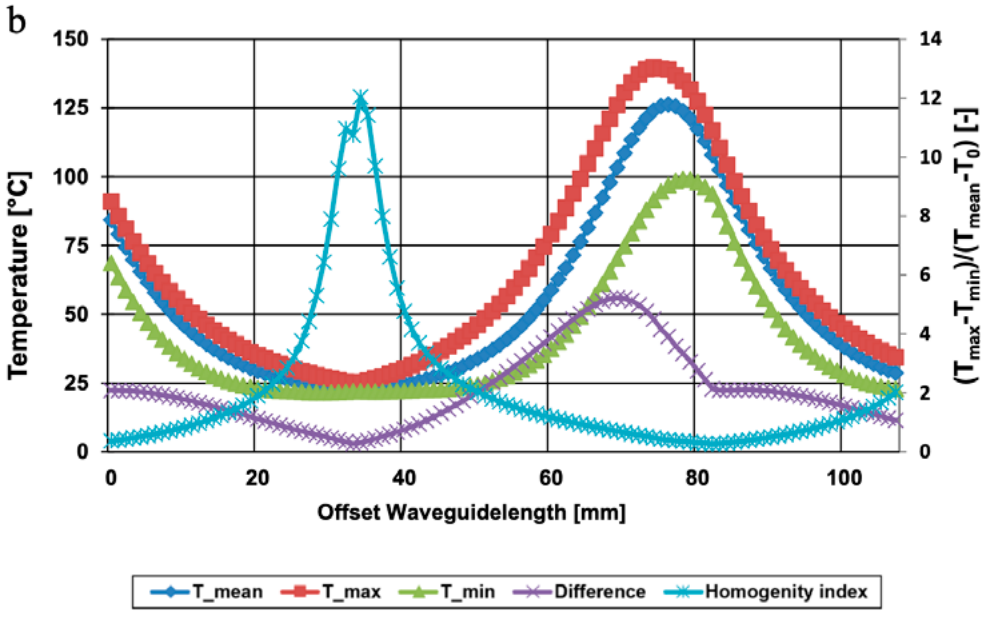

Figure 5. Temperature parameters – parameter sweep waveguide length
(a) cuboid – heating time t = 80 s, (b) sealing profile – heating time t = 28 s.

Conclusions and Outlook

The simulation results show a promising approach to facilitate the design of microwave vulcanization systems. The simulation showed that the waveguide length in particular has significant influence on the propagation of the electromagnetic field. As a result, the offset length varied in this model could be optimized to approximately 80 mm for both the cuboid and the sealing profile. Both high energy input and high homogeneity were achieved. The model also showed that smaller geometries experience more homogeneous heating in the single mode process.

The model will now be validated with more complex geometries and then scaled up to industrial scale. The focus will be on optimizing the geometry of the working shaft. Experimental data from an industrial solid-state plant will also be generated to validate the simulated results.

Acknowledgements

We would like to thank the “Zentrales Innovationsprogramm Mittelstand” (ZIM) for its financial support to the work, which is funded by the Federal Ministry of Economic Affairs and Climate Action (BMWK). In addition, we would like to thank our cooperation partner Gerlach Maschinenbau GmbH for the good collaboration.

References

1. G. Abts, *Einführung in die Kautschuktechnologie,* 2nd ed. München: Hanser, 2019. [Online]. Available: https://www.hanser-elibrary.com/doi/book/10.3139/9783446458550
2. L. Köster, H. Perz, and G. Tsiwikis, *Praxis der Kautschukextrusion*. München: Hanser, 2007.
3. W. Gohl et al., *Elastomere: Dicht- und Konstruktionswerkstoffe,* 3rd ed. Grafenau/Württ.: Expert-Verl., 1983.
4. I. Imenokhoyev, H. Windsheimer, R. Waitz, N. Kintsel, and H. Linn, "Mikrowellenerwärmungstechnik: Potentiale und Grenzen," *Ceramic Forum International*, vol. 2012, Vol.89 (11-12), pp. 19–27, 2012.
5. KERONE, "Microwave Heating Technology for Rubber Processing," 2020.
6. F. Röthemeyer and F. Sommer, *Kautschuk-Technologie: Werkstoffe–Verarbeitung–Produkte,* 3rd ed. München: Hanser, 2013.
7. J. Detlefsen and U. Siart, *Grundlagen der Hochfrequenztechnik,* 3rd ed. München: Oldenbourg, 2009.
8. E. Pehl, *Mikrowellentechnik: Grundlagen, Leitungen, Antennen, Anwendungen,* 3rd ed. Berlin, Offenbach: VDE-Verl., 2012.
9. B. Krieger, "Microwave Vulcanization: A Lesson in Business and Technology," *MRS Proc.*, vol. 347, pp. 57–69, 1994, doi: 10.1557/PROC-347-57
10. N. Makul and P. Rattanadecho, "Microwave pre-curing of natural rubber-compounding using a rectangular wave guide," *International Communications in Heat and Mass Transfer*, vol. 37, no. 7, pp. 914–923, 2010, doi: 10.1016/j.icheatmasstransfer.2010.03.001
11. K. Okumura, A. Saiki, M. Hojo, T. Takizawa, and S. Horikoshi, "Elucidation of the principle of microwave rubber vulcanization based on dielectric parameters and vulcanization of tire rubber by variable frequency microwave," *Journal of Applied Polymer Science*, vol. 139, no. 45, 2022, doi: 10.1002/app.52909
12. S. Schupp, "CST Studio Suite–Thermal and Mechanical Simulation," 2021.

DOI: https://doi.org/10.51573/Andes.PPS39.GS.MS.2

GENERAL SYMPOSIA | MODELING AND SIMULATION

Design Optimization of Rotationally Molded Hydrogen Pressure Vessels

Alex Pritchard, Peter Martin, Mark McCourt and Mark Kearns

DOI: https://doi.org/10.51573/Andes.PPS39.GS.MS.3

December 2024

Design Optimization of Rotationally Molded Hydrogen Pressure Vessels

Alex Pritchard, Peter Martin, Mark McCourt and Mark Kearns[1]

Abstract: Type IV hydrogen pressure vessels are made up of three components: a metallic boss, a polymer liner, and a composite overwrapping layer for reinforcement. Leakproof design of bosses is critical for safety, ensuring a gas-tight seal to prevent explosions due to leaks. Yet, their design has been largely overlooked. Using rotational molding it is possible to fully encapsulate bosses within liners during molding, but numerous challenges must be overcome relating to boss design for effective molding. FEA software was applied to virtually prototype boss designs and optimize their mechanical performance under pressure. CAD and FEA software were integrated in this work, enabling basic geometry constraints to be input in CAD, which were then fine-tuned in FEA in response to stress distribution results. This allowed the FEA model to optimize boss designs autonomously. To ensure moldability, initial boss designs were generated using existing rotational molding experience regarding the encapsulation of small inserts during molding. The autonomous optimization technique was then applied to minimize the boss weight by controlling the size of design features, while ensuring mechanical performance constraints were met.

Keywords: Rotational, Molding, Hydrogen, Boss, Simulation

1 The authors Alex Pritchard (a.pritchard@qub.ac.uk), Peter Martin, Mark McCourt and Mark Kearns are affiliated with the School of Mechanical and Aerospace Engineering at Queen's University Belfast in Northern Ireland.

DOI: https://doi.org/10.51573/Andes.PPS39.GS.MS.3

Introduction

Hydrogen is set to be an important energy vector as the world experiences more global warming and energy security challenges. With advances in technology and wider interest in storage vessels, the polymer industry could diversify their product offerings into new markets. Type IV hydrogen tanks are expected to become more important for storage in dynamic applications (such as cars, buses, trains, etc.). The tanks are made up of three major components, a polymer liner, a composite reinforcement, and metal bosses to allow gas management systems to be attached to the tank (see Figure 1).

Bosses facilitate the loading and unloading of gases from the tanks, and often serve as a mounting point to secure the tank within a larger assembly, such as a vehicle chassis, for example. Boss designs vary based on the process used to produce the tank liner. In blow molded tank liners, the bosses are added in a secondary welding process, however issues with hydrogen leakage have been acknowledged with liners made in this way [1]. Another technique used to produce the liners is rotational molding. This is a process used to produce hollow plastic components such as outdoor furniture and can feature small threaded inserts for assembly [2]. Rotationally molded tank liners can have the boss to fully encapsulated within the liner, providing a stronger connection to withstand leakage [3]. Figure 2 shows an example of a boss for a rotationally molded tank liner, illustrating the size and complexity of the dome that is embedded within the polymer liner.

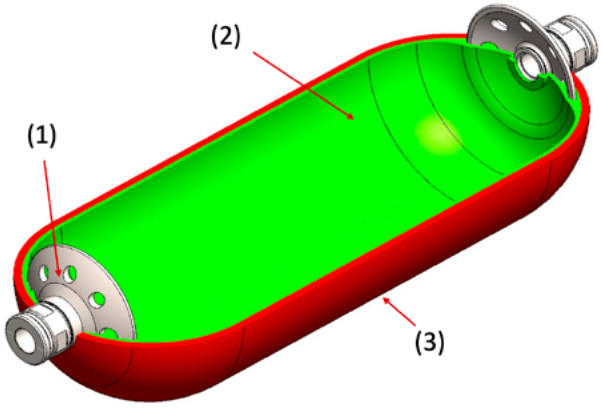

Figure 1. Schematic detailing the (1) bosses, (2) polymer liner, and (3) composite overwrapping of a Type IV hydrogen storage vessel.

DOI: https://doi.org/10.51573/Andes.PPS39.GS.MS.3

Figure 2. Example of a 316 stainless steel tank boss.

Hydrogen storage vessels usually have a nominal working pressure between 350 bar and 700 bar. The filament winding process has become the industry's leading technology for manufacturing Type IV hydrogen tanks. In general, there are two types of winding patterns, known as hoop and helical windings, as shown in Figure 3. High angle hoop windings are used to provide circumferential strength to the tank, while lower angle helical windings provide greater longitudinal/axial strength. As illustrated by the example of a wound tank in Figure 4, the process involves winding fibers (usually glass or carbon) under tension around a rotating mandrel, which is the tank liner and bosses itself for Type IV hydrogen tanks. While the liner rotates around a spindle, a delivery head moves back and forth horizontally in line with the rotating axis, laying down the fibers onto the rotating liner in the desired angle to the rotational axis. There are many factors involved in the winding process and careful consideration is needed to create a reliable product [4]. The major cost in hydrogen tank manufacturing is the carbon fiber layer, and hence there is research that has focused on understanding optimization and minimization [3-6].

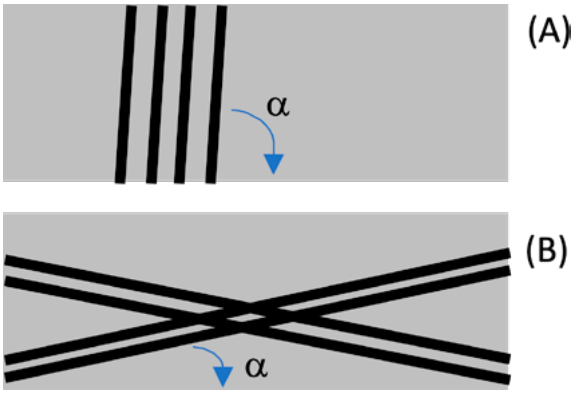

Figure 3. Schematic illustrating the difference between a (a) hoop and a (b) helical winding angle.

DOI: https://doi.org/10.51573/Andes.PPS39.GS.MS.3

Figure 4. Example of a filament wound Type IV hydrogen tank.

For rotational molders, the most challenging aspect of molding tank liners is the encapsulation of the metallic bosses within the polymer liner. Adequate encapsulation is vitally important as this junction poses a potential hydrogen leak path if the liner material were to separate from the metallic boss. To date there is very little research published regarding the optimization of boss designs for the rotational molding process. It is necessary to understand how design elements contribute to the performance of a boss both during molding and throughout its life in the tank. This work explores the of modeling and simulation to virtually prototype boss designs.

Method

Boss Design Simulation & Optimisation

Figure 5 summarizes the design methodology used in the work. The process began by establishing the design constraints of the tank, including the tank diameter, length, nominal working pressure, on-tank-valve thread size, and design safety factor. Following this, the boss diameter was found using the on-tank-valve thread size and nominal working pressure. Non-conformable tanks typically have a boss at one or both ends, forming a hole in the composite layer known as the polar opening (pole diameter). For optimal winding, the geodesic angle must be found using equation 1. At this angle, the angle of the fiber across the cylinder section results in the required polar opening size, when following the geodesic path over the dome. The geodesic angle is also the most stable path along the mandrel contour, where the least amount of friction is required to hold the fiber in place.

$$geodesic\ angle = \sin^{-1}\left(\frac{pole\ diameter}{cylinder\ diameter}\right) \quad 1)$$

DOI: https://doi.org/10.51573/Andes.PPS39.GS.MS.3

Figure 5. Type IV hydrogen pressure vessel design methodology followed in the work.

Netting theory, a tool commonly used to estimate the composite thickness needed to withstand the maximum design pressure of composite pressure vessels, was applied [7]. A geodesic winding angle of 13.4 degrees was obtained based on a polar opening size of 70 mm, and total laminate thickness of 14.8 mm were required. The simulation tools available in ANSYS were used to optimize the constituent components of the tank, refining the initial estimations. The models were simulated as axisymmetric models to reduce computation time, studying ¼ of the total tank. Certain dimensions, such as the diameter of the boss (the part embedded within the liner), were set as global parameters, allowing the simulation to drive their values. For improved accuracy, the laminate was modeled using the ANSYS Composite PrepPost (ACP) module, allowing fiber direction, fiber and resin properties, and stacking sequence to be taken into consideration. The materials properties are set out in Table 1 [8]. Standard materials of Nylon 6 (PA 6) for the liner and 316 Stainless Steel for the bosses were used, along with the default mesh settings. Surfaces where the boss to liner, and boss to laminate, were in contact were assumed to be bonded together. A pressure of 35 MPa was applied uniformly to the inner surfaces, representative of the working pressure of commericially available tanks used in heavy goods vehicles.

Prototype Boss Encapsulation Study

A final design was selected to be trialed using state-of-the-art robotically controlled electronically heated rotational molding equipment (courtesy of AMS, Belgium). The boss was 3D printed in stainless steel using a MetalX 3D printer and molded into a liner using settings typical of a PA6 moulding in the industry to access its encapsulation performance. An articulating borescope (Extech, HDV540) was used to inspect the encapsulation after demolding.

Table 1. Material properties for Teijin ITS50 [8].

Properties	
Bandwidth/ thickness (mm)	6.35 +/- 0.5 mm
Format	Pre-preg
Tex value or denier	>= 1600
Resin density	1.195 g/cm^3
Fibre density	1.80 g/cm^3

DOI: https://doi.org/10.51573/Andes.PPS39.GS.MS.3

Properties	
% Volume of fibre	65 +/- 2% fibre content
Ultimate fibre tensile stress	5100 MPa
Ultimate fibre tensile elongation	1.9 %
Modulus of elasticity for local axis 1, 2, 3	E_1 168 GPa, E_2 9 GPa, E_3 9GPa
Poisson's ratio for local plane 12, 13, 23	ν_{12} 0.1, ν_{13} 0.1, ν_{23} 0.3
Shear modulus of elasticity for local axis 12, 13, 23	G_{12} 5 GPa, G_{13} 5 GPa, G_{23} 3.7 GPa

Results and Discussion

Design Optimization

A range of boss designs were generated, making use of existing knowledge of sintering and densification during the molding process, and other boss features not typically considered due to machining constraints. Example designs are shown in Figure 6.

The direct optimization tool within ANSYS was used to identify the effect of the three common boss design features (holes, ribs, and castellations) by controlling their respective sizing within preset limits. The objective given to the tool was to minimize stress in the boss component while also minimizing weight. Figure 7 shows the optimal designs for each of the three scenarios. It was identified that the use of ribs resulted in the highest strength to weight part (σmax 340 MPa, weight 2.1 kg). Although holes are typically found on used rotationally molded metal inserts to encourage polymer bridging through the boss, to date no research has been conducted on the optimization of such features. In this study, it was found that stress concentrated at the edges of the holes (Figure 7[c]), which resulted in the optimization tool trying to make the holes as small as possible. To work effectively during molding though, the holes would need to be large enough to encourage polymer powder to pass freely through them during molding. It is acknowledged that for Type IV pressure vessels 'the dominating failure mode is directly related to the liner,' and that 'defects in the area of the connection between a boss and the liner material' are found during hydraulic testing of poorly constructed liners [9]. Although encouraging polymer bridging through holes in the boss could help to strengthen the connection between the boss and liner.

DOI: https://doi.org/10.51573/Andes.PPS39.GS.MS.3

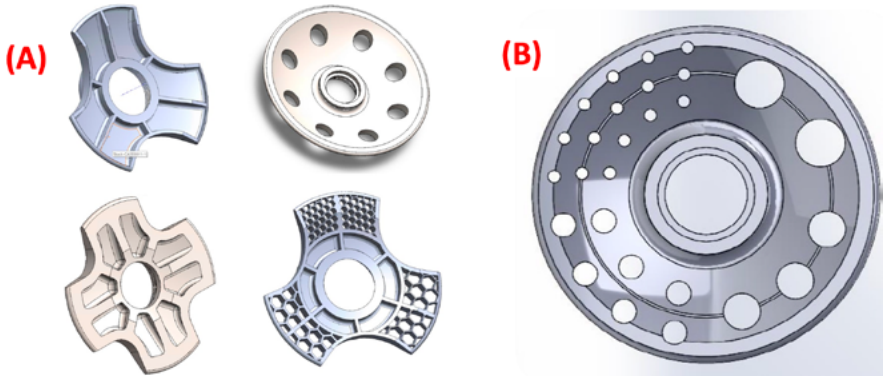

Figure 6. (a) Example boss designs based on parameters optimized for rotational molding, (b) Example of a boss design for identifying the optimum hole size for molding.

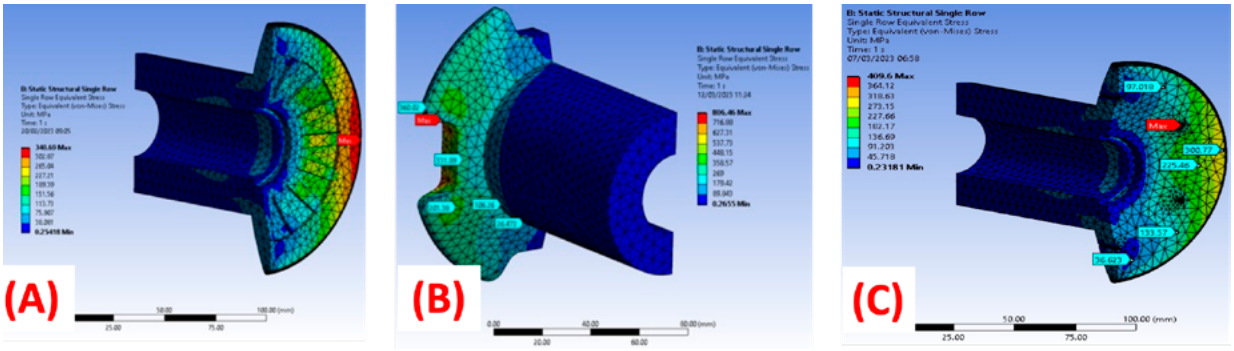

Figure 7. (a) Stress distribution on metal boss using ribs, (b) castellations, and (c) holes.

Industrial Encapsualtion Study

Molding trials were conducted using an electronically heated rotational molding tool, as shown in Figure 8(a). Tanks with 3D printed bosses encapsulated within them were produced, as shown in Figure 8(b). As previously indicated, bosses act as a heat sink and although additional metal may increase the part strength in a simulation, it may not perform well during molding. This effect is illustrated in Figure 8(c) and (d). Boss designs featuring thinner sections were found to be more encapsulated within the polymer during molding, due to their ability to absorb heat energy from the polymer being reduced. Designs featuring holes were found also to increase encapsulation of the polymer, bridging through the boss and acting to lock the boss in place, as illustrated in Figure 8(e).

DOI: https://doi.org/10.51573/Andes.PPS39.GS.MS.3

Figure 8. (a) Liner molded using electronically heated rotational molding tool, (b) Example of a single ended tank liner with a boss, (c) Boss acting as a heat sink resulting in poor encapsulation, (d) Onset of encapsulation on the inside face of a boss, (e) Part of a Metal Printed Boss Prior to Molding.

Conclusion

This work investigated the design of Type IV hydrogen tanks through virtual prototyping tools. ANSYS ACP was used, allowing the model to account for composite properties such as fiber direction and fiber and resin properties. Dimensions such as the diameter of the boss (the part embedded within the liner) were set as global parameters. The direct optimization tool was applied to study the effect of three common boss design features (holes, ribs, and castellations) by controlling their respective sizing within preset limits. The use of ribs resulted in the highest strength part with the lowest mass (σmax 340 MPa, weight 2.1 kg). Designs with holes showed high stresses around the hole, resulting in the optimization tool minimizing hole diameter. These designs which would not mold effectively as polymer powder would not pass through the holes. However, the polymer bridging caused larger holes during molding could be beneficial to strengthening the bond between the polymer and boss to prevent hydrogen leakage. Further work is ongoing to explore boss designs for polymer bridging while minimising stress.

DOI: https://doi.org/10.51573/Andes.PPS39.GS.MS.3

Acknowledgments

This work is supported by the Center for Advanced Sustainable Energy (CASE). CASE is funded through Invest NI's Competence Centre Programme. The author also thanks the Engineering and Physical Sciences Research Council (EPSRC) for supporting his participation in this conference.

References

1. Motaharinejad V, Delnaud L, Fouque M, Lucas A, Shirinbayan M, Fitoussi J, et al., "Enhancement of adhesion between the polymeric liner and the metallic connector of high-pressure hydrogen storage tank", *International Journal of Material Forming*, vol. 14, pp. 249-260, 2020.
2. Wallin, Steelcore Plastics, Johnson, Durus Industries, Inc. (Presentation), "Where Metal Meets Plastic", *19th Annual Fall Meeting, Association of Rotational Molders*, 1994.
3. Munzke D, Duffner E, Eisermann R, Schukar M, Schoppa A, Szczepaniak M, et al., "Monitoring of type IV com-posite pressure vessels with multilayer fully integrated optical fiber based distributed strain sensing", *Materials Today: Proceedings*, vol. 34, pp. 217-223, 2021.
4. Azeem M, Ya HH, Alam MA, Kumar M, Stabla P, Smolnicki M, et al., "Application of Filament Winding Technology" in Composite Pressure Vessels and Challenges: A Review. *Journal of Energy Storage*, vol. 49, 103468, 2022.
5. Alam S, Yandek GR, Lee RC, Mabry JM., "Design and development of a filament wound composite over-wrapped pressure vessel" *Composites Part C: Open Access*, vol. 2, 100045, 2020.
6. Nebe M., Asijee T.J., Braun C., van Campen J.M.J.F., Walther F., "Experimental and Analytical Analysis on the Stacking Sequence of Composite Pressure Vessels". *Composite Structures*, vol. 247, 112429, 2020.
7. Tew B.W., "Preliminary Design of Tubular Composite Structures using Netting Theory and Composite Degradation Factors", *Journal of Pressure Vessel Technology*, vol. 117, pp. 390-394, 1995.
8. Teijin Limited (Personal Communication, 2022). ITS50 24k/ Epikote 05940 (Epikure 05900 towpreg).
9. Gąsior P, Wachtarczyk K, Błachut A, Kaleta J, Yadav N, Ozga M, et al., "Validation of Selected Optical Methods for Assessing Polyethylene (PE) Liners Used in High Pressure Vessels for Hydrogen Storage", *Applied Sciences*, vol. 11, 5667, 2021.

GENERAL SYMPOSIA | MODELING AND SIMULATION

Optimizing Modeling the Multilayer Coextrusion Flow of Non-Newtonian Fluids Through Rectangular Ducts: Appropriate Shear Rate Definition for a Local Power Law Formulation

Thomas Naderer, Alexander Hammer, Wolfgang Roland, Maximilian Zacher and Gerald Berger-Weber

DOI: https://doi.org/10.51573/Andes.PPS39.GS.MS.4

December 2024

Optimizing Modeling the Multilayer Coextrusion Flow of Non-Newtonian Fluids Through Rectangular Ducts: Appropriate Shear Rate Definition for a Local Power Law Formulation

Thomas Naderer, Alexander Hammer, Wolfgang Roland, Maximilian Zacher and Gerald Berger-Weber[1]

Abstract: The accuracy of viscosity predictions is a crucial aspect of polymer melt flow modeling and essential for the design of coextrusion die systems. In the field of non-Newtonian fluid modeling for coextrusion flows through rectangular ducts, significant progress has been made in understanding multilayer flow dynamics. Our fundamental research, employing numerical techniques such as the shooting method, finite element method, and finite difference method for flow evaluation, has established a critical base for the field. Our current research advances fluid dynamics by refining our existing numerical solver, specifically developed for multilayer coextrusion flows. We aim to enhance the solver's performance by implementing more sophisticated calculations of shear rates that go beyond the traditional approach. The traditional approach often relies on average flow velocities and channel heights, which can underrepresent the complexity of experimentally studied polymer multilayer flows. Our study systematically compares various definitions for characteristic shear rates to describe the local shear rate dependent viscosity behavior using, for instance, a local power law model. A thorough error analysis quantifies the accuracy of each model and its predictive limitations for industrially relevant material combinations and operating conditions. This includes CFD simulations and experimental data comparisons, employing methods aligned with our fundamental research in

1 The authors Thomas Naderer (thomas.naderer@jku.at), Alexander Hammer, Wolfgang Roland, Maximilian Zacher and Gerald Berger-Weber are affiliated with the Institute of Polymer Processing and Digital Transformation at the Johannes Kepler University Linz in Austria.

DOI: https://doi.org/10.51573/Andes.PPS39.GS.MS.4

this area. Furthermore, our work paves the way for integrating these advanced fluid dynamics models into the evolving field of process digitalization, thereby contributing to the development of more efficient, digitally integrated manufacturing processes.

Introduction

Coextrusion is a pivotal technology in plastics processing that enables the creation of advanced polymeric multilayer structures, each layer imparting different functionalities within a single product. Accurate modeling of the coextrusion process is essential for fine-tuning process parameters, aiding in the design of feedblocks and dies, and preventing interfacial flow instabilities that can compromise product quality.

The numerical modeling of non-Newtonian fluid flows, particularly in the context of coextrusion, has experienced significant advancements. Traditional computational fluid dynamics (CFD) simulations, though effective, often require substantial computational resources and in-depth knowledge of the operators. Hence, our research leverages the shooting method [1], which is well-suited for such boundary value problems. Combined with a local power law formulation, coextrusion flows of non-Newtonian fluids with any number of layers can be predicted much more efficiently via the reduction of calculation time at simultaneously high accuracies.

This study specifically focuses on refining our numerical solver MultiSim [2] for multilayer flows. By implementing more sophisticated definitions of the representative shear rate for the local power law formulation, we aim to capture the rheological behavior of polymer melts more accurately. To this end, we compare various definitions of characteristic shear rates defined by: (i) the average flow velocity divided by channel height (i.e., reference shear rate), (ii) the representative shear rate as commonly employed in mono-extrusion flows to approximate the non-Newtonian flow behavior by a Newtonian one [3], and (iii) an average shear rate per layer of the flow. Through a thorough error analysis, we quantify the accuracy and limitations of each model both experimentally and by means of CFD simulation for industrially relevant material combinations and operating conditions. This research not only enhances the understanding of multilayer flow dynamics but also paves the way for integrating advanced fluid dynamics models into digitally integrated manufacturing processes, contributing to the development of more efficient production systems [1,4].

Experimental Setup

The coextrusion experiments were performed on a novel coextrusion demonstration die with a constant rectangular cross section, allowing for a well-controllable, stratified two-layer flow. To control the die temperature, heating cartridges grouped into 11 heating zones along the two die inlets, the vane-type feedblock, and the stratified flow region were used. Static mixing elements at the die inlet assured thermal homogeneity of the melt streams. Melt temperatures were determined

DOI: https://doi.org/10.51573/Andes.PPS39.GS.MS.4

just before the position of the junction. The pressure drop was recorded by five pressure transducers located along the stratified flow region. Furthermore, the die includes an optical viewport to assess the layer distribution by means of an optical coherence tomography (OCT) sensor. A detailed description of this experimental setup can be found in [5]. Two identical smooth-bore single-screw extruders with conventional three-zone screws with a diameter of 30 mm and an axial length of 20.2 times the diameter were used to provide the PMMA and the ABS melt streams. The rheological characteristics of the materials were determined using high shear capillary rheometry (HKR). The measured Carreau-Yasuda parameters are presented in Table 1.

Table 1. Carreau-Yasuda rheological parameters for PMMA and ABS melt streams used in the coextrusion experiments, characterized using high shear capillary rheometry (HKR).

Material -	η_0 Pa.s	η_∞ Pa.s	λ s	a -	n_{CY} -
ABS	16,628	0	0.1305	0.4324	0.1356
PMMA	6,211	0	0.0123	0.4164	0.0075

Numerical Methods

Predicting the stratified flow of two non-Newtonian fluids through a rectangular duct generally requires numerical solution procedures.

Shooting Method

The shooting method is a numerical technique used to solve boundary value problems by converting them into initial value problems. In the context of coextrusion flow modeling, the shooting method is used to determine both the velocity profile and the position of interface between different layers. The method involves guessing the initial conditions for the system and integrating the differential equations governing the flow. The results are then compared with the boundary conditions at the other end of the domain. If the boundary conditions are not satisfied, the initial conditions are adjusted, and the process is repeated iteratively until convergence is achieved [1].

The power law function is used to capture the shear thinning behavior of non-Newtonian fluids by relating the viscosity of the fluid to the shear rate:

$$\eta = K \cdot \dot{\gamma}^{n-1}, \quad 1)$$

DOI: https://doi.org/10.51573/Andes.PPS39.GS.MS.4

where η is the viscosity, K is the consistency index, $\dot{\gamma}$ is the shear rate, and n is the flow behavior index [6,7]. The main advantage of this rheological model is its mathematical simplicity, but it fails to describe the upper Newtonian plateau as well as the transition region to the shear thinning regime. Consequently, we aim to overcome this by employing a local power law approach, which can be interpreted by employing the tangent to the viscosity curve at a shear rate characteristic for the flow. The consistency and the flow index can then be evaluated using the parameters of more sophisticated rheological models, such as the Carreau-Yasuda model:

$$n = 1 + (\eta_0 - \eta_\infty) \cdot \left(\frac{(\lambda \cdot a_T \cdot \dot{\gamma})^a}{1 + (\lambda \cdot a_T \cdot \dot{\gamma})^a} \right) \cdot \frac{(n_{CY} - 1) - a}{a}, \tag{2}$$

$$\mathrm{K} = \left(\eta_\infty + (\eta_0 - \eta_\infty)(1 + (\lambda \cdot \mathrm{a_T} \cdot \dot{\gamma})^{\mathrm{a}})^{\frac{\mathrm{n}-1}{\mathrm{a}}} \right) \cdot \mathrm{a_T} \cdot \dot{\gamma}^{1-n_{CY}}. \tag{3}$$

The Carreau-Yasuda model provides a detailed description of non-Newtonian fluid behavior, incorporating additional parameters: zero shear rate viscosity η_0, infinite shear rate viscosity η_∞, a time constant related to the fluid's relaxation time λ, power law index n_{BCY}, and a, a dimensionless parameter describing the broadness of the transition region between the Newtonian plateau and the power law region. Additionally, a_T is the temperature shift factor that adjusts the viscosity based on the temperature T, accounting for temperature-dependent behavior of the fluid.

Local Shear Rate Formulations

The local shear rate, determined by one of the following formulations, is used to calculate the local power law parameters. We tested different formulations for local shear rates to better represent the complex flow behavior in multilayer coextrusion.

Reference Shear Rate

The reference shear rate $\dot{\gamma}_{ref}$ is given by:

$$\dot{\gamma}_{ref} = \frac{v_{ref}}{h}, \tag{4}$$

where v_{ref} is the average flow velocity and h is the channel height. This local shear rate is used for all layers and represents the default shear rate formulation in our inhouse software [4].

DOI: https://doi.org/10.51573/Andes.PPS39.GS.MS.4

Averaged Shear Rate

In a multilayer system, each layer of the flow – depending on its height position within the layer configuration and the rheological properties of the melts – is imposed by a particular range of shear rates. In general, layers located closer to the lower or upper boundary experience higher velocity gradients (i.e., shear rates) than layers located closer to the velocity maximum of the overall flow. The average shear rate is calculated from the velocity profile, which influences the viscosity and, consequently, the velocity profile itself. Therefore, an iterative solution is required.

For a system with N layers, each layer has a number of divisions N_{div} discretized shear rate values. Let $\dot{\gamma}_{i,j}$ represent the j-th shear rate value for the i-th layer, where $j = 1,2,\ldots,N_{div}$. The average shear rate for the i-th layer $\dot{\gamma}_{avg,i}$ is calculated as follows:

$$\dot{\gamma}_{avg,i} = \frac{1}{N_{div}} \sum_{j=1}^{N_{div}} \dot{\gamma}_{i,j}. \quad 5)$$

This equation provides the average shear rate for each layer by summing up the N_{div} discretized shear rate values and dividing by N_{div}. The solver is subsequently executed using the updated local shear rates. The shear profiles for each layer are then averaged using equation 5. This iterative process is repeated until convergence (precision threshold for $\dot{\gamma}_{avg,j}$ is set to 10^{-5} 1/s [2]) is achieved.

Representative Shear Rate

The representative shear rate $\dot{\gamma}_{rep}$ is well-known from monoextrusion pipe and slit flows and is designed to provide a single characteristic value that reflects the overall shear behavior of the flow. It is calculated using the volumetric flow rate and geometric parameters of the flow channel:

$$\dot{\gamma}_{rep} = \frac{6\dot{V}}{wh^2} \cdot 0.772, \quad 6)$$

where $\dot{V}$ is the volumetric flow rate, w is the width, and h is the height of the channel, whereas 0.772 is an empirical value for rectangular ducts [3].

DOI: https://doi.org/10.51573/Andes.PPS39.GS.MS.4

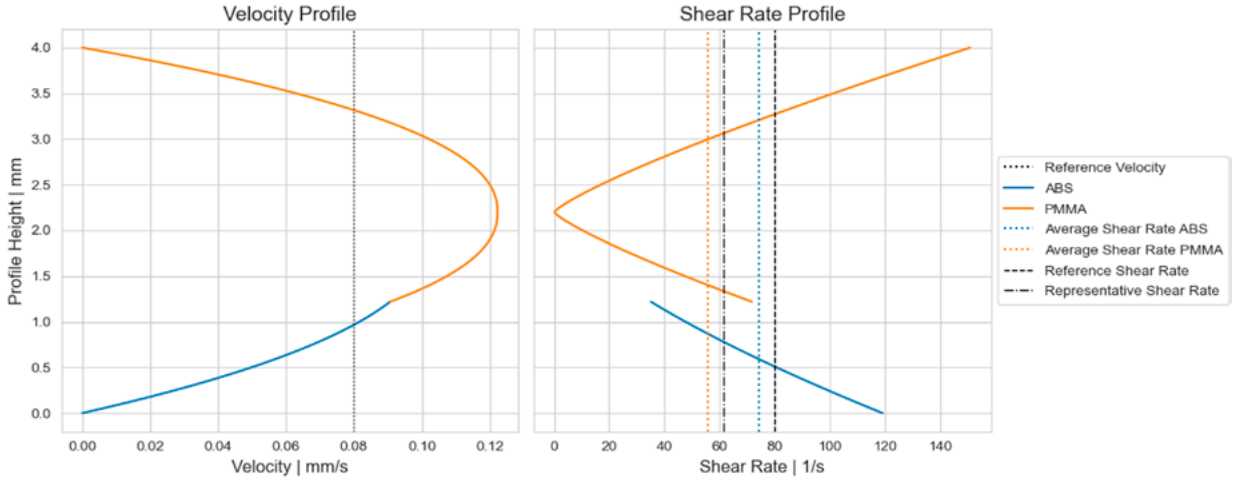

Figure 1. Velocity and shear rate profiles for ABS and PMMA two-layer coextrusion flow. The left panel shows the velocity profiles and the right panel displays the shear rate profiles. Reference, average, and representative shear rates are indicated to compare different shear rate formulations.

Figure 1 illustrates the velocity and shear rate profiles for ABS and PMMA layers in a multilayer coextrusion flow, representing one of the systems that were also experimentally examined. The left panel shows the velocity profiles, with the reference velocity v_{ref} marked by a dotted vertical line. The right panel presents the shear rate profiles, with vertical lines highlighting different shear rate formulations: the dotted orange line for the average shear rate of PMMA, the dashed line for the reference shear rate, and the dash-dot line for the representative shear rate.

Results

The results include a comparison of Ansys [8] CFD multiphase simulations (volume-of-fluid approach) with our solver calculations using the implemented shear rate formulations. The solver showed a significant reduction in computational time while maintaining accuracy (Table 2, Figure 2).

Table 2. Mean relative error (MRE) and standard deviation (in parentheses) for interface positions using different shear rate formulations in reference to the ANSYS CFD Multiphase Simulation. Pressure drop data is not included, as it was not available for the CFD simulation.

Shear Rate Formulation -	MRE Interface Positions %
Average Shear	1.12(±2.42)
Reference Shear	0.95(±2.67)
Representative Shear	1.05(±2.12)

DOI: https://doi.org/10.51573/Andes.PPS39.GS.MS.4

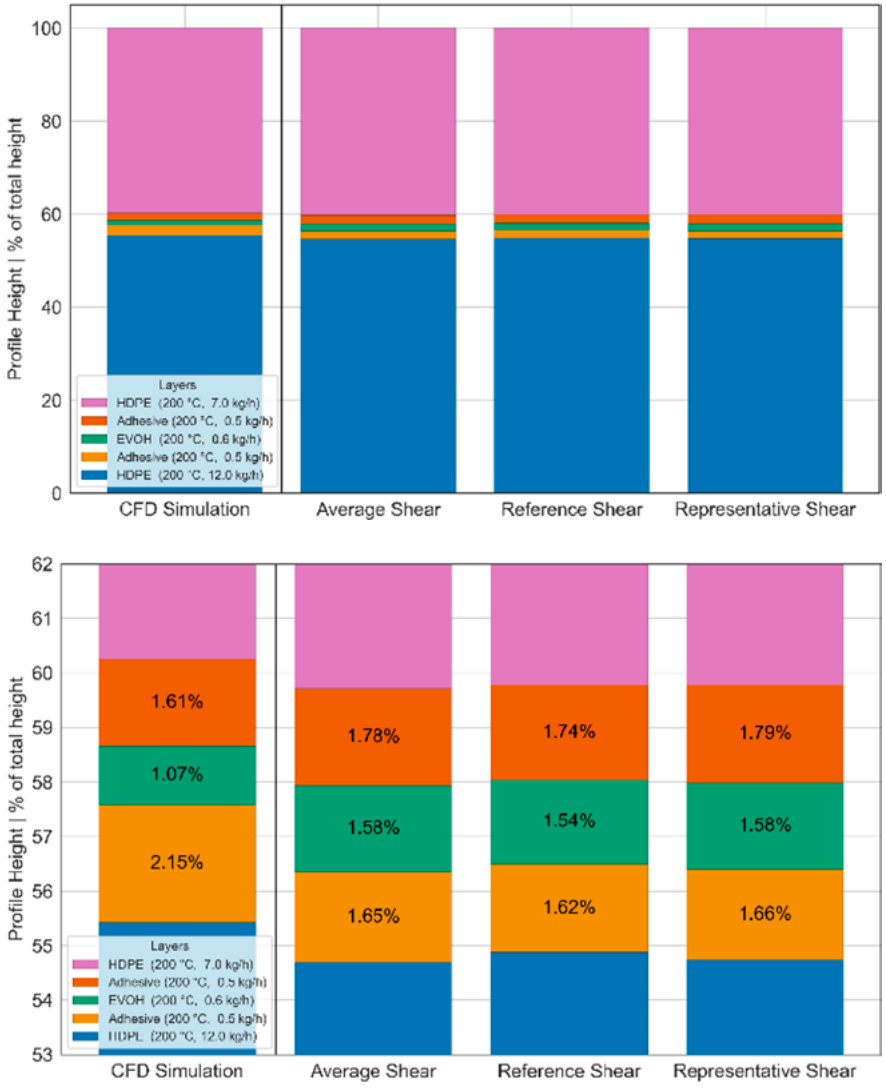

Figure 2. Comparison of numerical solver predictions and experimental results for interface positions in multilayer coextrusion. The left diagram shows the profile height percentages of different layers for the CFD simulation and the three shear rate formulations (average shear, reference shear, and representative shear). The right diagram provides a zoomed-in view of the height range from 53% to 62% of the total height, highlighting finer details of the interface positions for the different shear rate formulations.

Experimental Validation

The numerical results have been validated with experimental data from nine coextruded PMMA/ABS experiments. These experiments involved precise measurements of interface positions, pressure drop along the extrusion die, and comprehensive parameter studies. The mean relative error (MRE) was used to quantify the deviations between the solver predictions and experimental values,

DOI: https://doi.org/10.51573/Andes.PPS39.GS.MS.4

as shown in Table 3. This setup, consistent with previous studies [5], ensured reliable data collection and validation. The average deviation of the solver's prediction compared to the experimental data is shown in Table 3:

Table 3. Mean relative error (MRE) including standard deviation (in parentheses) for interface positions and pressure drop using different shear rate formulations compared to experimental values over nine experiments.

Shear Rate Formulation -	MRE Interface Positions %	MRE Pressure Drop %
Average Shear	11.42 (±1.69)	11.16 (±3.09)
Reference Shear	7.59 (±1.15)	12.23 (±7.76)
Representative Shear	13.74 (±9.02)	324.25 (±311.31)

Discussion

The results demonstrate that this refined numerical solver can accurately predict interface positions and shear rates in multilayer coextrusion flows. The newly implemented shear rate formulations provide a good match with experimental data and CFD simulations, enhancing the reliability and flexibility of our predictions for industrial applications.

Our results include a detailed comparison between Ansys CFD multi-phase simulations and our solver calculations using the implemented shear rate formulations. The solver demonstrated a significant reduction in computational time while maintaining accuracy. The mean relative error (MRE) for interface positions was 1.12% for the average shear rate, 0.95% for the reference shear rate, and 1.06% for the representative shear rate. These findings highlight the efficiency and effectiveness of our solver in reducing computational time without compromising on accuracy.

In our analysis of the shear rate formulations, the average shear rate generally provided better agreement with the experimental layer distribution, showing lower MRE in most cases compared to the reference shear rate. However, the representative shear rate, while sometimes showing good agreement with the kappa fraction, exhibited significantly higher MRE values for pressure drops. Specifically, the MRE for pressure drops using the representative shear rate was consistently high, indicating that this formulation may not be suitable for accurate pressure drop predictions in multilayer coextrusion flows.

These findings suggest that the average shear rate is more reliable for predicting layer thickness fractions, whereas the reference shear rate may offer a balanced performance, and the representative shear rate does not provide a benefit. The use of OCT technology has proven essential in obtaining precise interface measurements, further validating our model's accuracy.

DOI: https://doi.org/10.51573/Andes.PPS39.GS.MS.4

Overall, our refined numerical solver and improved shear rate formulations significantly enhance the predictive capabilities for multilayer coextrusion flows. This advancement not only aligns well with experimental observations but also offers a practical and efficient tool for industrial applications.

Conclusion and Outlook

Our study demonstrates that the refined numerical solver significantly reduces calculation time while maintaining precise predictions of interface positions and shear rates in multilayer coextrusion flows. The average shear rate formulation emerged as the most reliable for predicting layer thickness fractions, while the reference shear rate offered balanced performance. The representative shear rate, though useful in some scenarios, showed limitations in pressure drop predictions.

Future research should test the effectiveness of different shear rate formulations for various multilayer structures, including symmetrical, asymmetrical, and varying numbers of layers, to determine the best formulation for specific conditions. Additionally, developing and testing new shear rate formulations could enhance prediction precision.

More extensive experimental validations and CFD simulations are necessary to support these developments. Testing under diverse operating conditions and with a broader range of polymer materials will ensure the robustness and generalizability of the models. Continuous refinement of solver capabilities to handle complex geometries and multilayer dynamics will also be crucial.

References

1. A. Hammer, W. Roland, C. Marschik, and G. Steinbichler, “Applying the Shooting Method to Predict the Co-Extrusion Flow of Non-Newtonian Fluids Through Rectangular Ducts,” May 2021.
2. Thomas Naderer, Rene Huber, Alexander Hammer, Wolfgang Roland, Maximilian Zacher, Gerald Berger-Weber, “MultiSim–Multilayer CoExtrusion Solver Software.” Institute of Polymer Processing and Digital Transformation, Linz, 2024.
3. P. Schümmer and R. Worthoff, “An elementary method for the evaluation of a flow curve,” *Chemical Engineering Science*, vol. 33, no. 6, pp. 759–763, 1978.
4. A. Hammer, W. Roland, C. Marschik, and G. Steinbichler, “Predicting the Co-extrusion Flow of Non-Newtonian Fluids Through Rectangular Ducts – a Hybrid Modeling Approach,” *Journal of Non-Newtonian Fluid Mechanics*, vol. 295, p. 104618, Jul. 2021, https://doi.org/10.1016/j.jnnfm.2021.104618
5. A. Hammer, W. Roland, M. Zacher, S. Kohl, and G. Berger-Weber, “Experimental validation of non-Newtonian stratified co-extrusion prediction models using a digital process twin,” *Polymer Engineering & Science*, vol. 62, no. 12, pp. 3902–3922, 2022, https://doi.org/10.1002/pen.26147

DOI: https://doi.org/10.51573/Andes.PPS39.GS.MS.4

6. E. Mitsoulis and F. Heng, "Numerical simulation of coextrusion from a circular die," *Journal of Applied Polymer Science,* vol. 34, no. 4, pp. 1713–1725, 1987.

7. T. Koepplmayr and J. Miethlinger, "Application of the Network Simulation Method to Flat Dies with Inverted Prelands," *International Polymer Processing. Journal of the Polymer Processing Society*, vol. 28, pp. 322–330, Jul. 2013, https://doi.org/10.3139/217.2758

8. ANSYS, "ANSYS Fluent–CFD Software | ANSYS." 2016. [Online]. Available: http://www.ansys.com/products/fluids/ansys-fluent

DOI: https://doi.org/10.51573/Andes.PPS39.GS.MS.4

Investigation of Isotactic Polypropylene Crystallization in Processing Conditions

Vito Speranza and Roberto Pantani

DOI: https://doi.org/10.51573/Andes.PPS39.GS.MSD.1

December 2024

Investigation of Isotactic Polypropylene Crystallization in Processing Conditions

Vito Speranza and Roberto Pantani[1]

Abstract: Flow and pressure applied during polymer transformation processes of semi-crystalline polymers can significantly affect the kinetics of crystallization, final morphology, and properties of the part. In commonly used polymer transformation processes, the molten polymer is subjected to high pressure and thermal stress, as well as intense shear and elongational flow fields. The effect of pressure on crystallization kinetics is significant from both scientific and technological perspectives since the polymer solidifies under high pressure in important industrial processing techniques. On the other hand, the high shear rates experienced during the polymer processing can lead to the development of a highly non-uniform morphology that is typically very different from what is observed for quiescent crystallization of the same polymer. One example is injection molding, where the high shear rates experienced by a polymer melt close to the cold walls of the cavity can lead to a highly oriented layer ("skin" layer), whereas the low flow field close to sample mid-plane can lead to an isotropic layer ("core" layer) developing the so-called "skin-core" morphology. Thus, an understanding of polymer crystallization behavior with respect to the processing conditions is required to enable the rational design of materials and to optimize the final properties of the parts. This work explored the effects of the pressure and flow field on the kinetics of crystallization of isotactic polypropylene (i.e., iPP). The study of the effect of pressure on the crystallization kinetics of iPP was conducted using a dilatometer in the pressure range from 10 MPa to 100 MPa. Several isothermal flow experiments were carried out using two different devices: the Linkam shear cell and the Multi-Pass Rheometer (MPR). To describe the evolution into isotropic structures and fibrillar structures, a Kolmogoroff–Avrami–Evans model was adopted.

Keywords: Multipass Rheometer; Dilatometry, Flow-Induced Crystallization, Pressure Crystallization Birefringence, Orientation

1 The authors Vito Speranza (vsperanza@unisa.it) and Roberto Pantani are affiliated with the Department of Industrial Engineering at the University of Salerno in Italy.

DOI: https://doi.org/10.51573/Andes.PPS39.GS.MSD.1

Introduction

Isotactic polypropylene (iPP) is one of the most widespread polymers. It is an inert material that, when recycled, is environmentally harmless. The number of products based on iPP, from packaging to ballistic, from structural to biomedical applications, increases every day. Therefore, there's an growing interest in the optimization of production cycles of iPP parts.

Polymer transformation processes of semi-crystalline polymers can significantly affect the kinetics of crystallization, final structure, and properties of parts. In commonly used polymer transformation processes, such as extrusion, injection molding, and film blowing, the molten polymer is subjected to high pressure and thermal stress, as well as intense shear and elongational flow fields. These factors affect the polymers' crystallization and morphology that can occur during or after the imposition of flow, so the semi-crystalline morphology that develops in the final product is typically very different from what is observed for quiescent crystallization of the same polymer. Consequently, the properties of the material, mechanical as well as optical, electrical, transport, and chemical are closely related to these aspects: crystallinity and morphology. Thus, an investigation of the influence of pressure and shear field on the iPP crystallization is required to enable the rational design of materials and to tailor the final properties of the part. Pressure has been found to play a crucial role in the evolution of crystallization [1]. The dependence upon pressure on the iPP crystallization kinetics has been investigated using two main approaches: an off-line approach [2,3], and an on-line approach [3-5]. In the first approach, a thermal protocol, which also involves a given pressure, is adopted for the iPP sample solidification. After that, the final sample crystallization is investigated using several techniques. With such an approach, any data about the crystallinity evolution are missing. In the latter approach, a property directly related to crystallinity, such as heat or specific volume, is monitored during the iPP solidification under pressure conducted in a high-pressure calorimeter or dilatometer. Thus, the crystallinity evolution can be analyzed even if the cooling rates adopted are generally different from the ones experienced by the polymer during the real processing conditions.

Understanding of the nature of flow-enhanced crystallization remains a challenge, especially related to the availability of experimental data. Obtaining experimental data during flow-induced tests is quite challenging. However, several works have been proposed recently to investigate the morphology development under flow [6,7]. The influence of the processing conditions on the morphology distribution has been widely investigated [8]. A tool able to describe the effect of flow on the final microstructure distribution in the iPP sample is not yet available [9], but its development will surely be key to predicting the final product properties.

In this work, an on-line technique is adopted to study the effect of pressures and cooling rates on the crystallinity evolutions. A Gnomix apparatus is used to perform pressure-volume-temperature (PvT) acquisition during the dilatometric tests. Isobaric non-isothermal tests at different cooling rates in the pressure range from 10 MPa to 100 MPa are carried out. The effect of flow on both the

DOI: https://doi.org/10.51573/Andes.PPS39.GS.MSD.1

isothermal iPP kinetics and morphology has been investigated. A Multi-Pass Rheometer (MPR) has been adopted for the isothermal flow induced tests. A polarimeter has been coupled with the MPR to measure the birefringence evolution during the test.

A crystallization kinetics model coupled with a macromolecular evolution model was used to consider the effect of flow on crystallinity evolutions through the molecular stretch [10,11]. The kinetics model accounts for the formation of different morphologies (spherulites and fibers) in the iPP. Predictions of the evolution of molecular stretch, morphology, and degree of crystallinity were compared with experimental data.

Materials and Methods

For the iPP dilatometric and flow induced tests, a commercial grade iPP resin (T30G, Mw = 481000, Mn = 75000, tacticity=87.6%mmmm), kindly supplied by Montell (Ferrara, Italy), was adopted. A complete characterization of the adopted iPP (T30G, Basell, Switzerland) was conducted, considering the rheology, crystallinity, and interplay among these properties. One of the aims of this work was to study the variations of specific volume of the iPP in processing conditions. Dilatometry was the technique adopted to measure the bulk specific volume, both in the melt and solid state of polymers, as a function of pressure and temperature variations. Two measuring principles exist in the dilatometry technique: confining fluid dilatometers and piston-die dilatometers. A confining fluid dilatometer, Gnomix, was used in this work. In the Gnomix dilatometer, the polymer, in the form of pellets, is put into a rigid chamber where it is submerged in a fluid. This dilatometer subjects the polymer to a hydrostatic pressure in all directions. However, the drawback is that the measured volumetric changes are not exclusively due to the sample, but also affected by the presence of the confining fluid. The crystallization of materials was studied in isobaric conditions with varying values of pressure and cooling rates. Four values of pressure 10, 30, 50, and 100 MPa and two values of cooling rates, 1 and 2.5°C/min were considered. During the PvT tests, the iPP was first heated to 200°C, above the melting temperature, adopting a heating rate of about 3°C/min. After that, it was kept at 200°C for 10 min to delete all the effect on the sample of the previously applied thermo-mechanical history. Next, the sample was pressurized to the desired value and, finally, it was cooled at constant pressure to a temperature of 40°C adopting a constant cooling rate.

To obtain quantitative information about the flow-induced crystallization kinetics and the crystalline degree evolution into the material on this iPP grade, some isothermal flow experiments were carried out at a temperature of 140°C, using the multipass rheometer MPR to apply flow. The MPR is a double-piston capillary rheometer that adopts as flow geometry a 1.5 mm thick rectangular slit. Different piston speeds and shearing times were considered: 1 mm/s with 15 s and 10 mm/s with 2.5 s, respectively. The MPR was coupled with a polarimeter to monitor, for different shear conditions, the evolution of the transmitted light intensity passing through the sample. Ring-shaped samples obtained by a mini-injection molding machine, BABYPLAST 6/10 were used in the MPR.

DOI: https://doi.org/10.51573/Andes.PPS39.GS.MSD.1

The ring-shaped sample dimensions are 21 mm inner diameter, 22 mm outer diameter, and 2.5 mm height. The sample weight is about 60 mg. In situ optical techniques, such as the light depolarization technique (LDT), provide information about the formation of oriented and crystalline structures averaged over the thickness of the flow device. To describe the morphology evolutions during MPR tests, a recently developed crystallization kinetics model was adopted. The kinetics model describes the competing evolution of fibers and spherulites for the iPP alpha phase. The effect of flow on nucleation and growth processes of both morphologies is accounted for through the molecular stretch. A non-linear Maxwell model is adopted for the description of molecular stretch evolution during the flow experiments. The evolution of molecular stretch and of morphology and crystallinity degree predicted by the model were compared with experimental data.

The Alpha Phase Crystallization Model

The overall relative crystallinity degree ξ of the alpha crystalline phase is given by equation 1.

$$\frac{d\xi}{dt} = (1-\xi)\left(\frac{d\psi_0}{dt} + \frac{d\varphi_0}{dt}\right) \quad 1)$$

where ψ_0 is the space occupied by fibrils and ϕ_0 is the space occupied by spherulites described by adopting Kolmogoroff's equation:

$$\varphi_0 = \frac{4}{3}\pi \int_{-\infty}^{t} \dot{N}_s(s)\left[\int_s^t G_s(u)du\right]^3 ds \; ; \psi_0 = 2\pi \int_{-\infty}^{t} \dot{N}_f(s) \int_s^t G_f(u)\left[\int_u^t G_{lat}(p)dp\right]^2 du\, ds \quad 2)$$

where $\dot{N}_s$ and G_s are the nucleation and the growth rates of the spherulites, where $\dot{N}_f$ represents the nucleation rate of the fibrils (equal to $\dot{N}_s$), G_f is the fibrils axial growth rate (in other words the growth rate along the flow direction), and G_{lat} represents the growth rate in the direction transverse to the flow (equal to G_s). Spherulitic nucleation and growth rate under quiescent conditions are assumed function of temperature according to [10]:

$$N_s(T) = \frac{N_0}{\left(1+A_n exp(B_n(T-T_m))\right)} \; ; G_s(T) = G_0 exp\left(-\frac{U}{(R(T-T_\infty))}\right) exp\left(-\frac{K_g(T+T_m)}{(2T^2(T_m-T))}\right) \quad 3)$$

The effect of flow on crystalline kinetics functions is considered through the molecular orientation whose evolution is described with a non-linear Maxwell equation:

$$\frac{D}{Dt}\overline{\overline{A}} - \left(\overline{\overline{\nabla}}\overline{\mathrm{v}}\right)^T \times \overline{\overline{A}} - \overline{\overline{A}} \times \left(\overline{\overline{\nabla}}\overline{\mathrm{v}}\right) = -\frac{1}{\lambda}\overline{\overline{A}} + \left(\overline{\overline{\nabla}}\overline{\mathrm{v}}\right)^T + \left(\overline{\overline{\nabla}}\overline{\mathrm{v}}\right) \quad 4)$$

DOI: https://doi.org/10.51573/Andes.PPS39.GS.MSD.1

where $\overline{\overline{A}}$ is the molecular conformation tensor, $\overline{\nabla}\overline{v}$ is the velocity gradient, and λ is the relaxation time depending on the molecular stretch. The molecular stretch parameter Δ corresponds to the largest difference between the eigenvalues of the molecular conformation tensor $\overline{\overline{A}}$. λ is dependent upon Δ:

$$\lambda(T,P,\xi,\Delta) = \frac{\lambda_0 \cdot 10^{\frac{-C_1(T-T_0-C_3P)}{C_2+(T-T_0)}}}{1+(a\Delta)^b} \cdot exp^{h\xi^2} \quad 5)$$

The flow induced crystallization is considered adopted in the expression of growth rate (equation 3) a T_m depending on Δ. Furthermore, an additional nucleation rate was correlated to the excess of growth rate by effect of flow with respect to the quiescent growth rate [10,11]. The effect of molecular stretch is even more relevant for fibers, and according to the proposed model affects both growth and nucleation processes. The dependence of G_f upon molecular stretch can be expressed as:

$$G_f(\Delta) = A_0 \cdot \Delta^b \quad 6)$$

Values of the parameters adopted in equations 1-6 are reported in Table 1.

Table 1. Parameters adopted for the crystallization kinetics model (equations 1-6).

Parameter	Value	Parameter	Value	Parameter	Value	Parameter	Value
N_0 [nuclei/cm³]	1.95 10^9	G_0 [cm/s]	1380	T_0 [°C]	230	A_0 [μm/s]	0.0004
A_n [–]	1.3 10^8	K_g [K²]	371381	C_1 [–]	2.5	b [-]	5
Bn [K–1]	0.155	λ_0 [s]	14	C_2 [°C]	301.4		
U/R [K]	751.6	a [–]	3.8	C_3 [°C/bar]	0.18		
T_∞ [°C]	-74.44	b [–]	2.2	h [–]	180		

The model proposed to describe the crystallization process of iPP made it possible to evaluate the average spherulite radius, R, which can be obtained from equation 7:

$$R = \sqrt[3]{\frac{3\xi}{4\pi N_a}}; N_a = \int_0^t \frac{dN_s}{dt}\big(1-\xi(p)\big)dp \quad 7)$$

where ξ and the number N_a of active nuclei refer to the end of the crystallization process.

DOI: https://doi.org/10.51573/Andes.PPS39.GS.MSD.1

Results

Dilatometer experiments were carried out with pressure ranging between 10 to 100 MPa and two different cooling conditions. Figure 1 shows the specific volume evolution during the isobaric cooling performed at 1°C/min and 2.5°C/min, respectively Figures 1(a) and 1(b).

A volume reduction is observed at each pressure as the cooling proceeds. Moreover, considering the different pressures, as the pressure increases a volume reduction is observed. The effect of pressure on volume changes is larger at a high temperature (namely in melt state) with respect to the low temperature (namely in solid state). A transition can be observed between the melt and solid states. The transition corresponds to the material crystallization. The crystallization occurs at higher temperatures as the pressure increases. Differences between melt and solid state reduce as the pressure increases: Upon increasing the cooling rate (as shown in Figure 1[b]), the crystallization occurs at slightly lower temperatures with respect to the dilatometer experiment conducted at 1°C/min (Figure 1[a]). This can be attributed to the higher cooling rate experienced by the polymer, which shifts the crystallization process to a low temperature. In conclusion, for each cooling rate, the crystallization process shifts to a higher temperature and, moreover, completes over a broader range of temperatures as pressure increases. As the cooling rate increases, the crystallinity process shifts at lower temperatures.

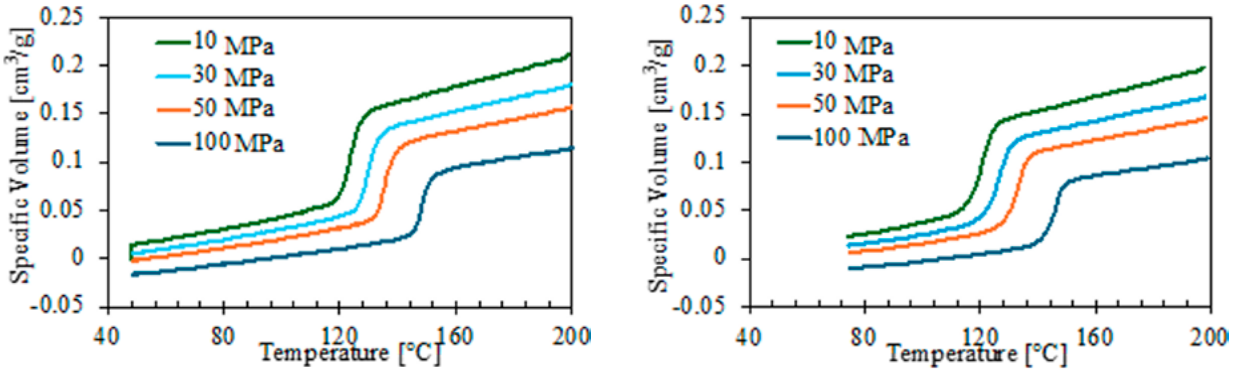

Figure 1. Specific volume evolution during the isobaric cooling performed at Gnomix PvT apparatus adopting 1°C/min cooling rate (a), 2.5°C/min cooling rate (b).

During the MPR isothermal shear flow experiments, the polarimeter began collecting data a few seconds before shear was applied and after shear continued for sufficient time to obtain the birefringence evolution during the iPP crystallization. Figure 2 shows the birefringence evolution during the MPR test conducted with 1 mm/s piston speed and 15 s shear time.

DOI: https://doi.org/10.51573/Andes.PPS39.GS.MSD.1

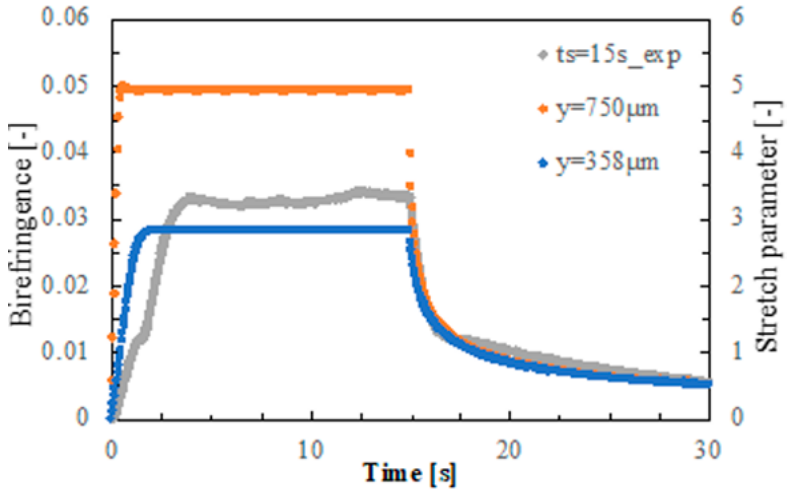

Figure 2. Birefringence evolution during the MPR test conducted with 1 mm/s piston speed and 15 s shear time. Predicted molecular stretch evolutions are also reported.

Birefringence starts to increase as the shear begins because of the molecule's orientation and stretch. After that, it reaches a plateau value that is maintained until the end of flow. After the end of shear, birefringence relaxes. Experimental acquisitions were compared with predictions obtained with the proposed model. Calculations were carried out by the proposed model at different layers from the sample midplane, considering that each layer is characterized by a different shear rate. The evolution of molecular stretch parameter and crystallinity at different layers from the sample midplane were compared with birefringence evolutions. In Figure 2, the molecular stretch parameter evolution at distances of 358 µm and 750 µm (namely at sample surface) are reported. Predictions rise up faster than measured birefringence at both distances from the sample midplane. Polymer experiences lower values of shear rate close to the sample midplane and thus the predicted stretch parameter exhibits a lower value plateau. Predictions correctly describe the birefringence relaxation. Furthermore, the model predicts that the orientation can relax after a shearing in the reported conditions, namely the sample is still completely amorphous.

Figure 3 shows the birefringence evolution for longer times in order to have information about iPP flow induced crystallization, for the tests obtained with 1 mm/s piston speed.

DOI: https://doi.org/10.51573/Andes.PPS39.GS.MSD.1

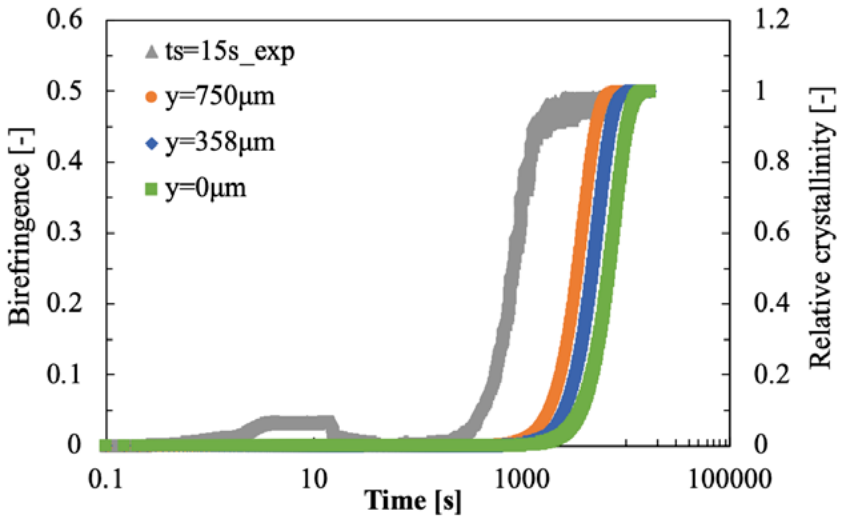

Figure 3. Birefringence evolution during the MPR test conducted with 1 mm/s piston speed and 15 s shear time. Predicted relative crystallinity evolutions are also reported.

In Figure 3, the predicted evolutions of the relative crystallinity at different distances from the sample midplane are also reported for the tests obtained with 1 mm/s piston speed. If compared with the evolution of birefringence, the predicted crystallinity evolution for the sample sheared for 15 s is slower. Evolution of crystallinity is faster at sample surface (namely 750 μm) with respect to the sample midplane (namely 0 μm).

Figure 4 shows the comparison of measured birefringence with calculated molecular stretch (Figure 4[a]) and relative crystallinity (Figure 4[b]) for the tests conducted with 10 mm/s piston speed.

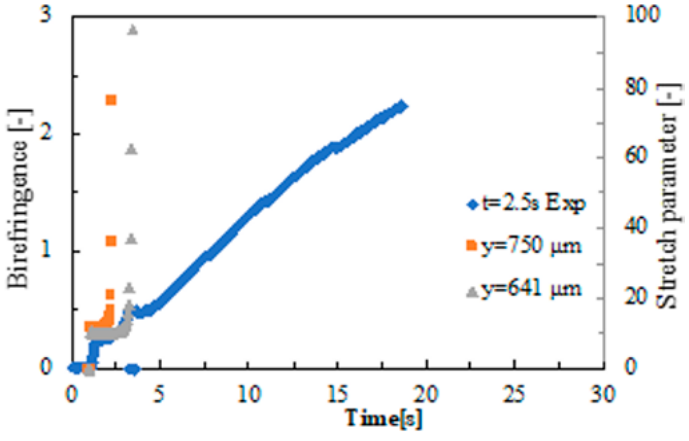

(a)

DOI: https://doi.org/10.51573/Andes.PPS39.GS.MSD.1

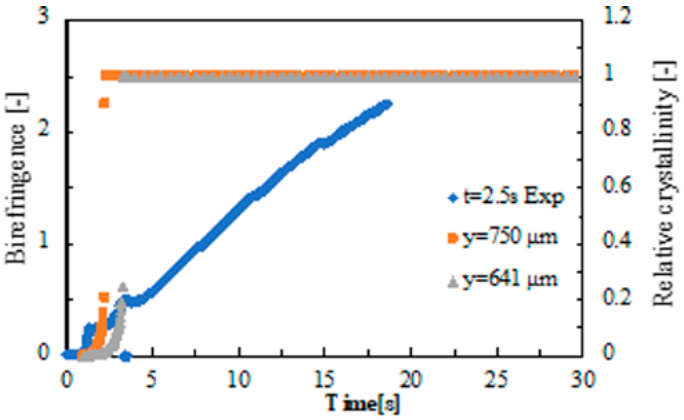

(b)

Figure 4. Birefringence evolution during the MPR test conducted with 10 mm/s piston speed and 2.5 s shear time. Comparison with predicted molecular stretch (a) and relative crystallinity evolutions (b).

A completely different situation is found for the sample sheared with a higher shear rate. As the piston speed is imposed, the calculated molecular stretch at sample surface abruptly increases after about 1 s of shear. In inner layer, the molecular stretch increases at the end of shearing time (see Figure 4[a]). In both layers, this happens because the crystalline structures rapidly fill all the available amorphous phase because of the high molecular orientation in the first seconds of shear (Figure 4[b]). This is confirmed by the experimental birefringence that continuously increases without any relaxation.

Cross-sections of the samples obtained with 10 mm/s piston speed were observed under polarized light microscopy to verify the effect of shear time on the final morphology of the structures. Figure 5 shows optical micrograph of the half-thickness of the samples sheared with a piston speed of 10 mm/s.

Near the wall (namely in the micrograph rightmost part) it is possible to observe a fibrillar layer of ~150 µm. Moving toward the sample midplane (namely in the leftmost part of the micrograph) spherulitic structure can be seen. Figure 5 shows the spherulites' size distribution along the sample half-thickness.

DOI: https://doi.org/10.51573/Andes.PPS39.GS.MSD.1

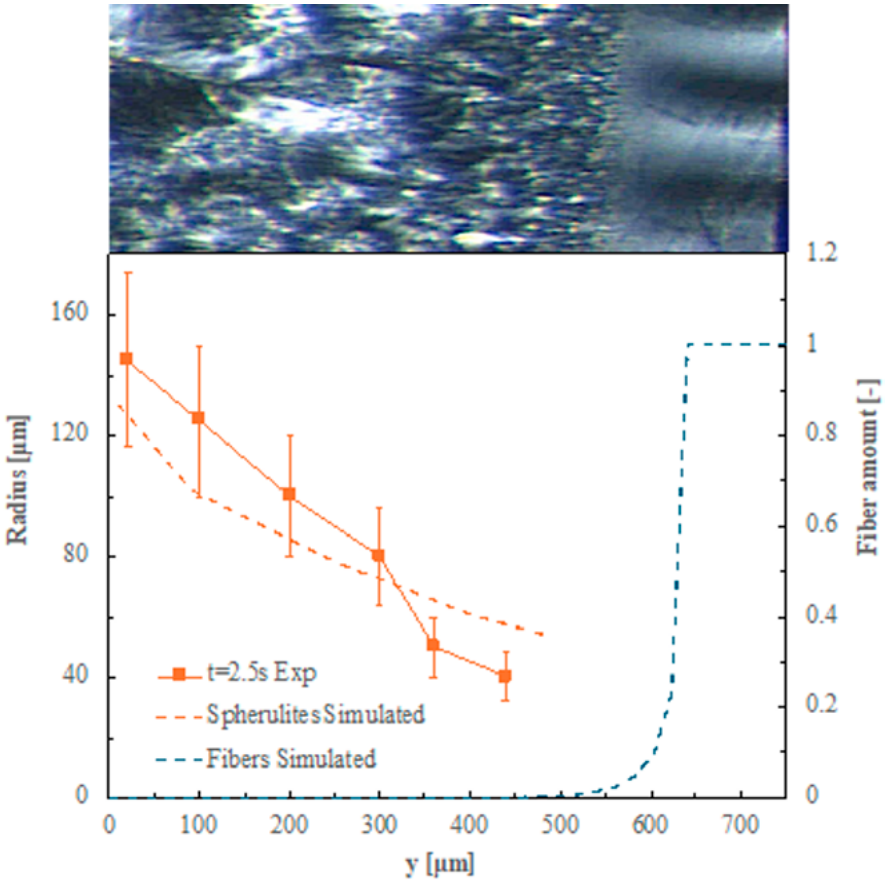

Figure 5. Morphology distribution for the samples obtained with a piston speed of 10 mm/s.

The model for crystallization kinetics adopted in this work predicts the morphology distribution along the sample thickness. In this case, simulations predict the formation of fibers close to the sample skin, whereas spherulites form closer to the midplane. The calculated number of fibers is compared with the sample micrograph in Figure 5. The fibrillar layer is only slightly underestimated. At complete crystallization, the predictions describe a fibrillar layer about 100 μm thick at the skin. Also, the predicted spherulites' dimensions are compared with the experimental results in Figure 5. Polarized optical micrographs were analyzed to determine the distribution of spherulites in the polymer sample. The optical micrographs were analyzed by the freeware software for image analysis, Fiji. Firstly, images were processed to better identify the spherulites in the micrographs. Secondly, the areas occupied by the spherulites were identified and the equivalent radii were evaluated. Finally, for each condition, the average and standard deviations of the radii distribution were determined. Consistent with the experimental observation, dimensions decrease as the distance from the sample midplane increases and thus the applied shear rate increases. Predicted dimensions concur with the measured radii of the spherulites.

DOI: https://doi.org/10.51573/Andes.PPS39.GS.MSD.1

Conclusions

This work examines the effect of pressure and flow on the crystallization kinetics of a well characterized polypropylene. Regarding pressure, specific volume measurements were performed using a confining fluid dilatometer, Gnomix, operating at pressures ranging from 10 to 100 MPa and cooling rates of 1 and 2.5°C/min. Changes in specific volumes due to the increase in pressure were larger at high temperatures (namely, in melt state) with respect to the increase at low temperatures (namely, in the solid state). Moreover, the polymer crystallization that characterizes the transition between the melt and solid states occurred at higher temperatures upon increasing the pressure and decreasing the cooling rates. In relation to flow, a rheometer, the MPR, that allows on-line measurement of the birefringence evolution and thus provides information regarding the orientation and the evolution of crystallinity, was adopted. The experimental data show that for the lowest applied shear rates, crystallization always takes place well after the end of the shear. For the largest applied shear rate, the birefringence monotonically increases, showing that crystallization takes place inside the sample during the shear step. A recently presented model to describe flow-induced crystallization was adopted to predict the evolution of crystallinity inside the samples. The results of the model in terms of the evolution of stretch and crystallinity inside the samples satisfactorily compare with the experimental data of birefringence. In particular, for the test carried out with the largest shear rate, the model predicts the start of crystallization during the shear step and a reasonable value of the thickness of the fibrillar layer at the sample skin.

References

1. C. Von Baeckmann, H. Wilhelm, F. Spieckermann, S. Strobel, G.Polt, P. Sowinski, E. Piorkowska, A. Bismarck, and M. Zehetbauer, "The influence of crystallization conditions on the macromolecular structure and strength of γ-polypropylene", *Thermochimica Acta*, vol.677, pp. 131-138, 2019. https://doi.org/10.1016/j.tca.2019.03.007
2. R. Pantani, I. Coccorullo, V. Speranza and G. Titomanlio, "Modeling of morphology evolution in the injection molding process of thermoplastic polymers", *Progress in Polymer Science*, vol. 30, no. 12, pp. 1185-1222, 2005. https://doi.org/10.1016/j.progpolymsci.2005.09.001
3. V. La Carrubba, V. Brucato, and S. Piccarolo, "Phenomenological approach to compare the crystallization kinetics of isotactic polypropylene and polyamide-6 under pressure", *Journal of Polymer Science: Part B Polymer Physics*, vol. 40, pp. 153-175, 2002. https://doi.org/10.1002/polb.10075
4. C. Nakafuku, "High pressure d.t.a. study on the melting and crystallization of isotactic polypropylene", *Polymer*, vol. 22, pp. 1673-1676, 1981. https://doi.org/10.1016/0032-3861(81)90384-0
5. M. Van Drongelen, T.B. Van Erp, and G.W.M. Peters, "Quantification of non-isothermal, multiphase crystallization of isotactic polypropylene: The influence of cooling rate and pressure", *Polymer*, vol. 53, pp. 4758-4769, 2012. https://doi.org/10.1016/J.POLYMER.2012.08.003

DOI: https://doi.org/10.51573/Andes.PPS39.GS.MSD.1

6. J. Sheng, W. Chen, K. Cui and L. Li, "Polymer crystallization under external flow", *Reports on Progress in Physics*, vol. 85, pp. 36-601, 2022. https://doi.org/10.1088/1361-6633/AC4D92

7. C. Nie, F. Peng, R. Cao, K. Cui, J. Sheng, W. Chen, and L. Li, "Recent progress in flow-induced polymer crystallization", *Journal of Polymer Science*, vol. 60, pp. 3149–3175, 2022. https://doi.org/10.1002/pol.20220330

8. S. C. Nian, C.Y. Wu and M.S. Huang, "Warpage Control of Thin-Walled Injection Molding Using Local Mold Temperatures". *International Communications in Heat and Mass Transfer*, vol. 61, pp. 102–110, 2015. https://doi.org/10.1016/j.icheatmasstransfer.2014.12.008

9. V. Speranza, S. Liparoti, and R. Pantani, "Prediction of Morphology Distribution within Injection Molded Parts Obtained with Fast Cavity Heating Cycles: Effect of Packing Pressure", *Macromolecular Materials and Engineering*, vol. 307, 2022. https://doi.org/10.1002/mame.202200436

10. R. S. Graham, "Understanding flow-induced crystallization in polymers: A perspective on the role of molecular simulations", *Journal of Rheology (N Y N Y)*, vol. 63, pp. 203–214, 2019. https://doi.org/10.1122/1.5056170

11. R. Pantani, V. Speranza, and G. Titomanlio, "Effect of Flow-Induced Crystallization on the Distribution of Spherulite Dimensions along Cross Section of Injection Molded Parts", *European Polymer Journal*, vol. 97, pp. 220–229, 2017. https://doi.org/10.1016/j.eurpolymj.2017.10.012

12. V. Speranza, S. Liparoti, V. Volpe, G. Titomanlio and R. Pantani, "Modelling of Morphology Development towards Spherulites and Shish–Kebabs: Application to Isothermal Flow-Induced Crystallization Experiments on Isotactic Polypropylene", *Polymer* (Guildf), vol.196, pp.122-459, 2020. https://doi.org/10.1016/j.polymer.2020.122459

GENERAL SYMPOSIA | RUBBER AND ELASTOMERS

Improvement of an Alternative Method for the Correction of Wall Slip Effects in Rheological Studies of Filled Rubber Compounds

Dennis Kleinschmidt, Jonas Petzke and Florian Brüning

DOI: https://doi.org/10.51573/Andes.PPS39.GS.RE.1

December 2024

Improvement of an Alternative Method for the Correction of Wall Slip Effects in Rheological Studies of Filled Rubber Compounds

Dennis Kleinschmidt, Jonas Petzke and Florian Brüning[1]

Abstract: Developing new and improved rubber compounds to meet increasing demands for application specific product properties requires detailed knowledge of material properties to be able to predict the processing behavior. Therefore, rheological material properties, which are traditionally determined using the high-pressure capillary rheometer (HPCR) are of crucial importance. Rubber compounds often exhibit flow anomalies and non-isothermal effects, influenced by the compound ingredients and processing parameters that are generally neglected in rheological studies and simulations. This work presents an improved model for describing wall slip effects based on the Coulomb wall slip model, taking into account dissipative material heating. Rheological studies were performed on a carbon black-filled SBR tire tread compound. Using slit capillaries with different geometric dimensions, the pressure dependence of wall slip effects was confirmed, allowing the separation of the flow curve into wall adherent and wall slip regions.

Keywords: High-Pressure Capillary Rheometry, Rheology, Rubber, Viscosity, Wall Slip

1 The authors Dennis Kleinschmidt (dennis.kleinschmidt@ktp.upb.de), Jonas Petzke (jonas.petzke@ktp.upb.de) and Florian Brüning (florian.bruening@ktp.upb.de) are affiliated with the Paderborn University in Germany.

DOI: https://doi.org/10.51573/Andes.PPS39.GS.RE.1

Introduction

The HPCR is widely used to characterize the flow behavior of thermoplastic melts and rubber compounds, allowing the determination of viscosity over the process-relevant shear rate range. Compared to round hole nozzles, the use of slit capillaries allows the measurement of direct pressure and temperature along the flow direction in the slit capillary, which significantly reduces the measurement effort and allows run-in effects to be neglected [1,2]. During rheological studies, a fully developed, steady flow with Newtonian flow behavior is assumed. Furthermore, dissipative material heating, wall slip, and pressure dependence of viscosity are neglected [2]. These assumptions are not fully valid for different types of complex fluids such as rubber compounds [3]. Accordingly, complex correction procedures are necessary to obtain the true viscosity data. As the shear rate increases, there is an intensification of both shear friction and shear heating. Due to the poor thermal conductivity of rubber compounds, heat accumulation and temperature rise in the material is initiated [4].

Wall slip leads to an incorrect determination of shear stresses and other material properties. When wall slip effects occur during processing, they cannot be minimized or prevented without affecting the process. Therefore, it is necessary to evaluate the wall slip behavior specific to the material and take it into account in modeling and simulation. In the literature, a differentiation is made between the Coulomb wall slip model and the slip film model. The Uhland [6] wall slip model is based on the occurrence of Coulomb friction between the flowing fluid and the flow-limiting wall. In analogy to solid friction, a certain frictional force, which is greater than the static frictional force, must be applied for the slip process. To maintain this condition, only the lower slip friction force must be exceeded. In the slip film model, a low-viscosity layer is assumed to form near the flow-limiting wall, which has a lower viscosity compared to the flowing fluid and thus represents a lubricating film. The fluid then slides on this low-viscosity layer. Therefore, this case of wall slip represents a cohesive failure [5-8].

For the quantification of wall slip velocities in rheological measurements, various approaches exist for different types of rheometers. In particular, the Mooney method [9] as well as the modified Mooney method by Geiger [10] have been used in recent work to determine slip velocities using HPCR. However, the application of the Mooney method to rubber compounds often leads to results that are not physically justifiable [13]. For a review of the main studies on wall slip effects focusing on filled rubber compounds, refer to [14], while Hatzikiriakos [3] provides a comprehensive overview of wall slip mechanisms in complex fluids, more generally.

Brockhaus describes an alternative approach for modeling the wall slip behavior of filled rubber compounds. In this approach, the total volumetric flow is separated into a slip and a shear component. This relation results from the equation of motion in conjunction with the continuity equation, taking into account the boundary condition of a wall slip velocity. It is shown that the velocity profile of the pressure flow in slit capillaries is not influenced by wall slip effects, since the slip velocity v_{slip} occurs as an increase of the total velocity in the form of a plug flow [15]:

DOI: https://doi.org/10.51573/Andes.PPS39.GS.RE.1

$$v_{slip} = \frac{\dot{V}_{total}}{WH} - \frac{nH}{2(1+2n)} \cdot \left(\frac{\tau_w}{K}\right)^{\frac{1}{n}} \quad 1)$$

v_{slip}	Wall slip velocity	$\dot{V}_{total}$	Total volume flow	W	Width of slit capillary
H	Height of slit capillary	n	Flow exponent	τ_w	Wall shear stress
K	Consistency factor				

This model approach uses the consistency factor K and the flow exponent n to characterize the wall slip velocity in order to consider the shear thinning material behavior. To determine these power law parameters, Brockhaus assumes isothermal conditions and the validity of the Coulomb slip model within the rheological investigations performed, without verifying these assumptions [15]. Since rubber compounds exhibit a shear thinning, non-Newtonian flow behavior, a shear rate correction is also required after the wall slip correction to determine the true viscosity data.

This work examined whether the wall slip behavior of filled rubber compounds depends on the flow channel geometry and can be described by the Coulomb slip model, which is the requirement for applying the wall slip correction method, according to Brockhaus. In addition, dissipative material heating is considered in rheological research in order to verify Brockhaus' assumption of an isothermal flow.

Materials

To demonstrate that the viscosity data for wall adhesion is independent of the flow channel geometry used, preliminary tests were performed on a low-density polyethylene (Lupolen 1840 D) from LyondellBasell used in blown film extrusion. A sulfur crosslinking styrene-butadiene rubber (SBR) tire tread compound was used for the wall slip studies. The base of the compound is a SBR 1502 to which 40 phr of carbon black N 347, 70 phr of silica, and 9.5 phr of processing oils, processing aids, and crosslinking chemicals have been added.

Equipment and Experimental Design

The characterization of the flow behavior was performed on a Rheograph 50 HPCR from Göttfert Werkstoff-Prüfmaschinen GmbH, Buchen (Germany), using four slit capillaries with different cross-sectional area (see Table 1). Three equidistant pressure transducers were used along the length of each slit capillary to determine the normal pressure orthogonal to the flow direction. A shear rate

DOI: https://doi.org/10.51573/Andes.PPS39.GS.RE.1

range of 0.1 to 1,000 s^{-1} was considered, with measurements taken from high to low shear rates at 200°C for the LDPE and from 80°C to 100°C for the rubber compound.

Table 1. Geometric data of the slit capillaries used.

	Cross-sectional area of the slit capillary (W x H)			
Dimension	10 mm x 0.5 mm	10 mm x 1 mm	12 mm x 1.2 mm	15 mm x 1.5 mm
Width	10 mm	10 mm	10 mm	10 mm
Height	0.5 mm	1 mm	1.2 mm	1.5 mm
Length	100 mm	100 mm	100 mm	100 mm

Results

To validate the assumption that the viscosity data is independent of the flow channel geometry used under conditions of wall adhesion, rheological tests were performed using an LDPE. The viscosity data obtained were corrected using the Weissenberg-Rabinowitsch method and approximated using the Carreau model [1]:

$$\eta = \frac{A}{(1 + B \cdot \dot{\gamma})^C} \qquad 2)$$

η	Viscosity	A	Zero viscosity	B	Transition time
$\dot{\gamma}$	Shear rate	C	Flow exponent		

Table 2 shows that the viscosity data in the considered shear rate range is approximately independent of the geometry and therefore the assumption of wall adhesion is valid.

Table 2. Carreau parameter for the LDPE at 200°C for the slit capillaries used.

Carreau parameter	Cross-sectional area of the slit capillary (W x H)			
	10 mm x 0.5 mm	10 mm x 1 mm	12 mm x 1.2 mm	15 mm x 1.5 mm
A [Pas]	83,774.6	50,401.6	44,981.8	47,453.1
B [s]	25.31	9.78	8.65	9.41
C [-]	0.59	0.60	0.60	0.60

DOI: https://doi.org/10.51573/Andes.PPS39.GS.RE.1

Figure 1 shows the apparent viscosity curves for the rubber compound at two different processing temperatures.

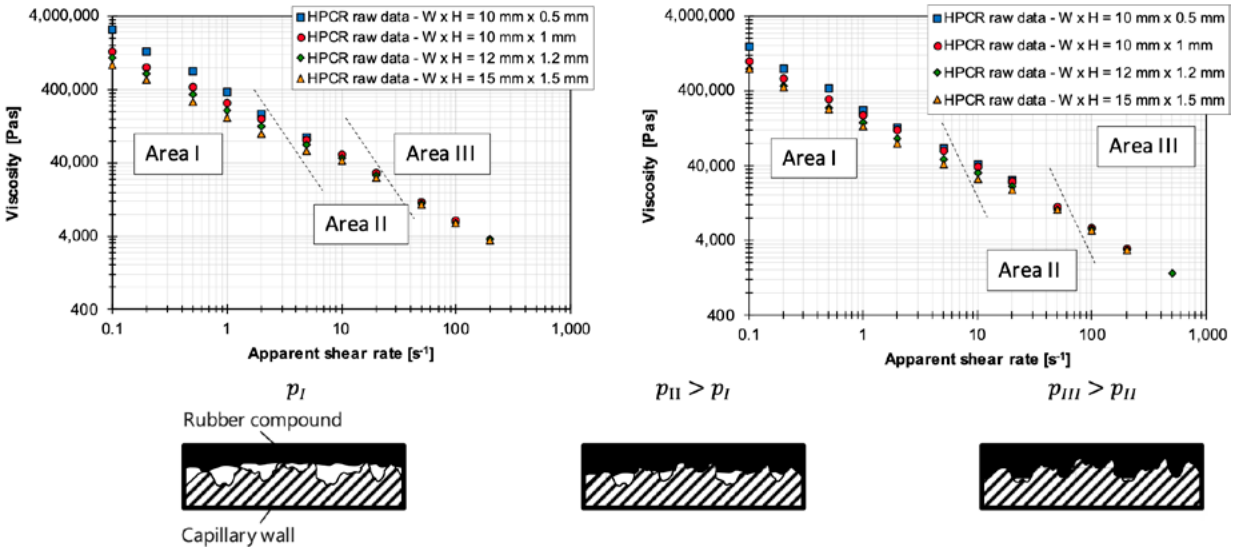

Figure 1. Subdivision of the apparent viscosity curves for 80°C (left) and 100°C (right) taking into account the pressure dependence of the contact area between the flowing rubber compound and the flow-limiting capillary wall.

The comparison clearly shows that there is a significant geometry dependence of the resulting apparent viscosity curve in the low apparent shear rate range. The geometry dependence of the data decreases with increasing apparent shear rate, equivalent to increasing wall shear stress ($\tau_w = \eta \cdot \dot{\gamma}$), until the viscosity data is approximately geometry independent.

The viscosity data available can be divided into three areas with sectionally valid power law functions, as already recognized by Brockhaus [15]:

$$\eta = K \cdot \dot{\gamma}^{n-1} \qquad 3)$$

η	Viscosity	K	Consistency factor	$\dot{\gamma}$	Shear rate
n	Flow exponent				

Using power law functions is sufficient for describing the shear thinning flow behavior of rubber compounds, since Leblanc et al. detected neither a yield point or a Newtonian viscosity plateau for highly filled rubber compounds at very low shear rates [16,17]. The determination of the partial

DOI: https://doi.org/10.51573/Andes.PPS39.GS.RE.1

areas is automated using the method of least squares. The power law parameters of the uncorrected viscosity data obtained for the different areas at 80°C are summarized in Table 3.

Table 3. Power law parameters of the uncorrected viscosity data for the different areas at 80°C.

Power law parameter	Area	Cross-sectional area of the slit capillary (W x H)			
		10 mm x 0.5 mm	10 mm x 1 mm	12 mm x 1.2 mm	15 mm x 1.5 mm
K [Pas]	I	355,762	262,133	209,013	165,080
	II		259,580	197,236	145,747
	III		428,565	342,317	301,798
n [-]	I	0.14	0.30	0.29	0.28
	II		0.28	0.36	0.43
	III		0.09	0.13	0.15

As the determined power law parameters have a direct influence on the wall slip velocity (see equation 1), the automated determination of the partial areas reduces the error rate compared to the manual and objective determination of Brockhaus. The accuracy of the range subdivision increases as the number of data points in the shear rate range under consideration increases.

For the description of the geometry dependence of the rheological data, the model concept of the pressure dependence of the contact surface between the rubber compound and the flow-limiting wall of the flow channel by Jepsen and Räbinger [18] is used. In rheological studies, an increase in the prevailing pressure with increasing shear rate causes the rubber compound to move into the surface roughness of the flow-limiting wall, thereby increasing the adhesion force (see Figure 1 bottom). At high shear rates, the adhesion force is large enough that any slip motion stops, and no slip motion occurs according to the Coulomb slip model [18]. The results are consistent with observations on wall slip for various materials in literature, where the wall slip effects are greatest when the pressure level reaches a minimum [8]. The nonlinear pressure gradient in the direction of the flow channel also indicates wall slip according to the Coulomb slip model [10]. The Uhland [11] wall slip model is based on the occurrence of Coulomb friction between the melt and the flow-limiting wall. In analogy to solid friction, a certain frictional force, which is greater than the static frictional force, must be applied for the slip process. To maintain this condition, only the lower slip friction force must be exceeded [11,12]. In addition, the experimental investigations yielded homogeneous, smooth extrudate strands throughout, confirming the model concept of Jepsen and Räbinger [18].

An infrared thermal imaging camera was used to determine the outlet temperature of the material strands during the rheological studies. In the shear rate range under consideration, an increase

in the shear rate leads to a measurable material heating of up to approximately 15°C on the rubber surface based on the set process temperature. Since an increase in temperature leads to a higher chain mobility and thus to a reduction in viscosity, the shear thinning material behavior of the rubber compound is overestimated, which requires a temperature correction of the viscosity data before the wall slip correction, which is neglected by Brockhaus. In order to have comparable starting points for the wall slip and shear rate correction both for the different apparent shear rates in the slit capillaries and between the slit capillaries, a temperature shift is carried out using the Arrhenius approach [1]:

$$\eta_{corr} = e^{\left(\frac{E_0}{R}\cdot\left(\frac{1}{T_{out}}-\frac{1}{T_{set}}\right)\right)} \cdot \eta \qquad 4)$$

η_{corr}	Temperature-corrected viscosity	E_0	Activation energy	R	Gas constant
T_{out}	Material outlet temperature	T_{set}	Set temperature		

The application of the wall slip correction to the temperature corrected viscosity data shows that an increase in the flow channel cross section leads to higher slip ratios, as the viscosity data is increasingly shifted to lower values (see Figure 2). The use of the Weißenberg-Rabinowitsch correction to take into account the shear thinning flow behavior of filled rubber compounds leads to the true viscosity data under the boundary condition of wall adhesion.

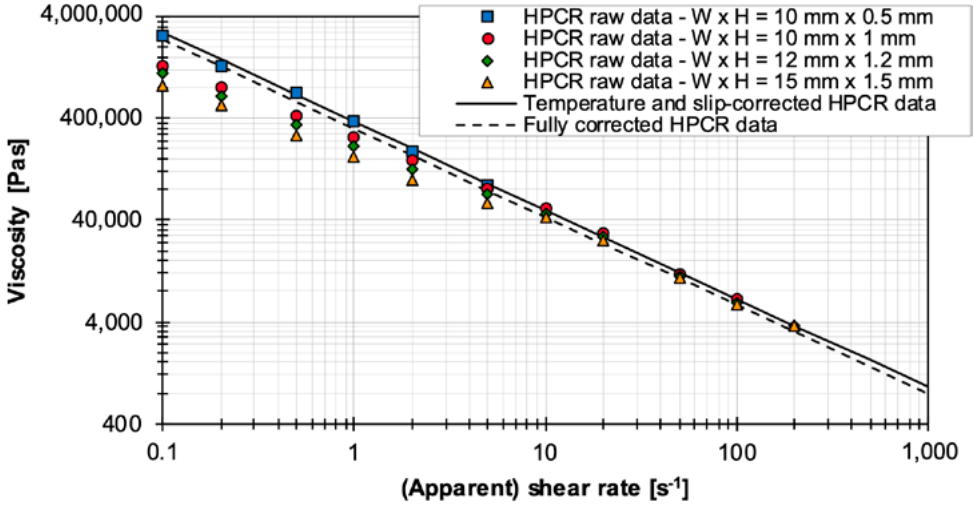

Figure 2. Comparison of viscosity data after different stages of the correction plan.

DOI: https://doi.org/10.51573/Andes.PPS39.GS.RE.1

The distinction between wall slip and wall adhesion is made on the basis of the critical wall shear stress. With respect to the available experimental data, the critical wall shear stress represents the transition wall shear stress between areas II and III. It is found that a temperature invariant critical wall shear stress of approximately 570 kPa is determined for the filled rubber compound (see Figure 1). Unlike the critical wall shear stress, the critical apparent shear rate is temperature dependent. An increase in temperature results in a shift in the critical apparent shear rate to higher values because higher temperature leads to higher chain mobility, which results in a shift in viscosity to lower values. Accordingly, a higher volume flow is required to achieve a comparable wall shear stress.

Conclusion and Outlook

The experimental investigations of the tire tread rubber compound have revealed that the wall slip behavior of filled rubber compounds is significantly influenced by the existing pressure level in the flow channel geometry and thus by the existing wall shear stress. The results show that the existing wall slip effects can be described with the Coulomb slip model, taking into account the model concept of the pressure dependence of the contact surface by Jepsen and Räbinger. This represents the starting point for the use of the wall slip correction method according to Brockhaus, which was extended by an automated partial area determination and the consideration of dissipative material heating. In further investigations, the evaluation routine presented is applied to EPDM rubber compounds used in the field of technical elastomer products.

Acknowledgements

This research was funded by the Deutsche Forschungsgemeinschaft (DFG, German Research Foundation) — SCHO551/48-1.

References

1. T. Schröder, *Rheologie der Kunststoffe*, München (Germany): Carl Hanser Verlag, 2018.
2. C. W. Macosko, *Rheology. Principles, Measurements and Applications*, New York: Wiley-VCH, 1994.
3. S. G. Hatzikiriakos, "Slip mechanisms in complex fluid flows." *Soft Matter Journal*, vol. 11, no. 40, pp. 7851-7856, 2015, https://doi.org/10.1039/c5sm01711d
4. R. Hornig, "Normal-stress-elasticity of FKM compounds basic observations on rheology and mixing process technology." *Gummi Fasern Kunststoffe*. vol. 12, no. 64, pp. 732-743, 2011.
5. M. Cloitre, R. T. Bonnecaze, "A review on wall slip in high solid dispersions." *Rheolgica Acta*, vol. 17, pp. 283-305, 2017, https://doi.org/10.1007/s00397-017-1002-7

6. E. Uhland, "Modell zur Beschreibung des Fließens wandgleitender Substanzen durch Düsen". *Rheologica Acta*, vol. 15, pp. 30-39, 1976, https://doi.org/10.1007/BF01538515

7. E. Uhland, "Das anomale Fließverhalten von Polyethylen hoher Dichte", *Rheologica Acta*, vol. 18, pp. 1-24, 1976, https://doi.org/10.1007/BF01515684

8. D. Schramm, "Möglichkeiten und Grenzen einer verbesserten Prozessbeschreibung für Kautschukextruder", Ph.D. Dissertation, Faculty Mech. Eng., Paderborn University, Paderborn, 2003.

9. M. Mooney, "Explicit Formulas for Slip and Fluidity", *Journal of Rheology.*, vol. 2, no. 2, pp. 210-222, Apr. 1931, https://doi.org/10.1122/1.2116364

10. K. Geiger, "Rheologische Charakterisierung von EPDM-Kautschukmischungen mittels Kapillarrheometer-Systemen." *Kautschuk Gummi Kunststoffe*, vol. 4, no. 42, pp. 273-283, 1989.

11. E. Uhland, "Modell zur Beschreibung des Fließens wandgleitender Substanzen durch Düsen", *Rheologica Acta*, vol. 15, pp. 30-39, 1976, https://doi.org/10.1007/BF01538515

12. E. Uhland, "Das anomale Fließverhalten von Polyäthylen hoher Dichte", *Rheologica Acta*, vol. 18, pp. 1-24, 1979, https://doi.org/10.1007/BF01515684

13. H.G. Buhrin, T. Rauschmann, "Viscosity Measurement of filled Rubber Compounds – New insight for Error free Measurements", *Kautsch. Gummi Kunststoffe*, vol. 2, pp. 61-66, 2021.

14. D. Kleinschmidt, V. Schöppner, "Improvement of a method for the correction of wall slip effects within the rheological measurements of filled rubber compounds", *SPE Polymers*, vol. 4, no. 2, pp. 63-79, 2023, https://doi.org/10.1002/pls2.10087

15. S. Brockhaus, "Theoretische und experimentelle Untersuchungen zum Temperatur- und Durchsatzverhalten von Kautschukextrudern", Ph.D. Dissertation, Faculty Mech. Eng., Paderborn University, Paderborn, 2017.

16. J. L. Leblanc, M. Cartault, "Evaluation of the Rheological Properties of Rubber Compounds for Die Flow Optimization" in *A Review of European Rubber Research in Practice – Mini Derucom and PRODESC*, Paderborn, Germany, 2002, pp. 301-315.

17. J. L. Leblanc, *Filled Polymers. Science and Industrial Applications,* Boca Raton: CRC Press, 2010.

18. C. Jepsen, N. Räbinger. "Untersuchungen zum Wandgleitverhalten von Kautschukmi-schungen an einem Hochdruck-Kapillarviskosimeter." *Kautsch. Gummi Kunstst.*, vol. 41, no. 4, pp. 342-352, 1988, (in German).

GENERAL SYMPOSIA | RUBBER AND ELASTOMERS

Processing of Thermoplastic Elastomers (TPE) by In-Situ Ground Tire Rubber (GTR) Vulcanization using Waste Ethylene-Vinyl-Acetate (wEVA) and Dicumyl Peroxide (DCP)

J. Suarez-Loor, M. Lazo, A. Rigail, E. Adrian and J. Vera

DOI: https://doi.org/10.51573/Andes.PPS39.GS.RE.2

December 2024

Processing of Thermoplastic Elastomers (TPE) by In-Situ Ground Tire Rubber (GTR) Vulcanization using Waste Ethylene-Vinyl-Acetate (wEVA) and Dicumyl Peroxide (DCP)

J. Suarez-Loor, M. Lazo, A. Rigail, E. Adrian and J. Vera[1]

Abstract: Tire rubber waste (TRW) is a complex mixture of materials, such as rubbers, steel, textile fibers, carbon black, and other additives. Its polluting capacity is a severe environmental problem, especially in landfills and waste management processes. As a practical solution to mitigate TRW's environmental impact, thermoplastic elastomers (TPE) commonly reuse the ground tire rubber (GTR). This work presents an in-situ devulcanization of ground tire rubber (DGTR) and re-vulcanization of devulcanized ground tire rubber using dicumyl peroxide (DCP) and waste ethylene-vinyl-acetate (wEVA). The GTR was devulcanized through thermo-mechanical action and then blended with waste ethylene-vinyl-acetate (wEVA) and dicumyl peroxide (DCP) to produce the thermoplastic elastomer (TPE). This blending process was monitored using a torque rheometer and analyzed with differential scanning calorimetry (DSC) to evaluate the crosslinking reactions and kinetic behavior. The results indicated that in-situ vulcanization took place within the rheometer mixing chamber, evidenced by an increase in torque. DSC analysis of the DGTR-DCP-wEVA system confirmed the curing reaction prior to vulcanization. The resulting in-situ vulcanized TPE ensures improved component adhesion. This research offers practical insights into a scalable, non-advanced process for local plastics industries in developing countries to incorporate vulcanized TPEs, thereby enhancing their knowledge and understanding of this innovative approach.

Keywords: Thermoplastic Elastomers, Vulcanization, Waste Plastic, Ground Tire Rubber

1 The authors J. Suarez-Loor (jossloor@espol.edu.ec), M. Lazo, A. Rigail and E. Adrian are affiliated with the Faculty of Mechanical Engineering and Production Sciences at the Escuela Superior Politécnica del Litoral (ESPOL) in Ecuador. The author J. Vera is affiliated with the Faculty of Natural Sciences and Mathematics at the same university.

DOI: https://doi.org/10.51573/Andes.PPS39.GS.RE.2

Introduction

Sustainable strategies focusing on developing plastic composites after their end-of-life cycle are crucial for the circular economy and pollution mitigation. Tire and plastic residues are ever-growing waste in developing countries, especially South America. This oversight prompts the exploration of a material derived from blending thermoplastic and tire waste, presenting a potential alternative to conventional practices. Thus, TPE are a common alternative to address these problems, employing recycled thermoplastic and elastomers. The main advantage of TPE is that they are easily produced using typical plastic processing methods (i.e., extrusion and injection molding) and the mechanical properties of a rubber [1].

TPE development methodologies from TRW usually use this material as it is received in a particle shape (GTR) without pretreatment. This causes a low interfacial adhesion and poor mechanical properties due to their limited compatibility and crosslinked structure [2]. Consequently, surface and structure modification of GTR can be achieved through chemical or physical methods. Reactive chemical techniques often involve peroxides, with common additives based on ethylene-octane copolymer (EOC), trans-polyoctenamer rubber (TOR), ethylene vinyl acetate (EVA), maleic acid grafted polyolefins (such as PE-g-MA), or ethylene propylene diene monomer (EPDM) [3-5].

This work presents a study of the processability, thermal, and kinetic properties of TPE blends composed from DGTR, wEVA, and DCP. This novel approach allows for the evaluation of the thermal and physical conditions of the devulcanization process by thermomechanical action and the synthesis of vulcanized TPE based on recycled and wasted materials.

Materials and Method

GTR with a particle size of 1 mm was used for the devulcanization process. wEVA with a 10% acetate content was employed as a binding agent. Additionally, DCP was utilized as a crosslinking agent for DGTR/wEVA blends [6]. The devulcanization process of GTR and the processability of composites were evaluated through a Brabender Plastograph® EC Plus torque rheometer at fixed conditions of velocity (90 rpm) and time (10 minutes). Thermal and kinetic analysis of composites was performed by a Differential Scanning Calorimeter (DSC) in non-isothermal conditions and a nitrogen atmosphere, from room temperature to 220°C at 20°C min^{1} to study the vulcanization reaction. The nomenclature of all samples was based on X parts of DGTR by Y parts of wEVA (XDGTR/YwEVA). All samples were mixed with 1.5%wt of DCP [6]. Table 1 depicts the nomenclature of the synthesized composites.

DOI: https://doi.org/10.51573/Andes.PPS39.GS.RE.2

Table 1. Nomenclature and compositions of TPE.

Sample (DGTR:wEVA)	Nomenclature
0:1	wEVA
2:1	2DGTR/wEVA
4:1	4DGTR/wEVA
6:1	6DGTR/wEVA

GTR devulcanization

Devulcanization of GTR was investigated at temperatures ranging from 170°C to 200°C, with increments of 10°C. Subsequently, the DGTR samples were analyzed using the torque rheometer to evaluate the torque increase with the DCP addition. The devulcanization conditions for the DGTR were selected based on the highest torque obtained during re-vulcanization with DCP at 180°C.

TPE synthesis

The composites were prepared at temperatures of 110°C and 180°C. At 110°C, the objective was to obtain the TPE without inducing vulcanization. On the other hand, at 180°C, the aim was to produce in-situ vulcanization in the composites due to the decomposition of DCP.

The kinetic study of composites was conducted using the Borchardt and Daniels (B/D) method (equations 1 and 2) and the Arrhenius equation in this logarithmic form (equation 3) [7], as shown in Table 2.

Table 2. Employed equations for kinetic analysis.

Crosslinking conversion (α)	$\alpha(T) = \frac{\int_{T_0}^{T_i}(dH/dT)dT}{\int_{T_0}^{T_\infty}(dH/dT)dT}$	1)
Reaction rate constant described by B/D method (k)	$\ln k(T_i) = \ln\left(\frac{q_{T_i}}{\Delta H_d}\right) - n \cdot \ln(1 - \alpha_{T_i})$	2)
Reaction rate constant described by Arrhenius (k)	$\ln k(T) = \ln(A) - \frac{E_a}{R}\left(\frac{1}{T}\right)$	3)

dH/dT is the reaction enthalpy at an infinitesimal temperature; T_0 is the onset reaction temperature; T_i is the reaction temperature on finishing the crosslinking process. q_{Ti} is the heat flow; n is the reaction order; and ΔH_d is the crosslinking energy. A is the pre-exponential factor; R is the universal gas; and E_a is the activation energy.

DOI: https://doi.org/10.51573/Andes.PPS39.GS.RE.2

Results and Discussion

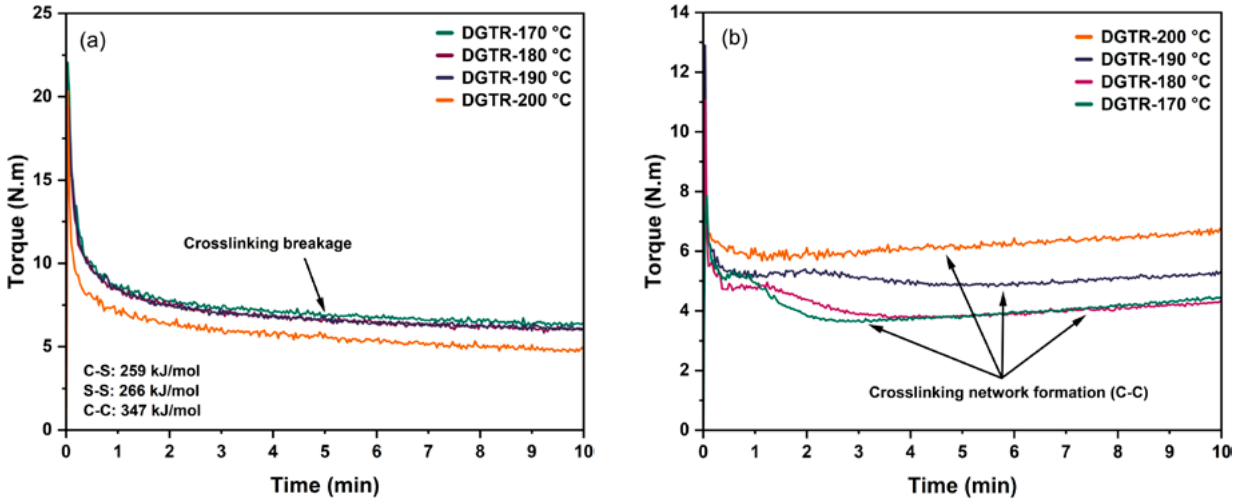

Figure 1. Devulcanization process by thermomechanical action at different temperatures. (b) In-situ re-vulcanization of DGTR by DCP decomposition in the Brabender mixing chamber at 180°C.

Figure 1(a) illustrates the torque-time profile of GTR devulcanization, while Figure 1(b) depicts its in-situ re-vulcanization process. Figure 1(a) shows a decreasing trend in torque values at elevated temperatures (i.e. 200°C). According to Ábel et al. [8], this reduction in torque values is due to the crosslinking breakage effect on carbon-sulfur (C-S), sulfur-sulfur (S-S), and carbon-carbon (C-C) bonds. Markl et al. [9], state that the devulcanization process by thermomechanical action is selective concerning bond breakage. Thus, C-S and S-S bonds are more likely to break in the devulcanized structure of GTR due to their lower bond energies than C-C bonds. Figure 1(b) presents the re-vulcanization torque-time curves measured when the temperature is set to 180°C in the presence of DCP. These results indicate an improved crosslinking behavior for DGTR when devulcanized at higher temperatures. Therefore, GTR devulcanized at 200°C (DGTR-200°C) was chosen as the base material for all compounds.

Figure 2(a) and (b) exhibit the rheological behavior of TPE composites at 110°C and 180°C, respectively. Figure 2(a) displays the processability of TPEs without DCP decomposition due to the lower process temperature to avoid any crosslinking reaction [10]. It can be observed that the torque values are related to the DGTR content in the composites. For example, a disturbance in the torque curve is predominant in 6DGTR/wEVA and 4DGTR/wEVA samples (in contrast to 2DGTR/EVA and EVA) due to DGTR particles in the molten wEVA, as these particles can alter the flow and viscoelastic properties of the polymer matrix, restricting the mobility of the chains [11]. Rigail et al. [12] mention that elevated torque levels are problematic in plastics manufacturing due to their complex processability. Figure 2(b) reveals the change in the torque profiles by vulcanization because of DCP decomposition in the DGTR/wEVA composites. This effect results from the increase in

DOI: https://doi.org/10.51573/Andes.PPS39.GS.RE.2

the molecular weight by the free radical polymerization between wEVA-wEVA, DGTR-DGTR, and wEVA-DGTR interfaces [13]. It is essential to highlight the different effects of DCP at different values of DGTR. For instance, wEVA and 2DGTR/wEVA samples show a torque stabilization curve after the polymerization, which, according to Dluzneski [10], is a synonym for a successful crosslinking reaction. Nonetheless, 4DGTR/wEVA and 6DGTR/wEVA composites expose a reversion in the vulcanization reaction. As indicated by Dluzneski [10], this phenomenon may be due to radical transfer and oxygenation due to the air presence in the mixing chamber. The first option is based on a possible stabilizing effect of the crosslinking reaction by wEVA molecules. Thus, at low DGTR contents, an equimolar reaction mechanism between DGTR and wEVA is presumed, which would explain the reversion in samples with higher DGTR content. This stabilizing effect is further enhanced by the abstraction of hydrogen from the methyl group of the acetate in wEVA [10,14,15].

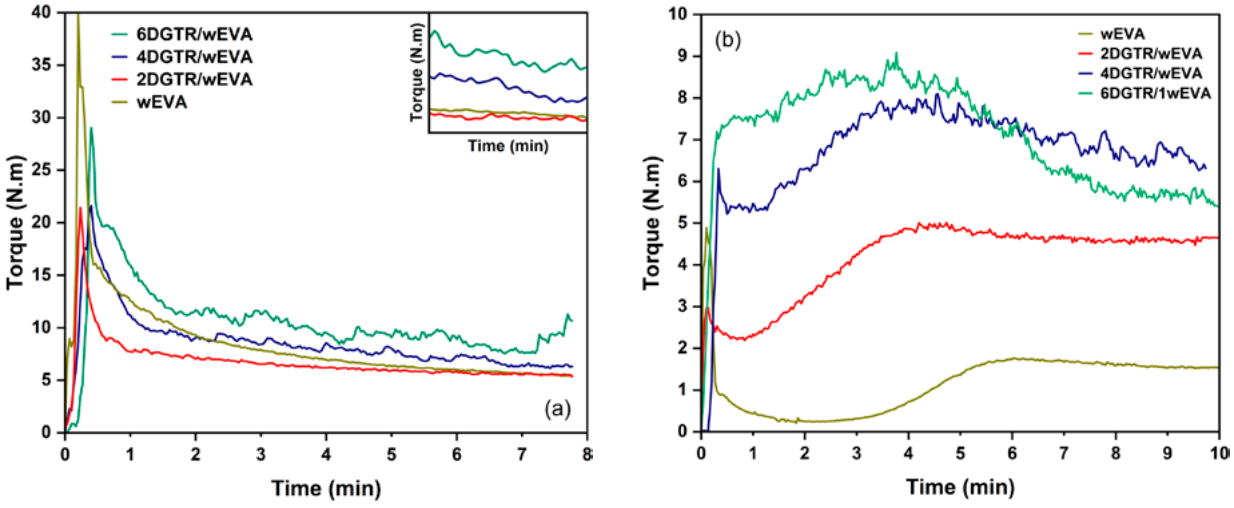

Figure 2. Processability of composites at different temperatures, (a) 110°C and (b) 180°C.

Figure 3(a) and (b) display the thermal behavior and crosslinking rate (α) of samples prepared in Table 1, respectively. Figure 3(a) shows two effects depending on the DGTR content. The first is based on the inverse proportional relation between the released energy and the DGTR content. This suggests that DGTR cannot correctly form free radicals in the presence of decomposed DCP, which supports the results obtained in torque rheometry at 180°C. The second effect is an elevation in the peak maximum temperature of the cross-linking reaction, which is related to the increase in activation energy, as shown in Table 3. The change in the crosslinking conversion rate or reaction order (n) states that crosslinking also occurs at the wEVA/DGTR interface, as Bianchi et al. [15] confirm in their study. From the DSC results, correlations from equations 1, 2, and 3 were employed to obtain crosslinking conversion versus temperature study (Figure 3[b]). These results state that samples containing increasing amounts of GTR showed longer times for the reaction induction, that is, a slower EVA crosslinking rate in the EVA/GTR blends [15], which is related to the higher values of activation energies. However, 6DGTR/wEVA is the only one that shows values of $\ln(A)$,

DOI: https://doi.org/10.51573/Andes.PPS39.GS.RE.2

E_a, and n different from the trend already discussed, which may be related to the predominance of DGTR, which could explain why these values are very similar to those of 4DGTR/wEVA. This hypothesis must be confirmed by an in-depth study at different DGTR grades up to 100 w/w.

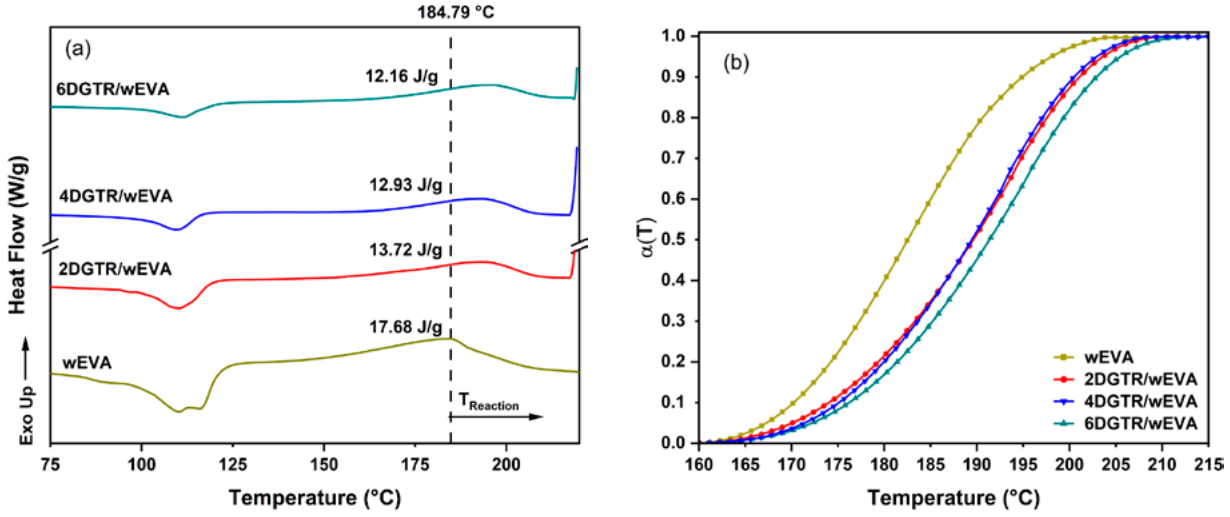

Figure 3. (a) DSC analysis for TPE composites at heating rate of 20°C min^{-1}, and (b) crosslinking conversion (α) of blends using B/D method.

Table 3. Kinetic parameters of DGTR/wEVA blends in DSC at 20°C min^{-1}.

DGTR:wEVA	ln(A)	E_a($kJ\ mol^{-1}$)	n	R^2
0:1	63.62	251.20	2.007	0.999
2:1	68.27	273.88	1.860	1.00
4:1	72.16	288.63	1.840	0.999
6:1	70.66	284.07	1.899	1.000

These results provide information on the efficiency of the devulcanization of GTR by thermomechanical action and manufacturing of TPE from plastics and tires, using recycled wEVA, and DCP as a crosslinking agent from a processing, thermal, and kinetic perspective.

Conclusion

This study investigated the influence of DGTR content on the processability, thermal behavior, and kinetics of composites comprising wEVA and DCP (1.5 wt%). Torque rheometry analysis revealed that increasing DGTR content intensified mixing instability, resulting in higher disruptive torque

DOI: https://doi.org/10.51573/Andes.PPS39.GS.RE.2

effects. Notably, wEVA demonstrated a stabilizing effect on the vulcanization process of TPE composites. Lower DGTR contents facilitated successful crosslinking of the TPE, whereas higher DGTR contents induced a reversion reaction. Moreover, samples with higher DGTR content exhibited higher activation energy values and lower crosslinking rates. Future research should explore additional properties (mechanical, acoustic, thermal, etc.) to fully assess the potential applications of these composites derived from recycled materials.

Acknowledgments

The authors thank the staff of the Instituto de Capacitación e Investigación del Plástico y del Caucho (ICIPC) for their technical support. We are grateful for the financial support of the Facultad de Ingeniería en Mecánica y Ciencias de la Producción of Escuela Superior Politécnica del Litoral (ESPOL).

References

1. R. C. V. Fletes, E. O. C. López, P. O. Gudiño, E. Mendizábal, R. G. Núñez, and D. Rodriguez, "Ground tire rubber/polyamide 6 thermoplastic elastomers produced by dry blending and compression molding," *Progress in Rubber, Plastics and Recycling Technology*, vol. 38, no. 1, pp. 38–55, Feb. 2022, https://doi.org/10.1177/14777606211038956
2. M. M. Hassan, N. A. Badway, A. M. Gamal, M. Y. Elnaggar, and E. S. A. Hegazy, "Studies on mechanical, thermal and morphological properties of irradiated recycled polyamide and waste rubber powder blends," *Nuclear Instruments and Methods Physics Research B*, vol. 268, no. 9, pp. 1427–1434, May 2010, https://doi.org/10.1016/J.NIMB.2010.01.021
3. J. Qin, H. Ding, X. Wang, M. Xie, and Z. Yu, "Blending LLDPE and ground rubber tires," *Polymer–Plastics Technology and Engineering*, vol. 47, no. 2, pp. 199–202, 2008, https://doi.org/10.1080/03602550701816217
4. L. Mészáros, M. Fejos, and T. Bárány, "Mechanical properties of recycled LDPE/EVA/ground tyre rubber blends: Effects of EVA content and postirradiation," *Journal of Applied Polymer Science*, vol. 125, no. 1, pp. 512–519, 2012, https://doi.org/10.1002/app.35675
5. H. M. Da Costa, V. D. Ramos, W. S. Da Silva, and A. S. Sirqueira, "Analysis and optimization of polypropylene (PP)/ethylene-propylene-diene monomer (EPDM)/scrap rubber tire (SRT) mixtures using RSM methodology," *Polymer Testing*, vol. 29, no. 5, pp. 572–578, 2010, https://doi.org/10.1016/j.polymertesting.2010.04.003
6. M. M. P. Lee, C. H. Hsieh, K. M. Yeh, C. I. Chang, and P. L. C. Hao, "Blends of PVC, PE, and PS Modified by Chlorinated Polyethylene (W E) and Dicumyl Peroxide (DCP)," *Journal of Vinyl & Additive Tecnology*, vol. 2, pp. 119-124, 1980, https://doi.org/10.1002/vnl.730020211

7. T. Chang, K. H. Hsueh, C. C. Liu, C. R. Cao, and C. M. Shu, "A Method to Derive the Characteristic and Kinetic Parameters of 1,1-Bis(tert-butylperoxy)cyclohexane from DSC Measurements," *Processes*, vol. 10, no. 5, May 2022, https://doi.org/10.3390/pr10051026

8. D. Á. Simon and T. Bárány, "Effective thermomechanical devulcanization of ground tire rubber with a co-rotating twin-screw extruder," *Polymer Degradation and Stability*, vol. 190, Aug. 2021, https://doi.org/10.1016/j.polymdegradstab.2021.109626

9. E. Markl and M. Lackner, "Devulcanization technologies for recycling of tire-derived rubber: A review," *Materials*, vol. 13, 2020. https://doi.org/10.3390/ma13051246

10. P. R. Dluzneski, "Peroxide Vulcanization of Elastomers," *Rubber Chemistry and Technology*, vol. 74, no. 3, pp. 451–492, Jul. 2001, https://doi.org/10.5254/1.3547647

11. M. M. Rueda et al., "Rheology and applications of highly filled polymers: A review of current understanding," *Progress in Polymer Science*, vol. 66, pp. 22–53, Mar. 2017, https://doi.org/10.1016/J.PROGPOLYMSCI.2016.12.007

12. A. Rigail-Cedeño et al., "Processability and Physical Properties of Compatibilized Recycled HDPE/Rice Husk Biocomposites," *Journal of Manufacturing and Materials Processing*, vol. 6, no. 4, p. 67, Jun. 2022, https://doi.org/10.3390/jmmp6040067

13. J. Suarez and M. Carrasco, "Diseño de un material para losetas a partir de residuos de neumáticos y termoplásticos reciclados," ESPOL, Guayaquil, 2022. Accessed: Mar. 06, 2024. [Online]. Available: https://dspace.espol.edu.ec/bitstream/123456789/57070/1/T-113001SU%c3%81REZ%20JOS%c3%89-CARRASCO%20MIGUEL-signed.pdf

14. F. Zeng, X. Guo, L. Sun, X. He, Z. Zeng, and Z. Liu, "Non-isothermal crosslinking of ethylene vinyl acetate initiated by crosslinking agents: kinetic modelling," *RSC Advances*, vol. 12, no. 24, pp. 15623–15630, May 2022, https://doi.org/10.1039/d2ra01994a

15. O. Bianchi, R. Fiorio, J. N. Martins, A. J. Zattera, C. H. Scuracchio, and L. B. Canto, "Crosslinking kinetics of blends of ethylene vinyl acetate and ground tire rubber," *Journal of Elastomers and Plastics*, vol. 41, no. 2, pp. 175–189, 2009, https://doi.org/10.1177/0095244308095015

SPECIAL SYMPOSIA | BIOPOLYMERS, BIOCOMPOSITES AND BIOPROCESSING

Optimization of Dosing Methodof Hybrid Filler (Cellulose/MgAl LDH) in Biopolymers Using Micro-Compounder for Preparation of Bio-Composites

Sajid Naseem, Sandra Heckel, Martin Zahel and Andreas Leuteritz

DOI: https://doi.org/10.51573/Andes.PPS39.SS.BBB.1

December 2024

Optimization of Dosing Method of Hybrid Filler (Cellulose/MgAl LDH) in Biopolymers Using Micro-Compounder for Preparation of Bio-Composites

Sajid Naseem, Sandra Heckel, Martin Zahel and Andreas Leuteritz[1]

Abstract: With growing environmental concerns about using conventional plastics in daily life, the demand for bio-based polymer products is increasing. Natural and biodegradable raw materials are alternatives for making plastic products more sustainable. Cellulose-based fibers have gained attention in preparing biodegradable polymer composites because of their biodegradable nature, bio-based origin, low cost and low weight compared to synthetic fibers (glass and carbon). In this research, hybrid fillers based on cellulose and hydrotalcite were used in biodegradable polymers such as in PLA and blend of PBAT/PLA to prepare bio composites. The loading of hybrid filler (cellulose/LDH) was done using a small-scale compounding machine. Hybrid fillers were used in compounding machines in different forms (paste, freeze dried, PLA dissolved, PEG mixed, and sheet based) with PBAT/PLA. The dosing method of hybrid filler in polymer was optimized in this work. Morphological analysis of hybrid filler and the mechanical properties of bio composites were also done. The tensile modulus of PLA was increased by about 33% when sheet-based hybrid filler was added to the PLA composite.

Keywords: Biodegradable, Cellulose, Bio-Composites, Hybrid Filler, MgAl LDH, Polylactic Acid (PLA), PBAT

1 The authors Sajid Naseem (naseem@ipfdd.de) and Andreas Leuteritz (leuteritz@ipfdd.de) are affiliated with the Leibniz-Institut für Polymerforschung Dresden in Germany. The authors Sandra Heckel (sandra.heckel@ptspaper.de) and Martin Zahel (martin.zahel@ptspaper.de) are affiliated with Papiertechnische Stiftung (PTS) in Germany.

DOI: https://doi.org/10.51573/Andes.PPS39.SS.BBB.1

Introduction

Plastic-based products produced by using petroleum raw materials are becoming a huge concern, as they are less environmentally friendly [1,2]. Global environmental safety issues and regulations encourage researchers to work on biodegradable products that could replace conventional plastic products [1,3]. Bio composites can be a good alternative for solving the problems that arise due to the use of non-degradable plastic products. Natural fillers and natural fibers are components used in many types of polymer composites to make them environmentally friendly products [4]. One of the important fillers is hydrotalcites [MgAl layered double hydroxides (LDH)] which are being used in many different polymers over the last few years and are available naturally and can also be easily synthesized [5-8]. The other common bio-based fiber is cellulose fibers, which are being used in polymers. The use of a combination of fillers such as mineral fillers with cellulose in polymers has gained special attention because they could improve the properties of polymers [3]. The improved form of cellulose and mineral filler is a hybrid filler, combining positive aspects of both when used in bio-polymers that may provide fully environmentally compatible products, as shown in Figure 1. These types of bio composites are getting attention but there is big challenge to mixing these cellulose based fillers in a given polymer matrix. The objective of this research is to optimize the loading method and mixing of hybrid filler (cellulose/LDH) in polymer matrices (PBAT, PLA) to make fully bio-compatible plastic products, as shown in Figure 1 below.

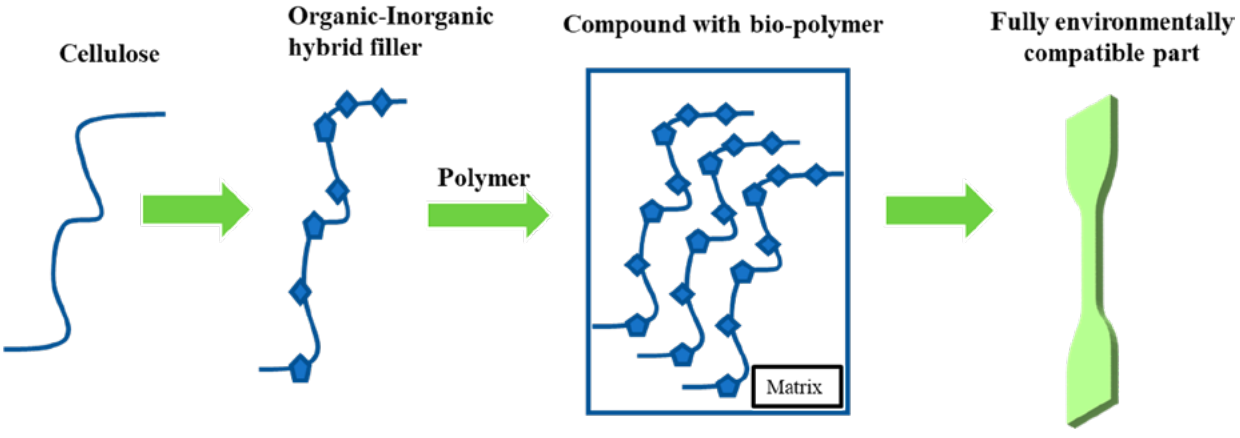

Figure 1. Schematic representation of hybrid filler/polymer bio-composites.

Materials and Methods

Hybrid fillers of cellulose and hydrotalcite [MgAl layered double hydroxides (LDH)] were supplied by Papiertechnische Stiftung (PTS), Heidenau, Germany. PLA (PLA: NW Ingeo 3251 injection molding grade), PBAT (Ecoflex F1200 film grade) (BASF), PLA (BioFed) (supplied by BioFed Germany),

DOI: https://doi.org/10.51573/Andes.PPS39.SS.BBB.1

poly(ethylene glycol) (PEG) (BioUltra 10K) (Sigma Aldrich), dichloromethane (Acros Organic now Thermo Scientific), and distilled water were used in this work.

Preparation Methods of Bio composites

Preparation of bio composites was done using a micro-compounder (X-plore, The Netherlands), as shown in Figure 2, which contains a compounding part and an injection molding part. Hybrid filler (cellulose/LDH) and PBAT, PLA were mixed with different techniques, as shown in Table 1. The dosing method of hybrid filler in matrix was optimized using 5 wt.% loading in polymer matrix.

Figure 2. Micro-compounding machine and injection molding setup used for preparation of hybrid filler/PBAT/PLA bio-composites [9].

Table 1. Description of composition of hybrid filler/PBAT/PLA bio-composites and types of hybrid filler dosing system.

Sr. No.	Form of hybrid filler	Hybrid Filler (wt. %)	Matrix (37 % PBAT + 63 %PLA (3251)) or PLA (BioFed) (95%) (wt. %)
1	Paste filler	5	95
2	Freeze dried filler	5	95
3	Solvent mixed PLA filler	5	95
4	PEG mixed filler	5	95
5	Sheet based filler	5	95

DOI: https://doi.org/10.51573/Andes.PPS39.SS.BBB.1

The pure PLA (BioFed) and the mixture of PBAT and PLA (3251) were used here as a matrix in this research, as shown in Table 1. The mixture of hybrid filler and polymer was compounded for 10 min at 100 rpm speed at a temperature of 190°C. The amount of hybrid filler used was 5 wt.% in each form of dosing system. The mixture was then delivered from a micro-compounder to a piston device for preparing samples for mechanical testing.

Characterization

SEM images were taken with a Zeiss Ultra Plus to visualize the hybrid filler of cellulose and MgAl layered double hydroxide (LDH). Tensile properties of bio-composites were measured according to DIN EN ISO 527-2/1BA/50 with a Zwick 1456 (Ulm, Germany). The Charpy impact strength of bio composites was measured using the standard ISO 179/1eU. The results of bio composites were averaged over five measurements for each sample for the tensile and Charpy impact testing.

Results and Discussion

Scanning Electron Microscopy (SEM) Images of Hybrid Filler

Figure 3 shows the SEM images of hybrid filler sample, which contain cellulose fibres and MgAl layered double hydroxide. The MgAl LDH particles are attached to the cellulose fibers, as can be observed in the SEM images. The hexagonal shape of MgAl LDH is also visible in Figure 3, which shows the well-ordered structure of MgAl LDH present in hybrid filler and attached to the cellulose fibers.

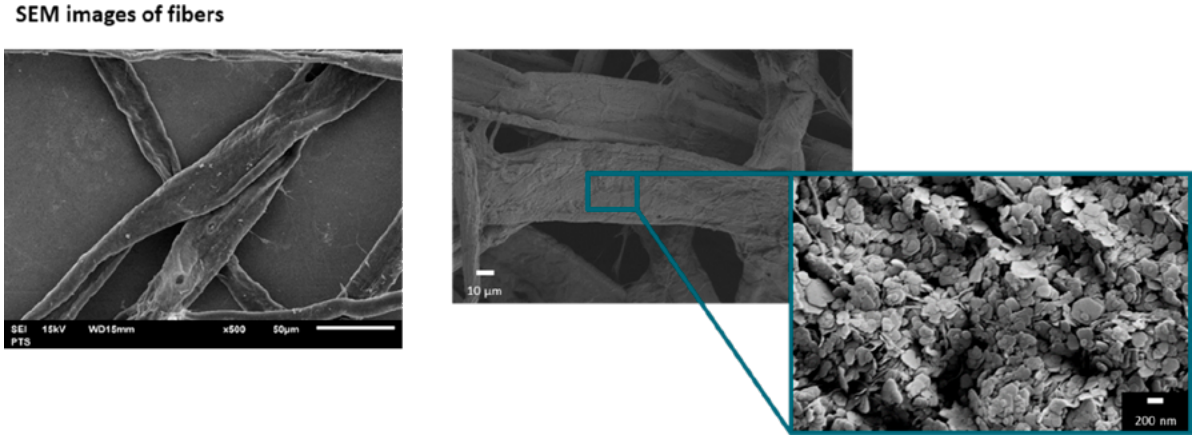

Figure 3. Scanning electron microscopy images of hybrid filler containing cellulose and MgAl layered double hydroxides (LDH).

DOI: https://doi.org/10.51573/Andes.PPS39.SS.BBB.1

Types of Dosing Systems of Hybrid Filler in PBAT/PLA Matrix

Figure 4 (a-e) show the form of hybrid filler that is used in the polymer matrix in the micro-compounding machine. The different forms of dosing are used here because the mixing of these hybrid filler in polymer was not easy. Initially, the hybrid filler in the form of paste (Figure 4[a]) was used during compounding. Freeze drying of paste (Figure 4[a]) was done and then used in the compounding machine to observe the mixing behavior. After freeze drying, the hybrid filler becomes fluffy and the volume of the freeze-dried hybrid filler (Figure 4[b]) increased. In the third option, freeze dried hybrid filler was first mixed in a solution of PLA (Figure 4[c]) and this mixture was then used in the compounding machine with the PBAT/PLA blend. In the fourth option, hybrid filler was first dispersed in PEG (Figure 4[d]) and then that PEG mixed hybrid filler was used in the compounding machine. Lastly, the sheet (Figure 4[e]) was made from the paste of hybrid filler and then used in the compounding machine with PLA(BioFed). All five dosing techniques were done to investigate which technique gives good mixing and good samples.

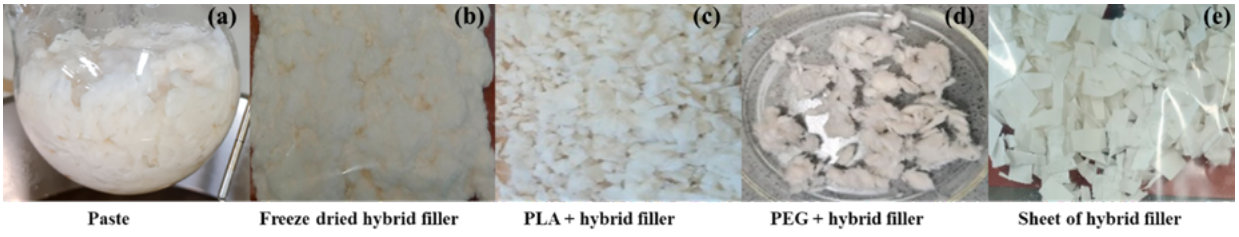

Figure 4. Hybrid filler dosing in different form (a) paste dosing (b) freeze dried filler dosing (c) hybrid filler dissolved in PLA (d) hybrid filler dissolved in PEG (e) sheet dosing.

Issues During the Dosing of Different Forms of Systems

Paste dosing was done with a polymer matrix in the micro-compounder and after mixing the polymer melt could not inject in the injector and in the end no sample could be made, as can be seen in Figure 5(a). The degradation of PBAT/PLA might occur during compounding in case of paste dosing due to the presence of water [10]. When freeze dried hybrid filler was used in the micro-compounder with PBAT/PLA, the filler was not mixed completely in polymer and some unmixed material was left in the mixing chamber, as can be seen in Figure 5(b). Due to the increase in volume and fluffiness of the hybrid filler after drying, the polymer melt could not infiltrate the hybrid filler. One reason might be the mismatch of surface properties leading to less interaction during mixing with PBAT/PLA. To overcome the issue of incomplete mixing of hybrid filler with polymer matrix, the freeze-dried hybrid filler was first mixed in the PLA solution and then dried that mixture. The dried mixture of hybrid filler/PLA was then used in the micro-compounder with PBAT/PLA. The mixing was done completely in this case but removing the sample from the mold was

DOI: https://doi.org/10.51573/Andes.PPS39.SS.BBB.1

difficult and the sample broke in most cases, as can be seen in Figure 5(c). This might be due to increase in brittleness in the bio composite.

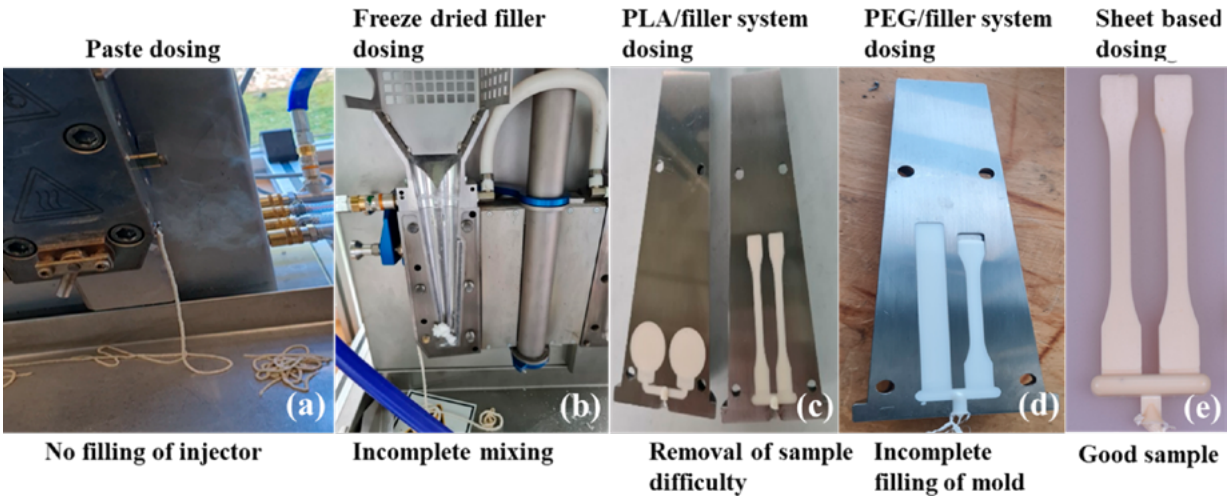

Figure 5. Different types of dosing system of hybrid filler (LDH/cellulose) in PBAT/PLA and issues during compounding process.

To overcome the issue of brittleness and broken samples after compounding, another option was used in which hybrid filler was dissolved in PEG and then used in PBAT/PLA in the micro-compounder. In this case, incomplete filling of the mold was observed, as can be seen in Figure 5(d). Lastly the sheet was made from hybrid filler paste in a press machine. The sheet was chopped and then used in PBAT/PLA. The mixing was relatively good and the sample was good in the end when compared to the other 4 methods of dosing, as can be seen in Figure 5(e). Finally, the sheet of hybrid filler was also used in PLA (BioFed) to compare the mechanical properties.

Mechanical Properties of Hybrid Filler-Based Bio Composites

The mechanical analysis was done on the sheet-based hybrid filler samples and is shown in Table 2. The bio composites of PLA (BioFed) were prepared using 5 wt.% of hybrid filler in PLA and the mechanical properties were compared with pure PLA. The tensile modulus and impact strength increased in the case of the hybrid filler samples. The tensile modulus in pure PLA was 2050 ± 152 MPa and in PLA composite was 2730 ± 230. The impact strength in case of pure PLA was 13.4 ± 1.18 and in case of composites was 19.1 ± 1.09.

DOI: https://doi.org/10.51573/Andes.PPS39.SS.BBB.1

Table 2. Mechanical properties (tensile and impact testing) of hybrid filler/PLA(BioFed) composites in which sheet dosing was used.

Sr. No.	Hybrid filler (sheet) (wt. %)	Tensile strength (MPa)	Tensile modulus (MPa)	Elongation at break (%)	Impact strength [kJ/m²]
1	0	35.37 ± 0.43	2050 ± 152	6.4 ± 0.89	13.4 ± 1.18
2	5	31.02 ± 0.73	2730 ± 230	4.8 ± 0.55	19.1 ± 1.09

Conclusion

The dosing technique of hybrid filler was optimized in this work. Five types of dosing methods were used and various issues in each dosing system were observed. The sheet made from paste of hybrid filler showed optimum results as the compounding was good and the sample obtained was also good as compared to other dosing systems of hybrid filler. Mechanical properties (modulus and impact strength) were enhanced at 5 wt.% loading of hybrid filler in case of the sheet-based dosing system. The tensile modulus was increased about 37% at only 5 wt.% loading of hybrid filler, which shows the potential of this hybrid filler in the bio composites field. As the amount of hybrid filler used in this research work was only 5 wt.%, the increased amount of hybrid filler in the polymer matrix could lead to other mixing issues, such as reduced homogeneity. The ratio of layered double hydroxide (LDH) and cellulose in hybrid filler could also lead to different mixing issues. The optimization of amount of filler loading such as more than 5 wt.% and ratios of LDH/cellulose in hybrid filler could show different results while compounding and need to be further investigated.

Acknowledgments

We thank BMWK Germany for financing the project under the project number IGF-22181.

References

1. N. Raddadi and F. Fava, "Biodegradation of oil-based plastics in the environment: Existing knowledge and needs of research and innovation," *Science of The Total Environment*, vol. 679, pp. 148-158, 2019.
2. T. A. Hottle, M. M. Bilec, and A. E. Landis, "Sustainability assessments of bio-based polymers," *Polymer Degradation and Stability*, vol. 98, no. 9, pp. 1898-1907, 2013.
3. B. Heinicke et al., "Preparation of cellulose-PCC fibre hybrids: Use as filler in polypropylene (PP) composites," *Cellulose*, vol. 31, no. 8, pp. 5043-5054, 2024.

4. H. Oosthuizen, L. Jones, S. Naseem, F. J. W. J. Labuschagne, and A. Leuteritz, "Tailoring materials for their need: Sustainable layered double hydroxide polymer composites," *Journal of Polymer Science*, vol. 61, no. 16, pp. 1749-1777, 2023.

5. S. Naseem, S. Wießner, I. Kühnert, F. J. W. J. Labuschagné, and A. Leuteritz, "Polypropylene (PP) nanocomposites with transition metal (MgCoAl, MgNiAl, MgCuAl, MgZnAl) layered double hydroxides (t-LDHs): Flammability, thermal and mechanical analysis," *Advanced Industrial and Engineering Polymer Research*, vol. 6, no. 2, pp. 203-213, 2023.

6. S. Naseem, S. Wießner, I. Kühnert, and A. Leuteritz, "Layered Double Hydroxide (MgFeAl-LDH)-Based Polypropylene (PP) Nanocomposite: Mechanical Properties and Thermal Degradation," *Polymers*, vol. 13, no. 19, pp. 3452, 2021.

7. S. Naseem, A. Leuteritz, and U. Wagenknecht, "Polymer Nanocomposites Based on Layered Double Hydroxides (LDHs)," in *Processing of Polymer Nanocomposites*: Carl Hanser Verlag GmbH & Co. KG, 2019, pp. 343-369.

8. S. Naseem, S. P. Lonkar, A. Leuteritz, and F. J. W. J. Labuschagné, "Different transition metal combinations of LDH systems and their organic modifications as UV protecting materials for polypropylene (PP)," *RSC Advances*, vol. 8, no. 52, pp. 29789-29796, 2018.

9. Xplore Together, "Micro Compounders," [Online]. Available: https://www.xplore-together.com/products/micro-compounders. [Accessed: Jun. 28, 2024].

10. W. Limsukon, M. Rubino, M. Rabnawaz, L.-T. Lim, and R. Auras, "Hydrolytic degradation of poly(lactic acid): Unraveling correlations between temperature and the three phase structures," *Polymer Degradation and Stability*, vol. 217, pp. 110537, 2023.

DOI: https://doi.org/10.51573/Andes.PPS39.SS.BBB.1

SPECIAL SYMPOSIA | BIOPOLYMERS, BIOCOMPOSITES AND BIOPROCESSING

Biochar Production, and Use: A Detailed Review of the Art

Farid Chejne, Valentina Sierra-Jiménez, Marlon Córdoba, María del Pilar Noriega and Manuel García-Pérez

DOI: https://doi.org/10.51573/Andes.PPS39.SS.BBB.2

December 2024

Biochar Production, and Use: A Detailed Review of the Art

Farid Chejne, Valentina Sierra-Jiménez, Marlon Córdoba, María del Pilar Noriega and Manuel García-Pérez[1]

Abstract: This study presents a detailed description of the technologies and processes for obtaining biochar and its formation from the fundamental structures of aromatic groups. These aromatic groups come from biomass pyrolysis; therefore, this document explores the complex relationship between biochar structural characteristics and the reactions involved in its formation during the pyrolysis process, specifically: analysis of the generation of a cross-linked network, structural features, and the impact of free radicals on biochar formation. This study will culminate with an analysis of microwave absorption and heat transfer dynamics among microwave absorbing materials and biomass or plastic particles. This examination aims to understand the temperature profiles in various heating modes, providing insights into their impacts on the overall performance of microwave-assisted reactors dedicated to these processes. Through this narrative, this study intends to provide an understanding of the multifaceted world of biochar and its diverse applications, drawing meaningful connections between its formation, structural attributes, and practical implementations.

Keywords: Biochar Production, Biochar Characterization, Biochar Application

1 The authors Farid Chejne and Valentina Sierra-Jiménez are affiliated with the Universidad Nacional de Colombia in Medellín, the Colombian Academy of Exact, Physical and Natural Sciences, the TAYEA Research Group, and the ABISURE Network. Manuel García-Pérez, as well as Valentina Sierra-Jiménez are affiliated with the Department of Biological Systems Engineering at the Washington State University in the United States. Marlon Córdoba is affiliated with the Faculty of Engineering at the Universidad de La Guajira in Colombia. María del Pilar Noriega is R&D and Innovation Director at DAABON Group.

DOI: https://doi.org/10.51573/Andes.PPS39.SS.BBB.2

Introduction

Biochar has many applications, including carbon storage and sequestration, soil enhancement, and pollution remediation [1]. Knowledge of its molecular structure and functionality is needed to engineer biochar for specific applications [2].

Biomass can be municipal, animal, forest, agroindustry, pulp and paper, industrial biowaste, and thermochemically or biologically treated food waste. Thermochemical processes (pyrolysis, gasification, combustion, hydrothermal carbonization) are suitable for dried waste; on the other hand, wet wastes are recommended for use in the biological processes route (extraction processing, anaerobic digestion, fermentation, microbial fuel cell, transesterification).

Biochar Production

Various thermochemical techniques convert waste polymer and lignocellulosic biomass into valuable products: syngas, hot gas, biochar, and bio-oil (pyrolysis oil). These products could become new, such as heat, power, fine chemicals, etc. The plastic waste can be mixed with biomass to increase the synergy between both to achieve products like biochar for multiple applications.

The type of thermochemical process depends on the operation conditions (see Figure 1). Torrefaction is a heating process at the lowest temperature (290°C) that is carried out at a slow heat rate (0.01-0.05°C/s) and long residence time (10-60 min) to obtain mostly solid products [5-7].

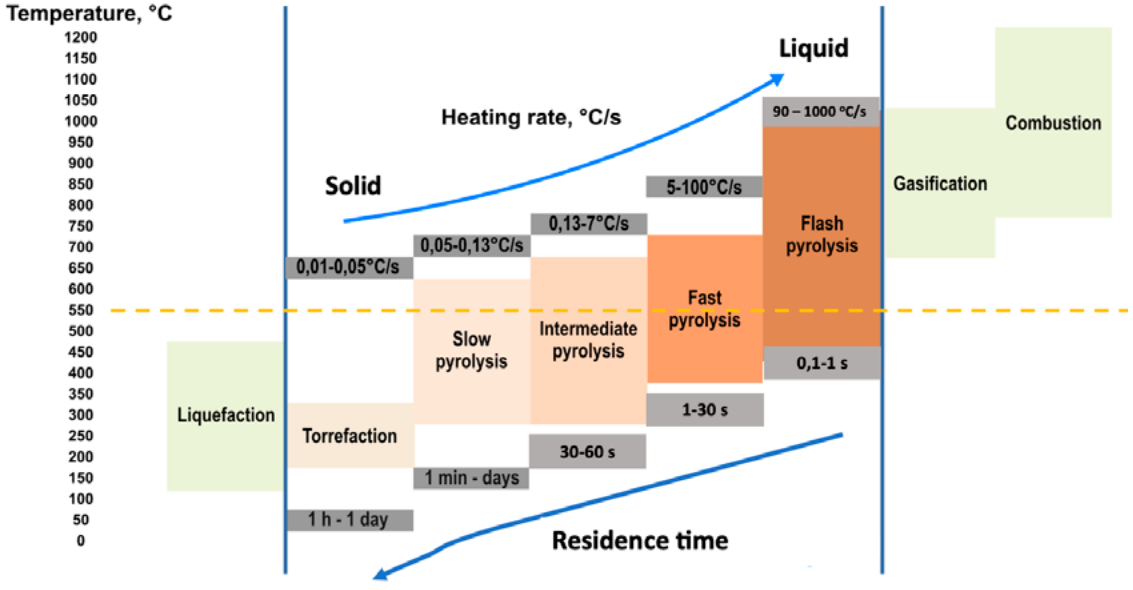

Figure 1. Description of figure above (prepared by authors and modified from [5]).

DOI: https://doi.org/10.51573/Andes.PPS39.SS.BBB.2

The products formed during the pyrolysis of biomass and commercial plastics depend on pyrolysis severity. Primary processes are carried out at the lowest heating rate and temperature. Still, when the severity is increased (e.g., increasing the heating rate and the temperature), secondary char, condensed oil (phenolics, aromatic), and low molecular weight products are formed.

Biomass is transformed during the heating process, e.g., condensation of aliphatic chains for ring formation from cellulose and hemicellulose become a solid part and all the benzene rings from lignin remain at low temperature (200-400°C). Condensation of branched structure for ring enlargement and polymerization of benzene rings by removing ether bonds occur as temperature increases up to 500°C. The organization process, removal of the ether bond of the interlayer sheet, condensation, and enlargement of fused rings occur at temperatures above 700°C.

The route to produce biochar from lignocellulosic biomass initializes with dehydration and cracking of functional groups from cellulose and hemicellulose will occur to permit the aromatization process and then the biochar formation [8-11]. Regarding lignin, its functional groups undergo cracking and heteroatoms are removed, resulting in the formation of biochar.

Concerning the pyrolysis of plastic material, it can be said that it is a depolymerization process in the formation of smaller polymers according to elementary reactions, such as those involved in the pyrolysis of Polystyrene (PS) [12]:

end initiation:	$P_n \rightarrow R_{n-1} + R_1$
random initiation:	$P_n \rightarrow R_{n-i} + R_i$
hydrogen abstraction:	$R_i + P_n \rightarrow P_i + R_n$
β-scission:	$R_n \rightarrow P_{n-j} + R_j$
depropagation:	$R_n \rightarrow R_{n-1} + P_1$
termination by disproportionation:	$R_i + R_j \rightarrow P_i + P_j$
termination by recombination:	$R_i + R_j \rightarrow P_{i+j}$

Polystyrene (PS) pyrolysis is considered to proceed via type-free radical reactions that include β-scission, hydrogen abstraction, hydrogen transfer, radical recombination, and disproportionation with the aromatic monomer, dimer, and trimer as the main products. Aromatic monomers are mainly produced via an unzipping reaction, where the terminal aromatic ring falls off due to the fracture of the C–C linkage between two aromatic rings.

Previously, the torrefaction process affected the biochar formation. This prior process increases biochar formation due to the last formation of crosslinking, depolymerization, and charring processes. In general terms, the pyrolysis of biomass is a process in which the oxygen and hydrogen are removed to obtain a product that seems like coal, kerogens, etc.

DOI: https://doi.org/10.51573/Andes.PPS39.SS.BBB.2

LDPE-biomass mixtures generated more char products than MBr-Np and MBr-Np-LDPE. In contrast, literature reports that co-pyrolysis of poly-olefinic plastics (such as LDPE) with biomass promotes bio-oil production. Some volatiles from biomass degradation were trapped within the residual solid, where they further reacted with the residual char and other volatiles to recombine. Such reactions led to the formation of secondary char, which is consistent with increased char yield at the expense of bio-oil production.

There are batch and continue reactors, such as screw kiln reactors, fluidized bed reactors, etc. The heating process can be external electric power by electrical resistance, hot gas from an external combustion process or a carrier that was hot outside a screw kiln, or by using microwaves, etc.

Screw kiln reactors can be used for slow pyrolysis to produce biochar if the raw material remains inside the kiln for an extended period (more than 20 minutes). However, they can also be used for fast pyrolysis to produce bio-oil, provided a short residence time for the gases inside the reactor (less than 1 second) is ensured. In the case of fluidized bed reactors, the residence times of solids and vapors are nearly identical and very brief (less than 1 second), making them well-suited for bio-oil production. Biochar can also be obtained through the gasification process, with a significant BET surface area that depends on the type of biomass used. This approach is essential for thermochemical processes aimed at simultaneously producing energy, liquid fuels, and biochar.

Biochar Characterization

It is essential to know what kind of biochar we are generating; it is therefore, necessary to characterize it in order to decide on a suitable application (see Figure 2). The physicochemical, surface, and structural/molecular characteristics make it possible to know the composition, pH, electrical conductivity, physical properties, internal structure and morphology, decomposition temperature, functional groups, aromaticity, etc. [9].

The biomass transforms the heating process, e.g., in biochar, the carbon increases, oxygen and hydrogen decrease, and several functional groups disappear, like the C=O group. Other data related to DTG analysis are necessary to determine the degradation temperature. Several plastic materials degrade at a single temperature and at temperatures higher than those of lignocellulosic biomass.

DOI: https://doi.org/10.51573/Andes.PPS39.SS.BBB.2

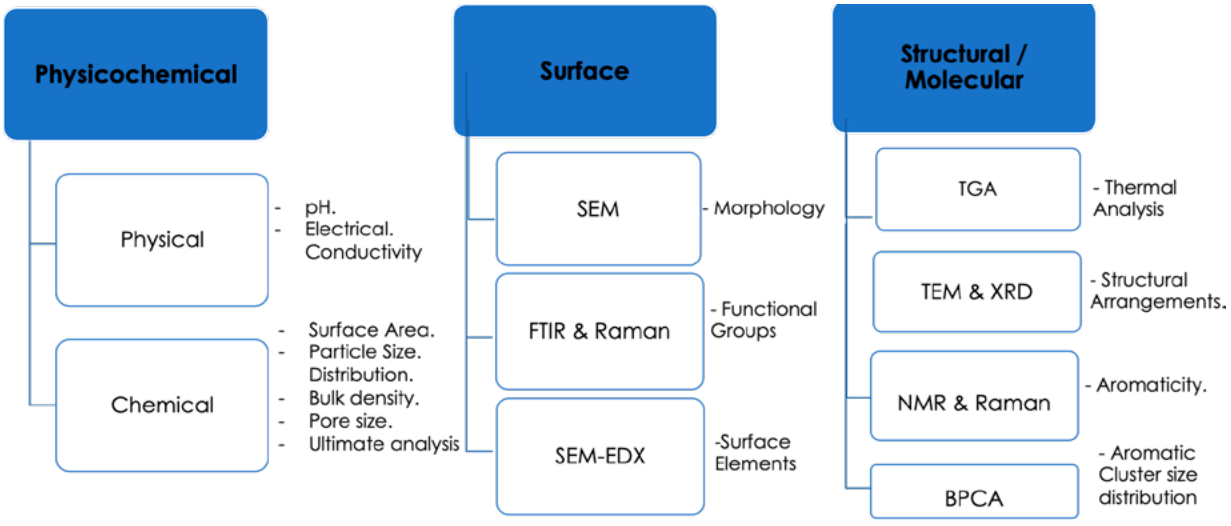

Figure 2. Analytical technique for characterization the biochar (prepared by authors).

The aromatic molecular structures within biochar can be defined by their aromaticity indices (the proportion of aromatic carbons) and their aromatic domain sizes (the number of conjugated aromatic rings within polyaromatic domains). ^{13}C Solid-State Nuclear Magnetic Resonance (ssNMR) can detect the different chemical environments within a biochar sample. The other most straightforward measure of aromaticity is to know the H/C ratio, which is related to aromatic domain size (n) by using the equation:

$$\frac{H}{C} = \frac{2\sqrt{n}+1}{2\sqrt{n}+n}$$

SEM analysis allows us to observe the structural change and transformation of the internal morphology of the biomass until it becomes biochar. On the other hand, theoretical analysis can determine how pyrolysis conditions influence the biochar structure. Simulation of the transformation of the biochar structure at different temperatures can be observed in Figure 3.

DOI: https://doi.org/10.51573/Andes.PPS39.SS.BBB.2

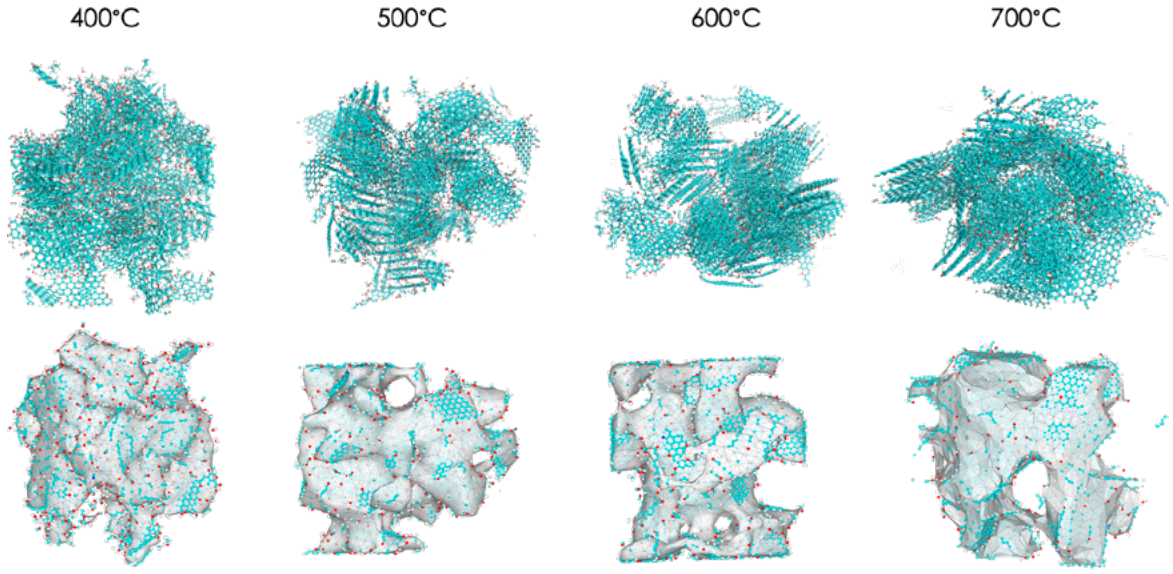

Figure 3. Simulation of biochar structure at different temperature (taken from [9]).

The internal surface of biochar depends on the thermochemical process [13,14]. It can increase from the slowest area of torrefied material to about 50 m2/g more than 2000 m2/g for activated biochar [14]. The internal surface of the biochar plays a crucial role in anaerobic digestion processes. The microporous can trap the smallest particles, the mesoporous can absorb medium sized particles, and the microporous provide a space for bacterial colonies to form. This high degree of selectivity significantly enhances methane production yields.

Biochar Application

Biochar has several applications. It can be used as an adsorbent, fuel, catalyst, catalyst support, soil amendment and additives. Modern application includes:

1. Using biochar derived from biomass waste as a catalyst provides the opportunity to develop a sustainable and efficient process to add value to plastic waste.

2. CO2 capture.

3. Biochar is a low-cost absorbent material.

4. Biochar contains significantly fewer functional groups than its biomass precursors. Depending on the nutrient composition of the initial biomass, a variety of nitrogen-, phosphorous- and sulfur-based functionalities may also appear. Nevertheless, those are found in significantly lower quantities than in oxygen-based groups.

DOI: https://doi.org/10.51573/Andes.PPS39.SS.BBB.2

5. Biochar as the conductive medium. The adsorption mechanism on the biochar surface is at two temperature ranges. The higher the pyrolytic temperature, > 450°C, the more suitable the biochar is for the adsorption of organic contaminants because of the improved surface area, the increased distribution of micropores, and the higher level of hydrophobicity. Biochar produced at lower temperatures, < 450°C, is suitable for the adsorption of inorganic and polar organic contaminants. The absorption rate that biochar creates over low temperatures is facilitated by electrostatic attraction, precipitation, and O- O-containing functional groups.

   The conductive properties of biochar could play an essential role in soil biogeochemistry and the microbial community, for instance, by promoting direct interspecies electron transfer (DIET), a mechanism for electron exchange between different species of microorganisms. After accepting electrons from an electron-donating microorganism, the conductive graphite-like sheet structures allow electrons to migrate to electron-accepting microorganisms, linking both metabolisms.

6. Role of biochar in anaerobic digestion processes [15]:

   - Improved digestion performance: accumulation of volatile fatty acids.
   - Improvement of the anaerobic environment: inhibitor adsorption, load shock resistance.
   - Promotion of substance exchange: increases the speed of transport of substances and direct interspecific electron transfer.
   - Biochar is very useful for integrating different technologies (see Figure 4).
   - Use of biochar for potable water production.
   - Use of biochar in the cement industry.
   - Production of nanostructures from tar using biochar.

DOI: https://doi.org/10.51573/Andes.PPS39.SS.BBB.2

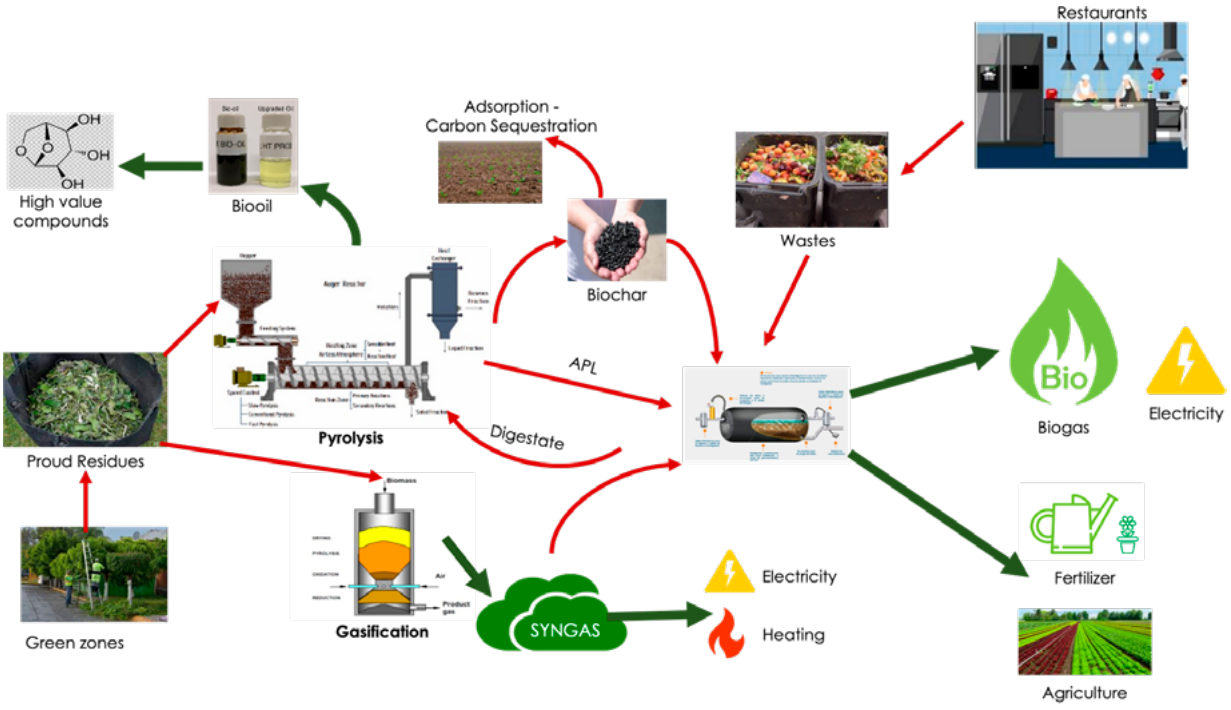

Figure 4. Outline of potential integrations between anaerobic digestion and pyrolysis (prepared by authors).

Conclusion

The second law of thermodynamics limits exploitation of agriculture and heat waste. Carrying out any process is linked to entropy generation due to irreversibility; therefore, this entropy creation means resources are lost, including materials, minerals, metals, and energy. It is vital to focus on developing complex engineering and high-level technology; working on soft engineering, specifically in advanced mathematical modeling; and developing the basic science for generating new efficient processes. These aspects are necessary to take advantage of biomass to implement a circular economy and reduce harmful environmental impacts.

Acknowledgments

The authors thank the Ministry of Science, Innovation, and Technology of the Colombian governmentfor supporting the project “Esquema híbrido de poligeneración (Termoquímico–Biológico) para la sustitución de fósiles a partir de residuos orgánicos” (ICETEX contract 2022-0666) under the ministry’s call for proposals 890.

References

1. A. Jain, S. Sarsaiya, M. K. Awasthi, R. Singh, R. Rajput, U. C. Mishra, J. Chen, and J. Shi, "Bioenergy and bio-products from bio-waste and its associated modern circular economy: Current research trends, challenges, and future outlooks," *Fuel*, vol. 307, p. 121859, 2022.
2. O. Dogu, M. Pelucchi, R. Van de Vijver et al., "Progress in Energy and Combustion Science," *Progress in Energy and Combustion Science*, vol. 84, p. 100901, 2021.
3. X. Zhou, L. J. Broadbelt, R. Vinu, and K. M. Van Geem, "Mechanistic understanding of thermochemical conversion of polymers and lignocellulosic biomass," in *Advances in Chemical Engineering*, vol. 49, Academic Press, 2016, pp. 95–198.
4. A. G. Adeniyi et al., "Green Chemical Engineering," *Green Chemical Engineering*, vol. 5, pp. 31–49, 2024.
5. F. Chejne J., M. García Pérez, and M. del P. Noriega E., *Applications of Biomass Derived Materials for Bioproducts and Bioenergy*, Hanser, Munich, Germany, 2024.
6. A. V. Bridgwater, "Review of fast pyrolysis of biomass and product upgrading," *Biomass and Bioenergy*, vol. 38, pp. 68–94, 2012, https://doi.org/10.1016/j.biombioe.2011.01.048
7. M. Sharifzadeh, M. Sadeqzadeh, and M. Guo et al., "Progress in Energy and Combustion Science," *Progress in Energy and Combustion Science*, vol. 71, pp. 1–80, 2019.
8. Y. Li, B. Xing, Y. Ding, X. Han, and S. Wang, "A critical review of the production and advanced utilization of biochar via selective pyrolysis of lignocellulosic biomass," *Bioresource Technology*, p. 123614, 2020, https://doi.org/10.1016/j.biortech.2020.123614
9. V. Sierra-Jimenez, J. P. Mathews, F. Chejne, A. Dufour, and M. Garcia-Perez, "Atomistic modeling of lignocellulosic and carbonaceous fuels and their pyrolysis reactions: A review," *Energy and Fuels*, 2024, https://doi.org/10.1021/acs.energyfuels.3c02901
10. A. Ngambia, O. Mašek, and V. Erastova, "Development of biochar molecular models with controlled porosity," *Biomass and Bioenergy*, vol. 184, p. 107199, 2024.
11. R. Wood, O. Mašek, and V. Erastova, "Biochars at the molecular level. Part 1 – Insights into the molecular structures within biochars," *ArXiv preprint arXiv:2303.09661*, 2023, https://doi.org/10.48550/arXiv.2303.09661
12. G. Martínez-Narroa, P. Prasertcharoensuk, L. S. Diaz-Silvarrey, L. Dixon, and A. N. Phan, "Chemical recycling of mixed plastic waste via catalytic pyrolysis," *Journal of Environmental Chemical Engineering*, vol. 10, p. 108494, 2022, https://doi.org/10.1016/j.jece.2022.108494
13. Y. P. Rago, F.-X. Collard, J. F. Görgens, D. Surroop, and R. Mohee, "Torrefaction of biomass and plastic from municipal solid waste streams and their blends: Evaluation of interactive effects," *Fuel*, vol. 277, p. 118089, 2020, https://doi.org/10.1016/j.fuel.2020.118089
14. M. Córdoba-Ramirez, F. Chejne, J. Alean, C. A. Gómez, Á. Navarro-Gil, J. Abrego, and G. Gea, "Experimental strategy for the preparation of adsorbent materials from torrefied palm kernel shell oriented to CO2 capture," *Environmental Science and Pollution Research*, 2024, https://doi.org/10.1007/s11356-024-32028-3
15. Z.-W. He et al., "Biochar regulates anaerobic digestion: Insights into the roles of pore size," *Chemical Engineering Journal*, vol. 480, p. 148219, 2024.

SPECIAL SYMPOSIA | BIOPOLYMERS, BIOCOMPOSITES AND BIOPROCESSING

Processability Study of Thermoplastic Starch/ Poly(Butylene Succinate Adipate) Blends in a Reactive Extrusion

Manuela Vargas Rojas, Felipe Salcedo Galán and Jorge Medina Perilla

DOI: https://doi.org/10.51573/Andes.PPS39.SS.BBB.3

December 2024

Processability Study of Thermoplastic Starch/ Poly(Butylene Succinate Adipate) Blends in a Reactive Extrusion

Manuela Vargas Rojas, Felipe Salcedo Galán and Jorge Medina Perilla[1]

Abstract: Growing concerns about ocean contamination from fossil fuel based polymers have created a demand for biodegradable alternatives, particularly for packaging applications. Thermoplastic starch (TPS) is a promising, eco-friendly biopolymer but has poor mechanical properties and high hydrophilicity. To address these issues, this article explores modifying starches through reactive extrusion and blending them with other biodegradable polymers. The study evaluates blends of native or acetylated starch with poly(butylene succinate) adipate (PBSA), using glycerol as a plasticizer and tartaric acid as a reactive agent. Films were processed using an internal mixer and compression molding. Results show tartaric acid improves processability and slightly enhances mechanical properties such as ductility and tensile strength, though limitations persist due to morphological and thermal stability issues. Despite these challenges, reactive extrusion with tartaric acid offers a promising approach for developing new packaging materials.

Keywords: Thermoplastic Starch, BioPBSA, Polymer Blend, Processability, Hydrophilicity

1 The authors Manuela Vargas Rojas (m.vargas12@uniandes.edu.co) and Jorge Medina Perilla are affiliated with the Department of Mechanical Engineering at the Universidad de los Andes in Colombia. The author Felipe Salcedo Galán is affiliated with the Department of Chemical and Food Engineering at the same university.

DOI: https://doi.org/10.51573/Andes.PPS39.SS.BBB.3

Introduction

The global production of fossil-based polymers for industrial sectors has been steadily increasing annually due to high demand since its creation. In 2020, its global production reached around 400 MT/year, with 44% from the packaging sector [1]. These polymers are difficult to recycle due to global economics and the physical impossibility of its degradation [2]. Consequently, polymers are often landfilled, incinerated, exported, or released into water sources and soil [3], particularly from the packaging industry. By 2030, an estimated 90 MT/year of these materials will be in the ocean [4], which threatens biodiversity, drinking water, and sustainable fishing. Biodegradable and compostable biopolymers are proposed as alternatives [5,6] to improve the management of single-use plastic pollution in the ocean.

Starch is a promising biopolymer due to its renewability, low cost, thermoplastic behavior, biodegradability, and compostability [7,8]. However, it faces issues such as difficult processability, fragility, and high hydrophilicity. Plasticizers are added to improve its behavior [7], creating thermoplastic starch (TPS). TPS is a low-density and cost-effective biopolymer, with limited stability due to its water absorption, and inferior mechanical properties [9]. To improve these issues, polymers blends are used. Several polymers have been tested [10,11], but degradability remains an issue when using fossil-based polymers for the blends. However, adding inherently biodegradable biopolymers to the blend can create materials that biodegrade quickly into non-toxic compounds.

Polybutylene succinate adipate (PBSA) is an aliphatic polyester biopolymer that degrades completely in water or soil over time. It also has good ductility, making it suitable for extrusion and injection molding [12]. Given these properties, blending TPS and PBSA is a potential solution to the problem. However, this blend has immiscibility issues due to the hydrophilic nature of starch and the hydrophobic nature of PBSA [13]. To overcome this, one strategy is to decrease the hydrophilic nature of the starch by replacing hydroxyl groups with carboxyl groups, via an esterification reaction. This article uses acetylated starch and reactive extrusion with tartaric acid to increase the substitution degree, by esterification, of modified and native starch in the blends with PBSA. This is expected to enhance mechanical properties, alter FTIR absorption wavelengths, and improve the microscopic structure observed in SEM images.

Materials and Methods

Materials

Native and acetylated modified corn starch was supplied by Ecobioplastic, Colombia. Glycerol (99%) and tartaric acid L(+) from Panreac AppliChem, USA was used as a plasticizer and esterification agent. Poly(butylene succinate adipate) (PBSA) pellets were supplied by Mitsubishi Chemical Performance Polymers, USA.

DOI: https://doi.org/10.51573/Andes.PPS39.SS.BBB.3

Blend and Films Preparation

To begin, the experimental design consists of 3 factors: type of starch (native and acetylated), proportion of TPS/TPSA and PBSA (60:40 and 70:30), and tartaric acid concentration (1, 2, and 3% wt. of starch weight). To plasticize the starch, glycerol was used in a 30% concentration based on TPS/TPSA weight. TPS refers to thermoplastic native starch, and TPSA refers to thermoplastic acetylated starch.

For the process, the raw materials were dried overnight at 80°C. Each material was then added to an internal mixer: PBSA was added first, followed by starch, tartaric acid, and glycerol. This was processed at 60 rpm and 150°C until the torque stabilized (10 min). The obtained blends were cut into pieces and placed in a molding press to form films of 0.3 mm thickness. Finally, the obtained films were die-cut into type V samples according to ASTM D638 and kept in a controlled environment to avoid moisture absorption.

Characterization of Blends

Chemical Analysis – FTIR Test

Films of raw materials and blends were used to analyze molecular interactions. A Thermo Scientific Nicolet iS50 spectrophometer was used, with a spectral range of 4000 to 400 cm^{-1} and 32 scans. No replicates were performed for this test. All spectra were baseline corrected and normalized.

Mechanical Analysis – Tensile Test

Type V samples were tested using a Universal Testing Machine INSTRON 3367 following ASTM D882 standards. Testing was performed at room temperature with a strain rate of 12.5 mm/min. At least eight specimens were tested for each sample, and the average and standard deviation results were reported.

Morphological Analysis – SEM Images

Films of raw materials and blends underwent cryogenic fracturing to expose the transversal plane. These fragments were gold metallized to ensure conductivity to the test. Subsequently, these samples were observed in the LYRA3 TESCAN machine with a magnification of ×3000. No replicates were conducted for this test.

DOI: https://doi.org/10.51573/Andes.PPS39.SS.BBB.3

Results and Discussion

Chemical Analysis – FTIR Test

To confirm the hypothesis that reactive extrusion increases the substitution degree of starch by replacing hydroxyl groups with carboxyl groups, FTIR analyses were conducted. This was assessed by the increase in carboxyl groups at the 1750 cm^{-1} wavelength and a decrease of hydroxyl groups at the 3250 cm^{-1} wavelength [14].

The IR spectra of TPS, PBSA, and their blends are shown in Figure 1. For the blends, no chemical interaction between raw materials is noted as no new peaks appeared. However, some absorbances changes were noted. For the 60:40 TPS and PBSA blends, contrary to expectations, the 3250 cm^{-1} peak increased with more tartaric acid and the 1750 cm^{-1} peak showed no clear trend. The same observations were made for the 70:30 TPS and PBSA blends. These results indicate that the esterification of native starch with tartaric acid did not occur. According to literature, starch tends to not esterify in the presence of glycerol and under thermal conditions. It needs an external catalytic agent to facilitate the reaction. In this case, the short mixing time was not enough to provide a self-catalytic reaction [15].

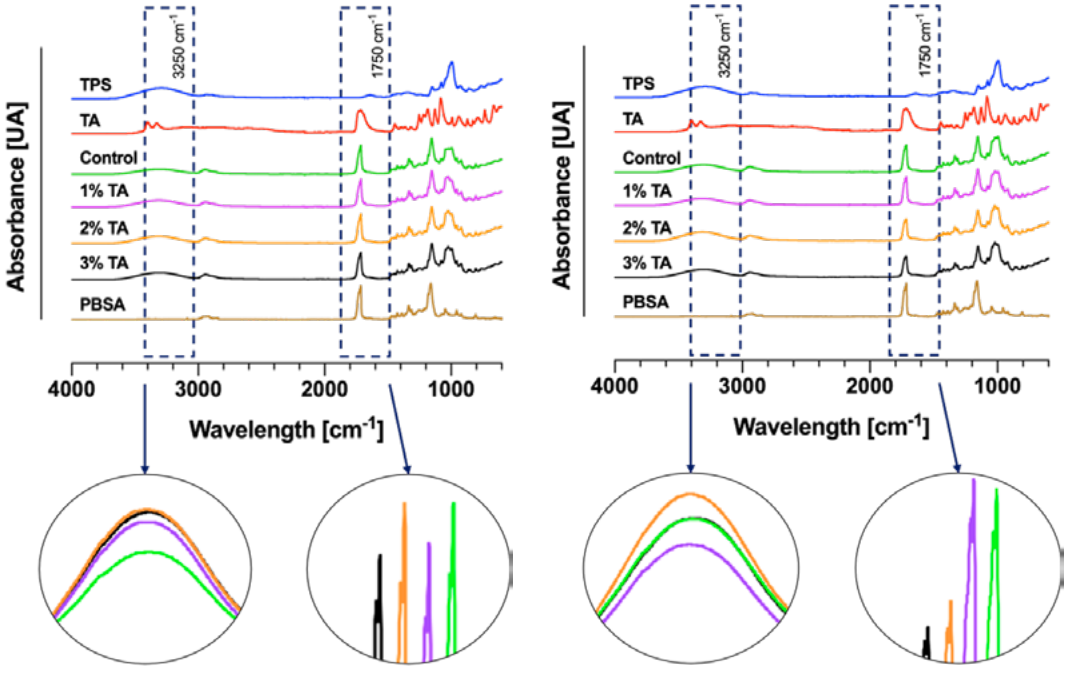

Figure 1. Comparative FTIR between the raw materials and the blends of TPS and PBSA (60:40 – left, 70:30 – right) with addition of tartaric acid (TA). The studied signals are shown in the graphs.

DOI: https://doi.org/10.51573/Andes.PPS39.SS.BBB.3

Figure 2 shows the IR spectra of TPSA, PBSA and their blends. With more tartaric acid, the 60:40 TPSA and PBSA blends shows the expected decrease in the hydroxyl peak (O – H) and increase in the carbonyl ester peak (C = O), indicating higher substitution degrees, similar to findings in other esterification studies [14]. For the 70:30 TPSA and PBSA blends, there is the expected change compared to the control. However, there are inconsistencies in the trend of the carbonyl ester peak and the hydroxyl peak, related with the change of tartaric acid. These changes can be related with the substitution degree of the starch, which will prove the initial hypothesis.

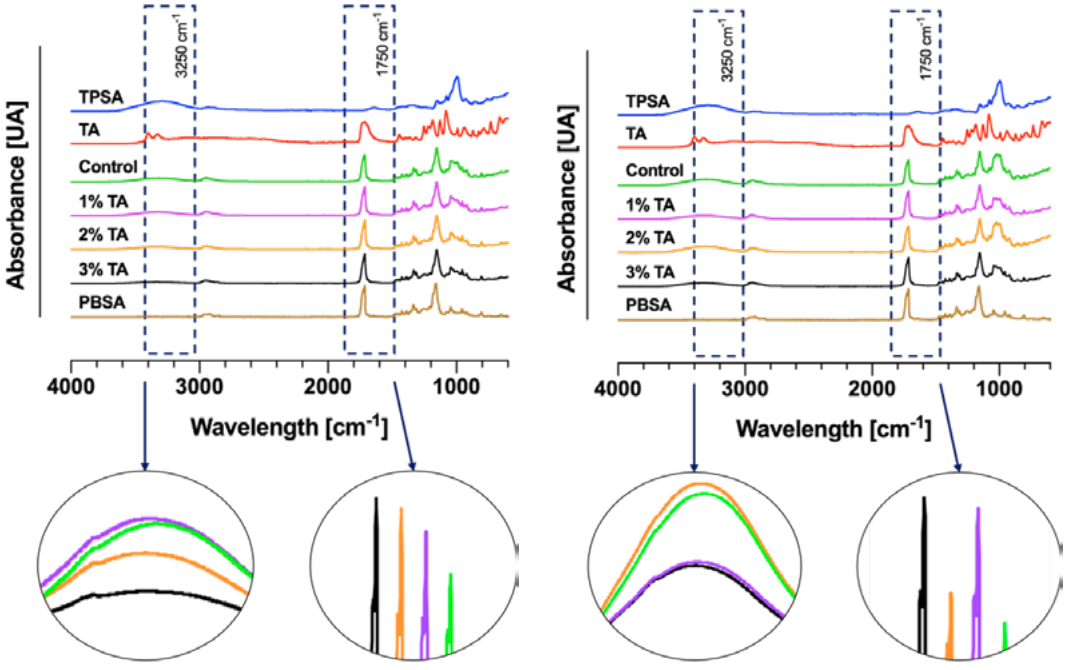

Figure 2. Comparative FTIR between the raw materials and the blends for TPSA and PBSA (60:40 – left, 70:30 – right) with addition of tartaric acid (TA). The studied signals are shown in the graphs.

Mechanical Analysis – Tensile Test

Tensile tests were performed to observe the consequences of a change in the substitution degree of the starch in the blends. For this study, the tensile strength and ductility were evaluated.

The tensile strength of the studied blends is shown in Figure 3. For blends with TPS, increasing tartaric acid results in a collective decrease in tensile strength, with a significant drop compared to the control. For blends with TPSA, the 60:40 blends show no significant change compared to the control, while the 70:30 blends show a slight decrease. All blend values fall between those of the raw materials. Comparing the controls for the blends with TPS and TPSA, there is a significant change where the higher value is for the TPSA blends. This result is expected as the acetylated

DOI: https://doi.org/10.51573/Andes.PPS39.SS.BBB.3

starch has fewer hydroxyl groups, which makes it more hydrophobic. The change in the chemical nature of the starch gives a better miscibility with the PBSA.

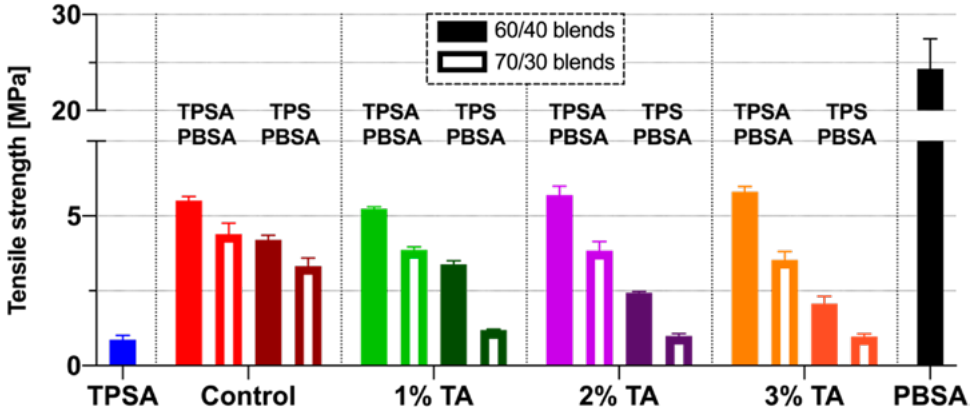

Figure 3. Comparative tensile strength between the raw materials and the blends between TPS/TPSA and PBSA (60:40, 70:30) with addition of tartaric acid (TA).

Subsequently, Figure 4 shows the ductility of the studied blends. For blends with TPS, increasing tartaric acid decreases ductility in the 60:40 blends, with no significant change in the 70:30 blends compared to the control. Using TPSA increases ductility compared to the control, more prominently in the 70:30 blends. All blend values fall between those of the raw materials.

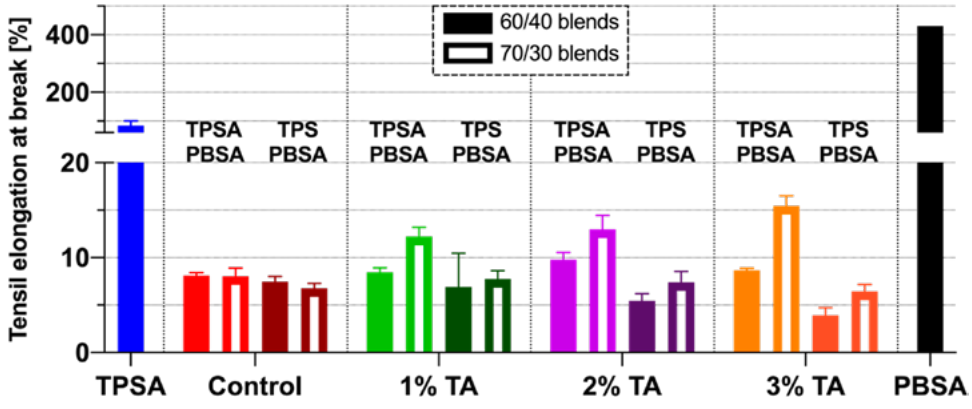

Figure 4. Comparative ductility between the raw materials and the blends between TPS/TPSA and PBSA (60:40, 70:30) with addition of tartaric acid (TA).

According to the FTIR analysis, the TPSA blends, especially those with 3% tartaric acid, showed changes in wavelengths related to starch esterification. These same blends did not show a significant change in tensile strength but had the highest increase in ductility. The tensile strength of polymers is linked to chain entanglement and organization, which suggest that the addition of

DOI: https://doi.org/10.51573/Andes.PPS39.SS.BBB.3

tartaric acid had little effect on these factors [16]. For ductility, fewer matrix imperfections, such as cavities, pores, and fractures, facilitate elongation of the films which is related to a better interfacial adherence [17]. With the obtained results, it is expected to see less of these features in SEM images for the mentioned blends.

Morphological Analysis – SEM Images

A SEM analysis was performed to observe the direct consequences of a change in the substitution degree of the starch in the blends, related to an improvement in the ductility of the film and its relationship with the microstructure of the transversal section of the film.

Figure 5 shows the microstructure of films made by TPS. Arrows in the pictures shows different features that indicates a poor interfacial adherence: cavities, pores, edges, cracks, and granules [17]. With the addition of tartaric acid there is a slight increase in cracks, which can explain the collective decrease of ductility for these blends, especially for the 60:40 blends.

Subsequently, the images for the blends with TPSA are shown in Figure 6. Unlike the TPS results, increasing tartaric acid in these blends results in progressively fewer granules, pores, and cracks. The surface shows small particles, likely from starch granule breakdown, compared to the control. These findings align with previous sections, where starch esterification indicated an increase in ductility and unchanged tensile strength, especially in the 3% tartaric acid blends. In this case, the images that show a better microstructure, related with the features mentioned before, are the ones with 3% tartaric acid, even more in the case of the 70:30 blend.

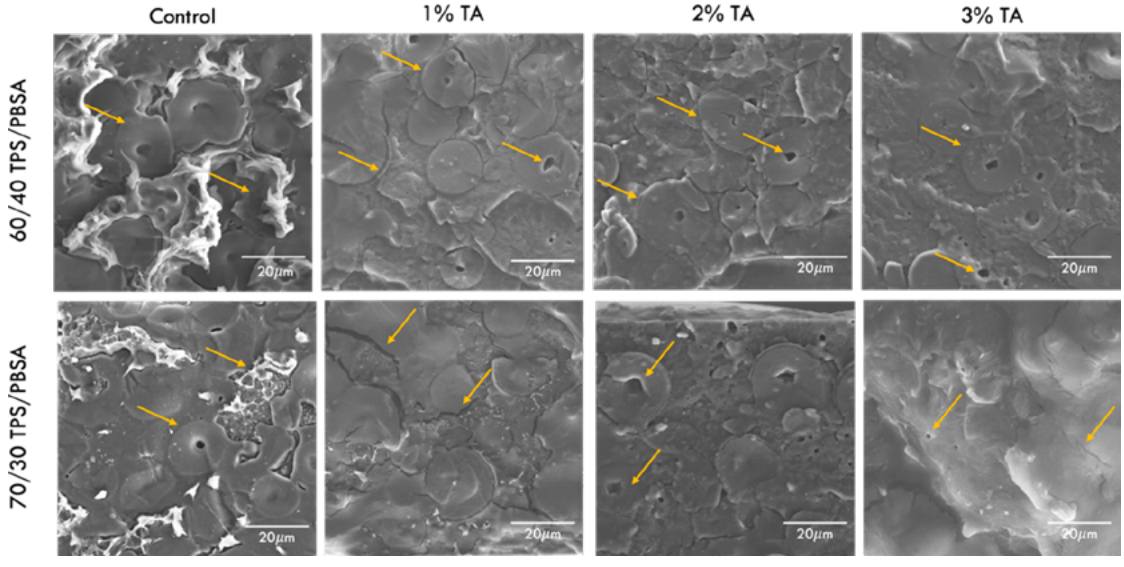

Figure 5. Comparative SEM images (×3000) between control and blends of TPS and PBSA (60:40, 70:30) with addition of tartaric acid (TA). Arrows indicate the important features of the microstructures.

DOI: https://doi.org/10.51573/Andes.PPS39.SS.BBB.3

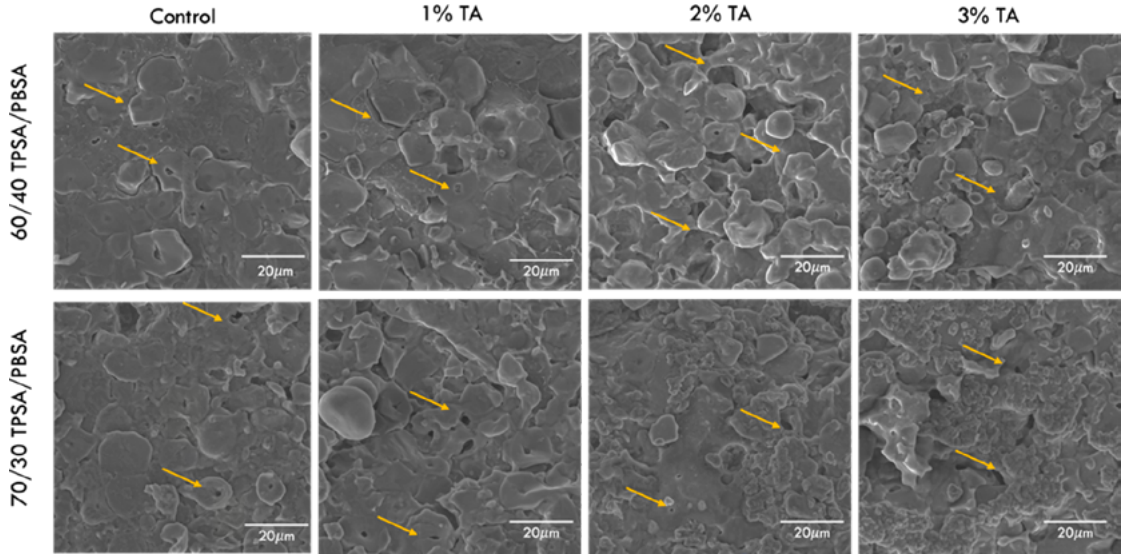

Figure 6. Comparative SEM images (×3000) between control and blends of TPSA and PBSA (60:40, 70:30) with addition of tartaric acid (TA). Arrows indicate the important features of the microstructures.

Conclusion

The use of tartaric acid as an esterification agent in TPS and PBSA blends did not present an improvement in the properties. On the contrary, it shown a greater incompatibility between the raw materials with a lower tensile strength and ductility and no change at the FTIR and SEM images. This decrease in compatibility was not the expected result, which provides the opportunity to conduct more tests and analyses to provide a possible response to the problem.

However, adding tartaric acid in TPSA and PBSA blends presented the expected changes in the FTIR analyses. The tensile strength did not significantly change, probably related to an unchanged structural organization of the chains. Ductility exhibited an improvement with the increase in tartaric acid, which is explained at the SEM images where a better microstructure is shown with the same trend. Nevertheless, the change in ductility is not enough for a flexible packaging application, which is why a new approach is needed.

References

1. Plastics Europe, “Plastics – The Facts 2023,” 2023.
2. J. Ackerman and D. B. Levin, “Rethinking plastic recycling: A comparison between North America and Europe”, *Journal of Environmental Management*, vol. 340, p. 117-859, Aug. 2023, https://doi.org/10.1016/j.jenvman.2023.117859

3. E. M. Foundation, "The new plastics economy: Rethinking the future of plastics", Ellen MacArthur Foundation. [Online]. Available in: https://ellenmacarthurfoundation.org/the-new-plastics-economy-rethinking-the-future-of-plastics
4. S. B. Borrelle et al., "Predicted growth in plastic waste exceeds efforts to mitigate plastic pollution", *Science*, vol. 369, no. 6510, pp. 1515-1518, Sep. 2020, https://doi.org/10.1126/science.aba3656
5. Acoplásticos, "ABC: Ley 2232 de 2022 'Plásticos de un solo uso'", Colombia, Review, 2022. [Online]. Available in: https://www.acoplasticos.org/index.php/mnu-noti/412-boletines-2022-abc-ley-de-plasticos-hd-pdf
6. T. M. Letcher, *Plastic Waste and Recycling: Environmental Impact, Societal Issues, Prevention, and Solutions*. Academic Press, 2020.
7. Z. N. Diyana et al., "Physical Properties of Thermoplastic Starch Derived from Natural Resources and Its Blends: A Review", *Polymers*, vol. 13, no. 9, p. 1396, Apr. 2021, https://doi.org/10.3390/polym13091396
8. D. Plackett and V. Katiyar, "Biopolymers–New Materials for Sustainable Films and Coatings", 2011, pp. 301-315. https://doi.org/10.1002/9781119994312.ch14
9. S. P. Bangar, W. S. Whiteside, A. O. Ashogbon, and M. Kumar, "Recent advances in thermoplastic starches for food packaging: A review", *Food Packaging and Shelf Life*, vol. 30, pp. 100-743, Dec. 2021, https://doi.org/10.1016/j.fpsl.2021.100743
10. S. Jayarathna, M. Andersson, and R. Andersson, "Recent Advances in Starch-Based Blends and Composites for Bioplastics Applications," *Polymers*, vol. 14, no. 21, 4557, Oct. 2022, https://doi.org/10.3390/POLYM14214557
11. A. Surendren, A. K. Mohanty, Q. Liu, and M. Misra, "A review of biodegradable thermoplastic starches, their blends and composites: recent developments and opportunities for single-use plastic packaging alternatives," *Green Chemistry*, vol. 24, no. 22, pp. 8606–8636, Nov. 2022, https://doi.org/10.1039/D2GC02169B
12. I. S. Yun, S. W. Hwang, J. K. Shim, and K. H. Seo, "A study on the thermal and mechanical properties of poly (butylene succinate)/thermoplastic starch binary blends", *International Journal of Precision Engineering and Manufacturing-Green Technology*, vol. 3, no. 3, pp. 289-296, Jul. 2016, https://doi.org/10.1007/s40684-016-0037-z
13. J. Li, X. Luo, X. Lin, and Y. Zhou, "Comparative study on the blends of PBS/thermoplastic starch prepared from waxy and normal corn starches", *Starch–Stärke*, vol. 65, no. 9-10, pp. 831-839, Sep. 2013, https://doi.org/10.1002/star.201200260
14. V. C. R. Schmidt et al., "Effect of the degree of acetylation, plasticizer concentration and relative humidity on cassava starch films properties", *Journal of Food Science and Technology*, vol. 39, no. 2, pp. 491-499, Jun. 2019, https://doi.org/10.1590/fst.34217
15. S. Zhang, Y. He, Y. Yin, and G. Jiang, "Fabrication of innovative thermoplastic starch bio-elastomer to achieve high toughness poly(butylene succinate) composites", *Carbohydrate Polymers*, vol. 206, pp. 827-836, Feb. 2019.
16. K. Balani, V. Verma, A. Agarwal and R. Narayan, "Physical, thermal, and mechanical properties of polymers", *Biosurfaces*, pp. 1-23, 2015.
17. W.Y. Jang, B.Y. Shin, T.J. Lee and R. Narayan, "Thermal Properties and Morphology of Biodegradable PLA/Starch Compatibilized Blends", *Journal of Industrial and Engineering Chemistry*, vol. 13, pp. 457-464, 2007.

SPECIAL SYMPOSIA | BIOPOLYMERS, BIOCOMPOSITES AND BIOPROCESSING

Production of a Starch-Based Polymeric Coating with Incorporation of Bioactive Principles from Chemical Synthesis to Extend the Shelf Life of Cavendish Banana

Felipe-Salcedo, Jose-Bejarano, Juan-Diaz, Yina-Ortega and Ariel-Vaca

DOI: https://doi.org/10.51573/Andes.PPS39.SS.BBB.4

December 2024

Production of a Starch-Based Polymeric Coating with Incorporation of Bioactive Principles from Chemical Synthesis to Extend the Shelf Life of Cavendish Banana

Felipe-Salcedo, Jose-Bejarano, Juan-Diaz, Yina-Ortega and Ariel-Vaca[1]

Abstract: Crown rot is a severe postharvest disease affecting tropical and subtropical fruits like mango, avocado, papaya, and banana. It is caused by fungal pathogens that penetrate the fruit, reducing its pulp and leading to premature ripening. Systemic fungicides have been used to control these fungi, typically applied to seeds, leaves, or fruits to prevent disease spread. However, traditional fungicides can pose toxicity risks to the environment and human health. Essential oils are chemical substances that can be found in plants and have antifungal capacity. Essential oils are being investigated as an alternative to traditional fungicides since they are less toxic to the environment and human health; however, they are more expensive and less efficient than traditional fungicides. Accordingly, chemically synthesizing the chemical compounds that are the active antifungal agent inside essential oils can be an ecological and effective approach to produce a new generation of antifungals. In this study, modified starch was investigated as a carrier for thymol (active antifungal agent in thyme oil) incorporation using four distinct methods. Emulsions of starch and thymol were prepared and spray dried to obtain a soluble powder that was used to produce coatings. The most effective method for thymol incorporation yields a retention of approximately 40% according to gas chromatography analysis. In-vitro results indicated that thymol incorporated into the matrix exhibited antifungal effects against key fungi responsible for crown rot disease in Cavendish bananas at concentrations greater than 6% w/w relative to the coating matrix.

Keywords: Crown Rot, Antifungal Coating, Banana Postharvest Treatment, Thymol

1 The authors Felipe-Salcedo (fesalced@uniandes.edu.co), Jose-Bejarano, Juan-Diaz and Ariel-Vaca are affiliated with the Department of Chemical and Food Engineering at the Universidad de los Andes in Colombia. The author Yina-Ortega is affiliated with the Universidad Popular del Cesar also in Colombia.

DOI: https://doi.org/10.51573/Andes.PPS39.SS.BBB.4

Introduction

In terms of export value, banana is the most important fruit globally. In 2022, global banana exportations reached 19.2 million tons [1]. Today, this fruit boasts a significant genetic diversity base that still exists due to natural crossbreeding [2]. One single variety, Cavendish, dominates 40% of global banana crops, representing nearly all large-scale export trade and a significant portion of local trade [3]. The Cavendish is a seedless sweet banana variety classified within the AAA group. The food security of less developed or low-income countries depends heavily on bananas due to their high consumption and potential [4]. The Cavendish banana currently dominates the global market but faces ongoing challenges, particularly in preventing postharvest diseases like crown rot, a damaging affliction affecting a wide range of tropical and subtropical fruits [5].

Crown rot is considered the primary postharvest disease affecting bananas, causing losses of around 20-25%. This critical disease is caused by fungi, including *Colletotrichum musae*, *Lasiodiplodia theobromae*, and *Fusarium sp.* [6,7]. Systemic fungicides have traditionally been used to control these fungi, but these products can be harmful to the environment and human health [8]. The European Union has restricted maximum residue limits (MRLs) for several fungicides, increasing the need to explore or develop safer alternatives [9]. Essential oils are a promising alternative due to their antifungal properties and lower toxicity. Studies have shown that essential oils from plants like thyme and lemongrass are effective against a wide range of pathogens [10-12].

In this context, to enhance control of crown rot in Cavendish bananas, the Integrated Design Group for Processes and Products (GDPP) at Universidad de los Andes has developed a natural coating based on modified cassava starch. This coating has been evaluated on Cavendish bananas incorporating thyme oil as an antifungal agent, demonstrating promising results as a postharvest treatment for maintaining banana quality and extending shelf life [13]. Therefore, it is possible to harness the primary bioactive compounds of essential oils, such as thymol and citral, which can be chemically synthesized to address their limitations, such as cost and efficacy [14,15]. This research investigates the effectiveness of this polymeric coating with thymol (from chemical synthesis) incorporation to improve the scalability of the coating as an alternative postharvest treatment for Cavendish bananas.

Materials and Methods

Materials

Native cassava starch, glycerol, citric acid, and other raw materials for coating matrix elaboration were supplied by Cimpa®. Sunflower oil was purchased from a commercial store and thymol crystals from Sigma Aldrich® were used. The *Fusarium sp.* and *Colletotrichum sp.* strains were provided by the Banana Research Center (Cenibanano), along with Cavendish bananas (*Musa AAA*).

DOI: https://doi.org/10.51573/Andes.PPS39.SS.BBB.4

Coating Preparation and Thymol Incorporation

The preparation of the coating matrix was carried out as reported by Vaca et al. [16]. This process, shown in Figure 1, began with the mixing of citric acid, glycerol, and cassava starch, and other raw materials, followed by modification and drying through spray drying. Detailed process information can be found in patent application WO2023026073. This coating matrix will hereafter be referred to as SM.

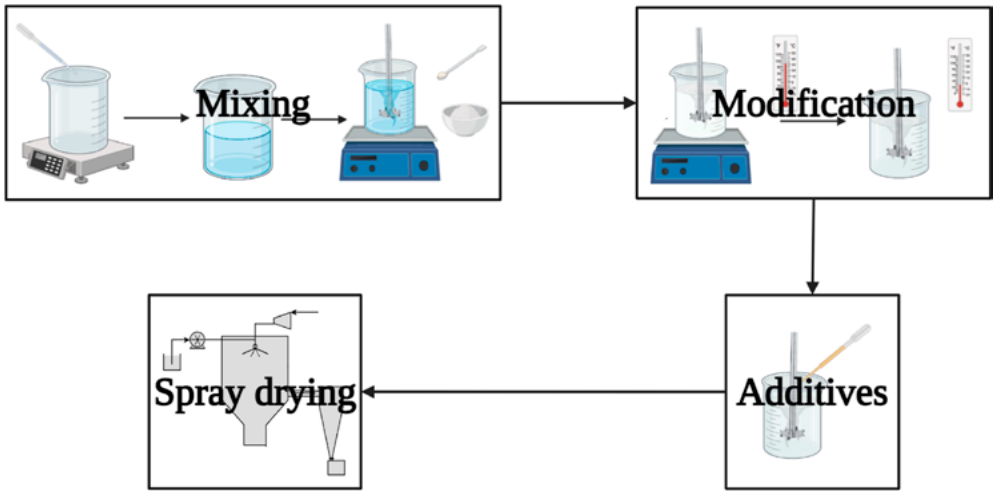

Figure 1. Coating matrix preparation method. Based on what is reported in the patent application WO2023026073. Created in Biorender.com

Once the SM coating matrix was obtained, thymol was incorporated by impregnating the obtained powder with a thymol solution in sunflower oil at a concentration of 10% w/v of thymol in oil. The solution of thymol in oil was added to SM powder through a dropwise method in a relation of 10% v/w relative to SM, to produce a 1% w/w thymol concentration in coating, then mixed and sealed hermetically in a vial, which was left to stabilize for 4 days. This formulation will hereafter be referred to as SM-TH.

Characterization of Thymol Incorporation

Thermogravimetric Analysis:

A thermogravimetric analysis was performed using a TA Instruments Q600® (New Castle, DE, USA). The method involved a ramp of 10°C/min up to 600°C in a nitrogen atmosphere with a flow rate of 10 mL/min. Using this methodology, the SM and SM-TH formulations were compared.

DOI: https://doi.org/10.51573/Andes.PPS39.SS.BBB.4

Gas Chromatography Analysis:

The presence of thymol in the coating sample was verified using gas chromatography (GC). An ethanol extraction was performed on the coating with thymol sample (SM-TH) and the non-thymol coating or coating matrix sample (SM) during 24 h in a 1:10 coating-to-ethanol ratio. These extracts were then compared to a thymol standard solution in ethanol. A calibration curve was constructed to quantify the incorporated thymol using this method.

A methodology previously used by the research group was employed for the GC analysis. A Shimadzu MDGC-2010 gas chromatograph was utilized, configured as follows: an RTX-WAX column (100% polyethylene glycol) measuring 30 m × 0.25 mm × 0.5 µm was used. The oven temperature was initially set at 35°C for 2 minutes, followed by a heating rate of 5°C/min until reaching 150°C. Subsequently, the temperature was increased to 250°C at a rate of 10°C/min and held for 7 min to eliminate residues. The injector temperature was fixed at 250°C, utilizing the splitless injection mode, with 2 µL of the sample being injected. A flame ionization detector (FID) was used at 250°C. Helium was employed as the carrier gas at a flow rate of 1 mL/min.

In-vitro evaluation:

Initially, *Fusarium sp.* and *Colletotrichum sp.* strains were activated and replicated to obtain mother cultures of each strain, received using the filter paper conservation method. Conidial suspensions of the pathogens were prepared from each mother culture, with a concentration of $1x10^3$ conidia per milliliter and a 1:1 ratio of conidia from each strain. For the in-vitro tests, 100 µL of the conidial suspension was inoculated, followed by the application of 400 µL of the coating formulations. The coatings were allowed to dry and then incubated at 27°C for 48 hours. This methodology is detailed in Figure 2. Starting from the formulation (SM-TH), the thymol concentration was increased until achieving a significant colonies inhibitory effect comparing to the conventionally used fungicide, Mertect®, containing thiabendazole as its active ingredient, which served as the positive control. The formulations used in the reported in vitro test are listed in Table 1. Each coating formulation was prepared by reconstituting 1.5 g of powder in 100 mL of sterile distilled water at room temperature.

DOI: https://doi.org/10.51573/Andes.PPS39.SS.BBB.4

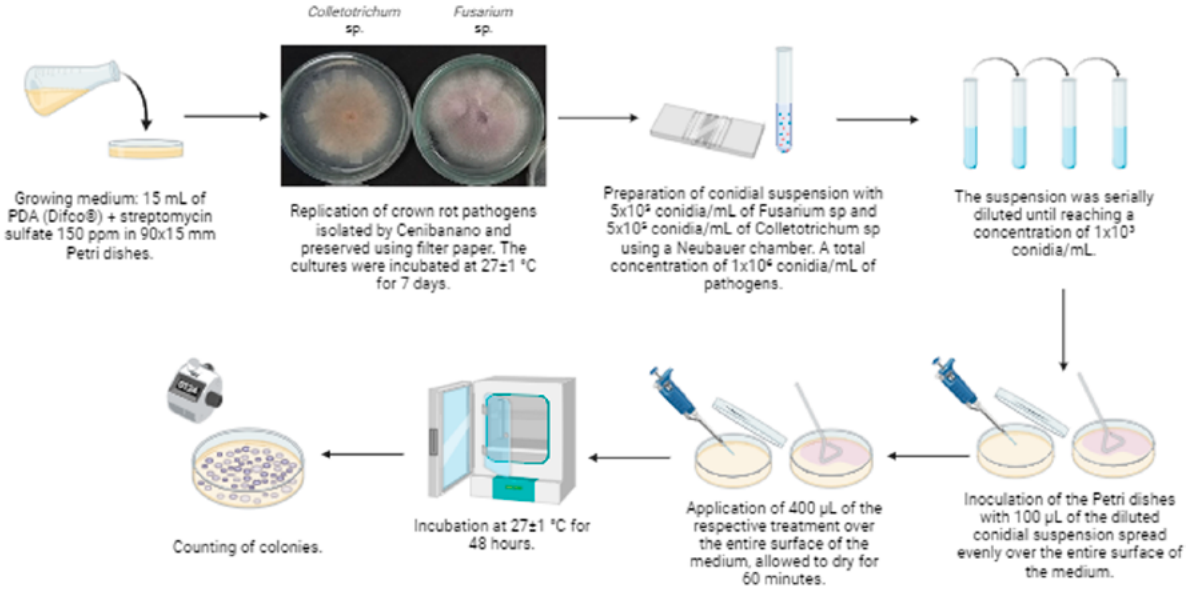

Figure 2. In-vitro evaluation methodology. Created in Biorender.com

Table 1. In-vitro coating formulations and control treatments.

Formulations	Inoculation	Thiabendazole[1]	Starch Matrix	Sunflower oil	Thymol[2]
C-	X	-	-	-	-
C+	X	396 ppm	-	-	-
SM	X	-	X	-	-
SM-TH	X	-	X	X	10 mg/g
SM-TH×6	X	-	X	X	30 mg/g
SM-TH×12	X	-	X	X	60 mg/g

[1] Thiabendazole was applied in sterile deionized water solution at the concentration shown in the table.
[2] The concentrations shown for thymol are relative to the coating matrix.

Results and Discussion

Characterization of Thymol Incorporation

Thermogravimetric Analysis:

Through the thermogram shown in Figure 3, it was observed that SM exhibits a significant drop around 50°C compared with SM-TH; typically, these drops at low temperatures are associated

with water loss, indicating that SM contains more water. Additionally, another weight loss occurs around 300°C; at this temperature, both formulations exhibit characteristic weight loss that is similar for both, associated with the degradation of the starch matrix, which is the main component of the coating. Another common drop for both occurs at 400°C, with SM-TH showing a higher loss, consistent with expectations due to the incorporation of oil as seen in Figure 3(a). Although the incorporation of oil in the coating through impregnation method is evident from TGA, the presence and loss of thymol are less distinct. Thymol typically exhibits characteristic weight loss around 140-160°C according to the planned methodology, yet no noticeable differences between SM and SM-TH are observed within this interval (see Figure 3[b]).

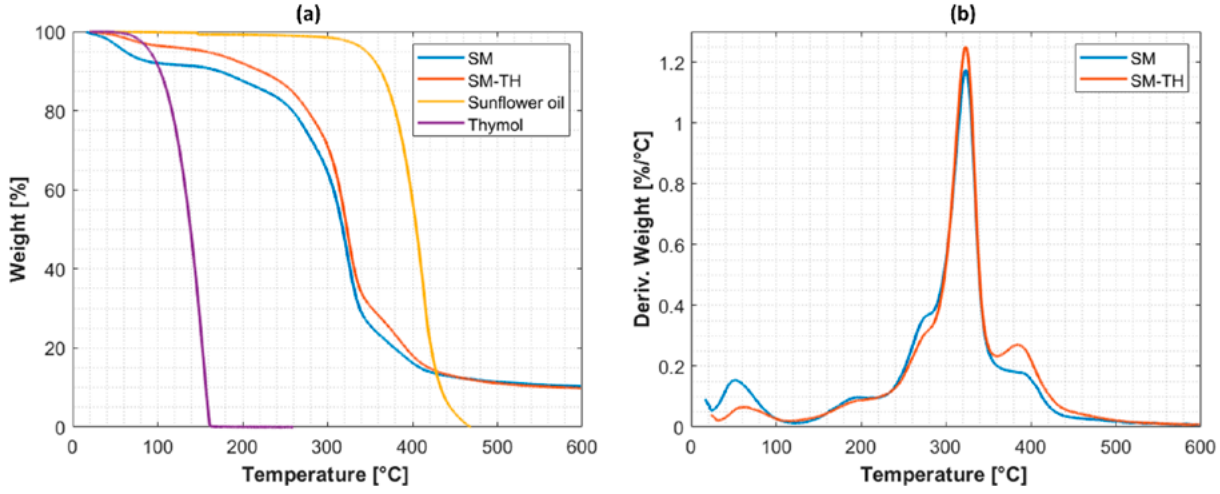

Figure 3. Thermograms of the coating matrix and the coating with thymol. (a) Weight percentage as a function of temperature (b) Derivative of weight as a function of temperature.

Gas Chromatography Analysis:

In contrast to the TGA, the chromatograms of the ethanol solutions resulting from thymol and the extracts of the coatings respectively show a notable presence of thymol in SM-TH. The results are shown in Figure 4. In the chromatogram of the ethanol-thymol standard solution, the solvent (ethanol) elution is observed early on, around 4 min, and a second peak corresponding to thymol is seen at a retention time of approximately 24.5 minutes. Comparing SM and SM-TH, it is evident that SM-TH has a prominent thymol peak at the same retention time, whereas SM shows a very faint peak. This small peak in SM might be due to sample contamination during storage or residuals in the chromatograph column. Considering these observations, the presence of thymol in SM-TH is evident. After constructing a calibration curve with standards, it was determined that the average concentration for SM-TH is around 4±1 mg/g, equal to 0.4% w/w relative to SM. This result is the average of three measurements indicating that the incorporation capacity through impregnation method is near 40% of added thymol.

DOI: https://doi.org/10.51573/Andes.PPS39.SS.BBB.4

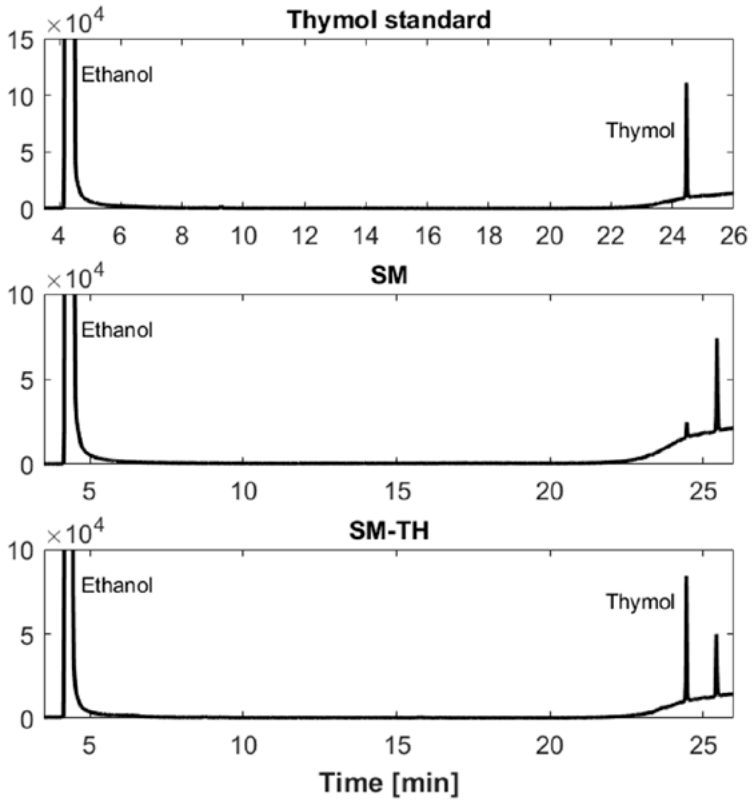

Figure 4. Chromatograms of thymol solution in ethanol and ethanol extracts of the coating matrix and coating with thymol incorporation.

In-vitro evaluation:

The results of pathogen colony inhibition by the coatings are depicted in Figure 5. It is noted that SM shows similarity to the negative control, suggesting no significant effect solely from the coating matrix. A similar result was obtained with SM-TH, where despite containing 1% w/w thymol relative to the matrix (equivalent to 10 mg/g), no significant inhibitory effect is observed. However, when evaluating SM-TH at different concentrations, a notable inhibitory effect on the colonies is observed starting from a thymol concentration of 60 mg/g relative to the matrix (SM-TH×6). Increasing the concentration to 120 mg/g of the matrix (SM-TH×12) resulted in an inhibitory effect comparable to the positive control (C+).

DOI: https://doi.org/10.51573/Andes.PPS39.SS.BBB.4

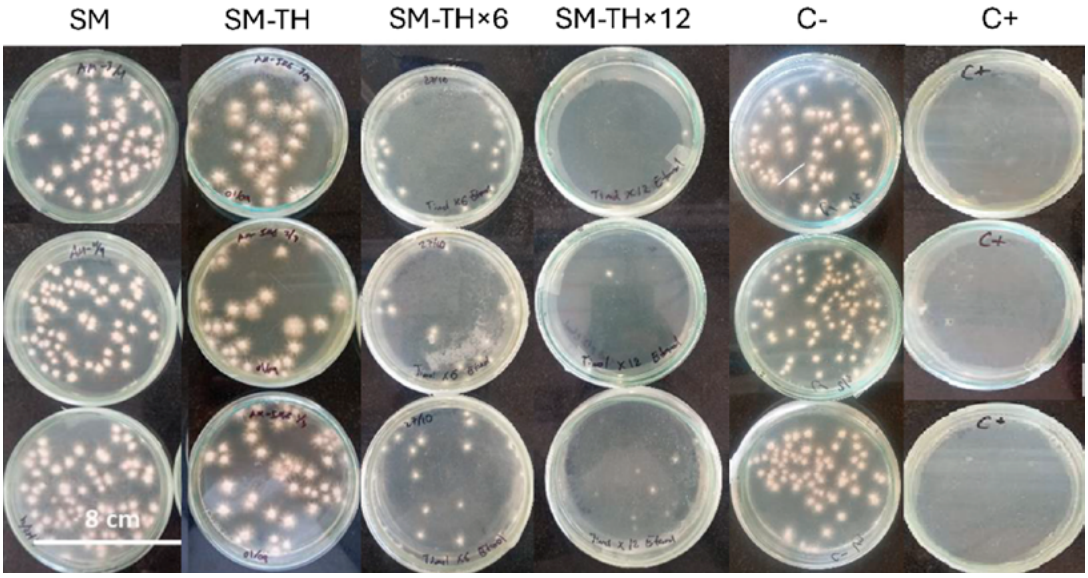

Figure 5. In-vitro pathogen colony inhibition test.

Conclusions

In this study, the effectiveness of thymol incorporation into modified starch-based coatings for antifungal control was achieved. Thermographic analysis (TGA) reveals distinct thermal behaviors between formulations, with SM-TH demonstrating oil integration and less water content. Chromatographic analysis confirmed substantial thymol presence in SM-TH, demonstrating successful thymol incorporation in coating. In vitro testing against fungal pathogens showed that while SM alone exhibited minimal inhibitory effects, SM-TH displayed significant colony inhibition at higher thymol concentrations (more than 60 mg/g), comparable to positive controls. These findings underscore the potential of thymol-enhanced coatings in effectively mitigating fungal growth, suggesting their utility as a viable postharvest treatment to enhance quality and extend the shelf life of Cavendish bananas.

References

1. FAO, "Banana Market Review 2022," 2023. Accessed: Nov. 01, 2023. [Online]. Available: https://www.fao.org/3/cc6952en/cc6952en.pdf
2. S. Debnath, A. A. Khan, A. Das, I. Murmu, A. Khan, and K. K. Mandal, "Genetic Diversity in Banana," *Sustainable Development and Biodiversity*, pp. 217-241, 2019, https://doi.org/10.1007/978-3-319-96454-6_8
3. A. Drenth and G. Kema, "The Vulnerability of Bananas to Globally Emerging Disease Threats," *Phytopathology*, vol. 111, no. 12, pp. 2146-2161, Dec. 2021, https://doi.org/10.1094/phyto-07-20-0311-rvw

4. I. Sulistyowarni, Sri Sundari, S. Halim, and U. Pertahanan, "The Potential of Banana Trading Commodity to Fulfill Market Demand and Support Food Security in Defense Economic Perspective (Study in Bogor District)," *Jurnal Pertahanan dan Bela Negara*, 2020, https://doi.org/10.33172/jpbh.v10i3.1114

5. R. Aguilar Anccota et al., "Hongos asociados a la pudrición de la corona en frutos de banano orgánico (Musa spp. L.) en Piura, Perú," *RIAA,* vol. 4, no. 1, pp. 81-88, 2013, Accessed: Jun. 29, 2024. [Online]. Available: https://dialnet.unirioja.es/servlet/articulo?codigo=5344992&info=resumen&idioma=ENG

6. D. Yagual et al., "Control of crown rot on Cavendish banana by high voltage atmospheric cold plasma treatment," *Journal of Food Engineering*, vol. 357, 111-654, Nov. 2023, https://doi.org/10.1016/j.jfoodeng.2023.111654

7. D. Triest and M. Hendrickx, "Postharvest Disease of Banana Caused by Fusarium musae: A Public Health Concern?," *PLoS Pathogens*, vol. 12, no. 11, p. e1005940, Nov. 2016, https://doi.org/10.1371/journal.ppat.1005940

8. World Health Organization, *Prevención de los riesgos para la salud derivados del uso de plaguicidas en la agricultura,* [Online]. Available https://iris.who.int/bitstream/handle/10665/42799/9243590995.pdf

9. The European Commission, *Commission Regulation (EU) No 10/2011*, [Online]. Available: https://eur-lex.europa.eu/eli/reg/2011/10/oj. [Accessed: Apr. 09, 2024].

10. R. Vilaplana, L. Pazmiño, and S. Valencia-Chamorro, "Control of anthracnose, caused by Colletotrichum musae, on postharvest organic banana by thyme oil," *Postharvest Biology and Technology*, vol. 138, pp. 56-63, Apr. 2018, https://doi.org/10.1016/j.postharvbio.2017.12.008

11. B. Safaiefarahani and R. Mostowfizadeh-Ghalamfarsa, "Fungal Plant Disease Management by Natural Essential Oils," *Plant Pathology Science*, vol. 8, no. 1, pp. 24-37, Mar. 2019, https://doi.org/10.29252/pps.8.1.24

12. K. H. S. Kouassi, M. Bajji, A. Zhiri, P. Lepoivre, and M. Jijakli, "Evaluation of three essential oils as potential sources of botanical fungicides," *Communications in Agricultural and Applied Biological Sciences*, vol. 75, pp. 525-529, 2010.

13. J. Diego et al., "Evaluación de coadyuvantes a base de almidón de yuca (incorporando agentes antifúngicos) sobre los procesos de maduración y pudrición de banano Cavendish," 2022, [Online]. Available: https://augura.com.co/wp-content/uploads/2023/04/Informe-anual-CENIBANANO-2022_VF.pdf. [Accessed: Oct. 22, 2023].

14. M. Kazemi, "Phytochemical Composition of Thymus vulgaris L. Essential Oil," *Journal of Essential Oil Bearing Plants*, vol. 18, no. 3, pp. 751-753, May 2015, https://doi.org/10.1080/097206 0x.2014.985733

15. H. J. Centorbi, O. E. Aliendro, and C. M. Mattana, "Effect of thymol and environmental factors on growth and biofilm formation by Listeria monocytogenes," *Boletín Latinoamericano y del Caribe de Plantas Medicinales y Aromáticas*, vol. 18, no. 4, pp. 411–424, Jul. 2019, https://doi.org/10.35588/blacpma.19.18.4.26

16. A. M. Vaca Bohórquez, A. D. Rojas Vera And F. Salcedo Galán, "Solid Soluble Compound for Application as a Carrier of Active Agents or Multifunctional Coating on Plant and Fruit Structures and Method of Obtainment Thereof," Mar. 02, 2023, [Online]. Available: https://patentscope.wipo.int/search/en/detail.jsf?docId=WO2023026073&_cid=P22-LEYA5R-19360-1. [Accessed: Sep. 28, 2023].

SPECIAL SYMPOSIA | BIOPOLYMERS, BIOCOMPOSITES AND BIOPROCESSING

Processability and Mechanical Properties of Spent Coffee Ground (SCG) and Polypropylene Biocomposites

A. Menendez, M. Coello, J. Suarez, M. Lazo, G Bravo, G. Baño, E. Adrian and A. Rigail-Cedeño

DOI: https://doi.org/10.51573/Andes.PPS39.GS.BBB.5

December 2024

Processability and Mechanical Properties of Spent Coffee Ground (SCG) and Polypropylene Biocomposites

A. Menendez, M. Coello, J. Suarez, M. Lazo, G Bravo, G. Baño, E. Adrian and A. Rigail-Cedeño[1]

Abstract: The circular economy encourages optimizing use of plastics, waste reduction, sustainable materials, and processing of plastic products. In this framework, the use of agricultural waste materials promotes waste reduction and eco-design in plastic product manufacturing. This study researched the preparation of an isotatic polypropylene (PP) matrix (MFI 50 grade) with spent coffee grounds (SCG) and various commercial additives. The biocomposites were analyzed to evaluate their mechanical properties and processability. PP and SCG composites were synthesized with 30% SCG content with maleic anhydride grafted polypropylene (PP-g-MA), stearic acid and epoxidized oil as compatibilizers. The study found that polypropylene grafted with maleic anhydride (PP-g-MA) as a compatibilizer improves SCG dispersion, enhancing processing stability. Epoxidized oil (EO) and stearic acid (SA) can also function as lubricants that significantly improve composite processability by decreasing specific energy and shear viscosity. The processability properties were accessed using a torque rheometer. A tensile test showed that while SCG addition decreases mechanical strength, PP-g-MA improves interfacial adhesion, and EO and SA increase flexibility by reducing brittleness.

Keywords: Biocomposites, Compatibilizers, Processability, Circular Economy

1 All the authors are affiliated with the Faculty of Mechanical Engineering and Production Sciences at the ESPOL Polytechnic University in Ecuador. The authors J. Suarez, M. Lazo, E. Adrian and A. Rigail-Cedeño (arigail@espol.edu.ec) are also affiliated with the Plastics Processing Laboratory at the same university.

DOI: https://doi.org/10.51573/Andes.PPS39.GS.BBB.5

Introduction

Finding environmentally friendly and sustainable materials is becoming essential in our society. One potential solution is incorporating agricultural and industrial waste into polymeric matrices [1]. Coffee is a widely consumed agricultural product in Ecuador and coffee drinks have become a trendy beverage. However, the preparation of coffee drinks generates organic waste. These wastes contain components that make them attractive as reinforcements in polymer matrix composites. They contain polyphenols, which are compounds that provide antioxidant properties that help protect materials from degradation. In addition, the presence of components such as cellulose, hemicellulose, lignin, and fatty acids improves the mechanical properties of the biocomposite [2].

Developing biocomposites based on thermoplastic matrices reinforced with natural fibers faces several problems due to the low compatibility and processability as a result of the hydrophobic matrix and hydrophilic reinforcement, affecting the final product's performance [3]. Garcia et al. [4] increased impact energy in the biocomposites to mitigate these drawbacks. Fuqua et al. [4] incorporated 5% by weight of PP-gMA into a corn fiber-reinforced polypropylene matrix, showing that the elastic modulus and strength of the biocomposites were improved compared to incompatible biocomposites. Regarding coffee residues, Leal et al. [5] incorporated ground coffee husk (GCH) in proportions of 20, 30, and 40% by weight to a PP and used PP-g-MA as a compatibilizer at 10% by weight relative to GCH. Relative to pure PP, the composite with 40% GCH increased flexural strength, flexural modulus, tensile modulus, and thermal distortion temperature. Similar findings in thermal, mechanical, and other physical properties occurred due to improved interface interaction between the maleic anhydride from PP-g-MA and the hydrophilic reinforcement particles [3,6]. Most studies examine the relationship between the formulation compound and the physical properties of the SGC biocomposite [7,8]. The processability and energy consumption of polymer composites reinforced with coffee wells are very relevant from the industrial perspective, especially those using polypropylene grafted with maleic anhydride as a compatibilizer. This area of research offers enormous potential for developing low-energy processing, sustainable materials, which require exploration to optimize their properties and processing energy efficiency.

In this study, a coffee-reinforced polypropylene thermoplastic composite material is investigated by evaluating the incorporation of three additives: polypropylene grafted with maleic anhydride (PP-g-MA), stearic acid (SA), and epoxidized oil (EO). The objective is to analyze how these additives interfere with the properties of the composite material. The interaction of the additives is evaluated in terms of the mechanical properties through tensile tests and the processability of the material.

DOI: https://doi.org/10.51573/Andes.PPS39.GS.BBB.5

Methodology

Materials

SCG used as reinforcements were supplied by Sweet & Coffee, a national coffee shop. Polypropylene (PP) with melt flow index (MFI) of 50 g/10min (230°C/2,16 kg) and the maleic anhydride grafted polypropylene (PP-g-MA) with MFI of 22.4 g/10min a density of 0.904 g·cm^{-3}, epoxidized oil (EO) with a density of 0.995 g·cm^{-3} and viscosity of 450 cP were kindly donated by Plasticos Industrial CA (PICA), and stearic acid (SA) with an acid value of 209-212 mgKOH/g was supplied by Dua Kuda, Indonesia.

Mixture Preparation

SCG was dried at 60°C for about 24 hours. Each component was weighed using a digital balance, following the formulations outlined in Table 1. Subsequently, the components were blended in a Brabender torque rheometer at 60 rpm and a temperature of 180°C for 10 minutes. The PP, PP-g-MA, EO, and SA were introduced initially, and the SCG was incorporated after 2 minutes.

Table 1. PP/SCG formulations.

	PP (%)	SCG (%)	PP-g-MA (%)	EO (%)	SA(%)
PP	100	—	—	—	—
SCG30	70	30	—	—	—
SCG30/PP-g-MA	65	30	5	—	—
SCG30/EO/SA	65	30	—	—	5
SCG30/PP-g-MA/EO/SA	60	10	—	5	5

Biocomposite Preparation

The mixtures obtained from the torque rheometer were pelletized using a plastic cutter. The pelletized material was placed inside a mold between the plates of a hydraulic press set to 180°C while maintaining a pressure of 0 psi for melting. Subsequently, a venting process was conducted, consisting of raising the pressure from 0 to 1500 psi and rapidly returning to 0 psi, repeated 10 times. The pressure was then raised to 1500 psi for 5 minutes and then increased to 2000 psi for another 5 minutes. Finally, the samples were cooled to room temperature and de-molded.

DOI: https://doi.org/10.51573/Andes.PPS39.GS.BBB.5

Characterization and Evaluation

Torque Rheometry

After processing in the torque rheometer, the torque vs. time curves were obtained using the Mixer Program for Windows Version 4.9.8 (WinMix) and BRABENDER® Data Correlation Version 4.0.6 software. The specific energy consumed in the processing of each compound, E (kWh/kg), and the viscosity have been successfully obtained previously [9,10].

Mechanical Strength

The test for determining the tensile properties was performed according to ASTM D638 on a Shimadzu AG-IS 10 kN universal testing machine. The test speed was 5 $mm \cdot min^{-1}$ under ambient conditions of 23°C.

Results and Discussion

Figure 1 illustrates the polymer composite behavior of mechanical energy and torque proposed in this study, simulating the twin screw process. Figure 1(b) shows the torque rheometer as a function of time. This graph illustrates how the torque is strongly related to the composite formulation. When the amount of PP was decreased in the formulation towards the biocomposite, the loading torque was shifted from about 30 N.m to a range of 5-10 Nm. This behavior is due to the apparent filling degree in the chamber, observed previously in neat polymers and composites [9]. The increase in torque and energy consumption in this process can be attributed to the higher solids content and particle agglomeration, which disturbs the movement of the PP chains and increases the flow resistance [12]. However, the epoxidized oil and stearic acid consistently decrease the torque after the feeding time. The effect of these low molecular weight additives diminished the loading torque and torque after this feeding time. It has been observed that the presence of a broad molecular weight of polymer decreases the loading torque and the viscosity [12]. When the SCG is added to the PP/additives mixture, the torque increases due to the loading of the SCG. Then, the mixture melts, which significantly influences the torque required for blending and the overall processability of the composite. The torque for pure PP and PP/SCG stabilized at 2.43 N.m and 5.32 Nm, respectively. The PP-gMA significantly stabilizes the melting mixture at earlier times (4.32 min) compared to other additives (5.30 and 5.56). PP-g-MA has a remarkable ability to be a compatibilizer and stabilize the extrusion process, as has been widely observed [13]. Also, the SCG is rich in phenolic compounds [14], which can potentially protect PP and SGS degradation during processing. The good affinity and processability characteristics of PP-g-MA in the PP/SCG blend could be inferred from a smooth and horizontal flat torque during the stabilized zone in a similar approach as observed in the neat PP.

DOI: https://doi.org/10.51573/Andes.PPS39.GS.BBB.5

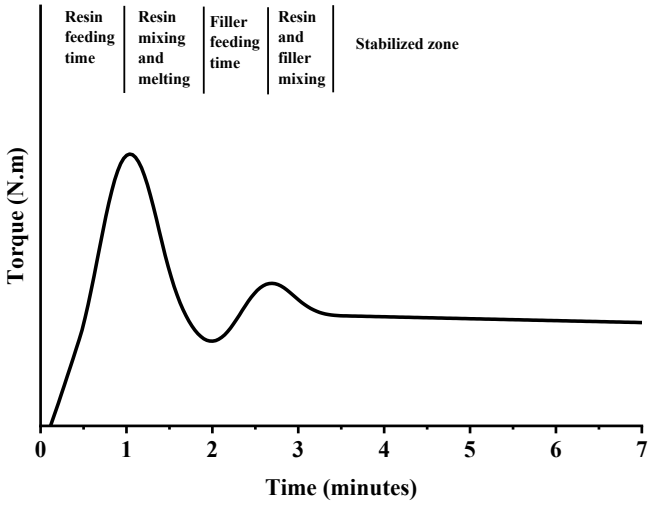

(a)

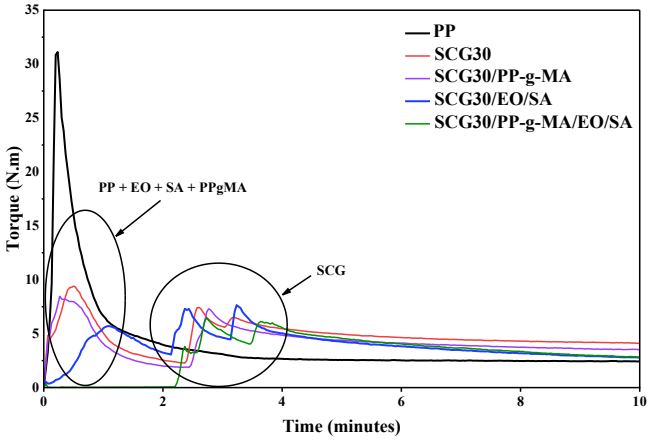

(b)

Figure 1. (a) Torque vs. Time for this research, adapted and modified from [11] and (b) Torque vs Time curves of compounds of coffee and compatibilizer additives.

In addition, EO and SA could act as lubricants; they could reduce the shear friction of the melt blending, and then the temperature and viscosity would decrease consistently. Figure 2(a) shows that EO/SA has the lowest viscosity and temperature for about 513,13 Pa.S and 182.23 C, respectively. However, Figure 1(b) shows that the ES and SA mixtures are still unstabilized at 10 minutes. For this reason, the PP-g-MA could help keep the melting quality during processing in this biocomposite. In general, it is observed that the temperature and the torque at 10 minutes are related to the viscosity and specific energy of the PP and biocomposite, so these results give a potential overview for the industrial scale process.

DOI: https://doi.org/10.51573/Andes.PPS39.GS.BBB.5

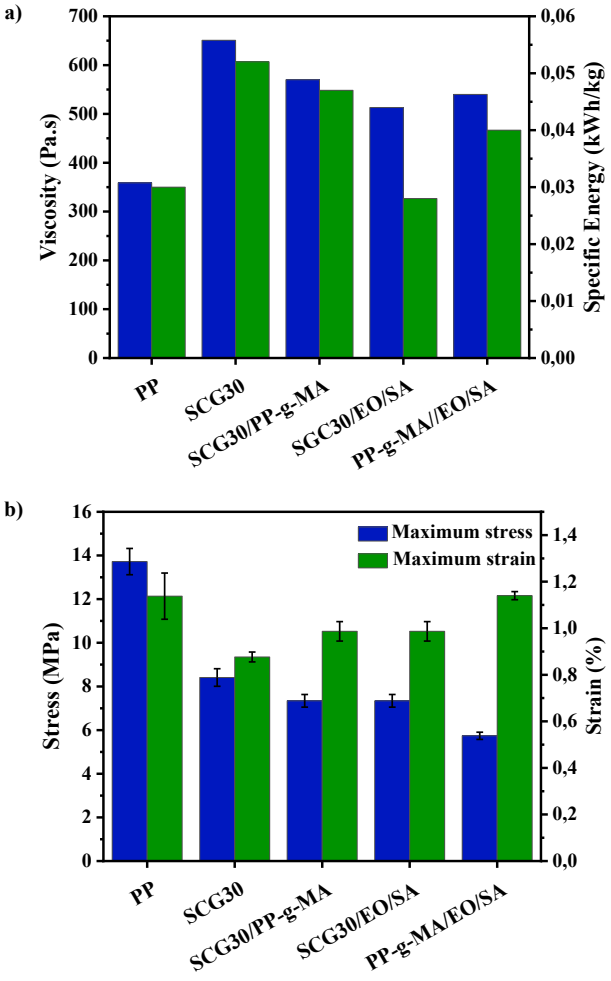

Figure 2. Results of (a) viscosity and specific energy (b) mechanical strength of the composites.

Figure 2(b) shows the maximum stress and strain properties of various PP/SCG composites, demonstrating the significant impact of SCG and different additives on these mechanical properties. A mixture of polyolefins and incompatible agro-industrial wastes generally produces poor mechanical properties [8,9]. Adding SCG to PP causes a substantial decrease in the maximum tensile stress, from about 14 MPa for pure PP to about 7 MPa for the SCG30 composite. This decrease indicates poor interfacial adhesion between the SCG fibers and the polymer matrix. It is also due to the low mechanical strength of voids and porosities, which give rise to significant stress concentration zones in composite materials [15].

On the contrary, the addition of PP-g-MA improves the strain of the biocomposite due to a slight improvement in the interfacial adhesion between the SGC and the polypropylene matrix, as observed in other polymer fiber biocomposites [16,17]. These results suggest that the compatibilizing agent promotes chemical interactions among the hydroxyl (OH-) cellulose, hemicellulose and lignin groups from coffee residues and the ester groups of PP-g-MA [18]. Using EO and SA as additives

further reduces the strength, with the SCG30/EO/SA composite showing maximum stress of 7.34 MPa. These additives significantly increase the strain, improving flexibility with values like neat PP. Therefore, the appropriate compatibilization and plasticizer effect plays an essential role in developing tailored mechanical properties of the biocomposite.

Conclusion

SCG increased the viscosity and torque at extrusion shear rates, as observed in the stationary torque rheometer. The polypropylene grafted with maleic anhydride (PP-g-MA), EO, and SA increases the feasibility of applying the extrusion process to this family of polyolefins SCG biocomposites. The PP-g-MA reduced by about 10-12% the torque, specific energy consumption, and viscosity from PP/SGC values, thus improving flow properties and processing stability. In addition, using EO and SA as lubricants significantly improves processability by reducing energy consumption and viscosity. Still, the melting processes were not stabilized after 10 minutes with EA/SA. While adding SCG decreases stress and strain, PP-g-MA slightly improves interfacial adhesion, and EO/SA mainly increases the flexibility and strain in the biocomposite formulations. This study gives an overview of agro-industrial waste polymer biocomposite processing and mechanical properties and puts forward an attractive industrial scale to be researched in this biocomposite family.

Acknowledgments

The authors thank the Laboratory of Testing Materials (LEMAT). This research was supported by the Plastic Processing Laboratory of the Faculty of Mechanical Engineering and Production Science at ESPOL.

References

1. M. A. Riera, S. Maldonado, and R. R. Palma, "Agro-Industrial Residues Generated in Ecuador for the Elaboration of Bioplastics," *Ingeniería Industrial*, vol. 3, pp. 227-246, 2018, [Online]. Available: https://doi.org/10.22320/S07179103/2018.13
2. L. M. Orejuela-Escobar, A. C. Landázuri, and B. Goodell, "Second generation biorefining in Ecuador: Circular bioeconomy, zero waste technology, environment and sustainable development: The nexus," *Journal of Bioresources and Bioproducts*, vol. 6, no. 2, pp. 83-107, 2021, https://doi.org/10.1016/j.jobab.2021.01.004
3. H. Awais, Y. Nawab, A. Amjad, A. Anjang, H. Md Akil, and M. S. Zainol Abidin, "Environmental benign natural fibre reinforced thermoplastic composites: A review," *Composites Part C: Open Access*, vol. 4, p. 100082, Mar. 2021, https://doi.org/10.1016/j.jcomc.2020.100082

4. M. A. Fuqua and C. A. Ulven, "Characterization of polypropylene/corn fiber composites with maleic anhydride grafted polypropylene," *Journal of Biobased Materials and Bioenergy*, vol. 2, no. 3, pp. 258-263, 2008, https://doi.org/10.1166/jbmb.2008.405

5. H. D. A. Leal, A. S. Babetto, and B. C. Bonse, "Properties of lignocellulosic composites of coffee husk filled polypropylene," in *AIP Conference Proceedings*, American Institute of Physics Inc., Jan. 2020. https://doi.org/10.1063/1.5142987

6. O. Das et al., "Natural and industrial wastes for sustainable and renewable polymer composites," *Renewable and Sustainable Energy Reviews*, vol. 158, no. May 2021, pp. 1-22, 2022, https://doi.org/10.1016/j.rser.2021.112054

7. M. Marques, L. F. F. F. Gonçalves, C. I. Martins, M. Vale, and F. M. Duarte, "Effect of polymer type on the properties of polypropylene composites with high loads of spent coffee grounds," *Waste Management*, vol. 154, pp. 232-244, Dec. 2022, https://doi.org/10.1016/j.wasman.2022.10.009

8. W. Song et al., "Utilization of spent coffee grounds as fillers to prepare polypropylene composites for food packaging applications," *Microscopy Research and Technique*, vol. 86, no. 11, pp. 1475-1483, Nov. 2023, https://doi.org/10.1002/jemt.24367

9. A. Rigail-Cedeño et al., "Processability and Physical Properties of Compatibilized Recycled HDPE/Rice Husk Biocomposites," *Journal of Manufacturing and Materials Processing*, vol. 6, no. 4, Aug. 2022, https://doi.org/10.3390/jmmp6040067

10. G. C. N. Lee and J. R. Purdon, "Brabender Viscometry: 1. Conversion of Brabender Curves to Instron Flow Curves," *Polymer Engineering and Science*, vol. 9, pp. 360-364, 1969, https://doi.org/10.1002/pen.760090508

11. M. Saddem, A. Koubaa, H. Bouafif, S. Migneault, and B. Riedl, "Effect of fiber and polymer variability on the rheological properties of wood polymer composites during processing," *Polymer Composites*, vol. 40, no. S1, Jan. 2019, https://doi.org/10.1002/pc.24909

12. C. R. Santi, E. Hage Jr, C. A. Correa, and J. Vlachopoulos, "Torque Viscometry of Molten Polymers and Composites," *Applied Rheology*, vol. 9, no. 1, pp. 17-26, 1999, https://doi.org/10.1515/arh-2009-0002

13. K. Xiao and C. Tzoganakis, "Rheological Properties of HDPE-Wood Composites," Jan. 2003, [Online]. Available: https://www.researchgate.net/publication/268179200

14. C. Feng, Z. Li, Z. Wang, B. Wang, and Z. Wang, "Optimizing torque rheometry parameters for assessing the rheological characteristics and extrusion processability of wood plastic composites," *Journal of Thermoplastic Composite Materials*, vol. 32, no. 1, pp. 123-140, Jan. 2019, https://doi.org/10.1177/0892705717744828

15. M. Poletto, M. Zeni, and A. J. Zattera, "Effects of wood flour addition and coupling agent content on mechanical properties of recycled polystyrene/wood flour composites," *Journal of Thermoplastic Composite Materials*, vol. 25, no. 7, pp. 821-833, Jul. 2011, https://doi.org/10.1177/0892705711413627

16. H. Hazrati, N. Jahanbakhshi, and M. Rostamizadeh, "Hydrophilic polypropylene microporous membrane for using in a membrane bioreactor system and optimization of preparation conditions by response surface methodology," *Polyolefins Journal*, vol. 5, no. 2, 2018, https://doi.org/10.22063/poj.2017.1945.1104

17. O. H. Margoto, K. D. S. Do Prado, R. C. Mergulhão, V. A. D. S. Moris, and J. M. F. de Paiva, "Mechanical and Thermal Characterization of Jute Fabric-Reinforced Polypropylene Composites: Effect of Maleic Anhydride," *Journal of Natural Fibers*, vol. 19, no. 5, pp. 1792-1804, May 2022, https://doi.org/10.1080/15440478.2020.1788489

18. A. Oromiehie, H. Ebadi-Dehaghani, and S. Mirbagheri, "Chemical Modification of Polypropylene by Maleic Anhydride: Melt Grafting, Characterization and Mechanism," *International Journal of Chemical Engineering and Applications*, vol. 5, no. 2, pp. 117-122, Apr. 2014, https://doi.org/10.7763/ijcea.2014.v5.363

SPECIAL SYMPOSIA | BIOPOLYMERS, BIOCOMPOSITES AND BIOPROCESSING

Reactive Extrusion of Lignocellulosic Biomass to Produce Biopolymer Monomers using High-Energy Radiation and Catalytic Acids

Adrian Krey, Vitus Zenz, Karolin Widera, Manuela List, Dirk Muscat and Nicole Strübbe

DOI: https://doi.org/10.51573/Andes.PPS39.SS.BBB.6

December 2024

Reactive Extrusion of Lignocellulosic Biomass to Produce Biopolymer Monomers using High-Energy Radiation and Catalytic Acids

Adrian Krey, Vitus Zenz, Karolin Widera, Manuela List, Dirk Muscat and Nicole Strübbe[1]

Abstract: The increasing prevalence of bio-based and biodegradable plastics as an alternative to traditional plastics derived from crude oil is a noteworthy trend. Polybutylene succinate (PBS), a plastic produced from succinic acid, is among the promising materials for the future. However, the production of bio-based succinic acid through biotechnical processes in controlled environments presents challenges. This process leads to increased costs and is currently not economically competitive compared to crude oil-based succinic acid production. In addition to succinic acid, levulinic acid is another monomer produced in the same process. A novel approach to the digestion of biomass has been developed to address the issue of biotechnological production of bio-based platform chemicals. This innovative process employs microwave radiation, pressure, and temperature to convert wood residues into succinic acid and levulinic acid. Various catalyst concentrations and biomass ratios were tested in a batch process, with high-pressure liquid chromatography (HPLC) and liquid chromatography–mass spectrometry (LC/MS) analyses revealing the formation of succinic acid, levulinic acid, formic acid, and 2-oxoglutaric acid. The results demonstrate that microwaves combined with a metal salt catalyst can be used to produce platform chemicals from lignocellulosic biomass. To further advance the continuous production of PBS, a twin-screw extruder was modified and adapted after the successful results obtained from the batch processes. This setup enables additional experiments to evaluate the transferability of batch process results to continuous reactions, facilitating the scale-up and the economic viability of the overall PBS production process in the future.

Keywords: Succinic Acid, Levulinic Acid, Biopolymer, Microwave, Wood

1 The authors are all affiliated with the Technical University of Applied Science Rosenheim in Germany.

DOI: https://doi.org/10.51573/Andes.PPS39.SS.BBB.6

Introduction

The annual production of plastics has expanded globally. In 2019, the volume was around 368 million tons [1]. A majority of these are derived from fossil raw materials. The bio-based plastics sector at present represents a niche, but it offers the advantage of reducing greenhouse gas emissions, specifically carbon dioxide [2], which is crucial in achieving temperature targets to combat climate change [3]. Bio-based plastics are primarily produced from plants containing carbohydrates that are fermented and dissolved by bacteria and yeasts in batch processes [4]. The resulting platform chemicals are subsequently separated through complex procedures [5]. The conversion process in these bioreactors is intricate. The biomass used as first-generation feedstock is competing with food production, as it can be used for sustenance, but it also occupies agricultural land and water [6]. The environmental impact of plastics is a pressing social issue, as plastic particles accumulate in the environment over a relatively short time due to the fact that a large portion of them biodegrade very slowly [7]. Biodegradable plastics offer the advantage of being mechanically broken down and disintegrating over time without creating microplastic. One example of a bio-based and biodegradable plastic is polybutylene succinate (PBS) [8]. The synthesis of PBS requires the platform chemical succinic acid. A newly developed process at the Technical University of Rosenheim enables the production of platform chemicals from lignocellulosic biomass through the utilization of catalysts, pressure, temperature, and microwave irradiation. This paper examines the batch process and the construction of a continuous production demonstrator on a laboratory scale.

Materials and Methods for Batch Process

Materials

Spruce wood chips (*picea abies*) from a local sawmill were used. A metal salt catalyst with a purity of over 95% was provided by VWR. The following chemicals were used for standard chemical analysis (Table 1). Hydrochloride Acid and Nitric Acid were used to clean the microwave digestion vessels.

Table 1. Raw Materials.

Chemicals	Purity in %	Producer
Levulinic Acid	98.0	Sigma Aldrich
Formic Acid	99.0	VWR
2-Oxoglutaric Acid	98.0	Sigma Aldrich
Succinic Acid	99.6	VWR
Hydrochloric Acid	30.0	Merck
Nitric Acid	69.0	Roth

DOI: https://doi.org/10.51573/Andes.PPS39.SS.BBB.6

Devices

A HAVER CPA 2-1 particle sizer from Haver & Boecker was used to determine the grain size of the spruce chips. The analysis of the products after hydrolysis of the wood was carried out using an HPLC Series 200 from Perkin Elmer and an LC/MSD iQ from Agilent Infinity Lab. The column used for the HPLC and LC/MSD is an Aminex® HPX-87H from Bio-Rad. The wood was hydrolyzed in a Multiwave 5000 with rotor (20SVT50) and Teflon pressure vessels (SVT50) from Anthon Paar.

Hydrolyses

The hydrolysis of the wood particles was carried out at a temperature of 200°C with a heating time of 10 min at a pressure of 1.5 MPa. The samples were stirred at the "high" level during the test. The exposure time of the samples was varied between 2 min, 5 min, and 10 min and cooled down to 65°C after microwave irradiation. Each test series comprised four samples.

A catalyst solution was mixed. A concentration of 1% mass was used for preparing a catalyst solution. This corresponds to 1.0 g metal salt catalyst per 100.0 g distilled water. Higher concentrations were also tested for samples (6 ml) with 2.0 g and 5.0 g catalyst. The biomass loading is calculated using the following formula:

$$Biomass\ loading\ in\ \% = \frac{0.20\ g\ Wood}{\mathrm{y}} \qquad 1)$$

y = amount of catalyst solution in g

Table 2 shows the concentrations of wood and water with the calculated biomass loading for each reaction time.

Table 2. Wood, Time, and Catalyst.

Reaction Time in min	Spruce in g	Catalyst Solution in g	Biomass loading in mass %
2.0	0.20	2.0; 4.0; 6.0	10.0; 5.0; 3.3
5.0	0.20	2.0; 4.0; 6.0	10.0; 5.0; 3.3
10.0	0.20	2.0; 4.0; 6.0	10.0; 5.0; 3.3

After each cycle, the reaction vessels were subjected to a cleaning program with distilled water, hydrochloric acid and nitric acid at 180°C in the microwave for 20 min.

DOI: https://doi.org/10.51573/Andes.PPS39.SS.BBB.6

Analytics

HPLC and LC/MS analysis were used to analyze the chemicals produced. The samples were diluted to 1:20 with distilled water before analysis. The method for the HPLC was isocratic with an analysis time of 25 min, a temperature of 35°C, an inlet volume of 20 µl with a flow rate of 0.6 ml/min and a mobile phase of 0.005 N H_2SO_4. The UV/VIS detector was set to 210 nm.

For the LC/MS analysis, an analysis time of 15 min, and an injection volume of 20 µl at a flow rate of 0.6 ml/min was set. The mobile phase is a 0.5% v/v formic acid. The scan range is 50-450 m/z, the gas temperature is 285°C, and the gas flow is 13 L/min. The fragmentor was operated at 75 V and the capillary at 3 kV.

Results Batch Process

The particles are on average 1.8 mm in size with a maximum size of 8 mm.

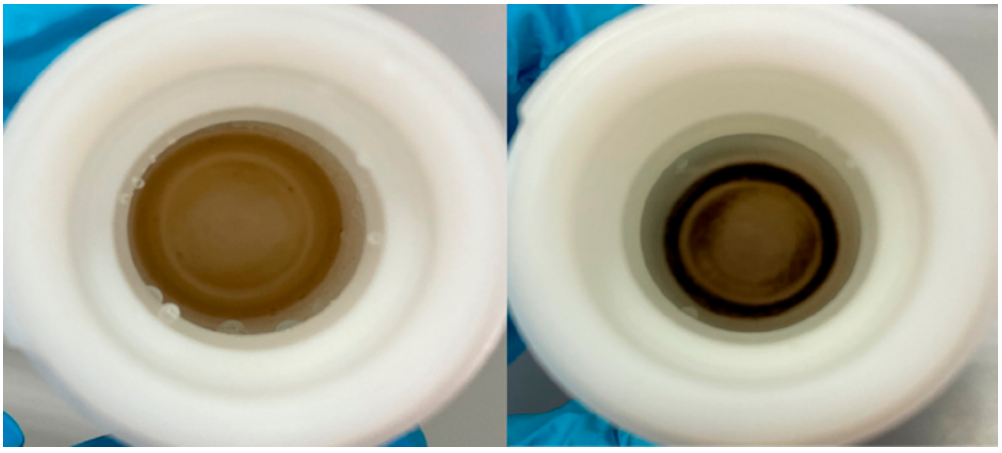

Figure 1. Solution after microwave radiation. 2 min (left), 10 min (right).
6 ml of catalyst solution with 1% metal salt catalyst and 0.2 g of wood.

After placing the sample in the microwave reactor for an extended period of time, a brown sediment formed, as compared to a 2-min irradiation where a transparent yellow solution was produced, as illustrated in Figure 1.

DOI: https://doi.org/10.51573/Andes.PPS39.SS.BBB.6

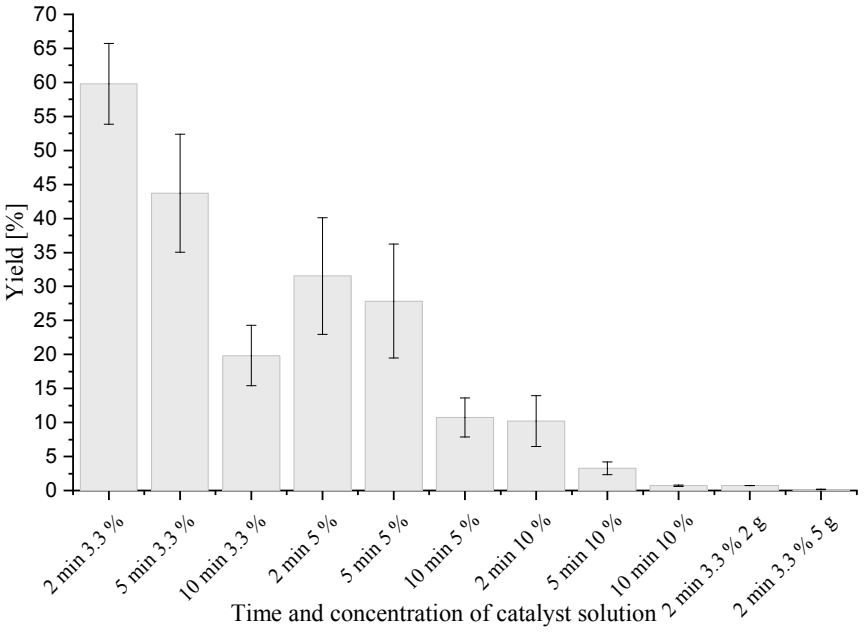

Figure 2. Yield of succinic acid.

The optimal succinic acid yield of 59.8% (±5.9%) was obtained at a biomass loading of 3.3% and a duration of 2 minutes, as seen in Figure 2. When the exposure time was increased, the yield significantly decreased, even with the same biomass loading. As the biomass increased, the yield of succinic acid decreased.

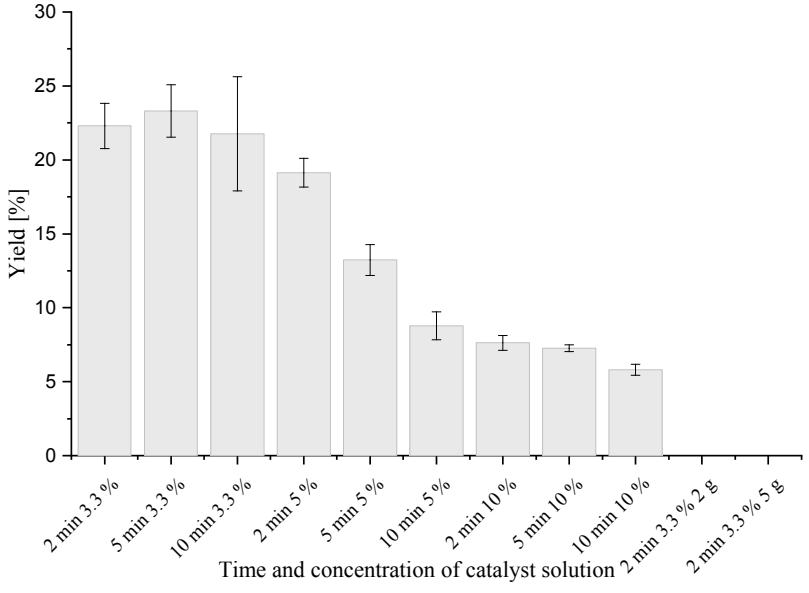

Figure 3. Yield of levulinic acid.

DOI: https://doi.org/10.51573/Andes.PPS39.SS.BBB.6

The output of levulinic acid diminished as the quantity of biomass expanded. The greatest concentration was attained at an irradiation of 5 minutes, which amounted to 23.3% (±1.8%), as illustrated in the bar graph in Figure 3. As the biomass loading increased, the concentration of the catalyst decreased.

In addition to succinic acid and levulinic acid, the production of smaller quantities of formic acid and 2-oxoglutaric acid was also observed. However, with higher amounts of catalyst, the yield of succinic acid and levulinic acid decreased, while the yield of 2-oxoglutaric acid increased. At 2 minutes, a biomass loading of 3.3% and a catalyst concentration of 5% yielded 11.2% (±1.5%).

Materials and Methods for Continuous Process

The outcomes of the laboratory experiments for the production of platform chemicals from lignocellulosic biomass were obtained via a batch process. The subsequent development step involves the design and construction of a laboratory-scale system for the continuous production of platform chemicals. To this end, a twin-screw extruder was modified. The extruder is two meters long and has a screw length of 80 D. Solid-state generators were adapted to the extruder at regular intervals along the conveying length to establish a lengthy reaction zone. A suspension of wood particles and water is fed into the twin-screw extruder by means of a pump. A separate dosing pump is used to administer the catalyst into the extruder after the wood particles. After the suspension has passed through, an aqueous solution containing the dissolved platform chemicals should be present at the outlet of the extruder. Excess water is recycled back into the process through evaporation and a heat exchanger, which also serves to conserve energy. The side view of the pilot machine is illustrated in Figure 4 below.

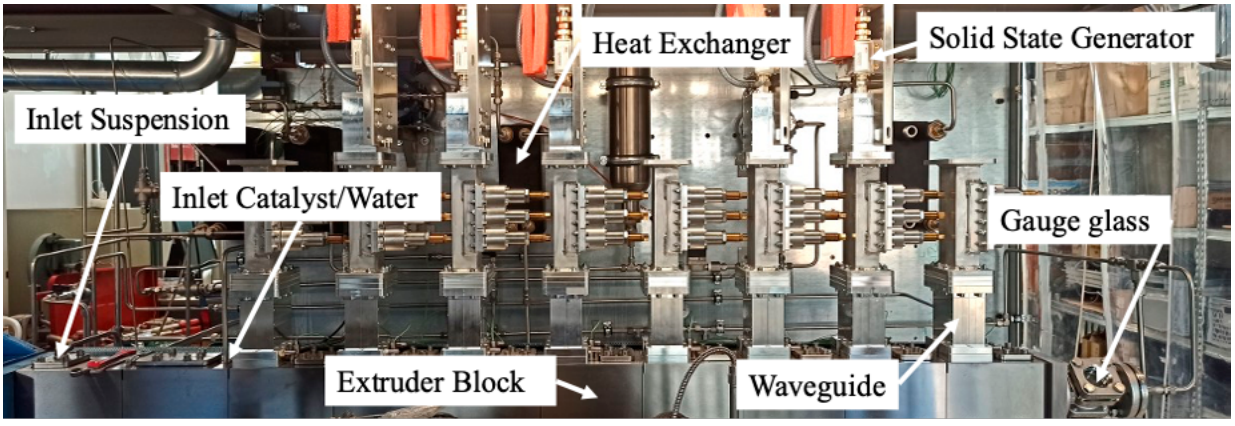

Figure 4. Modified Extruder with different components.

DOI: https://doi.org/10.51573/Andes.PPS39.SS.BBB.6

Conclusion

The research studies presented in this paper reveal the potential for producing platform chemicals through the degradation of wood on a laboratory scale. Utilizing microwaves in conjunction with metal salt as a catalyst, along with pressure and temperature, it is possible to break down wood and produce levulinic acid and succinic acid. The highest yield was achieved with a biomass loading of 3.3% and a process time of 2 minutes. The combined yield surpassed 80%, which is higher than the cellulose (43%) and hemicelluloses (35%) content of spruce wood. This exceptional yield can be attributed to the inherent inhomogeneity of wood as a natural product. The samples used in the study were relatively small, weighing 0.2 grams, and may have exhibited local variations in their compositions of celluloses, hemicelluloses, and lignin. Further experiments with a larger number of samples will be necessary to determine the optimal compositions for achieving the highest possible rates of platform chemicals.

In addition, a pilot plant for the continuous production of platform chemicals from wood residue has already been constructed. The next step is to operate and optimize the process parameters. Initially, this will involve using process parameters from batch processes. The continuous process allows the production of larger quantities of chemicals, which will be analyzed and used to optimize the process in subsequent steps.

Acknowledgments

The authors would like to thank the funding agencies Bayern Innovativ Gesellschaft für Innovation und Wissenstransfer mbH Projektträger Bayern and Projektträger Jülich Forschungszentrum Jülich GmbH.

References

1. L. Da Pires Mata Costa et al., "Capture and Reuse of Carbon Dioxide (CO2) for a Plastics Circular Economy: A Review," *Processes*, vol. 9, no. 5, p. 759, 2021, https://doi.org/10.3390/pr9050759
2. V. Piemonte and F. Gironi, "Land-use change emissions: How green are the bioplastics?," *Enviornmental Progress and Sustain Energy*, vol. 30, no. 4, pp. 685–691, 2011, https://doi.org/10.1002/ep.10518
3. D. I. Armstrong McKay et al., "Exceeding 1.5°C global warming could trigger multiple climate tipping points," *Science (New York, N.Y.)*, vol. 377, no. 6611, 2022, https://doi.org/10.1126/science.abn7950
4. T. Werpy, Pacific Northwest National Laboratory and G. Petersen: National Renewable Energy Laboratory, "Top Value Added Chemicals from Biomass: Volume I Results of Screening for Potential Candidates from Sugars and Synthesis Gas".

5. Y. S. Huh, Y.-S. Jun, Y. K. Hong, H. Song, S. Y. Lee, and W. H. Hong, "Effective purification of succinic acid from fermentation broth produced by Mannheimia succiniciproducens," *Process Biochemistry*, vol. 41, no. 6, pp. 1461–1465, 2006, https://doi.org/10.1016/j.procbio.2006.01.020

6. J. Brizga, K. Hubacek, and K. Feng, "The Unintended Side Effects of Bioplastics: Carbon, Land, and Water Footprints," *One Earth*, vol. 3, no. 1, pp. 45–53, 2020, https://doi.org/10.1016/j.oneear.2020.06.016

7. Khaled Ziani et al., "Microplastics: A Real Global Threat for Environment and Food Safety: A State of the Art Review," *Nutrients*, vol. 15, 2023.

8. S. Kato, T. Ueda, T. Aoshima, N. Kosaka, and S. Nitta, "BioPBS™ (Polybutylene Succinate)," in *Advances in Polymer Science, Synthetic Biodegradable and Biobased Polymers*, Cham: Springer International Publishing, 2024, pp. 269–304.

SPECIAL SYMPOSIA | BIOPOLYMERS, BIOCOMPOSITES AND BIOPROCESSING

Characterization of Oil Palm Biomass, Derived Materials, and Applications

Heidi-Teran, Diana-Giraldo, Gabriel-Chiappo, Maria del Pilar-Noriega and Farid-Chejne Janna

DOI: https://doi.org/10.51573/Andes.PPS39.SS.BBB.7

December 2024

Characterization of Oil Palm Biomass, Derived Materials, and Applications

Heidi-Teran, Diana-Giraldo, Gabriel-Chiappo, Maria del Pilar-Noriega and Farid-Chejne Janna[1]

Abstract: The aim of this case study is to identify the value added of existent biomass fibers (i.e., agro-industrial byproducts) and potential blends. The purpose is to explain the facts about sustainable and/or organic oil palm biomass in the energy recovery sector and in the biobased materials industry. Demand for sustainable biobased materials and energy recovery from biomass triggered the rapid growth experienced by the agricultural industry over recent years, leading to concerns about its impact on the environment and ecosystem. The agricultural industry is currently making efforts to improve sustainability practices, certifications, and to reduce carbon emissions based on innovative technologies. The used biomass, i.e. palm kernel shells (PKS), empty fruit bunches (EFB), and mesocarp fibers (MF), possesses widely accepted sustainability certifications for oil palm biomass, such as the Control Union certifications as a Roundtable on Sustainable Palm Oil (RSPO) approved certification body, the Regenerative Organic certification (ROC) for farms and products that meet the highest standards for soil health and biomass, and the EU Organic Certification in compliance with the standards and regulations of EC No. 834/2007 and EC No. 889/2008 on organic production of agricultural products. This work presents the main physicochemical characteristics of this studied biomass relevant to its energy recovery and a biobased material application. The characteristics of oil palm biomass can be summarized as a feedstock of medium energy content compared to fossil fuels and lower levels of sulfur, chlorine, and nitrogen than coal. Pellets of oil palm biomass are proven to meet expectations in both quality class A and B of non-woody pellets, i.e., characterized using the standards of solid biofuels, part 6, non-woody pellets, ISO 17225:2021. The application of biobased material ranges from pulp and paper to biobased polymer materials.

Keywords: Oil Palm Biomass, Solid Biofuel, Biobased Polymer Material, Characterization

1 The authors Heidi-Teran, Gabriel-Chiappo, Maria del Pilar-Noriega (mpnoriega@daabon.com.co) are affiliated with the Daabon Group in Colombia. The authors Diana-Giraldo and Farid-Chejne Janna are affiliated with the Universidad Nacional de Colombia.

DOI: https://doi.org/10.51573/Andes.PPS39.SS.BBB.7

Introduction

Agriculture in Colombia involves a variety of different crops, of which oil palm is an important economic and social contributor. Colombia is currently the fourth largest palm oil producer in the world and the first in the Americas, with 595,722 hectares planted, producing 7,882,225 tons of fresh fruit bunches (FFB), 1,747,377 tons of crude palm oil (CPO), and 312,512 tons of palm kernel oil (PKO). This generates total sales of 1,727,572 tons, which benefits thousands of families through 197,000 direct and indirect jobs [1].

Palm oil (PO) production involves several stages starting from palm planting to the extraction of CPO and PKO. Meanwhile, this system generates different by-products with specific characteristics to satisfy certain applications and thus develops the biorefinery concept, i.e. biomass conversion into products, such as bioenergy and biomaterials. On the one hand, wastewater from PO processing is used to generate biogas; on the other hand, the solid by-products include empty fruit bunches (EFB) and mesocarp fibers (MF), which are mainly used for composting, palm kernel shells (PKS), which are widely used as solid biofuel, and palm kernel expeller (PKE), which is suitable for ruminal feed. These renewable fibers correspond to 22%, 13%, 4.5%, and 2.3% of total FFB, respectively [2], and can be upgraded to obtain higher value added products, such as pellets for animal dietary and solid biofuel or for biobased material applications.

Ensuring quality while considering environmental and social responsibility is the current driver of fair trade. Thus, certifications, such as the Roundtable on Sustainable Palm Oil (RSPO), the Regenerative Organic Certification (ROC), the Rainforest Alliance, the NON-GMO project, organic practices under the European Union standards, among others, as well as practices like the Sustainable Palm Oil Transparency Toolkit (SPOTT), are important instruments that demonstrate ethical sourcing and high quality results: regenerating soil health and farm ecosystem; zero deforestation and biodiversity conservation; water, chemical, and pest management; community, land, and labor rights; among others.

The aim of this paper is to present the main physicochemical characteristics of oil palm biomass (OPB): EFB, MF and PKS, which are the most suitable for energy recovery and biobased material applications. The OPB will be characterized by lignocellulosic content (lignin, cellulose, hemicellulose), proximate analysis (fixed carbon, volatile matter, moisture, ash content), ultimate analysis (C, H, N, O), minor compounds (Cl, S), and calorific value. Furthermore, a case study on solid biofuel pellets will be expanded to show their suitability for energy recovery.

DOI: https://doi.org/10.51573/Andes.PPS39.SS.BBB.7

Materials and Methods

Sample Collection

The oil palm by-products EFB, MF, and PKS from sustainable plantations were collected according to the ISO 18135:2017 standard at the C.I. Tequendama SAS oil extraction plant in Fundación, Magdalena, Colombia, following the local plantation's internal sampling plan, to produce bio-pellets.

Biomass Physicochemical Characterization

Biomass sample preparation and determination of moisture, ash, and bulk density were performed following ISO standard 17225-6:2021. Proximate analysis was determined by a thermogravimetric method (TGA), in which the samples were treated in a two-stage process. In the first stage, under a nitrogen atmosphere to prevent burning, the samples were heated from room temperature to 120°C at a rate of 50°C/min. This stage was followed by a 3-minute isotherm at 120°C. In the second stage, the environment was switched to air and the temperature was further increased to 950°C at a rate of 100°C/min. On the other hand, carbon, hydrogen, and nitrogen content for the ultimate analysis was carried out according to the ASTM D5373-14 standard. Sulfur content was determined according to the ASTM D4329-18 standard and, based on the results, the oxygen content is calculated by difference. OPB calorific values were determined according to the ASTM D5865 standard. Furthermore, biomass pellets diameter, length, moisture, ash, mechanical durability, and bulk density were characterized according to ISO standard 17225-6:2021.

Results and Discussion

Colombian Biomass Characterization

A literature review was conducted to investigate the lignocellulosic composition of various Colombian biomass. OPB were compared to pine wood and sugar cane bagasse (SCB), common plantations in Colombia. Understanding this information is crucial for determining biomass suitability for various applications, such as biofuel production or biobased material development (Figure 1).

DOI: https://doi.org/10.51573/Andes.PPS39.SS.BBB.7

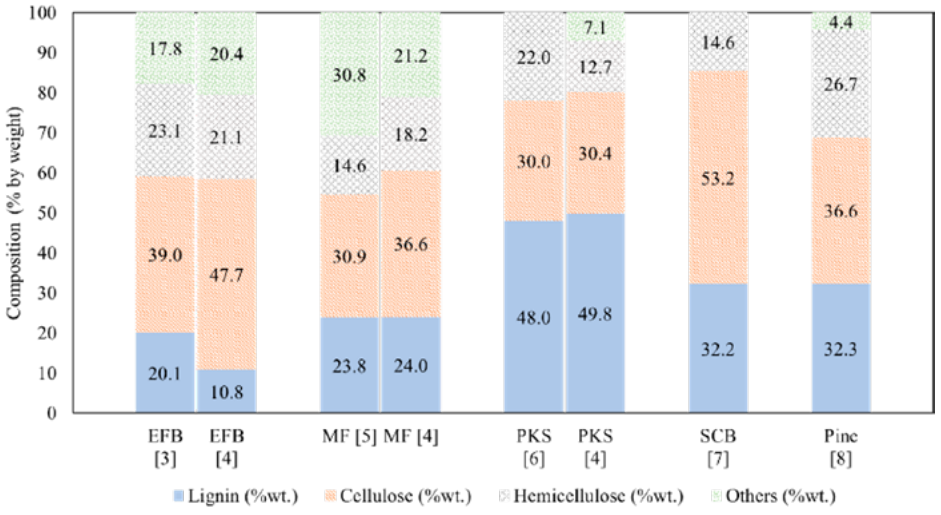

Figure 1. Lignocellulosic material from OPB: EFB, MF, PKS compared to SCB and pine wood.

Proximate analysis results (Figure 2) reveal several key characteristics of the OPB. Notably, all three types (EFB, MF, and PKS) have low ash content (EFB: 2.2%, MF: 3.1%, PKS: 1.4%) compared to sub-bituminous coal (Coal-SB: more than 9.2%) typically used in boilers. Moisture content varies across the samples. EFB and MF exhibit higher values (25% and 26%, respectively), while PKS has a lower moisture content (12.7%) analogous to Coal-SB. However, due to its biomass nature, PKS still requires drying to prevent fungal and microbial growth. In terms of volatile matter, both EFB and MF have values comparable to SCB. PKS, with 66.4% volatile matter, is quite similar to pine wood biomass. Finally, the fixed carbon content of the OPB is lower than pine wood or coal, but is still at least three times higher than the reported value for SCB.

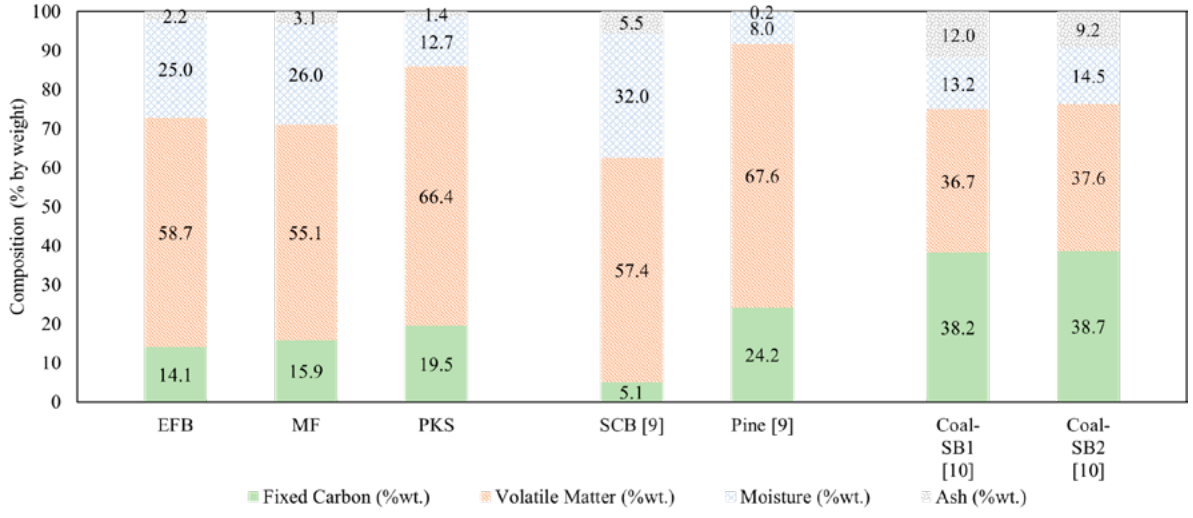

Figure 2. Proximate analysis of EFB, MF, PKS compared to SCB, pine wood and two sources of Coal-SB.

DOI: https://doi.org/10.51573/Andes.PPS39.SS.BBB.7

Ultimate analysis revealed key differences in the elemental composition of the OPB compared to Coal-SB, SCB, and pine wood (Table 1). Notably, EFB and PKS exhibited the highest oxygen content (44.2% and 41.5%, respectively), while MF oxygen content (38.8%) resembles SCB and pine wood. In terms of carbon content, EFB had the lowest value (45.9%), while MF and PKS possess 49.7% and 50.5%, respectively, which are comparable to Coal-SB. The most significant difference between the OPB and conventional coal was the sulfur content. The OPB had one order of magnitude lower sulfur content compared to the values presented in Table 1 for conventional coal. The OPB had lower levels of sulfur, chlorine, and nitrogen in compliance with ISO standard 17225-6:2021.

Table 1. Ultimate analysis of EFB, MF, PKS compared to SCB, pine wood, and two sources of Coal-SB.

	Composition					
	C (%wt.)	H (%wt.)	O (%wt.)	N (%wt.)	S (%wt.)	Cl (%wt.)
EFB	45.9	5.9	44.2	0.68	0.09	0.25
MF	49.7	6.5	37.9	1.41	0.15	0.27
PKS	50.5	5.8	41.5	0.39	0.07	0.11
SCB [9]	45.4	6.1	39.3	1.03	0.04	
Pine [9]	54.7	7.1	37.3	0.67	0.01	
Coal-SB1 [9]	62.2	4.5	18.0	1.25	1.71	
Coal-SB2 [9]	51.9	5.5	23.6	0.98	1.50	

Calorific value, in this case the higher heating value (HHV), corresponds to the upper limit for heat energy that can be released by a sample and is a crucial factor for evaluating the viability of biomass as a solid fuel. As shown in Figure 3, the calorific values of OPB (19.3–21.3 MJ/kg) are higher compared to SCB and pine wood, commonly used as solid biofuels. Even the calorific values of PKS, 21.3 MJ/kg, and MF, 20.5 MJ/kg, are comparable to reported values for Coal-SB, revealing their potential as sustainable solid biofuel alternatives. The calorific value of polyethylene terephthalate (PET) is shown as a basis of comparison.

DOI: https://doi.org/10.51573/Andes.PPS39.SS.BBB.7

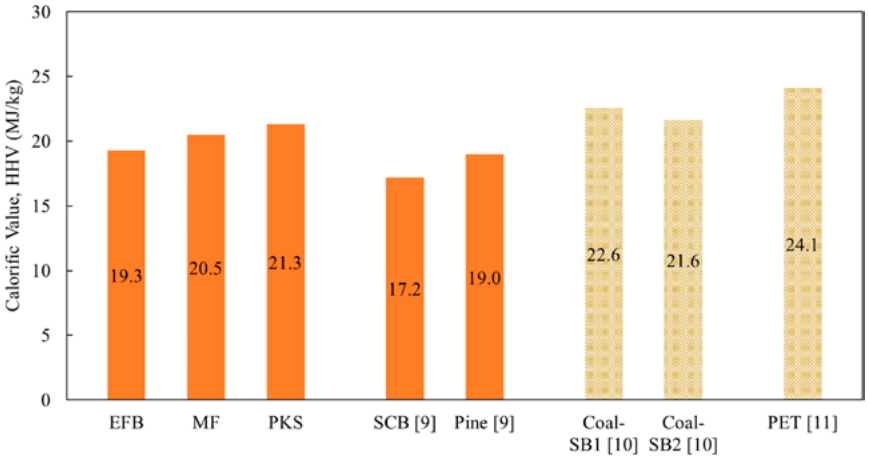

Figure 3. HHV of EFB, MF, PKS compared to SCB, pine wood and two sources of Coal-SB.

Case Study: Solid Biofuel Pellets

This case study describes some results from the project developed at CI Tequendama SAS, in partnership with the Daabon Group and the Universidad Nacional de Colombia. Pellets blends of PKS and/or MF for energy recovery were compared to ISO 17225-6 Class A and B solid biofuels specifications for non-woody pellets (see Table 2), as well as to SCB and pine wood pellets from the literature (see Table 3).

During pellet formation, the bulk density and moisture content are the most critical variables for pellets densification and its final quality. Bulk density is related to the potential for storing and long-range transporting of solids; the higher the value, the more the material can be transported or stored. This stands for logistic improvement and carbon footprint reduction. Moisture content of PKS/MF pellets blends and 100% pure MF pellets ranged from 9.1 to 12.08%, indicating compliance with ISO 17225 Class A. Nevertheless, this characteristic depends on the inlet moisture of the raw material, which could be controlled.

Table 2. OPB pellets from PKS and/or MF compared to ISO 17225-6 Class A and B solid biofuels specifications for non-woody pellets.

	Standard		Oil Palm		
	ISO 17225-6:2021		Solid Biofuel Pellets		
Parameter	Class A	Class B	Blend 1 PKS/MF	Blend 2 PKS/MF	MF100
Diameter, mm	6 to 25 ± 1	6 to 25 ± 1	8.11	8.16	8.19
Length, mm	3.15–40	3.15–40	9.28	13.64	14.13
Moisture (% Wet basis)	≤ 12	≤ 15	12.08	11.94	9.1

DOI: https://doi.org/10.51573/Andes.PPS39.SS.BBB.7

	Standard		Oil Palm		
	ISO 17225-6:2021		Solid Biofuel Pellets		
Parameter	Class A	Class B	Blend 1 PKS/ MF	Blend 2 PKS/ MF	MF100
Ash (% Dry basis)	≤ 6	≤ 10	3.61	4.63	4.63
Mechanical Durability (%)	≤ 97.5	≤ 96.0	93.4	91.78	90.43
Calorific value (HHV), MJ/kg	≥ 14.5	≥ 14.5	20.63	20.55	20.46
Bulk density, kg/m³	≥ 600	≥ 550	685.14	691.45	679.09

Table 3. OPB pellets from PKS and/or MF compared to SCB pellets and pine wood pellets.

	Oil Palm			Other Biomass	
	Solid Biofuel Pellets				
Parameter	Blend 1 PKS/ MF	Blend 2 PKS/ MF	MF100	SCB Pellets [12]	Pine Wood Pellets [13]
Diameter, mm	8.11	8.16	8.19	9.7	
Length, mm	9.28	13.64	14.13	22.7	
Moisture (% Wet basis)	12.08	11.94	9.1	5.49	7.29
Ash (% Dry basis)	3.61	4.63	4.63	8.7	0.33
Mechanical Durability (%)	93.4	91.78	90.43	98.2	97.52
Calorific value (HHV), MJ/kg	20.63	20.55	20.46	18.35	20.03
Bulk density, kg/m³	685.14	691.45	679.09	726.32	713.18

Ash content is an important characteristic when evaluating a material's potential for use in boilers, the lower the ash content, the better performance into the boiler. PKS/MF pellets blend and 100% MF pellets feature ash content values ranged from 3.61 to 4.63% according to ISO 17225 Class A. In contrast, SCB pellets report 8.7% of ash content, showing Class B. These biomasses are also compared to pine wood pellets, with only 0.33% ash content. It is important to note that wood pellets must meet other standards, and their values are shown for reference only.

The decisive issue up to this point is related to the need to densify the raw material into a pellet. Figure 4(a) presents the bulk density (BD) and energy density (ED) of raw OPB. It shows the clear reason for preferring to use PKS as solid biofuel: the raw material has a BD of 483 kg/m³ with an ED of 10299 MJ/m³. Nevertheless, in the case of EFB and MF, both the BD and ED are exceptionally low: BD is 30 and 75 kg/m³ for EFB and MF, respectively, while ED is 573 and 1524 MJ/m³ for EFB and MF, respectively. However, after pelletization (Figure 4[b]), all PKS/MF pellets blends and pure 100% MF pellets achieve BD values higher than 600 kg/m³, indicating compliance with

DOI: https://doi.org/10.51573/Andes.PPS39.SS.BBB.7

ISO 17225 Class A. Consequently, ED also increases up to 14206 MJ/m³ in the case of Blend 2, achieving an amount close to pine wood pellet ED which is 14285 MJ/m³. In Figure 4(b) is also noticeable that all OPB pellets exceed the 13328 MJ/m³ ED of SCB pellets, indicating that not only is a high BD necessary, but that the calorific value also plays an important role.

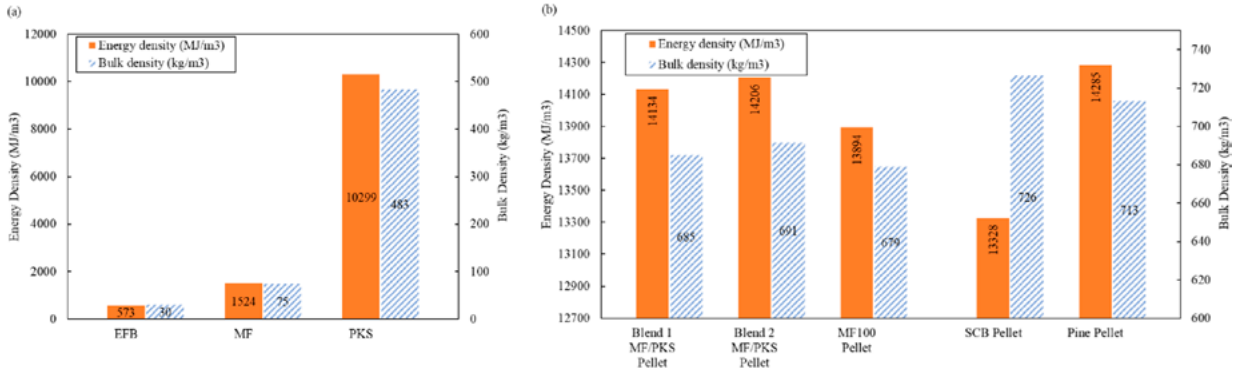

Figure 4. Energy density and bulk density of (a) EFB, MF, PKS OPB; (b) Pellets blends of PKS and/or MF compared to SCB pellets and pine wood pellets.

Conclusion

Oil palm is a sustainable oil crop from which many products could be obtained by implementing a biorefinery [14]. Current certifications related to organic farming and good social and ethical practices show the responsibility of manufacturers to the environment and the ecosystem. This work has shown that biomass from oil palm fulfils the required characteristics to be used in the energy recovery sector and in the biobased materials industry. From the proximate, ultimate, and minor compounds analysis, as well as the calorific value, it is concluded that the characteristics of OPB are comparable with those of SCB, pine wood, and subbituminous coal. In addition, the case study proves that OPB pellets could be used as sustainable solid biofuels analogous to SCB pellets and pine wood pellets. On the other hand, the lignocellulosic characterization of the different OPB fractions shows a structural difference which is suitable for developing biobased materials ranging from pulp and paper to polymeric composite materials.

Acknowledgments

The authors gratefully acknowledge the infrastructure and support of CI Tequendama SAS, part of Daabon Group, Universidad Nacional de Colombia, and the ABISURE network (Alliance for Biomass and Sustainability Research). The financial support of Daabon and the tax benefits project 1458-904-87192 of Colombian Ministry of STI are also gratefully acknowledged.

References

1. Cenipalma and Fedepalma, "La palma de aceite en Colombia." Accessed: Mar. 21, 2023. [Online]. Available: https://web.fedepalma.org/sites/default/files/files/Infografia_Colombia_2022_en_Espannol.pdf
2. J. A. Garcia-Nunez et al., "Evaluation of alternatives for the evolution of palm oil mills into biorefineries," *Biomass and Bioenergy*, vol. 95, pp. 310-329, 2016, https://doi.org/10.1016/j.biombioe.2016.05.020
3. B. Yimlamai, W. Choorit, Y. Chisti, and P. Prasertsan, "Cellulose from oil palm empty fruit bunch fiber and its conversion to carboxymethylcellulose," *Journal of Chemical Technology and Biotechnology*, vol. 96, no. 6, pp. 1656-1666, 2021, https://doi.org/10.1002/jctb.6689
4. J. A. Garcia-Nunez, M. Garcia-Perez, and K. C. Das, "Determination of kinetic parameters of thermal degradation of palm oil mill by-products using thermogravimetric analysis and differential scanning calorimetry," 2006.
5. A. C. Arévalo Vergel, D. S. Villamizar Fuentes, and B. R. Valencia, "Physicochemical characterization of the residual biomass obtained from oil palm (*Elaeis guineensis*) for uses in the manufacture of particle boards," *Revista Bistua*, vol. 17, no. 1, pp. 59-64, 2019.
6. R. K. Liew et al., "Production of activated carbon as catalyst supported by microwave pyrolysis of palm kernel shell: A comparative study of chemical versus physical activation," *Research on Chemical Intermediates*, vol. 44, no. 6, pp. 3849-3865, 2018, https://doi.org/10.1007/s11164-018-3388-y
7. G. Marrugo, C. F. Valdés, and F. Chejne, "Characterization of Colombian agroindustrial biomass residues as energy resources," *Energy and Fuels*, vol. 30, no. 10, pp. 8386–8398, 2016, https://doi.org/10.1021/acs.energyfuels.6b01596
8. L. T. López-Chalarca, L. Y. Vega Rodríguez, C. D. Rendón Colorado, and S. Tobón-Rojas, "Characterization of wood industry waste for use in different applications," *Ingeniería y Desarrollo*, vol. 38, no. 1, pp. 104-124, 2020, https://doi.org/10.14482/inde.38.1.691.1
9. A. Amell Arrieta et al., *Consultoría técnica para el fortalecimiento y mejora de la base de datos de factores de emisión de los combustibles colombianos–FECOC*, 2016.
10. UPME, *La Cadena del Carbón en Colombia*, 2005, [Online]. Available: http://www.digitosydisenos.com
11. M. Ioelovich, "Energy potential of natural, synthetic polymers and waste materials–A review," *Academic Journal of Polymer Science*, vol. 1, no. 1, 2018, https://doi.org/10.19080/ajop.2018.01.555553
12. L. F. Pedroso De Almeida, A. V. Herrero Sola, and J. J. Ramirez Behainne, "Sugarcane bagasse pellets: characterization and comparative analysis," *Acta Scientiarum–Technology*, vol. 39, no. 4, pp. 461-468, 2017, https://doi.org/10.4025/actascitechnol.v39i4.30198
13. J. I. Arranz, M. T. Miranda, I. Montero, F. J. Sepúlveda, and C. V. Rojas, "Characterization and combustion behaviour of commercial and experimental wood pellets in Southwest Europe," *Fuel*, vol. 142, pp. 199-207, 2015, https://doi.org/10.1016/j.fuel.2014.10.059
14. F. Chejne Janna, M. Garcia-Perez, and E. Noriega Maria, *Applications of Biomass Derived Materials for Bioproducts and Bioenergy*, Munich, Germany: Carl Hanser Verlag GmbH & Co. KG, 2024, ISBN: 978-1-56990-897-6.

SPECIAL SYMPOSIA | BIOPOLYMERS, BIOCOMPOSITES AND BIOPROCESSING

Evaluation of Dicumyl Peroxide as a Coupling Agent in Thermoplastic Starch and BioPBS Composites

Angie López-Galindo, Manuela Vargas-Rojas and Jorge Medina-Perilla

DOI: https://doi.org/10.51573/Andes.PPS39.SS.BBB.8

December 2024

Evaluation of Dicumyl Peroxide as a Coupling Agent in Thermoplastic Starch and BioPBS Composites

Angie López-Galindo, Manuela Vargas-Rojas and Jorge Medina-Perilla[1]

Abstract: To address plastic pollution from fossil fuel polymers, biodegradable alternatives like starch and polybutylene succinate (PBS) are proposed. However, starch is hydrophilic, while PBS and PBSA are hydrophobic. This research investigates the use of dicumyl peroxide (DCP) and tartaric acid (TA) as coupling agents in blends of thermoplastic starch (TPS) and PBS/PBSA, with glycerol as a plasticizer. Different weight/weight compositions of DCP and TA were added to blends in an internal mixer and subsequently compressed molded into films. DCP enhances tensile strength and ductility but increases torque and processing temperature. FTIR analysis show only a physical blend of components and no evidence of chemical interaction. TA reduces torque and tensile strength but increases ductility, with FTIR indicating that TA does not esterify starch but may form new bonds in the PBS carbonyl groups. SEM shows better compatibility in the blends.

Keywords: Thermoplastic Starch, PBS, PBSA, Dicumyl Peroxide, Tartaric Acid, Compatibilization

1 The authors Angie López-Galindo (as.lopez@uniandes.edu.co), Manuela Vargas-Rojas (m.vargas12@uniandes.edu.co) and Jorge Medina-Perilla (jmedina@uniandes.edu.co) are affiliated with the Department of Mechanical Engineering, Materials and Manufacturing Group (CIPP-CIPEM) at the Universidad de los Andes in Colombia.

DOI: https://doi.org/10.51573/Andes.PPS39.SS.BBB.8

Introduction

Several studies have investigated the combination of starch with PBS to obtain a sustainable polymeric material, with comparable mechanical properties and at a low cost [1,2]. However, these two compounds (TPS and PBS) are chemically opposite: starch is a hydrophilic polymer due to the polar groups (hydroxyl and carboxyl), while PBS is a hydrophobic polymer due to the aliphatic units [3]. For that reason, starch and PBS are immiscible and generate blends with low mechanical properties [4].

Therefore, to improve the chemical and mechanical behavior of the starch/PBS blends, different compatibilization mechanisms have been studied. In-situ compatibilization is a mechanism in which the compatibilizing agent is generated during the mixing procedure. Within these strategies, compatibilization with low molecular weight components is favorable due to its low economic and environmental cost [5]. When polymers are blended with peroxides, copolymers could be generated, and cross-linking and branching processes could occur through hydrogen abstraction reactions [5]. Organic peroxides produce free radicals when subjected to an increase in temperature, and in the presence of polymers this could generate a chain reaction: these radicals react with the PBS and starch polymer chains, eliminating a hydrogen atom from each carbon and, thus, generating the union (covalent bond) of monomers between the same or different polymers [6-8].

Furthermore, the use of tartaric acid as a reactive compatibilization agent for blends of starch and biodegradable polymers has been reported. Tartaric acid and other polycarboxylic acids promote esterification and transesterification between starch and PBS, thus increasing their compatibility and mechanical properties [9-11].

In this study, two different approaches were considered regarding TPS/PBS compatibilization: the preparation of a compatibilizer based on (i) DCP and (ii) DCP and TA. To evaluate the effect of the compatibilizers, the incorporation percentages were varied in the blends. In this study, PBS, starch, glycerol, DCP, and TA were processed in an internal mixer and then plastic films were manufactured by compression molding. The processability, morphology, chemical and mechanical properties were studied.

Methodology

Materials

Native cassava starch was obtained from Proyucal. PBS and PBSA were supplied by Mitsubishi Chemical Performance Polymers (MCPP) in references FZ91PM and FD92PM, respectively. Glycerol, 99.5% purity, was obtained from Panreac AppliChem. Dicumyl peroxide with 98% purity was supplied by Alfaesar and 98% tartaric acid was supplied by PanReac AppliChem.

DOI: https://doi.org/10.51573/Andes.PPS39.SS.BBB.8

Experiment Design

DCP Compatibilizer:

Two different factors were considered: type of PBS and relationship between TPS and type of PBS. The levels were: PBS and PBSA, and 60/40, 70/30, 80/20 and 90/10, respectively. The incorporation percentage of DCP was maintained at a constant value of 2% wt respect to the total blend. This value was proposed considering previous work found in literature.

DCP and TA Compatibilizer:

Three different factors were considered: (i) type of PBS, (ii) incorporation of DCP, and (iii) incorporation of TA. The levels correspond to: (i) PBS and PBSA, (ii) 0.5%, 1.0% and 2.0%, and (iii) 1.0%, 2.0% and 5.0%, respectively. The percentage of incorporation of DCP and TA was wt respect to the total blend.

Film Production:

Starch and BioPBS were dried at 80°C for 5 hours to remove moisture. The mixtures were blended using an internal mixer (CW Brabender 2553 or Brabender PLE 331) at 150°C and 60 rpm for 10 min. The proportion of glycerol used was always 30% wt respect to starch. The test films were compression molded in a Scientific LABTECH Engineering model LP-S-80 press (150°C, preheating of 5 minutes, 5 vents each one 5 seconds, pressure of 15 bars for 1 minute and, finally, pressure of 110 bars for 1 minute).

Characterization

Processability:

This consisted of obtaining torque and temperature data over time during the raw materials blend process. None of the formulations were duplicated. However, consistency was considered based on the evolution of the responses according to the change in composition.

Chemical characterization:

The raw materials and the films obtained were analyzed by Fourier Transform Infrared Spectroscopy (FTIR). For this, a Thermo Scientific Nicolet™ 380 spectrophotometer with an attenuated total reflectance (ATR) accessory and a germanium crystal were used. The spectral range analyzed was 400 to 4000 cm-1 with 32 scans. This test was not replicated.

DOI: https://doi.org/10.51573/Andes.PPS39.SS.BBB.8

Morphology:

A morphology study was carried out on the sampled films obtained through surfaces fractures by Scanning Electron Microscopy (SEM). For this, the films were subjected to cryogenic fracture with liquid nitrogen. Subsequently, the fractured fragments were coated with gold to obtain a conductive material compatible with the instrument. The samples were placed transversely on the LYRA3 TESCAN equipment at 10 kV with magnifications of ×800 and ×3000. No replications of this test were performed.

Mechanical properties:

The films obtained were die cut in modified type V specimens, in accordance with the ASTM D638 standard [12]. These were subjected to tension tests using an INSTRON 3367 universal testing machine following the ASTM D882 standard [12]. The separation between jaws was 25mm and the test speed was established at 12.5mm/min. The thickness of the specimens was measured using a model 549MM micrometer with a resolution of 0.0025mm. For each blend, 6 to 8 replicas were considered.

Results

The thickness of films manufactured by molding compression varied for both compatibilizers evaluated. The average thickness was 0.242mm ± 0.038 mm.

DCP Compatibilizer

Processability Analysis:

All blends present steady state torques between the reference values of the raw materials (6Nm (PBS) or 5Nm (PBSA) and 33Nm (TPS)). For all cases, the addition of DCP generates an increase in torque, related to the increase in the molar mass and viscosity of the blends. This could indicate the copolymers or cross-linkers formation [13].

Similarly, the processing temperatures of the blends fall within the average values of the raw materials. The inclusion of DCP to the formulation results in higher processing temperatures, suggesting a potential reaction between the blend components.

DOI: https://doi.org/10.51573/Andes.PPS39.SS.BBB.8

Fourier Transform Infrared Spectroscopy (FTIR) Analysis:

Considering the hydrogen abstraction mechanism, changes were expected in the signal related to the stretching of the hydrogen atoms in PBS (2880 cm^{-1}) and in the band associated with the OH groups of starch (3000 -3700 cm^{-1}) [14]. The spectra of the TPS/BioPBS blends are a combination of the spectra of the raw materials (TPS and PBS or PBSA). However, despite the addition of DCP, there were no discernible changes in the spectra compared to the control blends. This suggests that there may have been no chemical reaction as proposed in the previous section.

Scanning Electron Microscopy (SEM) Analysis:

The fracture surface images for the samples at x800 magnification are presented in Figure 1. In the case of TPS (a), central voids are observed on a smooth surface, which correspond to the fracture of starch granules with water content [15]. In the case of PBS (b) and PBSA (c), there is a completely smooth matrix in which only the propagation lines are observed.

The morphologies of both the control formulations and those including DCP were observed. In all formulations (d-g), distinct cavities and edges are visible. Upon comparing formulations without DCP to those with DCP, it becomes apparent that there is no improvement in the compatibility of the mixtures, as starch granules and clear phase differentiation remain evident. This indicates that the blends still have compatibility issues.

Mechanical Properties:

For Figure 2(a), it is shown that as the incorporation of TPS increases, the tensile strength of the films simultaneously decreases.

For the blends with PBS, the inclusion of DCP either maintains or increases the tensile strength. These enhancements range from 36.60% to 47.03% for the 80/20 formulation. However, for the blends with PBSA, the effect of DCP is less clear. In instances where there is an increase in this property, it ranges between 99.54% and 132.96% for the 70/30 blend.

On the other hand, regarding ductility (Figure 2[b]), an expected decrease in elongation was observed with increasing incorporation of BioPBS. This is because the inclusion of BioPBS, while improving tensile strength, typically reduces the material's ductile behavior. The effect of adding DCP to the PBS mixtures is less clear. Increases were observed for the 70/30 (40.38%) and 80/20 (495.22%) mixtures. However, in the case of PBSA, DCP generates higher elongation until fracture in the films, ranging from 25.87% to 238.20%.

DOI: https://doi.org/10.51573/Andes.PPS39.SS.BBB.8

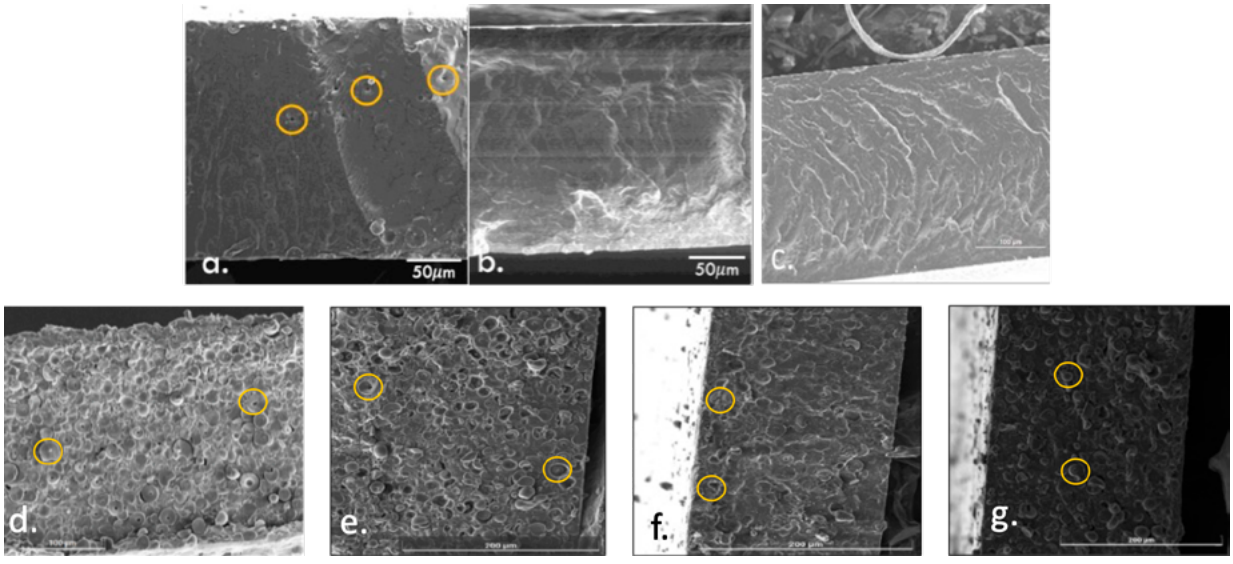

Figure 1. SEM images in x800. (a) TPS, (b) PBS, (c) PBSA, (d) 60TPS40PBS, (e) 60TPS40PBS DCP, (f) 60TPS40PBSA, (g) 60TPS40PBSA DCP.

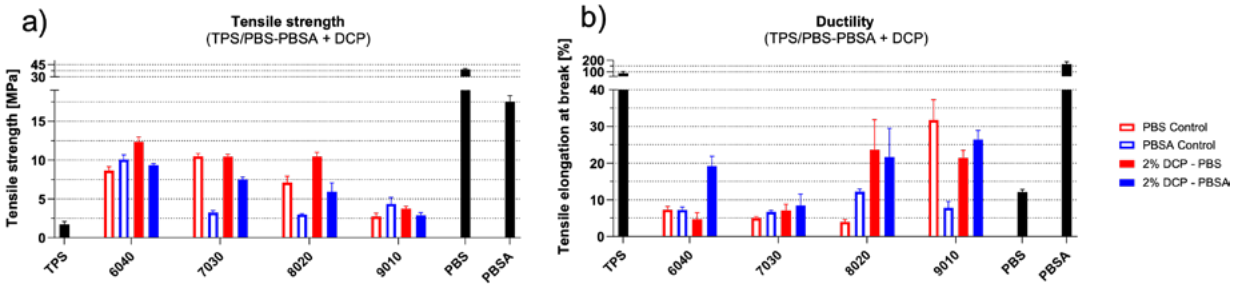

Figure 2. Mechanical properties for films. a) Tensile strength, b) Ductility.

DCP and TA Compatibilizer

Processability Analysis:

For all formulations, the inclusion of tartaric acid reduces the torque in steady state, with the 5% TA group presenting the lowest torque, even reaching values lower than the torque of the control sample that does not include DCP. This result indicates that the processing of mixtures with 5% TA, independent of the DCP incorporation level, are easier to process than the pure TPS and PBS or PBSA mixture. In contrast, by increasing the percentage of DCP incorporation, the torques always increase; so in terms of processability it is recommended to use the lowest DCP level.

DOI: https://doi.org/10.51573/Andes.PPS39.SS.BBB.8

In relation to the processing temperatures, higher percentages of DCP lead to increased maximum temperatures within each % TA group. This may be related to the formation of free radicals at high temperature. Regarding the amount of TA, it is evident that at higher % TA the maximum temperatures decrease, reaching values below the control mixture.

Fourier Transform Infrared Spectroscopy (FTIR) Analysis:

Figures 3(a) and 3(c) show that maintaining the DCP composition, increasing the % TA increases the signal intensity. Likewise (Figures 3[b] and 3[d]), by leaving the TA constant and increasing the DCP composition, the signal intensity will also increase. This indicates that neither the DCP nor the TA reacted with the OH groups of the starch. That is, the TA is not functionalizing the starch through esterification. However, although the addition of DCP and TA always generates higher signal intensities, the magnitude of the effect of the incorporation percentage is different for the PBS and the PBSA.

Now, in Figure 4(a) and 4(c) we see that by leaving the % DCP constant, increases in TA generate a decrease in the intensity of the OH groups of the PBS. For both the formulations with PBS and PBSA, the higher the % TA, the more significant the decrease in peak intensity. Now, by leaving the TA constant and increasing the amount of DCP, it is evident that the peak related to the OH groups is also reduced. In this case, the largest drops in intensity are also presented with the highest percentages of DCP.

Based on literature review, when TA is introduced into polyesters/starch blends, the anticipated outcome is the heightened intensity of peaks at 1712 cm-1, which correlates with the esterification process [16]. On the contrary, the absence of heightened intensity in this signal suggests that TA did not facilitate esterification of TPS. However, the observed decrease in signal intensity suggests that the carbonyl group bonds of PBS were substituted by new bonds.

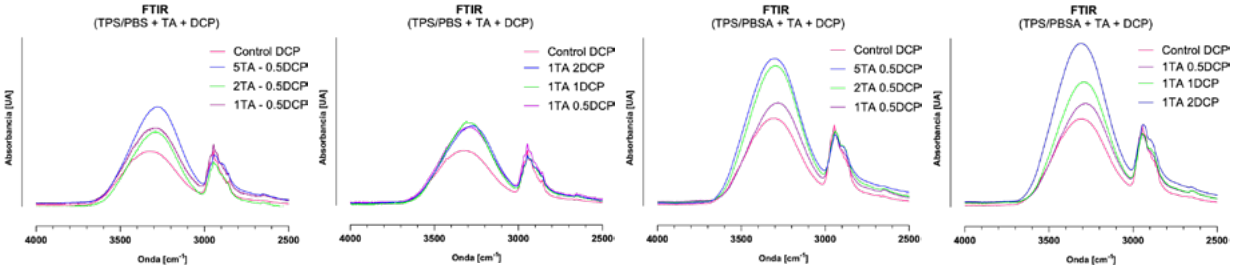

Figure 3. FTIR spectrum between 2600 and 4000 cm^{-1}. (a)(b) formulations with PBS, and (c)(d) formulations with PBSA.

DOI: https://doi.org/10.51573/Andes.PPS39.SS.BBB.8

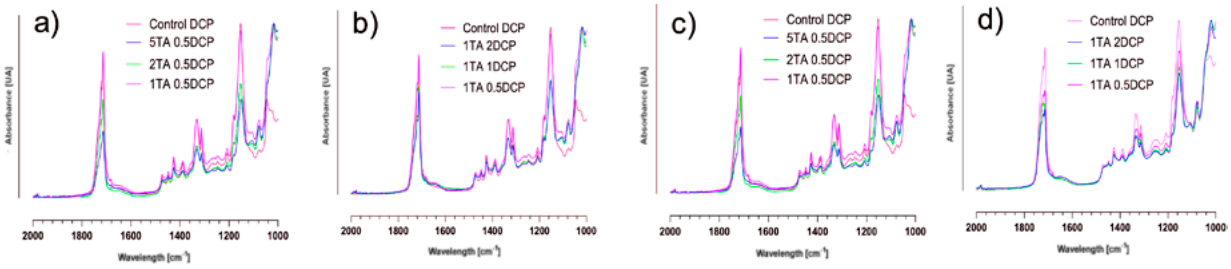

Figure 4. FTIR spectrum between 1000 and 2000 cm^{-1}. (a)(b) formulations with PBS, and (c)(d) formulations with PBSA.

Scanning Electron Microscopy (SEM) Analysis:

Figure 5 shows that the simultaneous incorporation of TA and DCP, as opposed to the exclusive incorporation of DCP, has a positive effect on the morphology of the fracture surfaces of the films. Films with TA and DCP have a considerable reduction in cavities or holes, and their surface is noticeably smoother. By increasing the percentage of TA, the interfacial adhesion between TPS and BioPBS improves. Additionally, an increase in the percentage of DCP in the blends produces the same effect. These changes indicate a better interaction between TPS and BioPBS, so TA and DCP would have the desired effect: promoting the compatibility of the polymers. Considering the above, it is expected to have a positive effect on the mechanical properties of the material, especially on ductility, since this property is related to imperfections. As the amount of starch granules and/or cavities is reduced, the transfer of stress in the material would then increase, thus facilitating ductility.

In some images (Figure 5[f-k]), it is possible to distinguish some darker and irregular regions on the surface of the sample (indicated by the arrows in yellow). These regions could indicate that the material has fractured or cracked or could be related to the presence of a second phase.

By contrasting with literature, it is possible to relate the morphology of the films as co-continued morphology. In this, there is the simultaneous presence of at least two continuous three-dimensional structures within the same volume [17]. However, considering that it is a 3D network morphology, SEM images are not conclusive and other tests are necessary, such as confocal microscopy, dynamic mechanical analysis (DMA) or solvent extraction.

DOI: https://doi.org/10.51573/Andes.PPS39.SS.BBB.8

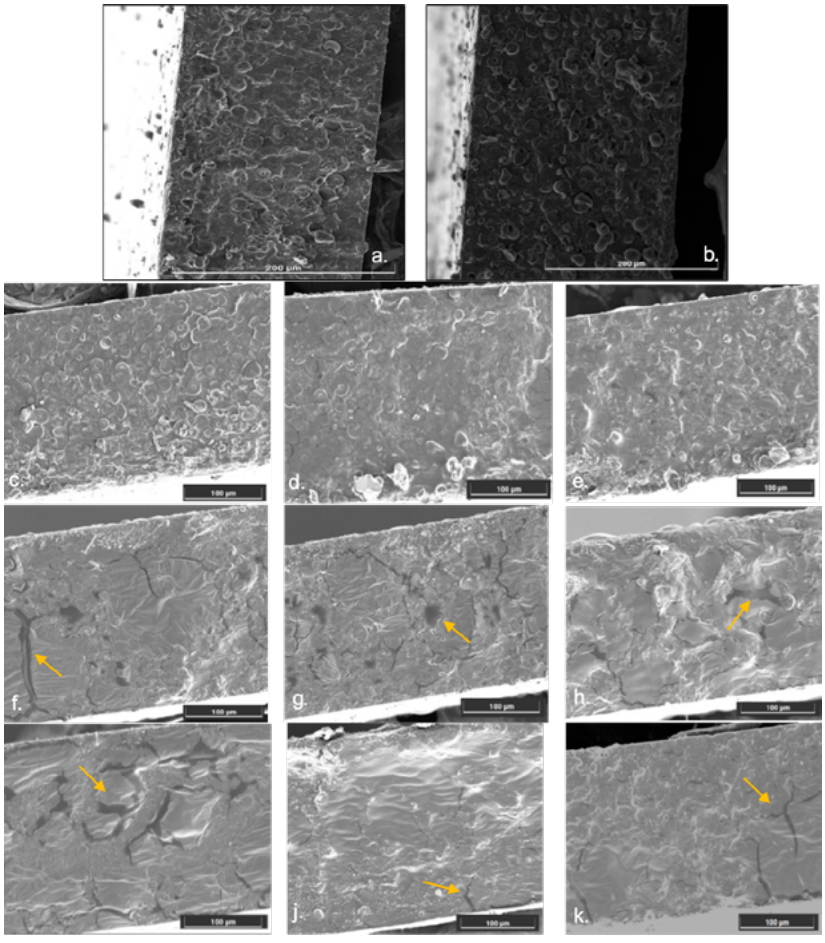

Figure 5. SEM images in x800. (a) Control, (b) DCP Control, (c) 1TA 0.5DCP, (d) 1TA 1DCP, (e) 1TA 2DCP, (f) 2TA 0.5DCP, (g) 2TA 1DCP, (h) 2TA 2DCP, (i) 5TA 0.5DCP, (j) 5TA 1DCP, (k) 5TA 2DCP.

Mechanical Properties:

For tensile strength (Figure 6[a]), as the percentage of TA incorporation increases, this mechanical property decreases. The effect of the DCP variation is not so clear. When comparing the tensile strength values obtained for the formulations with DCP+TA with respect to their control values, it is evident that there is an increase in the property using both compatibilizers only for the group of formulations with PBS. This increase is 11.06% for the 1TA-0.5DCP mixture and 7.17% for the 1TA-1DCP mixture.

DOI: https://doi.org/10.51573/Andes.PPS39.SS.BBB.8

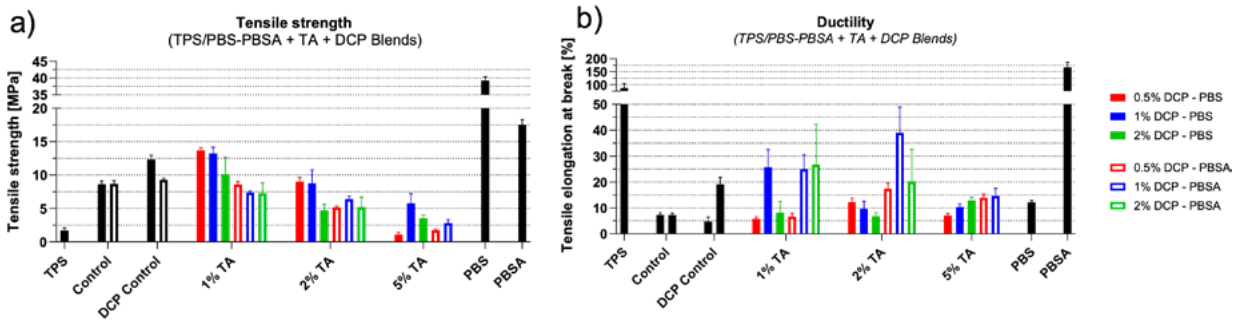

Figure 6. Mechanical properties for films. (a) Tensile strength, (b) Ductility.

In contrast, the results obtained for the ductility of the films (Figure 6[b]) are not conclusive. This is because it is not possible to identify a clear trend for the variations in %T A nor % DCP. The mixtures with PBS increase or at least maintain ductility compared to their control with only DCP, which does not occur with the PBSA group. However, when comparing formulations with PBS and formulations with PBSA, the latter has higher elongation values until fracture.

Conclusion

The use of compatibilization agents DCP and DCP+TA improved the tensile strength and ductility of the material. DCP increases torque and processing temperatures but enhances tensile strength and ductility, especially in mixtures with PBS (12.34 MPa) and PBSA (26.40%) with respect to their control blends without compatibilizer, respectively. However, SEM and FTIR analyses show no improved compatibility or chemical reaction between components. Adding DCP and TA simultaneously modifies processing conditions: TA decreases torque and temperature, while DCP increases them. Increased TA decreases tensile strength, especially in PBS formulations, but the effect of DCP on tensile strength is inconclusive. Ductility showed no clear trend. SEM suggests better compatibility for the blends, and FTIR indicates that TA is not esterifying starch, however, bonds of carbonyl groups in PBS could have been replaced by new bonds.

References

1. Y. Yan y Q. Dou, "Effect of Peroxide on Compatibility, Microstructure, Rheology, Crystallization, and Mechanical Properties of PBS/Waxy Starch Composites", *Starch–Stärke*, vol. 73, no. 3-4, Mar. 2021, https://doi.org/10.1002/star.202000184

2. B. Fahrngruber, M. Fortea-Verdejo, R. Wimmer, and N. Mundigler, "Starch/Poly(butylene succinate) Compatibilizers: Effect of Different Reaction-Approaches on the Properties of Thermoplastic Starch-Based Compostable Films", *Journal of Polymers and the Environment*, vol. 28, no. 1, pp. 257-270, Jan. 2020, https://doi.org/10.1007/s10924-019-01601-0

3. K. Suchao-in, P. Koombhongse, and S. Chirachanchai, "Starch grafted poly(butylene succinate) via conjugating reaction and its role on enhancing the compatibility", *Carbohydrate Polymers*, vol. 102, pp. 95-102, Feb. 2014, https://doi.org/10.1016/j.carbpol.2013.11.001

4. J.-B. Zeng, L. Jiao, Y.-D. Li, M. Srinivasan, T. Li, and Y.-Z. Wang, "Bio-based blends of starch and poly(butylene succinate) with improved miscibility, mechanical properties, and reduced water absorption", *Carbohydrate Polymers*, vol. 83, no. 2, pp. 762-768, Jan. 2011, https://doi.org/10.1016/j.carbpol.2010.08.051

5. R. Muthuraj, M. Misra, and A. K. Mohanty, "Biodegradable compatibilized polymer blends for packaging applications: A literature review", *Journal of Applied Polymer Science*, vol. 135, no. 24, June 2018, https://doi.org/10.1002/app.45726

6. X. Hu, T. Su, P. Li, and Z. Wang, "Blending modification of PBS/PLA and its enzymatic degradation", *Polymer Bulletin*, vol. 75, no. 2, pp. 533-546, Feb. 2018, https://doi.org/10.1007/s00289-017-2054-7

7. P. Srimalanon, B. Prapagdee, T. Markpin, and N. Sombatsompop, "Effects of DCP as a free radical producer and HPQM as a biocide on the mechanical properties and antibacterial performance of in situ compatibilized PBS/PLA blends", *Polymer Testing*, vol. 67, pp. 331-341, May 2018, https://doi.org/10.1016/j.polymertesting.2018.03.017

8. R. Wang, S. Wang, Y. Zhang, C. Wan, and P. Ma, "Toughening modification of PLLA/PBS blends via in situ compatibilization", *Polymer Engineering & Science*, vol. 49, no. 1, pp. 26-33, Jan. 2009, https://doi.org/10.1002/pen.21210

9. J. B. Olivato, C. M. O. Müller, G. M. Carvalho, F. Yamashita, and M. V. E. Grossmann, "Physical and structural characterisation of starch/polyester blends with tartaric acid", *Materials Science and Engineering: C*, vol. 39, pp. 35–39, June 2014, https://doi.org/10.1016/j.msec.2014.02.020

10. J. B. Olivato, M. M. Nobrega, C. M. O. Müller, M. A. Shirai, F. Yamashita, and M. V. E. Grossmann, "Mixture design applied for the study of the tartaric acid effect on starch/polyester films", *Carbohydrate Polymers*, vol. 92, no. 2, pp. 1705-1710, Feb. 2013, https://doi.org/10.1016/j.carbpol.2012.11.024

11. J. B. Olivato, M. V. E. Grossmann, A. P. Bilck, and F. Yamashita, "Effect of organic acids as additives on the performance of thermoplastic starch/polyester blown films", *Carbohydrate Polymers*, vol. 90, no. 1, pp. 159-164, Sep. 2012, https://doi.org/10.1016/j.carbpol.2012.05.009

12. D20 Committee, "Test Method for Tensile Properties of Thin Plastic Sheeting", *ASTM International,* https://doi.org/10.1520/D0882-18

13. W. R. Waldman and M.-A. De Paoli, "Influence of compatibilizer on blends degradation during processing", *Polímeros*, vol. 23, no. 1, pp. 7-12, Feb. 2013, https://doi.org/10.1590/S0104-14282013005000015

14. Monika, A. K. Pal, S. M. Bhasney, P. Bhagabati, and V. Katiyar, "Effect of Dicumyl Peroxide on a Poly(lactic acid) (PLA)/Poly(butylene succinate) (PBS)/Functionalized Chitosan-Based Nanobiocomposite for Packaging: A Reactive Extrusion Study", *ACS Omega Journal*, vol. 3, no. 10, pp. 13298-13312, Oct. 2018, https://doi.org/10.1021/acsomega.8b00907

15. W. Yeul Jang, B. Young Shin, T. Jin Lee, and R. Narayan, "Thermal Properties and Morphology of Biodegradable PLA/Starch Compatibilized Blends", *Journal of Industrial and Engineering Chemistry*, vol. 13, pp. 457-464, 2007.

16. J. B. Olivato, C. M. O. Müller, G. M. Carvalho, F. Yamashita, and M. V. E. Grossmann, "Physical and structural characterisation of starch/polyester blends with tartaric acid", *Materials Science and Engineering: C*, vol. 39, pp. 35–39, June 2014, https://doi.org/10.1016/j.msec.2014.02.020

17. P. Pötschke and D. R. Paul, "Formation of Co-continuous Structures in Melt-Mixed Immiscible Polymer Blends", *Journal of Macromolecular Science, Part C: Polymer Reviews*, vol. 43, no. 1, pp. 87-141, Jan. 2003, https://doi.org/10.1081/MC-120018022

SPECIAL SYMPOSIA | BIOPOLYMERS, BIOCOMPOSITES AND BIOPROCESSING

Evaluation of the Effect of Cellulose Nanofibers in Thermoplastic Starch Films

Johan Sebastián Garcia Aramendiz, Leonardo Forero Varela and Jorge Alberto Medina Perilla

DOI: https://doi.org/10.51573/Andes.PPS39.SS.BBB.9

December 2024

Evaluation of the Effect of Cellulose Nanofibers in Thermoplastic Starch Films

Johan Sebastián Garcia Aramendiz, Leonardo Forero Varela and Jorge Alberto Medina Perilla[1]

Abstract: Thermoplastic starches (TPS) are important bio-based, biodegradable polymers used in flexible packaging. However, their mechanical properties, processability, and high hydrophilicity limit their applications. This study examines the effects of chemical modifications and mechanical reinforcements on TPS matrices. Combinations of native and acetylated TPS, reinforced with native (CNF) and acetylated cellulose nanofibers (CNFA) at 1%, 2%, 3%, and 10%, were analyzed. TPS films were prepared with CNF using compression molding, followed by structural, morphological, mechanical, and hygroscopic analyses. Results show that higher CNF percentages increase tensile strength, slightly reduce moisture absorption, and decrease surface hydrophilicity. High material compatibility was observed, with proper phase interaction and mechanical homogeneity, especially at the highest fiber addition level. Further evaluation with higher acetylation degrees is needed to clarify the effects of this modification.

Keywords: Thermoplastic Starch, Nano Cellulose Fibers, Biopolymeric Films

1 The authors are affiliated with the CIPP-CIPEM Materials and Manufacturing Research Group as part of the Department of Mechanical Engineering at the Universidad de los Andes in Colombia.

DOI: https://doi.org/10.51573/Andes.PPS39.SS.BBB.9

Introduction

The global production of polymers reached approximately 400.3 million tons in 2022, with 44% used for packaging in 2021 [1,2]. While traditional polymers offer advantages such as durability and low cost, their non-renewable origins and low recycling rate (9%) pose significant environmental issues [3]. Only 0.5% of annual production consists of biopolymers, although a substantial increase is projected by 2028 [1]. In response to these challenges, thermoplastic starches (TPS) have emerged as biodegradable alternatives, though limited by suboptimal mechanical properties and high hydrophilicity [4].

A promising strategy is reinforcing TPS with cellulose nanofibers (CNF), which enhance the mechanical and thermal properties of TPS matrices [5]. However, CNF's high hydrophilicity and polarity complicate their dispersion in the matrix. Chemical modification, such as acetylation, can improve compatibility and reduce hygroscopicity, resulting in enhanced materials [6]. This study evaluates the effect of reinforcing native and acetylated TPS matrices with native and acetylated CNF, anticipating combined improvements in hygroscopic and mechanical properties. Additionally, the study researches the potential of these biopolymer composites to offer a viable alternative to conventional plastics, thereby expanding their range of applications. The resulting films are characterized in terms of their chemical, mechanical, morphological, and processability properties, providing a comprehensive assessment of their performance and potential uses.

Materials and Method

Materials

The materials used include native cassava starch (Ingredion Proyucal 4701), acetylated corn starch (Ingredion E1420), native cellulose nanofibers (SAPPI Valida L), acetylated cellulose nanofibers (SAPPI Valida S231C), and 99.5% glycerol (Panreac Applichem).

Thermoplastic Starch Processing

The premixing of starch and nanofibers was carried out using a torque rheometer. The mixture was then dried in an oven for 8 hours at 85°C. After drying, it was blended with glycerol at a weight ratio of 70:30 in a Brabender 2553 internal mixer for 7 min. The resulting mixture was cut into small pieces and compression molded in a Scientific Labtech LB-S80 press at 150°C with 5 venting cycles.

Atomic Force Microscopy (AFM)

Morphological characterization of the nanofibers was conducted using an Asylum Research microscope, model MFP-3D-BIO, equipped with a silicon tip. Topographic measurements were performed

DOI: https://doi.org/10.51573/Andes.PPS39.SS.BBB.9

on the samples to obtain reference values for the diameters and lengths of the fibers. An initial area scan of 20x20 μm was conducted to visualize the dispersion and distribution of the fibers, followed by multiple scans in areas of 5x5 μm to measure the diameter and elastic modulus of the fibers.

Fourier Transform Infrared Spectroscopy (FTIR)

Infrared spectra were obtained using a Thermo Scientific Nicolet 380 spectrophotometer in ATR mode with a germanium crystal. Measurements were taken at a 3 cm^(-1) resolution over a spectral range of 400-4000 cm^(-1), with 32 scans. This analysis covered raw materials (native and acetylated starch, CNF, CNFA) and produced films for all formulations and loading levels. No replicates were performed.

Tension Test–Mechanical Properties

The mechanical properties of the films were measured using an INSTRON 3367 universal testing machine, following ASTM D638 standards. Type V specimens were used with a jaw separation of 50 mm and a separation speed of 12.5 mm/min. Seven specimens were tested for each sample, and the average value was reported. Film thickness, measured with a TMI micrometer model 549MM (resolution 0.0025 mm), averaged 0.2292 mm ± 0.0103 mm. This test determined tensile strength and elongation at break. Due to the time, temperature, and humidity sensitivity of thermoplastic starches, all tests were conducted within 5 days of film manufacture to minimize these effects.

Scanning Electron Microscopy (SEM)

The morphology of the films was characterized using a LYRA3 TESCAN scanning electron microscope. The samples underwent cryogenic fracture using liquid nitrogen, with the fracture area subsequently coated in gold for observation. SEM micrographs were taken at magnifications of x800 and x3000 with an acceleration voltage of 10 kV.

Confocal Laser Scanning Microscopy (CLSM)

To identify fiber dispersion and distribution within the matrices, film samples were observed using a confocal microscope (Olympus Fluoview 300) at x20 magnification with a wavelength of 426 cm^{-1}. Two replicates were performed for all films and their controls.

DOI: https://doi.org/10.51573/Andes.PPS39.SS.BBB.9

Results and Discussion

Atomic Force Microscopy (AFM)

Figure 1 shows the results of microscopy for native and acetylated fibers. No significant morphological differences were observed between them, with noticeable dispersion in both fiber diameter and length.

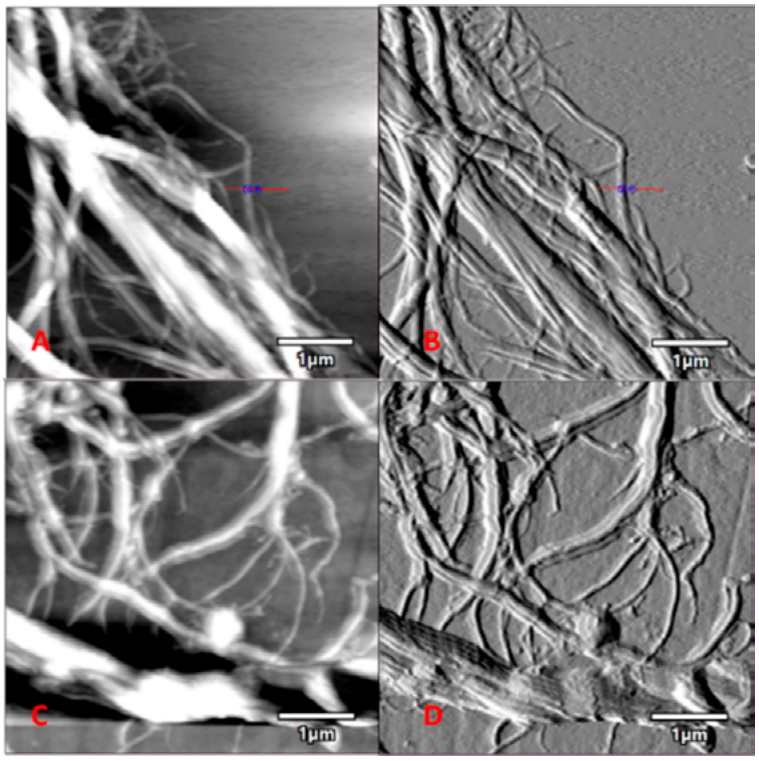

Figure 1. AFM Results (a) CNF Photograph, (b) CNF Topography, (c) CNFA Photograph, (d) CNFA Topography.

Topographical analysis showed fiber lengths from 0.5 µm to 7 µm, consistent with literature values (5 nm to 150 µm) [7]. The average fiber diameter, determined using Z-axis profile analysis and ImageJ software, was 14.5 nm for CNFA and 16.5 nm for CNF in thinner branches, with main fibers averaging 500 nm, aligning with theoretical values [7]. Thus, the nanofibers span from nano- to microscale. Diameter variability and branching result from the mechanical production process, with morphologies expected for "high-pressure homogenization" [8]. Given their similar sizes, shapes, and production processes, both fiber types are expected to have the same physical reinforcement effect. Differences in the films mechanical properties can be attributed to chemical variations and interactions between materials.

DOI: https://doi.org/10.51573/Andes.PPS39.SS.BBB.9

Fourier Transform Infrared Spectroscopy (FTIR)

To compare the structural differences of the raw materials and their consequences, Figure 2(a) presents the spectra of native and acetylated starch, while Figure 2(b) presents the spectra of CNF and ACNF. Key differences in the spectra include the band at 1730 cm^{-1} (carbonyl groups, C=O), the band at 1375 cm^{-1} (CH^{-} group), and the band at 1250 cm^{-1} (C-O bond of acetyl groups). These bands are associated with the acetylation process. The intensity of the carbonyl group signal (1730 cm^{-1}) in both cases suggests a low degree of acetylation, suitable for food-grade starch.

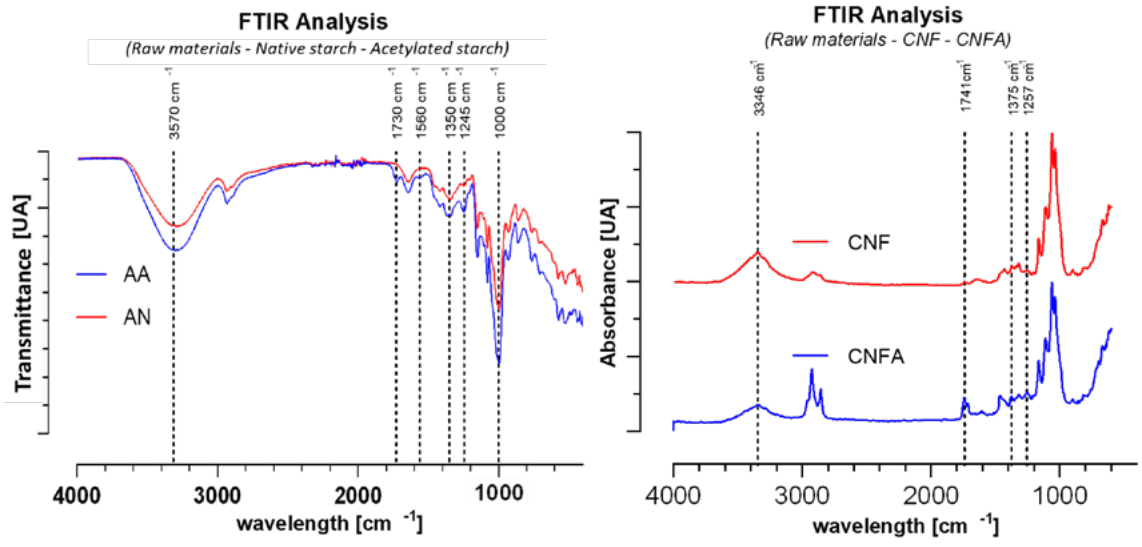

Figure 2. FTIR Results for raw materials, (a) Left -Native and acetylated starches, (b) Right – CNF.

Figure 3 shows the overlaid spectra corresponding to the films of different mixtures with a 3% fiber addition. An enlargement of the regions of interest is also presented, highlighting the changes between formulations. Small increases are observed in the characteristic bands of carbonyl and C-O groups (1720 cm^{-1} C=O, 1560 and 1260 cm^{-1} C-O), as well as a slight decrease in the signal associated with free hydroxyl groups (3330 cm^{-1}). A notable difference is the signal of the TPSA/CNFA formulation in Figure 3(a), where the interaction effect of the two acetylated materials on the OH group signal is observed, resulting in the lowest intensity signal. These slight differences coincide with a low degree of acetylation for the set of materials, indicating that while there is a cumulative effect of acetylation, the primary effect of the nanofibers is mechanical reinforcement. The impact of the chemical modification is too small to be clearly distinguished.

DOI: https://doi.org/10.51573/Andes.PPS39.SS.BBB.9

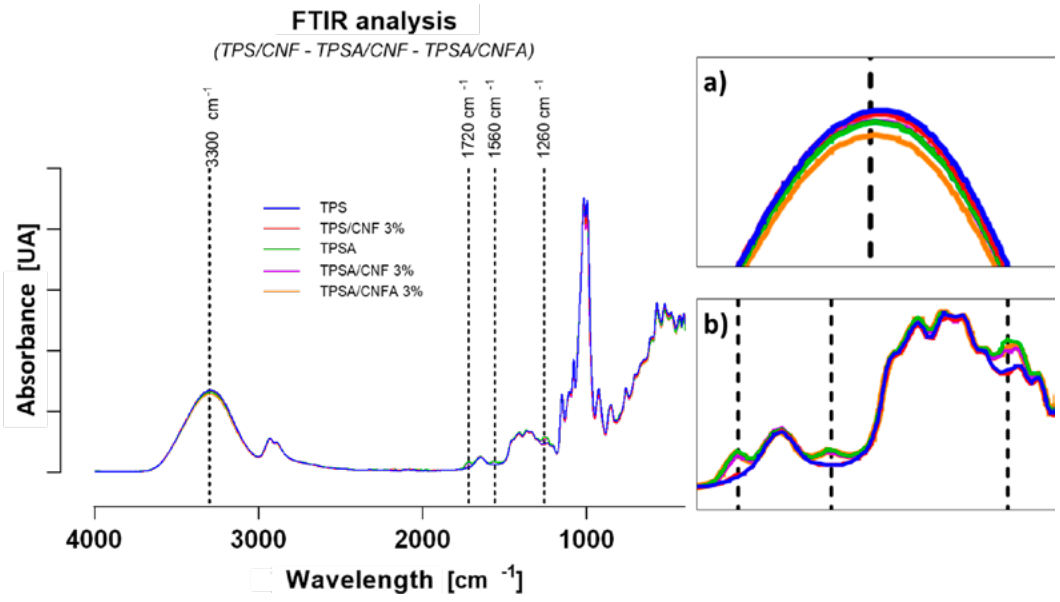

Figure 3. Comparative FTIR of the 3% blends: (a) OH Region, (b) C-O and Carbonyl Region.

Mechanical Properties

Table 1. Mechanical properties results.

	Ductility [%]			Tensile strength [MPa]		
Formulation	TPS/CNF	TPSA/CNF	TPSA/CNFA	TPS/CNF	TPSA/CNF	TPSA/CNFA
Control	62,77 ± 6,34	98,03 ± 2,30	98,03 ± 2,30	1,70 ± 0,16	1,19 ± 0,20	1,19 ± 0,20
1%	19,88 ± 2,43	20,19 ± 2,85	27,22 ± 2,62	2,52 ± 0,18	2,90 ± 0,15	2,24 ± 0,24
2%	20,18 ± 2,15	21,51 ± 1,61	16,86 ± 3,87	3,84 ± 0,19	2,66 ± 0,30	2,63 ± 0,40
3%	25,31 ± 6,30	19,70 ± 1,13	25,49 ± 2,26	4,02 ± 0,74	2,79 ± 0,15	3,07 ± 0,46
10%	11,13 ± 5,40	16,19 ± 4,77	21,51 ± 6,69	12,99 ± 2,80	8,25 ± 2,59	3,60 ± 0,59

Table 1 presents the tensile strength (TS) and elongation at break (E) values obtained for all formulations and load levels. The tensile properties of the films were analyzed based on stress-strain curves obtained at 20°C and 45% relative humidity.

Control ductility values initially show that TPSA film is more ductile than the TPS sample, aligning with literature reports that higher degrees of acetylation increase elongation but reduce strength [6]. The addition of CNF significantly decreases ductility in all samples, with drops of approximately 76.8% (TPSA/CNFA), 80.2% (TPSA/CNF), and 44.5% (TPS/CNF) compared to their respective controls, with the most substantial reductions occurring in the TPSA matrices. Chemical modification

DOI: https://doi.org/10.51573/Andes.PPS39.SS.BBB.9

exposes cellulose's active hydroxyl groups, promoting reactions with the matrix, resulting in greater mechanical interlocking and stronger secondary bonds [9]. The overall decrease in ductility due to CNF addition is expected, as reinforcing agents typically reduce the ductility and flexibility of matrices. However, an increase in the tensile strength of the films is also anticipated.

Comparing the results for each formulation, no significant differences were observed for 1%, 2%, and 3% loadings, with values remaining close to each other. For the 10% addition, ductility decreased for all three formulations; however, no drastic drop was noted. These results align with the previously stated logic, where ductility decreases due to both the mechanical effect of reinforcing agents and the expected chemical interactions occurring on the fiber surfaces. Thus, an increase in strength is anticipated with minimal ductility loss. However, no conclusive behavior regarding the degree of fiber incorporation was observed.

Figure 4 shows the comparison of tensile strength values, where the addition of nanofibers increases this property for all samples. For 1% to 3% loadings, similar increases of approximately 130% compared to control values were observed. However, for 10% CNF, a significant increase in film strength was recorded: 594% and 663% for TPSA/CNF and TPS/CNF formulations, respectively, while the TPSA/CNFA blend showed an increase of approximately 203%.

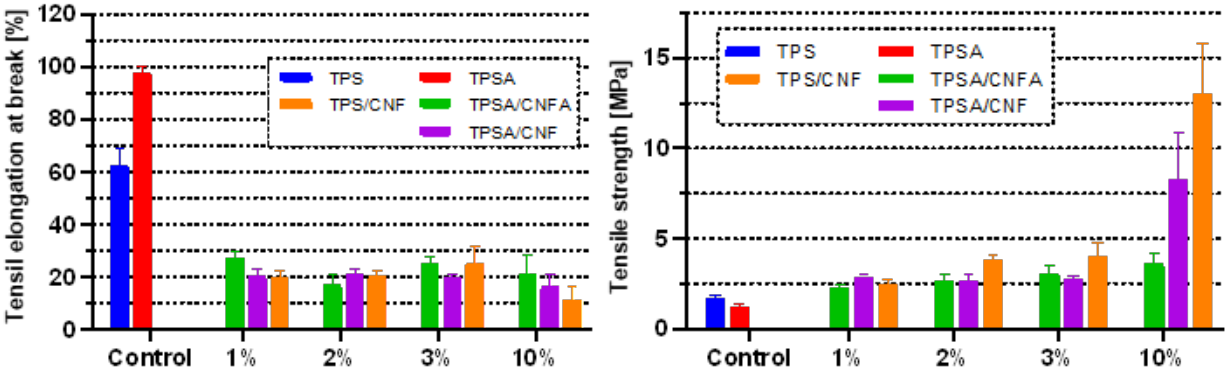

Figure 4. Mechanical properties comparison (a) Left -Ductility (b) Right–Tensile strength.

Upon analyzing the observed behaviors, it is evident that the addition of a higher amount of CNF results in a considerable increase in tensile strength, with a reduction in ductility like that observed at lower addition levels. This result suggests that a 10% loading offers a better balance between the loss of ductility and the increase in strength, aligning with previous studies that indicate the optimal fiber addition range is between 12% and 15% [10].

Additionally, the mechanical characterization results do not show a clear differentiation between the effects of native and acetylated materials, particularly concerning the impact of the nanofibers. Therefore, it is necessary to verify the structural changes in the mixtures.

DOI: https://doi.org/10.51573/Andes.PPS39.SS.BBB.9

Scanning Electron Microscopy (SEM)

The morphological analysis aims to verify the interaction between materials and confirm the starch gelatinization process, given the strong relationship between morphology and the mechanical properties of polymers [11]. Figure 5 (a) and (b) presents the results for the TPS and TPSA control samples. These images show a smooth, continuous surface with a few starch granules having a central void, typical of granules with moisture content at equilibrium, indicating correct gelatinization for both cases.

Figure 5 (c-e) shows the micrographs for various formulations with a 3% fiber load, as well as for the TPS/CNF formulation at a 10% load (f). The SEM results do not show significant cavities, agglomerations, branches, or holes, suggesting appropriate interaction between the phases, regardless of chemical modification [11]. This is positive, as it indicates no agglomerations, stress concentrators, or discontinuities in the matrix, implying that the mechanical property measurements are not significantly affected by such defects. Proper phase interaction is crucial for the mechanical response of the films.

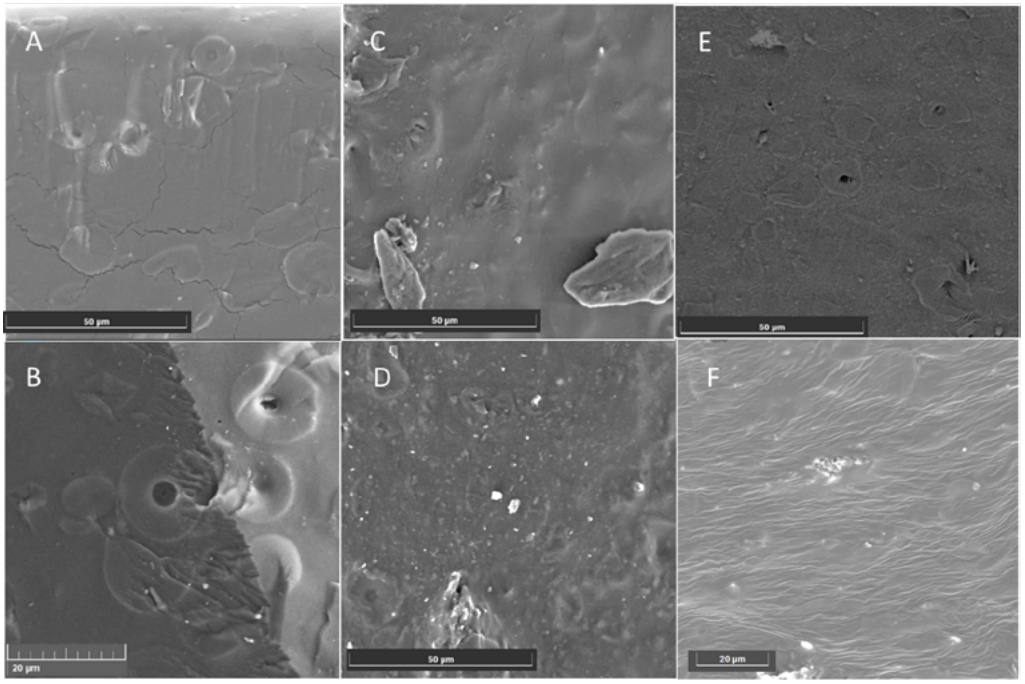

Figure 5. SEM Images at x3000. (a) TPS, (b) TPSA, (c) TPS/CNF 3%, (d) TPSA/CNFA 3%, (e) TPSA/CNF 3%, (f) TPS/CNF formulation at a 10% load.

This behavior was observed in all samples, with no changes when increasing the CNF content and without varying by the type of material used. Therefore, when comparing the results of the TPS/CNF formulation with 3% (Figure 5[e]) and 10% (Figure 5[f]) fiber load, the main difference found is

DOI: https://doi.org/10.51573/Andes.PPS39.SS.BBB.9

the presence of fracture lines attributed to breakage, without the appearance of new or unexpected morphologies. The good interaction between the phases is attributed to the structural similarity between starch and cellulose, as well as the nanoscale of the fibers, combined with the interaction of hydrogen bonds between the CNFs and starch [5].

Confocal Laser Scanning Microscopy (CLSM)

Verifying the dispersion and distribution of nanofibers within the matrices is crucial given the previously evidenced correct phase interaction. Figure 9 shows confocal microscopy results: panels a-c for different formulations with 3% fiber addition and panel d for TPSA/CNFA at 10%.

TPS/CNF and TPSA/CNF formulations show mainly free and oriented fibers across all fiber levels, improving mechanical properties, especially at 10% fiber load. This uniform CNF distribution stems from the excellent compatibility between starch and CNF, facilitating efficient stress transfer from the matrix to the CNF [10]. SEM and CLSM results confirm correct phase interaction and proper fiber distribution within these matrices.

However, TPSA/CNFA (Figure 6 [c-d]) displays smaller loose fibers and sheets across all fiber levels. At a 10% load, there is no significant increase in mechanical properties, contrary to expectations. The interaction between the two acetylated materials was hypothesized to enhance mechanical strength and fiber dispersion, but this was not observed.

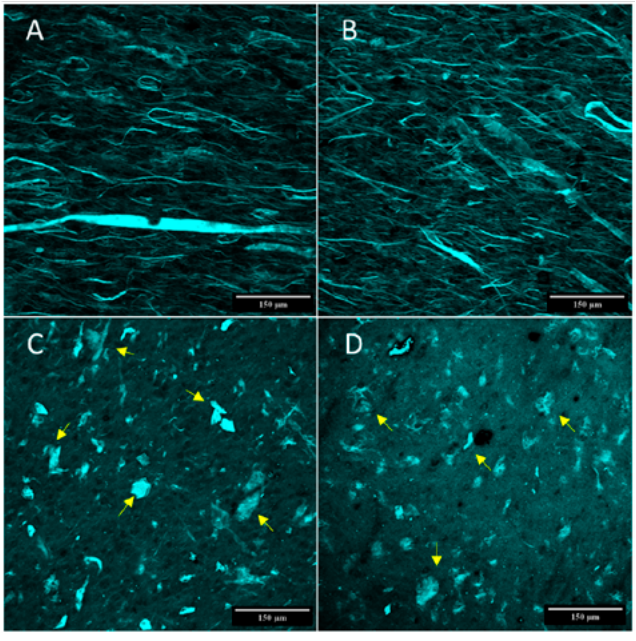

Figure 6. CLSM Results at X20. (a) TPS/CNF 3%, (b) TPSA/CNF 3%, (c) TPSA/CNFA 3%, (d) TPSA/CNFA 10%.

DOI: https://doi.org/10.51573/Andes.PPS39.SS.BBB.9

Similarly, when evaluating the film profiles in Figure 7, it is observed that fiber distribution tends towards one surface in all cases. This behavior and fiber orientation can be attributed to the compression molding process, where material fusion and applied pressure cause fibers to migrate to the lower surface and align themselves. This suggests that fiber distribution within the matrices is influenced by the film manufacturing process.

The correct fiber distribution on one surface indicates uniformity in the mechanical response of the films. However, ideally, uniform distribution should occur throughout the entire matrix. Therefore, it would be necessary to evaluate this test by altering the manufacturing method to achieve uniform distribution across the matrix.

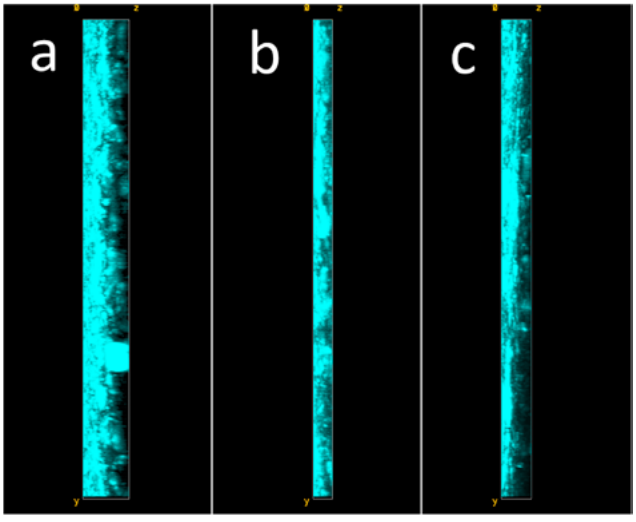

Figure 7. CLSM profiles at x20. (a) TPS/CNF 3%, (b) TPSA/CNF 3%, (c) TPSA/CNFA 3%.

Conclusions

The addition of cellulose nanofibers (CNF) to TPS matrices resulted in increased tensile strength across all cases, with the 10% CNF additions providing the best balance between ductility loss and strength gain.

Mechanical and morphological analyses indicate good compatibility and interaction for the TPS/CNF and TPSA/CNF formulations, correlating with the observed mechanical performance. However, the degree of acetylation was insufficient to significantly influence the mechanical properties of the films, suggesting that higher degrees of acetylation should be evaluated.

DOI: https://doi.org/10.51573/Andes.PPS39.SS.BBB.9

References

1. PlasticsEurope, "Plastics – the fast Facts shows preliminary global and European plastics production data," [Online].
2. Plastics Europe, "Plastics-the Facts 2022," 2022. Accessed: Jun. 14, 2024. [Online]. Available: https://plasticseurope.org/knowledge-hub/plastics-the-facts-2022/
3. OECD, "Global Plastics Outlook Economic Drivers, Environmental Impacts and Policy Options," 2022.
4. A. Akhavan, F. Khoylou, and E. Ataeivarjovi, "Preparation and characterization of gamma irradiated Starch/PVA/ZnO nanocomposite films," *Radiation Physics and Chemistry*, vol. 138, pp. 49–53, Sep. 2017, https://doi.org/10.1016/j.radphyschem.2017.02.057
5. Y. Lu, L. Weng, and X. Cao, "Biocomposites of plasticized starch reinforced with cellulose crystallites from cottonseed linter," *Macromolecular Bioscience*, vol. 5, no. 11, pp. 1101–1107, Nov. 2005, https://doi.org/10.1002/mabi.200500094
6. R. Colussi et al., "Acetylated rice starches films with different levels of amylose: Mechanical, water vapor barrier, thermal, and biodegradability properties," *Food Chemistry*, vol. 221, pp. 1614–1620, Apr. 2017, https://doi.org/10.1016/j.foodchem.2016.10.129
7. Ahmed Barhoum, *Handbook of Nanocelluloses*. Springer International Publishing, 2022. https://doi.org/10.1007/978-3-030-62976-2
8. K. J. Nagarajan et al., "A comprehensive review on cellulose nanocrystals and cellulose nanofibers: Pretreatment, preparation, and characterization," *Polymer Composites*, vol. 42, no. 4, pp. 1588–1630, Apr. 01, 2021. https://doi.org/10.1002/pc.25929
9. P. R. Fitch-Vargas et al., "Mechanical, physical and microstructural properties of acetylated starch-based biocomposites reinforced with acetylated sugarcane fiber," *Carbohydrate Polymers*, vol. 219, pp. 378–386, Sep. 2019, https://doi.org/10.1016/j.carbpol.2019.05.043
10. M. Li, X. Tian, R. Jin, and D. Li, "Preparation and characterization of nanocomposite films containing starch and cellulose nanofibers," *Industrial Crops and Products*, vol. 123, pp. 654–660, Nov. 2018, https://doi.org/10.1016/j.indcrop.2018.07.043
11. W. Yeul Jang, B. Young Shin, T. Jin Lee, and R. Narayan, "Thermal Properties and Morphology of Biodegradable PLA/Starch Compatibilized Blends," 2007.

SPECIAL SYMPOSIA | BIOPOLYMERS, BIOCOMPOSITES AND BIOPROCESSING

On the Cryo-Molding Process and Subsequent Forming Processes of Biopolymers with Low Glass Transition Temperature

Julius Petrausch, Daniel Klein, Johannes Zimmer and Markus Stommel

DOI: https://doi.org/10.51573/Andes.PPS39.SS.BBB.10

December 2024

On the Cryo-Molding Process and Subsequent Forming Processes of Biopolymers with Low Glass Transition Temperature

Julius Petrausch, Daniel Klein, Johannes Zimmer and Markus Stommel[1]

Abstract: Bio-based as well as biodegradable polymers are increasingly finding their way into applications such as food packaging. Here, certain biopolymers with a high degree of crystallinity may be of interest due to their superior barrier properties. Conversely, forming processes including high deformations often require an almost amorphous material state to avoid the brittle behavior associated with crystal structures. For some of those biopolymers, the narrow window in which they can be processed has delayed their potential use for packaging applications. In rigid packaging, two-step processes are commonly used for the production of containers from thermoplastic polymers. These processes, such as thermo forming or injection stretch blow molding, are a combination of a conversion step, e.g. film extrusion or injection molding, and a deformation step. However, to enable a forming process, the material properties after the first (conversion) step need to fulfil the mechanical requirements of the forming process. For semi crystalline polymers, these requirements are closely linked to the morphology of the converted material. A new process is presented to prevent crystallization and allow for a subsequent forming step. The efficiency of this process is evaluated on tailored lab scale equipment. This publication will provide insights into the opportunities as well as potential challenges presented by the "Cryo-Injection-Molding" (CIM) process. The CIM uses a mold that is cooled by liquid nitrogen. This mold is insulated and used in a lab scale injection process. This process is capable of cooling specimens down to their amorphous state (or semi-crystallin state with a very low degree

1 The authors Julius Petrausch (petrausch@IPFdd.de) and Markus Stommel (stommel@IPFdd.de) are affiliated with the Leibniz Institute of Polymer Research Dresden in Germany. Daniel Klein (daniel.klein@waters.nestle.com) is affiliated with the Nestlé Product Technology Center Waters in France. Johannes Zimmer (johannes.zimmer@rd.nestle.com) is affiliated with the Nestlé Institute of Packaging Science in Switzerland. Markus Stommel is also affiliated with the Institute of Material Science at the Technical University Dresden in Germany.

DOI: https://doi.org/10.51573/Andes.PPS39.SS.BBB.10

of crystallinity) and allows the mechanical characterization in a softened state at a temperature above glass transition. To prevent unintended changes of the morphology, after the production process, the samples are stored at a temperature below glass transition and later heated using custom convectional heaters in a setup of a tensile testing machine. In this context, PBAT, PBS and PHA biopolymers are tested exemplarily.

Keywords: Cryo-Molding, Injection Molding, CIM, Morphology, Amorphous, Biopolymer, Processing, PHA, PBAT, PBS

Introduction

Packaging materials must fulfill many requirements, including mechanical and chemical requirements, with the product's shelf life being one of the key performance indicators. The packaging shelf life is also linked to the barrier of the packaging material. Typically, water vapor and gases like oxygen and carbon dioxide should be blocked.

In general, for many thermoplastic packaging materials, this barrier depends on the degree of crystallinity i.e. poly(ethylene terephthalate) (PET) [1]. An increase of crystallinity thereby leads to improved barrier properties, among other effects, due to an increased packing density leading to a reduction of free volume [2]. In contrast, high crystallinity will prevent materials from being easily formable. This causes technical challenges in two stage processes like thermoforming or injection stretch blow molding (ISBM). In thermoforming as in ISBM the morphology of the precursors can define the processability. A high degree of crystallinity in those precursors will prevent the downstream processability, since large deformations might no longer be reached.

This conflict between high barrier and good formability can potentially be resolved by the decomposition of both requirements by avoiding the formation of crystalline structures for the time until the final packaging shape is reached. This approach is investigated by processing bio-based thermoplastics that differ in their crystallization rate and formability.

Materials

The investigated materials are biopolymers that are made from bio and fossil-based sources and are categorized as biodegradable [3]. Commercial grades were used, to access processable amounts for the specimen production. The used material grades are listed in Table 1.

DOI: https://doi.org/10.51573/Andes.PPS39.SS.BBB.10

Table 1. Materials used in this investigation.

	Supplier	Application	Similar conventional plastics	Source / Degradability
PBAT Polybutylene adipate terephthalate				
Ecoflex® F Blend C1200	BASF	Blown Films, Cast Film	LDPE	Fossil based / Biodegradable
PHA (polyhydroxyalkanoates)-based thermoplastic				
ErcrosBio® PH 110	Ercros	Injection Moulding	Mechanical: LDPE Barrier: PET Haptic: PP	Bio based / Biodegradable
PBS Bio-based polybutylene succinate				
BioPBS™ FZ91PM	Misubishi Chemical	Blown Films, Cast Films	LDPE	Bio based / Biodegradable

To identify the mechanical behavior of amorphous biopolymers, three materials with low glass transition temperature are studied. Their low glass transition temperature suggests that they crystallize at room temperature, making their amorphous behavior previously unknown. PHA, PBAT, and PBS are selected to showcase the bandwidth of processability. PHAs are difficult to use in forming processes, due to their brittleness, associated to spherulitic crystallization [4]. PBAT and PBS are suitable for conventional forming processes due to their high maximum strains [5]. All of these materials are compared by their processing and mechanical properties with LDPE.

For semi-crystalline thermoplastic materials, the cooling rate has an influence on the degree of crystallinity when cooling from the molten state. The effect of two different cooling rate on the crystallization enthalpy, as measured by DSC, are given in Table 2.

Table 2. Selected thermal properties of PHA, PBS and PBAT.

Material	Tg (°C)	Tm according to TDS (°C)	Relative change in Crystallization Enthalpies (10 K/min vs. 100 K/min, DSC) (%)
PBAT	-29.2	110–120	-19.2
PHA	-1.8	124	-15.5
PBS	-34.9	115	-15.5

An increase of the cooling rate from 10 K/min to 100 K/min in DSC measurements yields a significant reduction (>15%) in the recrystallisation peak. The crystallinity can be further suppressed by increasing the cooling rate. For the injection molding process, this is tested by minimizing the mold temperature by using liquid nitrogen.

DOI: https://doi.org/10.51573/Andes.PPS39.SS.BBB.10

Process

The method of changing the morphology for precursors in forming processes allows reconsideration of the thermal history of the processing of biomaterials. In Figure 1, a possible temperature history for the novel CIM process is presented schematically.

The CIM process is characterized by an injection process above the specific melt temperature of the material, followed by cooling at mold temperatures at around -100°C. After demolding the specimens at that temperature, the specimens are kept cold by keeping them in liquid nitrogen, or a deep freezer at approximately -80°C.

Due to the expected low degree of crystallinity, it is assumed that the material will become formable once reheated to temperatures above glass transition. Therefore, in the subsequent process step the material is reheated to temperatures above the glass transition. This is indicated for the bio polymers with temperatures above 0°C in Figure 1. To assess the mechanical behavior of the material at those temperatures, the heated specimens are immediately subjected to tensile testing. This uniaxial testing mimics a subsequent forming process and makes it possible to study the formability of the material in its amorphous condition. Finally, the specimens rest at environmental conditions to slowly recrystallize. During the forming process, this recrystallization could assist a formed packaging in achieving the required specifications, due to a greater stiffness of the recrystallized material and to possibly enhanced barrier properties of the same.

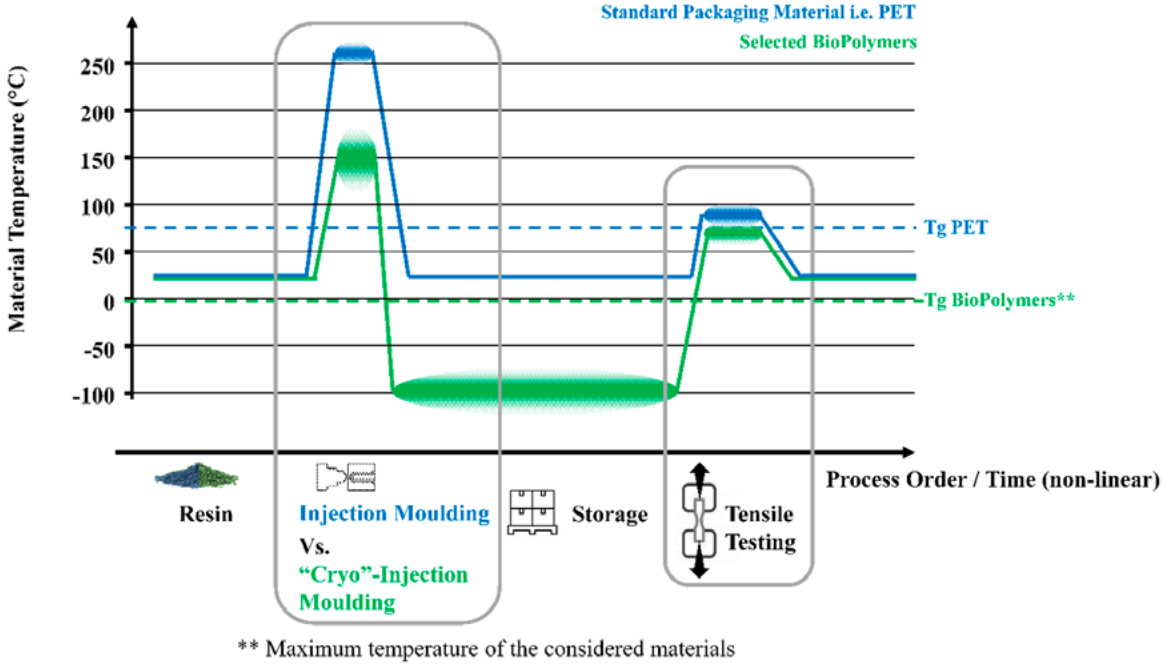

Figure 1. Schematics to compare the thermal history of the processing–Biopolymers vs. PET.

DOI: https://doi.org/10.51573/Andes.PPS39.SS.BBB.10

Specimen Production with the Use of "Cryo-Injection-Molding"

The CIM process uses a custom build tool, that can be used in conjunction with a commercially available micro compounder (Xplore MC 15 HT & IM 12). The "cryo"-tool contains a cavity for an ISO 527 type "1BA" specimen. The cooling mechanism is realized by two open cooling circuits that use the negative pressure created by two venturi pumps to slowly transfer the liquid nitrogen into the molds. An excerpt of a resulting temperature evolution of the mold during testing can be seen in Figure 2.

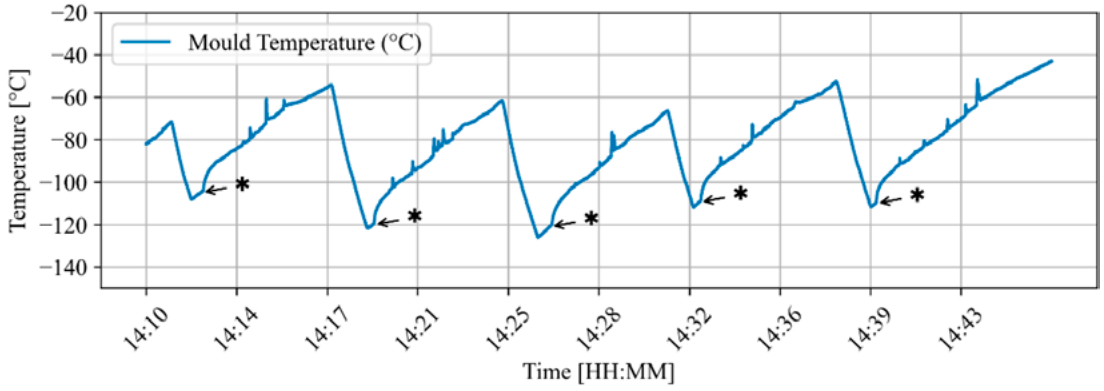

Figure 2. Mold temperature during the injection. The * indicates the time of the injection.

Due to the manual valve opening and closing, the temperature of the mold is oscillating between 40°C and 130°C. The injection process starts after cooling down the mold and reaching temperatures below -100°C. At that temperature, the mold heats up about 9 K due to the injection of the hot polymer. This shows that the thermal mass of the mold is dominant, compared to the thermal mass of the specimen. The unmolding begins right after the injection and the specimens are transferred into the cold storage.

Due to the extreme low temperatures on the mold surfaces and parting plane, humidity condenses on theses surfaces and thin ice layers occur. At some point the extensive ice on the parting surfaces leads to non-closed mold and therefore to flashing.

In conventional processes the used PHA type must be kept in the mold for about 60 seconds at 60°C or higher. The resulting crystallization is needed, since otherwise the polymer at that stage is too soft to be ejected by most ejection systems. Additionally, in the conventional process the material is very sticky to the mold surfaces, as long it is not crystallized. It was observed that this stickiness is avoided below its glass transition temperature in the CIM process. At the low temperatures these biomaterials can be demolded easily and right away. This could lead to an economic advantage due to shorter cycle times in the processing of PHA and other biopolymers.

DOI: https://doi.org/10.51573/Andes.PPS39.SS.BBB.10

Evaluation of the Mechanical Properties by Tensile Testing

Since these materials' glass transition temperatures are well below environmental temperatures and they recrystallize at those temperatures, their behavior in their amorphous state is still unknown.

To quickly and reliably heat up the tensile specimens, a convectional heating device is used to heat up the specimens from both sides. The actual temperature of the specimens right before the deformation with 1000 mm/s is evaluated using thermal imaging technology.

In Figure 3, the specimens made of PBS and PBAT show similar results for both processes, for the CIM and for the regular injection molding. Still, the CIM materials break at larger strains and show overall lower stresses.

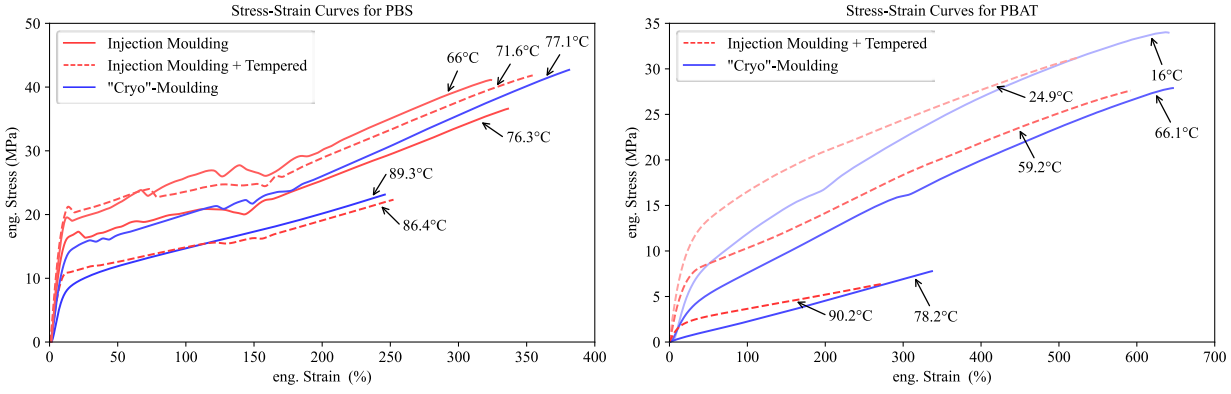

Figure 3. Tensile testing results for PBS (left) and PBAT (right) for selected temperatures and conditions.

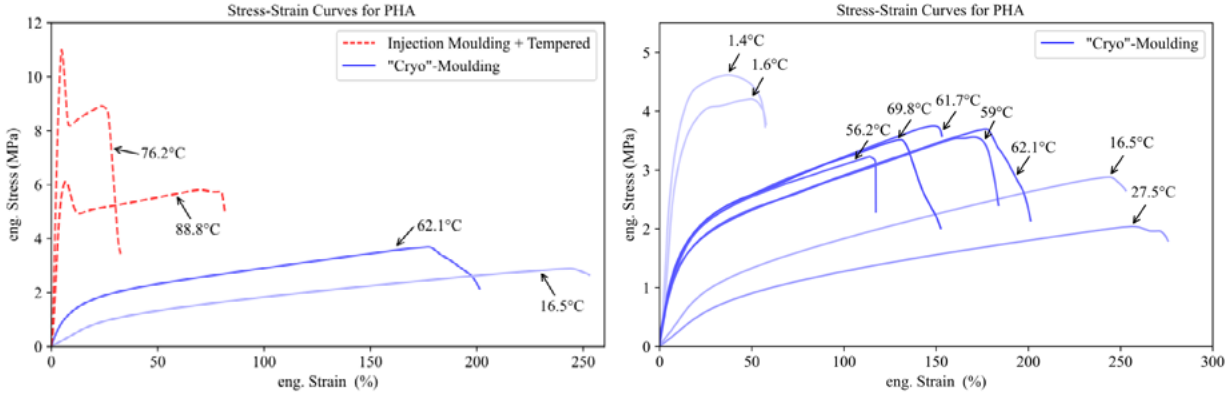

Figure 4. Tensile testing results for PHA. Comparison of the conventional and CIM process (left). Comparing the ductile behavior of the CIM process (right).

DOI: https://doi.org/10.51573/Andes.PPS39.SS.BBB.10

In contrast, the revealed stress-strain behavior of the specimens made of PHA in its amorphous state is significantly different from the known crystalline condition. In Figure 4, the different processes change the material from a brittle and stiff state to a ductile and stretchable material. This leads to a significantly higher elongation at break and lower stresses. In the comparison for the behavior of the ductile material for different temperatures, at low temperatures of approximately 1.5°C the core of the material is assumable still colder than glass transition and behaves stiffer with a strain at break at around 50%. With rising temperatures (16.5°C and 27.5°C) the material softens and the elongation at break is at approximately 250%. From temperatures of approximately 56°C and higher, the material behaves stiffer again and the measured strains at break range from 100% to 200%. This gain in stiffness could be assigned to the thermal induced crystallization that might already occur at these temperatures.

Conclusion

The presented CIM process and tensile testing is capable of revealing the behavior of thermoplastic materials in a highly amorphous state, although they are usually in their semi crystalline state, when processed and handled conventionally. A method with its thermal processing history is presented and mechanical material properties are compared. Particularly for PHA, the mainly amorphous state is difficult to achieve and the characterization of the stress-strain behavior for this state is unobserved. With the presented process, strains of more than 250% have been observed for PHA. These strains are multiple times higher compared to those achieved with the same material in its crystallized state, demonstrating a ductile material behavior. This observed material behavior could be advantageous to produce formed containers.

Alongside this finding, a significant improvement of the molding process for biopolymers was found by CIM. Since the specimens are cooled down to temperatures far below their glass transition, they are stiff and therefore they can be unmolded fast and easily.

The study demonstrates how biopolymers, especially PHA, become more deformable under amorphous conditions. Besides rapid cooling and keeping the material below Tg, there are other methods to avoid big spherulitic crystals, such as using nucleation additives to change the material structure or forming it from the melt, for example, as done in the one-stage injection stretch blow molding process.

Acknowledgments

This work is part of a joined project between the Leibniz-Institut für Polymerforschung Dresden e.V. (IPF), Nestlé Research (NR) and NPTC Waters. The IPF has received funding from NR to conduct this research.

References

1. A. A. Natu, E. A. Lofgren, and S. A. Jabarin, "Effect of morphology on barrier properties of poly(ethylene terephthalate)," *Polymer Engineering & Science*, 2005, https://doi.org/10.1002/pen.20288
2. K. Yamane, H. Sato, Y. Ichikawa, K. Sunagawa, and Y. Shigaki, "Development of an industrial production technology for high-molecular-weight polyglycolic acid," *Polymer Journal*, vol. 46, no. 11, pp. 769–775, Nov. 2014, https://doi.org/10.1038/pj.2014.69
3. European Bioplastics, "What are bioplastics?," [Online]. Available: http://docs.european-bioplastics.org/publications/fs/EuBP_FS_What_are_bioplastics.pdf. [Accessed: Jun. 28, 2024].
4. M. Koller, *The Handbook of Polyhydroxyalkanoates*. Informa, 2020, https://doi.org/10.1201/9781003087663
5. V. Jost, "Packaging related properties of commercially available biopolymers – An overview of the status quo," *Express Polymer Letters*, 2018, https://doi.org/10.3144/expresspolymlett.2018.36

DOI: https://doi.org/10.51573/Andes.PPS39.SS.BBB.10

SPECIAL SYMPOSIA | BIOPOLYMERS, BIOCOMPOSITES AND BIOPROCESSING

Transforming Agriculture: Advancements in Compost-Biopolymers Composites for Enhanced Sustainability

Yina-Ortega and Felipe-Salcedo

DOI: https://doi.org/10.51573/Andes.PPS.SS.BBB.11

December 2024

Transforming Agriculture: Advancements in Compost-Biopolymers Composites for Enhanced Sustainability

Yina-Ortega and Felipe-Salcedo[1]

Abstract : In the Cesar Department in Colombia, sustainable agriculture faces critical challenges despite its thriving livestock sector. Extensive cattle ranching and poor soil management worsen soil conditions. Additionally, significant environmental concerns arise from the substantial discharge of wastewater in the dairy processing industry. This study aims to valorize biosolids derived from wastewater during dairy plant disinfection to enhance sustainable livestock production. It explores the use of biosolids as the primary matrix for creating composted compounds and biopolymers for agricultural purposes. These composite materials utilize composted biosolids from the dairy industry as the main matrix (60%), blended with biodegradable polymers such as polybutylene adipate succinate (PBSA) and polylactic acid (PLA) as functional agents. This innovative approach contrasts with the prevailing literature on composite polymer materials, where polymers typically form the matrix and agricultural residues serve as fillers. Biosolids from Freskaleche S.A. undergo controlled thermal treatment and composting before being combined with PBSA and PLA polymers using an internal mixer. The development of these new compounds includes the evaluation of thermal stability, Fourier-transform infrared spectroscopy (FTIR), and mechanical properties. It is noteworthy that Compost/PBSA composites exhibit promising compatibility and thermomechanical properties resembling pure PBSA, suggesting their potential as thermoplastic materials for producing plastic-based agricultural products. Regarding Compost/PLA blends, compost enhances chemical reactions in PLA polymeric chains, significantly altering their thermomechanical properties. This research provides valuable insights into the use of biosolids for manufacturing composite materials, offering a sustainable approach to address agricultural challenges in the Cesar region.

Keywords: Composite materials, Dairy industry, Polymers, Soil erosion, Waste treatment

1 Yina Ortega (yp.ortega@uniandes.edu.co) is affiliated with the Department of Agroindustrial Sciences at the Universidad Popular in Colombia. Felipe Salcedo is affiliated with the Department of Chemical and Food Engineering at the Universidad de los Andes in Colombia.

DOI: https://doi.org/10.51573/Andes.PPS.SS.BBB.11

Introduction

Livestock farming in the department of Cesar, Colombia, is distinguished by the generation of wastewater, known as "biosolids," with a high load of organic contaminants, representing approximately 90% of processed milk, depending on the type of plant [1]. This wastewater mainly originates from the cleaning of equipment, machines, and production plants containing residues of dairy and chemical products such as acids, alkalis, detergents, and disinfectants.

Biosolids, composed primarily of water (> 90%) and organic matter (around 30% on a dry basis) [2], have been studied globally for over half a century. In developed countries, these materials have been regulated for over a decade for use in various activities, both agricultural and non-agricultural, including soil recovery, landfill cover, and utilization in the forestry industry [3]. Therefore, the dairy industry must focus on managing these wastewater streams, both due to their volume and organic content.

The excessive use of non-degradable plastics poses another significant challenge to agricultural sustainability, as these materials are widely used in greenhouses, irrigation systems, and packaging due to their durability and environmental resistance. Although bioplastics offer the advantage of biodegradability, their adoption in agricultural applications has been limited compared to conventional plastics, which remain dominant due to their lower cost and established performance [4]. The research focuses on utilizing biosolids as a rich source of essential nutrients for crop development, leveraging their high biodegradation capacity due to significant organic content.

This makes them ideal for compost production and agricultural application; however, it is crucial to extend their beneficial effects on soil and plants. Thus, integrating biodegradable and compostable biopolymers such as polybutylene succinate-co-adipate (PBSA) and polylactic acid (PLA), known for their biodegradability, strength, and flexibility, into compost-polymers composites derived from composted dairy biosolids could offer a promising pathway to explore potential agricultural applications that enhance soil and crop improvement over an extended period [5].

Materials and Methods

Materials

The biosolids from Freskaleche S.A.'s wastewater formulation plant, constituting 18% of the compost, underwent thermal treatment at 200°C for 90 minutes. Subsequently, its were composted with other organic components: black soil (54%), rice husks (7%), cocoa husks (13%), orange peel (3.5%), and Efficient Microorganisms (4.5%) to improve the compost. For the composite material, Poly butylene succinate adipate (PBSA) pellets from Mitsubishi Chemical Performance Polymers,

DOI: https://doi.org/10.51573/Andes.PPS.SS.BBB.11

USA, and Luminy® LX175, a transparent, amorphous, low-flow, high-viscosity polylactic acid (PLA) (96% L-Isomer) from Total Corbion PLA, were used.

Blend and samples preparation

The production process of the composite material began with drying composted biosolids at 65°C for 3 hours, followed by grinding to 0.25 mm using a blade mill. Polymer and compost homogenization was made by a C.W. Brabender 2553 internal mixer, where PBSA and PLA polymers were first incorporated, followed by the compost after one minute of mixer operation. The mixtures, as detailed in Table 1, were processed at 40 rpm and 120°C for PBSA, and 170°C for PLA, until the torque stabilized, typically taking about 10 minutes.

Characterization of blends

Thermal analysis (DSC and TGA):

Thermal analysis utilized a TA Instruments SDT-Q600 Thermogravimetric Analyzer in a nitrogen atmosphere (100 ml/min). Samples (~10 mg) were heated at 10°C/min to 500°C, measuring residual weight, moisture loss, and the DTG peak.

Differential Scanning Calorimetry (DSC) with an SDT-Q2000 analyzer assessed thermal properties: Glass Transition Temperature (Tg) during heating (25°C to 250°C at 10°C/min), Crystallization Temperature (Tc) during cooling (with a 1-minute hold at 250°C) and Melting Temperature ™ from the second endothermic peak. Enthalpy of Crystallization (ΔHc) was calculated based on the area under the crystallization peak.

Comparing ΔHc values between biocomposites and pure polymers provides insights into their relative crystallinity, offering a detailed assessment of how the crystalline characteristics of biocomposites compare to those of pure polymers.

$$\text{Equation} = \text{Ci}\ (\%) = \frac{\Delta Hm - \Delta Hc}{\Delta H^0 * f} * 100\% \quad (1)$$

$$\text{Equation} = \quad \text{Ci}\ (\%) = \frac{\Delta Hm}{\Delta H^0 * f} * 100\% \quad (2)$$

The crystallinity index (Ci) of the films was determined by DSC, according to equation 1 for PLA, and equation 2 for PBS, where ΔH^0 is 135.0 J/g for PBSA [6] and 93,0 J/g for PLA [7].

DOI: https://doi.org/10.51573/Andes.PPS.SS.BBB.11

Fourier Transform Infrared Spectroscopy (FTIR):

FTIR-ATR was used to study the bonds and interactions between the components of the prepared composites. The FTIR spectra of the composite materials were collected with a resolution of 4 cm-1 using a Nicolet™ iS50 spectrometer in the range of 400-4000 cm-1. Three measurements were taken for each specimen, and the average spectrum is shown.

Analysis of Mechanical Properties:

Mechanical properties (tensile strength, percentage elongation at break, and Young's modulus) were evaluated using an INSTRON 3367 universal testing machine per ASTM D638, with results averaged from ten specimens.

Results and Discussion

Thermal analysis (DSC and TGA)

The thermal stability of all prepared samples was evaluated by thermogravimetric analysis. Figures 1(a) and (b) show the TG and DTG curves of the pure polymers and composites produced under the different compost ratios.

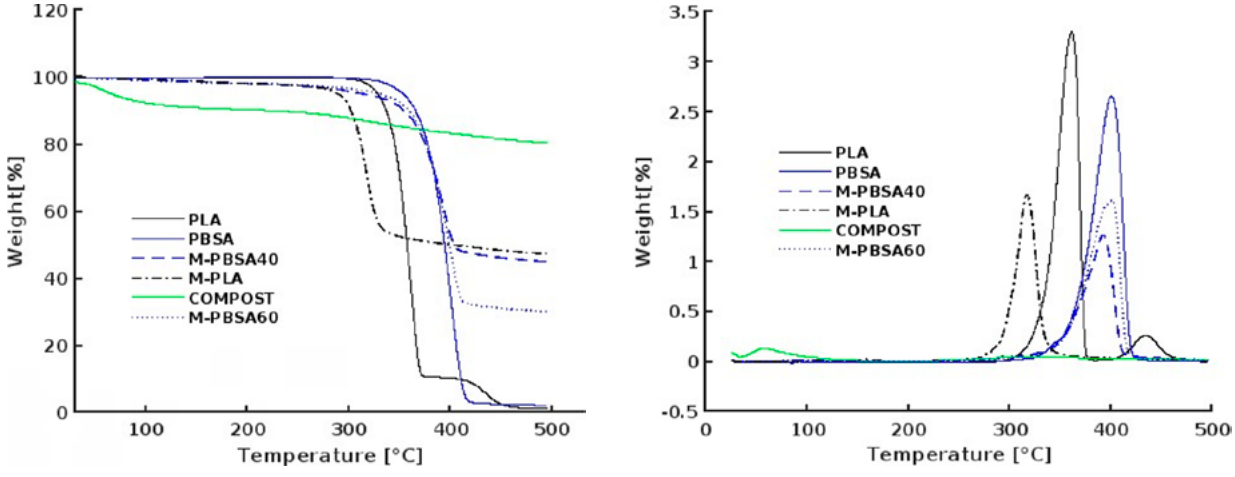

Figure 1. Thermograms of the proposed mixtures. (a) Temperature and weight % Thermogram; (b) Weight % Derivative /°C Thermogram.

DOI: https://doi.org/10.51573/Andes.PPS.SS.BBB.11

When examining the thermograms in Figure 1, it is evident that the thermal degradation temperatures for pure PBSA and the blends with 60% and 40% compost do not differ significantly. For example, pure PBSA has a degradation temperature of 400°C, while the PBS biocomposite blends with 40% and 60% compost show degradation temperatures of 391°C and 398°C, respectively.

Table 1. TGA and DSC thermal properties of PBSA , PLA and Biocomposites.

Formulation			TGA Parameters		DSC Parameters					
	% Compost	% Polymers	T0 (°C)	Tmax (°C)	Tg(°C)	Tc(°C)	ΔHcc (Jg-1)	Tm(°C)	ΔHm(Jg-1)	Ci (%)
PLA	0	100	329	361	55,4	104,8 (Tcc)*	18,69	145,6	21,41	2,7
M-PLA	60	40	354	400	55,2	107,4	9,139	145,7	9,145	0,8
PBSA	0	100	331	398	-43,7	44,3	41,16	52,3a – 75,3b	36,7	27,2
M-PBSA60	40	60	316	391	-45	50,4	26,77	61,9a–78,5b	19,1	23,6
M-PBSA40	60	40	290	316	-46,4	53,3	14,26	70,9a – 79,7b	8,496	15,7
COMPOST	100	0	67	58	——-	———	———	——-	——-	

* Tcc = Cold cristalization

The decrease in degradation temperature is closely related to the presence of cellulose and lignin in the compost. At temperatures above 350°C, cellulose undergoes thermal decomposition due to the random cleavage of the main chains of 1,4-β-d-glucopyranose. Furthermore, at these high temperatures, the cleavage of C-O and C-C bonds in cellulose leads to the generation of volatile compounds such as CO and CH4, as observed in previous studies incorporating pineapple and yucca flour fillers [8].

On the other hand, when exposed to high temperatures, PLA exhibits a notably different thermal response. In its thermogram (Figure 1[a]), two distinct decomposition zones are identified, linked to various reactions occurring during PLA's thermal degradation. Typically, PLA degrades in a single step around 350 °C [9,10]. However, in some cases, two degradation stages have been reported, at 300 °C and 340-360 °C [4], as presented in this study. This difference could be explained by the complexity of PLA's thermal degradation or its chemical structure in terms of polymer stereoisomerism. The stereoisomerism of PLA, influenced by the presence of L or Disomers, can impact the polymer's thermal properties [11].

DOI: https://doi.org/10.51573/Andes.PPS.SS.BBB.11

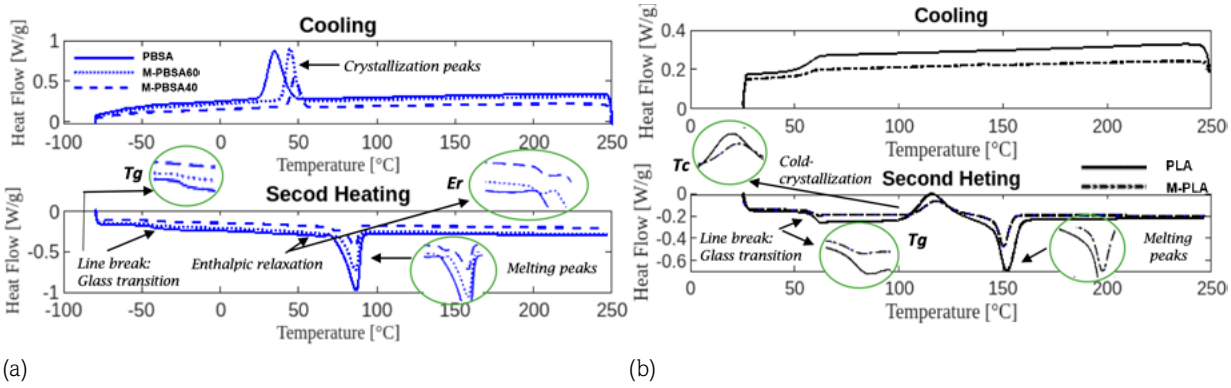

(a) (b)

Figure 2. Thermal transitions observed for formulations. (a) Thermogram of PBSA, M-PBSA60 and M-PBSA40; (b) Thermogram of PLA and M-PLA.

Differential scanning calorimetry (DSC) identified the melting temperatures (Tm) and crystallization temperatures (Tc) and calculated the melting enthalpies (ΔHm) and crystallization enthalpies (ΔHc), as well as the crystallinity index (CI) of the samples (Table 1, Figure 2[a] and [b]). The addition of 60% compost does not significantly alter the Tg of pure PLA or its biocomposites, which remains around 55°C, nor does it affect the Tm values, maintaining them at 145°C [12], as reported by Cacciotti et al. in their study on PLA with functional diatomite loaded with coffee extracts [13].

Similarly, the Tg of PBSA and its biocomposites remains close to -45°C, with the Tm also remaining constant in the range of 75°C to 78°C, consistent with previous studies that show no significant differences with additions of up to 20% cellulose [14].

For PBSA, the exothermic peak associated with crystallinity is found at 44.3°C, shifting to 50.4°C and 53.3°C in M-PBS60 and M-PBS40, respectively, indicating that compost acts as a nucleating agent [15]. Cellulose in the compost promotes crystal formation at higher temperatures [16,17]. In the formulation with 40% compost (M-PBSA40), the crystallinity index (CI) is barely affected, with a reduction of approximately 3%. However, with compost content increased to 60% (M-PBSA60), the CI decreases by around 12%, possibly due to homogeneous dispersion hindering lamellar crystallization compared to the pure polymer. Additionally, both in PBSA and its biocomposites, a multiple melting behavior (identified as Tma in Table 1) associated with partial melting, recrystallization, and re-melting phenomena is observed, characteristic of PBSA as reported in previous studies [18].

The thermogram of PLA shows a sharp endothermic peak just before the glass transition, due to enthalpy relaxation from the polymer's physical aging [19]. This peak is more pronounced in pure PLA than in the M-PLA composite, likely because the addition of compost results in lower molecular weight products with higher mobility. The cold crystallization process of PLA has a peak at 104.8°C. Adding 60% compost raises the Tcc to 107.4°C, possibly due to stereocomplexation. However, a decrease in the material's crystallinity index is observed, similar to that seen in PBSA, due to the difficulty in forming crystallites [12,20].

Fourier Transform Infrared Spectroscopy (FTIR):

The FTIR spectra for the biopolymer's PLA and PBSA, as well as for the biocomposites M-PLA, M-PBSA60, M-PBSA40, and Compost are shown in Figure 3.

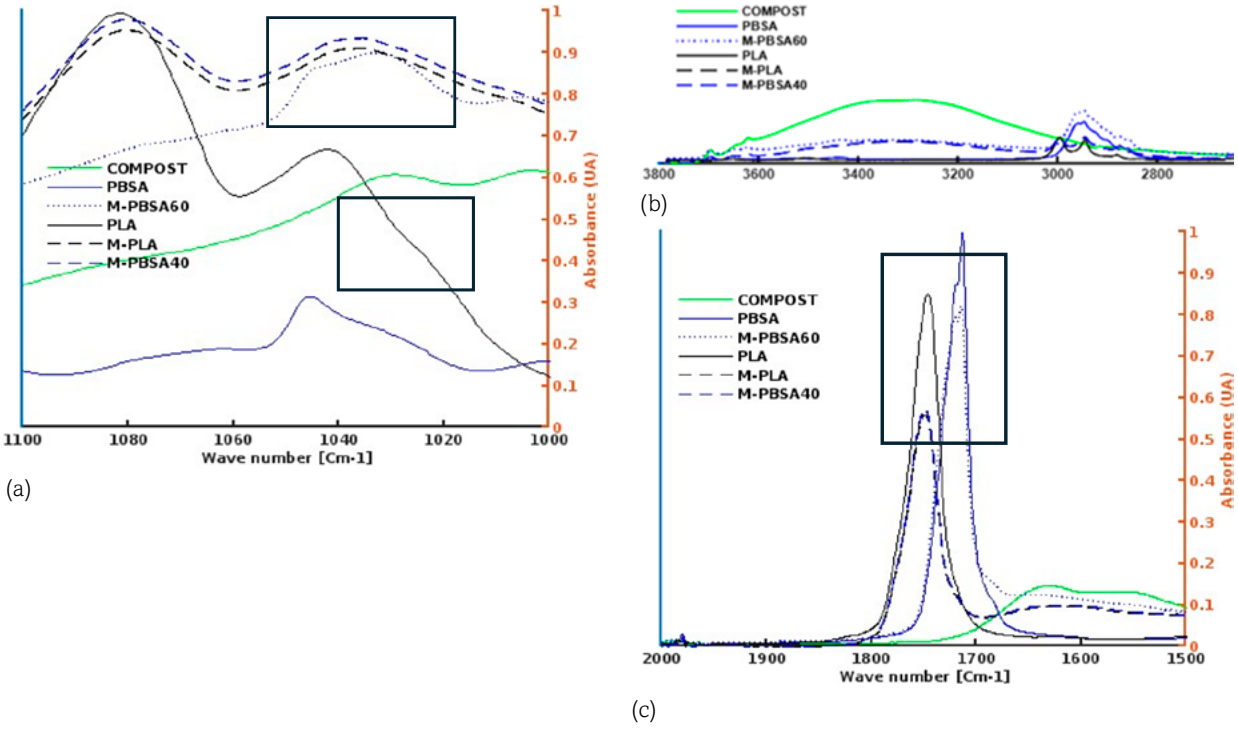

Figure 3. FTIR Analysis for formulations. (a) Hydroxyl groups region (2800- 3800 cm-1); Cellulose region (1020–1050 cm-1); (c) Carbonyl group region (1600–1700 cm-1).

The spectral signals in Figure 3(a), identified in the range of 3600 to 3000 cm 1, indicated the presence of numerous hydroxyl (OH) groups and methyl groups in the lignocellulose section of the compost. This observation is confirmed by the strong absorption peak in the range of 1020 to 1050 cm−1 in the spectra of both the compost and the composites (Figure 3[b]), related to cellulose. These findings are consistent with previous studies on the effect of coffee husk in the production of biocomposites.

On the other hand, the region corresponding to the carbonyl group (-C=O) in the 1700 cm−1 range presents several overlapping peaks (Figure 3[c]), a characteristic behavior of semicrystalline polyesters, such as PLA and PBS. This behavior is equally evident in the biocomposites M-PLA, M-PBS40, and M-PBS60, despite the high percentage of compost added to the formulation. This phenomenon is attributed to the stretching of the ester carbonyl groups in both amorphous and crystalline regions. The confirmed presence of cellulose in the samples explains the decrease in the thermal stability of the composites provided by it [15-21].

DOI: https://doi.org/10.51573/Andes.PPS.SS.BBB.11

Analysis of Mechanical Properties:

When comparing the results between the pure polymers and their derived blends, Figure 4 is obtained.

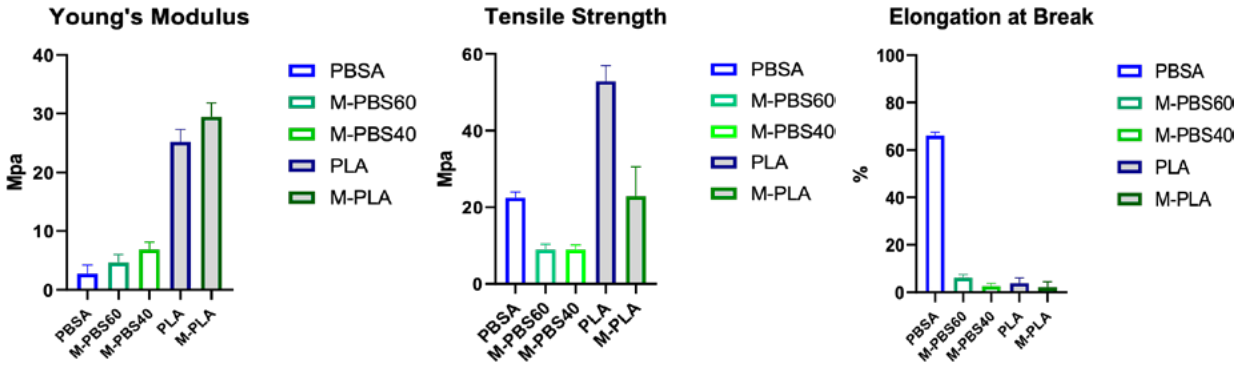

Figure 4. Mechanical properties of PBSA and PLA neat polymers and composites.

The results of the Figure 4 show that the M-PBS60, M-PBS40, and M-PLA blends are stiffer but less ductile than the pure PBS and PLA polymers. The stiffness increased by 17% for M-PLA, 70% for M-PBS60, and 150% for M-PBS40, while tensile strength decreased by 57% for M-PLA and around 48% for M-PBS60 and M-PBS40. Elongation at fracture also significantly decreased. These results align with torque rheometry tests and literature, which indicate that the excessive addition of fibrous material reduces ductility due to non-uniform load and stress transfer within biocomposites [22].

Conclusion

The results show that biocomposite blends with composted biosolids are stiffer but less ductile than pure polymers, due to the addition of fibrous material that reduces ductility.

Spectral analysis confirmed the presence of cellulose in the compost, contributing to lower thermal stability but promoting crystal formation at higher temperatures. Despite the high compost concentration, the thermal and rheological properties of the biocomposites remained similar to those of pure polymers, with compost acting as a nucleating agent.

Based on these findings, the incorporation of composted biosolids as the primary matrix in biocomposites is expected not only to enhance material stiffness but also to provide additional benefits to soil and crop growth, offering a sustainable and effective solution in agriculture.

DOI: https://doi.org/10.51573/Andes.PPS.SS.BBB.11

Acknowledgments

We wish to extend our sincere gratitude to the Ministry of Science, Technology, and Innovation (MINCIENCIAS) in Colombia for their invaluable contributions to this research. We are particularly thankful for the funding provided through the doctoral scholarship awarded to Yina Ortega under the "Bicentenario 2" program. Additionally, we appreciate the support of the Agroindustrial Engineers from the Universidad Popular del Cesar—Marcela Quimbayo, Melissa Segura, Ariana Sierra Vera, and Yerfry Castro—for their assistance in producing the organic amendment.

References

1. H. Escalante, L. Castro, M. P. Amaya, L. Jaimes, and J. Jaimes-Estévez, "Anaerobic digestion of cheese whey: Energetic and nutritional potential for the dairy sector in developing countries," *Waste Management*, vol. 71, pp. 711–718, 2018, https://doi.org/10.1016/j.wasman.2017.09.026
2. Y. Freiberg, P. Fine, I. Levkovitch, and S. Baram, "Effects of the origins and stabilization of biosolids and biowastes on their phosphorous composition and extractability," *Waste Management*, vol. 113, pp. 145–153, 2020, https://doi.org/10.1016/j.wasman.2020.06.002
3. M. Buta, J. Hubeny, W. Zieliński, M. Harnisz, and E. Korzeniewska, "Sewage sludge in agriculture – the effects of selected chemical pollutants and emerging genetic resistance determinants on the quality of soil and crops – a review," *Ecotoxicology and Environmental Safety*, vol. 214, 2021, https://doi.org/10.1016/j.ecoenv.2021.112070
4. S. ElHady, O. Amin, A. Elhussieny, and I. S. Fahim, "Bioplastics, biodegradable plastics, and degradation in natural environments," in *Biodegradability of Conventional Plastics: Opportunities, Challenges, and Misconceptions*, Elsevier, 2022, pp. 47–67, https://doi.org/10.1016/B978-0-323-89858-4.00008-7
5. R. Dziuba, M. Kucharska, L. Madej-Kiełbik, K. Sulak, and M. Wiśniewska-Wrona, "Biopolymers and biomaterials for special applications within the context of the circular economy," *Materials*, vol. 14, no. 24, 2021, https://doi.org/10.3390/ma14247704
6. V. Siracusa, N. Lotti, A. Munari, and M. Dalla Rosa, "Poly (butylene succinate) and poly (butylene succinate-co-adipate) for food packaging applications: Gas barrier properties after stressed treatments," *Polymer Degradation and Stability*, vol. 122, pp. 10–16, 2015, https://doi.org/10.1016/j.polymdegradstab.2015.04.026
7. S. Wang, L. Daelemans, R. Fiorio, G. Maling, R. D. D'hooge, K. De Clerck, and L. Cardon, "Improving mechanical properties for extrusion-based additive manufacturing of poly(lactic acid) by annealing and blending with poly(3-hydroxybutyrate)," *Polymers*, vol. 11, no. 9, p. 1529, 2019, https://doi.org/10.3390/polym11091529
8. G. Dorez, A. Taguet, L. Ferry, J. Lopez-Cuesta, and J. M. Lopez-Cuesta, "Thermal and fire behavior of natural fibers/PBS biocomposites," *Polymer Degradation and Stability*, vol. 98, no. 1, pp. 1–10, 2013, https://doi.org/10.1016/j.polymdegradstab.2012.10.026

9. D. Aydemir and D. J. Gardner, "Biopolymer blends of polyhydroxybutyrate and polylactic acid reinforced with cellulose nanofibrils," *Carbohydrate Polymers*, vol. 250, p. 116867, Dec. 2020, https://doi.org/10.1016/j.carbpol.2020.116867

10. I. Armentano et al., "Processing and characterization of plasticized PLA/PHB blends for biodegradable multiphase systems," *Express Polymer Letters*, vol. 9, no. 7, pp. 583–596, 2015, https://doi.org/10.3144/expresspolymlett.2015.55

11. H. Tsuji and I. Fukui, "Enhanced thermal stability of poly(lactide)s in the melt by enantiomeric polymer blending," *Polymer*, vol. 44, no. 10, pp. 2891–2896, May 2003, https://doi.org/10.1016/S0032-3861(03)00175-7

12. A. Aguero, L. Quiles-Carrillo, A. Jorda-Vilaplana, O. Fenollar, and N. Montanes, "Effect of different compatibilizers on environmentally friendly composites from poly(lactic acid) and diatomaceous earth," *Polymer International*, vol. 68, no. 5, pp. 893–903, 2019, https://doi.org/10.1002/pi.5779

13. I. Cacciotti, S. Mori, V. Cherubini, and F. Nanni, "Eco-sustainable systems based on poly(lactic acid), diatomite and coffee grounds extract for food packaging," *International Journal of Biological Macromolecules*, vol. 112, pp. 567–575, 2018, https://doi.org/10.1016/j.ijbiomac.2018.01.144

14. R. Avolio et al., "Effect of cellulose structure and morphology on the properties of poly(butylene succinate-co-butylene adipate) biocomposites," *Carbohydrate Polymers*, vol. 133, pp. 408–420, 2015, https://doi.org/10.1016/j.carbpol.2015.07.072

15. Z. C. Lule and J. Kim, "Organic-inorganic hybrid filler for improved thermal conductivity and anti-dripping performance of polybutylene succinate composite," *Journal of Cleaner Production*, vol. 340, 2022, https://doi.org/10.1016/j.jclepro.2022.130781

16. M. M.-U. Haque, M. E. Errico, G. Gentile, M. Avella, and M. Pracella, "Properties of macromolecular materials," *Macromolecular Materials and Engineering*, vol. 297, pp. 985–992, 2012.

17. L. Jiang, E. Morelius, J. Zhang, M. Wolcott, and J. Holbery, "Sustainable composite materials from cellulose fiber and polylactic acid," *Journal of Composite Materials*, vol. 42, pp. 2629–2639, 2008, https://doi.org/10.1177/0021998308097740

18. J. Amaya-Pinos, "Thermo-mechanical study of the mixture of polylactic acid PLA obtained from potato starch with an aliphatic copolyester PBSA (polybutylene succinate adipate)," *Dyna*, vol. 89, no. 221, pp. 142–150, 2022

19. I. Armentano et al., "Processing and characterization of plasticized PLA/PHB blends for biodegradable multiphase systems," *Express Polymer Letters*, vol. 9, pp. 583–596, 2015.

20. A. N. Frone, S. Berlioz, J. F. Chailan, D. M. Panaitescu, and D. Donescu, "Cellulose fiber-reinforced polylactic acid composites," *Polymer Composites*, vol. 32, pp. 976–985, 2011, https://doi.org/10.1002/pc.21120

21. M. R. Nobile, A. Crocitti, M. Malinconico, G. Santagata, and P. Cerruti, "Preparation and characterization of PBS and PBAT biodegradable blends," *AIP Conference Proceedings*, vol. 1981, 2018, https://doi.org/10.1063/1.5046042

22. M. R. Rahman, "Engineering materials acacia wood bio-composites towards bio-sustainability of the environment," Springer, 2019, [Online]. Available: http://www.springer.com/series/4288

SPECIAL SYMPOSIA | CIRCULAR ECONOMY OF POLYMERS

Effect of Jatropha Curcas Oil on the Thermorheological Properties of Asphalt Binder Modified with Recycled HDPE

Ana Machute, Lucas Tamele Jr., Arão Manhique, Afonso Macheca and Hermínio Muiambo

DOI: https://doi.org/10.51573/Andes.PPS39.SS.CEP.1

December 2024

Effect of Jatropha Curcas Oil on the Thermorheological Properties of Asphalt Binder Modified with Recycled HDPE

Ana Machute, Lucas Tamele Jr., Arão Manhique, Afonso Macheca and Hermínio Muiambo[1]

Abstract: The application of bio-oils in asphalt and polymer-modified asphalt (PMA), has recently received considerable attention as a pivotal method for enhancing the high-temperature performance of asphalt mixtures while maintaining good binder's workability. In this study, *Jatropha curcas* oil (JCO) was selected and evaluated as an PMA modifier. JCO-rHDPE-modified bio-asphalt was prepared with different JCO contents: 1, 3, and 5 wt.%. Physical tests (penetration, softening point, and ductility), rheological tests (dynamic viscosity and rolling thin-film oven test–RTFOT), and thermogravimetric analysis (TGA) were employed to evaluate the effect of JCO on the rheological, aging, and thermal properties of unmodified and HDPE-modified asphalt. The addition of JCO was effective in reducing the age hardening of asphalt binders due to an increase in penetration and ductility and a decrease in the softening point, and penetration index values. Aged asphalt binder with a combination of JCO and rHDPE has improved resistance to thermo-oxidative aging, exhibiting lower oxidation and volatilization after RTFOT. TGA indicated that the addition of JCO and rHDPE increases the thermal stability of modified binders by delaying the initial decomposition temperature of neat asphalt by 10°C. The incorporation of JCO leads to a decrease in the viscosity of both virgin and rHDPE-modified asphalt. Thus, JCO-rHDPE-modified asphalt has better workability as well as potentially reduced fuel consumption and harmful emissions at pavement service temperatures.

Keywords: Asphalt, *Jatropha Curcas* Oil, HDPE, Rheological Properties, Thermal Properties

1 The authors Ana Machute, Lucas Tamele Jr., Arão Manhique and Hermínio Muiambo (hmuiambo@uem.mz) are affiliated with the Department of Chemistry at the Eduardo Mondlane University in Mozambique. Afonso Macheca is affiliated with Center of Studies in Oils and Gas Engineering Technology at the same university.

DOI: https://doi.org/10.51573/Andes.PPS39.SS.CEP.1

Introduction

Roads, are one of the most important assets of a country, they provide easy access to basic social amenities. Road extension has increased by approximately 12 million kilometers globally and construction of new surface roads is expected to reach 25 million kilometers by the year 2050 [1]. A growing demand for asphalt in road engineering and declining crude oil reserves around the world have impacted large-scale highway construction and maintenance [2]. Therefore, it is important to seek alternative binders to reduce the use of petroleum asphalt [3].

A good method for reducing fresh petroleum asphalt use is to apply polymers as binder modifiers [1]. Polymer modifiers reportedly possess the capacity to improve the properties of bitumen and thus the overall properties of hot mix asphalt (HMA) used in flexible pavement works [4]. Incorporating polymers into asphalt has many advantages that include, but are not limited to, enhanced fatigue resistance, improved thermal stress cracking, decreased temperature susceptibility, and reduced rutting [5]. Despite these improvements, the polymer loads level usually added to an asphalt matrix is limited (3 to 7 wt.%) [6]. This is because the use of high molecular mass polymers can produce thermodynamically unstable modified bitumen, and phase separation readily occurs during its storage at higher temperatures [7]. Moreover, the process of mixing polymer-modified asphalt binders (PMA) requires high shear and processing temperatures (170°C -180°C) to overcome the viscosity differences between bitumen and polymer and achieve adequate polymer dispersion, significantly impacting the technical properties and costs of the process [5].

To solve this issue, some authors attempted to mix the polymer-modified asphalt with bio-oil [8]. Several vegetable oils have been used as raw materials for flexible pavement applications including waste cooking oil (WCO), soybean oil, rapeseed, linseed, Jatropha curcas, mustard oil, corn oils, palm oil, coconut oil, sunflower oil, tung oil, and palm kernel oils [1,5]. JCO is a non-edible oil that cannot be used for nutritional purposes and does not compete with the food chain. It is thus considered more sustainable for pavement applications than any other food-based crop thanks to the presence of anti-nutritional factors, such as phorbol esters [5]. Ahmad et al. [9] investigated the feasibility of utilizing JCO as a bio-based agent. Their results derived from the positive penetration index (PI) results, which indicate good resistance to low-temperature cracking and storage stability and a higher softening point, showing that JCO was capable of rejuvenating and recycling aged bituminous mixtures as well as reducing construction and maintenance costs. It could also improve workability and the resistance to crack at low temperatures. To the best of our knowledge, no research on the incorporation of JCO in polymer-modified asphalt has been carried out. In this study, polymer bio-asphalt (PBA) binders were produced by modifying the base bitumen with recycled HDPE and JCO with enhanced engineering and thermal properties that can also be a sustainable way to avoid flexible pavements.

DOI: https://doi.org/10.51573/Andes.PPS39.SS.CEP.1

Materials and Methods

Materials

A 50/70 penetration grade base asphalt binder from Puma Energy Mozambique was used. The rHDPE was obtained from the mechanical shredding of HDPE plastic bottles. They were washed and dried to remove residual material before extrusion and pelletizing. JCO seeds were collected in the Administrative Post of Sabié, Moamba District, Maputo, Mozambique (26° 02' 36'' S, 32° 19' 36'' E). The air-dried seeds were cracked, and the kernels were finely ground using mortar and pestle and stored at -14°C in screw-capped 15 mL polypropylene vials. The Soxhlet method was used to extract JCO oil, according to Shivani et al. [10], with slight modifications.

Sample Preparation

The preparation of the specimens was based on Langa et al. [11]. First, the base binder was heated up to 170 ± 5°C and the JCO was added. The binder was then mixed, using an IKA® EUROSTAR 20 high-speed shear emulsifying machine, for 15 min at a rotation speed of 500 rpm. Lastly, rHDPE was added and mixed for 45 min at a constant rotation speed of 4 000 rpm. The modified asphalts considered in this study are asphalt modified by (i) 5 wt.% HDPE (AH5); 5 wt.% JCO (AJ5); 5 wt.% HDPE and 1 wt.% JCO (AH5J1); 5 wt.% HDPE and 3 wt.% JCO (AH5J3); 5 wt.% HDPE, and 5 wt.% JCO (AH5J5).

Experimental Procedures

The physico-chemical properties of JCO were determined by a titration method, following the American Oil Chemists Society (AOCS) test procedure. Hence, the acid value (AV) and free fatty acid (FFA) were determined following AOCS Te 2a-64 standard method; the iodine value – AOCS Cd 1-25; and the saponification value (SV) – AOCS Cd 3c-91. The conventional rheological properties were measured by penetration (ASTM-D5), softening point (ASTM-D36), ductility at 25°C (ASTM-D113), and rotational viscosity at 165°C (ASTM-D4402). The short-term aging (RTFOT) experiment was conducted according to ASTM D2872 and evaluated through various aging indexes including mass change (%ΔW), ductility retention (DR), and viscosity aging index (VAI). Thermogravimetric analysis (TGA) was performed using a TA instrument, model STA 6000 TGA/DSC, where 15 ± 1 mg of the sample was heated in aluminum pans from 25°C to 600°C, with a heating rate of 10°C/min under N_2 atmosphere, with a flow rate of 100 mL/min.

DOI: https://doi.org/10.51573/Andes.PPS39.SS.CEP.1

Results and Discussion

Physicochemical Properties of JCO

This study obtained a high extraction yield of JCO (54.35 wt.%). The JCO showed FFA, AV, SV, and iodine values (IV) of 1.63%, 3.25 ± 0.51 mg(KOH)/g, 181.21 ± 8.48 mg KOH/g, and 121.45 ± 3.17 g/100 g, respectively. The JCO extraction yield obtained in this study is within the yield in the works by Zimila et al. [12] (57.9 ± 3.6 wt.%). Previous studies show that FFA content in JCO from different countries varies from 0.4 to 2.3%, and according to Zhang et al. [13], AV in the range of 0.40 to 3.50 mg(KOH)/g are preferable with regard to the high-temperature rheology of asphalt binder. Ideal SV values for asphalt modification are between 177 to 187 mg(KOH)/g. Lower FFA values are required for asphalt modification as FFA are more prone to oxidation. On the other hand, the JCO obtained has good potential to reduce the viscosity of the polymer composite in line with the report from Mumtaz et al. [14], who suggested that low FFA improves lower kinematic viscosity.

Rheological Properties of Asphalt Binders

Table 1 shows that the addition of 5 wt.% rHDPE decreased the penetration value of virgin asphalt (VA) from 54 to 20 dmm and increased the softening point by 36% (from 47 to 64°C). On the other hand, the addition of 5 wt.% JCO to VA binder increased the penetration value by 28%, from 54 to 69 dmm, and the softening point decreased from 47 to 42°C. As for penetration, the addition of 5 wt.% rHDPE decreased the ductility of VA binder and 5 wt.% JCO increased the VA ductility. In ternary composites binders, the increase in JCO loads from 1 to 5 wt.% increased penetration and ductility and steadily decreased the softening point of HDPE-modified asphalt by 7, 20, and 52%. The change in asphalt consistency as a function of temperature was studied through the penetration index (PI). Lesueur [15] states that the typical range for paving-grade asphalts is -2 to +2.0, and for blown asphalt from +2 to +8. All prepared asphalt binders, except AJ5 and AH5J5, were within the range of the conventional paving asphalt binder. The results obtained showed that the addition of rHDPE leads to binder stiffness [15]. This increase in asphalt binder stiffness can be explained mainly by the formation of the polymeric network in the asphalt matrix, with absorption of the light fractions of the asphalt (maltenes) causing greater internal strength, a beneficial factor that increases binder resistance to permanent deformation at high temperatures [16]. Previous research reported that the addition of bio-oils increases penetration and softening point. These observations can be explained by the decrease in the ratio of asphaltenes to maltenes as a result of the increase in the ratio of lower molecular mass oily medium [17].

DOI: https://doi.org/10.51573/Andes.PPS39.SS.CEP.1

Table 1. Asphalt classification for the paving purpose.

Binders	Viscosity at 165°C, mPa.s		Ductility at 25°C, cm		%			Penetration, dmm	Softening point, °C	PI
	Before RTFOT	After RTFOT	Before RTFOT	After RTFOT	Mass change	VAI	DR			
Virgin 50/70	77	91	>100.00	>100	0.077	18.18	-	54.00	47.00	-1.8
AH5	297	351	24.63	21.63	0.029	18.18	87.82	20.00	64.00	-0.2
AJ5	57	73	>100.00	>100	0.070	28.07	-	69.00	42.00	-2.7
AH5J1	261	310.5	26.4	23.47	-0.047	18.97	88.90	25.00	58.00	-0.9
AH5J3	252.5	290	29.63	26.67	-0.040	14.85	90.01	26.00	54.00	-1.6
AH5J5	230	285.5	37.66	34.55	0.035	24.13	91.74	31.00	48.00	-2.6

Table 1 shows that the AH5 binder has the highest viscosity value (297 mPa.s). This increase in viscosity might be explained by higher binder stiffness [15]. High viscosity reduces binder workability, causes non-uniform binder coating with aggregates, and requires higher temperatures for mixing and compaction stages [18]. The HDPE-modified asphalt binder viscosity decreased steadily by adding JCO from 1 to 5 wt.%. The observed viscosity reduction may be explained by the high unsaturated component content in JCO (JCO has a high iodine value). Hence, the JCO balances the chemical composition of the asphalt matrix, enhancing the activity of the molecules in the asphalt binder, and increases the intermolecular distance, or weakens the intermolecular forces [17].

Table 1 shows that VA, AH5, and AJ5 asphalt binders gained mass after aging (oxidation reactions). However, ternary binders registered a mass loss (evaporation of volatile components), except for the AH5J5 binder, which gained mass. All binders comply with the acceptable range of ±0.5% recommended by European standard EN 12607-1 for 50/70 asphalt binders. The aging proprieties of binders was also evaluated through VAI and DR. According to Galooyak et al. [19], lower VAI and higher DR values mean greater aging resistance. The results showed that VA and AH5 binders displayed the same VAI value (18.2%), while AJ5 binder presented a higher VAI value (28.1%). The AH5J3 binder had the lowest VAI value. In the ternary composite, the addition of JCO steadily increase the DR. These results demonstrate that, after aging, addition of HDPE and JCO decreases the viscosity and improves the resistance to thermal-oxidative aging of asphalt binder. This might occur because, during aging, naphthene aromatics are partially converted into polar aromatics, and the polar aromatics are converted into asphaltenes, causing an increase in asphaltene content [17].

Thermal Analysis

Figure 1 shows the TGA and DTG thermograms for asphalt, HDPE-modified asphalt, JCO-modified asphalt, and HDPE-JCO-modified asphalts. These thermograms illustrate that in non-oxidative

(N_2 atmosphere) conditions, VA thermal decomposition occurs in a single stage. This observation corroborated those found by Tamele et al. [20]. The TGA results show that the initial and final decomposition temperatures for virgin asphalt were registered at 373 and 504°C, respectively, with a maximum degradation temperature of 448°C. According to Tamele et al. [20], below 400°C, the asphalt thermal decomposition can be attributed to the cracking of maltenes fractions, such as saturated and aromatic compounds. Above 400°C, decomposition of asphaltenes fractions and the formation of a coke residue occurs [20].

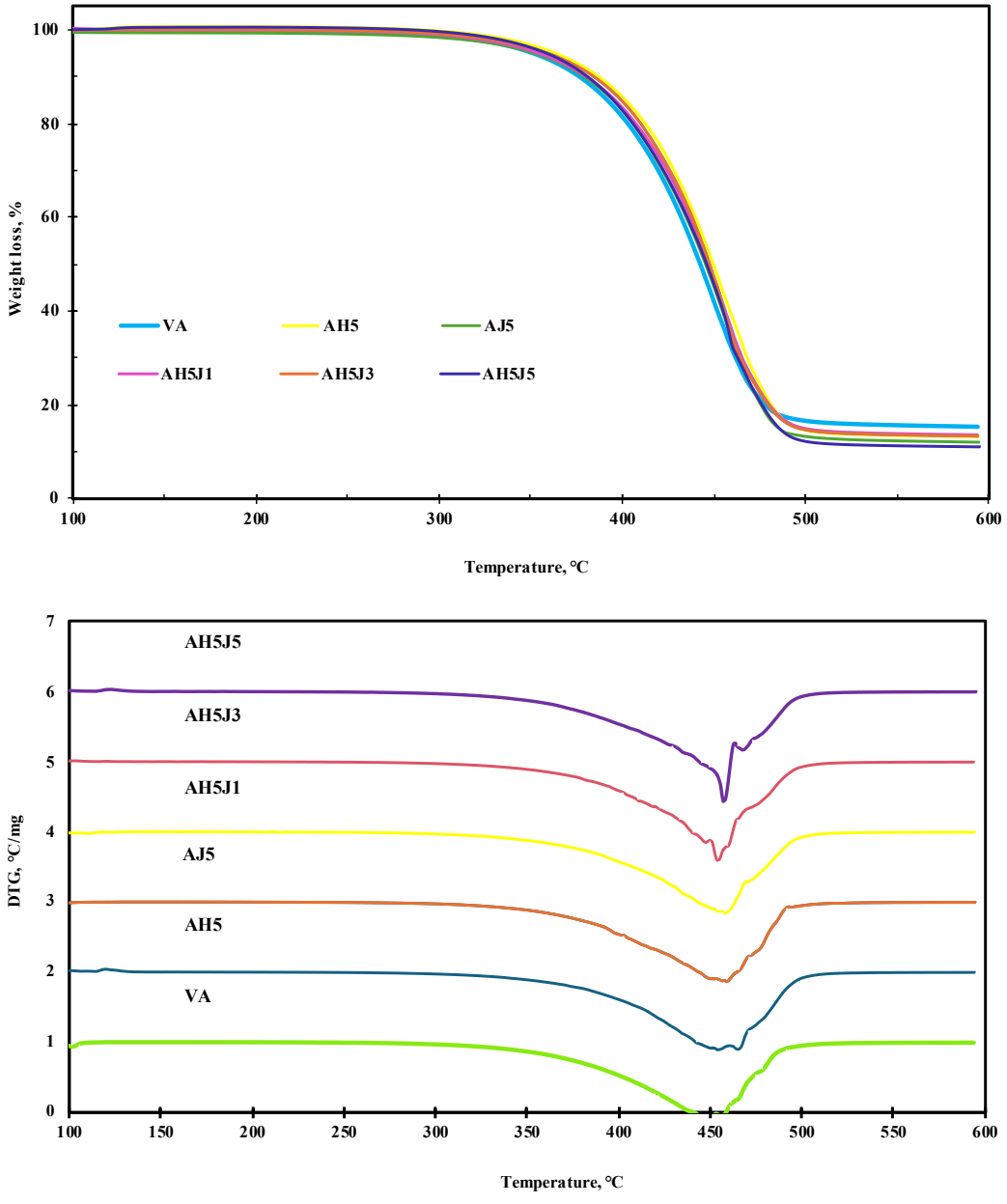

Figure 1. TGA thermograms of asphalt binders. (a) TG-curves; (b) DTG-curves.

DOI: https://doi.org/10.51573/Andes.PPS39.SS.CEP.1

The TGA-curves (Figure 1[a]) show that modified binders displayed a similar decomposition pattern to that of neat asphalt binder. However, in DTG curves (Figure 1[b]) of modified binders, there is a superimposition of two decomposition events, in agreement with results from [21]. For the first and more pronounced event, the overlapped peaks in the DTG-curves are due to the occurrence of polymer chains degradation [22], decomposition of cellulosic materials, and lignin compounds of JCO and evaporation of the maltene fraction of asphalt [11]. It can also be seen that the maximum decomposition temperature has been significantly improved. Thus, the incorporation of HDPE and JCO to the binder reduces its susceptibility to thermal decomposition, as specifically demonstrated by the AH5J3 sample. The shift to high observed temperatures could be a consequence of the interactions between the polar compounds of the HDPE and JCO with the asphalt polar fractions, which create forces that prevent the thermal rupture of bonds at relatively lower temperatures. The combination of JCO and HDPE to modify asphalt binders makes it more thermally resistant and consequently more stable to heating.

Conclusions

This study researched the feasibility of JCO as a bio-based modifier agent for unmodified asphalt and HDPE-modified asphalt. Based on this work, JCO was found to be effective in reducing age-hardening of asphalt. Specifically, the experimental data obtained showed that the addition of 1, 3, and 5 wt.% JCO can counteract the stiffening effect of the HDPE-modified asphalt, due to a noticeable increase in penetration and ductility, and a decrease in the softening point and PI values. The addition of 5 wt.% HDPE increases PI value while the addition of JCO reduces the PI value. At higher temperatures, the addition of JCO leads to a decrease in the viscosity of both VA and rHDPE-modified asphalt. Therefore, the addition of JCO to rHDPE-modified asphalt improves binder workability, reducing fuel consumption. At pavement service temperatures, the presence of rHDPE enhances the stability of the asphalt pavement. The interaction of JCO and HDPE is responsible for promoting significant improvements in asphalt binder thermos-oxidative aging resistance and preventing binder failures during the processing, storage, mixing, and compaction stages by exhibiting higher ductility retention, lower mass gain/loss, and lower viscosity aging ratio. The simultaneous incorporation of HDPE and JCO delays the initial decomposition temperature, especially when 3 wt.% JCO is used, which restricts decomposition by 10°C. Thus, it is recommended that the JCO content be kept at less than 3 wt.% for better bio-binder performance.

References

1. S. M. Saeed et al., "Optimization of rubber seed oil content as bio-oil rejuvenator and total water content for cold recycled asphalt mixtures using response surface methodology," *Case Studies in Construction Materials*, vol. 15, Dec. 2021, https://doi.org/10.1016/j.cscm.2021.e00561

2. R. Zhang, H. Wang, X. Jiang, Z. You, X. Yang, and M. Ye, "Thermal Storage Stability of Bio-Oil Modified Asphalt," *Journal of Materials in Civil Engineering*, vol. 30, no. 4, Apr. 2018, https://doi.org/10.1061/(asce)mt.1943-5533.0002237

3. M. Bilema, Y. Bin Aman, N. A. Hassan, Z. Al-Saffar, K. Ahmad, and K. Rogo, "Performance of aged asphalt binder treated with various types of rejuvenators," *Civil Engineering Journal (Iran)*, vol. 7, no. 3, pp. 502-517, Mar. 2021, https://doi.org/10.28991/cej-2021-03091669

4. S. Köfteci, P. Ahmedzade, and B. Kultayev, "Performance evaluation of bitumen modified by various types of waste plastics," *Construction and Building Materials*, vol. 73, pp. 592-602, Dec. 2014.

5. M. A. Emmanuel, "Polymer-Modified Bio-Asphalt: A Sustainable Panacea to Greenhouse Gas Emissions," in *Asphalt and Asphalt Mixtures*, IntechOpen, 2019, pp. 1-15. https://doi.org/10.5772/intechopen.86832

6. A. Mansourian, A. Rezazad, and F. Karimian, "Performance evaluation of asphalt binder modified with EVA / HDPE / nanoclay based on linear and non-linear viscoelastic behaviors," *Construction and Building Materials*, vol. 208, pp. 554-563, 2019, https://doi.org/10.1016/j.conbuildmat.2019.03.065

7. I. L. Howard, J. D. Doyle, J. M. Hemsley, G. L. Baumgardner, and L. A. Cooley, "Emergency paving using hot-mixed asphalt incorporating warm mix technology," *International Journal of Pavement Engineering*, vol. 15, no. 3, pp. 202-214, Mar. 2014, https://doi.org/10.1080/10298436.2012.721549

8. R. Zhang, H. Wang, J. Gao, X. Yang, and Z. You, "Comprehensive Performance Evaluation and Cost Analysis of SBS-Modified Bioasphalt Binders and Mixtures," *Journal of Materials in Civil Engineering*, vol. 29, no. 12, Dec. 2017, https://doi.org/10.1061/(asce)mt.1943-5533.0002098

9. K. A. Ahmad, M. E. Abdullah, N. A. Hassan, N. Usman, and K. Ambak, "Investigating the Feasibility of Using Jatropha Curcas Oil (JCO) as Bio Based Rejuvenator in Reclaimed Asphalt Pavement (RAP)," *MATEC Web of Conferences* , vol. 103, pp. 1-9, 2017, https://doi.org/10.1051/matecconf/20171030

10. P. Shivani, P. Khushbu, N. Faldu, V. Thakkar, and R. B. Shubramanian, "Extraction and analysis of Jatropha curcas L. seed oil," *African Journal of Biotechnology*, vol. 10, no. 79, pp. 18210-18213, Dec. 2011, https://doi.org/10.5897/AJB11.776

11. E. Langa, G. Buonocore, A. Squillace, and H. Muiambo, "Effect of Vegetable Oil on the Properties of Asphalt Binder Modified with High Density Polyethylene," *Polymers (Basel)*, vol. 15, no. 3, Feb. 2023.

12. H. Zimila, J. S. Mandlate, H. Muiambo, E. M. Artur, H. F. Muiambo, and A. A. Uamusse, "Vortex-assisted solid-liquid extraction for rapid screening of oil content in jatropha Seed: An alternative to the modified Soxhlet method," *South African Journal of Chemistry*, vol. 75, pp. 00-00, 2021, https://doi.org/10.17159/0379-4350/2020/v73a00

13. D. Zhang, M. Chen, S. Wu, J. Liu, and S. Amirkhanian, "Analysis of the relationships between waste cooking oil qualities and rejuvenated asphalt properties," *Materials*, vol. 10, no. 5, 2017, https://doi.org/10.3390/ma10050508

14. M. W. Mumtaz, A. Adnan, H. Mukhtar, U. Rashid, and M. Danish, "Biodiesel production through chemical and biochemical transesterification: Trends, technicalities, and future perspectives," in *Clean Energy for Sustainable Development: Comparisons and Contrasts of New Approaches*, Elsevier Inc., pp. 465-485, 2017.

15. D. Lesueur, "The colloidal structure of bitumen: Consequences on the rheology and on the mechanisms of bitumen modification," *Advances in Colloid and Interface Science*, vol. 145, no. 1-2, pp. 42-82, 2009, https://doi.org/10.1016/j.cis.2008.08.011

16. E. A. A. Siddig, C. P. Feng, and L. Y. Ming, "Effects of ethylene vinyl acetate and nanoclay additions on high-temperature performance of asphalt binders," *Construction and Building Materials*, vol. 169, pp. 276-282, 2018, https://doi.org/10.1016/j.conbuildmat.2018.03.012

17. C. Rodrigues, S. Capitão, L. Picado-Santos, and A. Almeida, "Full recycling of asphalt concrete with waste cooking oil as rejuvenator and LDPE from urban waste as binder modifier," *Sustainability (Switzerland)*, vol. 12, no. 19, Oct. 2020, https://doi.org/10.3390/su12198222

18. H. A. R. Quintana and W. D. F. Gómez, "Mechanical resistance of a chemically-modified warm mix asphalt (Resistencia mecánica de una mezcla asfáltica modificada con un aditivo químico)," *Tenura*, vol. 18, pp. 97-108, 2014, https://doi.org/10.14483/udistrital.jour.tecnura.2014.DSE1.a09

19. S. S. Galooyak, B. Dabir, A. E. Nazarbeygi, and A. Moeini, "Rheological properties and storage stability of bitumen/SBS/montmorillonite composites," *Construction and Building Materials*, vol. 24, no. 3, pp. 300-307, 2010.

20. L. Tamele, H. Muiambo, G. Buonocore, and C. Cumbane, "Thermal proprieties and decomposition kinetics of asphalt binder modified by thermoplastic polymer and nanoclay Dellite 43B," *Journal of Applied Science and Engineering (Taiwan)*, vol. 26, no. 1, 2022, https://doi.org/10.6180/jase.202301_26(1).0002

21. L. V. E. Ruiz, "Analysis of bio-binders for paving as a total substitute for asphalt binder," Master Thesis, Escola Politecnica of the Universidade de Sao Paulo, Sao Paulo, 2020.

22. H. Yu, Z. Leng, and Z. Gao, "Thermal analysis on the component interaction of asphalt binders modified with crumb rubber and warm mix additives," *Construction and Building Materials*, vol. 125, pp. 168-174, Oct. 2016, https://doi.org/10.1016/j.conbuildmat.2016.08.032

SPECIAL SYMPOSIA | CIRCULAR ECONOMY OF POLYMERS

Unlocking the Potential of Recycled Polypropylene in Food Packaging

N. Krempl, M. Fruehwirth, Z. Shahroodi, C. Holzer, E. Pinter, E. Jahn, V.H. Gabriel and F. Aschermayer

DOI: https://doi.org/10.51573/Andes.PPS39.SS.CEP.2

December 2024

View Online

Export Citation

Unlocking the Potential of Recycled Polypropylene in Food Packaging

N. Krempl, M. Fruehwirth, Z. Shahroodi, C. Holzer, E. Pinter, E. Jahn, V.H. Gabriel and F. Aschermayer[1]

Abstract: This study aims to enhance recycled polypropylene (rPP) for yogurt cups, promoting sustainable resource use and waste reduction. Analysis of sorting, recycling, and decontamination shows mechanical recycling of PP effectively generates new products. Experiments reveal pre-sorted, hot-washed, and color-sorted rPP has superior quality and is processable up to 100% recyclate content. Adding a masterbatch additive improves oxidative stability and reduces degradation. Biological, chemical, and sensory analyses confirm rPP cups match virgin PP in odor and appearance, with no mutagenic substances detected. This demonstrates the feasibility of high-quality rPP in food packaging, supporting sustainable practices in the circular economy.

Keywords: Mechanical Recycling, Polypropylene, Sustainable Packaging, Circular Economy, Material Characterization, Industrial Testing, Quality Assurance, Research Collaboration

1 The authors N. Krempl, M. Fruehwirth, Z. Shahrood and C. Holzer are affiliated with the Institute of Polymer Processing at the University of Leoben in Austria. E. Pinter is affiliated with the Department of Packaging, Recycling and Dangerous Goods, at the Austrian Research Institute for Chemistry and Technology in Austria. The authors E. Jahn and V.H. Gabriel are affiliated with the Packaging and Resource Management at the University of Applied Life Sciences in Austria. Finally, F. Aschermayer is affiliated with Greiner Packaging International GmbH in Austria.

DOI: https://doi.org/10.51573/Andes.PPS39.SS.CEP.2

Introduction

Guided by the Circular Economy Action Plan, the European Union aims to achieve climate neutrality by 2050. This includes making all plastic packaging recyclable and recycling 55% of plastic packaging and 60% of municipal waste. In 2022, 54 million tons of plastics were processed in Europe, with packaging leading at 21.1 million tons. Of the total processed polymers, 32 million tons were collected and nearly 38% of packaging waste was recycled [1].

Several European countries, including Austria and Germany, have banned landfill plastics, leading to higher recycling rates despite increased incineration. Polypropylene (PP) is the most commonly used plastic, constituting about 19% of the total. Austria, for example, has a PET beverage bottle recycling rate of about 73% and is expected to reach 90% by 2030 with its new deposit system.

Austria's yellow bag system for collecting plastic packaging aims to improve sustainability. Collected waste is being sorted, but challenges persist. For example, the trade sector's choice between recycling or using virgin packaging significantly impacts market dynamics. Advanced sorting technologies are needed to handle complex materials and outdated regulations hinder progress.

The Pack2theLoop project, funded by the Austrian Research Promotion Agency (FFG), involves 40 companies represented by ecoplus, the Business Agency of Lower Austria and four research teams collaborating to develop quality-assured recyclates from post-consumer packaging for new packaging applications. This article focuses on rPP for food packaging, ensuring the recyclates meet stringent quality requirements. The project, conducted on an industrial scale, aims to improve recycling processes and material quality, enhancing the sustainability and efficiency of the packaging sector.

Materials and Methods

In order to improve the recycling processes and material quality, the first step involved establishing a status quo by examining a specific Austrian material stream using state-of-the-art sorting and recycling methods and technologies in 2021 (Material Loop 1). Building on these initial insights, the project progressed to a second phase that focused on enhanced quality improvement steps (Material Loop 2).

Material Loop 1

Initial industrial sorting employed the Austrian output fraction ARA 414 (a mix of PP and PS), whose input and output were analyzed in detail in manual sorting trials. The sorted materials underwent industrial recycling with water separation, comparing cold vs. hot washing methods. At the Starlinger facility, decontamination involved extrusion, filtration, degassing, and hot air treatment.

DOI: https://doi.org/10.51573/Andes.PPS39.SS.CEP.2

Biological, chemical, and sensory analyses evaluated quality and contamination levels for potential conversion into yogurt cups.

Sorting trials in separate collection were conducted manually at three locations from 2021 to 2024 to assess the potential of PP recycling from Austrian household plastic packaging waste. Detailed analysis focused on PP lightweight packaging collected from yellow bags or bins. Initially, waste was separated by material type, followed by sorting based on criteria including food/ non-food, shape (cup, hollow body, etc.), color, labeling(L) (direct printing, sleeve, L>50%, L<50%, etc.) and closure (with/without). Quantities were documented by weight and number of units to evaluate recycling feasibility.

Initial findings showed significant inhomogeneity in colored rPP recycling stream, promoting characterization of hot-washed, color-sorted rPP granules decontaminated to PET standards.

Material Loop 2

Given its availability, PP with the material specification 324-0 polypropylene [2] from Der Grüne Punkt, Germany, was selected for Material Loop 2. In contrast to Material Loop 1, this phase included additional pre-sorting of white and natural-colored rigid PP for food contact to enhance input purity. The recycling process comprised float-sink separation using saline solution and cold water, followed by drying, dedusting, flake sorting, and a hot wash for thorough cleaning. Decontamination at the Starlinger facility involved extrusion, filtration, degassing, and hot air treatment of the granules.

Proof of concept through an industry study

The study analyzed the processability of decontaminated material from Loop 2 using an inline thermoforming process involving extrusion and thermoforming of monolayer films. The process utilized standard settings designed for virgin cups, with the material demonstrating excellent processability and requiring minimal adjustments. Despite a high melt flow index (MFI) of 17 g/10 min (230°C, 2.16 kg), for the decontaminated rPP, up to 100% rPP content did not present any thermoforming issues. However, challenges in long-term serial production could potentially arise.

Biological, chemical, and sensory analyses

The analyses included migration studies using HS-SPME-GC/MS for volatile substances assessment. Toxicological evaluations were conducted via the miniaturized Ames test to detect DNA-reactive mutagens in decontaminated recyclate and yogurt cup samples. Samples underwent migration in 95% ethanol at 60°C for 10 days, followed by analysis or concentration for methodological purposes. Additionally, sensory evaluation by a trained panel assessed odor profiles to compare with virgin samples.

DOI: https://doi.org/10.51573/Andes.PPS39.SS.CEP.2

Material quality improvement taking into account multiple processing

Here, a twin screw extruder and a combination masterbatch (MAXITHEN® PP7AB4750AO) from Gabriel Chemie GmbH were conducted to enhance the property profile of decontaminated recyclate within the circular economy framework. The extrusion process employed a Leistritz Extrusion GmbH ZSE 27 MAXX compounder operating at 350 rpm, with processing parameters set at 210°C and L/D ratio of 44.3 wt.-% of the masterbatch additive was incorporated during the initial cycle. Pelletization was performed using an Econ GmbH underwater pelletizer (type EUP 50 D). The resulting compounds underwent ten extrusion cycles and was subsequently analyzed thermally, rheologically, and by gel permeation chromatography to assess the material properties.

Thermal analyses involved measuring the oxidation induction time (OIT) using differential scanning calorimetry (DSC 1, Mettler Toledo GmbH, Switzerland). Granules were uniformly pressed into 1 mm plates for consistent sample surfaces. Samples with a diameter of 5 mm and weighing 10 mg were prepared and heated under inert gas (N_2) at 185°C for 2 minutes, followed by exposure to oxygen for 60 minutes to induce oxidation.

Rheological measurements (MCR702, Anton Paar GmbH, Austria) were conducted in a nitrogen atmosphere, evaluating complex viscosity, storage, and loss moduli across an angular frequency range of 0.1–500 rad/s at 185°C and 1% deformation. The crossover point of storage and loss moduli was utilized to qualitatively assess average molecular weight and molecular weight distribution, indicating material degradation [3].

Gel permeation chromatography (GPC) was employed to quantitatively analyze the results obtained from rheological measurements. The analysis utilized 1,2,4-trichlorobenzene (TCB) as the solvent, which was stabilized with butylated hydroxytoluene (BHT) and n-heptane. High-temperature GPC coupled with an IR detector was conducted at 160°C, employing three mixed bed columns and a guard column with a flow rate of 1 mL/min. The analysis, calibrated using narrow PP standards, spanned 40 minutes per sample to determine molecular weight distribution. Prior to analysis, samples were prepared by mixing 8 mg of each with a flow marker and TCB, followed by dissolution, filtration, and measurement using an external filtration system.

Results and Discussion

Sorting trials in separate collection

Manual sorting resulted in approximately 8 wt.-% rigid PP packaging in Austrian separate waste collection of household lightweight packaging waste. A significant share of approximately three quarters represents food packaging in the PP sorting. PP food cups account for 1.4 wt.-% in the yellow bag, which are mainly white coloured with 71 wt.% Figure 1. In addition, approximately 12 wt.-% of the identified PP food cups have an aluminium platine attached.

DOI: https://doi.org/10.51573/Andes.PPS39.SS.CEP.2

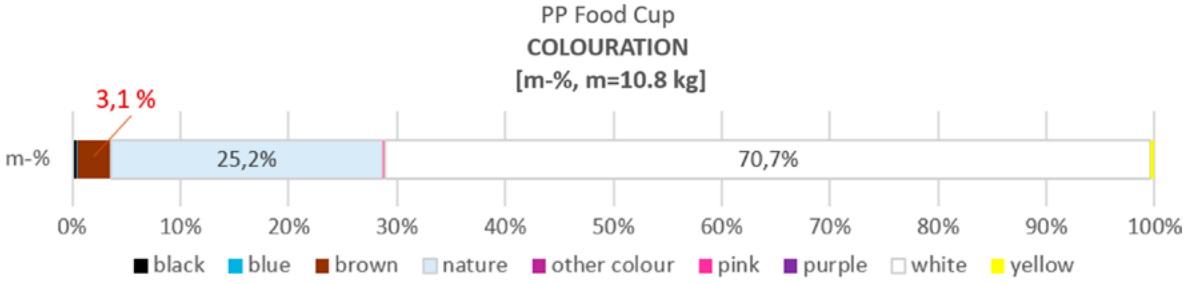

Figure 1. Packaging waste analysis of PP food cups concerning coloration of the main packaging body. 10.8 kg were identified as PP food cups in the sorting input of which 71 wt.-% were white and a quarter transparent.

Industrial Study

In the industrial evaluation of decontaminated rPP production, several key insights into its properties and performance were identified. A high melt flow index of 17 g/10 min (30°C, 2,16 k) was found also to be suitable for up to 100% rPP content, although ongoing production may require continuous monitoring to address potential long-term issues. Material processability was excellent, with minimal adjustments needed, though rPP cups exceeding 30% rPP sometimes exceeded weight specifications. Introducing 30% rPP into virgin material showed acceptable variations in color and odor, indicating minor sensory differences were manageable at this concentration. Uniform lower diameter limits were hardly achieved, but the deviations remained small and acceptable. In general, large fluctuations were found in the measurement protocol of the cup dimensions. The material's top load capacity remained unaffected up to 70% rPP, indicating robustness and macroscopic impurities (Figure 2) probably require better filtration during decontamination.

Figure 2. PP yoghurt cup with 40 w.% rPP and 60% vPP with several marked black spots [4].

DOI: https://doi.org/10.51573/Andes.PPS39.SS.CEP.2

Biological, chemical, and sensory analyses confirmed the potential of decontaminated granulates for use in food packaging. Under worst case migration conditions, chemical screening revealed no deviations compared to virgin material, and bioassay results indicated no DNA-reactive mutagenic effects. The odor of the decontaminated PP resembled that of virgin PP granulates, supporting its application in cup production. Further analyses of 100% rPP cups, considered most critical, showed no adverse effects in bioassays and no anomalies in chemical composition across varying recycling contents (30%, 60%, 100% rPP). Although fewer high volatile substances were detected compared to virgin PP, attributed to effective decontamination processes, sensory analysis indicated no perceptible differences with increasing recyclate content, affirming comparable odor profiles to cups made from virgin PP.

Material quality improvement taking into account multiple processing of the decontaminated recyclate by adding additive involved systematic exploration within the circular economy framework. The material underwent rigorous testing to explore its capabilities through multiple processing cycles, focusing on degradation behavior. Analysis centered on the impact of a masterbatch, integrating oxidation stabilization and compatibilizer, on OIT and molecular mass, illuminating the material's degradation process.

Addition of 3 wt% of the masterbatch extended OIT by a factor of 4.5, maintaining 2.5 times higher stability than unstabilized samples even after 10 cycles (Table 1).

Table 1. OIT at a temperature of 185°C for rPP and rPP with 3 wt% masterbatch.

Cycle	$OIT_{185°C}$ in min		factor x
	rPP	rPP+3wt.% MB	
1x comp	9	42	4,5
5x comp	8	23	3,0
10x com	7	17	2,5

The rheological findings were consistent with those from GPC. Figure 4 illustrates the correlation between these methods for pure rPP and the rPP masterbatch compound. Over successive cycles, all compounds showed gradual material degradation, as evidenced by the upward and rightward shift of the crossover points (Gc) of G' and G'' (left diagram of Figure 3). The polydispersity index (PDI) in the right diagram of Figure 3, which indicates the breadth of molecular weight distribution, revealed a 28% degradation in the rPP compound after 10 cycles due to molecular chain breakdown. Incorporating 3 wt% masterbatch reduced this degradation by approximately 5%.

DOI: https://doi.org/10.51573/Andes.PPS39.SS.CEP.2

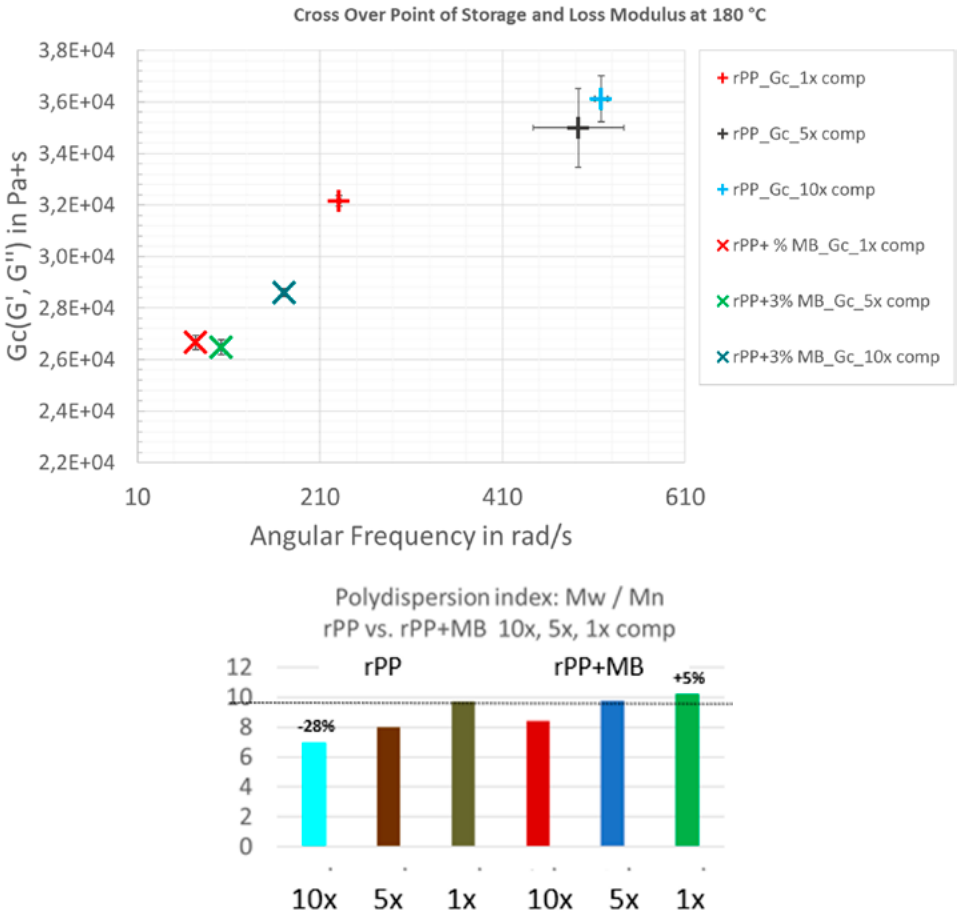

Figure 3. Above: Crossover Point Gc (G', G'') as a function of angular frequency ω at a temperature of 185°C. Below: Polydispersity for rPP without and with masterbatch (MB).

Conclusion

This study conclusively supports the use of rPP in food packaging, aligning with the European Union's Circular Economy Action Plan goals. Through advanced sorting, recycling, and decontamination methods, rPP demonstrated suitability for stringent quality standards without compromising processability, even at high content levels (up to 100%). Sensory evaluations indicated minimal odor differences compared to virgin PP cups, supporting consumer acceptance. Biological and chemical analyses confirmed the safety of decontaminated rPP, showing no mutagenic effects or chemical deviations under worst case migration scenarios. The study highlights the effectiveness of additives like masterbatch in enhancing oxidative stability and mitigating material degradation during multiple processing cycles, crucial for scaling up rPP adoption in packaging. Continued innovation and regulatory support will be vital to further advance sustainable practices and achieve higher recycling rates across Europe.

DOI: https://doi.org/10.51573/Andes.PPS39.SS.CEP.2

Acknowledgments

We gratefully acknowledge the funding support from the Austrian Research Promotion Agency (FFG) for the Pack2theLoop project. We also extend our appreciation to the 40 companies represented by ecoplus, the Business Agency of Lower Austria, and the four research teams whose collaboration was instrumental in the success of this project. Their contributions have significantly advanced our understanding and capabilities in developing quality-assured recyclates from post-consumer packaging for new packaging applications.

References

1. N.N., Plastics Europe, Conversion Market & Strategy GmbH, and nova-Institut, *The Circular Economy for Plastics: A European Analysis*, 2024. [Online]. Available: https://plasticseurope.org/knowledge-hub/the-circular-economy-for-plastics-a-european-analysis-2024/. Accessed: Jun. 20, 2024.
2. N. Wallus, Der Grüne Punkt, "Raw material fraction specification 324-0 Polypropylene," Version 1.00.0001, Doc. No. DOC-23-50686, 2024. [Online]. Available: https://www.gruener-punkt.de/fileadmin/Dateien/Downloads/PDFs/Rohstofffraktionsspezifikationen2024/April/DOC-23-50686_-Rohstofffraktionsspezifikation_324-0_Polypropylen-_v1.00.0001.pdf.
3. N.N., Thermo Fisher Scientific – Materials & Structural Analysis, "Optimizing Polymeric Materials with Rheological Analysis," 2023. [Online]. Available: https://www.azom.com/article.aspx?ArticleID=20979. Accessed: Aug. 28, 2023.
4. F. Aschermayer, Greiner Packaging International GmbH, "PP yoghurt cup with 40 w.% rPP and 60 % vPP with several marked black spots," *Pack2theLoop User Meeting Presentation*, Nov. 29, 2023.

SPECIAL SYMPOSIA | CIRCULAR ECONOMY OF POLYMERS

Recyclates for Sustainable Food Contact Method Development for the Validation of Migration Barriers

Ali Cetin and Rainer Dahlmann

DOI: https://doi.org/10.51573/Andes.PPS39.SS.CEP.3

December 2024

Recyclates for Sustainable Food Contact Method Development for the Validation of Migration Barriers

Ali Cetin and Rainer Dahlmann[1]

Abstract: Ideological changes in industrial approaches require greater ecological thinking. Regarding plastics, the integration of plastic waste into the circular economy arises from the urgent need to design and develop sustainable alternatives. The primary objective of a recycling process is to ensure that the quality of recycled plastics consistently matches that of the original product. Regional authorities and regulations require the assessment and prevention of the potential safety hazards of possible contaminants in recycling streams, recycling processes, and recycling technologies. The specific limits on migrating substances are difficult to achieve through recycling, especially in food packaging. Since food packaging accounts for the largest global share of plastic use, alternative approaches for assessing the value of recyclates as food contact materials need to be considered. One possible way to achieve this goal is barrier development via plasma-enhanced chemical vapor deposition (PECVD) to potentially prevent migration of contamination and barrier function as food contact materials. To efficiently evaluate migrations and barrier efficiencies, a novel contamination approach for virgin materials is introduced to simulate model recyclates. Achieving higher concentrations inside a virgin polypropylene matrix simplifies the analytical approaches. Further, an analysis chain regarding migration evaluation via gas chromatography coupled mass spectrometry and barrier developments are shown.

Keywords: Model Contaminants, Migration, Contaminant Characterization, Migration Barrier

1 The authors Cetin Ali and Dahlmann Rainer are affiliated with the IKV–Institute In Plastics Processing in Industry and the Skilled Craft at the RWTH Aachen University in Germany. They can be contacted through publications@ikv.rwth-aachen.de

DOI: https://doi.org/10.51573/Andes.PPS39.SS.CEP.3

Introduction

Accounting for the largest global plastic production, packaging plastic leads to the rapid accumulation of plastic waste and significant environmental harm due to inadequate waste management. Consequently, recycling of post-consumer packaging plastics and circularity in this sector are indispensable to promote sustainability. In general, the post-consumer lifecycle and material stream of plastics determine their recycling through energy recovery and chemical or mechanical recycling processes. From an ecological and energetic perspective, mechanical recycling is advantageous, particularly when dealing with pure material streams. The primary focus of mechanical recycling is to substitute virgin materials with recyclates of consistent quality, hence the challenge of dealing with extensive sorting, materials charges, and purification efforts [1-3] Taking post-consumer recyclates into account, the resulting unknown history of the materials life cycle and origins limit their applications, as unknown impurities and miscibility's of different polymers affect the resulting quality of the recyclates. In this context, contaminants arise from various sources, including substances that form during the recycling processes, degradation of plastic composition, intentionally added substances like additives, polymeric impurities, chemical substances from both intended and unintended use [2-4]. The regulatory bodies divide contaminants into intentionally and unintentionally added substances and classify them according to their chemical nature. At the same time, regulatory bodies like the European Food and Safety Authority (EFSA) or the U. S. Food and Drug Administration (FDA) limit the quantity and quality of contaminants within the recyclate matrices respective to the application region and according to the application scenario to prevent human harm [5-7]. Therefore, to ensure suitability, an assessment of any technology application related to recyclates should be conducted before implementing these material streams in their respective fields (see Figure 1).

Figure 1. Analytical assessment to determine recyclate suitability.

DOI: https://doi.org/10.51573/Andes.PPS39.SS.CEP.3

Before applying technologies such as decontamination plants, it is crucial to quantitatively and qualitatively assess the contaminations present in the input stream. This assessment allows for determination of the efficiency of the decontamination technology through a subsequent re-evaluation of residual or migrating contaminants. In particular, food contact materials require high demands to meet the threshold of toxicological concerns and safety assessment limits [3]. Despite advancements in recycling pathways in recent years, mechanically recycled post-consumer polypropylene materials still fail to meet the quality threshold imposed by regulatory authorizations for the food contact material stream, which constitutes the largest share of global plastic usage. Intensive research is conducted to analyze, identify, and reduce contaminants in recycled plastics to optimize their life cycles [2,3]. A viable approach to enable the use of post-consumer recycled polypropylene in the food contact material sector is to inhibit or mitigate impurity migration by barrier applications. Therefore, a complete test path, including analyzes prior to barrier migration testing, is the key factor in efficient barrier development to meet specific application legislation thresholds.

Plasma-Based Migration Barriers

Surface coatings have been a promising approach as physical and chemical material property enhancers to suit certain applications, especially in the food contact materials sector [8]. Since avoiding degradation and migration processes are the highest disciplines for food contact materials, one possible pathway to evade these limitations is the use of surface coatings based on plasma-induced barriers [9,10]. Plasma-based barriers have a high potential to overcome gas permeation and migrations of inorganic and organic substances in packaging materials [11]. In particular, barriers by plasma-enhanced chemical vapor deposition (PECVD) inherit uniform surface properties while maintaining low operation and materials costs [10]. The PECVD represents a platform for fast coating depositions on low temperature substrates, yielding nanoscale functional coatings with outstanding chemical and physical properties. In industrial approaches, silicon-based coatings are highly valued in the application fields due to their excellent properties and efficient processabilities [10,11]. As a result, silicon oxide (SiO_x) barrier coatings became highly relevant in the packaging industry due to their excellent gas barrier properties and quick, non-destructive, and environmentally friendly deposition possibilities. By transferring the SiO_x barrier methodology of plasma-based coatings by PECVD to containers made of post-consumer recyclates, a promising pathway to preventing migration of contaminants in addition to the good gas barrier properties can be pursued (see Figure 2).

DOI: https://doi.org/10.51573/Andes.PPS39.SS.CEP.3

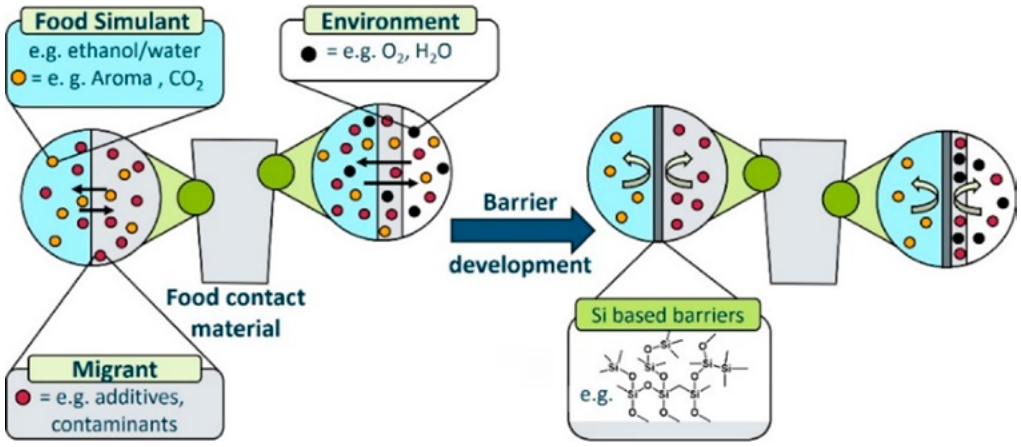

Figure 2. Concept of plasma-based barriers for migration inhibition.

According to regulatory authorizations by EFSA and FDA, the use of SiO_x coatings in food contact materials is permissible. Furthermore, the integration of nanoscale PECVD coatings into existing plastic recycling processes has been confirmed to have no adverse effects, enhancing the overall sustainability of packaging solutions [5-7]. The methodology and challenges of PECVD related to barrier deposition of Si-based barriers on recyclates can be read elsewhere [10,11].

Method Development for the Validation of Plasma-Induced Barriers

Since regulatory authorizations guide approval processes of any kind of technologies related to recyclates, barrier applications also need to meet certain thresholds of migration inhibition after testing under defined conditions [6,7]. But before taking on any approval processes on real recyclate products, the key is to understand the migration processes of chemical substances of all kinds and design barriers to prevent migration weaknesses [9,10]. To reduce the complexity of contamination matrices in real recyclates, model recyclates consisting of virgin materials contaminated with defined chemicals can be used for an efficient barrier development and barrier evaluation (see Figure 3).

Through the selection of specific chemicals, migration mechanisms and the effects of contaminants of a similar chemical nature related to the barriers and the plastic itself can be concluded. Taking the barrier evaluation into account, it is necessary to conduct an analysis chain prior to the introduced model contaminants in a designed sample, in addition to barrier development to approve barrier efficiencies. The evaluation consists of migration testing and analysis regarding the quantification and qualification of the migration of contaminants by gas chromatography coupled mass spectrometry (GC/MS) after barrier deposition. The testing procedures and analysis depend on the application fields and region and are set by official authorizations [3,5,6]. Regarding the contamination procedure, particularly for the recycling decontamination evaluation, the guidelines

DOI: https://doi.org/10.51573/Andes.PPS39.SS.CEP.3

recommend introducing model contaminants known as challenge test chemicals through surrogation. This involves a specific protocol where pristine plastics are stored under defined conditions with the addition of model contaminants, followed by purification [5,6]. The resulting contaminant concentrations in the virgin plastic matrices are mostly insufficient, introducing a certain complexity for the subsequent barrier evaluation. Alongside the resulting insufficient concentration of the contaminations, only one recycling cycle is considered, neglecting further possible accumulation of contaminations by several circular recycling cycles, which are not governed by these challenge tests. To address these points, a novel contamination approach for polypropylene PP [Moplen HP640J] is conducted at the IKV along with the barrier development and analysis chain improvement strategies, hereby introducing certain chemical contaminants via compounding. By implementing effective migration barriers, the aim is to overcome contamination challenges and facilitate the reintegration of post-consumer polypropylene into the circular economy.

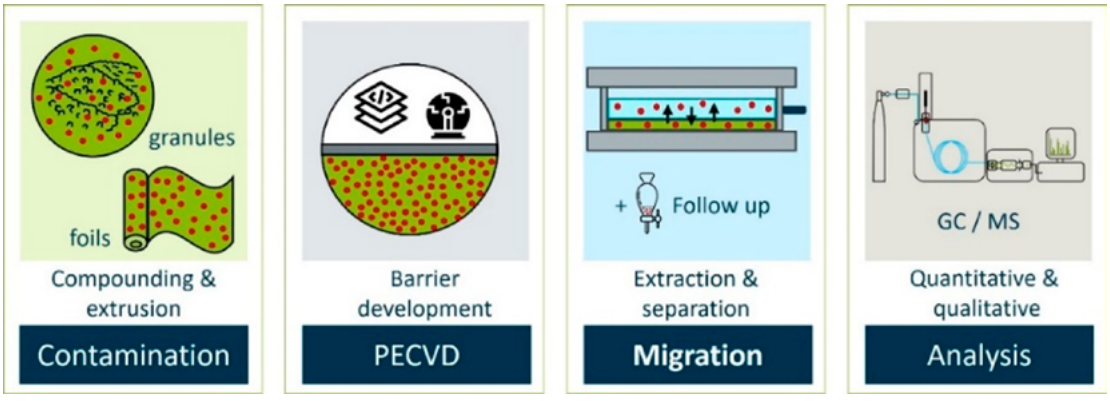

Figure 3. Method development for efficient analysis.

Novel Contamination Method

Since the novel contamination method aims to directly introduce high amounts of contaminants into the virgin PP matrix, the right choice of contaminants is crucial. Through intensive research, the contaminants were chosen respective to their volatilities and polarities in accordance with the regulatory authorities FDA and EFSA representing a broad spectrum of contaminants [5,6], while enabling rapid compounding in the PP samples under certain aspects like their solubilities or application in plastics, e.g. plasticizers. Since the accumulation of contaminants in recycled plastics can be assumed for chemicals with higher boiling points and molecular weights due to their slow evaporation and diffusion out of plastics in decontamination plants, in general contaminants with high boiling points were taken into account for this compounding approach. The volatile contaminants were selected based on their boiling points, positioned near the upper threshold of their definitional range, to ensure a significant retention within the polypropylene (PP) matrix during compounding at an elevated temperature of 180°C. Furthermore, by utilizing this strategy the

DOI: https://doi.org/10.51573/Andes.PPS39.SS.CEP.3

contaminants will be more quickly introduced into the plastic matrix leading to a more efficient and flexible migration evaluation and barrier development. Through infrared spectroscopy and thermogravimetric analysis, the quantitative and qualitative characterization of the contaminants inside the PP samples are accessible (see Figure 4) [12].

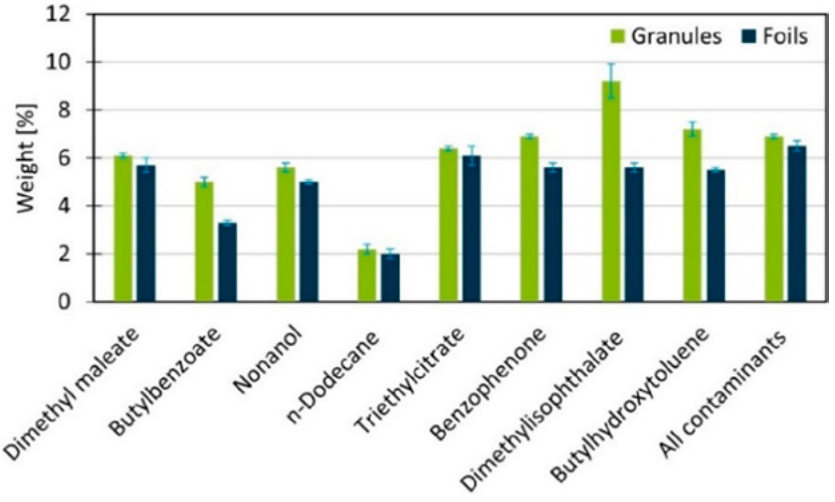

Figure 4. Content of model contaminants in the compounded and extruded PP matrices.

Regarding the differentiation of contaminants based on their polarity and volatility, specifically polar and volatile (dimethyl maleate, butyl benzoate), non-polar and volatile (nonanol, n-dodecane), polar and non-volatile (triethyl citrate, benzophenone), and non-polar and non-volatile (dimethyl isophthalate, butylhydroxytoluene), no clear trends can be observed in their incorporation into the polypropylene matrices during the compounding to granules. The variations in the resulting weight percentages can be attributed to the differing solubilities and boiling points of the contaminants introduced. Originally, a target compounding of 10 weight percent was desired. However, this was not achieved due to evaporation during the contamination procedure, uneven distribution of model substrates within the granules, and loss of contaminants in the water bath during compounding. Furthermore, the weight losses observed in contaminations during subsequent foil extrusion processes can be attributed to the volatilization occurring during thermal processing.

Migration Analysis

With respect to the barrier migration evaluation, it is imperative to conduct migration analysis in accordance with the specific food contact material testing protocols relevant to different application regions. Considering the varying application fields, testing under defined regulatory contact conditions with various food simulants is necessary to quantitatively and qualitatively evaluate the migrating substances, determining their suitability in accordance with the regulatory authorities

DOI: https://doi.org/10.51573/Andes.PPS39.SS.CEP.3

[3,5,6,9]. To ensure the migration testing of the novel contamination method the contaminants are characterized by GC/MS (see Figure 5).

All contaminants and the internal standard in a dichloromethane solution of 10 ng/µL are identified by their resulting mass spectra and assigned to the peaks in the resulting clean chromatogram. This demonstrates the suitability of GC/MS in the method development chain for quantifying and qualifying the migrating substances. The next steps involve performing quantifications to meet regulatory detection thresholds and validating the extractability of contaminants in food simulant matrices with dichloromethane, ensuring the analysis through GC/MS and following the suggested path to initiate barrier development.

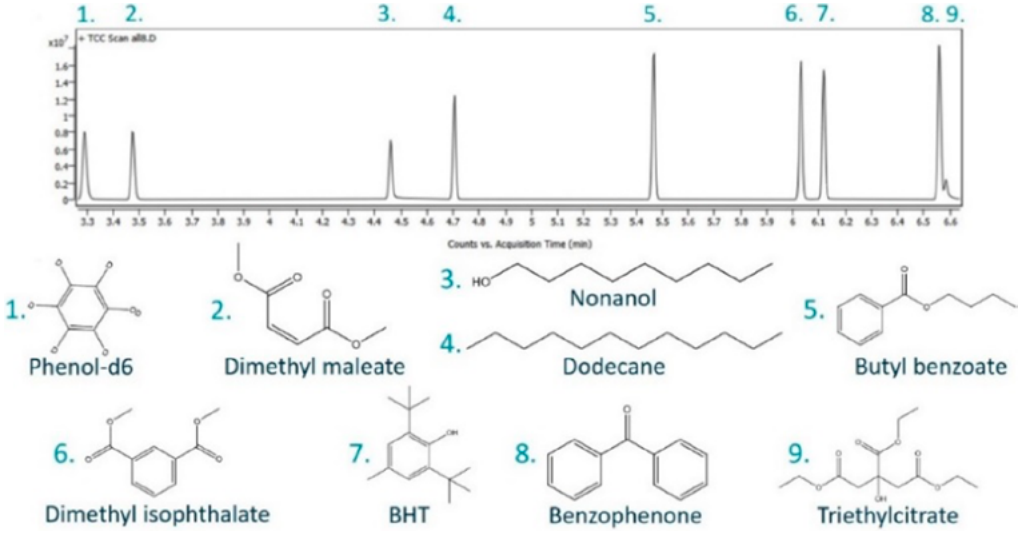

Figure 5. Gas chromatography spectrum of all contaminants and internal standard Phendol-d6.

Conclusion and Outlook

In accordance with regulations from Europe and the United States, a novel contamination method was integrated into a migration evaluation chain for the efficient development of barriers or any recycling technology. By direct compounding specific contaminants in virgin, high concentrations of PP were obtained. Further, the basis for the GC/MS analysis of the contaminants post migration were validated. Building on these fundaments, the next step involves ensuring qualitative and quantitative migration evaluation via GC/MS to facilitate efficient barrier development. The final step entails transferring the methodology to recyclates, following successful migration studies with model substrates. This will pave the way for developing barriers in recyclates for food contact materials, to achieve specific migration limits.

DOI: https://doi.org/10.51573/Andes.PPS39.SS.CEP.3

Acknowledgments

This research was funded by the Deutsche Forschungsgemeinschaft (DFG, German Research Foundation) under the Sonderforschungsbereich Transregio 87 (SFB TR-87). We would like to cordially extend our thanks to the DFG. Additionally, we would like to thank Professor Grundmeier and his team from University Paderborn and our partners GIZEH Verpackungen GmbH & Co. KG, DSD – Duales System Holding GmbH & Co. KG.

References

1. Z. O. G. Schyns and M. P. Shaver, "Mechanical Recycling of Packaging Plastics: A Review," *Macromolecular Rapid Communications*, vol. 42, no. 3, 2021.
2. R. Franz and F. Welle, "Recycling of Post-Consumer Packaging Materials into New Food Packaging Applications—Critical Review of the European Approach and Future Perspectives," *Sustainability*, vol. 14, no. 2, p. 824, 2022.
3. A. K. Undas, M. Groenen, R. J. B. Peters, and S. P. J. van Leeuwen, "Safety of recycled plastics and textiles: Review on the detection, identification and safety assessment of contaminants," *Chemosphere*, vol. 312, no. 1, p. 137175, 2023.
4. J. Saleem, F. Tahir, M. Z. K. Baig, T. Al-Ansari, and G. McKay, *Environmental Technology & Innovation*, vol. 32, p. 103-289, 2023.
5. EU Commission, *Commission Regulation (EU) No 10/2011 of 14 January 2011 on plastic materials and articles intended to come into contact with food*, Official Journal of the European Union, 2011.
6. Food and Drug Administration, *Guidance for industry: use of recycled plastics in food packaging: chemistry considerations*, 2006.
7. EU Commission, *On good manufacturing practice for materials and articles intended to come into contact with food*, Official Journal of the European Union, 2023.
8. M. Forrest, *Coatings and inks for food contact materials*. Shrewsbury: Rapra Technology, 2006.
9. F. Welle and R. Franz, "SiO*x* layer as functional barrier in polyethylene terephthalate (PET) bottles against potential contaminants from post-consumer recycled PET," *Food Additives & Contaminants: Part A*, vol. 25, no. 6, pp. 788–794, 2008.
10. L. Kleines, T. Blasius, and R. Dahlmann, "PECVD barrier coating systems on post-consumer recyclates for food contact applications," *Surface Engineering*, vol. 38, 10-12, pp. 968–976, 2022.
11. R. Snyders, D. Hegemann, D. Thiry, O. Zabeida, J. Klemberg-Sapieha, and L. Martinu, "Foundations of plasma enhanced chemical vapor deposition of functional coatings," *Plasma Sources Science and Technology*, vol. 32, no. 7, p. 74001, 2023.
12. A. Cetin, R. Dahlmann, *32nd International Colloquium Plastics Technology*, 2024.

DOI: https://doi.org/10.51573/Andes.PPS39.SS.CEP.3

SPECIAL SYMPOSIA | CIRCULAR ECONOMY OF POLYMERS

Polymeric Blends Containing Different Carboxylic Acids

Fabiula Danielli Bastos de Sousa and
Matheus Alves Rodrigues

DOI: https://doi.org/10.51573/Andes.PPS39.SS.CEP.4

December 2024

Polymeric Blends Containing Different Carboxylic Acids

Fabiula Danielli Bastos de Sousa and Matheus Alves Rodrigues[1]

Abstract: A single-screw extruder was used to produce polymeric blends comprising recycled high-density polyethylene (HDPE) and thermoplastic starch (TPS). Carboxylic acids with varying lengths of carbon chains were used as compatibilizing agents in the blends. While the mechanical properties did not show significant differences among the blends containing compatibilizing agents, all exhibited superior results compared to those without a compatibilizing agent. Therefore, opting for the more cost-effective acid is advisable.

Keywords: HDPE, TPS, Carboxylic Acid, Polymer Blend, Mechanical Properties

1 The authors Fabiula Danielli Bastos de Sousa (fabiuladesousa@gmail.com) and Matheus Alves Rodrigues (matheusar@gmail.com) are affiliated with the Technology Development Center at the Universidade Federal de Pelotas-UFPel in Brazil.

DOI: https://doi.org/10.51573/Andes.PPS39.SS.CEP.4

Introduction

Synthetic thermoplastic/thermoplastic starch blends are formulated as a substitute material for disposable packaging to mitigate the adverse environmental effects of polymers [1]. Most synthetic polymers, such as polyethylene, are immiscible with starch at the molecular level, resulting in deficient mechanical properties in these blends [2]. One option to resolve this issue is to use compatibilizing agents. Maleic anhydride (MA) is extensively used as a compatibilizing agent in polymeric blends. However, MA is costly, difficult to produce, and non-biodegradable, similar to petroleum-based polymers [3]. One potential solution is to utilize carboxylic acids derived from renewable sources as a compatibilizing agent [4]. These acids have a compatible chemical structure, are available in the environment, and are biodegradable [5].

In this work, thermoplastic starch and recycled high-density polyethylene (HDPE) were mixed with carboxylic acids of different carbon chain lengths as compatibilizing agents to produce polymeric blends using a single-screw extruder.

Materials and Methods

Materials

The materials used were recycled HDPE, cornstarch commonly used in bakeries (Cornmill), glycerin PA (Synth), stearic acid (Synth), myristic acid (Dinâmica), and palmitic acid (Dinâmica).

The packaging thrown away for recycling by the cleaning department of the Universidade Federal de Pelotas was the source of the recycled HDPE. Based on ABNT NBR 13230:2008, all packages are code 2.

Preparation of the HDPE

The packages were separated, the labels removed, and then washed and dried at room temperature. Subsequently, the samples were cut manually and ground using a Marconi knife mill.

Preparation of the Starch/Glycerol Mixture

The starch and glycerol mixture (60/40 ratio by mass) was prepared in an industrial mortar mixer. The materials were mixed for 30 minutes until a homogeneous mixture was achieved. Subsequently, the mixture was dried in an oven at 50°C for 24 hours.

DOI: https://doi.org/10.51573/Andes.PPS39.SS.CEP.4

Processing of the Blends

The blends were processed in a single-screw extruder ECO, at the following temperatures: 96°C (first zone), 177°C (second zone), 180°C (third zone), and 180°C (die), and with a rotation speed of 100 rpm. The blends were chopped using a shredder connected to the extruder.

Blends of 60% HDPE and 40% starch (along with glycerol, known as TPS) were produced. Within each blend, 10% of the total mass of HDPE consisted of various carboxylic acids, which were used as compatibilizing agents. The formulations and terminologies of the produced blends are detailed in Table 1

Injection of the Blends

The blends were injected using a Spazio reciprocal screw injector, model DW130 Plus, at the following temperatures: 100°C (first zone), 150°C (second zone), 190°C (third zone), 190°C (injection nozzle), and the mold at room temperature. Specimens were prepared for tensile tests following ASTM D638.

Tensile Properties Analysis

An Instron tensile test machine model 3369 was used for the tensile strength test with a displacement speed of 5mm/min.

Table 1. Formulations and nomenclatures of the produced blends.

Sample	HDPE (% mass)	TPS (% mass)	Compatibilizing agent		
			Myristic acid (M)	Palmitic acid (P)	Stearic acid (S)
HDPE	100	-	-	-	-
Zero	60	40	-	-	-
M	60	40	X	-	-
P	60	40	-	X	-
S	60	40	-	-	X

DOI: https://doi.org/10.51573/Andes.PPS39.SS.CEP.4

Results and Discussion

The results of the tensile tests are shown in Figure 1.

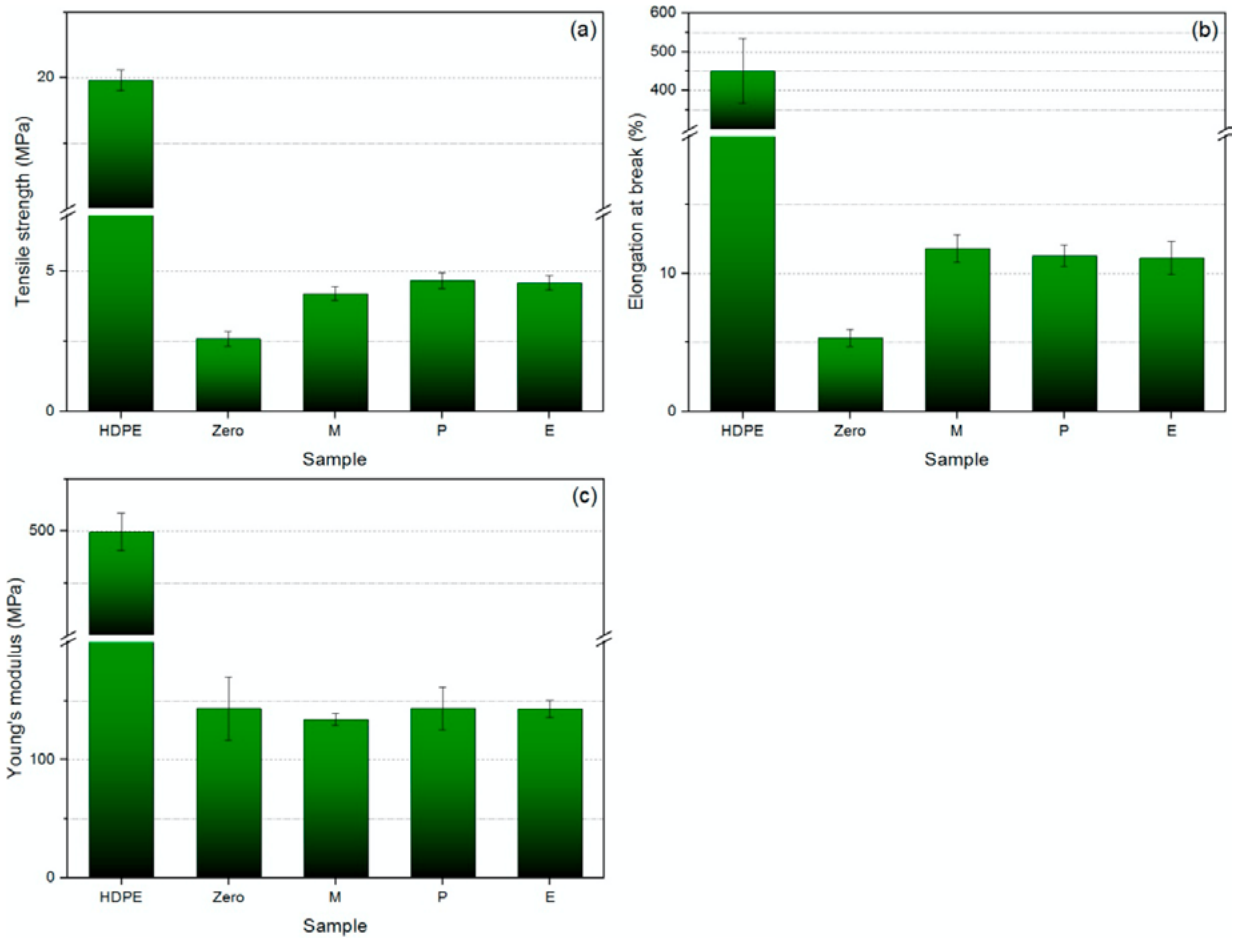

Figure 1. Tensile properties of the samples: (a) tensile strength, (b) elongation at break, and (c) Young's modulus.

In general, a reduction in the tensile properties of the Zero blend can be observed compared to the recycled HDPE. One potential reason for the decrease in tensile strength after adding starch to the HDPE is the inadequate interfacial interaction between the components of the blend, which may lead to mechanical rupture at the interface [6]. Moreover, the elongation at break is significantly influenced by the interfacial interaction between the blend phases [7]. Similar behavior was observed by Ning et al. [8] in glycerol/starch/linear low-density polyethylene (LLDPE) blends, which was attributed to the weak interfacial adhesion between two distinct polarity materials and unthermoplastic starch granules.

DOI: https://doi.org/10.51573/Andes.PPS39.SS.CEP.4

The blends containing compatibilizing agents exhibited higher tensile strength values and elongation at break. Elongation at break is a high-strain property influenced by interfacial interaction [1]. The results underscored the effectiveness of the compatibilizing agents employed. Conversely, Young's modulus values did not display significant variations across all blends.

No significant difference was observed among the blends containing compatibilizing agents (M, P, and E blends). In this case, opting for the less expensive acid is a more suitable choice.

Martins and Santana [1] produced polypropylene (PP)/TPS blends using the same compatibilizing agents employed in the current study and PP-grafted maleic anhydride (PPgMA). According to the researchers, compared to the PP/TPS blend, those containing stearic acid, PPgMA, and myristic acid exhibited enhancements of 25%, 22%, and 17% in tensile strength at break, and 180%, 194%, and 259% in elongation at break, respectively. Consequently, stearic acid displayed superior performance compared to PPgMA.

Conclusion

Recycled HDPE/TPS blends were produced in a single-screw extruder. Blends containing carboxylic acids exhibited superior tensile strength and elongation at break compared to those without a compatibilizing agent. However, the carbon chain length of the acids did not significantly influence the mechanical properties of the blends. The enhancement in the properties of the HDPE/TPS blends was attributed to the increased compatibility facilitated by the carboxylic acids.

References

1. A. B. Martins and R. M. C. Santana, "Effect of carboxylic acids as compatibilizer agent on mechanical properties of thermoplastic starch and polypropylene blends," *Carbohydrate Polymers*, vol. 135, pp. 79-85, Jan. 2016.
2. R. Chandra and R. Rustgi, "Biodegradation of maleated linear low-density polyethylene and starch blends," *Polymer Degradation and Stability*, vol. 56, no. 2, pp. 185-202, May 1997.
3. W. Shujun, Y. Jiugao, and Y. Jinglin, "Preparation and characterization of compatible thermoplastic starch/polyethylene blends," *Polymer Degradation and Stability*, vol. 87, no. 3, pp. 395-401, Mar. 2005.
4. F. D. B. de Sousa and D. J. Carastan, "Reinforced polymer blends composed of coffee capsules/thermoplastic starch," *AIP Conference Proceedings*, vol. 2884, no. 1, p. 190001, Oct. 2023.
5. M. Poletto, A. J. Zattera, and R. M. C. Santana, "Effect of natural oils on the thermal stability and degradation kinetics of recycled polypropylene wood flour composites," *Polymer Composites*, vol. 35, no. 10, pp. 1935-1942, Oct. 2014.

DOI: https://doi.org/10.51573/Andes.PPS39.SS.CEP.4

6. A. G. Pedroso and D. S. Rosa, "Mechanical, thermal and morphological characterization of recycled LDPE/corn starch blends," *Carbohydrate Polymers*, vol. 59, no. 1, pp. 1-9, Jan. 2005.

7. N. St-Pierre, B. D. Favis, B. A. Ramsay, J. A. Ramsay, and H. Verhoogt, "Processing and characterization of thermoplastic starch/polyethylene blends," *Polymer (Guildf).*, vol. 38, no. 3, pp. 647-655, Feb. 1997.

8. W. Ning, Y. Jiugao, M. Xiaofei, and W. Ying, "The influence of citric acid on the properties of thermoplastic starch/linear low-density polyethylene blends," *Carbohydrate Polymers*, vol. 67, no. 3, pp. 446-453, Feb. 2007.

DOI: https://doi.org/10.51573/Andes.PPS39.SS.CEP.4

SPECIAL SYMPOSIA | CIRCULAR ECONOMY OF POLYMERS

The Effect of Clays on the Mechanical Properties of Dynamically Revulcanized Blends Composed of Ground Tire Rubber/High-Density Polyethylene

Fabiula Danielli Bastos de Sousa

DOI: https://doi.org/10.51573/Andes.PPS39.SS.CEP.5

December 2024

The Effect of Clays on the Mechanical Properties of Dynamically Revulcanized Blends Composed of Ground Tire Rubber/High-Density Polyethylene

Fabiula Danielli Bastos de Sousa[1]

Abstract: This study examines the impact of adding Cloisite 20A and Halloysite clay on the mechanical properties of dynamically revulcanized blends composed of high-density polyethylene (HDPE) and ground tire rubber (GTR), which have been previously devulcanized via microwaves. Blends were prepared, containing different concentrations of the phases. Halloysite clay seems to have acted as a compatibilizer agent between the phases of the blends, whereas Cloisite 20A clay seems to have acted as a reinforcement in the revulcanized blends. However, slight deviations were noticed in the variations in the phases' concentrations. This study explored the possibility of utilizing end-of-life tires in polymeric blends.

Keywords: Clays, Cloisite 20A, Halloysite, Mechanical Properties, Morphology

1 The author Fabiula Danielli Bastos de Sousa (fabiuladesousa@gmail.com) is affiliated with the Technology Development Center at the Universidade Federal de Pelotas-UFPel in Brazil.:

DOI: https://doi.org/10.51573/Andes.PPS39.SS.CEP.5

Introduction

As a result of growing ecological consciousness and global concern about the continuous accumulation of end-of-life tires, the scientific community is encouraged to research alternative methods of recycling them [1]. Microwave devulcanization is a method of recycling ground tire rubber (GTR) using microwave energy to break down the cross-links. However, this method may degrade the material, so a thorough understanding of the process and its variables is crucial. When GTR is a phase of a polymeric blend, devulcanization improves the interaction between the polymeric phases. This helps reduce the deterioration of the final product's properties and increases the concentration of recycled elastomer in the blend [2].

Thermoplastic vulcanized polymeric blends require sufficient adhesion between the phases to achieve mechanical behavior similar to an elastomer. The revulcanization of the GTR phase is beneficial, but researchers have incorporated nanofillers such as nanoclays to enhance adhesion between the blend phases [3,4]. A substantial lack of literature on the issue still exists.

This work aims to analyze the influence of Cloisite 20A and Halloysite clays on the mechanical properties of dynamically revulcanized blends composed of high-density polyethylene (HDPE) and GTR. The results indicate that each clay behaved differently with Halloysite acting as a compatibilizer agent and Cloisite 20A clay acting as a reinforcement.

Materials and Methods

Materials

Ground truck tire (GTR) waste separated from non-elastomeric components; vulcanization additives: rubber accelerator TBBS (N-tert-Butyl-2-benzothiazole sulfenamide) and sulfur (vulcanization agent); HDPE (trade name IA-59 from Braskem); organically modified Montmorillonite Cloisite 20A® (Bentonit União Nordeste); halloysite nanotubes of specification #685445 (Sigma-Aldrich); and maleic anhydride grafted HDPE (HDPE-MA) Polybond® 3029 (Chemtura).

The methodology is based on earlier works [5,6].

Devulcanization of GTR and Production of the Nanocomposites

The maximum power (820 W) was used to devulcanize GTR in a conventional microwave oven that had been modified with a motorized stirring system with speed control. Approximately 65 g of the GTR sample was placed in a 250 mL glass beaker and stirred at 100 rpm for 5.5 minutes.

DOI: https://doi.org/10.51573/Andes.PPS39.SS.CEP.5

After the devulcanization process, the samples were homogenized in a laboratory two roll mill, and 1 phr (parts per hundred of rubber) of TBBS and 1 phr of sulfur were added, respectively. The resulting tacky rubber sheets were manually cut into pieces of approximately 3 mm x 3 mm to produce blends in a twin-screw extruder.

The HDPE granules were pulverized using a cryogenic mill (Micron Powder Systems, model Mikro-Bantam) and then dried in an oven at 60°C for 24 hours. To create masterbatches, they were mixed with Cloisite 20A clay (resulting in the nanocomposite HDPE/Cloisite 20A) and with Halloysite clay and a compatibilizer agent (resulting in the nanocomposite HDPE/Halloysite). The resulting nanocomposites were then dried for eight hours at 60°C in a vacuum oven.

A Werner & Pfleider model ZSK 30 co-rotating twin-screw extruder was utilized to prepare the nanocomposites. The processing temperatures were as follows: 160°C (zone 1), 170°C (zone 2), 180°C (zone 3), 190°C (zone 4), 200°C (zone 5), and 210°C (zone 6). The final concentrations of clay and compatibilizer agent (when using Halloysite clay) in the matrix were both five wt%.

Production of the Blends in Twin-Screw Extruder

A Thermo Scientific twin-screw extruder, model Process 11, was equipped with two feeders to prepare the blends. The temperatures of the barrel zones were set at 180°C, except for the third zone in the second feeder, which was set at 120°C to facilitate the introduction of the rubber phase (Figure 1). The screw speed was set to 250 rpm.

The materials were taken directly from the extruder die and injected using a 12cc Explore micro injection molding machine. The temperature of the injection unit was set to 180°C while the mold temperature was maintained at 45°C. The material inside the mold was maintained at 15 bars for 10 s. The mold dimensions were in accordance with ASTM D 412 type A.

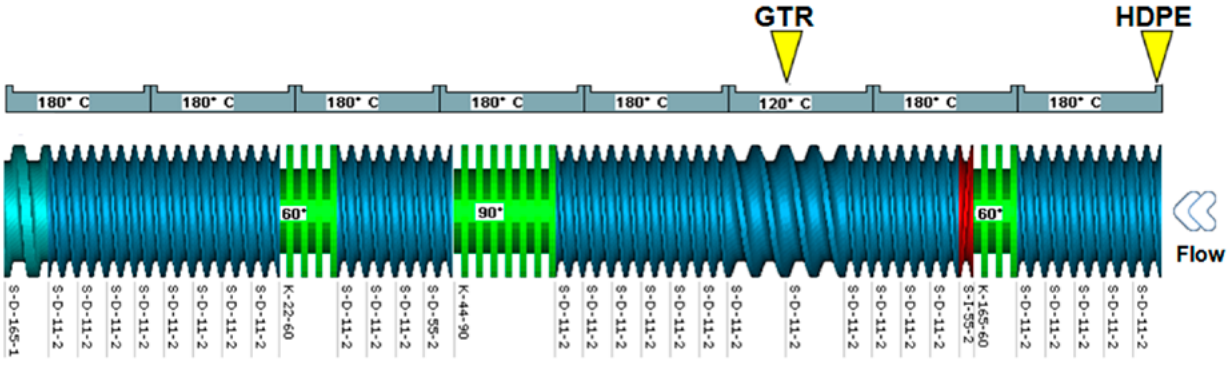

Figure 1. Screw profile employed in the processing of the polymeric blends.

DOI: https://doi.org/10.51573/Andes.PPS39.SS.CEP.5

The nomenclature of the samples is X GTR Y+ad/Z HDPE+W. In this notation, 'Y' represents the time of exposure of the GTR to microwaves, '+ad' the presence of vulcanization additives in the sample, and 'X' and 'Z' the amount of GTR and HDPE in the sample (in mass), respectively. 'W' represents the presence of clay, in which '20A' corresponds to the presence of the Cloisite 20A and 'Hal' corresponds to Halloysite.

Morphology and Tensile Properties

The specimens for tensile tests were cut and cryogenically fractured. They were then dried and coated with gold using a sputter coater. The morphology of the blends was analyzed using a Scanning Electron Microscope (SEM) model JMS-6701F–Jeol.

The mechanical properties of the samples were measured using a Universal Testing Machine Instron 5569 equipped with a 50 kN load cell. The test speed was 50 mm/min.

Results and Discussion

The SEM images of the samples are shown in Figure 2.

The revulcanized blends appear to have better dispersion of GTR particles in the matrix because of the addition of clays, especially Halloysite clay. This clay acts as a compatibilizer agent between phases, leading to a noticeable enhancement in particle dispersion in blends containing 80% GTR. Halloysite clay also seems to have enhanced the toughness and roughness of the HDPE phase. Li et al. [7] added an unidentified powdered rubber scrap, consisting of a polar and another apolar rubber, to a blend of ethylene-octate copolymer (POE) and HDPE, which acted as a filler. A significant enhancement in the toughness of the HDPE phase was observed. The authors proposed two potential causes for this increase: the POE particles varied in size from submicron to micron and were finely dispersed throughout the matrix; and the POE capsized the particle of the fillers on the surface, increasing the matrix's deformation ability around the fillers and its toughness. In this study, the first possibility was observed, while the second possibility may have occurred in the case of blends containing Halloysite clay.

In general, it was shown that the polymeric blends did not have satisfactory mechanical properties (Figure 3), even when the particles were more evenly dispersed in the matrix. This was particularly evident in the low elongation at break values. Upon analyzing the SEM images of blends at low amplifications, it was observed that, overall, GTR particles were well dispersed, but poorly distributed in the thermoplastic matrix. The analysis was conducted using cryogenic breakage of dumbbell-shaped tension tests, which were injection molded. Therefore, the morphology was likely influenced by the injection process.

DOI: https://doi.org/10.51573/Andes.PPS39.SS.CEP.5

The mechanical properties of the blends containing Cloisite 20A significantly decreased (as shown in Figure 3). This decrease can be attributed to voids between the GTR particles and the matrix, indicating a lack of adhesion between the phases (Figure 4). Babu et al. [8] also observed this behavior in vulcanized thermoplastic blends EOC/polypropylene (PP), where particle detachment led to poor physical properties. In regions with a lower concentration of rubber particles, white lines are visible on the fractured surfaces due to stretch-induced crystallization, suggesting that the clay has acted as a nucleation agent in the HDPE phase [9].

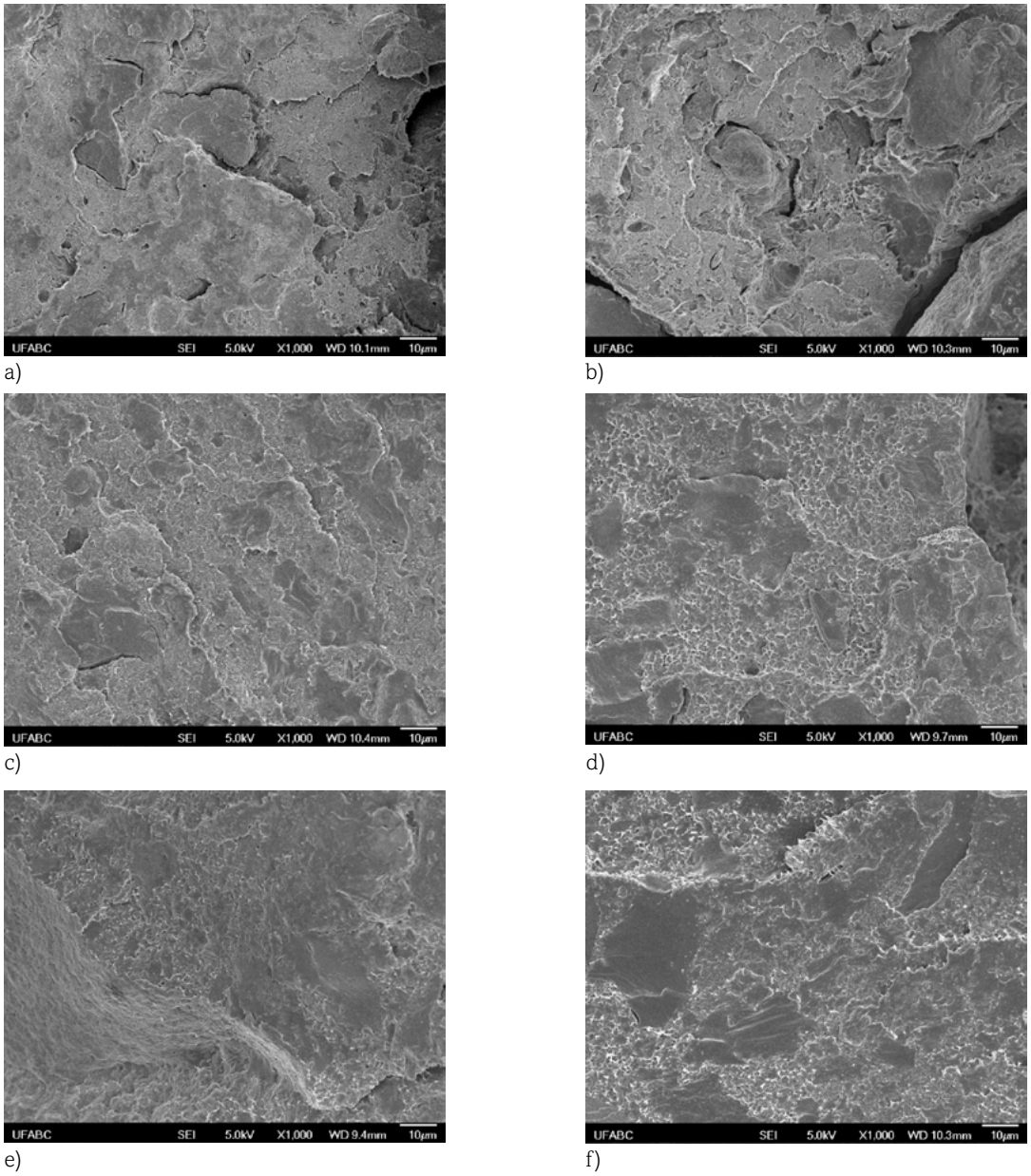

Figure 2. SEM images of the blends: (a) 60GTR5.5+ad/40HDPE, (b) 60GTR5.5+ad/40HDPE+20A, (c) 60GTR5.5+ad/40HDPE+Hal, (d) 80GTR5.5+ad/20HDPE, (e) 80GTR5.5+ad/20HDPE+20A, and (f) 80GTR5.5+ad/20HDPE+Hal.

DOI: https://doi.org/10.51573/Andes.PPS39.SS.CEP.5

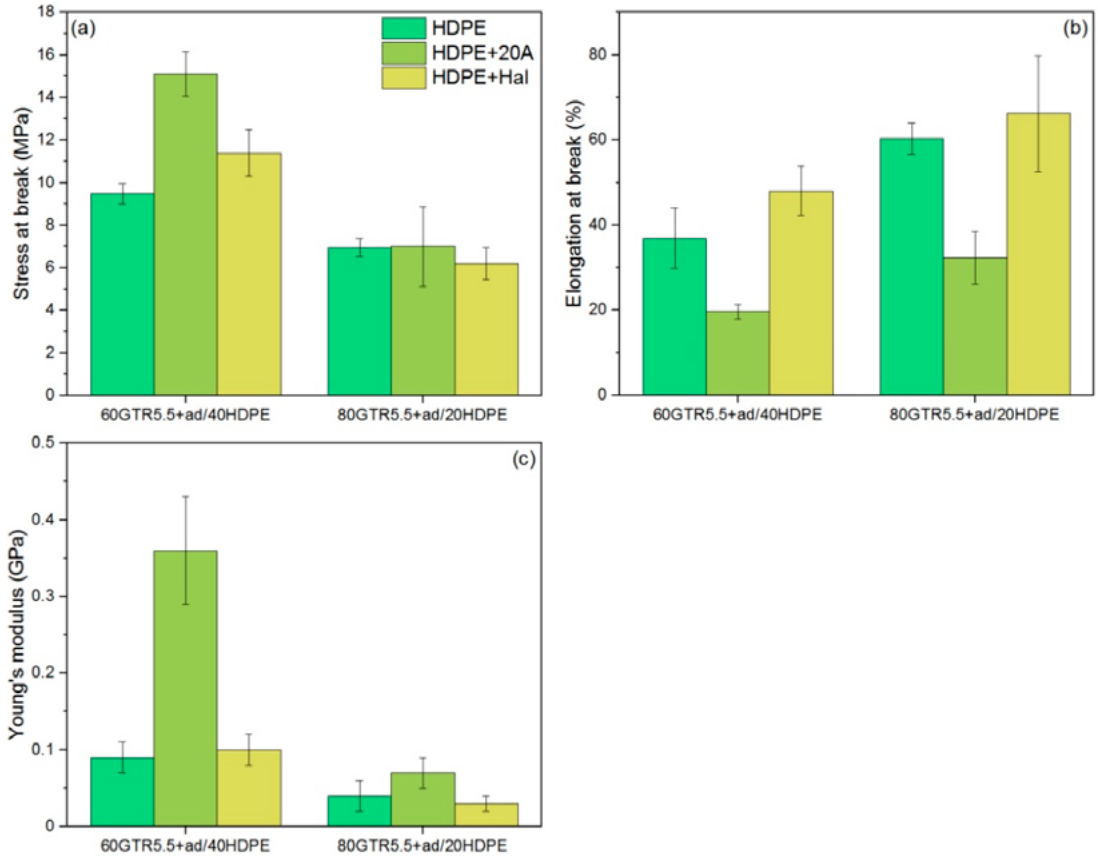

Figure 3. Mechanical properties of the polymeric blends: (a) Stress at break, (b) Elongation at break, and (c) Young's modulus.

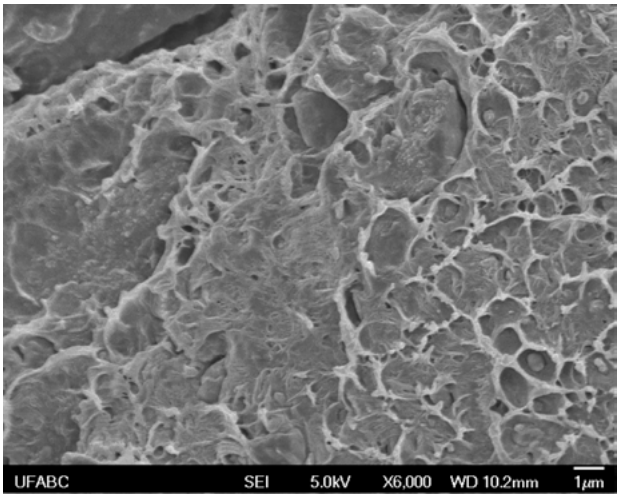

Figure 4. SEM image of the blend 60GTR5.5+ad/40HDPE+20A. The circle shows the presence of a GTR particle, and the valley between it and the matrix indicates the lack of adhesion between the phases.

DOI: https://doi.org/10.51573/Andes.PPS39.SS.CEP.5

Additionally, the poor mechanical properties obtained are also a result of the degradative processes that occurred during all stages of recycling GTR [10-12]. Some authors have analyzed the properties of revulcanized GTR (GTR devulcanized by microwaves and then revulcanized in a hydraulic press at 180°C) [10,11]. The results showed that the revulcanized material was oxidized and contained more carbon black. GTR, which is composed of natural rubber (NR) and styrene butadiene rubber (SBR), was degraded during all the stages of the recycling, being that NR was preferably degraded during the devulcanization by microwaves stage [12]. SBR was primarily degraded during the revulcanization stage [10,11].

Conclusion

The research results indicated that the inclusion of clays impacted the morphology and mechanical properties of the dynamically revulcanized blends composed of HDPE/GTR devulcanized via microwaves. Halloysite clay appeared to enhance the compatibility between the phases of the blends, while Cloisite 20A seemed to enhance the crystallinity of the matrix and/or reinforce the revulcanized blends.

Acknowledgments

The author thanks Prometeon Pneus, Braskem, Bentonit União Nordeste, Chemtura, and Prof. Dr. Rosario Bretas for the donation of the material. CAPES, FAPESP (process number 2010/15799-6) and CNPq (process number 201891/2011-5) for the financial support.

References

1. C. Rosales, N. A. Hocine, C. Bernal, and V. Pettarin, "Toughness improvement of LLDPE/PP blend by incorporation of GTR waste," *Polymer Bulletin*, vol. 81, no. 8, pp. 6743-6760, Jun. 2024.
2. V. Y. Levin, S. H. Kim, A. I. Isayev, J. Massey, and E. VonMeerwall, "Ultrasound devulcanization of sulfur vulcanized SBR: Crosslink density and molecular mobility," *Rubber Chemistry and Technology*, vol. 69, no. 1, pp. 104-114, 1996.
3. F. D. B. de Sousa, "Dynamic-mechanical properties of dynamically revulcanized blends composed of ground tire rubber/high-density polyethylene reinforced with different clays," *AIP Conference Proceedings*, vol. 2884, no. 1, p. 190002, Oct. 2023.
4. F. D. B. de Sousa, "Influence of the addition of clays in the rheological properties of dynamically revulcanized blends composed of high-density polyethylene/ground tire rubber devulcanized by microwaves," *AIP Conference Proceedings*, vol. 2607, no. 1, May 2023.

5. F. D. B. de Sousa, G.-H. Hu, S. Hoppe, and C. H. Scuracchio, "Influence of devulcanization and revulcanization of ground tire rubber in dynamic mechanical properties of blends ground tire rubber/high density polyethylene," *AIP Conference Proceedings*, vol. 2139, no. 090002, pp. 090002-1-090002-4, Aug. 2019.

6. F. D. B. de Sousa and C. H. Scuracchio, "Influence of dynamic revulcanization of ground tire rubber in blends composed of high-density polyethylene/ground tire rubber devulcanized by microwaves ," *AIP Conference Proceedings*, vol. 2289, pp. 020051-1-020051-5, 2020.

7. Y. Li, Y. Zhang, and Y. X. Zhang, "Morphology and mechanical properties of HDPE/SRP/elastomer composites: effect of elastomer polarity," *Polymer Testing*, vol. 23, no. 1, pp. 83-90, 2004.

8. R. R. Babu, N. K. Singha, and K. Naskar, "Effects of mixing sequence on peroxide cured polypropylene (PP)/ethylene octene copolymer (EOC) thermoplastic vulcanizates (TPVs). Part. I. Morphological, mechanical and thermal properties," *Journal of Polymer Research*, vol. 17, no. 5, pp. 657-671, 2010.

9. Y. Tsai, J. H. Wu, Y. T. Wu, C. H. Li, and M. T. Leu, "Reinforcement of dynamically vulcanized EPDM/PP elastomers using organoclay fillers," *Science and Technology of Advanced Materials*, vol. 9, no. 4, 2008.

10. F. D. B. de Sousa, A. Zanchet, and C. H. Scuracchio, "From devulcanization to revulcanization: Challenges in getting recycled tire rubber for technical applications," *ACS Sustainable Chemistry & Engineering Journal*, vol. 7, no. 9, pp. 8755-8765, May 2019.

11. F. D. B. de Sousa, A. Zanchet, H. L. Ornaghi Júnior, and F. G. Ornaghi, "Revulcanization kinetics of waste tire rubber devulcanized by microwaves: Challenges in getting recycled tire rubber for technical application," *ACS Sustainable Chemistry & Engineering Journal*, vol. 7, no. 18, p. 15413-15426, Aug. 2019.

12. F. D. B. de Sousa, C. H. Scuracchio, G. H. Hu, and S. Hoppe, "Devulcanization of waste tire rubber by microwaves," *Polymer Degradation and Stability*, vol. 138, pp. 169-181, 2017.

DOI: https://doi.org/10.51573/Andes.PPS39.SS.CEP.5

SPECIAL SYMPOSIA | CIRCULAR ECONOMY OF POLYMERS

From PP Waste to High-Quality Products: Decontamination of the Material Throughout the Entire Recycling Process Chain Using State-of-the-Art Technologies

Sandra Czaker, Thomas Wieland, Moritz Mager, Mohammad Hassan Akhras and Jörg Fischer

DOI: https://doi.org/10.51573/Andes.PPS39.SS.CEP.6

December 2024

From PP Waste to High-Quality Products: Decontamination of the Material Throughout the Entire Recycling Process Chain Using State-of-the-Art Technologies

Sandra Czaker, Thomas Wieland, Moritz Mager, Mohammad Hassan Akhras and Jörg Fischer[1]

Abstract: Turning waste into high-quality products should be the aim of recycling, but it requires considerable effort to separate specific materials from others, clean them properly, and reconvert them into products. Such a process chain of mechanical recycling of post-consumer polypropylene (PP) from a mixed waste collection was conducted with an advanced combination of state-of-the-art technologies considering the material's decontamination throughout the different process steps. The levels of solid and volatile contamination were analyzed with an optical control system and a gas chromatographic method, respectively, and were found to decrease in varying amounts throughout the process. The results of this study represent the currently achievable qualities of recycled PP in mechanical recycling and, based on these findings, the recycling process can be further improved.

Keywords: Volatile Organic Compounds (VOC), Plastics Recycling, Decontamination, Polypropylene

1 All the authors, including Sandra Czaker (sandra.czaker@jku.at) are affiliated with the Institute of Polymeric Materials and Testing & LIT Factory and the Competence Center CHASE GmbH at the Johannes Kepler University Linz in Austria.

DOI: https://doi.org/10.51573/Andes.PPS39.SS.CEP.6

Introduction

One of the 17 United Nations Sustainable Development Goals aims to achieve circularity, including recycling plastics [1]. Obtaining a high-quality product from waste material via recycling requires several elaborate steps. In a common mechanical recycling process for plastics, the material is collected, sorted, shredded, and cleaned in the pre-treatment stage, and subsequently heated, filtered, degassed, and granulated in the extrusion stage [2]. Finally, products are produced that can be distributed and used until they are disposed of and collected again. For polyethylene terephthalate (PET), recycling processes to obtain high-quality recyclates are already being implemented [3]. In contrast, polyolefins, such as polypropylene (PP), are usually down-cycled into products with lower specifications, despite holding the highest global market share [4,5]. This results from a detrimental change in the properties, which are affected by mixing different property profiles, contaminations, and material degradation. Solid contaminations, e.g. labels, sand, or other polymer types, have a significant impact on mechanical properties and aesthetics [6,7]. Additionally, volatile contaminations lead to odor or can even be a health hazard, which must be eliminated according to regulations [8,9]. Thus, this study aimed to evaluate how solid and volatile contaminations in PP waste are changing throughout the different stages of a mechanical recycling process. The contaminations were analyzed via optical and gas chromatographic methods to obtain data on the achievable qualities of recycled PP (rPP) with state-of-the-art technologies and to identify potential avenues for further process improvements.

Material and Methods

Post-consumer PP waste from mixed collection of Dutch household waste was separated, sorted in several loops, pre-treated, extruded, and used to produce two types of cups. The detailed recycling process is depicted in Figure 1. While the injection molded cups contained 100% recyclate, the thermoformed cups had a multilayer structure with a middle layer of 60% recyclate content and two top layers of virgin material. Excluding the application stage, all the used technologies were state-of-the-art.

DOI: https://doi.org/10.51573/Andes.PPS39.SS.CEP.6

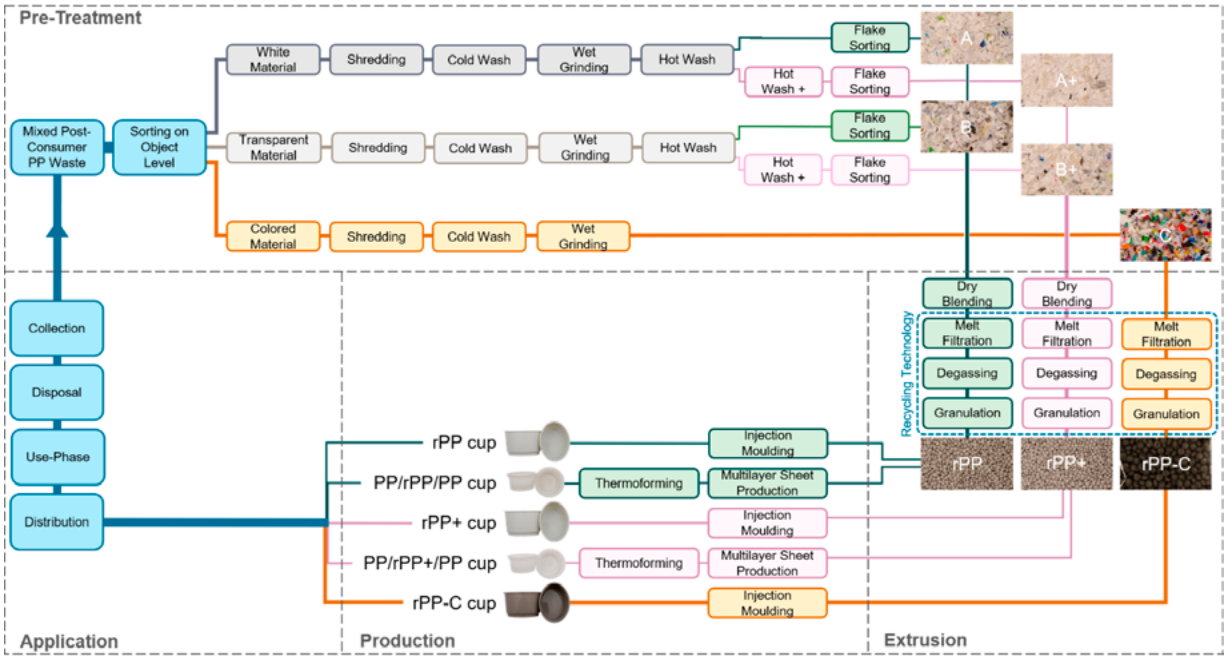

Figure 1. Scheme of the mechanical recycling process. The photographs show the analyzed samples.

For the analysis of solid contaminations in the flakes and granules, a Modular Film Analyzer equipped with a Film Surface Analyzer FSA100 and a Measuring Extruder ME30 (OCS) (OCS Optical Control Systems GmbH, Germany) were used. As the flakes from the pre-treatment stage still contained some PET flakes, they were separated via density in a water bath and dried in a drying and heating chamber at 50°C for 3 h (BINDER GmbH, Germany) before the film extrusion at a processing temperature of 200°C. The solid contaminations were categorized according to size x into those with $x \leq 100$ µm, $100 < x \leq 300$, $300 < x \leq 500$ µm, and $x > 500$ µm. To enable counting of the solid contaminations, the film thickness was reduced to a minimum of about 100 µm, the grey value was set to 219 and the threshold to 15%. An area of 5 m² was analyzed for each sample.

The volatile organic compounds (VOC) were analyzed via a gas chromatograph including a flame ionization detector Clarus 690, which was equipped with a mass spectrometer Clarus SQ 8 T and an analytical thermal desorption unit TurboMatrix 650 (ATD-GC/FID-MS) (PerkinElmer Inc., USA). For separation, an HP Ultra 2 Column with 50 m x 0.32 mm size and 0.52 µm stationary phase (Agilent, USA) was installed. The system was calibrated with an external one-point calibration of a 0.5 µg/µL Toluene (Merck, Germany) solution in Methanol (Merck, Germany). Of this solution, 4 µL were injected into a sample tube filled with the adsorbent TenaxTA (PerkinElmer Inc., USA) under a nitrogen flow of 100 mL/min for 6 min. Pieces of 5 x 40 mm were cut from 250 µm thick film sheets previously produced on the OCS or from the side walls of the cups. A blank was conducted before each sample triplicate. The parameters for the ATD-GC/FID-MS are listed in Table 1.

DOI: https://doi.org/10.51573/Andes.PPS39.SS.CEP.6

Table 1. Parameters of ATD-GC/FID-MS.

ATD Parameters		GC/FID-MS Parameters	
Mode	2 Stage Desorption	Temperature Program:	60°C, 13min, 6°C/min to 215°C, 25°C/min to 280°C, 12 min
Column Flow [kPa]	130		
Desorption Flow [mL/min]	40		
Inlet Split Flow [mL/min]	44	FID Temperature [°C]	300
Outlet Split Flow [mL/min]	19	Hydrogen Flow [mL/min]	30
Transfer Line Temperature [°C]	290	Synthetic Air Flow [mL/min]	450
Trap Temperature [°C]	-30 to 280	Transfer Line Temperature to MSD [°C]	280
Heating Rate [°C/s]	99		
Trap Hold [min]	20	Scan Mode Range [amu]	29-450
Valve Temperature [°C]	280	MS Solvent Delay [min]	4.5

Results and Discussion

After the pre-treatment, extrusion, and production stages, we took samples and evaluated them for optical changes, solid contaminations, and volatile contaminations.

Optical Evaluation Results

The separation of white (A) and colored material (C) was good. In contrast, the material intended to be transparent (B) had a lot of white and even some colored mis-sorts. Adding a deinking step (hot wash +) for materials A (A+) and B (B+) visibly removed the color of the residual labels. In the extrusion stage, the white and transparent materials were again blended due to the required amount of material for the recycling technology. This resulted in light grey granules and just slightly brighter granules for the hot washed rPP and for the deinked material (rPP+), respectively. Nevertheless, the color of both was acceptable for a potential new coloration compared to the dark granules resulting from material C (rPP-C).

DOI: https://doi.org/10.51573/Andes.PPS39.SS.CEP.6

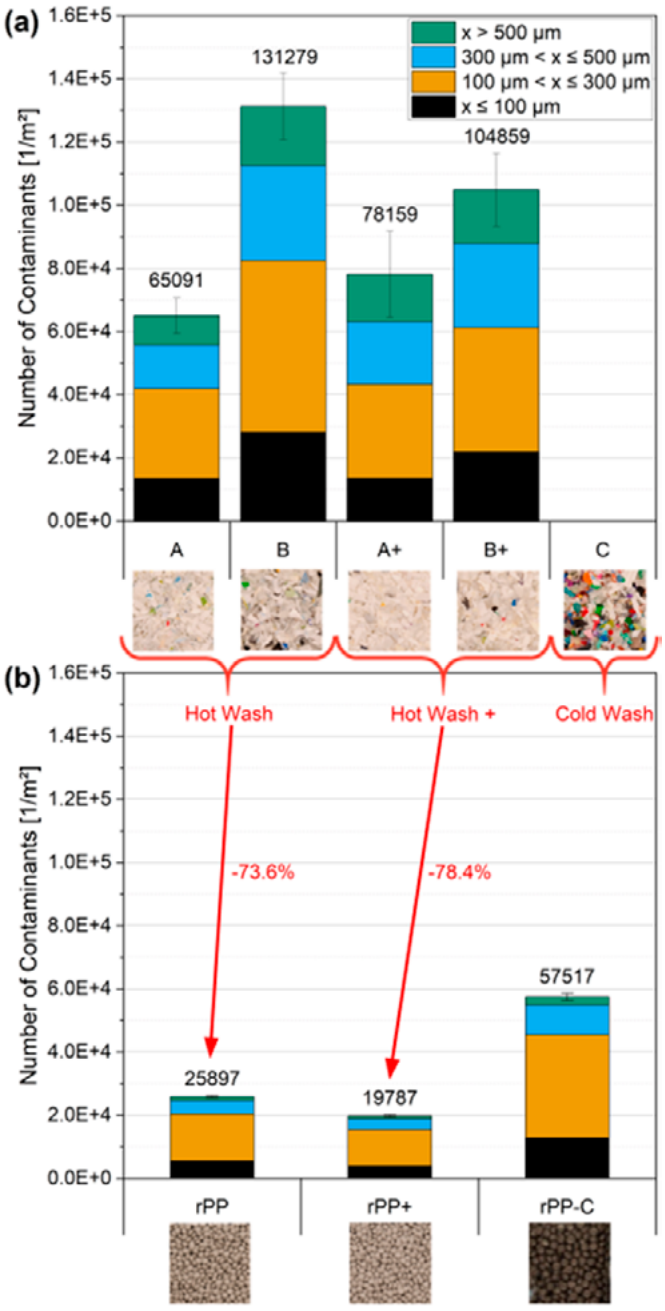

Figure 2. Numbers of solid contaminations that are categorized by size for (a) the flakes after the pre-treatment and (b) the granules after the extrusion.

DOI: https://doi.org/10.51573/Andes.PPS39.SS.CEP.6

Solid Contaminations

Figure 2 displays various size categories of detected solid contaminations, with the category of $100 < x \leq 300$ µm exhibiting the highest values across the samples from the pre-treatment stage (as shown in Figure 2[a]) and from the extrusion stage (as shown in Figure 2[b]). Due to the high contamination level of the colored material with a high number of contaminants larger than 500 µm, we were not able to produce films thin enough for light transmission to be analyzed by the OCS. Solid contaminations were reduced by 74 to 78% for material PP and rPP via the laser filter with 90/110 µm in the extrusion stage. We assume similar results for material rPP-C since the same extrusion parameters were used as for the other two materials. Thus, rPP-C has the highest amount of solid contaminations, which is a result of the less extensive washing at the pre-treatment stage. The granules rPP+ showed the lowest amount of solid contaminations, which reflects the additional effect of removing residual inks and labels by multiple washing steps.

Volatile Contaminations

The VOC emitted from the solid samples at elevated temperatures should represent the volatile contaminations trapped in the material. The results are depicted in Figure 3. In the pre-treatment stage, the VOC values were similarly high throughout almost every material except for material C, which was unexpectedly lower (as shown in Figure 3[a]). This may indicate that, compared to the cold washing procedure, surface contaminations are reduced in the hot washing procedures, while volatile degradation products increase with temperature and washing agent. In contrast, the VOC values of material rPP-C are higher than for the other materials in the extrusion stage (as shown in Figure 3[b]). Due to the residual surface contaminations of the cold washed material C, the generation of degradation products during the extrusion may be triggered, and in addition to the residual contaminations result in a high VOC value for rPP-C. Nevertheless, the VOC values of all three rPP samples were still higher than a commercial virgin PP grade for injection molding. In the end, when considering the product level, there was a decrease in VOC throughout the entire mechanical recycling process, but with similar results for the different cups after the production stage (as shown in Figure 3[c]).

DOI: https://doi.org/10.51573/Andes.PPS39.SS.CEP.6

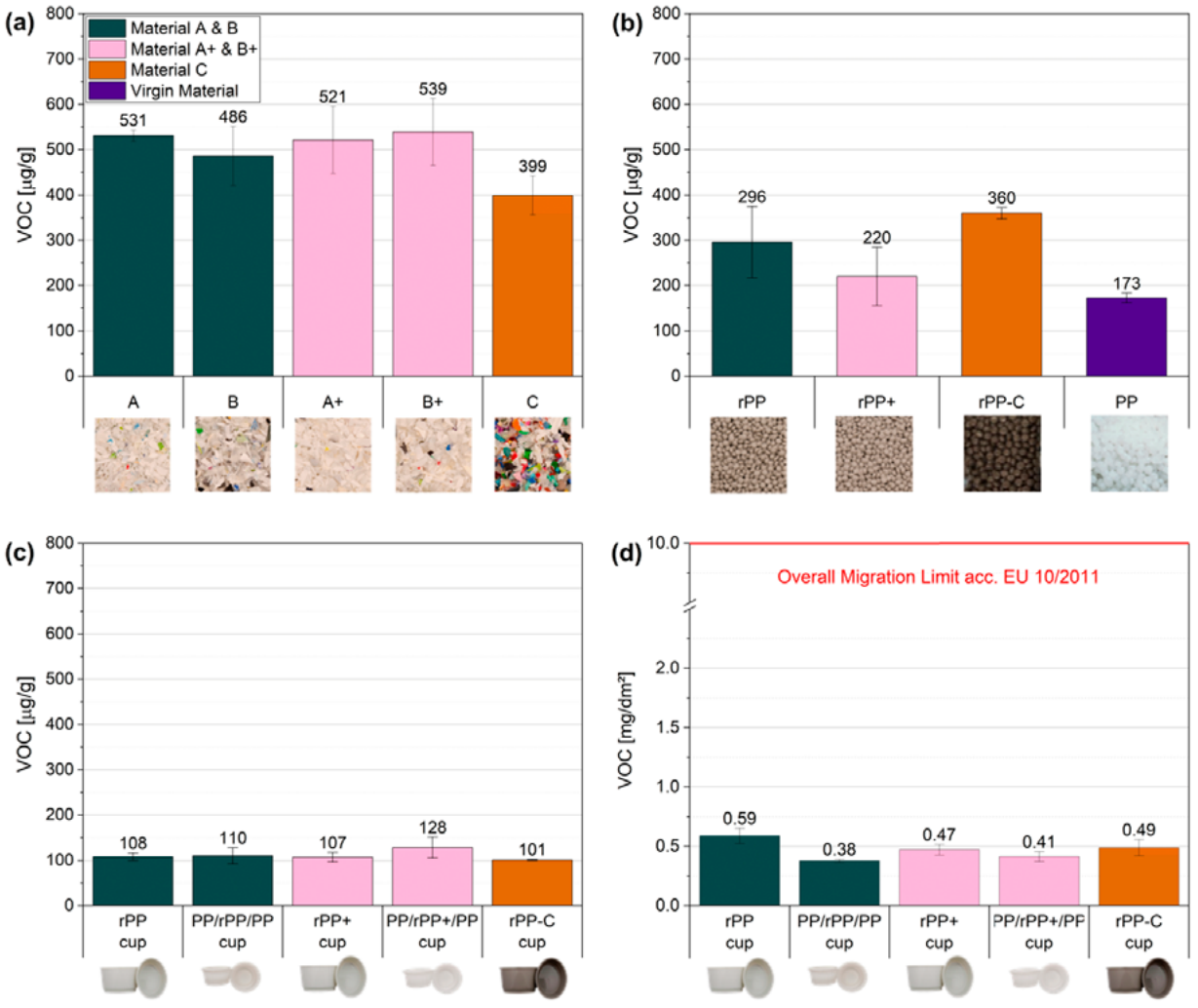

Figure 3. VOC values of (a) the flakes after the pre-treatment, (b) granules after the extrusion, (c) cups after production and (d) overall migration limits set out by the European Commission.

Since cups are usually used as food contact material, we also calculated the VOC values correlated to the contact surface and compared the results with the recent overall migration limits (OML) set out by the European Commission (as shown in Figure 3[d]) [8]. This OML specifies the allowed level of substances that can migrate from the packaging into the food without posing a health risk for the consumer. The resulting values, which were significantly lower than this OML, showed already high purity and high quality of the PP recyclate. Nevertheless, further investigation should be conducted to provide a full picture of the composition of the volatile contaminations.

DOI: https://doi.org/10.51573/Andes.PPS39.SS.CEP.6

Conclusion

This study provides an overview of the changes in solid and volatile contaminations throughout the entire mechanical recycling process. The pre-treatment aiming for white material leads to high-quality PP regarding contamination and can be easily colored. In contrast, combining state-of-the-art sorting technologies did not lead to the intended transparent post-consumer recycled PP. Furthermore, choosing the right filter size in the extrusion stage can reduce solid contaminations by around 76%. The OCS can be a helpful method to determine the required filter size. Regarding volatile contaminations, in the end the VOC values of the products did not seem to be affected by the different washing steps, but mainly by the extrusion and processing steps. When removing labels, deinking is efficient but has no significant effect on the VOC values of the end product and only leads to a slight reduction in solid contaminations. Using all the information gathered, there are possibilities to make the recycling processes more efficient by e.g., evaluating the required washing steps for the intended product. In order to do so, we require further information regarding the composition of the VOC. It would be also advantageous to analyze the cold washed references of the white and transparent materials to confirm the decontamination efficiency of the cold washing step. Ultimately, mechanical characterization of the samples should be conducted to obtain a full picture of all the effects on the post-consumer recycled PP throughout the whole mechanical recycling process with state-of-the-art technologies.

Acknowledgments

The authors acknowledge the support from the FTI circular economy initiative "circPLAST-mr," funded by the BMK (Federal Ministry for Climate, Environment, Energy, and Innovation) and the FFG (Austrian Research Promotion Agency) (funding nr 889843); the COMET Centre CHASE, funded within the COMET (Competence Centers for Excellent Technologies) program by the BMK, the BMDW, the Federal Provinces of Upper Austria and Vienna, and managed by FFG; and thank the NTCP for their support with this study.

References

1. United Nations, "Sustainable Development Goals." [Online]. Available: https://unric.org/en/united-nations-sustainable-development-goals/. Accessed: Jun. 5, 2024.
2. N. Niessner, Ed., *Recycling of Plastics*. Munich, Germany: Hanser Publishers, 2022.
3. P. Benyathiar, P. Kumar, G. Carpenter, J. Brace, and D. K. Mishra, "Polyethylene Terephthalate (PET) Bottle-to-Bottle Recycling for the Beverage Industry: A Review," *Polymers*, vol. 14, no. 12, 2022, https://doi.org/10.3390/polym14122366

4. Plastics Europe AISBL, "Plastics the fast facts 2023." [Online]. Available: https://plasticseurope.org/knowledge-hub/plastics-the-fast-facts-2023/. Accessed: Jun. 14, 2024.

5. Plastics Europe AISBL, *The Circular Economy for Plastics – A European Analysis 2024*. [Online]. Available: https://plasticseurope.org/knowledge-hub/the-circular-economy-for-plastics-a-european-analysis-2024/. Accessed: Jun. 14, 2024.

6. M. Gall, P. J. Freudenthaler, J. Fischer, and R. W. Lang, "Characterization of Composition and Structure-Property Relationships of Commercial Post-Consumer Polyethylene and Polypropylene Recyclates," *Polymers*, vol. 13, no. 10, 2021, https://doi.org/10.3390/polym13101574

7. I. Traxler, K. Fellner, and J. Fischer, "Influence of macroscopic contaminations on mechanical properties of model and post-consumer polypropylene recyclates," in *SPE ANTEC 2023–Proceedings*, Society of Plastics Engineers, 2023.

8. Commission Regulation (EU) No 10/2011 of 14 January 2011 on plastic materials and articles intended to come into contact with food: *EU 10/2011*, 2020.

9. A. Cabanes, F. J. Valdés, and A. Fullana, "A review on VOCs from recycled plastics," *Sustainable Materials and Technologies*, vol. 25, e00179, 2020, https://doi.org/10.1016/j.susmat.2020.e00179

SPECIAL SYMPOSIA | CIRCULAR ECONOMY OF POLYMERS

Mechanical Recycling of Bulk Molding Compound: A Technical and Environmental Assessment

A. Salvi, M. Ostrowska and G. Dotelli

DOI: https://doi.org/10.51573/Andes.PPS39.SS.CEP.7

December 2024

Mechanical Recycling of Bulk Molding Compound: A Technical and Environmental Assessment

A. Salvi, M. Ostrowska and G. Dotelli[1]

Abstract: This study evaluates the technical and environmental feasibility of mechanically recycling post-industrial bulk molding compound (BMC) waste from the manufacturing of low-voltage circuit breakers. Testing reveals that incorporating up to 10% recycled BMC as filler substitute maintains the required mechanical and electrical properties. A life cycle assessment shows that while replacing virgin fillers with recycled BMC has limited effects on the carbon footprint of the material, the overall product system benefits significantly by avoiding waste incineration. Moreover, optimized scenarios like maximizing recycled content and reducing transportations substantially reduce the environmental impacts. This study underscores the potential of circular production models to enhance sustainability in the thermoset composite industry.

Keywords: Bulk Molding Compound, Thermoset Composites, Mechanical Recycling, Life Cycle Assessment (LCA), Environmental Impact, Circular Economy

1 The authors A. Salvi (alessandro.salvi@polimi.it) and G. Dotelli are affiliated with the Department of Chemistry, Materials and Chemical Engineering "Giulio Natta" at the Politecnico di Milano in Italy. M. Ostrowska is affiliated with ABB SACE also located in Italy.

DOI: https://doi.org/10.51573/Andes.PPS39.SS.CEP.7

Introduction

Bulk molding compound (BMC) and sheet molding compound (SMC) are widely produced materials in the thermoset glass fiber reinforced plastic (GFRP) industry. Their production reaches a volume of 268,000 tons per year (2022), reaching a market share of 23.5% within the composite thermoset industry [1]. Both materials are based on an unsaturated polyester (UP) matrix reinforced with varying contents of glass fibers and mineral fillers, like aluminum hydroxide (ATH) or calcium carbonate [2]. BMC is broadly exploited for a variety of applications, ranging from the automotive to the electrical industry [3], but its complex composition poses important challenges for waste management [4]. Specifically, thermal reprocessing is impossible due to the cross-linked nature of the polymeric matrix, and the considerable inorganic content (roughly 70%) reduces its GCV to about 10 MJ/kg [5,6], hindering its use in incineration plants.

In recent years, there has been growing interest in developing sustainable waste management practices for thermoset GFRP. Mechanical recycling, which involves reprocessing post-industrial BMC waste into reusable material, is one such practice [7]. This study evaluates the technical feasibility and environmental sustainability of mechanically recycling pre-consumer BMC waste used in the production of low-voltage circuit breakers.

By comparing the traditional linear production model with circular systems that incorporate mechanically recycled BMC, we aim to understand the potential environmental benefits of this practice. This comprehensive approach allows us to assess the benefits and challenges of transitioning from a linear to a circular production model, contributing to a more sustainable future for the industry.

Materials and Methods

Materials

The composition of the BMC used in this study, as provided by ABB through their suppliers, is reported in Table 1. Such formulation is optimized for use in structural components of low-voltage circuit breakers. The specific chemical composition of the resin, initiator, and other additives is not explicitly disclosed in this paper.

Additionally, the pre-consumer BMC waste sent to recycling is assumed to be sourced from the same supplier, therefore having approximately the same composition.

DOI: https://doi.org/10.51573/Andes.PPS39.SS.CEP.7

Table 1. Composition of Bulk Molding Compound.

Material	Weight %
Aluminum hydroxide (ATH)	52%
Chopped glass fibers (GF)	20%
Unsaturated Polyester Resin (UPR)	18%
Styrene monomer	4%
Polyethylene (PE)	3%
Initiator and additives	3%

Mechanical Recycling and Testing

The mechanical recycling process adopted in this study involves the milling of post-industrial waste (i.e., manufacturing scraps). Such waste is generated during the molding of BMC parts and is typically sent to incineration. In our process, this scrap is collected and milled into a fine material. This milled material is then reused in the formulation of new BMC, substituting the alumina trihydrate (ATH) used as a filler and flame retardant in BMC production, resulting in parts containing up to 10% wt. of recycled material. Specifically, three types of samples were produced, with recycled contents of 0% (i.e., virgin), 5%, and 10%.

To assess the quality of the mechanically recycled BMC, some standardized tests were conducted on the samples. Tensile tests were performed using a INSTRON 5584 universal testing machine, to measure the tensile strength of the parts. Tests were directly conducted on the molded components to allow immediate comparison with the maximum load requirements set by ABB for the final application in circuit breakers. Up to 20 measurements per sample were taken to determine a statistical error. Additionally, Comparative Tracking Index (CTI) tests were conducted to evaluate electrical insulation properties following the IEC 1102 standard, and vertical burning tests (UL-94 standard) were executed to assess flame retardancy class.

The results of these tests provided valuable insights into the performance of the recycled BMC and its suitability for application in low-voltage circuit breakers.

Life Cycle Assessment: Goal and Scope

The LCA was conducted following ISO 14040 standards, which provide a robust framework for conducting a comprehensive environmental impact assessment.

The product system considered encompasses three distinct phases: (1) BMC production, (2) BMC parts molding, and (3) end-of-fife (EoL) treatment of production scrap.

DOI: https://doi.org/10.51573/Andes.PPS39.SS.CEP.7

This LCA is cradle-to-gate, with system boundaries including raw material extraction, transportation, BMC production, manufacturing (molding), and end-of-life treatments (of manufacturing waste only). The use phase and product end-of-life are excluded from the system boundary. The declared unit is one kilogram of molded BMC parts.

In order to maintain a physically consistent mass balance among the defined scenarios, the following parameters were introduced:

- **P**: Reference flow of each system, always equal to 1 kg of molded parts, representing the output of phase 2 (molding).
- **W:** Amount of waste generated by the molding process.
- **F**: Amount of BMC fed to the molding process. Therefore, F represents the output to phase 1 (BMC production) and it is equal to P+W.
- **Y**: Ratio of W to F, representing the percentage of waste relative to the total BMC fed to the molding process. Since the values of both P and W are provided by the molder on an annual basis, the value of y is known and constant for all scenarios (y=0.1435).
- **R1**: Fraction of W which is fed to the recycling (milling) process
- **I1**: Fraction of W which is sent to incineration.
- **R2**: Amount of recycled material produced by the milling process, net of any losses.
- **I2**: Amount of waste generated by the milling process, sent to incineration.
- **L**: Ratio of I2 to R1, representing the percentage of material lost during milling.
- **x**: Recycled content in BMC, ranging from 0 to 12.5% (maximum recycled content achievable if all post-industrial waste from molding is recycled without loss).
- **V:** Amount of virgin material used in BMC production, the main input to phase 1 (BMC production), along with R2.

Consequently, three scenarios were defined for the LCA, namely:

- **Linear (L)**: Linear production system, where BMC is produced entirely from virgin resources and any waste generated during the molding phase is incinerated. Moreover, the current transportation distances are respected. Therefore, x=0 and D=1.
- **Circular (C)**: Currently implemented closed loop recycling chain, taking into account the technical constraints (maximum recycling content = 5%, material losses in recycling = 10%) and the actual transportation distances. In this case, the manufacturing waste is partially recycled and partially incinerated. Therefore, the variables for this scenario are x=0.05, L=0.1, and D=1.

DOI: https://doi.org/10.51573/Andes.PPS39.SS.CEP.7

- **Optimized (O)**: Realistically achievable improvement with respect to scenario C. All the BMC waste is looped back into the production chain, achieving a recycled content of 12.5% (x=0.125), losses are minimized (L=0), and transportation distances are reduced by 75% (D=0.25).

A graphical visualization of scenarios L and O is reported in Figure 1. Scenario C is omitted from the figure for the sake of conciseness, as it can be seen as an intermediate situation between the two other cases.

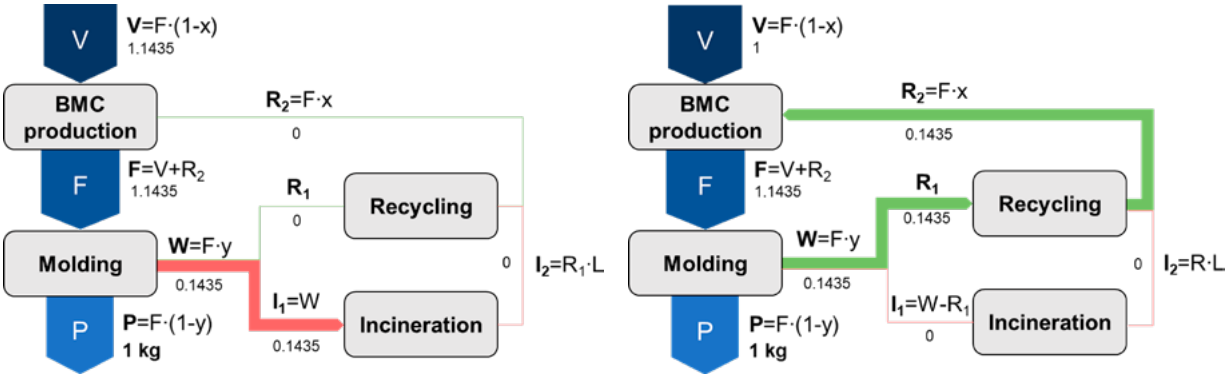

Figure 1. Flow diagram for two of the possible scenarios (L and O). The thickness of the arrows is proportional to the mass flow. Note that these two schemes represent two extremes: a number of intermediate situations are possible.

Life Cycle Assessment: Inventory

Primary data for this LCA study were sourced from two primary contributors. Data pertaining to BMC production (phase 1) and recycling (phase 3) were provided, through ABB, by the BMC supplier, located in northern Germany, while data concerning the molding (phase 2) and scrap incineration were provided by the molder, located in central Italy. Secondary data were either derived from literature or from the ecoinvent 3.9.1 database [8].

For phase 1 and 2, data concerning raw materials, utilities and energy consumption, transport distances and modes, direct emissions, packaging materials, and waste management were provided. Moreover, the specific energy-mix compositions were used in the modeling.

For phase 3, primary data were available only for the use of electrical energy and other utilities in the milling process, along with the efficiency of the process in terms of material losses. The incineration process was modeled using the ecoinvent dataset for the incineration of plastic from electrical waste, adapted to the composition of BMC in terms of carbon and inorganic content.

DOI: https://doi.org/10.51573/Andes.PPS39.SS.CEP.7

Specific quantitative information on the full LCA inventory is not disclosed in this paper but may be available upon request to the authors.

Results and Discussion

In the following sections, the results of the mechanical testing and the LCA study are presented and discussed.

Mechanical Recycling and Testing

As shown in Figure 2, substituting alumina trihydrate (ATH) with recycled BMC has a noticeable detrimental effect on the load at break of parts, even at low recycled contents. Specifically, the sample with 5% recycled content showed a 7% reduction in load at break compared to the virgin sample. The mechanical performance further declined for the sample with 10% recycled BMC, with a total reduction of 13% compared to the virgin sample. Nonetheless, all samples met the minimum requirement set by ABB for low-voltage circuit breakers (2400 N), even when considering the standard deviation.

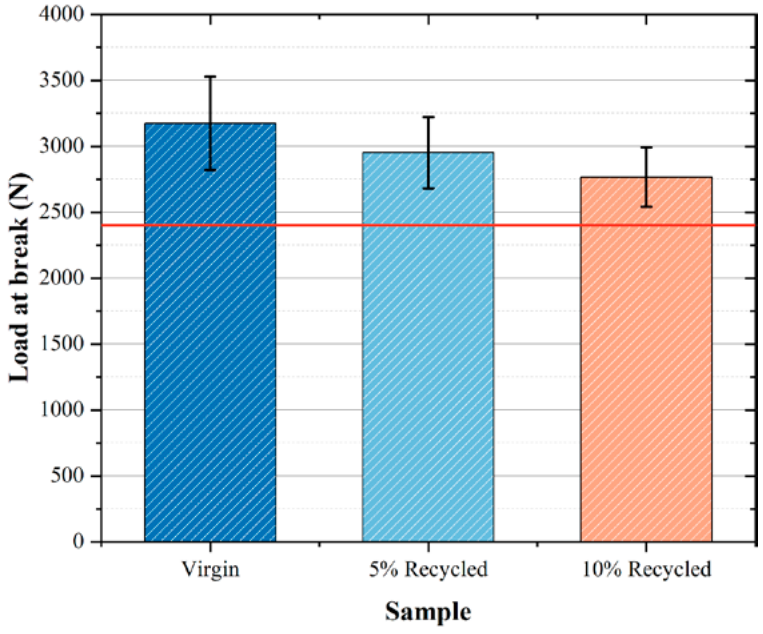

Figure 2. Load at break measurements for molded parts with a variable content of recycled material. The red line represents the minimum requirement set by ABB.

DOI: https://doi.org/10.51573/Andes.PPS39.SS.CEP.7

Table 2. Results of tensile, vertical burning, and CTI tests for the three samples.

Recycled Content	Load at break	UL94 rating	CTI
	[N]	[-]	[V]
0%	3174.3	V-0	600
5%	2951.7	V-0	600
10%	2765.7	V-0	600

Other measured properties confirmed the suitability of all samples for use in circuit breakers. Specifically, as reported in Table 2, the CTI requirement of 600V and the UL94 V-0 classification were achieved, even for the sample with 10% recycled content.

Life Cycle Impact Assessment (LCIA)

All scenarios were analyzed using the Environmental Footprint 3.1 impact assessment method, encompassing all midpoint impact categories, with a primary focus on the climate change indicator. A cut-off approach (100:0) was adopted, choosing the "Allocation, cut-off by classification" system model in the LCA software SimaPro.

Focusing on phase 1 (BMC production), as shown in Figure 3, the main contributors to the climate change indicator are the polyester resin and glass fibers. In contrast, ATH accounts for only 18% of the total impact, despite constituting more than 50% by weight of the final material. This suggests that replacing ATH with another filler, such as milled BMC, might have a limited effect on the climate change impact category. This is further confirmed by Figure 4, which shows that the impacts of the two fillers (milled BMC and ATH) are quite similar.

DOI: https://doi.org/10.51573/Andes.PPS39.SS.CEP.7

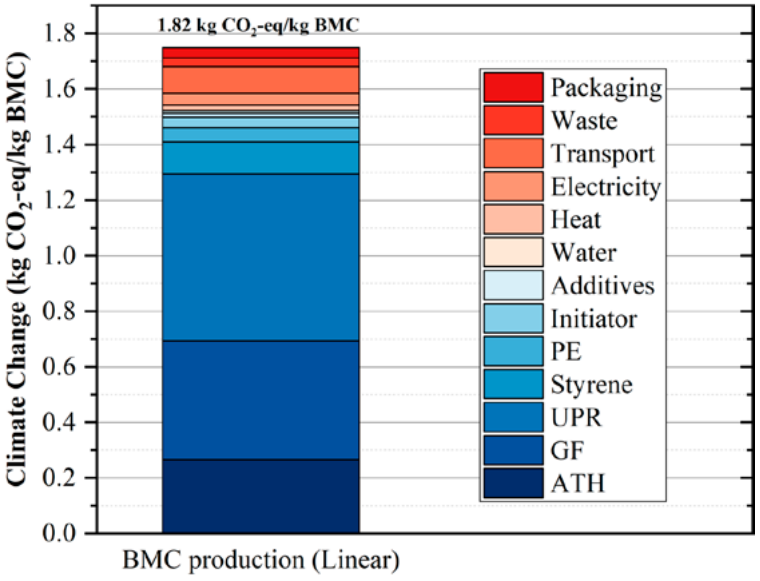

Figure 3. LCIA result and process contributions for BMC production (phase 1) in the Linear scenario; Climate Change.

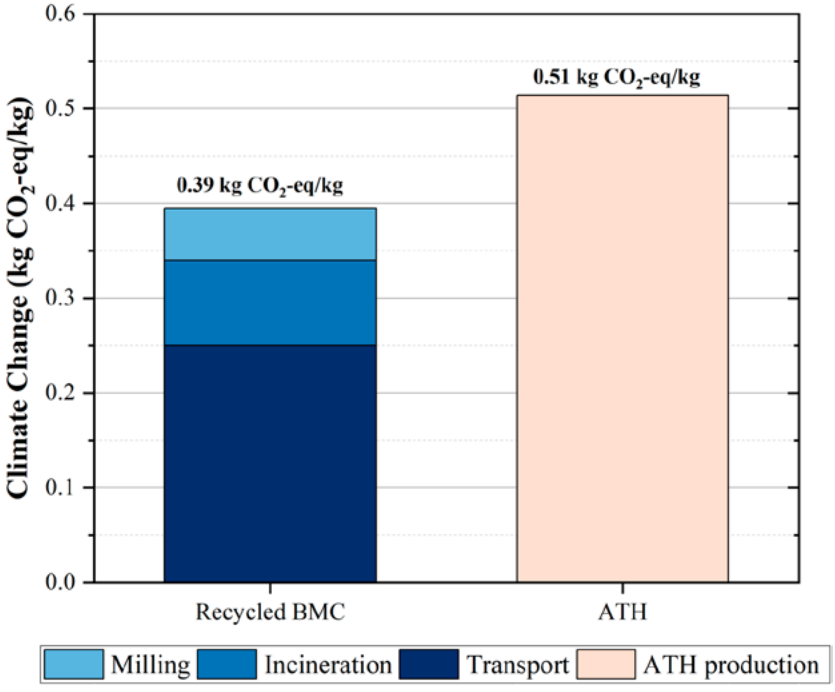

Figure 4. Impact comparison between the two possible fillers: milled BMC and virgin ATH (Aluminum Trihydrate), Climate Change.

DOI: https://doi.org/10.51573/Andes.PPS39.SS.CEP.7

When the entire product system is considered by including the molding phase and the end-of-life treatment of BMC scraps, the impact for the linear scenario increases to 2.96 kg of CO_2-eq/kg, with the main contributors being the production of virgin BMC, the electricity used for molding, and the transportation of BMC from Germany to Italy (Figure 5).

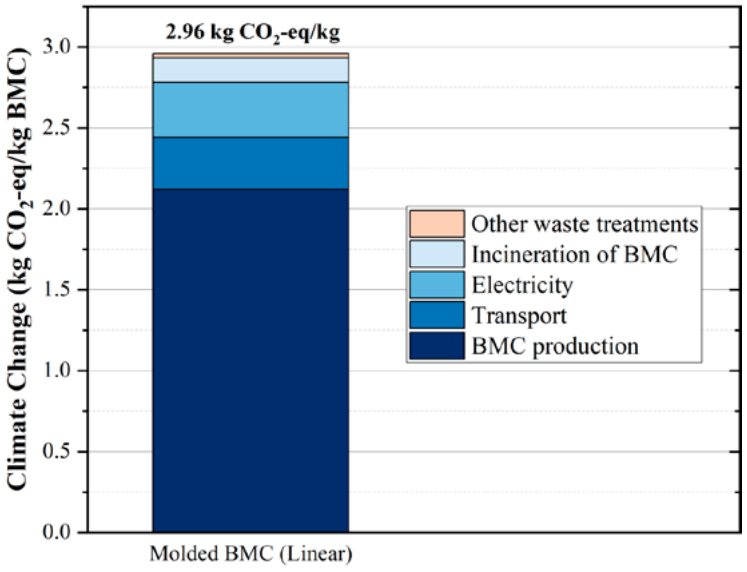

Figure 5. LCIA result and process contributions for 1 kg of BMC molded parts in the Linear scenario; Climate Change.

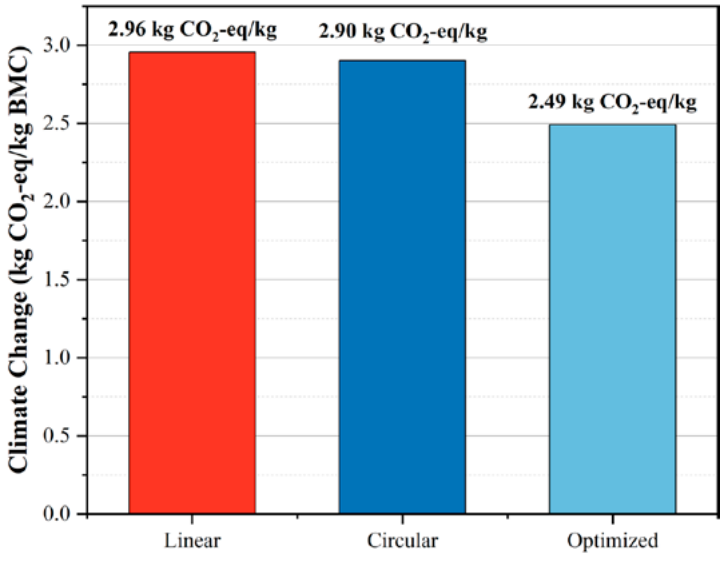

Figure 6. Impact comparison between the three scenarios: Linear, Circular, and Optimized for 1 kg of BMC molded parts; Climate Change.

DOI: https://doi.org/10.51573/Andes.PPS39.SS.CEP.7

Comparing the linear system with the circular and the optimized scenario (Figure 6), the impact reduction in the circular scenario is almost negligible (-1.8%). On the other hand, in the case of an optimized system, where the recycled content is maximized and transportation distances are minimized, a much better result is obtained, with an impact reduction of 15.8%. The main reasons for such an improvement are the avoided incineration of BMC waste and the reduction of the transportation distances.

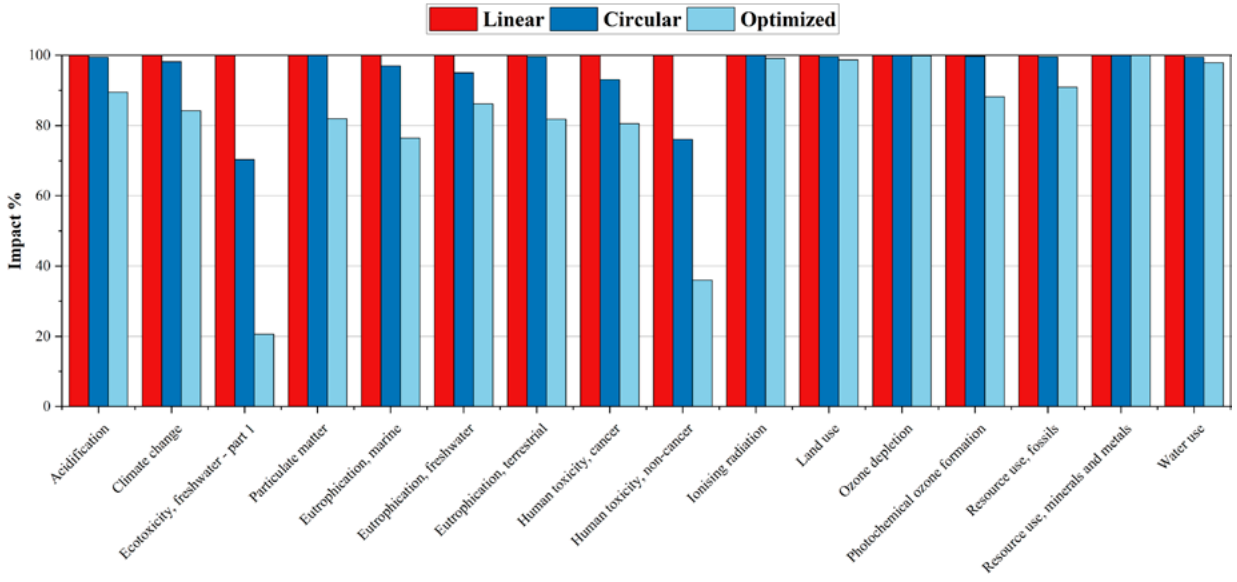

Figure 7. LCIA results comparison between the three scenarios: Linear, Circular, and Optimized for 1 kg of BMC molded parts. Method: Environmental Footprint 3.1.

Considering the full LCIA results (Figure 7), all the impact categories are improved or, at worst, unchanged by introducing the circular and optimized scenario. The avoided incineration of waste plays a major role in reducing the impacts, particularly for the two impact categories that are most affected by such process: ecotoxicity and human toxicity.

Finally, considering the optional LCA phases of normalization and weighting, the single score indicator provides a valuable indication of the overall environmental performance of the scenarios. Specifically, the linear scenario obtains a single score of 370 μPt/kg, while the circular and optimized scenarios achieve reductions of 4.3% (354 μPt/kg) and 17.5% (305 μPt/kg), respectively.

DOI: https://doi.org/10.51573/Andes.PPS39.SS.CEP.7

Conclusion

This study evaluates the technical and environmental sustainability of mechanically recycling BMC used in low-voltage circuit breakers. The incorporation of recycled post-industrial waste as a filler replacement up to 10% by weight in BMC, maintains acceptable mechanical, electrical, and thermal properties, meeting the industry standards. The life cycle impact assessment reveals that replacing ATH with recycled BMC has a limited effect on the climate change impacts of the material production stage. However, considering the entire product system, a beneficial effect is obtained thanks to the avoided incineration of the waste. Moreover, an optimized system that maximizes recycled content and minimizes transportation distances can achieve a significant reduction in environmental impacts, particularly in the climate change, ecotoxicity, and human toxicity categories. The results underscore the potential benefits of transitioning from a linear to a circular production model, highlighting the importance of recycling and optimized logistics in reducing the environmental footprint of BMC production.

Acknowledgments

We would like to express our gratitude to ABB for their invaluable support in providing data, facilitating contacts with suppliers, and supplying the necessary testing equipment.

References

1. E. Witten and V. Mathes, "The Market for Glass Fibre Reinforced Plastics (GRP) in 2020." [Online]. Available: www.avk-tv.de
2. P. M. Spasojevic, "Thermal and rheological properties of unsaturated polyester resins-based composites," in *Unsaturated Polyester Resins: Fundamentals, Design, Fabrication, and Applications*, Elsevier, 2019, pp. 367-406. https://doi.org/10.1016/B978-0-12-816129-6.00015-6
3. L. B. Manfredi, E. S. Rodríguez, M. Wladyka-Przybylak, and A. Vázquez, "Thermal degradation and fire resistance of unsaturated polyester, modified acrylic resins and their composites with natural fibres," *Polymer Degradation and Stability*, vol. 91, no. 2, pp. 255-261, Feb. 2006, https://doi.org/10.1016/J.polymdegradstab.2005.05.003
4. X. Xue, S. Y. Liu, Z. Y. Zhang, Q. Z. Wang, and C. Z. Xiao, "A technology review of recycling methods for fiber-reinforced thermosets," *Journal of Reinforced Plastics and Composites*, vol. 41, no. 11-12, pp. 459-480, Jun. 2022, https://doi.org/10.1177/07316844211055208
5. R. DeRosa, E. Telfeyan, and J. S. Mayes, "Current State of Recycling Sheet Molding Compounds and Related Materials," *Journal of Thermoplastic Composite Materials*, vol. 18, no. 3, pp. 219-240, Aug. 2005, https://doi.org/10.1177/0892705705045006

6. S. J. Pickering, "Recycling technologies for thermoset composite materials—current status," *Composites Part A: Applied Science and Manufacturing*, vol. 37, no. 8, pp. 1206-1215, Aug. 2006, https://doi.org/10.1016/j.compositesa.2005.05.030

7. J. Palmer, O. R. Ghita, L. Savage, and K. E. Evans, "Successful closed-loop recycling of thermoset composites," *Composites Part A: Applied Science and Manufacturing*, vol. 40, no. 4, pp. 490-498, Apr. 2009, https://doi.org/10.1016/j.compositesa.2009.02.002

8. G. Wernet, C. Bauer, B. Steubing, J. Reinhard, E. Moreno-Ruiz, and B. Weidema, "The ecoinvent database version 3 (Part I): Overview and methodology," *International Journal of Life Cycle Assessment*, vol. 21, no. 9, 2016, https://doi.org/10.1007/s11367-016-1087-8

SPECIAL SYMPOSIA | CIRCULAR ECONOMY OF POLYMERS

Investigating the Effect of Liquid State Decontamination on the Material Properties of Post-Consumer High Impact Polystyrene Recyclate

D. Mittermayr, W. Roland and J. Fischer

DOI: https://doi.org/10.51573/Andes.PPS39.SS.CEP.8

December 2024

Investigating the Effect of Liquid State Decontamination on the Material Properties of Post-Consumer High Impact Polystyrene Recyclate

D. Mittermayr, W. Roland and J. Fischer[1]

Abstract: The global focus on environmental sustainability has intensified the need for innovative plastic waste management solutions, especially in the food packaging industry. This study explores liquid state decontamination processes of recyclates produced by post-consumer waste recycling of polystyrene yogurt cups and their effects on the material properties of the recycled material. For this purpose, different decontamination processes based on a twin-screw extruder with vacuum degassing and an industrial-scale recycling machine were applied. Tests such as tensile testing, Charpy impact testing, melt flow rate (MFR) measurement, plate-plate rheometry, high-pressure capillary rheometry (HCR), and differential thermal analysis (DTA) were conducted to assess the mechanical and thermo-rheological properties as well as the oxidation induction temperature as an indicator of polymer degradation. The findings provide a comprehensive understanding of the achievable properties of polystyrene from post-consumer waste and reveal insights into the different process-induced degradation processes of the recycled polystyrene.

Keywords: Recyclate, Post-Consumer, Polystyrene, High Impact Polystyrene, Liquid State Decontamination, Food Packaging

1 The authors D. Mittermayr (David.Mittermayr@jku.at) and J. Fischer are affiliated with the Institute of Polymeric Materials and Testing at the Johannes Kepler University Linz in Austria. W. Roland is affiliated with the Next Generation Recyclingmaschinen GmbH, also located in Austria.

DOI: https://doi.org/10.51573/Andes.PPS39.SS.CEP.8

Introduction

The global challenge of plastic waste management has gained increasing attention. In 2021, 390.7 million tons of plastic were produced worldwide, and this trend is on the rise. The environmental impact of plastic pollution, particularly from the food packaging industry, highlights the need for recycling. The European Union is aiming for a 50% recycling rate for plastic packaging by the end of 2025, up from 32% in 2020. In addition, the new targets for the recycling rates consider new points of calculation, which leads to the even bigger challenge of meeting these targets. Sustainable food packaging must have high mechanical integrity and comply with food safety standards, which requires innovative recycling solutions [1,2].

High impact polystyrene (HIPS) is commonly used in the food packaging industry due to its robustness and versatility [3]. However, recycling post-consumer HIPS, such as polystyrene yogurt cups, is challenging due to contamination issues. Recycled plastic contamination can affect both mechanical properties and potential health risks [4]. One promising approach is the decontamination process in the liquid state (melt phase super-cleaning), which offers the possibility of improving the quality and safety of recycled plastics [5].

This study examines the effects of different decontamination processes and their vacuum influences on the mechanical and thermo-rheological properties of recycled post-consumer HIPS. A twin-screw extruder with a vacuum degassing unit and an industrial scale recycling machine were used for liquid state decontamination and the properties of the post-consumer recycled HIPS produced were studied.

A comprehensive series of tests were carried out to investigate the influence of liquid state decontamination on the properties of recycled material and to gain insight into its capabilities for closed loop recycling. These tests included tensile testing, Charpy impact testing, melt flow rate (MFR) measurement, plate-plate rheometry, high pressure capillary rheometry (HCR), and differential thermal analysis (DTA).

Material and Methods

Material and Decontamination Processes

A company partner processed material from the German waste fraction DSD331. This waste fraction is defined as used, residue-free, rigid, system-compatible plastic items made of polystyrene, volume ≤ 1 liter, such as cups and trays, including ancillary components such as closures, labels, etc. [6]. The waste fraction was sorted on an object-related scale, shredded, hot-washed (>80°C, at least 2.5% NaOH), and sorted on a flake scale.

DOI: https://doi.org/10.51573/Andes.PPS39.SS.CEP.8

After the pre-treatment, the material was extruded with a mass flow of 1300 kg/h and granulated. The extrusion step included a laser filtration and a vacuum degassing system. This was the initial material batch, henceforth referred to as "input".

In the following processing steps, different liquid state decontamination (LSD) processes were applied. On the one hand, a Leistritz ZSE 18 MAXX twin-screw extruder (Leistritz AG, Germany) was used, equipped with two vacuum ports connected to a pump. The vacuum levels of the two ports, set to "High" (300 mbar) and "Low" (700 mbar), were varied to assess their effect on the material. Other machine parameters remained unchanged: 240°C, 258 rpm, no filtration, and a mass flow of 3 kg/h. Three balanced vacuum settings were used:

- High-High
- Low-Low
- Non-Non

Two other settings were used to determine the effects of a dual versus single vacuum degassing system. In this setting, only the vacuum port on the die side of the extruder was used, leaving the other port open to draw in air.

- High-Non
- Low-Non

Additionally, an industrial-scale super-cleaning process derived from PET recycling was used. The process used high vacuum to extract volatiles, with a residence time of ~25 min to achieve a "super-cleaned" material batch [5].

Characterization

Mechanical properties were examined by conducting tests on injection-molded multipurpose and Charpy specimens following ISO 294-1 and ISO 19063-2. A victory 60 injection molding machine (Engel, Austria) was used to produce the specimen. Specimens were stored for 48 hours at testing conditions prior to testing.

Tensile tests were performed with a Z005 universal testing machine (Zwick Roell, Germany) with a 5 kN load cell and strain gauges, following ISO 527-2. Young's modulus was measured within a strain range of 0.05 to 0.25% at a testing speed of 1 mm/min. The testing speed was then increased to 50 mm/min until failure. Tests were conducted at 23°C and 50% relative humidity.

Charpy impact tests were carried out using an HIT25P impact tester (Zwick Roell, Germany), according to ISO 179-1. Specimens were notched with a type A notch utilizing an RM2265 microtome (Leica, Germany). Unnotched and notched tests used 5 J and 0.5 J pendulums, respectively, at 23°C and 50% relative humidity.

DOI: https://doi.org/10.51573/Andes.PPS39.SS.CEP.8

MFR tests used an Mflow Extrusion Plastometer (Zwick Roell, Germany) at just one temperature of 200°C with a 5 kg weight, following ISO 1133-1. The other rheological measurements (plate-plate rheometry and HCR) were performed at 200°C, 220°C, and 240°C.

Plates for plate-plate rheometry were pressed at 230°C and 1 bar using a Manual Hydraulic Press 15 Ton (Specac Ltd, UK). For the measurements, an MCR 502e (Anton Paar, Austria) following ISO 3219-2 was used. Tests covered a frequency range from 628 to 0.05 rad/s at the three temperatures mentioned above.

HCR viscosity measurements on a Rheograph 25 (Göttfert, Germany) used pellets and a 1 mm die of either 20 or 0.1 mm length, allowing the Bagley correction to be applied. The tests were carried out according to ISO 11443 with three different material batches (input, super-cleaned, and high-high) in the shear rate range between 10^4 and 10^1 s^{-1}. Results were corrected using the Weißenberg-Rabinowitsch method.

DTA measurements to examine material degradation were performed to characterize oxidation induction temperature (OIT) following ISO 11357-6. Specimens were cut into plates, put into aluminum pans, and heated from 30°C to 240°C at 10 K/min using a DSC 4000 (Perkin Elmer, USA). The onset of the oxidation peak was measured.

Results and Discussion

Mechanical Properties

The tensile properties and in particular the tensile modulus (E_t) are very important for a thermoformed product, such as a cup [7]. The input batch reached a modulus of 2176 MPa, which was not significantly different from the other batches, shown in Table 1. Characterization of the yield stress (σ_y) indicated that processing had a positive influence, especially at higher vacuum levels, with an almost 10% improvement due to the super-cleaning process. All the extruded material batches showed higher values for the strain at break (ε_b). The influence of vacuum setting during extrusion showed only a slight trend towards higher strain at break for higher vacuum levels. The most significant differences can be observed in the super-cleaned batch with high yield and post-yield stresses but low strains at break values. The respective stress-strain curves are depicted in Figure 1. Only small standard deviations were detected in tensile testing.

The Charpy impact tests of the unnotched specimens showed high standard deviations (σ_a_{cU}) due to imperfections in the material. The input material achieved the lowest Charpy impact strength of the unnotched specimens (a_{cU}) as shown in Table 1. Due to the high spread of the result values, notched specimens (a_{cN}) were additionally characterized. The results obtained revealed a trend that was opposite to that of the unnotched specimens (see Figure 1[b]). With these specimens, the

DOI: https://doi.org/10.51573/Andes.PPS39.SS.CEP.8

input batch shows the highest impact strength values followed by the extruded material batches, where the vacuum level had no significant influence. The lowest impact strength was achieved by the super-cleaned batch.

Table 1. Mechanical properties of the tensile testing and of the Charpy unnotched & notched impact testing.

	E_t	σ_y	ε_b	a_{cU}	σ_a_{cU}	a_{cN}	σ_a_{cN}
	MPa	MPa	%	[kJ/m²]	[kJ/m²]	[kJ/m²]	[kJ/m²]
Input	2176	27.3	21.1	38.3C*	6.1	6.5C*	0.12
High-High	2178	28.1	25.3	56.6C*	14.5	5.7C*	0.11
Low-Low	2163	28.2	25.3	53.7C*	16.0	5.7C*	0.09
Non-Non	2174	27.2	24.0	56.2C*	17.4	6.2C*	0.11
High-Non	2169	29.0	24.2	54.0C*	11.6	5.6C*	0.06
Low-Non	2164	28.9	24.9	50.6C*	10.6	5.5C*	0.10
Super-cleaned	2153	29.7	19.3	52.3C*	11.3	4.7C*	0.12

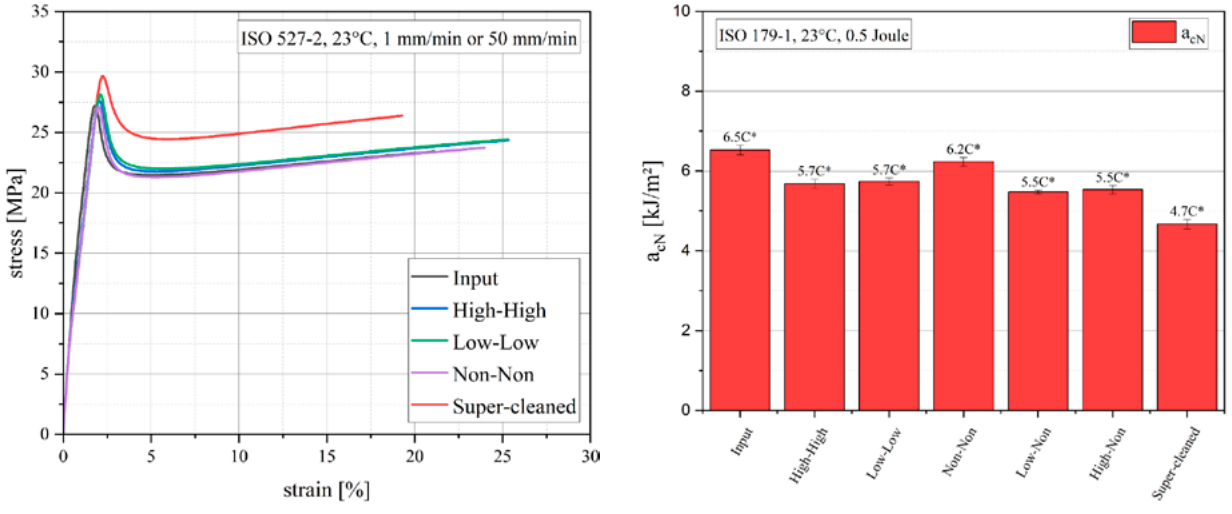

(a) (b)

Figure 1: (a) Stress-strain-curves from tensile testing and (b) Charpy notched impact strengths.

Rheological Properties

First, the MFR was measured. The input batch achieved an MFR of 4.8 g/10min that corresponds to a melt volume rate (MVR) of 5.0 cm³/10min, resulting in a melt density of 0.97 kg/dm³. The melt density remained unchanged, but every extruded material batch achieved higher MFR values than

DOI: https://doi.org/10.51573/Andes.PPS39.SS.CEP.8

the input batch, regardless of vacuum level, as shown in Table 2. The lowest MFR value can be observed in the super-cleaned batch.

The oscillating plate-plate rheological measurement showed no major differences in the vacuum setting while extruding. The differences between the input and extruded material batches were also not significant. The comparison between the input and the super-cleaned batch confirmed the results of the MFR. With small differences, the super-cleaned batch achieved a higher complex viscosity at all temperatures and all circular frequencies.

The rheological measurements were completed by the HCR viscosity analysis to show the behavior of the materials at higher shear rates. The input and the high-high batches revealed the same result as in the plate-plate rheological measurements: no significant differences. The super-cleaned batch again achieved the highest viscosities, with differences approaching zero at the highest shear rates.

Combining the plate-plate and HCR rheological measurements revealed the possibility of superpositioned curves to provide information over a wide shear rate range, indicating the applicability of the Cox-Merz rule [8]. After correcting the HCR results, all curves showed a good overlap between the two different test systems, as illustrated in Figure 2(a). The curves were merged at the intersection, shown in Figure 2(b). This gave us single curves from shear rates of 0.5 s^{-1} to 20,000 s^{-1}.

Looking at the rheological properties revealed a controversial change in properties caused by the processing. The viscosity, in particular the MFR, showed that the extrusion process increased the MFR, and the LSD process decreased it. The increase might have been due to degradation of the polystyrene matrix by chain scission, and the decrease indicated cross-linking of the polybutadiene particles in the polystyrene matrix due to the increased process time and thermal stress on the material [9].

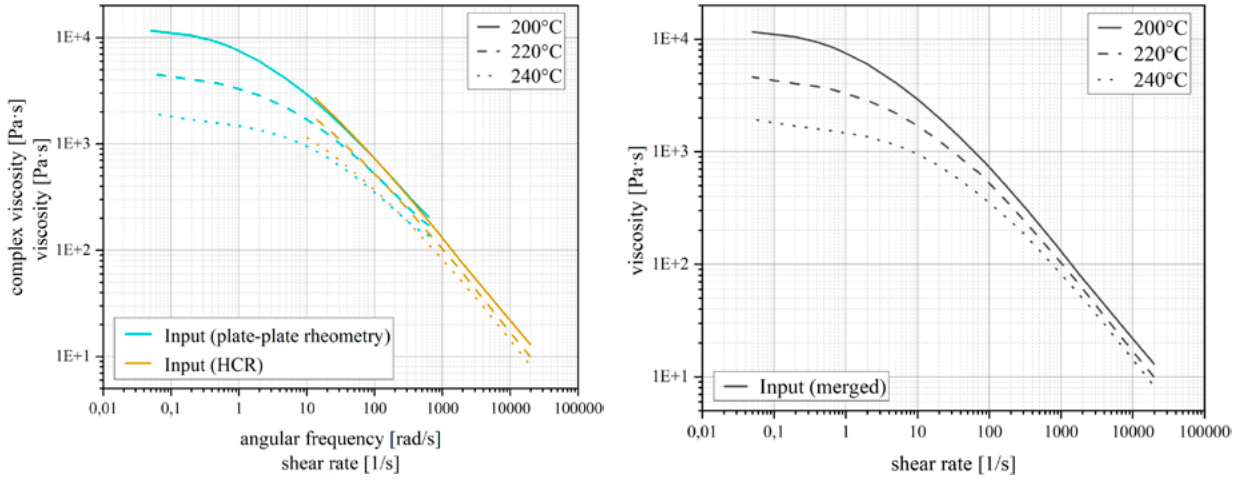

Figure 2: Viscosity curves of the input material: (a) overlapping curves from plate-plate rheometry & HCR rheometry and (b) merged viscosity curves.

DOI: https://doi.org/10.51573/Andes.PPS39.SS.CEP.8

Thermal Properties

DTA characterization revealed several transition temperatures: polystyrene glass transition at 95-100°C, small peaks at 125°C and 165°C from traces of foreign polymers (polyethylene and polypropylene), and the crucial oxidation peak onset. The input batch achieved an OIT of 181.6°C. The extruded material batches, independent of the vacuum level, showed similar values within the standard deviation. The super-cleaned batch, on the other hand, only reached 173.4°C, indicating measurable degradation through the LSD process. This demonstrated a clear difference in degradation between the extrusion and the LSD processes due to different processing times at high thermal stresses. This finding is consistent with the duality of degradation in the rheological properties mentioned above.

Table 2. Rheological properties of MFR testing and thermal properties of DTA measurements.

	MFR	σ_MFR	MVR	σ_ MVR	ρ_m	OIT	σ_OIT
	g/10min	g/10min	cm³/10min	cm³/10min	kg/dm³	[°C]	[°C]
Input	4.8	0.07	5.0	0.08	0.970	181.6	1.67
High-High	5.2	0.11	5.3	0.11	0.968	179.9	0.81
Low-Low	5.6	0.09	5.8	0.09	0.968	180.3	0.60
Non-Non	5.2	0.07	5.4	0.08	0.969	182.2	1.27
High-Non	5.2	0.09	5.4	0.09	0.968	181.1	0.64
Low-Non	5.4	0.09	5.5	0.10	0.968	180.3	1.39
Super-cleaned	4.3	0.09	4.5	0.09	0.969	173.4	1.15

Conclusion

The vacuum setting during twin-screw extrusion had an almost negligible influence on the mechanical, rheological, and thermal properties. Comparing input with any extruded material batches, the extrusion itself showed only a minor influence on the mechanical properties. The rheological or thermal properties were not significantly affected, except for a higher MFR due to the chain scission degradation caused by extrusion. The super-cleaned batch showed the greatest changes in properties. Here, the mechanical properties displayed that it could withstand higher tensile stresses but lost some of its impact strength. The rheological properties revealed higher viscosities in each test method due to the cross-linking degradation of the polybutadiene in the LSD process, which also correlates with the higher tensile strength and lower ductility measured in the mechanical tests. The OIT results showed almost no degradation in the extruded material batches but high degradation in the super-cleaned batch, in line with the degradation hypothesis. In conclusion, multiple closed-loop recycling of HIPS with an LSD process could cause problems due to material degradation and, therefore, this type of recycled product requires good quality control.

DOI: https://doi.org/10.51573/Andes.PPS39.SS.CEP.8

References

1. Official Journal of the European Union L 150/141, "Directive (EU) 2018/852 of the European Parliament and of the Council of 30 May 2018 amending Directive 94/62/EC on packaging and packaging waste," Accessed: Jun. 6, 2024. [Online]. Available: https://eur-lex.europa.eu/eli/dir/2018/852/oj
2. Plastics Europe AISBL, "Plastics – the Facts 2022," Oct. 2022. Accessed: Jun. 6, 2024. [Online]. Available: https://plasticseurope.org/knowledge-hub/plastics-the-facts-2022/
3. M. F. Martin, J. P. Viola, and J. R. Wuensch, "Preparation, Properties and Applications of High-impact Polystyrene," in *Modern Styrenic Polymers: Polystyrenes and Styrenic Copolymers*, J. Scheirs and D. B. Priddy, Eds.: Wiley, 2003, pp. 247-280.
4. F. Welle, "Recycling of Post-Consumer Polystyrene Packaging Waste into New Food Packaging Applications—Part 1: Direct Food Contact," *Recycling*, vol. 8, no. 1, p. 26, 2023, https://doi.org/10.3390/recycling8010026
5. N. Niessner, Ed., *Recycling of plastics*. Munich: Hanser Publishers, 2022.
6. Der Grüne Punkt, "Rohstofffraktionsspezifikation 331 Polystyrol," Quality Assurance. Accessed: Jun. 11, 2024. [Online]. Available: https://www.gruener-punkt.de/fileadmin/Dateien/Downloads/PDFs/Rohstofffraktionsspezifikationen2023/DOC-23-50746_-_Rohstofffraktionsspezifikation_331_Polystyrol_-_v0.01.0004.pdf
7. I. Traxler, J. Fischer, C. Marschik, S. Laske, M. Eckerstorfer, and H. Reckziegel, "Structure-property relationships of thermoformed products based on recyclates," *AIP Conference Proceedings*, 2023, https://doi.org/10.1063/5.0168248
8. W. P. Cox and E. H. Merz, "Correlation of dynamic and steady flow viscosities," *Journal of Polymer Science*, vol. 28, no. 118, pp. 619–622, 1958, https://doi.org/10.1002/pol.1958.1202811812
9. Y. Israeli, J. Lacoste, J. Lemaire, R. P. Singh, and S. Sivaram, "Photo- and thermoinitiated oxidation of high-impact polystyrene. I. Characterization by FT-IR spectroscopy," *Journal of Polymer Science Part A: Polymer Chemistry*, vol. 32, no. 3, pp. 485-493, 1994, https://doi.org/10.1002/pola.1994.080320310

SPECIAL SYMPOSIA | DEGRADATION, BIODEGRADATION AND COMPOSTING

Modelling Hydrolytic, Thermal, and Mechanical Degradation of PLA During Single-Screw Extrusion

Ineke Velghe, Bart Buffel, Veerle Vandeginste, Wim Thielemans and Frederik Desplentere

DOI: https://doi.org/10.51573/Andes.PPS39.SS.DBC.1

December 2024

Modelling Hydrolytic, Thermal, and Mechanical Degradation of PLA During Single-Screw Extrusion

Ineke Velghe, Bart Buffel, Veerle Vandeginste, Wim Thielemans and Frederik Desplentere[1]

Abstract: Since melt processing causes degradation of poly(lactic acid) or PLA, it is crucial to understand the effect of extrusion conditions on the molecular weight reduction. Kinetic models found in literature are promising tools to describe hydrolytic, thermal, and mechanical degradation during extrusion. In order to use these models, extrusion parameters (that are equipment dependent) should be translated into the four fundamental parameters that determine degradation: moisture content in PLA, residence time, shear stress history and temperature history. This work presents a methodology to use numerical simulations to translate extrusion parameters into fundamental parameters. The results show that numerical simulations can be used successfully to describe the extrusion process based on residence time, shear stress history, and temperature history.

Keywords: Extrusion, PLA, Numerical Simulation, Process-Induced Degradation

1 The authors Ineke Velghe (ineke.velghe@kuleuven.be), Bart Buffel (bart.buffel@kuleuven.be), Veerle Vandeginste (veerle.vandeginste@kuleuven.be), Wim Thielemans (wim.thielemans@kuleuven.be) and Frederik Desplentere (frederik.desplentere@kuleuven.be) are affiliated with KU Leuven in Belgium.

DOI: https://doi.org/10.51573/Andes.PPS39.SS.DBC.1

Introduction

The sensitivity of the ester bonds in poly(lactic acid) or PLA is a major concern in processing bio-polyesters. The potential presence of moisture in the granules combined with high shear stresses and temperatures during the melt processing can lead to a significant molecular weight reduction due to hydrolytic, thermal, and mechanical degradation [1-3]. Previous research has presented a kinetic degradation model to successfully predict the decrease of viscosity (and thus molecular weight) over time by studying the effect of processing temperature and moisture content in the granules using a rheometer [4]. Extending the kinetic degradation model to estimate degradation during single-screw extrusion implies differences in two aspects. First, mechanical degradation should be included in addition to hydrolytic and thermal degradation. Second, since the processing temperature and shear stress inside the barrel vary throughout the extrusion process, the temperature history and shear stress history as a function of time need to be understood. Degradation of PLA is expressed in terms of four fundamental parameters (moisture content in the granules, processing temperature, shear stress, and residence time), while extruding PLA requires a set of processing parameters (e.g., screw rotation speed, die and screw geometry, and processing temperature build-up in different heating zones). The combined processing parameters determine the total residence time, shear stress history, and temperature history, thus the essential data required to apply the aforementioned kinetic degradation model on extrusion [4]. The goal of this paper is to translate extrusion parameters to fundamental parameters using numerical simulations, enabling a description of the extrusion process in a universally applicable (equipment-independent) manner. This approach allows other researchers or companies to compare data, even if another extruder, die or screw geometry is used.

Materials and Method

PLA 2500HP Ingeo™ (supplied by NatureWorks) is selected as the material of interest. This PLA grade is characterized by a high molecular weight ($\overline{Mn}$ 65 kDa, $\overline{Mw}$ 124 kDa) and a D-isomer content of less than 0.5%. To remove moisture from the PLA granules, the material is dried in a Moretto Mini Dryer D4 for a minimum of 24h at 80°C.

A COLLIN single-screw extruder with a diameter D of 30 mm and an L/D ratio of 28 was used. The extruder is equipped with five pressure and temperature transducers along the barrel and can be used in combination with FECON software, that enables monitoring the stability of the extrusion process and capturing data. The screw geometry and locations of the pressure and temperature transducers are presented in Figure 1. Behind the barrel, the die section starts as seen in Figure 2. The die section consists of a coupling piece (inner diameter 25.6 mm, length 102 mm) and a round capillary die (diameter either 2, 3, or 4 mm, length 30 mm) or open (no capillary die).

DOI: https://doi.org/10.51573/Andes.PPS39.SS.DBC.1

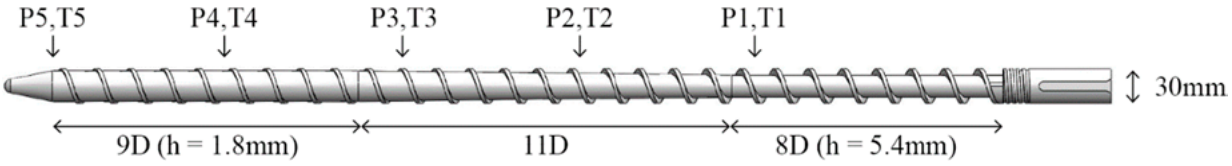

Figure 1. Screw geometry and locations of five pressure and temperature transducers.

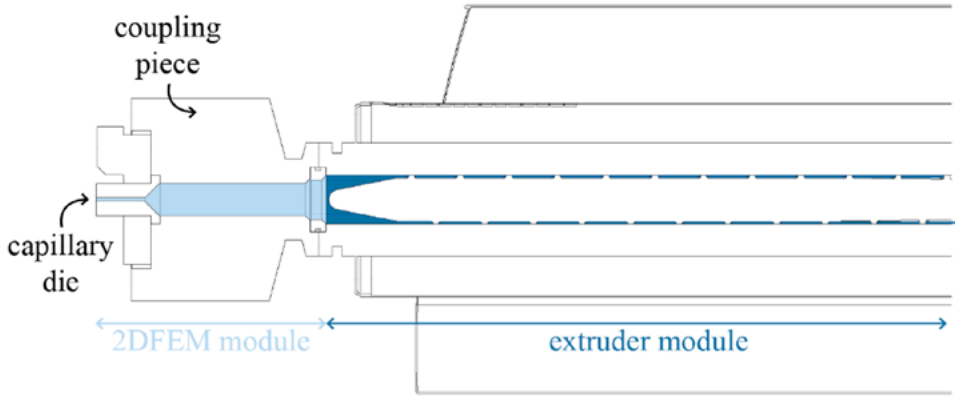

Figure 2. Use of an *extruder module* for screw section and a *2DFEM module* for die section in VEL.

Twelve extrusion experiments are performed, as shown in Table 1. In each experiment, one variable is changed compared to the reference set of parameters (210°C, 30 rpm and a capillary die with a diameter of 4 mm). During each experiment, the pressure is measured at the five locations along the extruder, as reported in Figure 3. The highest pressure, measured at location 3 (P3), is reported in Table 1, together with the measured mass flow rate (MFR) in each experiment.

Table 1. Processing combinations and results for P3 (pressure at location 3) and MFR (mass flow rate).

Name	Processing parameters			Experiment		Simulation		Difference	
[-]	T [°C]	n [rpm]	die [-]	P3 [MPa]	MFR [kg/h]	P3 [MPa]	MFR [kg/h]	ΔP3 [%]	ΔMFR [%]
190°C	190	30	4 mm	22.7	4.08	23.3	4.19	-2.78	-2.74
200°C	200	30	4 mm	21.1	4.01	20.0	4.26	5.65	-6.05
210°C	210	30	4 mm	18.2	4.17	18.3	4.42	-0.37	-5.76
220°C	220	30	4 mm	16.6	4.15	15.7	4.54	6.19	-8.62
230°C	230	30	4 mm	14.2	4.25	13.5	4.68	5.36	-9.26
20rpm	210	20	4 mm	13.7	2.70	14.1	2.96	-3.07	-8.67
25rpm	210	25	4 mm	17.8	3.56	16.2	3.69	9.98	-3.45

DOI: https://doi.org/10.51573/Andes.PPS39.SS.DBC.1

Name [-]	Processing parameters			Experiment		Simulation		Difference	
	T [°C]	n [rpm]	die [-]	P3 [MPa]	MFR [kg/h]	P3 [MPa]	MFR [kg/h]	ΔP3 [%]	ΔMFR [%]
30rpm	210	30	4 mm	18.2	4.17	18.3	4.42	-0.37	-5.76
35rpm	210	35	4 mm	21.3	4.87	20.4	5.16	4.53	-5.74
40rpm	210	40	4 mm	23.5	5.54	22.3	5.90	5.43	-6.05
open	210	30	open	18.6	4.24	17.7	4.53	4.94	-6.42
4 mm	210	30	4 mm	18.2	4.17	18.3	4.42	-0.37	-5.76
3 mm	210	30	3 mm	21.2	3.97	19.5	4.21	8.86	-5.80
2 mm	210	30	2 mm	22.2	3.64	22.3	3.90	-0.22	-6.72

The extrusion combinations named *210°C, 30 rpm* and *4 mm* refer to the same measurement and are repeated in Table 1 for better comparison with other data. The mentioned temperature (e.g., 210°C) is the set temperature of the last of seven heater bands on the extruder (30–170–190–210–210-210-210°C). The actual, measured temperature is 10°C higher for all processing combinations due to shear heating.

The simulations are performed in a Virtual Extrusion Laboratory (VEL) developed by Compuplast. Two modules in VEL are used: *extruder module* to model the process from hopper until the end of the screw, and *2DFEM module* to model the process in the die, as shown in the geometry (Figure 2). The used screw geometry and measured material properties are presented in Figure 1 and Table 2. The Carreau model is used to describe the rheological properties of the PLA melt (equation 1):

$$\eta(\gamma, T) = \frac{A * f(T)}{[1 + (r * \gamma * f(T))^a]^{\frac{1-n}{a}}} \quad 1)$$

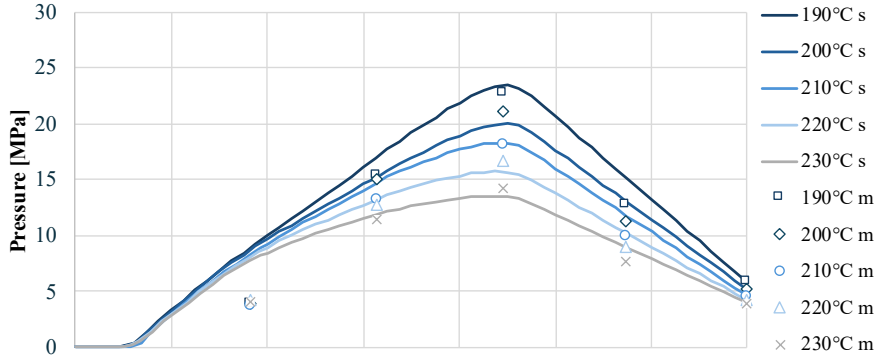

DOI: https://doi.org/10.51573/Andes.PPS39.SS.DBC.1

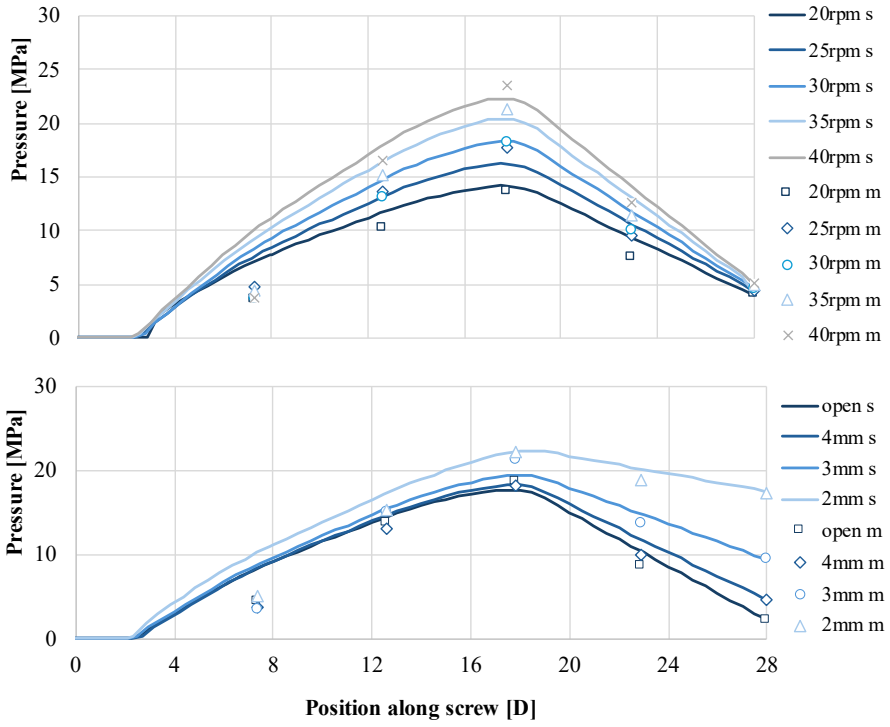

Figure 3. Measured (m) and simulated (s) pressure evolution throughout the extruder.

Table 2. Measured material properties used for simulations.

ρ_{solid} [kg/m³]	ρ_{melt} [kg/m³]	ρ_{bulk} [kg/m³]	$T_{freezing}$ [°C]	T_{melt} [°C]	Cp_{solid} [J/kg/°C]	Cp_{melt} [J/kg/°C]	ΔH_f [J/kg]	k [W/mK]
1240	992	790	143.5	173	1682	2258	40780	0.16

With zero shear viscosity A (1795.28 Pa.s), constant r (0.004611), constant a (0.65161), constant n (0.1) and $f(T) = e^{-b\,(T-Tr)}$ with temperature dependency parameter b (0.03836 1/°C), and reference temperature Tr (210°C). The same extrusion combinations (Table 1) are simulated and compared with P3 and MFR of the experimental results (Figure 3) to check the quality of the simulation results. The percentage deviations of P3 and MFR are calculated and reported in Table 1.

Results and Discussion

As the relative deviations between experimental and simulation results are less than 10% for P3 and MFR (Table 1), it can be concluded that the simulation is able to correctly describe the actual experiments. Thereby, the simulation output of VEL can be used to extract information about the residence time of the material inside the extruder, temperature throughout the extrusion process, and shear stress throughout the extrusion process.

DOI: https://doi.org/10.51573/Andes.PPS39.SS.DBC.1

Results residence time

The residence time of the material starts when the material exceeds the melting temperature of 173°C. This point was selected as in this work the authors assumed that process-induced degradation occurs in the melt state. Figure 4 presents the residence time of the material inside the feeding, compression, and metering zone of the screw, and the die section of the extrusion line. The temperature of the material exceeds 173°C around position 6D (slightly different for each experiment) while the feeding zone has a length of 8D. Therefore, the reported residence time in the feeding zone in Figure 4 is around 25% of the total feeding zone residence time that is calculated in VEL. It is assumed that no process-induced degradation occurs in the first 75% of the feeding zone, since the granules are in a solid state. To estimate the residence time in the die section, the volume of the die section and the measured MFR are used. The residence time results indicate that the residence time is longer at a lower processing temperature, a lower screw rotation speed, and when a smaller die is used, which was expected.

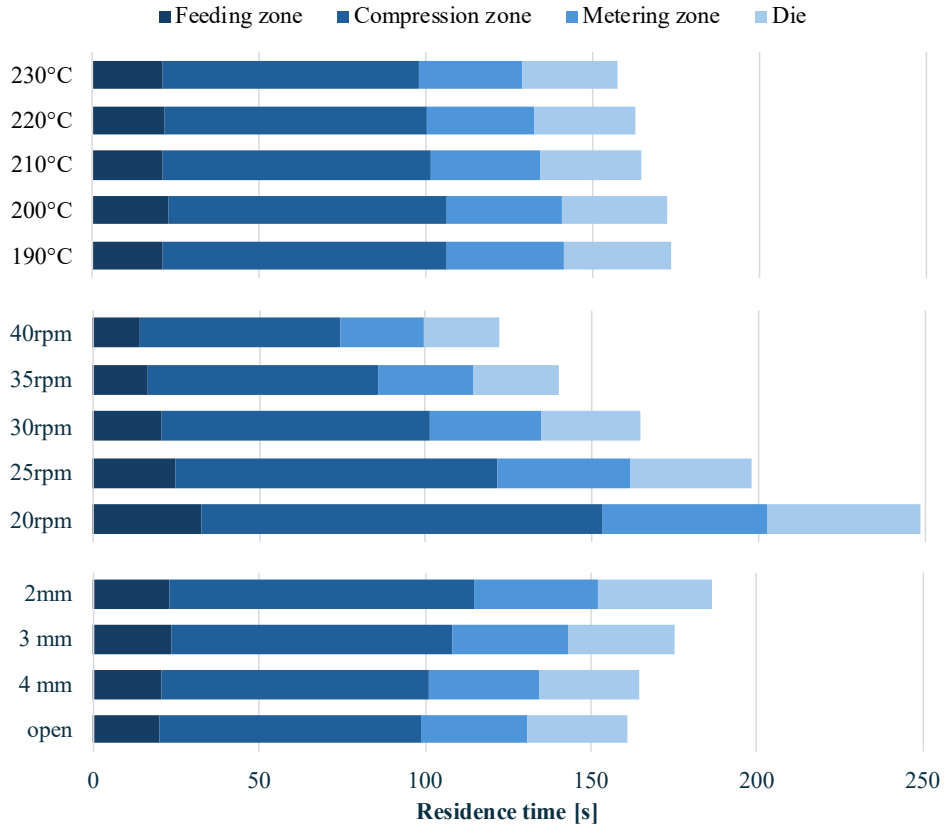

Figure 4. Residence time in each zone for the different extrusion combinations.

DOI: https://doi.org/10.51573/Andes.PPS39.SS.DBC.1

Results Temperature History

During extrusion, the temperature of the melt varies along its screw position, caused by the heating or cooling of the barrel and the shear heating energy dissipation. The material temperature along the screw is calculated at each location as an average value over the screw channel cross-section. The common output in VEL is temperature as a function of position along the screw (expressed in D), which is therefore linked to the extrusion geometry and inevitably equipment-dependent. In this work, the desired output is the temperature as a function of time, which makes the results equipment-independent. The residence time data is known at five positions along the extruder, as seen in the previous section: start of the degradation when the temperature exceeds 173°C (t = 0s), end of feeding zone 8D, end of compression zone 19D, end of the metering zone 28D, and end of the die section. Due to the changing channel depth in the compression zone, a sixth location at 13.5D is defined. The residence time inside the compression zone is divided proportionally to the volume of the channel in this section that is 62% between 8-13.5D and 38% between 13.5D-19D. This allows us to express the bulk temperature throughout the process as a function of time, presented in Figure 5. The temperature evolution occurs as expected: an increase in temperature occurs more rapidly at a higher processing temperature and a faster screw rotation speed, particularly when a larger die diameter is used, after which the temperature stabilizes.

Results Shear Stress History

Similar to the bulk temperature, shear stress as a function of position along the extruder (in D) should be translated into the shear stress as a function of time. The same six locations are used as described in the previous section. The reported shear stress at the six locations is the weighted average shear stress across the screw section (Figure 5). A higher shear stress is obtained at a lower processing temperature and a higher screw rotation speed. When comparing the effect of the die diameter, it can be concluded that the shear stress is not significantly affected. This range of dies mainly affects the residence time of the material, but the effect on the shear stress is less pronounced, due to the short residence time of the material in the capillary die.

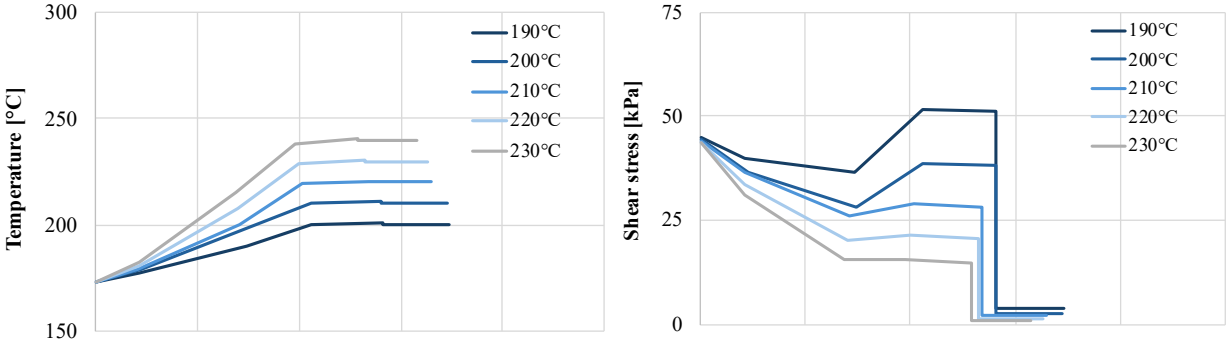

DOI: https://doi.org/10.51573/Andes.PPS39.SS.DBC.1

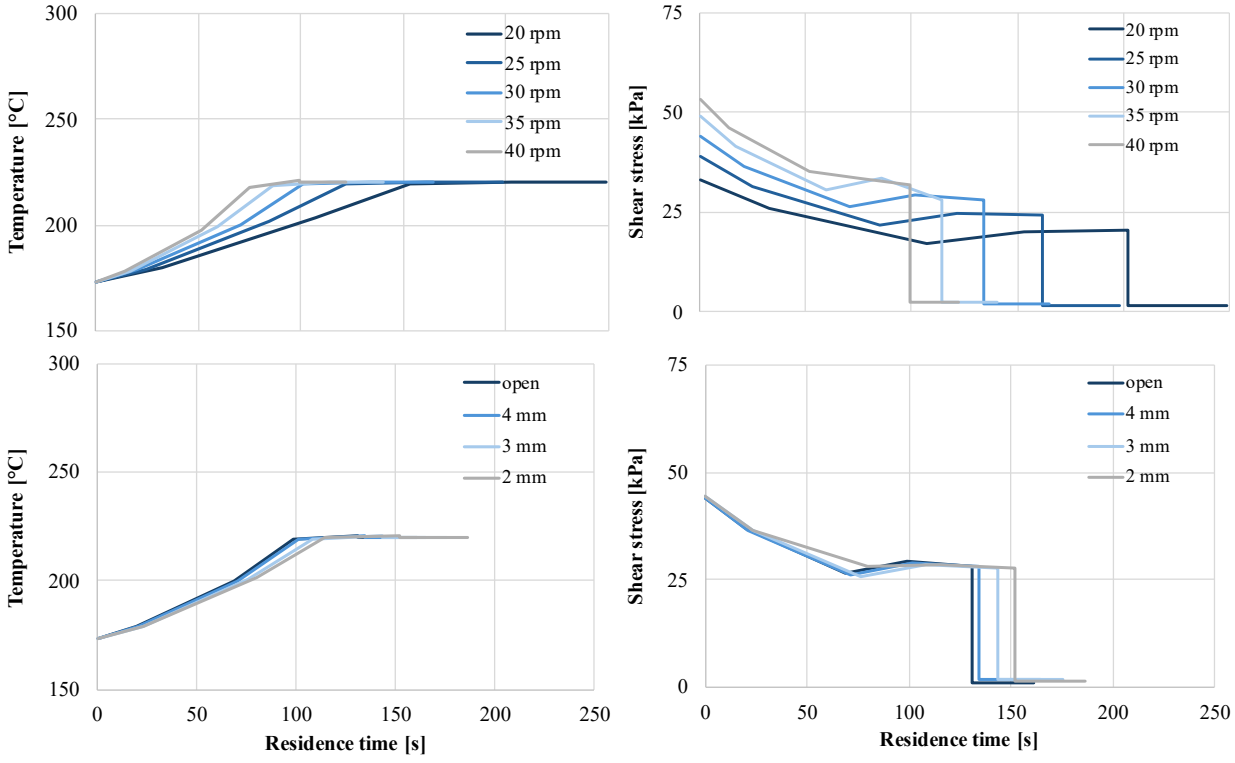

Figure 5. Plots of bulk temperature and shear stress against residence time.

Conclusion

The goal of this work is to translate extrusion parameters to fundamental parameters using numerical simulations. The results indicate that numerical simulations in VEL enable reconstruction of the temperature history, shear stress history, and residence time of the molten PLA inside the extruder. The method, combining experimental results with numerical simulations, can be used to describe the extrusion process in a way that is universally applicable (equipment-independent). This means that the results are no longer linked to the screw geometry, processing parameters, and die selection, enabling comparison of results with other researchers or processors working with PLA or other types of polyesters.

Outlook

The translation step from processing to fundamental variables is a critical step to prepare data for further use in a kinetic degradation model. In future work, this translated data is the basis for predicting thermal and mechanical degradation during processing with a kinetic model. A next step will be to perform extrusion experiments and simulations with PLA that contains moisture, in order to also investigate hydrolytic degradation.

DOI: https://doi.org/10.51573/Andes.PPS39.SS.DBC.1

Acknowledgments

This study was supported by the Research Foundation – Flanders (FWO), grant number 1S16122.

References

1. A. A. Cuadri and J.E. Martin-Alfonso, "Thermal, thermo-oxidative and thermomechanical degradation of PLA: A comparative study based on rheological, chemical and thermal properties", *Polymer Degradation and Stability*, vol. 150, pp. 37-45, 2018.
2. G. Gorrasi and R. Pantani, "Hydrolysis and biodegradation of poly(lactic acid)", *Advances in Polymer Science*, vol. 279, pp. 119-151, 2018.
3. I. Velghe, B. Buffel, V. Vandeginste, W. Thielemans and F. Desplentere, "Review on the Degradation of Poly(lactic acid) during Melt Processing", *Polymers*, vol. 15, 2023.
4. V. Sperzanza, A. De Meo and R. Pantani, "Thermal and hydrolytic degradation kinetics of PLA in the molten state", *Polymer Degradation and Stability,* vol. 100, pp. 37-41, 2014.

SPECIAL SYMPOSIA | POLYMERS IN THE SUSTAINABLE DEVELOPMENT GOALS OF THE UNITED NATIONS

Plastics and the United Nations Sustainable Development Goals

Fabiula Danielli Bastos de Sousa

DOI: https://doi.org/10.51573/Andes.PPS39.SS.PSDGUN.1

December 2024

Plastics and the United Nations Sustainable Development Goals

Fabiula Danielli Bastos de Sousa[1]

Abstract: Recent literature on the role of plastics in achieving the United Nations Sustainable Development Goals (SDGs) was analyzed. Despite contributing to the accomplishment of at least 15 SDGs, plastic pollution, especially marine pollution, outweighs the positive contributions of plastic to accomplishing the 2030 Agenda. The study, however, emphasized the vital importance of the circular economy, highlighting practices such as recycling as viable solutions to the socio-environmental problems that may be created by plastics.

Keywords: Sustainable Development Goals, SDGs, Plastic, Pollution, Circular Economy, Recycling

1 The author (fabiuladesousa@gmail.com) is affiliated with the Technology Development Center at the Universidade Federal de Pelotas-UFPel in Brazil.

DOI: https://doi.org/10.51573/Andes.PPS39.SS.PSDGUN.1

Introduction

Plastics are ubiquitous in the global economy. However, we must consider the adverse effects of our throwaway culture and poor waste management practices to balance out any benefits that plastics may provide. We cannot ignore the fact that improper disposal of plastic waste has led to an increase in water pollution. It is a delicate balance that we need to maintain for the well-being of our planet.

Plastic significantly impacts our societal lives and the progress and attainment of the 2030 Agenda for Sustainable Development. During the Rio+20 Conference in 2015, the 2030 Agenda for Sustainable Development was deliberated, leading to an action plan comprising 17 Sustainable Development Goals (SDGs) [1]. Previous research [2] suggests that the negative impact of plastic pollution (primarily marine pollution) on the 2030 Agenda outweighs its positive contributions to achieving at least 15 SDGs.

To demonstrate the impact of plastic on the achievement of the UN SDGs, a bibliometric analysis and mapping of the data obtained from a Scopus search on the subject was conducted. Trends, directions, and gaps were identified.

Methodology

A search in the Scopus database was performed on April 29, 2024, to record the data inputs. The terms used in the search were (sustainable development goal* OR SDG*) and (plastic* OR polymer*), searching within article titles, abstracts, and keywords.

Subject areas such as biochemistry, genetics, molecular biology, immunology, microbiology, and medicine often employ specific terminology, such as "SDG*," which has a distinct meaning unrelated to the 2030 Agenda. So, these subject areas were excluded.

Articles and reviews in English from 2020 to 2024 were considered to assess the literature on the subject concerning previous works [2,3]. The data was exported to a.csv file, which was examined using the R-package Bibliometrix and VOSviewer version 1.6.18. Graphs were created in Biblioshiny for Bibliometrix and VOSviewer. The network generated by VOSviewer displays 47 keywords with at least five occurrences, and the full counting approach was applied.

Results and Discussion

The Scopus search resulted in 622 publications in English, including 452 articles and 170 reviews. Figure 1 demonstrates the evolution of the number of publications per year. Comparing this result with a previous publication [3], there has been a significant increase in the number of publications per year. In the present work, the annual growth rate is of 18.67%.

DOI: https://doi.org/10.51573/Andes.PPS39.SS.PSDGUN.1

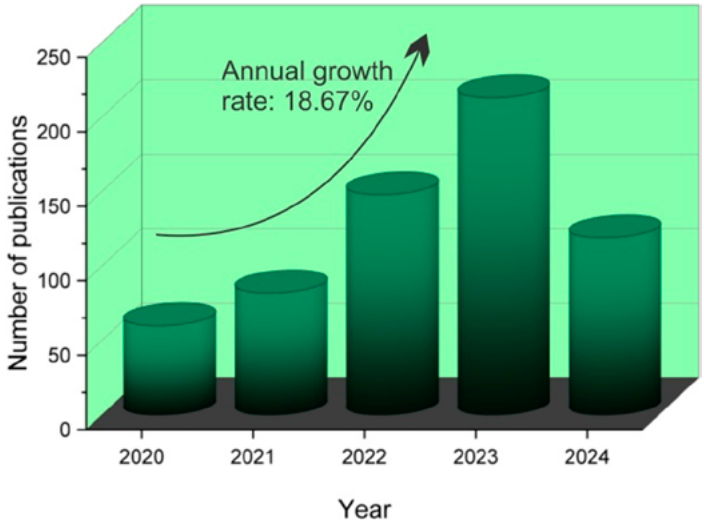

Figure 1. Evolution of the number of publications per year.

This is a multidisciplinary research area, and the fields with the highest number of publications are Environmental Science (283), Materials Science (173), Engineering (137), Energy (124), and Chemistry (122). There has been a shift in the profile of the areas with the highest number of publications compared to the results obtained in the 2020 Scopus database search [3]. Environmental Science, Chemistry, Chemical Engineering, Materials Science, and Agricultural and Biological Sciences had the highest number of publications in 2020.

Keyword analysis is crucial for identifying research trends, directions, and gaps in a research field. Figure 2 shows word clouds comprising the 50 most frequent authors' keywords from the Scopus searches performed in 2020 [3] and 2024. The frequency of a keyword is proportional to the size of its letters.

In 2020 (Figure 2[a]), the most frequent authors' keywords were (number of occurrences in parenthesis) sustainable development goals (11) (it is not shown in Figure 2[a]), circular economy (7), sdgs (4), sustainability (4), life cycle assessment (3), green chemistry (2), India (2), marine debris (2), optical properties (2), and polymers (2). On the other hand, in 2024 (Figure 2[b]), from a total of 2,319 authors' keywords, the most frequent are (number of occurrences in parenthesis) sustainability (70), sustainable development goals (52), circular economy (47), sustainable development (31), plastic pollution (26), life cycle assessment (22), waste management (21), recycling (19), microplastics (18), and plastic waste (17). The number of occurrences of the keywords in Figure 2(a) is lower than those in Figure 2(b) because the search in the Scopus database in 2020 resulted in fewer publications. The available literature on the subject increased significantly in the search conducted in 2024.

DOI: https://doi.org/10.51573/Andes.PPS39.SS.PSDGUN.1

Figure 2. Word clouds comprising the 50 most frequent keywords from the Scopus searches performed in 2020 (a) and in 2024 (b).

By comparing the word clouds (Figures 2[a] and [b]), current literature trends differ from those in 2020. Recent research has increasingly revealed the significance of the circular economy and life cycle assessment regarding the impact of plastic on the SDGs. Current literature provides evidence of the pollution caused by plastic. This literature mainly focuses on the adverse impacts of microplastic (MP) pollution [4] on the environment.

The co-occurrence network of the 47 main authors' keywords is displayed in Figure 3. The keywords are divided into 7 clusters, each marked with a different color. The network has 208 links, with a total link strength of 377.

Each cluster represents a specific direction within the subject area. The red cluster, which has 13 items and focuses on applications, contains the majority of the items. The green cluster focuses on life cycle assessment and has 10 items. The blue cluster has 9 items and is about plastic pollution. The yellow cluster is about biomass and contains 5 items. The purple cluster focuses on geopolymers and consists of 5 items. The light blue cluster consists of 3 items and focuses on the circular economy. The orange cluster is about biopolymers and contains 2 items.

DOI: https://doi.org/10.51573/Andes.PPS39.SS.PSDGUN.1

The keyword 'circular economy' (the largest light blue circle) holds a central position in the network, representing a crucial factor in plastics' role in achieving the SDGs. According to Maaskant et al. [5], decoupling from fossil feedstocks, optimizing recycling strategies, and manufacturing less frequently discarded items from easily biodegradable materials are crucial steps in establishing a renewable circular economy for thermoplastic polymers. Based on this, some examples from the literature will be briefly described below.

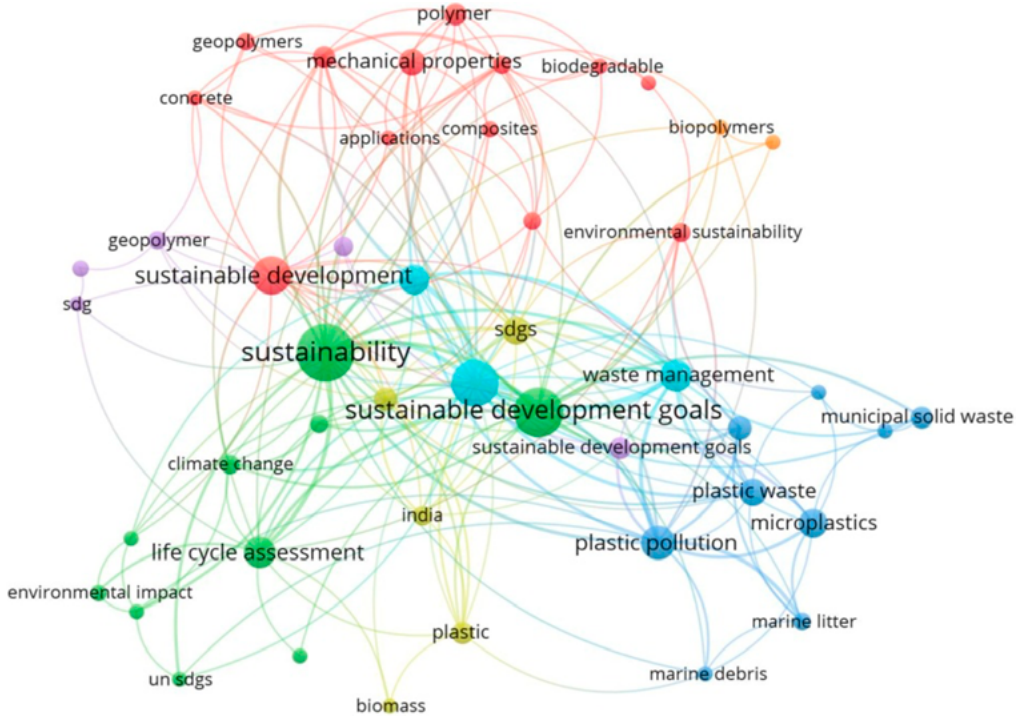

Figure 3. Co-occurrence network of the 47 primary authors' keywords.

As potential alternatives to the polymers currently used in packaging, literature suggests using edible pectin-alginate films reinforced with orange peel powder [6]. Additionally, Salas et al. [7] discussed the possibility of using "Nejayote," a byproduct of the maize snack industry, as a compound to create a new sustainable bioplastic. Some authors [8] have demonstrated that an azido triazine-based grafting agent enables polyolefin blends to be directly converted into high-performance materials through reactive extrusion at processing temperatures commonly used in the industry. Other authors have studied the properties of recycled composites and have developed composites incorporating recycled materials [9-14] for diverse applications. Some authors [15] used ground tire rubber (GTR) to produce GTR-based composite material using a fused filament fabrication desktop 3D printer, thereby enhancing damping properties.

The connections among specific keywords in the network shown in Figure 3 will be analyzed in Figure 4.

DOI: https://doi.org/10.51573/Andes.PPS39.SS.PSDGUN.1

When considering the keyword 'sustainable development goals' (Figure 4[1]), it is important to examine the connections between it and the keywords 'circular economy' and 'waste management'. These links are highly interconnected and frequently co-occur in publications. No correlation was found between the keywords 'waste management' and 'sustainable development goals' in the database search conducted in 2022 [2]. Hence, this recent correlation suggests that effective waste management strategies are crucial for achieving the SDGs.

Despite their relative distance, the concepts of 'circular economy' (Figure 4[2]), 'waste management', and 'recycling' are intricately connected and have a high total link strength of 10 and 11, respectively. Furthermore, they belong to the same cluster, suggesting their interdependence in advancing the circular economy of plastics. The distance between the 'circular economy' and the keywords of the application cluster (the red cluster) is worrisome. This indicates that more literature is needed in this area to enhance it. Mere recycling is insufficient; the crucial issue lies in developing viable applications for recycled materials. Therefore, current literature fails to address the potential of recycled plastics to contribute to the circular economy of plastics, which represents a gap.

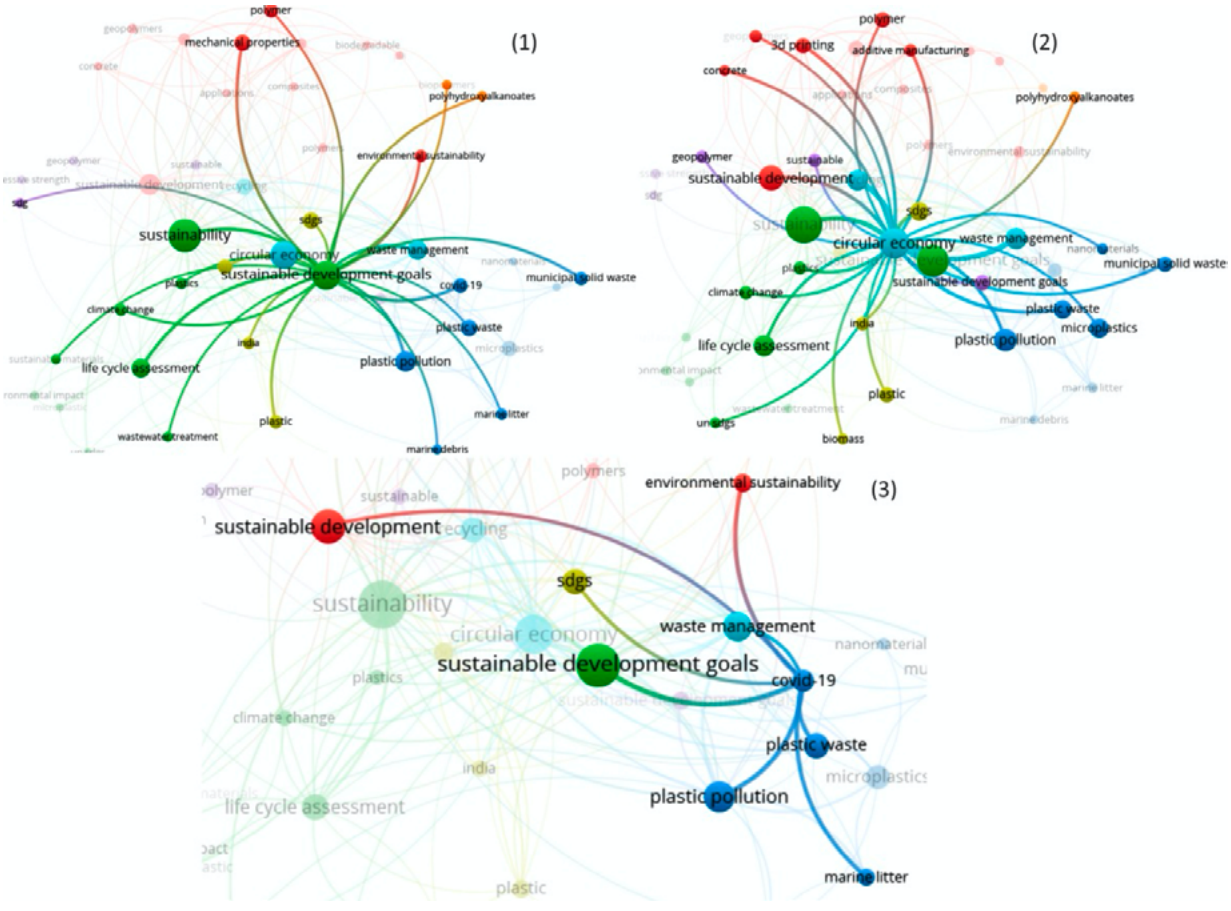

Figure 4. Connections among the keywords: Sustainable development goals (1), circular economy (2), and COVID-19 (3).

DOI: https://doi.org/10.51573/Andes.PPS39.SS.PSDGUN.1

Regarding the keyword 'covid-19' (Figure 4[3]), it is established that the COVID-19 pandemic contributed to plastic pollution [16-18]. Due to the restrictions imposed, the number packaging waste generated at home has increased as a result of internet or app purchases and deliveries. However, the lockdown impacted the recycling sector and waste management systems as a whole [19,20]. At the same time, using personal protective equipment, particularly face masks, was essential, and their improper disposal contributed to increased plastic pollution. Literature confirmed the release of MP from face masks [21,22]. MP pollution directly or indirectly affects at least 12 SDGs [23]. Although the literature proposes solutions to the residues generated during the COVID-19 pandemic [24-26], overall, it has negatively and significantly impacted progress towards achieving the SDGs.

Conclusion

In this study, a bibliometric analysis and mapping of the data retrieved from a Scopus search was conducted on the role of plastic in achieving the UN SDGs. The main trends are the circular economy and life cycle assessment. The directions are applications, life cycle assessment, plastic pollution, biomass, geopolymers, circular economy, and biopolymers. Plastic recycling is essential for the circular economy of plastic; however, literature has demonstrated a gap in recycled plastic applications. These observations are crucial for mitigating the socio-environmental issues that plastics may cause and are a significant ally in achieving the UN SDGs. These results not only contribute to current understanding but also inspire and guide future research efforts on the role of plastics in achieving the UN SDGs.

References

1. "#Envision2030: 17 goals to transform the world for persons with disabilities" [Online]. Available: https://www.un.org/development/desa/disabilities/envision2030.html.
2. F. D. B. de Sousa, "Plastics: Sustainable development goals and circular solutions," in *The circular economy: Meeting sustainable development goals*, S. K. Ghosh and G. Eduljee, Eds. London: The Royal Society of Chemistry, 2023, pp. 165-179.
3. F. D. B. de Sousa, "The role of plastic concerning the sustainable development goals: The literature point of view," *Cleaner and Responsible Consumption*, vol. 3, p. 100020, 2021.
4. F. D. B. de Sousa, "Plastic effects on marine and freshwater environments," *Water Biology and Security*, p. 100228, 2023.
5. E. Maaskant, W. Post, M. T. Brouwer, D. S. van Es, and E. U. Thoden van Velzen, "Strategic selection tool for thermoplastic materials in a renewable circular economy: Identifying future circular polymers," *Sustainable Production and Consumption*, vol. 38, pp. 174-185, 2023.
6. M. Mocan and S. B. Uncu, "Structure-property relationship in edible pectin-alginate/orange peel biocomposite films," *Green Materials*, 2023.

DOI: https://doi.org/10.51573/Andes.PPS39.SS.PSDGUN.1

7. R. Salas, M. Ruiz, and M. Felix, "Revalorisation of a residue from the maize-snack industry through the development of bio-based materials. Effect of the plasticiser," *Journal of Food Engineering*, vol. 370, p. 111964, 2024.

8. T. Vialon et al., "Upcycling polyolefin blends into high-performance materials by exploiting azidotriazine chemistry using reactive extrusion," *Journal of American Chemical Society*, vol. 146, no. 4, pp. 2673-2684, 2024.

9. M. G. Faga et al., "Ethylene-Vinyl Acetate (EVA) Containing Waste Hemp-Derived Biochar Fibers: Mechanical, Electrical, Thermal and Tribological Behavior," *Polymers (Basel).*, vol. 14, no. 19, 2022.

10. J. von Freeden, B. Rodenwaldt, and D. Nebel, "Investigation of the influence of multiple thermoforming processes on the properties of continuous fiber-reinforced thermoplastics to enable structural reuse," *SN Applied Sciences*, vol. 5, no. 2, 2023.

11. F. Stojcevski et al., "Inverse Vulcanisation of canola oil as a route to recyclable chopped carbon fibre composites," *Sustainable Materials and Technologies*, vol. 32, 2022.

12. X. Colom, J. Cañavate, and F. Carrillo-Navarrete, "Towards circular economy by the valorization of different waste subproducts through their incorporation in composite materials: Ground tire rubber and chicken feathers," *Polymers*, vol. 14, no. 6, 2022.

13. P. Sintharm, A. Nimpaiboon, Y.-C. Liao, and M. Phisalaphong, "Bacterial cellulose reinforced with skim/fresh natural rubber latex for improved mechanical, chemical and dielectric properties," *Cellulose*, vol. 29, no. 3, pp. 1739-1758, 2022.

14. P. Sintharm and M. Phisalaphong, "Green natural rubber composites reinforced with black/white rice husk ashes: Effects of reinforcing agent on film's mechanical and dielectric properties," *Polymers (Basel).*, vol. 13, no. 6, 2021.

15. H. T. Nguyen, K. Crittenden, L. Weiss, and H. Bardaweel, "Recycle of waste tire rubber in a 3D printed composite with enhanced damping properties," *Journal of Cleaner Production*, vol. 368, 2022.

16. F. D. B. de Sousa, "Pros and cons of plastic during the COVID-19 pandemic," *Recycling*, vol. 5, no. 4, p. 27, 2020.

17. F. D. B. de Sousa, "Plastic and its consequences during the COVID-19 pandemic," *Environmental Science and Pollution Research 2021*, pp. 1–12, Jul. 2021.

18. N. Parashar and S. Hait, "Plastics in the time of COVID-19 pandemic: Protector or polluter?," *Science of the Total Environment*, vol. 759. Elsevier, p. 144274, 2021.

19. W. L. Filho *et al.*, "COVID-19 and waste production in households: A trend analysis," *Science of the Total Environment*, vol. 777, p. 145997, 2021.

20. D. Hantoko, X. Li, A. Pariatamby, K. Yoshikawa, M. Horttanainen, and M. Yan, "Challenges and practices on waste management and disposal during COVID-19 pandemic," *Journal of Environmental Management*, vol. 286, p. 112140, 2021.

21. F. Saliu, M. Veronelli, C. Raguso, D. Barana, P. Galli, and M. Lasagni, "The release process of microfibers: from surgical face masks into the marine environment," *Environmental Advances*, vol. 4, p. 100042, 2021.

22. O. O. Fadare and E. D. Okoffo, "Covid-19 face masks: A potential source of microplastic fibers in the environment," *Science of the Total Environment*, vol. 737, p. 140279, 2020.

23. T. R. Walker, "(Micro)plastics and the UN Sustainable Development Goals," *Current Opinion in Green and Sustainable Chemistry*, vol. 30, p. 100497, 2021.

24. C. Crespo, G. Ibarz, C. Sáenz, P. Gonzalez, and S. Roche, "Study of recycling potential of FFP2 face masks and characterization of the plastic mix-material obtained. A way of reducing waste in times of Covid-19," *Waste and Biomass Valorization*, vol. 12, no. 12, pp. 6423-6432, 2021.

25. O. Zabihi et al., "Mechanical upcycling of single-use face mask waste into high-performance composites: An ecofriendly approach with cost-benefit analysis," *Science of the Total Environment*, vol. 919, 2024.

26. Q. L. Aung, W. S. Chow, Y. P. Yong, and C. N. Lam, "Nanokaolin reinforced carboxylated nitrile butadiene rubber/polyurethane blend-based latex with enhanced tensile properties and chemical resistance," *Progress in Rubber, Plastics and Recycling Technology*, vol. 39, no. 3, pp. 281-293, 2023.

DOI: https://doi.org/10.51573/Andes.PPS39.SS.PSDGUN.1